

T2K Replica Target Hadron Production Measurements in NA61/SHINE and T2K Neutrino Flux Predictions

THÈSE

présentée à la Faculté des Sciences de l'Université de Genève
pour obtenir le grade de Docteur ès sciences, mention physique

par

Alexis Häsler

de Gsteigwiler (BE)

Thèse N° 4803

Cette thèse donne lieu à une publication à paraître sous le titre:
*Measurements of π^\pm yields from the surface of the T2K replica target
for incoming 31 GeV/c protons with the NA61/SHINE spectrometer at the CERN SPS*



UNIVERSITÉ
DE GENÈVE

FACULTÉ DES SCIENCES

**Doctorat ès sciences
Mention physique**

Thèse de **Monsieur Alexis HÄSLER**

intitulée :

**"T2K Replica Target Hadron Production Measurements in
NA61/SHINE and T2K Neutrino Flux Predictions"**

La Faculté des sciences, sur le préavis de Monsieur A. BLONDEL, professeur ordinaire et directeur de thèse (Département de physique nucléaire et corpusculaire), Monsieur A. BRAVAR, docteur (Département de physique nucléaire et corpusculaire), Monsieur X. WU, professeur associé (Département de physique nucléaire et corpusculaire), Monsieur M. GAZDZICKI, professeur (Institut für Kernphysik, Johann-Wolfgang-Goethe-Universität, Frankfurt am Main, Deutschland), Monsieur M. HARTZ, professeur (Kavli Institute for the Physics and Mathematics of the Universe, University of Tokyo, Kashiwa, Japan) et Monsieur B. POPOV, docteur (Laboratoire de Physique Nucléaire et Hautes Energies, Université Paris Diderot, Paris VI et VII, Paris, France), autorise l'impression de la présente thèse, sans exprimer d'opinion sur les propositions qui y sont énoncées.

Genève, le 22 juin 2015

Thèse - 4803 -

Le Décanat

N.B. - La thèse doit porter la déclaration précédente et remplir les conditions énumérées dans les "Informations relatives aux thèses de doctorat à l'Université de Genève".

Abstract

Accelerator based neutrino experiments generate their neutrino beams by impinging high energy protons on thick targets. The neutrino beam predictions are thus based on modeling the interactions of the beam protons inside the targets. Different hadronic models can be used with different accuracies depending on the energy range of the incident protons and on the target material. Nevertheless, none of the models can be seen as perfectly describing all different interactions. In order to reach high precision neutrino flux predictions, it is thus mandatory to be able to test and constrain the models with hadron production measurements.

The T2K experiment in Japan uses the ancillary NA61/SHINE facility at CERN to constrain the production of hadrons resulting from the interactions of proton beam particles impinging on a 90cm long graphite target. Data taken by NA61/SHINE with a 30 GeV proton beam on a thin (4% interaction length) graphite target have been recorded in 2007 and 2009. They have been analysed and extensively used by T2K. These data allow to constrain up to 60% of the neutrino flux at the beam peak energy. The remaining 40% are generated by re-interactions of secondary particles within the target or with the material surrounding the target. These re-interactions cannot be directly constrained with the p+C at 30 GeV thin target measurements. By measuring the production of hadrons off a replica of the T2K target, up to 90% of the neutrino flux can be constrained.

In 2007, the NA61/SHINE took a first pilot run with a replica of the T2K target. These data were analyzed and demonstrated the feasibility of such measurements. This first pilot run did not give a large enough statistical dataset to allow for a reduction in the uncertainty regarding the neutrino flux prediction. In 2009 and 2010, two larger data sets were recorded. In this thesis, the analysis of the 2009 data set is presented. Pion multiplicities at the surface of the target are extracted and systematic uncertainties are computed. The results are given in bins of momentum p , polar angle θ and longitudinal position z at the surface of the target. The uncertainties on these results are typically of the order of 7% for the statistical component and between 4% and 10% for the systematic component.

A procedure based on some of the work developed within T2K is presented in order to compare the thin target and T2K replica target results of NA61/SHINE. This procedure consists of re-weighting each modeled interactions in the 90cm long target with the NA61/SHINE thin target measurements. The re-weighted pion multiplicities at the surface of the target can then be directly compared to the T2K replica target analysis results. Finally, the neutrino flux predictions are constrained by using the 2009 T2K replica target data and the uncertainties on this data set are propagated to the neutrino flux predictions.

The 2010 data set will allow to reach ultimate precision with respect to hadron production off the T2K replica target. As a result of higher recorded statistical datasets, kaon multiplicities at the surface of the target could also be extracted.

All future projects proposing long baseline neutrino experiments mention the need for high precision hadron production measurements in order to reach their physics goals. This opens new perspectives for NA61/SHINE. Its neutrino physics program will certainly remain of interest for the neutrino physics community.

Résumé

Les expériences de physique des neutrinos basées sur les accélérateurs produisent leurs flux de neutrinos en faisant interagir un intense faisceau de protons sur une épaisse cible. Les prédictions des flux de neutrinos sont donc basées sur la modélisation des interactions des protons avec la cible. Différents modèles hadroniques peuvent être utilisés afin de décrire, au mieux, en fonction de l'énergie spécifiques des protons incidents, le faisceau à simuler. Néanmoins, aucun modèle ne peut, avec précision, prédire toutes les interactions différentes engendrées par un proton à l'intérieur de la cible. Pour atteindre un haut degré de précision sur la simulation des flux de neutrinos, il est donc nécessaire de tester et contraindre les modèles avec des mesures de production de hadron.

L'expérience T2K au Japon utilise les mesures effectuées par NA61/SHINE au CERN pour contraindre la production de hadron créés par l'interaction d'un faisceau de proton sur une cible de carbone de 90 cm de long et 1.3 cm de diamètre. Les données prises en 2007 et 2009 par NA61/SHINE avec un faisceau de protons de 30 GeV bombardant une fine cible (4% de la longueur d'interaction) de carbone ont déjà été analysées et sont largement utilisées par T2K. Ces données permettent de contraindre 60% du flux de neutrino au pique d'énergie du faisceau. Les 40% restant proviennent de re-interactions, soit à l'intérieur de la cible elle-même, soit dans les matériaux entourant la cible. Ces re-interactions ne peuvent pas directement être contraintes par les mesures effectuées avec les protons à 30 GeV sur la cible fine. Par contre, en mesurant la production de hadrons sortant de la surface de la cible de T2K, toutes les re-interactions sont alors incluses dans les mesures. Jusqu'à 90% du flux de neutrino peut ainsi être contraint avec ces mesures.

En 2007, une première série de données a été enregistrée avec un faisceau de proton de 30 GeV bombardant une réplique de la cible de T2K. Ces données ont été analysées et ont permis de prouver la faisabilité de telles mesures. Le nombre d'événements enregistrés était cependant relativement faible et l'incertitude de ces mesures n'a pas malheureusement permis de contraindre le flux de neutrino de T2K de manière plus précise que ce qui n'avait déjà été fait auparavant avec les données de la cible fine. En 2009 et 2010, deux nouveaux sets de données ont été enregistrés avec une réplique de la cible de T2K. Cette thèse présente l'analyse des données prises en 2009. Les multiplicités des pions à la surface de la cible sont extraites et les erreurs systématiques sur ces mesures sont estimées. Les résultats sont présentés en bins d'impulsion p , d'angle polaire θ et de position longitudinal de sortie de la cible z . Les incertitudes statistiques sont typiquement de l'ordre de 7% alors que l'ensemble des erreurs systématiques se situent entre 4% et 10%.

Une procédure basée sur un travail accompli par la collaboration de T2K est présentée dans le but de comparer les mesures prises par NA61/SHINE avec la cible fine de celles prises avec la réplique de la cible de T2K. Cette procédure repose sur la repondération, avec les résultats de la cible fine, de chacune des interactions ayant été préalablement simulées tout au long des 90 cm de la cible. Les multiplicités de pions ainsi repondérées peuvent alors directement être comparées aux mesures effectuées avec la réplique de la cible de T2K.

Finalement, les résultats de l'analyse de la réplique de la cible de T2K sont implémentés dans la prédiction des flux de neutrinos de T2K. Les incertitudes sur ces résultats sont propagées afin d'évaluer une erreur systématique sur les flux de neutrinos.

Les données 2010, avec leur large nombre d'événements enregistrés, permettront d'atteindre l'ultime degré de précision sur la production de hadron sortant de la réplique de la cible de T2K. Non seulement les spectres de pions pourront être extraits de ces données, mais également

les spectres de kaons, qui, eux aussi, jouent un rôle important dans la production de flux de neutrinos.

Tous les projets de physique des neutrinos basés sur des accélérateurs soulignent l'importance de la connaissance de production de hadron. Ceci assure à l'expérience NA61/SHINE au CERN de continuer à jouer un rôle de premier plan dans ce domaine pour la physique des neutrinos.

Remerciements

During the years I spent at the DPNC for my PhD thesis, I always had lots of pleasure to meet and discuss with my group colleagues. I would like to specially and sincerely thank Prof Alain Blondel, my thesis supervisor. He always gave me a lot of freedom in my work, but never forgot to ask precise questions that would push me in the right direction for my research and the development of my thesis. We had many interesting discussions, and not only about physics, but also about adventure and mountaineering, a passion we certainly have in common. A very special thanks goes to Alexander Korzenev for his always very pertinent advices and all the cross checks and corrections he did on my work during my PhD. Thank you very much to Alessandro Bravar with whom it has always been a great pleasure to discuss about the different analysis strategies in NA61/SHINE but also more widely about neutrino physics. Thanks to Nicolas Abgrall who spent lots of his time teaching me the basics of the different softwares of the NA61/SHINE and T2K. He also introduced me to the analysis techniques and showed me the important steps to follow. Many thanks to all my colleagues from the neutrino group: Melody, Leïla, Antoaneta, Fanny, Sébastien, Mark, Enrico, Jordan, Etam and François. It was particularly enriching to discuss about everyone's projects, allowing me to discover many different topics.

Thank you to Boris Popov from LPNHE for his very good and relevant advices and for having always followed carefully all my presentations over the different meetings. Thank you to Laura Zambelli from LPNHE who shared with me her knowledge of simulation softwares and provided me many useful technical tricks that saved me certainly lots of time. Thank you to Dimitar Kolev from Sofia University, whose work helped me to cross check my own results and gave me confidence in the analysis I was conducting.

Many thanks to the Professors Marek Gazdzicki, Mark Hartz and Xin Wu for having accepted to be part of the jury of this thesis. To me, it is a very important and appreciated recognition of the work I have tried to deliver.

Thanks to Catherine Blanchard, who always knows how to transform the complicated administrative tasks into an easy and straight forward job.

Thank you to David Haesler for the time invested in reading and correcting the grammar of important parts of this thesis.

Finally, I would like to thank my family for always supporting me in all my different projects, this thesis being one of them.

Contents

1	Introduction to Neutrino Physics	1
1.1	Historical Introduction	1
1.2	Neutrinos in the Standard Model	2
1.3	Neutrino Masses	7
1.3.1	Dirac Mass Term	7
1.3.2	Majorana Mass Term	9
1.3.3	Dirac+Majorana Mass Term	11
1.4	Accelerator based neutrino experiments	12
1.4.1	Neutrino beams and hadron production measurements	14
1.4.2	Present knowledge and future goals of oscillation experiments	20
1.4.3	Present knowledge and future goals of cross-section experiments	23
2	The T2K experiment	29
2.1	The experimental setup	30
2.1.1	The SK far detector	31
2.1.2	The beam line	35
2.1.3	The ND280 near detector complex	40
2.2	The importance of an accurate neutrino flux predictions	47
2.3	The neutrino flux simulation	48
2.3.1	Primary proton beam	49
2.3.2	Sources of neutrino production	51
2.3.3	Re-weighting of the hadron production	58
2.3.4	Uncertainties on the neutrino flux predictions	65
3	The NA61/SHINE Experiment	79
3.1	Data sets for the T2K neutrino physics program	79
3.1.1	Data taking periods	79
3.1.2	Thin target results	81
3.2	The experimental setup	86
3.2.1	Beam line and triggers	88
3.2.2	Data calibration, reconstruction and simulation	90
3.2.3	The Time Projection Chambers	91
3.2.4	The Forward Time Of Flight	93
3.3	Monte-Carlo simulations	95
3.3.1	Specific Monte-Carlo productions for the T2K replica target	95
3.3.2	Flat phase-space simulations	96

4 The T2K Replica Target Analysis	97
4.1 Incident proton beam	97
4.2 Determination of intersection point of track on target surface	100
4.3 Target alignment and target position	101
4.3.1 Target alignment	101
4.3.2 Target position	101
4.4 Combined ToF-dE/dx analysis	105
4.4.1 Track selection	105
4.4.2 Analysis binning	108
4.4.3 Geometrical acceptance	108
4.4.4 Particle identification	109
4.4.5 Monte-Carlo corrections	116
4.5 Systematic uncertainties	117
4.6 Results	123
4.7 Comparisons of thin target and T2K replica target results using the T2K hadron production re-weighting procedure	132
5 Implementation of the T2K Replica Target Results in the T2K Neutrino Flux Prediction	143
5.1 Calculation of neutrino flux using T2K Replica Target Results	144
5.2 Flux systematics using T2K replica target data	148
5.3 Proton Beam Profiles	151
6 Conclusion	165
A Pion correction factors	169
B T2K replica target weights	175
C Comparisons of pions spectra at the surface of the target for different beam profiles	181
D Numerical Tables	195

List of Figures

1.1	Elementary particles of the Standard Model	3
1.2	Measurements of the hadron production cross-section around the Z resonance. The curves indicate the predicted cross-section for two, three and four neutrino species with SM couplings and negligible mass (from Ref. [18]).	4
1.3	Higgs potential as given by eq. (1.3) for $\mu^2 > 0$ (left) and $\mu^2 < 0$ (right)	4
1.4	Typical event in the BEBC experiment interpreted as the production of a charmed particle in a neutrino nucleus interaction and the subsequent decay of this particle. [27].	13
1.5	Typical components of a neutrino beam line. Example taken from the T2K experiment	15
1.6	Percent difference between the best-fit prediction of the parameterization proposed in Ref. [38] and experimental data for pions (left) and kaons (right) as a function of x_R [38].	16
1.7	Comparison between the proposed parameterization of NA56/SPY and NA20 data (dotted line) and the one-pion (left) and one-kaon (right) inclusive invariant cross-sections in pBe interactions at 24 GeV as measured by Eichten et al. [38].	17
1.8	Comparison between the proposed parameterization of NA56/SPY and NA20 data (line) and the one-pion inclusive invariant cross-section in $p + C$ interactions at 100 GeV as measured by Barton et al. Positive (negative) pions are shown in the left (right) panel [38].	18
1.9	Yields of π^+ [42] (left) and ratios of data points to the GEANT4-based MC [43] (right) as a function of p_z in bins of p_T . Different colors and markers represent bins of p_T , and the yields are scaled and the ratios offset such that the points in different p_T bins do not overlap. Both statistical and systematic error bars are plotted.	20
1.10	The expected $\Delta\chi^2$ significance to resolve $\sin\delta_{CP} \neq 0$ as a function of δ_{CP} for various values of $\sin^2\theta_{23}$ in case of normal (left) and inverted (right) mass hierarchy. The T2K statistical and systematic uncertainties are included. A constraint based on the reactor measurements is used.	21
1.11	The expected $\Delta\chi^2$ significance to resolve $\sin\delta_{CP} \neq 0$ as a function of CP for T2K(red), NO ν A (blue), and T2K+NO ν A (black) with(dashed) and without (solid) systematics for 'true' values $\sin^2\theta_{23} = 0.5$. The 'true' MH is the NH (top) or the IH (bottom) while the test MH is unconstrained	22
1.12	The expected $\Delta\chi^2$ significance to determine MH as a function of CP for T2K(red), NO ν A (blue), and T2K+NO ν A (black) with(dashed) and without (solid) systematics for 'true' values $\sin^2\theta_{23} = 0.5$. The 'true' MH is the NH (top) or the IH (bottom) while the test MH is constrained to the opposite MH.	23

1.13 Total ν_e CC inclusive cross-section. The T2K data point is placed at the ν_e flux mean energy. The vertical error represents the total uncertainty, and the horizontal bar represents 68% of the flux each side of the mean. The T2K flux distribution is shown in grey. The NEUT and GENIE predictions are the total ν_e CC inclusive predictions as a function of neutrino energy. The NEUT and GENIE averages are the flux-averaged predictions. The Gargamelle data is taken from Ref. [46].	24
1.14 Neutrino and antineutrino cross-sections as a function of energy [46].	25
1.15 Total neutrino and antineutrino per nucleon CC cross-sections (for an isoscalar target) divided by neutrino energy and plotted as a function of energy. Also shown are the various contributing processes. These contributions include quasi-elastic scattering (dashed), resonance production (dot-dash), and deep inelastic scattering (dotted). Example predictions for each are provided by the NUANCE generator [48]. Note that the quasi-elastic scattering data and predictions have been averaged over neutron and proton targets and hence have been divided by a factor of two for the purposes of this plot [47].	26
1.16 Diagram representations for the different processes of neutrino-nucleus scattering	26
1.17 Schematic of the $2p2h$ process, where two nucleons are involved along with the neutrino interaction	27
2.1 The T2K experiment layout [52].	30
2.2 Energy of the emitted neutrino in the pion decay as a function of the parent pion energy for different angle between the parent pion and neutrino directions.	31
2.3 Muon neutrino survival probability at Super Kamiokande and the neutrino fluxes for different off-axis angles [60].	32
2.4 Layout of the Super-Kamiokande detector. The inner and outer detectors are marked. A support structure optically separates them and holds the PMTs [52].	32
2.5 Example of reconstructed events in Super Kamiokande. A muon like ring (top left) and electron like ring (top right) [52]. The muons are less sensitive to multiple scattering and give a sharper ring than the electrons. A multiple ring event (bottom) [70] is a typical candidate for a π^0 event. If the two rings are not well separated or one of the two rings is not reconstructed, it can fake a electron like event. Fully contained events draw a ring on the detector walls.	34
2.6 Accumulated number of protons on target versus time and related beam power. .	35
2.7 Overview of the neutrino beam line with the two sections: the primary and the secondary beam line [60]	36
2.8 Schematic layout of the primary beam line monitor in the final focusing section [60]	36
2.9 Side view of the secondary beam line [60].	37
2.10 Drawing of the target inserted inside the first horn.	38
2.11 The predicted flux of ν_μ at the SK far detector for operation at different horn currents. The flux histogram (top) ranges from 0 to 3 GeV, while the ratios (bottom) range from 0 to 10 GeV [60].	39
2.12 Layout of the off-axis detectors of ND280 embedded in the UA1 magnet [52] . .	41
2.13 INGRID on-axis detector	41
2.14 Example of Neutrino beam profiles for x (left) and y (right) directions as measured by INGRID [60].	41
2.15 Neutrino events per 10^{14} POT measured by INGRID (points) overlaid with mean value (dashed lines). The error bar represents the statistical error on INGRID measurement [60].	41

2.16	Technical drawing of the TPC design. The outer dimensions are apporximately $2.3m \times 2.4m \times 1.0m$ [75].	43
2.17	A schematic of the pi-zero detector. The beam is coming from the left and going right. Insets show details of the Water Target super-P0Dule layers and Central ECal layers [76].	43
2.18	Momentum resolution for a single TPC is shown as a function of momentum perpendicular to the magnetic field as predicted by the Monte Carlo simulation of muons generated with the standard neutrino event generator of T2K. The dashed lines represents the momentum resolution goal.	44
2.19	Distribution of the energy loss as a function of the momentum for negatively charged particles produced in neutrino interactions, compared to the expected curves for muons, electrons, protons, and pions.	44
2.20	The discrimination between track-like (muon-like) and shower-like (electron-like) samples in the barrel-ECal (left) and in the Ds-ECal (right). Solid lines show Monte Carlo information and points show data [78].	45
2.21	SMRD counter sliced view with the start of the serpentine route for the wavelength shifting fiber [79].	46
2.22	Time resolution of a SMRD counter versus light yield. The data are recorded in response to cosmic muons penetrating the center of the scintillator slab [79].	46
2.23	Far-to-near flux ratio for the ν_μ flux as a function of the neutrino energy	47
2.24	ν_μ (left) and ν_e (right) flux predictions at SK for GCALOR (black), GFLUKA (purple), GHEISHA (blue) [80].	48
2.25	Far to near flux ratio for ν_μ (left) and ν_e (right) for GCALOR (black), GFLUKA (purple), GHEISHA (blue) [80].	48
2.26	Two dimensional view of the geometrical set-up in the FLUKA simulation of the baffle and the target [60].	51
2.27	Energy spectra for ν_μ (black), $\bar{\nu}_\mu$ (red), ν_e (blue) and $\bar{\nu}_e$ (purple) at the ND280 near detector (left) and at the far detector (right) [80].	52
2.28	Contributions of neutrino parent particles	53
2.29	Position in the XZ plane of the production of the neutrino parent particles. Points in red correspond to parent particles produced inside the target or during the decay chain of a particle produced in the target. Blue points correspond to parent particles produced by re-interactions in the material of the beam line [80].	53
2.30	Ratios of neutrino flux related only to neutrinos having parent particles produced in re-interactions outside the target over total neutrino flux for ν_μ (top left), $\bar{\nu}_\mu$ (top right), ν_e (bottom left), $\bar{\nu}_e$ (bottom right) at SK [80].	54
2.31	Schematic of the interactions in the target. The pion is labeled as secondary hadrons as it is a product of the interaction of the primary beam proton, the kaon is labeled as tertiary hadron as it has been produced in re-interaction.	55
2.32	Ratio of tertiary to total contribution for ν_μ top left, $\bar{\nu}_\mu$ top right, ν_e bottom left, $\bar{\nu}_e$ bottom right neutrino fluxes at SK [80].	56
2.33	Schematic of the placement of the particles along the target surface for the study of the effect of the longitudinal binning on the neutrino flux predictions	57
2.34	Effect of different number of bins along the target surface. The black curve shows the nominal neutrino flux prediction by placing precisely the particles at the exact exit position. Other curves show binning with 1 to 5 bins.	58
2.35	Stacked histograms showing the contribution of each different longitudinal bin to the muon neutrino flux at SK.	59

2.36 Differential cross-section as a function of momentum transfer $ t $ from Bellettini [83]. The low $ t $ region corresponds to the elastic interactions while the higher $ t $ region is interpreted as the quasi-elastic interactions.	60
2.37 Phase space of π^\pm , K^\pm and K_s^0 that contribute to the neutrino flux at SK with the NA61/SHINE analysis phase space for each particle species overlaid on top.	62
2.38 The meson multiplicity weights from NA61/SHINE data over FLUKA 2011. Outside the NA61/SHINE analysis phase-space, the weights are computed with respect to the BMPT fits to the NA61/SHINE data.	70
2.39 This figure shows the phase space covered by the different data sets and the FLUKA secondary proton distribution. The colored background is the FLUKA MC, rectangles are the NA61/SHINE bins, green triangles are the Eichten data and pink stars are the Allaby data. The Allaby and Eichten data were scaled according to the x_F scaling procedure in order to plot the data with the T2K beam energy. Lines of constant x_F are drawn, which are used as various cuts in the analysis.	71
2.40 Secondary baryon weights for FLUKA MC are shown. These are the weights used to calculate the nominal neutrino flux in this flux release. The fading effect seen in the neutrons, Λ s and Σ s is a result of only tuning the leading baryons in these regions.	72
2.41 Comparisons of σ_{prod} measurements and the values used in the simulation (solid line for FLUKA and dashed line for GCALOR), for incident protons (top left) and charged pions (top right), K^+ (bottom left) and K^- (bottom right).	73
2.42 Ratio of the hadron interaction re-weighted flux over the nominal flux for ν_μ (black), $\bar{\nu}_\mu$ (red), ν_e (blue), $\bar{\nu}_e$ (magenta) at SK	73
2.43 Meson multiplicity tuning uncertainties for SK fluxes in positive focussing horn mode operation; top left ν_μ , top right $\bar{\nu}_\mu$, bottom left ν_e and bottom right $\bar{\nu}_e$. The 13av1 labeled uncertainty is the current version of the estimated flux uncertainties in T2K as of summer 2015. It uses the latest preliminary results of NA61/SHINE thin target dataset recorded in 2009. The 11bv3.2 labeled uncertainty is the previous version of the estimated flux uncertainties that used the NA61/SHINE 2007 thin target data in the tuning.	74
2.44 Relative effect of the baryon production tuning at SK for the ν_μ (top left), $\nu_{\bar{\mu}}$ (top right), ν_e (bottom left), $\nu_{\bar{e}}$ (bottom right) fluxes in positive focusing horn mode operation. The relative uncertainties are shown along with effect.	74
2.45 Different ranges considered for the production cross-section following the available data set from table 2.5.	75
2.46 The hadron interaction model uncertainties evaluated for the different ND280 fluxes; top left ν_μ , top right $\bar{\nu}_\mu$, bottom left ν_e and bottom right $\bar{\nu}_e$. The 13av1 labeled uncertainty is the current version of the estimated flux uncertainties in T2K as of summer 2015. It uses the latest preliminary results of NA61/SHINE thin target dataset recorded in 2009. The 11bv3.2 labeled uncertainty is the previous version of the estimated flux uncertainties that used the NA61/SHINE 2007 thin target data in the tuning.	76

2.47 The hadron interaction model uncertainties evaluated for the different SK fluxes; top left ν_μ , top right $\bar{\nu}_\mu$, bottom left ν_e and bottom right $\bar{\nu}_e$. The 13av1 labeled uncertainty is the current version of the estimated flux uncertainties in T2K as of summer 2015. It uses the latest preliminary results of NA61/SHINE thin target dataset recorded in 2009. The 11bv3.2 labeled uncertainty is the previous version of the estimated flux uncertainties that used the NA61/SHINE 2007 thin target data in the tuning.	77
2.48 An example of the fractional change of SK ν_μ flux when the beam center position (Y) and center angle (θ_Y) measured in Run 1 are changed by 1σ , i.e. set to 1.42 mm and 0.29 mrad, respectively [60].	77
2.49 The total uncertainties evaluated for the SK flux predictions and the ND280 flux predictions. The 13av1 uncertainty is the current version. The 11bv3.2 is the previous version.	78
3.1 Photo of the T2K replica target mounted at NA61/SHINE. The aluminium flanges can be seen at the upstream part of the target (left).	80
3.2 Production cross-section for the 2007 and 2009 data sets. Results from other experiments taken from Ref. [83, 88, 91] are shown for comparisons.	81
3.3 Multiplicities for positively charged pions (left) and negatively charged pions (right). Results are the weighted average of the 2007 and 2009 data sets.	82
3.4 Multiplicities for positively charged kaons (left) and negatively charged kaons (right). Results for positively charged kaons are the weighted average of the 2007 and 2009 data sets. Results for negatively charged kaons have only been extracted for the 2009 data set.	83
3.5 Multiplicities for protons. Results are the weighted average of the 2007 and 2009 data sets.	84
3.6 Schematic view of the vertical plane of the H2 beamline in the configuration used for the ion fragment separation. The dimensions are not to scale, e.g. the beamline is more than 600 m long, the height difference between T2 and the EHN1 is about 12 m, the aperture of the quadrupoles is ± 45 mm [103].	86
3.7 NA61/SHINE experimental set-up seen from above. The beam is coming from the left, impinging on the T2K replica target shown in this figure.	87
3.8 Schematic layout (horizontal cut in the beam plane, not to scale) of the beam detectors in two configurations of the beam line. a) for the thin target measurements where the S4 counter plays the role of interaction counter; b) for the T2K replica target measurements where the S3 counter insures that the proton beam hit the target upstream face.	89
3.9 Counts of hadrons per incident beam particle from the CEDAR counter as a function of the gas pressure within the pressure range which covers maxima of pions, kaons and protons at 13 (left), 31 (middle) and 158 GeV/c (right) [103].	89
3.10 Momentum resolution as a function of the measured momentum for the 2009 T2K replica target data set. The forward going tracks going through GTPC MTPC show a lower resolution than those having a stronger bending.	92
3.11 Specific energy losses in the TPCs for positively (left) and negatively (right) charged particles as a function of momentum. Data taken from the 2009 T2K replica target data set.	93
3.12 Resolution of the energy loss as a function of the number of measured points along the track.	93
3.13 Schematic layout of scintillators in the ToF-F detector.	94

3.14	Mass squared versus momentum as measured by the ToF-F	95
3.15	Distribution of the difference between a particle's time of flight measured independently by the overlapping scintillator bars of the ToF-F detector. The width of the distribution is about 155 ps, indicating a <i>tof</i> resolution of about 110 ps for a single measurement.	95
4.1	Schematic layout (horizontal cut in the beam plane, not to scale) of the beam detectors for the T2K replica target configuration.	97
4.2	Distributions for the <i>x</i> (left) and <i>y</i> (right) coordinates of the chi-square for the fitted proton beam track in the BPDs.	98
4.3	Distributions of the residuals at BPD3 for the <i>x</i> (left) and <i>y</i> (right) coordinates.	99
4.4	Distributions under T2 (left) and T3 (right) triggers of the proton beam profile at the <i>z</i> position of the target upstream face.	99
4.5	Example of tracks to determine the point of closest approach.	101
4.6	<i>x</i> (left) and <i>y</i> (right) positions for each 17 slices of the center of the 1.3cm radius circle at which the number of tracks within the circle is maximized.	102
4.7	A transverse misalignment between the beam particles and the tracks extrapolated backward from the TPCs is translated into a longitudinal shift of the vertex distributions when comparing the two sets of tracks composed of positive RST and negative WST with positive WST and negative RST	103
4.8	Distribution of the vertexes between the beam tracks and the reconstructed tracks in the TPCs along the <i>z</i> axis for the Monte-Carlo simulation.	104
4.9	Distribution of the vertexes between the beam tracks and the reconstructed tracks in the TPCs along the <i>z</i> axis for the data.	105
4.10	Layout of the NA61/SHINE detector showing the azimuthal coverage. The track shows the example of a positive pion of 3 GeV/c with a polar angle of 60 mrad and an azimuthal angle of 30 degrees.	107
4.11	Distribution of the azimuthal angle ϕ of the tracks at the surface of the target. On the left for $40 < \theta < 60$ mrad and on the right for $100 < \theta < 140$ mrad.	107
4.12	Sketch of the longitudinal binning of the target.	108
4.13	Analysis binning overlaid on the (p, θ) distributions of the pion parent particles exiting the target surface and producing ν_μ at SK.	109
4.14	Representation of Wrong Side Track (WST) in red and Right Side Track (RST) in blue.	110
4.15	Right side tracks acceptance maps for the different longitudinal bins <i>z</i> in the (p, θ) phase-space. The acceptance is defined as the fraction of tracks that passes the analysis cuts.	110
4.16	Wrong side tracks acceptance maps for the different longitudinal bins <i>z</i> in the (p, θ) phase-space. The acceptance is defined as the fraction of tracks that passes the analysis cuts.	111
4.17	Example of a two-dimensional $m^2 - dE/dx$ distribution for positively charged particles in the second longitudinal bin <i>z2</i> in the polar angle interval $60 < \theta < 80$ mrad and momentum $2.27 < p < 2.88$ GeV/c.	111
4.18	Parameterization of the dE/dx resolution for pion-like particles used for the initialization of the two-dimensional fits	113
4.19	Bethe-Bloch curves for the different particle species. Theoretically, they should all fall on the same curve. Some small differences can be seen at low $\beta\gamma$	113
4.20	The dE/dx distributions as a function of momentum for positive particles (left) and negative particles (right) with the Bethe-Bloch curves superimposed.	114

4.21	Mass squared distribution and resolution as functions of momentum.	114
4.22	Two dimensional histogram with contour plot showing the fit result for the second longitudinal bin $z2$ in the polar angle bin $60 < \theta < 80$ mrad and momentum $2.27 < p < 2.88$ GeV/c (top). The different particle species are well separated in different “islands”. Bottom plots show the projection on the m^2 (left) and dE/dx (right) axes.	115
4.23	Correction factors for positively charged pions, in the polar angle range from 60 to 80 mrad, and for the six longitudinal bins as a function of momentum.	117
4.24	Components of the systematic uncertainties for positively charged pions, in the polar angle range from 0 to 140 mrad, and for the six longitudinal bins as a function of momentum.	119
4.25	Components of the systematic uncertainties for positively charged pions, in the polar angle range from 140 to 340 mrad, and for the six longitudinal bins as a function of momentum.	120
4.26	Components of the systematic uncertainties for negatively charged pions, in the polar angle range from 0 to 140 mrad, and for the six longitudinal bins as a function of momentum.	121
4.27	Components of the systematic uncertainties for negatively charged pions, in the polar angle range from 140 to 340 mrad, and for the six longitudinal bins as a function of momentum.	122
4.28	Fully corrected spectra for positively charged pions, in the polar angle range from 0 to 140 mrad, and for the six longitudinal bins as a function of momentum. The normalization is done on the number of protons on target.	124
4.29	Fully corrected spectra for positively charged pions, in the polar angle range from 140 to 340 mrad, and for the six longitudinal bins as a function of momentum. The normalization is done on the number of protons on target.	125
4.30	Fully corrected spectra for negatively charged pions, in the polar angle range from 0 to 140 mrad, and for the six longitudinal bins as a function of momentum. The normalization is done on the number of protons on target.	126
4.31	Fully corrected spectra for negatively charged pions, in the polar angle range from 140 to 340 mrad, and for the six longitudinal bins as a function of momentum. The normalization is done on the number of protons on target.	127
4.32	Statistical and systematic uncertainties for positively charged pions, in the polar angle range from 0 to 140 mrad, and for the six longitudinal bins as a function of momentum.	128
4.33	Statistical and systematic uncertainties for positively charged pions, in the polar angle range from 140 to 340 mrad, and for the six longitudinal bins as a function of momentum.	129
4.34	Statistical and systematic uncertainties for negatively charged pions, in the polar angle range from 0 to 140 mrad, and for the six longitudinal bins as a function of momentum.	130
4.35	Statistical and systematic uncertainties for negatively charged pions, in the polar angle range from 140 to 340 mrad, and for the six longitudinal bins as a function of momentum.	131
4.36	pp and pn elastic cross-sections and σ_{qe} as computed in eq. (2.21) as function of momentum p.	133

4.37 Nominal and modified Fluka production cross-sections compared with available data. The modified FLUKA production cross-section has been computed from the nominal values of the FLUKA production cross-section σ_{prod}^{FLUKA} and using eq. (4.7) with a scaling factor $S = -0.6$ and a quasi-elastic cross-section σ_{qe} given by eq. (4.8)	134
4.38 T2K replica target results for positively charged pions with nominal FLUKA predictions (blue), FLUKA re-weighted for the multiplicities (green) and FLUKA re-weighted for multiplicities and production cross-section σ_{prod} for the three upstream longitudinal bins and in the polar angles between 0 and 80 mrad plotted as a function of momentum	135
4.39 T2K replica target results for positively charged pions with nominal FLUKA predictions (blue), FLUKA re-weighted for the multiplicities (green) and FLUKA re-weighted for multiplicities and production cross-section σ_{prod} for the three upstream longitudinal bins and in the polar angles between 80 and 220 mrad plotted as a function of momentum	136
4.40 T2K replica target results for positively charged pions with nominal FLUKA predictions (blue), FLUKA re-weighted for the multiplicities (green) and FLUKA re-weighted for multiplicities and production cross-section σ_{prod} for the three upstream longitudinal bins and in the polar angles between 220 and 340 mrad plotted as a function of momentum	136
4.41 T2K replica target results for positively charged pions with nominal FLUKA predictions (blue), FLUKA re-weighted for the multiplicities (green) and FLUKA re-weighted for multiplicities and production cross-section σ_{prod} for the three downstream longitudinal bins and in the polar angles between 0 and 80 mrad plotted as a function of momentum	137
4.42 T2K replica target results for positively charged pions with nominal FLUKA predictions (blue), FLUKA re-weighted for the multiplicities (green) and FLUKA re-weighted for multiplicities and production cross-section σ_{prod} for the three downstream longitudinal bins and in the polar angles between 80 and 220 mrad plotted as a function of momentum	138
4.43 T2K replica target results for positively charged pions with nominal FLUKA predictions (blue), FLUKA re-weighted for the multiplicities (green) and FLUKA re-weighted for multiplicities and production cross-section σ_{prod} for the three downstream longitudinal bins and in the polar angles between 220 and 340 mrad plotted as a function of momentum	138
4.44 T2K replica target results for negatively charged pions with nominal FLUKA predictions (blue), FLUKA re-weighted for the multiplicities (green) and FLUKA re-weighted for multiplicities and production cross-section σ_{prod} for the three upstream longitudinal bins and in the polar angles between 0 and 80 mrad plotted as a function of momentum	139
4.45 T2K replica target results for negatively charged pions with nominal FLUKA predictions (blue), FLUKA re-weighted for the multiplicities (green) and FLUKA re-weighted for multiplicities and production cross-section σ_{prod} for the three upstream longitudinal bins and in the polar angles between 80 and 220 mrad plotted as a function of momentum	140

4.46 T2K replica target results for negatively charged pions with nominal FLUKA predictions (blue), FLUKA re-weighted for the multiplicities (green) and FLUKA re-weighted for multiplicities and production cross-section σ_{prod} for the three upstream longitudinal bins and in the polar angles between 220 and 340 mrad plotted as a function of momentum	140
4.47 T2K replica target results for negatively charged pions with nominal FLUKA predictions (blue), FLUKA re-weighted for the multiplicities (green) and FLUKA re-weighted for multiplicities and production cross-section σ_{prod} for the three downstream longitudinal bins and in the polar angles between 0 and 80 mrad plotted as a function of momentum	141
4.48 T2K replica target results for negatively charged pions with nominal FLUKA predictions (blue), FLUKA re-weighted for the multiplicities (green) and FLUKA re-weighted for multiplicities and production cross-section σ_{prod} for the three downstream longitudinal bins and in the polar angles between 80 and 220 mrad plotted as a function of momentum	142
4.49 T2K replica target results for negatively charged pions with nominal FLUKA predictions (blue), FLUKA re-weighted for the multiplicities (green) and FLUKA re-weighted for multiplicities and production cross-section σ_{prod} for the three downstream longitudinal bins and in the polar angles between 220 and 340 mrad plotted as a function of momentum	142
5.1 Spectra of neutrino parent particles for ν_μ (top left), $\bar{\nu}_\mu$ (top right), ν_e (bottom left) and $\bar{\nu}_e$ (bottom right) at SK calculated using JNUBEAM.	145
5.2 Fraction of neutrino fluxes at ND280 generated by re-interactions along the beam line (solid blue line) and by particles not being a pion when exiting the target surface (dashed black line) as calculated using JNUBEAM.	146
5.3 Fraction of neutrino fluxes at SK generated by re-interactions along the beam line (solid blue line) and by particles not being a pion when exiting the target surface (dashed black line) as calculated using JNUBEAM.	147
5.4 Ratio of ν_μ flux re-weighted with thin target procedure over T2K replica target. Left plot shows result when the production cross-section is not re-weighted, on the right the production is rescaled by -0.6 of the quasi-elastic contribution . . .	147
5.5 Coefficient matrix for pions exiting the target surface contributing to each bin of the ν_μ spectra at SK	148
5.6 Coefficient matrix for pions exiting the target surface contributing to each bin of the $\bar{\nu}_\mu$ spectra at SK	149
5.7 Propagated statistical and systematic uncertainties for the T2K replica target results to the ν_μ (left) and $\bar{\nu}_\mu$ (right) fluxes at SK (top) and ND280 (bottom). The statistical uncertainties are considered as not being correlated between the different NA61/SHINE analysis bins, while for each component of the systematic uncertainties the correlation is considered to be maximal. The different components of the systematic uncertainties are considered as not being correlated between each others.	151
5.8 Proton beam divergence versus momentum for T2K (top) and NA61/SHINE (bottom) for the x coordinate (left) and y coordinate (right) at the upstream face of the target	154
5.9 Radial distributions for the NA61/SHINE (black) and T2K (red) beam profiles at the upstream face of the target	155

5.10 (x, y) distributions of the proton beams at the surface of the target for NA61/SHINE (top left) and for T2K (top right). The ratio of these two distributions is shown in the bottom plot. The (r, ϕ) binning is overlaid on top of the color histograms	156
5.11 (r, ϕ) distributions of the proton beams at the surface of the target for NA61/SHINE (top left) and for T2K (top right). The ratio of these two distributions is shown in the bottom plot. The (r, ϕ) binning is overlaid on top of the color histograms	157
5.12 Two dimensional distribution showing the contribution of each beam bin to the different (p, θ, z) bins for positively charged pions using the NA61/SHINE simulation. The normalization is such that the sum over each row is one.	158
5.13 Distributions of the number of entries in three different (p, θ, z) bins generated by using the 100 bootstrap samples. The left plot is for the second longitudinal bin Z2, polar interval between 180 and 220 mrad and momentum between 2.93 and 3.50 GeV/c. The middle plot is for the fourth longitudinal bin Z4, polar interval between 40 and 60 mrad and momentum between 4.90 and 5.95 GeV/c. The right plot is for the downstream face of the target (i.e. Z6 bin), polar interval between 60 and 80 mrad and momentum between 4.23 and 4.95 GeV/c.	158
5.14 Ratio of re-weighted NA61/SHINE π^+ spectra with respect to the T2K beam profile over the T2K simulated π^+ spectra for the three upstream longitudinal bins and in the polar angles between 0 and 80 mrad plotted as a function of momentum	159
5.15 Ratio of re-weighted NA61/SHINE π^+ spectra with respect to the T2K beam profile over the T2K simulated π^+ spectra for the three upstream longitudinal bins and in the polar angles between 80 and 220 mrad plotted as a function of momentum	160
5.16 Ratio of re-weighted NA61/SHINE π^+ spectra with respect to the T2K beam profile over the T2K simulated π^+ spectra for the three upstream longitudinal bins and in the polar angles between 220 and 340 mrad plotted as a function of momentum	161
5.17 Ratio of re-weighted NA61/SHINE π^+ spectra with respect to the T2K beam profile over the T2K simulated π^+ spectra for the three downstream longitudinal bins and in the polar angles between 0 and 80 mrad plotted as a function of momentum	162
5.18 Ratio of re-weighted NA61/SHINE π^+ spectra with respect to the T2K beam profile over the T2K simulated π^+ spectra for the three downstream longitudinal bins and in the polar angles between 80 and 220 mrad plotted as a function of momentum	163
5.19 Ratio of re-weighted NA61/SHINE π^+ spectra with respect to the T2K beam profile over the T2K simulated π^+ spectra for the three downstream longitudinal bins and in the polar angles between 220 and 340 mrad plotted as a function of momentum	164
6.1 Example of a new proposed position for a replica target closer to the central part of VTPC1.	167
A.1 Corrections factors for positively charged pions, in the polar angle range from 0 to 140 mrad, and for the six longitudinal bins as a function of momentum.	170
A.2 Corrections factors for positively charged pions, in the polar angle range from 140 to 340 mrad, and for the six longitudinal bins as a function of momentum.	171

A.3	Corrections factors for negatively charged pions, in the polar angle range from 0 to 140 mrad, and for the six longitudinal bins as a function of momentum.	172
A.4	Corrections factors for negatively charged pions, in the polar angle range from 140 to 340 mrad, and for the six longitudinal bins as a function of momentum.	173
B.1	T2K replica target weights for positively charged pions computed as the ratio of the NA61/SHINE measurements over the FLUKA 2011 predictions, in the polar angle range from 0 to 140 mrad, and for the six longitudinal bins as a function of momentum. The normalization is done on the number of protons on target.	176
B.2	T2K replica target weights for positively charged pions computed as the ratio of the NA61/SHINE measurements over the FLUKA 2011 predictions, in the polar angle range from 140 to 340 mrad, and for the six longitudinal bins as a function of momentum. The normalization is done on the number of protons on target.	177
B.3	T2K replica target weights for negatively charged pions computed as the ratio of the NA61/SHINE measurements over the FLUKA 2011 predictions, in the polar angle range from 0 to 140 mrad, and for the six longitudinal bins as a function of momentum. The normalization is done on the number of protons on target.	178
B.4	T2K replica target weights for negatively charged pions computed as the ratio of the NA61/SHINE measurements over the FLUKA 2011 predictions, in the polar angle range from 140 to 340 mrad, and for the six longitudinal bins as a function of momentum. The normalization is done on the number of protons on target.	179
C.1	Positively charged pion spectra at the surface of the target produced with FLUKA for the NA61/SHINE beam profile (green) and the T2K beam profile (blue) for the three upstream longitudinal bins and in the polar angles between 0 and 80 mrad plotted as a function of momentum. The spectra are normalized to momentum bin size and number of protons on target	182
C.2	Positively charged pion spectra at the surface of the target produced with FLUKA for the NA61/SHINE beam profile (green) and the T2K beam profile (blue) for the three upstream longitudinal bins and in the polar angles between 80 and 220 mrad plotted as a function of momentum. The spectra are normalized to momentum bin size and number of protons on target	183
C.3	Positively charged pion spectra at the surface of the target produced with FLUKA for the NA61/SHINE beam profile (green) and the T2K beam profile (blue) for the three upstream longitudinal bins and in the polar angles between 220 and 340 mrad plotted as a function of momentum. The spectra are normalized to momentum bin size and number of protons on target	184
C.4	Positively charged pion spectra at the surface of the target produced with FLUKA for the NA61/SHINE beam profile (green) and the T2K beam profile (blue) for the three downstream longitudinal bins and in the polar angles between 0 and 80 mrad plotted as a function of momentum. The spectra are normalized to momentum bin size and number of protons on target	185
C.5	Positively charged pion spectra at the surface of the target produced with FLUKA for the NA61/SHINE beam profile (green) and the T2K beam profile (blue) for the three downstream longitudinal bins and in the polar angles between 80 and 220 mrad plotted as a function of momentum. The spectra are normalized to momentum bin size and number of protons on target	186

C.6	Positively charged pion spectra at the surface of the target produced with FLUKA for the NA61/SHINE beam profile (green) and the T2K beam profile (blue) for the three downstream longitudinal bins and in the polar angles between 220 and 340 mrad plotted as a function of momentum. The spectra are normalized to momentum bin size and number of protons on target	187
C.7	Negatively charged pion spectra at the surface of the target produced with FLUKA for the NA61/SHINE beam profile (green) and the T2K beam profile (blue) for the three upstream longitudinal bins and in the polar angles between 0 and 80 mrad plotted as a function of momentum. The spectra are normalized to momentum bin size and number of protons on target	188
C.8	Negatively charged pion spectra at the surface of the target produced with FLUKA for the NA61/SHINE beam profile (green) and the T2K beam profile (blue) for the three upstream longitudinal bins and in the polar angles between 80 and 220 mrad plotted as a function of momentum. The spectra are normalized to momentum bin size and number of protons on target	189
C.9	Negatively charged pion spectra at the surface of the target produced with FLUKA for the NA61/SHINE beam profile (green) and the T2K beam profile (blue) for the three upstream longitudinal bins and in the polar angles between 220 and 340 mrad plotted as a function of momentum. The spectra are normalized to momentum bin size and number of protons on target	190
C.10	Negatively charged pion spectra at the surface of the target produced with FLUKA for the NA61/SHINE beam profile (green) and the T2K beam profile (blue) for the three downstream longitudinal bins and in the polar angles between 0 and 80 mrad plotted as a function of momentum. The spectra are normalized to momentum bin size and number of protons on target	191
C.11	Negatively charged pion spectra at the surface of the target produced with FLUKA for the NA61/SHINE beam profile (green) and the T2K beam profile (blue) for the three downstream longitudinal bins and in the polar angles between 80 and 220 mrad plotted as a function of momentum. The spectra are normalized to momentum bin size and number of protons on target	192
C.12	Negatively charged pion spectra at the surface of the target produced with FLUKA for the NA61/SHINE beam profile (green) and the T2K beam profile (blue) for the three downstream longitudinal bins and in the polar angles between 220 and 340 mrad plotted as a function of momentum. The spectra are normalized to momentum bin size and number of protons on target	193

Chapter 1

Introduction to Neutrino Physics

1.1 Historical Introduction

The history of weak interactions started in 1896 with the discovery of the radioactivity of uranium by H. Becquerel. Three years later, J. Chadwick could demonstrate the existence of two different radiations, the α and β radiations. In 1914, J. Chadwick conducted measurements of the β -spectrum and demonstrated it was a continuous spectrum in energy [1], while α -spectrum was observed as a monochromatic peak in energy. The continuous energy spectrum in radioactive decays led to the idea that a new particle could explain the presence of the missing energy. In 1930, in a famous letter addressed to “Liebe Radioaktive Damen und Herren”, Wolfgang Pauli proposed the existence of a new weakly interacting neutral particle that would explain the continuous β -spectrum and solve the problem of spin statistics in β -decay. W. Pauli called this new particle *neutron*. In 1932, J. Chadwick discovered the neutron (as we know it today) [2, 3] and E. Fermi renamed the Pauli particle *neutrino*. The first theory of weak interactions was proposed in 1934 by E. Fermi [4] and proved to be very successful in describing the experimental results of the β -decay. Nevertheless, no observation of neutrinos had been confirmed.

R. Davis, following the theoretical work of B. Pontecorvo, proposed to use chlorine as a target for neutrino interactions. In this process, a neutrino should interact with a chlorine atom to produce argon and an electron. Finding argon atoms in the chlorine tank would be a proof of neutrino interactions. He attempted to run his experiment using a nuclear reactor as the anti-neutrino source. A first experiment was conducted at the Brookhaven experimental reactor and a second, with a more powerful reactor, at the Savannah River site. None of these experiments could measure a signal for the detection of antineutrinos. As it has since been understood, only electron neutrino can interact with chlorine to produce argon, but not antineutrinos. Nevertheless, at that time, no such conclusion was possible and R. Davis could only conclude that the interaction rate was so low that he didn't get any signal.

F. Reines and C. Cowan, on their side, were also hunting for neutrinos. Their experiment was using a nuclear reactor as the intense source of antineutrinos, but the detection of interactions was based on a different process. They would use a water tank as target with addition of cadmium to the water. The antineutrino from the reactor would interact with the proton, creating a neutron and a positron. Cadmium, as a highly efficient neutron absorber, would give a gamma ray after having captured the neutron. A detection from the gamma ray of the cadmium 5 microseconds after the detection of the gamma ray from the positron would be the signal for a neutrino interaction. In contrast to the experiment proposed by R. Davis, such reaction is possible with a flux of antineutrinos from a nuclear reactor. In 1956, 26 years after the open

letter of W. Pauli, F. Reines and C. Cowan could finally prove the existence of neutrinos [5, 6] !

This same year, T.D. Lee and C.N. Yang published a paper questioning parity conservation in weak interactions [7]. By the end of 1956, C.S. Wu had demonstrated in an experiment based on polarized ^{60}Co that parity was indeed violated in β -decays [8]. Soon after, other experiments confirmed parity violation in weak interactions. Two years later, in 1958, M. Goldhaber could determine the helicity of the neutrino in a subtle experiment, using the electron capture in the ^{152}Eu nucleus, transforming it into ^{152}Sm with the production of γ and one ν_e [9]. His results were consistent with a left-handed particle being massless. The Standard Model of particle physics would be built on this assumption.

Despite its lack of results with reactor (anti)neutrinos, R. Davis pursued his chlorine experiment with the famous Homestake experiment in order to try to detect neutrinos emitted by the burning process of the Sun. J. Bahcall had made a prediction of the number of neutrinos reaching the earth [10] and R. Davis wanted to confirm it experimentally. It turned out that R. Davis could count only one third of the number of neutrinos predicted by J. Bahcall [11]. This became the well-known solar neutrino problem. Other experiments like Kamiokande and Super-Kamiokande in Japan confirmed R. Davis' results. The solution to this problem was finally explained by the theory of neutrino oscillations.

B. Pontecorvo was the first to mention a theory of neutrino oscillation. Based on the idea of the oscillation of neutral Kaons $K^0 \rightleftharpoons \bar{K}^0$, Pontecorvo proposed the possible oscillation $\nu \rightleftharpoons \bar{\nu}$ for Majorana particles [12]. After the discovery of the muon neutrino ν_μ in 1962 by L. Lederman, M. Schwartz and J. Steinberger [13], and with the results of observations based on atmospheric neutrinos it was understood that the oscillations were happening between the different neutrino flavors [14].

In 2002, the SNO experiment finally confirmed the theory of neutrinos oscillating between three flavor eigenstates [15]. Since then, neutrino oscillation experiments have allowed to measure the three mixing angles, the value of the squared-mass difference Δm_{21}^2 and the absolute value of $\Delta m_{31}^2 \sim \Delta m_{32}^2$.

To this date, the CP phases, the absolute scale of neutrino masses and the sign of Δm_{31}^2 remain unknown.

1.2 Neutrinos in the Standard Model

With the discovery of the Higgs Boson at the CERN LHC [16] [17], all particles predicted by the Standard Model have been observed. They are categorized depending on their nature. Quarks and leptons are the elementary building blocks of matter. They are called fermions and have spin 1/2. Bosons are responsible for the interactions between particles. They have integer spin. The common representation of the Standard Model is given in fig. 1.1. The Standard Model has proved to be very successful in explaining most of the observed phenomena in high energy physics. It is a $SU(3) \times SU(2)_L \times U(1)_Y$ gauge theory describing the strong, weak and electromagnetic interactions of elementary particles. The strong interactions are described by the Quantum ChromoDynamics (QCD) which involves quarks and gluons only. Leptons do not interact with gluons. $SU(3)$ is the gauge group of QCD. Weak and electromagnetic interactions can be unified in an electroweak theory. $SU(2)_L \times U(1)_Y$ is the gauge group of the electroweak theory. Spontaneous breaking of this symmetry leads to the $U(1)_{em}$ group of the Quantum ElectroDynamics (QED).

Neutrinos are represented as left-handed massless fermion fields and are classified into three generations (also called flavors). They are called electron ν_e , muon ν_μ and tau ν_τ neutrinos. Being neutral and massless particles, their flavor can only be defined by the associated charged

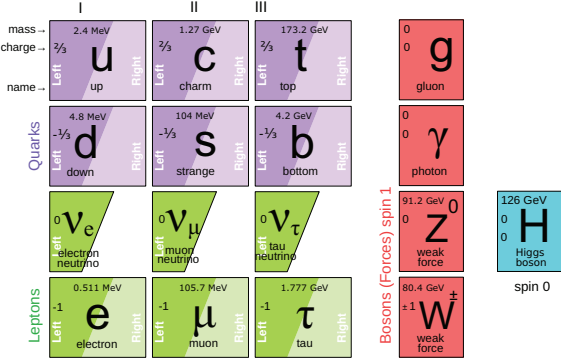


Figure 1.1: Elementary particles of the Standard Model

leptons involved in the neutrino interactions. Experimentally, it was observed that only three neutrino flavors can take part to the weak interaction process. This was done at CERN [18] by measuring the width of the Z boson. As this boson couples to all fermions, the width is directly related to the number of neutrino species. Figure 1.2 shows the measured data with the predictions assuming two, three and four flavors of neutrinos.

Before the correct understanding and the observation of neutrino oscillation phenomenon, the picture of the neutrinos being left-handed and massless particles was consistent with the experimental measurements. The Goldhaber experiment proved that neutrinos are left-handed particles and no other observation could show that neutrinos could have masses. Hence it was a reasonable assumption to base the Standard Model as in fig. 1.1.

The Higgs mechanism (also known as Brout-Englert-Higgs mechanism [19] [20]) included in the Standard Model allows to explain the origin of the masses of the particles but still keeping the neutrinos as massless. It is embedded in the $SU(2)_L \times U(1)_Y$ local gauge symmetry of the electroweak sector of the Standard Model. The minimal Higgs model is built on a weak isospin doublet of two complex scalar fields (with a charge difference of one between the two component of the doublet as it is prescribed by the electroweak sector):

$$\Phi = \begin{pmatrix} \phi^+ \\ \phi^0 \end{pmatrix} = \frac{1}{\sqrt{2}} \begin{pmatrix} \phi_1 + i\phi_2 \\ \phi_3 + i\phi_4 \end{pmatrix} \quad (1.1)$$

and a Lagrangian of the form

$$\mathcal{L} = (\partial_\mu \Phi)^\dagger (\partial^\mu \Phi) - V(\Phi) \quad (1.2)$$

with the Higgs potential given by

$$V(\Phi) = \mu^2 \Phi^\dagger \Phi + \lambda (\Phi^\dagger \Phi)^2 \quad (1.3)$$

Figure 1.3 shows the shape of the potential for the two cases $\mu^2 > 0$ and $\mu^2 < 0$. Considering $\mu^2 < 0$ gives an infinite number of minima for the potential. Choosing one specific minima leads to spontaneous symmetry breaking.

Two strong constraints have to be applied to the Higgs mechanism. First it has to be a local gauge theory. This means that the partial derivatives in the kinetic part of the lagrangian in eq. (1.2) should be replaced by the usual covariant derivatives. This produces the gauge fields of the electroweak theory related to the photons, W and Z bosons. The second constraint is

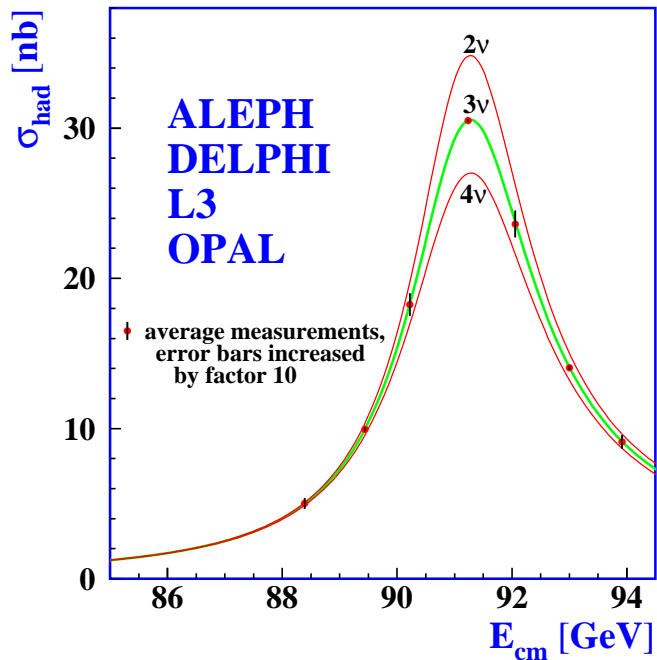


Figure 1.2: Measurements of the hadron production cross-section around the Z resonance. The curves indicate the predicted cross-section for two, three and four neutrino species with SM couplings and negligible mass (from Ref. [18]).

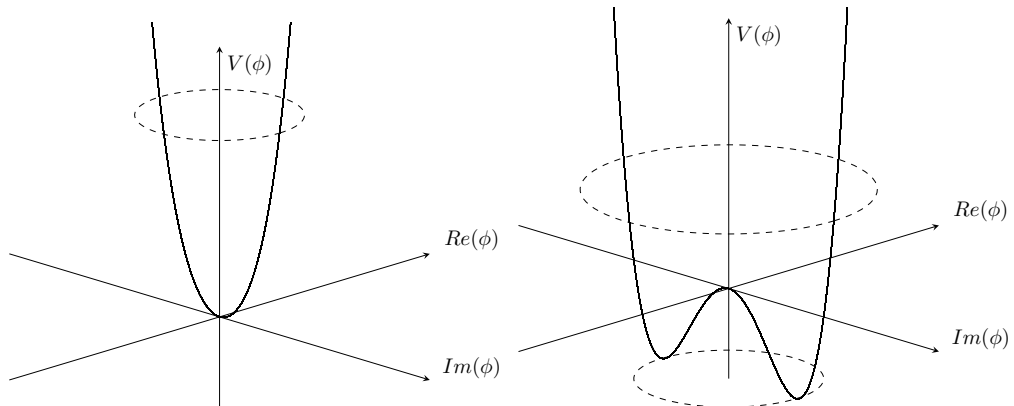


Figure 1.3: Higgs potential as given by eq. (1.3) for $\mu^2 > 0$ (left) and $\mu^2 < 0$ (right)

related to the fact that the Higgs mechanism has to give masses to the W and Z bosons but leave the photon massless. This can be done by considering a non-zero value only for the neutral component of the Higgs doublet. Equation (1.1) can then be written as:

$$\Phi = \frac{1}{\sqrt{2}} \begin{pmatrix} 0 \\ \phi_3 + i\phi_4 \end{pmatrix} \quad (1.4)$$

Choosing one specific minima of the Higgs potential when $\mu^2 < 0$ leads to spontaneous symmetry breaking. Considering an expansion of the field around the chosen potential minimum, the Higgs doublet from eq. (1.4) can be written as:

$$\Phi = \frac{1}{\sqrt{2}} \begin{pmatrix} 0 \\ v + H(x) + i\xi \end{pmatrix} \quad (1.5)$$

where v is the vacuum expectation value, H and ξ represent the expansions around the minimum.

Inserting eq. (1.5) in eq. (1.2) reveals that the field H has an associated mass term corresponding to

$$m_H = \sqrt{-2\mu^2} \quad (1.6)$$

while the field ξ remains a massless field which is associated to a Goldston boson [21].

Requesting the theory to be gauge invariant, it is possible to show that this massless field is not physical and can be “eaten” by properly choosing the gauge transformations of the gauge fields present in the covariant derivative. This specific transformation in which only the physical fields remain present is called the *Unitary Gauge*.

As a conclusion of the two constraints we have listed above and after spontaneous symmetry breaking, the minimal Higgs doublet can be written as

$$\Phi = \frac{1}{\sqrt{2}} \begin{pmatrix} 0 \\ v + H(x) \end{pmatrix} \quad (1.7)$$

and H is the only remaining physical field. Inserting it in the Lagrangian from eq. (1.2) with the correct form of the covariant derivatives allows to extract mass terms for the W and Z bosons while keeping the photon as a massless field.

This Higgs mechanism is very powerful at describing how the gauge bosons get their masses, but it can also be used to generate the masses of the fermions. Being spin 1/2 particles, fermions are described by the Dirac Lagrangian ¹

$$\mathcal{L} = i\bar{\psi}\gamma^\mu\partial_\mu\psi - m\bar{\psi}\psi \quad (1.8)$$

The mass term $-m\bar{\psi}\psi$ is not invariant under $SU(2)_L \times U(1)_Y$ local gauge transformation and cannot be directly included in the Standard Model. Nevertheless, in the Standard Model, the same $SU(2)_L$ local gauge transformation apply on the Higgs doublet Φ

$$\Phi \rightarrow \Phi' = \left(I + ig\vec{\alpha}(x) \cdot \vec{T} \right) \Phi \quad (1.9)$$

and on the left-handed chiral fermion doublet L

$$L \rightarrow L' = \left(I + ig\vec{\alpha}(x) \cdot \vec{T} \right) L \quad (1.10)$$

¹ γ matrices satisfy the anti-commutation relation $\{\gamma^\mu, \gamma^\nu\} = 2g^{\mu\nu}$, where $g^{\mu\nu} = \text{diag}(1, -1, -1, -1)$ is the Minkowski metric tensor; the γ^5 matrix is defined by $\gamma^5 \equiv \gamma_5 \equiv i\gamma^0\gamma^1\gamma^2\gamma^3\gamma^4$

$$\bar{L} \equiv L^\dagger \gamma^0 \rightarrow \bar{L}' = \bar{L} \left(I - ig\vec{\alpha}(x) \cdot \vec{T} \right) \quad (1.11)$$

where

$$L \equiv \begin{pmatrix} \nu_{\ell L} \\ \ell_L \end{pmatrix} \quad (1.12)$$

Hence, a term $\bar{L}\Phi$ is $SU(2)$ invariant. In order to get a $SU(2)_L \times U(1)$ invariant term, the right-handed chiral fermion singlet can be used to form a term like

$$\bar{L}\Phi R \quad \text{where } R \equiv \ell_{\alpha R}; \quad \alpha = e, \mu, \tau \quad (1.13)$$

Such terms can be directly applied to the lepton sector and the proper $SU(2)_L \times U(1)_Y$ invariant mass term for the Lagrangian of the Standard Model is written as

$$\mathcal{L} = - \sum_{\alpha, \beta = e, \mu, \tau} Y_{\alpha\beta}^{\ell} \bar{L}'_{\alpha L} \Phi \ell'_{\beta R} + \text{H.c} \quad (1.14)$$

In the unitary gauge we have described above, it will become

$$\mathcal{L} = - \left(\frac{v + H}{\sqrt{2}} \right) \sum_{\alpha, \beta = e, \mu, \tau} Y_{\alpha\beta}^{\ell} \bar{\ell}'_{\alpha L} \ell'_{\beta R} + \text{H.c} \quad (1.15)$$

and the terms related to the neutrino fields have disappeared. Hence, the Higgs mechanism of the Standard Model does not allow to generate masses for the neutrinos.

The prime subscript indicates that, in general, the Yukawa coupling matrix $Y_{\alpha\beta}^{\ell}$ is not diagonal. In order to find the charged lepton it is necessary to diagonalize this matrix. It is done by using two 3×3 unitary matrices and the transformation

$$V_L^{\ell\dagger} Y^{\ell} V_R^{\ell} = Y^{\ell} \quad \text{with} \quad Y_{\alpha\beta}^{\ell} = y_{\alpha}^{\ell} \delta_{\alpha\beta} \quad (\alpha, \beta = e, \mu, \tau) \quad (1.16)$$

Introducing the following notation for the chiral lepton array

$$\ell_L = V_L^{\ell\dagger} \ell'_L = \begin{pmatrix} e_L \\ \mu_L \\ \tau_L \end{pmatrix} \quad \text{and} \quad \ell_R = V_R^{\ell\dagger} \ell'_R = \begin{pmatrix} e_R \\ \mu_R \\ \tau_R \end{pmatrix} \quad (1.17)$$

the Lagrangian in eq. (1.15), in the eigenbasis where Y^{ℓ} is diagonal, can be written as

$$\mathcal{L} = - \sum_{\alpha = e, \mu, \tau} \frac{y_{\alpha}^{\ell} v}{\sqrt{2}} \bar{\ell}_{\alpha} \ell_{\alpha} - \sum_{\alpha = e, \mu, \tau} \frac{y_{\alpha}^{\ell}}{\sqrt{2}} \bar{\ell}_{\alpha} \ell_{\alpha} H \quad (1.18)$$

where

$$\ell_{\alpha} = \ell_{\alpha L} + \ell_{\alpha R} \quad (\alpha = e, \mu, \tau) \quad (1.19)$$

are the fields of the charged leptons with definite masses. The masses of the charged leptons are thus identified by

$$m_{\alpha} = \frac{y_{\alpha}^{\ell} v}{\sqrt{2}} \quad \text{with} \quad \alpha = e, \mu, \tau \quad (1.20)$$

At the time the standard model was built, the neutrinos were seen as left-handed massless particles. Hence the above theory was very successful at explaining the lepton sector.

It should be noted that if the same method is applied to the quark sector, only those quarks

classified in the lower part of the doublets would acquire masses. In order to remedy to this problem and also give masses to the up-type quark with the Higgs mechanism, it is possible to construct the conjugate of the Higgs doublet as

$$\tilde{\Phi} = -i\sigma_2 \Phi^* = \begin{pmatrix} -\phi^{0*} \\ \phi^- \end{pmatrix} \quad (1.21)$$

and consider terms in the Lagrangian of the form $\bar{L}\tilde{\Phi}R$. These terms are $SU(2)_L \times U(1)_Y$ invariant and allow to generate masses for the upper components of the quark doublets.

The Standard Model has proved to be very powerful at describing nature. It has even been used to make predictions that revealed to be correct. It was constructed to match with the observations made by experiments. Before neutrino oscillations were experimentally confirmed, it was justified to introduce the neutrinos in the Standard Model as left-handed massless fermions.

Since we know that neutrinos oscillate and hence have masses, it is mandatory to expand the Standard Model. In the following sections, we will see three different propositions for physics beyond the Standard Model by adding masses to the neutrinos

1.3 Neutrino Masses

In this section, we will show how the Standard Model can be extended to add masses to the neutrinos. For simplicity, we will consider three flavor states and three massive states for the neutrinos. But it is important to note that, while the number of flavor states involved in the weak interactions has been experimentally measured as being three, the number of massive neutrino states is not constrained. Considering more than three massive states open the door to the existence of sterile neutrinos.

1.3.1 Dirac Mass Term

A Dirac neutrino mass can be generated in the same way the up-type quark mass was introduced in the previous section. But the introduction of right-handed components of the neutrinos is then needed. The Lagrangian in the unitary gauge for the fermion mass terms in this minimally extended Standard Model can be written in matrix form as

$$\mathcal{L} = -\frac{v + H}{\sqrt{2}} \left[\bar{\ell}_L Y^{\prime\ell} \ell'_R + \bar{\nu}_L Y^{\prime\nu} \nu'_R \right] + \text{H.c} \quad (1.22)$$

with the new right-handed neutrino array

$$\nu'_R = \begin{pmatrix} \nu'_{eR} \\ \nu'_{\mu R} \\ \nu'_{\tau R} \end{pmatrix} \quad (1.23)$$

and where $Y^{\prime\nu}$ is a new matrix with Yukawa coupling terms. As for leptons and quarks, it is, in general, not a diagonal matrix. It can be diagonalized by using two 3×3 unitary matrices V_L^ν and V_R^ν

$$V_L^{\nu\dagger} Y^{\prime\nu} V_R^\nu = Y^\nu \quad \text{with} \quad Y_{kj}^\nu = y_{kj}^\nu \delta_{kj} \quad (k, j = 1, 2, 3) \quad (1.24)$$

Introducing the massive chiral neutrino arrays

$$n_L = V_L^{\nu\dagger} \nu'_L = \begin{pmatrix} \nu_{1L} \\ \nu_{2L} \\ \nu_{3L} \end{pmatrix} \quad \text{and} \quad n_R = V_R^{\nu\dagger} \nu'_R = \begin{pmatrix} \nu_{1R} \\ \nu_{2R} \\ \nu_{3R} \end{pmatrix} \quad (1.25)$$

eq. (1.22) expressed in the basis in which the Yukawa matrices are diagonal becomes:

$$\mathcal{L} = -\frac{v+H}{\sqrt{2}} \left[\sum_{\alpha=e,\mu,\tau} y_\alpha^\ell \bar{\ell}_{\alpha L} \ell_{\alpha R} + \sum_{k=1}^3 y_k^\nu \bar{\nu}_{k L} \nu_{k R} \right] + \text{H.c} \quad (1.26)$$

Defining the Dirac charged lepton fields (as in the previous section) and Dirac neutrino fields as

$$\ell_\alpha = \ell_{\alpha L} + \ell_{\alpha R} \quad (\alpha = e, \mu, \tau) \quad \text{and} \quad \nu_k = \nu_{k L} + \nu_{k R} \quad (k = 1, 2, 3) \quad (1.27)$$

eq. (1.26) can finally be written as

$$\mathcal{L} = - \sum_{\alpha=e,\mu,\tau} \frac{y_\alpha^\ell v}{\sqrt{2}} \bar{\ell}_\alpha \ell_\alpha - \sum_{k=1}^3 \frac{y_k^\nu v}{\sqrt{2}} \bar{\nu}_k \nu_k - \sum_{\alpha=e,\mu,\tau} \frac{y_\alpha^\ell}{\sqrt{2}} \bar{\ell}_\alpha \ell_\alpha H - \sum_{k=1}^3 \frac{y_k^\nu}{\sqrt{2}} \bar{\nu}_k \nu_k H \quad (1.28)$$

The neutrino mass terms can then be identified by

$$m_k = \frac{y_k^\nu v}{\sqrt{2}} \quad (k = 1, 2, 3) \quad (1.29)$$

and are related to the Higgs vacuum expectation value v as for the charged leptons and quarks. The last term of eq. (1.28) represent the interaction of the neutrinos with the Higgs boson.

In order to see the practical effect of the matrices $V_{L,R}^\nu$ and $V_{L,R}^\ell$, let's consider the charged current weak interaction part of the Lagrangian. It is given by

$$\mathcal{L}_{W,L}^{CC} = -\frac{g}{2\sqrt{2}} \bar{\nu}_L^\nu \gamma^\mu (1 - \gamma^5) \ell'_L W_\mu + \text{H.c} = -\frac{g}{2\sqrt{2}} j_{W,L}^\mu W^\mu + \text{H.c} \quad (1.30)$$

With the above notations, the leptonic weak charged current $j_{W,L}^\mu$ can be written as

$$j_{W,L}^\mu = 2\bar{\nu}_L^\nu \gamma^\mu \ell'_L = 2\bar{n}_L V_L^{\nu\dagger} \gamma^\mu V_L^\ell \ell_L = 2\bar{n}_L V_L^{\nu\dagger} V_L^\ell \gamma^\mu \ell_L \quad (1.31)$$

where we can define the matrix U as

$$U = V_L^{\nu\dagger} V_L^\ell \quad \text{and} \quad \nu_L = U n_L \quad \nu_L = \begin{pmatrix} \nu_{eL} \\ \nu_{\mu L} \\ \nu_{\tau L} \end{pmatrix} \quad (1.32)$$

With this definition, the mixing matrix is directly applied to the neutrinos and not to the leptons. The reason is that leptons can be treated as particles with definite masses. The flavor of each lepton is identified by its mass and its decay modes which can be directly observed. Hence, a charged lepton with definite flavor is a particle with a specific mass. Neutrinos, on the other hand, can only be detected indirectly via the charged lepton they produce or annihilate. Hence, flavor neutrinos are not required to have definite mass. They can be seen as superposition (or linear combination) of massive neutrinos.

The 3×3 unitary matrix U characterizes the superposition of massive neutrinos for each flavor neutrino. It can be described by three mixing angles and six phases. Nevertheless, the Lagrangian in eq. (1.28) is invariant under transformations of the form

$$\nu_k \rightarrow e^{i\phi_k} \nu_k \quad (k = 1, 2, 3) \quad (1.33)$$

$$l_\alpha \rightarrow e^{i\phi_\alpha} l_\alpha \quad (\alpha = e, \mu, \tau) \quad (1.34)$$

This invariance of the Lagrangian can be used to rephase and eliminate five of the six phases that do not have any physical effect. Only one physical phase remains and is actually of significance in the current given in eq. (1.31).

Noether's theorem stresses that for each transformation that leaves the Lagrangian invariant, there exist an associated conserved current and conserved charge. It is thus interesting to see under which global transformation the Lagrangian eq. (1.28) remain invariant. The most general global transformation of the form

$$\nu_{kL} \rightarrow e^{i\phi} \nu_{kL}, \quad \nu_{kR} \rightarrow e^{i\phi} \nu_{kR} \quad (k = 1, 2, 3) \quad (1.35)$$

$$l_{\alpha L} \rightarrow e^{i\phi} l_{\alpha L}, \quad l_{\alpha R} \rightarrow e^{i\phi} l_{\alpha R} \quad (\alpha = e, \mu, \tau) \quad (1.36)$$

with a common phase ϕ , leaves eq. (1.28) invariant. The conserved value associated to this transformation is the total lepton number.

It should be noted that the values of the Yukawa couplings are not constrained by the Standard Model. Therefore, the origin of the values of quark and lepton masses remain a mystery in the Standard Model. The absolute masses of the neutrinos haven't been measured yet but they are known to be much smaller than the masses of the other fermions.

Adding Dirac mass terms for the neutrinos to the Standard Model has the advantage to be a very minimal extension that can be considered in order to explain the confirmed observations in current neutrino oscillation experiments. No further considerations or hypothesis would be required. Nevertheless this minimal extension would not be sufficient to explain theories like the baryon asymmetry of the universe or the predicted neutrinoless double beta decay process that requires the neutrinos to be Majorana particles. It would also not allow to predict the existence of heavy neutrinos which are proposed as potential candidates for dark matter. Hence, it is believed that some other basic underlying processes should be responsible for the masses of the neutrinos.

1.3.2 Majorana Mass Term

Two component spinors are sufficient to describe massless spin-1/2 fermions. Indeed, for massless fermions, left-handed and right-handed chiral fields are decoupled (as can be seen through the Dirac equation). E. Majorana showed in 1937 that two-component spinors could also be sufficient to describe massive particles. Nevertheless, this assumes some relations connecting the right-handed and left-handed chiral fields. The specific relation for the fermion field can be deduced from the Dirac equation and is given by the Majorana condition

$$\psi = \psi^C \quad (1.37)$$

where C is the charge conjugate operator and ψ^C is the charge conjugated field of ψ . Hence, the Majorana condition implies that the particle is equal to its antiparticle. Therefore, only neutral fermions can have the property to be Majorana particles.

The Majorana mass term in the Lagrangian can be written as

$$\mathcal{L} = \frac{1}{2} \sum_{\alpha, \beta = e, \mu, \tau} \nu'_{\alpha L}^T C^\dagger M_{\alpha \beta}^L \nu'_{\beta L} + \text{H.c.} \quad (1.38)$$

M is the Majorana mass matrix. It is a 3×3 complex symmetric matrix which is, in general, not diagonal. The fields of massive neutrinos are obtained by diagonalizing M . This can be written as

$$(V_L^\nu)^T M^L V_L^\nu = M \quad \text{with} \quad M_{kj} = m_k \delta_{kj} \quad (k, j = 1, 2, 3) \quad (1.39)$$

Expressing the left-handed flavor fields as unitary linear combination of the left-handed components of fields with definite mass

$$\nu'_L = V_L^\nu n_L \quad \text{with} \quad n_L = \begin{pmatrix} \nu_{1L} \\ \nu_{2L} \\ \nu_{3L} \end{pmatrix} \quad (1.40)$$

we can write eq. (1.38) as

$$\mathcal{L} = -\frac{1}{2} \sum_{k=1}^3 m_k \overline{\nu_{kL}^C} \nu_{kL} + \text{H.c.} \quad (1.41)$$

It is important to note that this mass term is not invariant under the global $U(1)$ gauge transformation (in opposition to the Dirac mass case)

$$\nu_{kL} \rightarrow e^{i\phi} \nu_{kL} \quad (k = 1, 2, 3) \quad (1.42)$$

with the same phase ϕ for all massive neutrinos. This fact implies that the total lepton number does not need to be conserved anymore, opening the door for interesting processes like neutrino-less double- β -decay.

Furthermore, from eq. (1.41) one can see that the Lagrangian is also not invariant under a transformation of the form

$$\nu_{kL} \rightarrow e^{i\phi_k} \nu_{kL} \quad (k = 1, 2, 3) \quad (1.43)$$

where the phases ϕ_k are different for each flavor. Therefore, it is not possible, as for the Dirac fields, to rephase the left-handed neutrino fields and it is not possible to remove five phases. Only three phases can be removed by rephasing and three CP phases remain in the mixing matrix. The mixing matrix can be written as a product of two matrices

$$U = U^D D^M \quad (1.44)$$

where U^D represent the Dirac mixing matrix with three mixing angles and one phase and D^M contains the two extras phases related to Majorana mass term.

The common parametrization for U^D and D^M is written as

$$U^D = \begin{pmatrix} c_{12} c_{13} & s_{12} c_{13} & s_{13} e^{i\delta_{CP}} \\ -s_{12} c_{23} - c_{12} s_{23} s_{13} e^{i\delta_{CP}} & c_{12} c_{23} - s_{12} s_{23} s_{13} e^{i\delta_{CP}} & s_{23} c_{13} \\ s_{12} s_{23} - c_{12} c_{23} s_{13} e^{i\delta_{CP}} & -c_{12} s_{23} - s_{12} c_{23} s_{13} e^{i\delta_{CP}} & c_{23} c_{13} \end{pmatrix} \quad (1.45)$$

where $c_{ij} \equiv \cos(\theta_{ij})$, $s_{ij} \equiv \sin(\theta_{ij})$ and

$$D^M = \text{diag}(1, e^{i\phi_1}, e^{i\phi_2}) \quad (1.46)$$

We have introduced here the notation δ_{CP} for the phase related to the Dirac mixing matrix as it is the notation commonly used in neutrino oscillation experiments.

Adding only a Majorana mass term to the Standard Model would allow to explain the present observations in neutrino experiments. Furthermore it is a mandatory term for the theory of neutrinoless double beta decays. Nevertheless, it does not bring by itself a clear explanation for the origin of the very small values of the masses of the neutrinos with respect to the other fermions.

1.3.3 Dirac+Majorana Mass Term

The chiral fields ν_L and ν_R are the building blocks of the neutrino Lagrangian. If only ν_L exists, then the neutrino Lagrangian can only contain the Majorana mass term

$$\mathcal{L}_{mass}^L = \frac{1}{2} m_L \nu_L^T C^\dagger \nu_L + \text{H.c} \quad (1.47)$$

If ν_R also exists, then the neutrino Lagrangian can contain the Dirac mass term

$$\mathcal{L}_{mass}^D = -m_D \bar{\nu}_L \nu_R + \text{H.c} \quad (1.48)$$

However, the neutrino Majorana mass term for ν_R can also be considered

$$\mathcal{L}_{mass}^R = \frac{1}{2} m_L \nu_R^T C^\dagger \nu_R + \text{H.c} \quad (1.49)$$

Therefore, in general, if we assume that ν_R exists, we can write the general Dirac-Majorana mass term

$$\mathcal{L}_{mass}^{D+M} = \mathcal{L}_{mass}^D + \mathcal{L}_{mass}^L + \mathcal{L}_{mass}^R \quad (1.50)$$

Defining the left-handed chiral field as a column matrix

$$N_L = \begin{pmatrix} \nu_L \\ \nu_R^C \end{pmatrix} = \begin{pmatrix} \nu_L \\ C \bar{\nu}_R^T \end{pmatrix} \quad (1.51)$$

eq. (1.50) can be written as

$$\mathcal{L}_{mass}^{D+M} = \frac{1}{2} N_L^T C^\dagger M N_L + \text{H.c} \quad \text{with} \quad M = \begin{pmatrix} m_L & m_D \\ m_D & m_R \end{pmatrix} \quad (1.52)$$

To find the fields for massive neutrinos, we again have to diagonalize the mass matrix M via

$$U^T M U = \begin{pmatrix} m_1 & 0 \\ 0 & m_2 \end{pmatrix} \quad (1.53)$$

The massive neutrino fields are then given by

$$n_L = \begin{pmatrix} \nu_{1L} \\ \nu_{2L} \end{pmatrix} \quad \text{and} \quad N_L = U n_L \quad (1.54)$$

Equation (1.50) becomes then

$$\mathcal{L}_{mass}^{D+M} = \frac{1}{2} \sum_k m_k \nu_{kL}^T C^\dagger \nu_{kL} + \text{H.c} = -\frac{1}{2} \sum_k m_k \bar{\nu}_k \nu_k \quad (1.55)$$

where we have defined

$$\nu_k = \nu k L + \nu_{kL}^C = \nu_{kL} + C \bar{\nu}_{kL}^T \quad (1.56)$$

This is exactly the Majorana relation which describes Majorana particles. So, a Dirac-Majorana mass term implies that massive neutrinos are Majorana particles.

An interesting case is when $m_D \ll m_R$ and $m_L = 0$. In this case, from the characteristic equation when diagonalizing the mass matrix M , one gets

$$m_1 \simeq \frac{m_D^2}{m_R} \quad \text{and} \quad m_2 \simeq m_R \quad (1.57)$$

If one assumes that m_R is large, ν_2 becomes as heavy as m_R and ν_1 is a very light neutrino because its mass is suppressed with respect to m_D by the large value of m_R . This mechanism is known as see-saw mechanism, where light neutrinos are linked to very heavy neutrinos. As these very heavy neutrinos are right handed, they do not participate in weak interactions and cannot be detected by Standard Model processes. They are called sterile neutrinos.

Adding a Dirac+Majorana mass term to the standard model is of course not the minimal extension. But it is probably the most interesting one. We can cite two examples to underline the interest into a Dirac+Majorana mass term.

The first one relates to dark matter. Still a large part of the mass of the universe cannot be explained by the quarks and charged leptons of the Standard Model. Right-handed heavy neutrinos could be interesting dark matter candidates. Assuming their masses are large (as it would be the case from a see-saw mechanism) it is possible that modern accelerators like the LHC haven't been yet able to reach the requested energy to experimentally generate them. Future accelerator projects like Fcc-ee might probe new theories and help to shed light on the nature of neutrinos [22].

The second example relates to the baryon asymmetry of the universe. A proposed theory shows that the baryogenesis could be understood as based on the leptogenesis under different conditions. One condition state that the lepton number should be violated. A second condition requests C- and CP-symmetries to be violated as well in the lepton sector. These conditions can be fulfilled in the case of Dirac+Majorana mass term included as an extension of the Standard Model.

In conclusion, even if the nature of neutrinos is still unknown, the addition of a Dirac+Majorana mass term is favored by many physicists as it would allow to predict other potential phenomena.

1.4 Accelerator based neutrino experiments

The concept of accelerator neutrino beam was first proposed by M. Schwartz [23] and B. Pontecorvo [24] in two independent articles. The first experiment to use an accelerator to produce a neutrino beam was carried out by L. Lederman, M. Schwartz and J. Steinberger, which allowed them to discover the muon neutrino in 1962. In 1963, research using neutrino beams started at CERN and resulted in two very important successes. The first one was the discovery of weak neutral currents in the Gargamelle Experiment [25]. The large bubble chamber had the capacity to accurately display the vertexes of the interactions as well as the products of the interactions. In December 1972, the observation of an isolated electron was the clear signature for the process $\nu_\mu + e^- \rightarrow \nu_\mu + e^-$ which can only be due to the exchange of a Z^0 boson. This inspired the collaboration to look for the more complicated hadronic neutral current candidates. A precise understanding of the neutrino flux was mandatory and a dedicated hadron production experiment was conducted with the Allaby spectrometer. The careful understanding of the background,

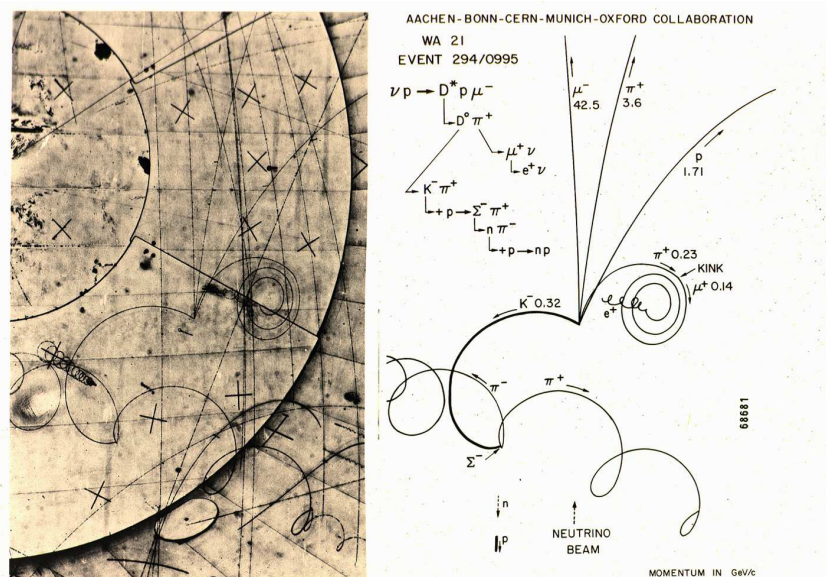


Figure 1.4: Typical event in the BEBC experiment interpreted as the production of a charmed particle in a neutrino nucleus interaction and the subsequent decay of this particle. [27].

mainly due to induced neutrons out of the chamber, was a key point for the confirmation of the observation of neutral current events. In July 1973, the Gargamelle collaboration published their results [26], confirming the discovery of neutral current events in neutrino interactions. The second important success of the CERN neutrino programme was the direct observation of charmed particles. Charm quarks had been postulated by the GIM (Glashow, Iliopoulos, Maiani) mechanism. The interactions of neutrinos with the quarks of the nucleons would allow for the production of charmed particles, themselves decaying into leptons. Hence, the experimental signature for the production of charmed particles would be the detection of two leptons with opposite signs in the final state. We quote two experiments that reported such observations. The BEBC experiment, with its bubble chamber, could clearly identify the different tracks of the product of the interaction of the incident neutrinos with the nucleons, and hence identify events with the production of charmed particles and their subsequent decays. Figure 1.4 shows a typical candidate of such event. The CDHS experiment, thanks to its larger mass and its detection technique using emulsions, could record a large number of dileptons events and could conclude, in an article published in 1982 [28], that “Neutrino- and antineutrino-induced dimuon events show all the properties expected for a charged-current reaction and charm production and decay”.

Since the confirmation of the neutrino oscillation phenomenon by experiments like SNO [15] and KamLAND [29], neutrino physics has entered an era of precise measurements of the mixing parameters (presented in eq. (1.45)) as well as of cross-sections. Accelerator-based neutrino experiments quickly showed to be very suitable to reach these goals.

Two different concepts have been used to produce neutrino beams at accelerator. In the beam dump approach, a proton beam is shot onto a large solid target. The goal is to absorb the protons as well as their secondaries in order to minimize the probability for the conventional sources of neutrinos to decay. With this method, the electron neutrino component is enhanced with respect to the muon neutrino component in the beam. The Gargamelle experiment at CERN has been

using the beam dump approach to study electron neutrino interactions in its detector.

In the second approach, the proton beam impinges on a nuclear target producing secondary particles, mainly pions and kaons. Those secondaries leave the target, boosted in the forward direction, and are let to travel through a decay volume so that they can decay to neutrinos. In conventional neutrino beams, additional focusing horns are used to collect and focus as much hadrons as possible in the direction of the neutrino detectors.

In this section we discuss present knowledge and future challenges of accelerator-based neutrino experiments. We concentrate on currently running experiments and proposed future projects

1.4.1 Neutrino beams and hadron production measurements

Conventional neutrino beams at accelerator are created by the interactions of protons on a long nuclear target. Hadrons are produced as a result of these interactions. Predominantly pions will exit the target with a smaller amount of kaons. A long decay volume placed after the target let the hadrons decay into neutrinos. The decays $\pi^\pm \rightarrow \mu + \nu_\mu$ (BR $\sim 100\%$), $K^\pm \rightarrow \mu + \nu_\mu$ (BR = 63.4%) and $K_L \rightarrow \pi + \mu + \nu_\mu$ (BR = 27.2%) produce the dominant contribution of the muon neutrino beams. Other decays like $K_L \rightarrow \pi + e + \nu_e$ (BR = 27.2%) or the subsequent decays of muons $\mu \rightarrow e + \nu_e + \nu_\mu$ are usually seen as a background for a muon neutrino beam. Nevertheless, sometimes they can be used to exploit the small component of ν_e for e.g. cross-section measurements. The target is usually made out of a low density material, like carbon or beryllium, to let the pions exit its surface. Different geometries have been used, but with always the same idea: a few interaction lengths along the beam direction to compensate for the low density material and a small diameter to get as many particles escaping the skin of the target.

The length of the decay volume can be optimized with respect to the pion energy spectra so that it maximizes the number of pion decays while it keeps the number of muon decays as low as possible. Typical lengths in currently running and proposed future experiments are such that they correspond to the decay length of the pions around the peak energy of the pion distribution exiting the target. As the muon life time (2.2 μs) is nearly 100 times as long as the pion life time (0.026 μs), most of the muon will not decay before reaching the end of the decay volume. Hence, it minimizes the ν_e contamination in the ν_μ beam generated by those muon decays. The volume can be filled with helium or be under vacuum to reduce the number of pion loss due to interactions and to avoid air activation.

The use of magnetic horns, first proposed by Simon van der Meer [30], placed around and just after the target allow to collect as many hadrons as possible exiting the nuclear target and to focus them in a chosen direction. It allows to increase the neutrino flux by more than an order of magnitude around the beam peak energy. Changing the polarity of the magnetic field allows to select either positively charged particles or negatively charged particles. Positive pions and kaons will create a muon neutrino beam while focusing negatively charged pions and kaons will generate a muon antineutrino beam.

At the end of the decay volume, a beam dump will absorb the remaining pions and muons. In order to control the evolution of the beam, its intensity and its direction, a muon monitor is usually placed just after the beam dump. Only high energy muons will be recorded with a low event rate. Figure 1.5 shows a schematic of a typical beam line (here T2K as an example) with the different components listed above.

Modern conventional neutrino beams run with different primary proton energies, different repetition cycles as well as different number of protons per spill. The proton beam power gives a typical number to qualify neutrino beams. Currently, this number is of the order of hundred kW. Next generation neutrino beam are expected to exceed one MW. These beams are qualified as Superbeams. Table 1.1 gives the typical proton parameters for currently running experiments

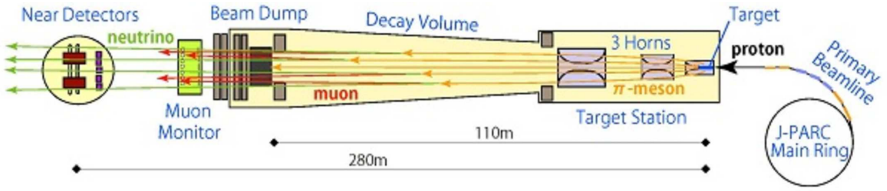


Figure 1.5: Typical components of a neutrino beam line. Example taken from the T2K experiment

and proposed upgrades and projects.

Beam Line	Turn-on	Proton energy (GeV/c)	Beam Power (kW)	Protons per spill	Cycle time (sec)
BNB [31]	2003	8	26	4.5×10^{12}	0.14
NuMI [32]	2005	120	375	4.0×10^{13}	1.87
T2K*	2009	30	371	1.2×10^{14}	2.54
CNGS [33]	2006	400	512	2.4×10^{13}	6
Upgrades					
NuMI [32]	2015	120	700	4.9×10^{13}	1.33
T2K [34]	2017	30	750	2.0×10^{14}	2.48
Projects					
LBNE [35]	-	80 - 120	1200	7.5×10^{13}	0.8 - 1.2
LBNE II [35]	-	60 - 120	2400	1.5×10^{14}	0.6 - 1.2
CENF [36]	-	100	200	2.25×10^{13}	3.6
LBNO [37]	-	400	750	7.0×10^{13}	6
LBNO II [37]	-	50	2000	2.5×10^{14}	1
T2HK [34]	-	30	1500	2.2×10^{14}	1.3

* achieved in 2015

Table 1.1: Proton beam parameters for different running beam lines, upgrades and projects.

The simulation of the proton interactions within a long target is a very complex task involving many different processes at various energies. Hadronic generators are usually good at describing specific interactions in some well defined energy ranges. But none of them is able to precisely describe all different particles interactions over large ranges of momenta. Hence, it is not possible to rely only on model predictions to account for all the different subsequent re-interactions in the long target and beam-line elements. Hadron production measurements can help to constrain the models.

All modern accelerator-based neutrino experiments have used hadron production measurements in the prediction of their neutrino fluxes. We can cite different examples from past experiments. The HARP data were used by the MiniBooNE and SciBooNE experiments at Fermilab. The NA20 and NA56/SPY data used for NOMAD and CHORUS experiments, as well as the experiments on the CNGS beam line. The MIPP data used by the experiments on the NuMi beam line (Minos, Minerva, NO ν A). The NA61/SHINE data are being used by the T2K experiment.

Among all these experiments, MIPP, HARP and NA61/SHINE conducted specific measurements for the neutrino experiments.

Three approaches will be shortly explained here on how one can predict the hadron production for neutrino beam simulations. The first approach is based on parameterizations, the second and

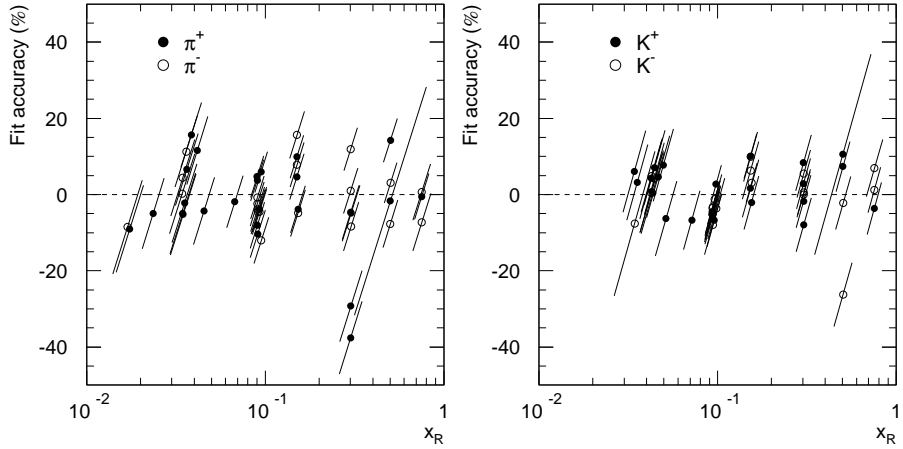


Figure 1.6: Percent difference between the best-fit prediction of the parameterization proposed in Ref. [38] and experimental data for pions (left) and kaons (right) as a function of x_R [38].

third approaches are based on constraining hadronic models with measured data.

The first approach was proposed by Bonesini *et al.* [38] after a careful study of the measurements of the NA20 and NA56/SPY experiments. The goal of the study was to find a suitable parameterization for the inclusive cross-sections of secondary meson production in proton target interactions. The NA20 and NA56/SPY experiments measured cross-sections for pions, kaons and protons in different transverse momenta as a function of secondary meson momenta for incident protons on a Beryllium target at 400 and 450 GeV/c. The proposed parameterization was given as:

$$\left(E \times \frac{d^3\sigma}{d^3p} \right) = A(1 - x_R)^\alpha(1 + Bx_R)x_R^{-\beta}(1 + \alpha'(x_R)p_T + b'(x_R)p_T^2)e^{-a'(x_R)p_T} \quad (1.58)$$

where $x_R \equiv E/E_{\max}$ is the ratio of the particle's energy to its maximum possible energy in the center of mass frame and the functions $a'(x_R) \equiv a/x_R^\gamma$ and $b'(x_R) \equiv a^2/x_R^\delta$ control the scale breaking of p_T . A fit to the data allowed to estimate the parameters of the empirical formula. The accuracy of the empirical formula can be tested by taking the ratio between the results of the parameterization and the measured data. This is showed in fig. 1.6.

The conclusion of the authors was that the proposed empirical formula are adequate to describe NA20 and NA56/SPY data with a 10% accuracy.

If the above formula seems to give a decent accuracy for the specific process of the interactions of 400 GeV/c protons on a beryllium target, it was further proposed by the authors to probe the formula once scaled to different incident proton momenta or different target materials. The scaling of the invariant cross-section to different incident proton momenta assumed to follow the Feynman scaling. Bonesini et al. compared their parameterization, scaled down to an incident proton energy of 24 GeV, with the measurements done by Eichten et al. [39] for proton berillyum interactions at 24 GeV. As can been seen on fig. 1.7, the estimated production of π^+ is about 35% lower than that measured while the agreement seems to be better for kaons.

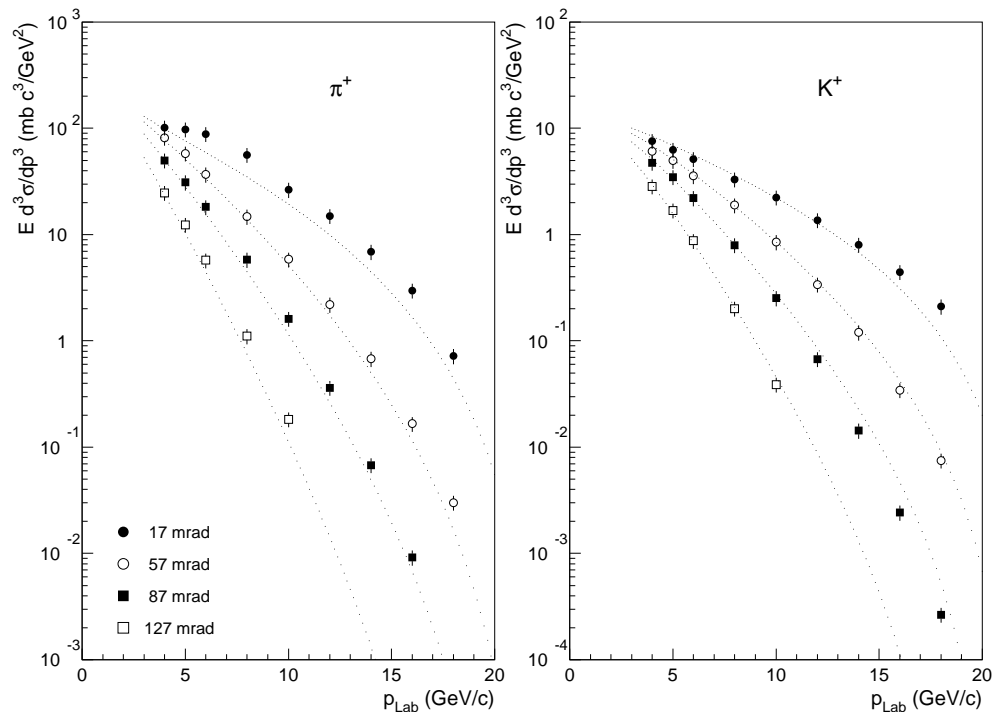


Figure 1.7: Comparison between the proposed parameterization of NA56/SPY and NA20 data (dotted line) and the one-pion (left) and one-kaon (right) inclusive invariant cross-sections in pBe interactions at 24 GeV as measured by Eichten et al. [38].

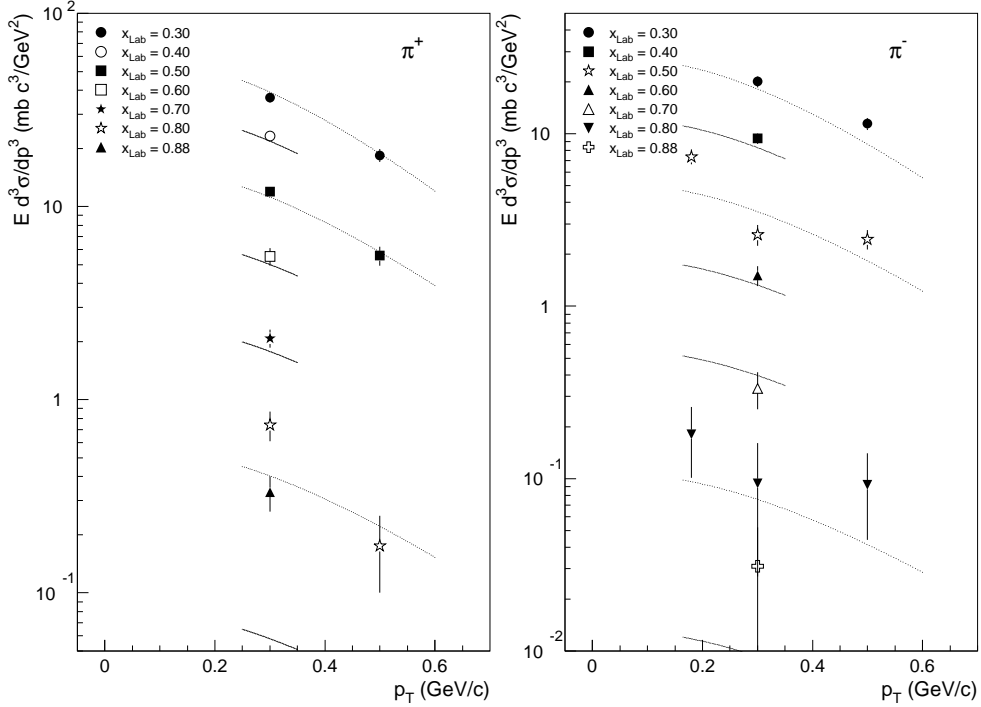


Figure 1.8: Comparison between the proposed parameterization of NA56/SPY and NA20 data (line) and the one-pion inclusive invariant cross-section in $p + C$ interactions at 100 GeV as measured by Barton et al. Positive (negative) pions are shown in the left (right) panel [38].

The scaling to different target material had already been studied by Barton et al. [40] and Skubic et al. [41]. It was concluded that the invariant cross-sections for hadron-nucleus interactions ($hA \rightarrow h'X$) depend on the mass number A of the target nucleus via parameterizations of the type:

$$E \frac{d^3\sigma^{hA_1}}{dp^3} = \left(\frac{A_1}{A_2} \right)^\alpha \cdot E \frac{d^3\sigma^{hA_2}}{dp^3} \quad (1.59)$$

where α is parameterized for different values of p_T as

$$\alpha(x_F) = (a + b \cdot x_F + c \cdot x_F^2) \cdot (d + e \cdot p_T^2) \quad (1.60)$$

To probe this scaling, a comparison of the proposed re-scaled parameterization with the measurements of Barton et al. for interactions of protons on carbon at 100 GeV was computed. Results can be seen on fig. 1.8. The agreement between pion data and the empirical parameterization is excellent at low x_{Lab} but gets quite far off at large x_{Lab} ($x_{Lab} = p/p_{inc}$, where p and p_{inc} are the momenta of the detected particle and of the incident proton in the laboratory reference frame).

It is easy to conclude that the above proposed parameterizations are of interest for a fast estimate of hadron production for a given target material and proton beam energy. Nevertheless, for a detailed prediction of produced particles on a thick target, uncertainties will rapidly become very important as many scalings to different incident nucleon momenta will be needed to describe re-interactions along the target. It is then not possible to use only these parameterization

methods to reach uncertainties as small as a few percent on neutrino predictions.

The second method consists of generating a prediction of neutrino flux by using Monte-Carlo simulation techniques. The full chain of interactions that enter into the generation of hadrons producing neutrinos is recorded. Using ancillary hadron production measurements it is then possible to re-weight each interaction along the chain and hence to constrain the model predictions with data. This method can make use of several hadron production data already available. Nevertheless, most of these data will have some discrepancies with the exact condition of the simulated neutrino beam. Either the incident nucleon momentum will have to be scaled or an extrapolation for different target material will have to be performed. Hence, when using this second method, different factors must be taken into account:

- interpolating between a sparse set of measurements at fixed values of produced particle momenta p or transverse momenta p_T
- extrapolating from measured yields off one nuclear target material to the one of relevance for the neutrino beam
- extrapolating to the correct incident projectile momentum on the target

For each of these factors, a systematic uncertainty will have to be estimated and will contribute in a non-negligible manner to a total uncertainty on the flux prediction.

The parameterizations as well as the scaling methods mentioned in the previous approach can be used for each of these factors. Nevertheless, as already mentioned, parameterizations and scalings do not always agree well with measured data and hence systematic uncertainties have to be estimated.

In a third approach, one can consider measuring hadron production yields off a replica target exploited in the neutrino beam line. In this case, the entire interaction chain does not need to be considered and the constraint on the hadron production is only made at the surface of the replica target. This approach should be less model dependent than the previous one but has the disadvantage that a very specific ancillary experiment has to be performed, using exactly the same target as the one exploited by the neutrino experiment.

This approach was followed by the MIPP experiment that took data with a replica of the NuMI target and more recently by the NA61/SHINE experiment that recorded events with a replica of the T2K target. In the case of MIPP, results are given as integrated multiplicities of π^+ for the whole target for different bins in transverse momenta as a function of longitudinal momentum. They are further normalized to the number of protons on target. As can be seen in fig. 1.9, comparisons with the MC predictions show large discrepancies of more than a factor two at low transverse momenta. No segmentation of the target in the longitudinal direction was considered. Nevertheless, particles produced at the upstream face of the target will contribute differently to the neutrino flux with respect to those exiting the downstream part of the target. This can be understood, in an intuitive way, with a geometrical argument. Particles exiting the upstream face of the target will be mainly produced at high angles with respect to the incident proton direction and hence have smaller momenta. They will contribute to the lower energy spectrum of the neutrino. Particles exiting the downstream part of the target might be produced at small angles with higher momenta and hence, contributing to the high tail of the neutrino energy spectrum. This means that giving integrated multiplicities over the entire length of the target could allow to constrain the integrated neutrino fluxes but probably not to constrain the shape of the spectra.

This aspect will be further discussed in the next sections. The analysis of the NA61/SHINE measurements of the T2K replica target will be discussed in details in the following chapters.

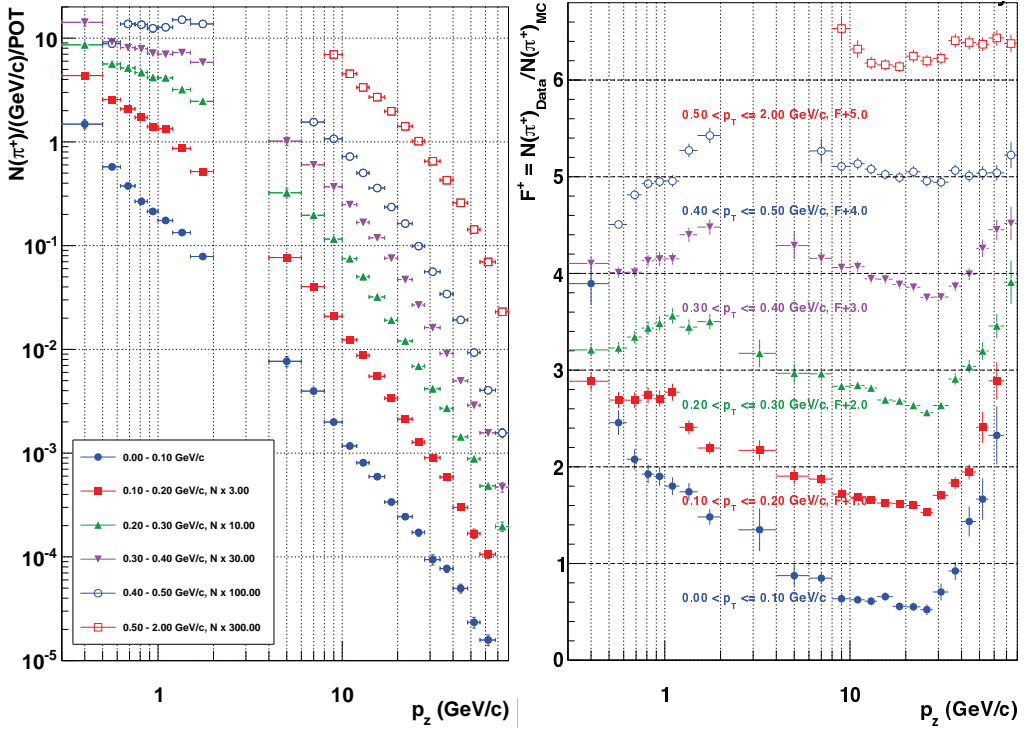


Figure 1.9: Yields of π^+ [42] (left) and ratios of data points to the GEANT4-based MC [43] (right) as a function of p_z in bins of p_T . Different colors and markers represent bins of p_T , and the yields are scaled and the ratios offset such that the points in different p_T bins do not overlap. Both statistical and systematic error bars are plotted.

1.4.2 Present knowledge and future goals of oscillation experiments

Since the discovery of a non-zero value of θ_{13} by the Daya Bay experiment [44] and its further high precision measurements, all mixing angles are known with good accuracy. The two mass splittings have been measured as well. The current values are listed in table 1.2.

The present goals of long baseline neutrino experiments are to measure the δ_{CP} phase, determine the mass ordering of the three neutrino mixing as well as to look for evidences for sterile neutrinos.

T2K and NO ν A are the two currently running experiments that could shed light on the above questions. Both experiments can run with a neutrino beam or antineutrino beam. Hence, measuring the oscillation probabilities $P(\nu_\mu \rightarrow \nu_e)$ and $P(\bar{\nu}_\mu \rightarrow \bar{\nu}_e)$ is a powerful tool for these experiments to extract information about the CP phase. As in June 2015, the T2K experiment's exposure is of 1.1×10^{21} protons on target, which represent $\sim 14\%$ of its proposed full statistics of 7.8×10^{21} protons on target.

Detailed studies have been conducted in order to show the future expected sensitivity for T2K on the δ_{CP} phase. In the studies, the reactor measurements are used to constrain the fits and the parameters related to θ_{12} and Δm_{12}^2 are fixed. All other parameters are allowed to vary. Systematic uncertainties used with the T2K analysis are included. Assuming that T2K will run for a time sharing of 50:50 between neutrino and antineutrino running, the expected sensitivity on δ_{CP} is presented in fig. 1.10. It is very important to note the strong dependence

	Normal Ordering ($\Delta\chi^2 = 0.97$)		Inverted Ordering (best fit)		Any Ordering
	bfp $\pm 1\sigma$	3σ range	bfp $\pm 1\sigma$	3σ range	3σ range
$\theta_{12}/^\circ$	$0.304^{+0.013}_{-0.012}$	$0.270 \rightarrow 0.344$	$0.304^{+0.013}_{-0.012}$	$0.270 \rightarrow 0.344$	$0.270 \rightarrow 0.344$
$\sin^2 \theta_{23}$	$33.48^{+0.78}_{-0.75}$	$31.29 \rightarrow 35.91$	$33.48^{+0.78}_{-0.75}$	$31.29 \rightarrow 35.91$	$31.29 \rightarrow 35.91$
$\theta_{23}/^\circ$	$0.452^{+0.052}_{-0.028}$	$0.382 \rightarrow 0.643$	$0.579^{+0.025}_{-0.037}$	$0.389 \rightarrow 0.644$	$0.385 \rightarrow 0.644$
$\sin^2 \theta_{13}$	$42.3^{+3.0}_{-1.6}$	$38.2 \rightarrow 53.3$	$49.5^{+1.5}_{-2.2}$	$38.6 \rightarrow 53.3$	$38.3 \rightarrow 53.3$
$\theta_{13}/^\circ$	$0.0218^{+0.0010}_{-0.0010}$	$0.0186 \rightarrow 0.0250$	$0.0219^{+0.0011}_{-0.0010}$	$0.0188 \rightarrow 0.0251$	$0.0188 \rightarrow 0.0251$
$\frac{\Delta m_{21}^2}{10^{-5} \text{ eV}^2}$	$8.50^{+0.20}_{-0.21}$	$7.85 \rightarrow 9.10$	$8.51^{+0.20}_{-0.21}$	$7.87 \rightarrow 9.11$	$7.87 \rightarrow 9.11$
$\delta_{CP}/^\circ$	306^{+39}_{-70}	$0 \rightarrow 360$	254^{+63}_{-62}	$0 \rightarrow 360$	$0 \rightarrow 360$
$\frac{\Delta m_{31}^2}{10^{-3} \text{ eV}^2}$	$7.50^{+0.19}_{-0.17}$	$7.02 \rightarrow 8.09$	$7.50^{+0.19}_{-0.17}$	$7.02 \rightarrow 8.09$	$7.02 \rightarrow 8.09$
$\frac{\Delta m_{32}^2}{10^{-3} \text{ eV}^2}$	$+2.457^{+0.047}_{-0.047}$	$+2.317 \rightarrow +2.607$	$-2.449^{+0.048}_{-0.047}$	$-2.590 \rightarrow -2.307$	$\begin{bmatrix} +2.325 \rightarrow +2.599 \\ -2.590 \rightarrow -2.307 \end{bmatrix}$

Table 1.2: Three-flavor oscillation parameters from our fit to global data after the NOW 2014 conference. The results are presented for the “Free Fluxes + RSBL” in which reactor fluxes have been left free in the fit and short baseline reactor data (RSBL) with $L \lesssim 100$ m are included. The numbers in the 1st (2nd) column are obtained assuming normal ordering (inverted ordering) of the masses, *i.e.*, relative to the respective local minimum, whereas in the 3rd column we minimize also with respect to the ordering. Note that $\Delta m_{3\ell}^2 \equiv \Delta m_{31}^2 > 0$ for NO and $\Delta m_{3\ell}^2 \equiv \Delta m_{32}^2 < 0$ for IO. All values taken from Ref. [45].

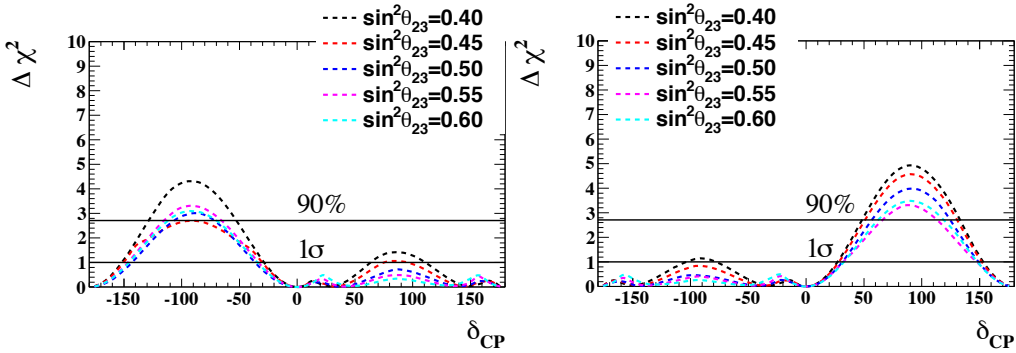


Figure 1.10: The expected $\Delta\chi^2$ significance to resolve $\sin \delta_{CP} \neq 0$ as a function of δ_{CP} for various values of $\sin^2 \theta_{23}$ in case of normal (left) and inverted (right) mass hierarchy. The T2K statistical and systematic uncertainties are included. A constraint based on the reactor measurements is used.

of the sensitivity on the value of $\sin^2 \theta_{23}$. T2K is well equipped for precise measurements of the θ_{23} mixing angle through disappearance analysis. This will play a crucial role on the exclusion plots of δ_{CP} .

Because the NO ν A experiment has a longer baseline than T2K (810km versus 295km) and the neutrino energy is higher (~ 2 GeV versus ~ 0.6 GeV) by a factor three, the matter effect is three times larger in NO ν A than in T2K. Therefore, NO ν A would have higher sensitivity to determine the mass hierarchy. The sensitivity study for the combination of T2K and NO ν A is based on the statistics quoted in the NO ν A assumed run plan: 1.8×10^{21} protons on target for the neutrino beam and 1.8×10^{21} protons on target for the antineutrino beam. Systematic uncertainties have been assumed to be the same for both experiments. Figure 1.11 shows the significance for $\sin \delta_{CP} \neq 0$ as a function of δ_{CP} and fig. 1.12 shows the significance on the mass hierarchy determination.

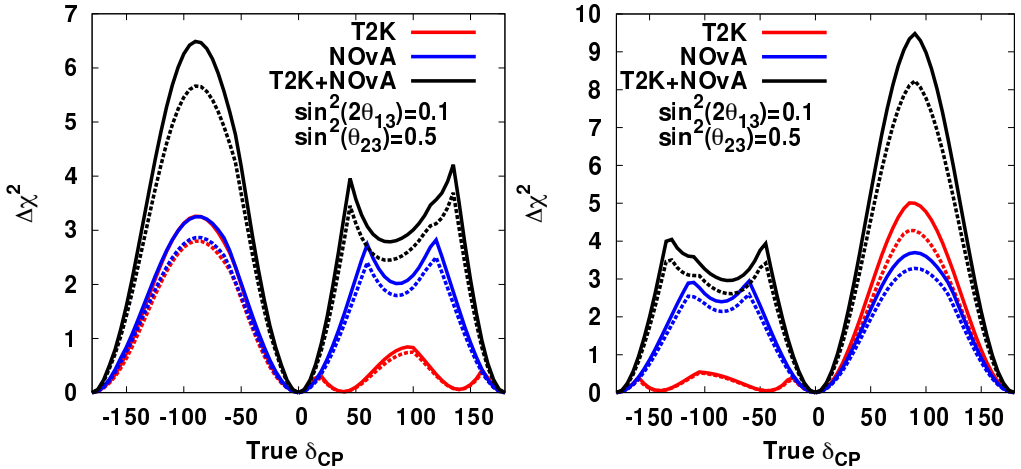


Figure 1.11: The expected $\Delta\chi^2$ significance to resolve $\sin \delta_{CP} \neq 0$ as a function of CP for T2K (red), NO ν A (blue), and T2K+NO ν A (black) with (dashed) and without (solid) systematics for 'true' values $\sin^2 \theta_{23} = 0.5$. The 'true' MH is the NH (top) or the IH (bottom) while the test MH is unconstrained

From fig. 1.10 to fig. 1.12 we can conclude that it will be mandatory to combine both experimental results in order to resolve the degeneracies between the mass ordering and the values of δ_{CP} .

Three future long base line oscillation experiments have been proposed with the last few years to try and resolve, with high significance, the mass ordering and the measurement of the CP phase. The LBNO in Europe propose an experiment with a beam from CERN to Finland. This base line of 2300km will be strongly sensitive to matter effects. As neutrino and antineutrino do not have the same behavior when they travel through matter, the important length of the base line will allow to have clearly different oscillation probabilities for $P(\nu_\mu \rightarrow \nu_e)$ and $P(\bar{\nu}_\mu \rightarrow \bar{\nu}_e)$. By running with neutrino and antineutrino beams, the LBNO predicts to reach a sensitivity better than 5σ for the determination of the mass hierarchy over the entire range of δ_{CP} . Knowing the mass hierarchy allows to disentangle the degeneracy for the measurement of the CP phase. The LBNO, after having determined the mass hierarchy predicts that CP-violation can be determined at the 90% C.L. for 60% of the CP parameter space.

The LBNE experiment (lately re-named DUNE) proposed in the US has comparable sensitivity. The base line of 1300km is shorter than the one of the LBNO and hence the significance

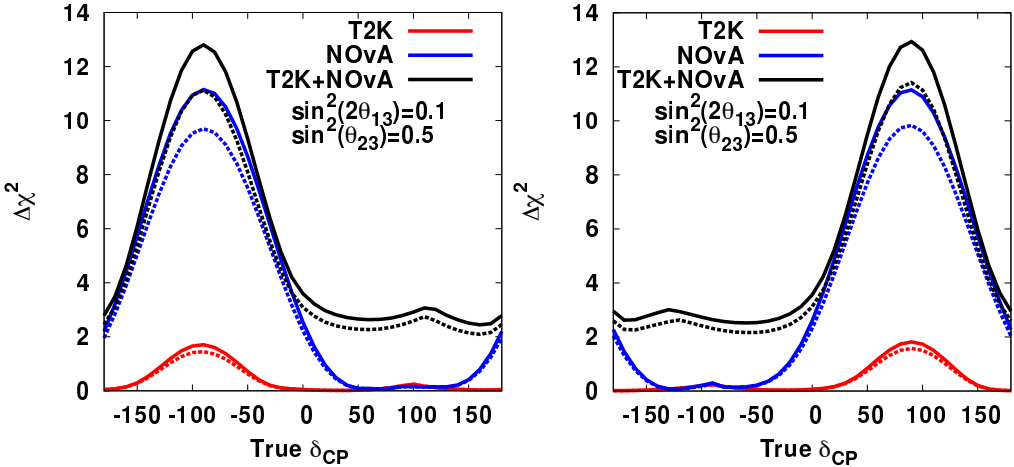


Figure 1.12: The expected $\Delta\chi^2$ significance to determine MH as a function of CP for T2K(red), NO ν A (blue), and T2K+NO ν A (black) with(dashed) and without (solid) systematics for 'true' values $\sin^2 \theta_{23} = 0.5$. The 'true' MH is the NH (top) or the IH (bottom) while the test MH is constrained to the opposite MH.

of the determination of mass hierarchy is a bit lower.

The proposed T2HK (Tokai to Hyper-Kamiokande) experiment has the shorter base line of the proposed future projects with 295km. It would use the same beam line for the generation of the neutrino beam as T2K and rely on the proton accelerator of the J-PARC laboratory in Tokai. Its sensitivity to mass hierarchy is well below the other two experiments. Nevertheless, the predicted sensitivity on δ_{CP} shows good values, with an exclusion of $\sin \delta = 0$ for 76% of the δ range at 3σ level and 58% of δ at 5σ level.

Obviously, all future accelerator-based neutrino experiments will need to handle very high intensity beams (of the order of MW) and very large mass detectors. Systematic uncertainties will need to be further reduced, which means a better knowledge of the neutrino beam generation as well as a better understanding of neutrino-nucleus cross-sections.

1.4.3 Present knowledge and future goals of cross-section experiments

Neutrino cross-section experiments play an increasingly important role in neutrino physics.

In neutrino oscillation experiments, the ability to reconstruct the neutrino energy is crucial to extract oscillation parameters in ν_μ disappearance measurements. The mixing angles and mass squared differences are inferred by comparing the far and near neutrino flux spectra. However, neutrino beams in present accelerator based experiments have a broad spectra in energy. Even with an "off-axis" technique, the beam cannot be approximated as being monochromatic in energy. Thus, an approximate reconstruction of the neutrino energy at the detectors would lead to an uncertain determination of the flux spectra, conducting to large errors on the extraction of oscillation parameters. Unfortunately, the neutrino energy is not measurable directly but has to be reconstructed from the reaction products, as for example in the interaction $\nu + N \rightarrow \ell^- + X$, from the measured energy of the lepton ℓ^- and the energy difference between the target nucleon N and the hadron final state X . Hence, a precise knowledge of neutrino cross-sections is a key point to know how to reconstruct, from the reaction products measured in a detector, the incident neutrino energy.

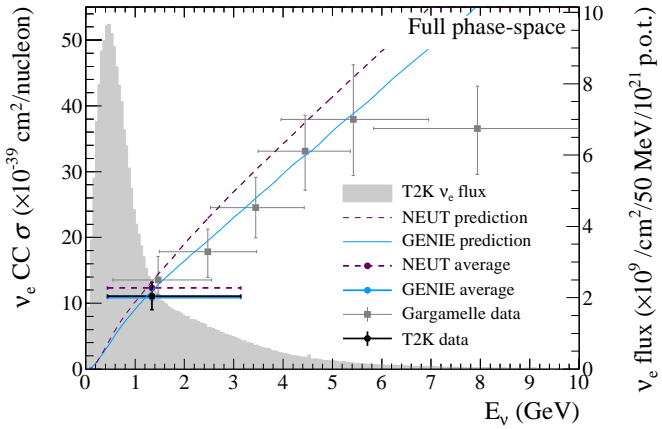


Figure 1.13: Total ν_e CC inclusive cross-section. The T2K data point is placed at the ν_e flux mean energy. The vertical error represents the total uncertainty, and the horizontal bar represents 68% of the flux each side of the mean. The T2K flux distribution is shown in grey. The NEUT and GENIE predictions are the total ν_e CC inclusive predictions as a function of neutrino energy. The NEUT and GENIE averages are the flux-averaged predictions. The Gargamelle data is taken from Ref. [46].

Current knowledge of neutrino cross-sections is diverse over energy ranges and neutrino flavor. Many measurements are available for muon neutrino and muon antineutrino while for electron neutrino and antineutrino only very few data are available.

In the electron flavor sector, experiments were mainly conducted with reactor antineutrinos or solar neutrinos. Hence, most of the cross-section results are available in the MeV energy range. The Gargamelle collaboration published some data at the GeV energy range and more recently the T2K experiment has released a measurement of inclusive electron neutrino charged current cross-section on carbon. Figure 1.13 shows the T2K results overlaid on the Gargamelle data. The Gargamelle collaboration published also results for electron antineutrino cross-section in the GeV range. They are presented in fig. 1.14.

In the muonic sector, even if neutrino and antineutrino cross-sections have been more extensively measured, there is still a lack of data in the energy range where future neutrino oscillation experiments plan to run, i.e. in the GeV range. Furthermore, as can be seen in fig. 1.15, where a summary of the current data is given, the GeV region is exactly where different processes contribute to the cross-section. Figure 1.15 shows all the available data (for references to all the different experiments the reader should consult [47]).

In the case of quasi-elastic scattering, the neutrino changes a nucleon in the nuclei but does not break it. For the resonance processes, the nucleon is put in a excited state that produces a new particle. In the deep inelastic regime, the neutrino has sufficient energy to break up the nucleon producing many subsequent particles. The Feynman diagrams of these three processes are represented in fig. 1.16.

It is easy to understand that a precise prediction of π production is mandatory for a strong constrain of the background coming from these particles being misidentified as electrons from $\nu_e n \rightarrow e^- p$.

In addition to these processes, it is also mandatory to take into account all nuclear effects, as most of neutrino interactions happen on nucleus (typically carbon, oxygen, iron) and not on a

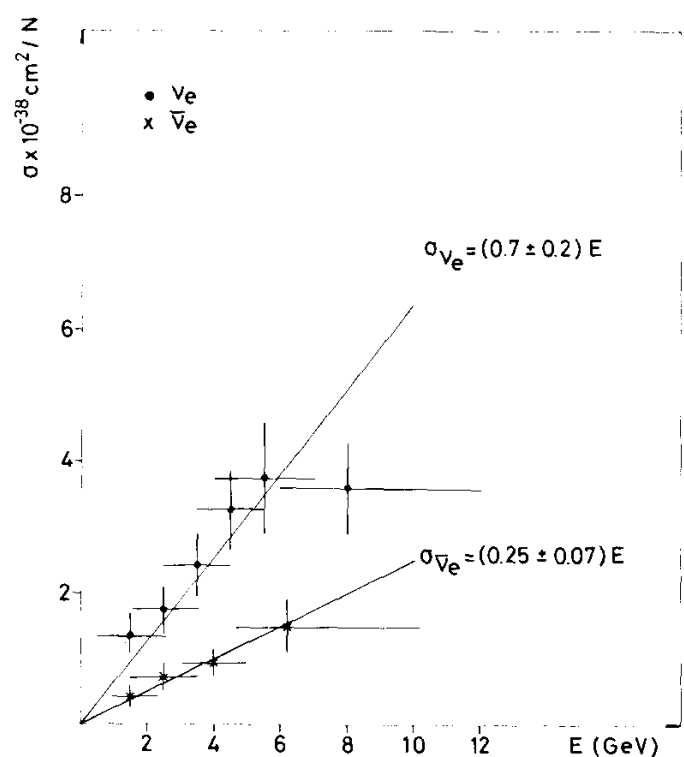


Figure 1.14: Neutrino and antineutrino cross-sections as a function of energy [46].

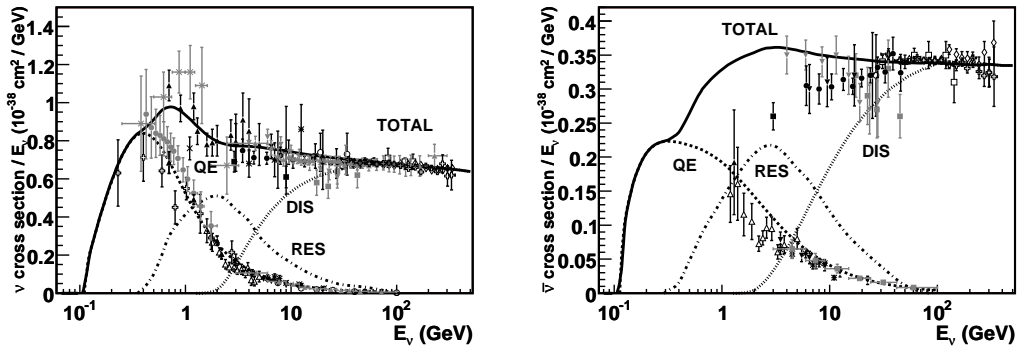


Figure 1.15: Total neutrino and antineutrino per nucleon CC cross-sections (for an isoscalar target) divided by neutrino energy and plotted as a function of energy. Also shown are the various contributing processes. These contributions include quasi-elastic scattering (dashed), resonance production (dot-dash), and deep inelastic scattering (dotted). Example predictions for each are provided by the NUANCE generator [48]. Note that the quasi-elastic scattering data and predictions have been averaged over neutron and proton targets and hence have been divided by a factor of two for the purposes of this plot [47].

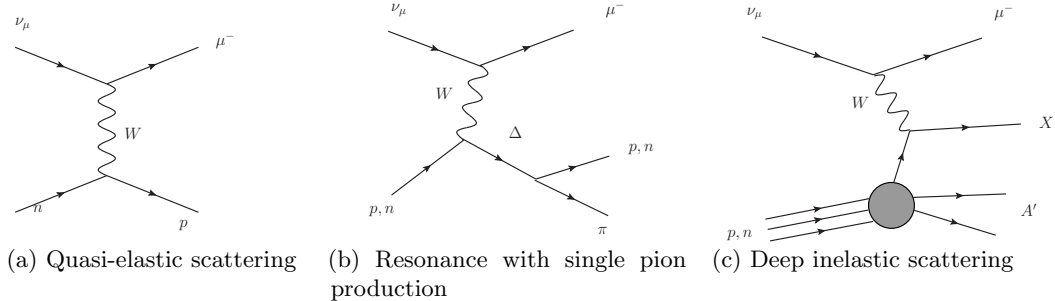


Figure 1.16: Diagram representations for the different processes of neutrino-nucleus scattering

simple free nucleon. We can mention here the effects known as meson exchange current (MEC), final state interactions (FSI) and random phase approximation (RPA).

In final state interactions, it is thought that within the nucleus, a particle (typically a pion) can be produced and directly re-interact with the other nucleon of the same nucleus. In this case, the intermediate particle would not be detected, as it does not leave the nucleus. And the measured energy of the particles exiting the target would be misinterpreted.

The meson exchange current process has also been tested to explain the recent neutrino cross-section results. Sometimes it is also mentioned as nph model. A schematic diagram of this process is presented in fig. 1.17. This naming comes from the fact that, as a product of the process, n protons can be extracted out of the nucleus, leaving n holes. In order for this process to happen, a particle exchange takes part between the n nucleons exiting the nucleus.

The random phase approximation is explained as a change of the weak interaction strength in nuclear media due to the presence of strongly interacting nucleons. This effect is non negligible for certain energies of incident neutrinos and can be as large as the FSI or MEC effects.

All these different nuclear effects will of course have different contributions for different incident neutrino energy. Hence, in order to properly understand the neutrino cross-section, it will be

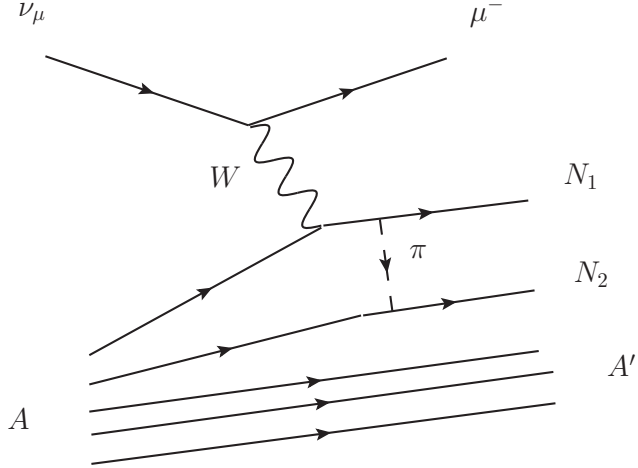


Figure 1.17: Schematic of the $2p2h$ process, where two nucleons are involved along with the neutrino interaction

mandatory to be able to understand these underlying effects as a function of neutrino energy.

A detailed study [49] showed the potential effect of these processes on the determination of the charged current quasi-elastic cross-sections for typical neutrino energies of 1 GeV as it is the case for present long base line experiments.

Cross sections are different for neutrino and antineutrino. As the strategy of neutrino oscillation experiments to measure δ_{CP} is based on the comparisons of neutrino and antineutrino oscillation probabilities through the asymmetry:

$$A = \frac{P(\nu_\mu \rightarrow \nu_e) - P(\bar{\nu}_\mu \rightarrow \bar{\nu}_e)}{P(\nu_\mu \rightarrow \nu_e) + P(\bar{\nu}_\mu \rightarrow \bar{\nu}_e)} \quad (1.61)$$

a poor knowledge of the differences between neutrino and antineutrino cross-section could produce a spurious CP violation effect. In addition, the oscillation probability is experimentally extracted from the observed signals in a set of near and far detector. This signal can be written in terms of the fluxes $\Phi_{ND}(\nu_\mu)$ and $\Phi_{FD}(\nu_\mu)$ at the near and far detectors, $\sigma_{ND}(\nu_\mu)$ and $\sigma_{FD}(\nu_e)$ the cross-sections at the near and far detectors, and $\epsilon_{ND}(\nu_\mu)$ and $\epsilon_{FD}(\nu_e)$ detector efficiencies as:

$$N_{FD}^{exp.}(\nu_e) = N_{ND}^{data}(\nu_\mu) \times \frac{\Phi_{FD}(\nu_\mu)}{\Phi_{ND}(\nu_\mu)} \times P(\nu_\mu \rightarrow \nu_e) \times \frac{\epsilon_{FD}(\nu_e)}{\epsilon_{ND}(\nu_\mu)} \times \frac{\sigma_{FD}(\nu_e)}{\sigma_{ND}(\nu_\mu)} \quad (1.62)$$

A poor knowledge of the ν_e and ν_μ cross-sections could again, potentially, give a fake CP violating effect through the $\sigma_{FD}(\nu_e)/\sigma_{ND}(\nu_\mu)$ term.

Furthermore, future experiments would surely not be satisfactory if they remain simple “counting” experiments. To learn more and extract more information on the oscillation parameters, it will be important to study as well the shape distortions due to oscillation process. Hence, it will become even more important to be able to precisely reconstruct the shape in energy of the measured neutrino flux in both, the far and near detectors of long base line experiments.

Neutrino cross-section measurements are also interesting by themselves in the sense that they allow for probing the $\mu - e$ universality. If the leptons are assumed to be different only by their masses but not by the way they interact, then their weak hypercharges should be identical. Hence,

probing the cross-sections for ν_e , $\bar{\nu}_e$, ν_μ and $\bar{\nu}_\mu$ allow to test this universality. The CHARM [50,51] and Gragamelle [46] experiments published comparisons of ν_e to ν_μ and $\bar{\nu}_e$ to $\bar{\nu}_\mu$ cross-sections. Their results confirmed the predictions from the Standard Model. Nevertheless, larger statistics and better constrains on systematics would surely bring interesting results.

Chapter 2

The T2K experiment

The T2K (Tokai to Kamioka) experiment [52] is a long baseline neutrino oscillation experiment located in Japan. An intense beam of muon neutrinos is generated at the Japan Proton Accelerator Research Complex (J-PARC) in Tokai. The beam is directed towards the Super-Kamiokande detector located under the mountains of western Japan, 295km from Tokai.

T2K was designed to pursue the following physics goals: to observe the $\nu_\mu \rightarrow \nu_e$ transition (and the measurement of non-zero value of $\theta_{13} \neq 0$), to take precision measurements of oscillation parameters in ν_μ disappearance (with expected precision of $\delta(\Delta m_{23}^2) \sim 10^{-4} \text{eV}$ and $\delta(\sin^2 \theta_{23}) \sim 0.04$), to search for sterile components in ν_μ disappearance by observation of neutral-current events and to have world-leading contributions to neutrino-nucleus cross-section measurements.

The T2K neutrino beam is created by the extraction of high energy 30 GeV protons from the J-PARC main ring accelerator and shooting them on a fixed graphite target. Hadrons (mainly pions and kaons) are produced as a product of the interaction of the primary beam protons with the target. A set of three magnetic horns collect the pions exiting the target surface and focus them in the direction of Super-Kamiokande. The polarity of the horn currents can be set to a positive or negative value and this allows the T2K experiment to run in so-called neutrino mode or antineutrino mode. Focusing positively charged pions allow to create a beam of muon neutrino while focusing negatively charged pion produces a antineutrino beam. A detailed description of this process will be given in the following sections. To study the neutrino oscillations, T2K uses the combination of a near detector (ND280) located at 280 meters from the target and a far detector (Super-Kamiokande (SK)) located 295 km from the target. The determination of the oscillation parameters is based on the comparisons between the predicted and measured observables at the far detector. In order to reduce the systematic uncertainties of the model dependent simulations, the near detector is used to constrain the predictions at SK.

At the near detector site, the effect of the oscillation is expected to be negligible. The simplest way to determine the oscillation parameters would then be to compute a far to near flux ratio. Nevertheless, it should be noted that the near detector, located at only 280 meters from the target sees a line source of neutrinos, while the far detector sees a point source of neutrinos. The extrapolation of the flux from the near to the far detector (without taking into account any oscillation phenomena) does not follow a simple $1/L^2$ behavior and is energy dependent. Hence, the measurements at ND280 are a necessary but not sufficient condition to reach the expected sensitivity by T2K on the oscillation parameters. A detailed knowledge of the hadron production off the graphite target is mandatory to further constrain the prediction of the neutrino flux. This will be further discussed in section 2.2. The precision on the far to near flux ratio has to be better than 3% in order to reach the T2K physics goals.

T2K started data taking for physics runs in January 2010. In the first paper published in 2011 [53], the indication of electron neutrino appearance in a muon neutrino beam could be demonstrated. Two following papers [54, 55] showed the evidence and observation of $\nu_\mu \rightarrow \nu_e$ transition. These measurements allowed to confirm a non-zero value for the θ_{13} mixing angle at a 7.3σ level.

The near detector complex has been also used to measure neutrino cross-sections. ND280 is a composite detector (see section 2.1.3) and was designed to record neutrino interactions on carbon and water. The first paper on inclusive ν_μ charged current cross-section on carbon in the near detector has been published in 2013 [56]. Since then, other studies have been conducted and published [57–59].

2.1 The experimental setup

The experimental setup of the T2K experiment can be divided into three parts: the beam line at J-PARC, the near detector complex (ND280) and the far detector (SK). The layout of the experiment is shown in fig. 2.1.

T2K is the first neutrino oscillation experiment to use an off-axis beam. The center of the beam points with a 2.5 degrees angle away from the SK detector. This method allows to generate a narrow band beam at the far detector. It is based on the kinematics of the pion decay. In this two-body decay, the energy of the emitted neutrino can be estimated, in a first approximation, as:

$$E_\nu = \frac{m_\pi - m_\mu}{2E_\pi - p_\pi \cos(\theta)} \quad (2.1)$$

where θ is the angle between the neutrino and its parent pion. The energy of the emitted neutrino can hence be plotted as a function of the pion parent energy for different θ angle. This is illustrated on fig. 2.2. For an on-axis beam, the neutrino energy is proportional to the pion energy. In the case of an off-axis beam, the neutrino energy varies slightly at low pion energy but then reaches a plateau and become independent of the pion parent energy. The neutrino beam will hence get peaked around this plateau. By varying the off-axis angle, the neutrino beam peak energy changes and can be set such that its maximum matches the neutrino oscillation maximum.

In the case of T2K, the base line is of 295km. Assuming a simple two neutrino flavor scheme with a maximal mixing angle and a square mass difference of $\Delta m^2 = 2.4 \times 10^{-3} eV^2/c^4$, the

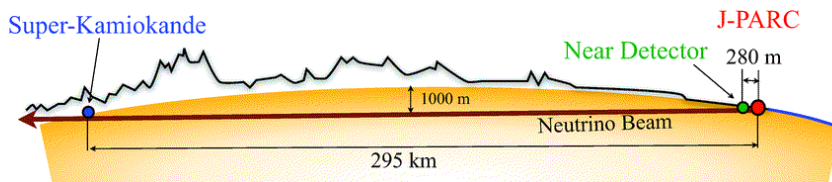


Figure 2.1: The T2K experiment layout [52].

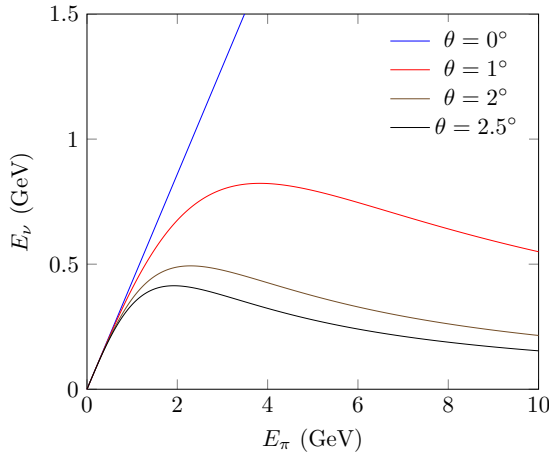


Figure 2.2: Energy of the emitted neutrino in the pion decay as a function of the parent pion energy for different angle between the parent pion and neutrino directions.

$P(\nu_\mu \rightarrow \nu_\mu)$ can easily be plotted on a graph as a function of the neutrino energy. The off-axis angle is then chosen so that the beam peak energy matches the minimum of $P(\nu_\mu \rightarrow \nu_\mu)$. Figure 2.3 shows the different fluxes for different off-axis angles and the comparison to the oscillation survival probability. It is clear that a 2.5 off-axis angle is the preferred value in the case of the T2K experiment.

2.1.1 The SK far detector

The Super Kamiokande detector is located in the Mozumi Mine in the Gifu Prefecture of Japan. It was built as (and still is) the world's largest water Cherenkov detector. It is a cylindrical tank, 39 m in diameter and 42 m in height. The capacity of the tank is 50 ktons of pure water. A layout of the Super-Kamiokande detector is presented on fig. 2.4. The volume of the tank is divided into 2 optically separated volumes. The inner dimensions are 33.8 m diameter and 36.2 m high. It defines the inner detector which contains 32 ktons of water. The inward-facing 11,129 photo-multiplier-tubes (PMTs) are instrumented in the inner tank. The coverage of the PMTs photocathode amounts to 40% of the inner detector surface. The outer detector is covered by 1,885 outward-facing PMTs. The main purpose of the outer detector is to distinguish between neutrino events and cosmic ray muon events. Neutrinos, as neutral particles, do not leave any Cherenkov signal before they interact within the detector. Cosmic ray muons, as high energy charged particles, will produce Cherenkov light as soon as they enter the detector. Hence, vetoing any signal in the outer detector allows to reduce the background from charged particles entering the detector.

Super-Kamiokande has a long data taking history and has produced well known results. It has participated to the explanation of the solar neutrino puzzle [61–64] as well as to the atmospheric neutrino problem [14, 65, 66]. It also holds the best upper limit on proton decay [67, 68]. The data taking started in 1996 and has gone through 4 phases. The first phase SK-I lasted from 1996 until 2001, when a shut down took place to upgrade the detector. During maintenance work, an accident occurred that made implose about half of the PMTs. The second period SK-II started in 2002 with only 19% of photo cathode coverage as the damaged PMTs could not all be changed before the planned restart of data taking. This second phase ended in 2005 and the replacement

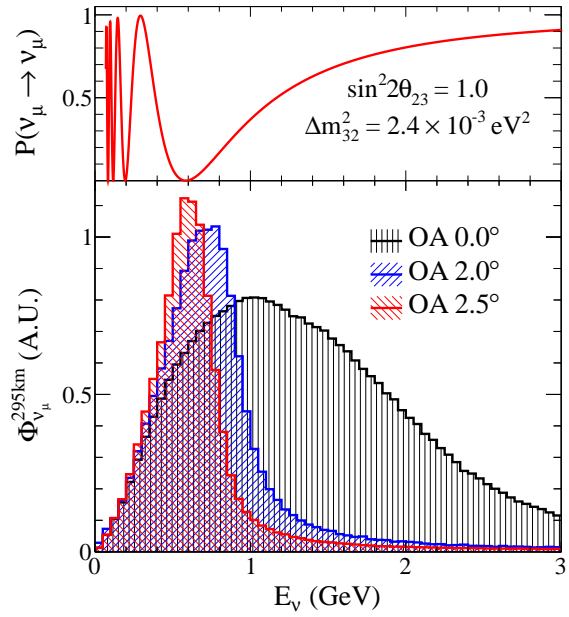


Figure 2.3: Muon neutrino survival probability at Super Kamiokande and the neutrino fluxes for different off-axis angles [60].

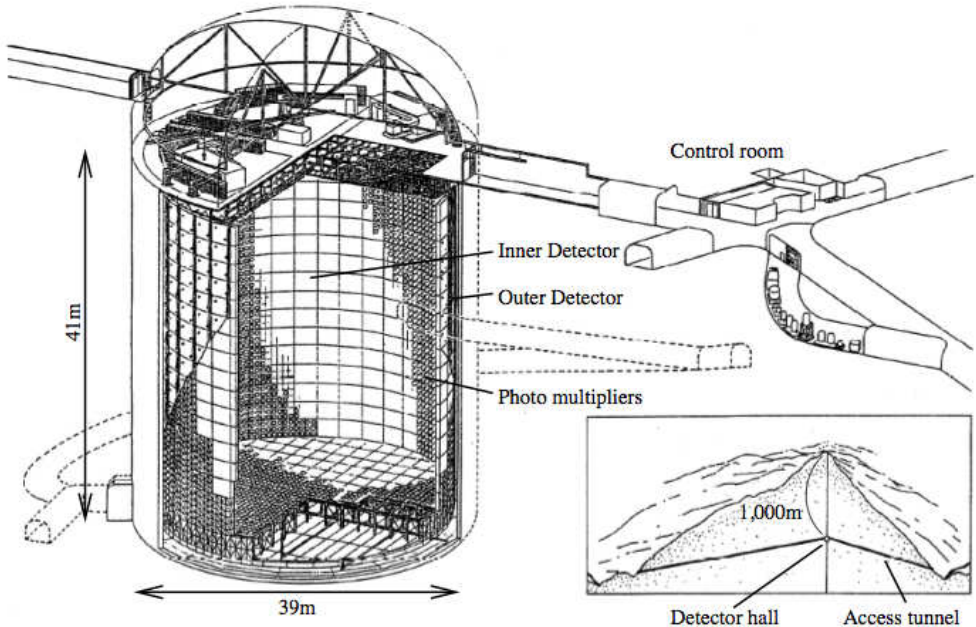


Figure 2.4: Layout of the Super-Kamiokande detector. The inner and outer detectors are marked. A support structure optically separates them and holds the PMTs [52].

of the dead PMTs could be conducted before the beginning of phase SK-III in July 2006. At the end of 2008, an upgrade of the electronics was conducted which allowed to handle a higher data rate processing. The T2K experiment is part of the present phase SK-IV which started at the end of 2008. For this phase, the DAQ was further extended so that it can trigger in time with the beam spills produced by the J-PARC accelerator. A 1ms window is open around each beam spill and all hits in SK are recorded. In addition, a GPS time stamp is passed to the SK computers for each beam spill. The offline processing of the SK events uses a software trigger to extract the neutrino candidates and pass them to T2K.

The events of interest in SK are the fully contained (FC) events, where the starting vertex is within the inner detector and the outgoing particle stopped with the inner volume. In this case only, all the relevant information can be extracted. The reconstruction of these events occur in four stages. First, the initial vertex is reconstructed, using the time difference between the fired PMTs and an initial track direction is calculated by searching for a well defined edge in the PMT charges. Second, an iterative algorithm is used to search for Cherenkov ring candidates. Third, an algorithm classifies the particle in electron-like or muon-like candidates by comparing the measured pattern to a calculated muon-like ring and to a Monte-Carlo generated pattern in case of electron. Finally, the reconstructed momentum for each particle is determined from the distribution of observed charge assigned to the particle's Cherenkov ring. The relationship between the observed charge and the particle momentum is established using Monte-Carlo simulation and detector calibrations from a number of different sources. It is clear that a well understood calibration of the detector is mandatory for a succesfull event reconstruction. Thanks to the long time running of the detector, the calibration processes are well controlled. The accuracy of the absolute energy scale is better than 1%, the timing resolution is better than 2ns, which gives very precise vertex reconstruction. The matching between the simulation of events in the detector and the calibration sample is better than 1% [69].

Figure 2.5 shows an example of events reconstructed in SK. Muons, as massive particles, create a sharp ring. Electrons, due to their small mass, undergo multiple scattering and produce electromagnetic showers. The created Cherenkov ring is more fuzzy.

The main goal of SK for T2K is to measure the neutrino flavor components of the beam in order to extract the relevant information concerning the disappearance of ν_μ and the appearance of ν_e . A charged current (CC) interaction is necessary because neutral current (NC) interactions are flavor independent. Of the CC interactions, the optimal signal is a charged current quasi-elastic (CCQE) interaction, given by:

$$\nu_e + n \rightarrow p + e^- \quad (2.2)$$

The proton does not usually acquire sufficient momentum to reach the Cherenkov threshold. So, only the electron can be observed in Super Kamiokande. The dominant background for the process eq. (2.2) will come from neutral pion decays, producing two gammas. If one of these two gammas is not reconstructed, or if the two gammas are not geometrically well separated, the event will be identified as an electron.

Thanks to its large mass and its very well understood calibration techniques, Super Kamiokande is a perfect detector for neutrino experiments at the energies of interest for T2K (~ 600 MeV). Muons and electrons at a few hundreds MeV leave a very clear track in the detector. Those energy correspond to a distance for a long base line neutrino oscillation experiments of a few hundreds km in order to match with the peak of the oscillation probability. It has then become very interesting to combine the Japan Accelerator Research Complex and its 30 GeV proton accelerator with the Super Kamiokande detector in order to set up a well designed neutrino oscillation experiment capable of conducting very precise studies on ν_μ disappearance and

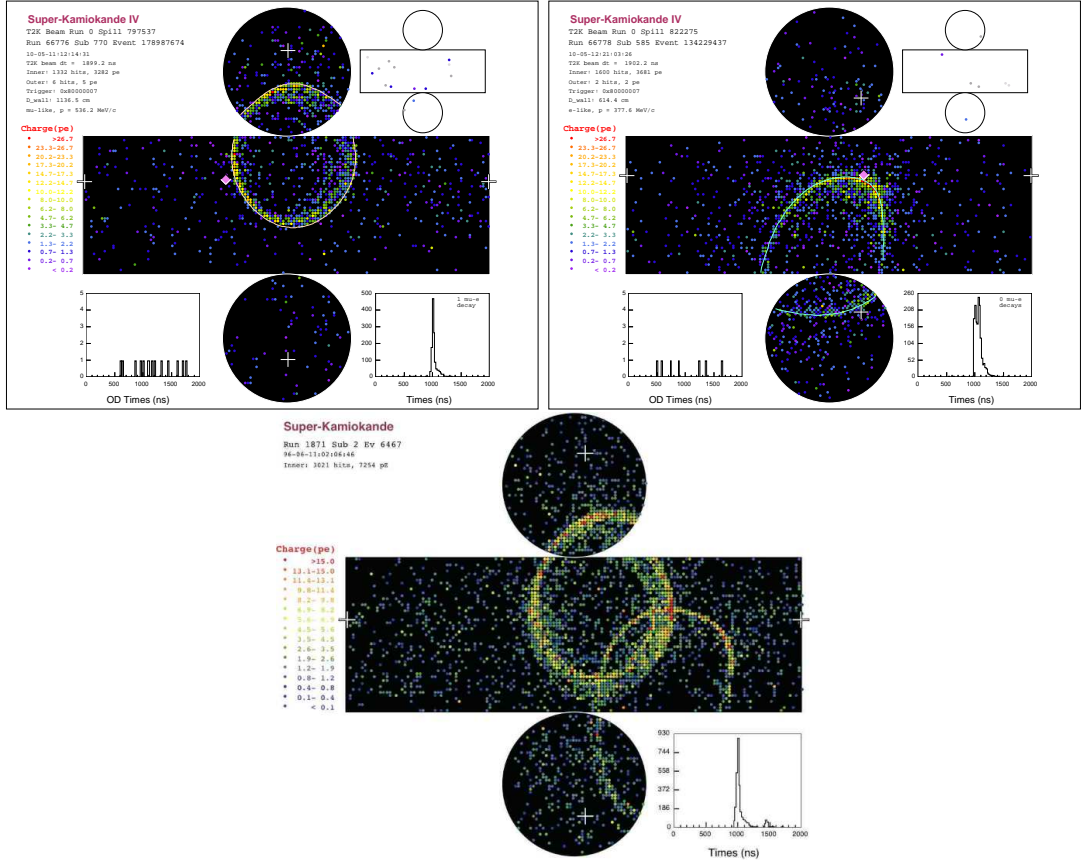


Figure 2.5: Example of reconstructed events in Super Kamiokande. A muon like ring (top left) and electron like ring (top right) [52]. The muons are less sensitive to multiple scattering and give a sharper ring than the electrons. A multiple ring event (bottom) [70] is a typical candidate for a π^0 event. If the two rings are not well separated or one of the two rings is not reconstructed, it can fake a electron like event. Fully contained events draw a ring on the detector walls.

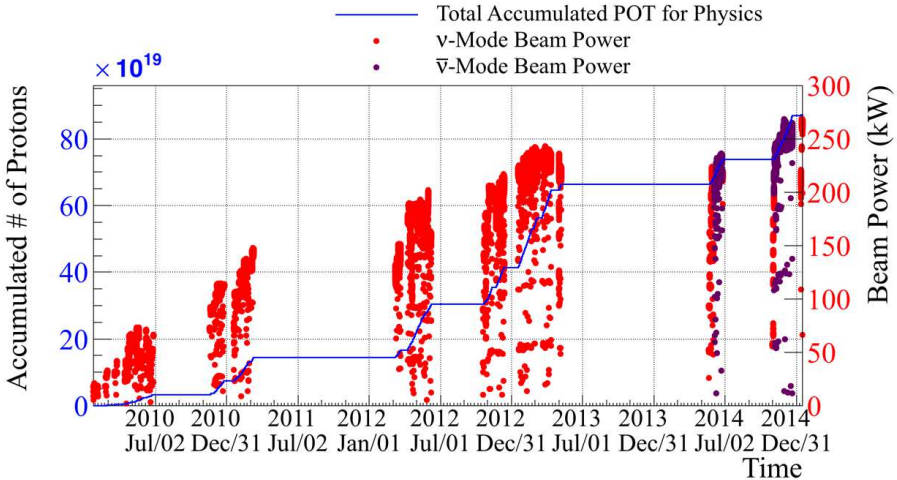


Figure 2.6: Accumulated number of protons on target versus time and related beam power.

ν_e appearance phenomenon.

2.1.2 The beam line

The T2K beam line is located at the Japan Accelerator Research Complex (J-PARC) on the east coast of Japan in Tokai. The J-PARC main ring accelerates protons to 30 GeV. A fast extraction from the main ring send the proton beam every 2.54 sec to the T2K beam line in form of spills. Each spill contains eight bunches in about $5\mu s$. The specifications of the designed beam line were based on an expected 750kW proton beam with 3.3×10^{14} protons per pulse. In June 2015, the beam power reached 371kW. Figure 2.6 shows the proton beam history.

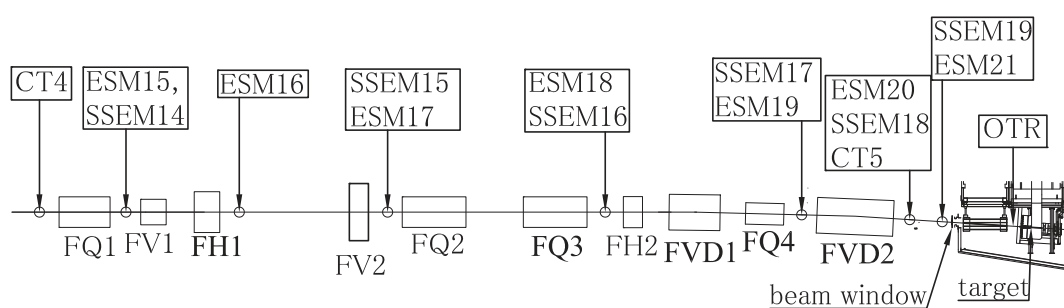
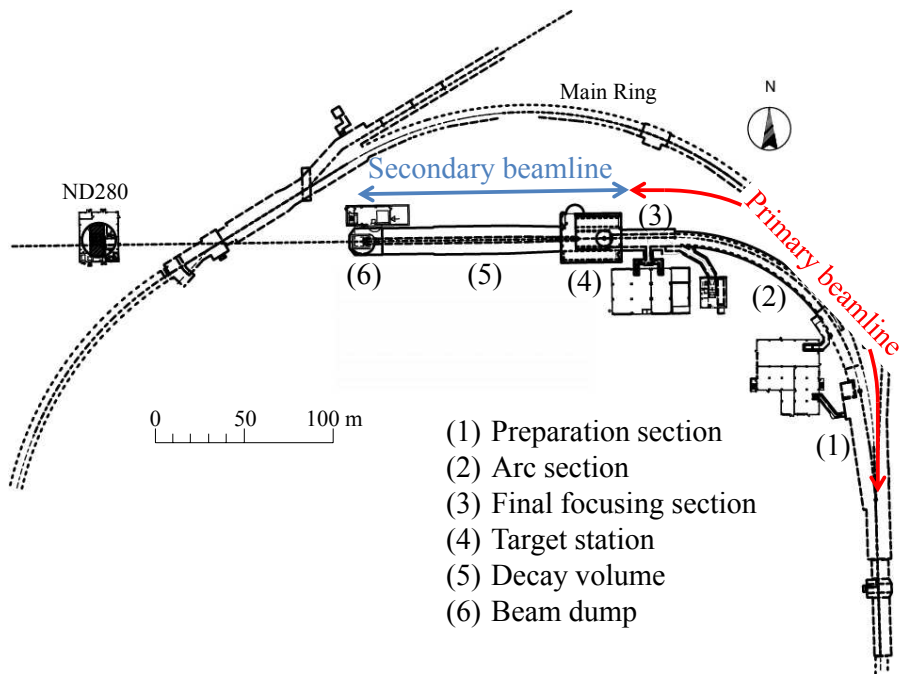
The neutrino beam line can be subdivided into two parts: a primary and a secondary beam line. Figure 2.7 shows an overview of the neutrino beam line with the two sections.

Primary beam line

The primary beam line guides and focuses the beam from the extraction point of the main ring to the T2K target upstream face. The arc section is composed of twenty eight superconducting magnets, each producing dipole (2.59T) and quadrupole (18.6 T/m) fields. In the final focusing section, a set of normal conducting magnets (four steering, two dipole and four quadrupole magnets) allow to control the beam profile and the beam direction to point downwards by 3.64 degrees with respect to the horizontal. Different type of detectors allow to monitor different aspects of the beam. A schematic layout of the beam monitors is presented in fig. 2.8. Five current transformers (CTs) allow to measure the beam intensity. Each CT is a 50-turn toroidal coil around a cylindrical ferromagnetic core. The uncertainty on the beam intensity from the CTs is 2%.

Twenty one electrostatic monitors (ESMs) determine the beam center position by measuring the top-bottom and left-right asymmetry of the beam induced current on the electrodes of the ESMs. This is a non destructive method as no interaction with the beam itself is required. The precision of the beam position determination with this method is better than $450\mu m$.

Nineteen segmented secondary emission monitors (SSEMs) measure the horizontal and vertical projections of the proton beam profile. A set of $5\mu m$ thick titanium foil strips is placed



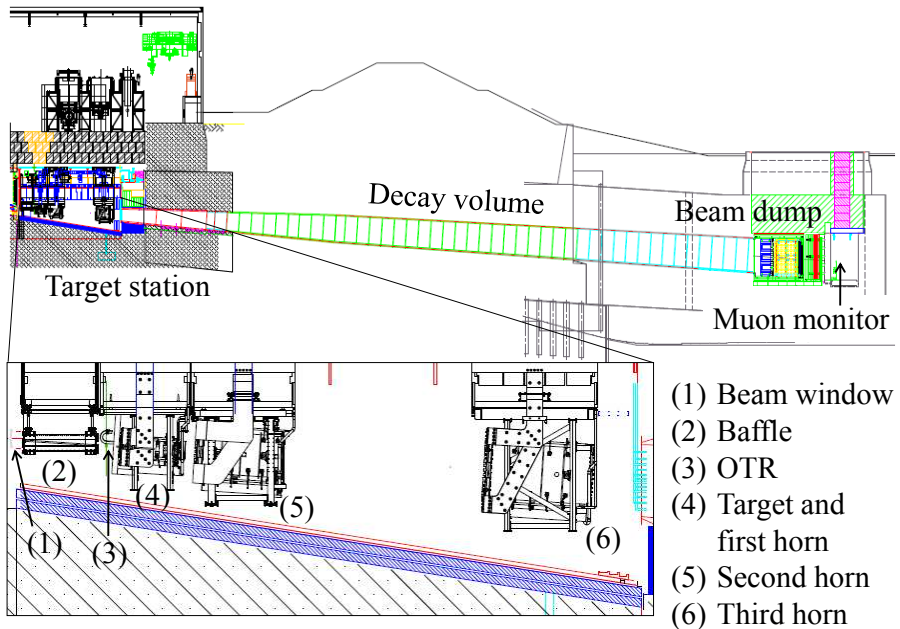


Figure 2.9: Side view of the secondary beam line [60].

horizontally and vertically in the plane perpendicular to the beam axis. A high voltage anode foil is placed between them. The measurements of the induced current on the strips give an image of the projections of the beam profile. The systematic uncertainty on the beam width measurements is $200\mu\text{m}$. This method causes a small loss of the beam. Hence SSEMs are in place only during the beam tuning and removed during the data taking period, except for the most downstream monitor.

Finally, an optical transition radiation (OTR) monitor, placed 30cm before the target upstream face allows to measure the two dimensional beam profile. This is done by imaging the transition radiation produced when the beam passes through the $50\mu\text{m}$ thick titanium allow foil. A detailed explanation of the OTR monitor can be found in Ref. [71].

The use of all monitors in the final focusing section allows to reconstruct the beam position at the entrance of the baffle with an accuracy better than 0.7 mm. These precise measurements of the beam characteristics will be extensively used to model the neutrino flux predictions for the near and the far detectors of T2K. It will be further discussed in section 2.3.

Secondary beam line

The secondary beam line covers the target station (including the focusing horns), the decay volume and the beam dump (with the following muon monitor). A side view of the secondary beam line is presented in figure fig. 2.9.

The target station includes a baffle, the OTR monitor (already described in the primary beam line section), the target and the three focusing horns. The baffle is a collimator whose role is to protect the rest of the target station from badly focused primary protons. It is a simple graphite block with a 30mm hole. The primary proton beam goes through this hole. It is cooled down by water cooling pipes. The target core is a 1.9 interaction length (91.4cm) and 2.6cm diameter graphite rode of density 1.83 g/cm^3 . A flow of cold gaseous helium circulates around the target

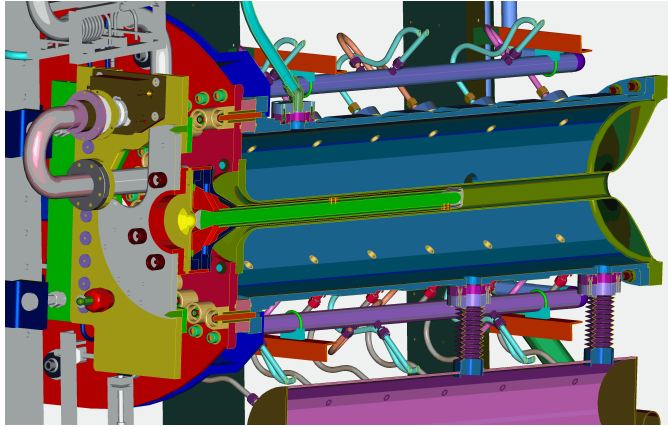


Figure 2.10: Drawing of the target inserted inside the first horn.

to cool it down during operation as an increase of 700 degrees in temperature is expected at the center of the target for the full 750kW beam power. The target is inserted into the first magnetic horn as it is shown in fig. 2.10.

T2K uses the combination of three magnetic horns. A detailed design study allowed to fix the sizes of the horns as well as their position with respect to the target [72]. Each horn consist of two coaxial conductors (an inner and an outer conductor). The toroidal magnetic field is generated by a current flowing into the conductors. The generated magnetic field decrease as $1/r$ with the distance from the center of the horn axis. A low frequency pulsed current, synchronized with the arrival time of the primary proton beam, is loaded into the horn. The design study shows that operating the horns with a current of 250kA allows to increase the neutrino flux at Super Kamiokande by a factor of 17 at the beam peak energy. This is shown in fig. 2.11.

The role of the first horn is to collect the pions exiting the target surface while the second and third horns have been designed to focus the pion beam to the decay volume. A 250kA current in the horns will produce a magnetic field that collects and focuses positively charged particles (π^+ and K^+), while defocussing negatively charged particles. This will produce a muon neutrino beam (with a small contamination of ν_e as it will be discussed later). In this case, the T2K experiment is said to run in “neutrino mode”. By reversing the current flow in the horns, negatively charged particles will be brought to the decay volume while positively charged particles will be tracked away from the beam axis. This will produce a muon antineutrino beam. We speak of “antineutrino mode”.

The decay volume is a 96m long tunnel filled with helium. The dimensions perpendicular to the beam at the upstream part of the tunnel are 1.4m in width and 1.7m in height. At the downstream end these dimensions are 3.0m wide by 5.0m high. Along the beam axis, 40 plate coils are welded on the steel wall, whose thickness is 16 mm, to cool the wall and concrete to below 100°C using water.

The beam dump, at the end of the decay tunnel, is still part of the helium volume. It consists of a core of 75 tons of graphite and is 3.174 m long, 1.94 m wide and 4.69 m high. Iron plates surround the graphite core. The beam dump is cooled by water so that its core will stay at a temperature around 150°C for a beam power of 750kW. Only muons above $\sim 5\text{GeV}/c$ can go through the beam dump and reach the muon detector.

The muon detector is located in a pit just after the beam dump. Measuring the muon beam profile and intensity on a bunch-by-bunch basis allows to monitor the neutrino beam intensity and

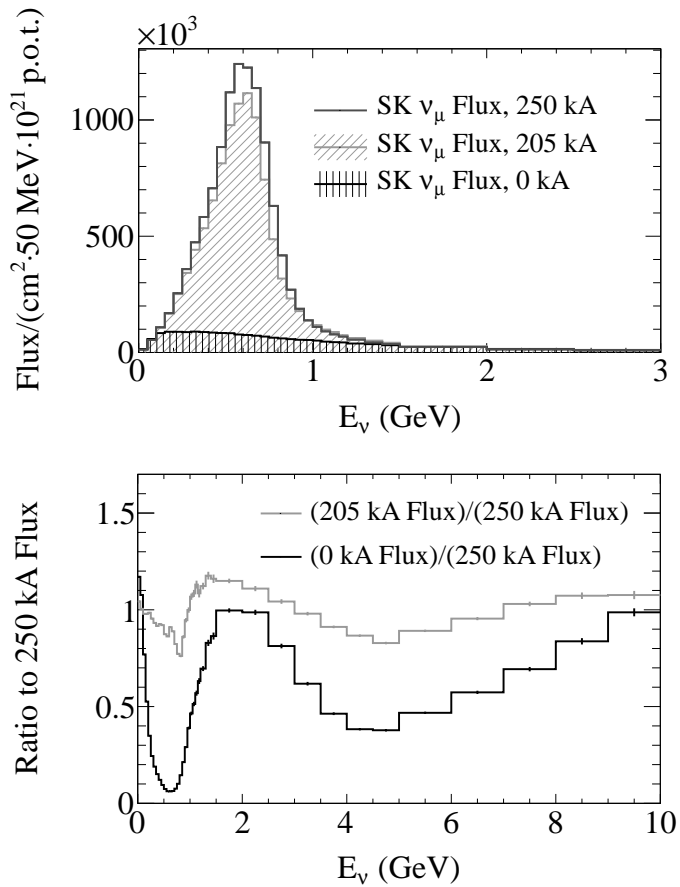


Figure 2.11: The predicted flux of ν_μ at the SK far detector for operation at different horn currents. The flux histogram (top) ranges from 0 to 3 GeV, while the ratios (bottom) range from 0 to 10 GeV [60].

direction as each muon is produced along with a neutrino in the pion decay. The neutrino beam direction is measured as the direction from the center of the target to the center of muon profile at the muon monitor. Two kind of detector arrays have been built. Silicon PIN photodiodes of dimensions $10 \times 10\text{mm}^2$ are followed by ionization chambers of dimensions $100 \times 100\text{mm}^2$. The silicon PIN photodiodes are not radiation tolerant and hence cannot be reliable on a long term scale in a full power beam operation. Nevertheless, for the actual beam intensity, the detector does bring interesting measurements. Packages of the photodiodes were designed so that installation or replacement of the photodiodes can be quickly done in situ.

An emulsion tracker has also been installed next to the muon monitor. It consists of two types of modules. One module, composed of eight emulsion films, which allow to measure the muon flux with a systematic uncertainty of 2%. The second module, composed of 25 emulsion films interleaved by 1 mm lead plates, allows to measure the momentum of each muon by multiple Coulomb scattering with a precision of 28% for a muon energy of 2 GeV/c. These films are analyzed by scanning microscopes.

The overall precision on the center of the muon profile is 2.95cm, which corresponds to 0.25 mrad precision on the beam direction.

2.1.3 The ND280 near detector complex

The Near Detector (ND280) is located 280 meters downstream from the target. As mentioned earlier, its primary goal for the oscillation studies, is to observe the unoscillated neutrino beam. It is also used to conduct neutrino-nucleus cross-section measurements. ND280 comprises an on-axis detector (INGRID) whose main role is to monitor the intensity and direction of the neutrino beam. A set of off-axis detectors are contained inside the magnet recycled from the UA1 and NOMAD experiments at CERN. It comprises a Pi zero Detector (P0D), three Time Projection Chambers (TPCs), two Fine Grained Detectors (FGDs), an Electromagnetic Calorimeter (ECal) and a Side Muon Range Detector (SMRD). Figure 2.12 shows the layout of the different ND280 off-axis sub-detectors in the UA1 magnet.

The INGRID on-axis detector

INGRID (Interactive Neutrino GRID) is a neutrino detector. It is shaped as a cross, centered in the neutrino beam axis. It consists of fourteen identical modules: two identical groups along the horizontal and vertical axis, and two additional separate modules located at off-axis directions outside the main cross, as shown in fig. 2.13. The center of the cross, with two overlapping modules, is aligned with the primary proton beam line. The accuracy of the positioning of the 16 modules is 2mm in the direction perpendicular to the beam.

Each module is composed of a sandwich structure of nine iron plates and eleven tracking scintillator planes. The dimensions of the iron plates are $124\text{cm} \times 124\text{cm}$ in the x and y directions and 6.5 cm along the beam direction. The total iron mass serving as a neutrino target is 7.1 tons per module. Each of the 11 tracking planes consists of 24 scintillator bars in the horizontal direction glued to 24 perpendicular bars in the vertical direction. The light emitted by the scintillator bars is collected by wavelength shifting fibers which are read out by MPPC's. The timing resolution of each channel is measured to be 3.2 ns.

Using the number of observed neutrino events in each module, the beam center is measured to a precision better than 10 cm. This corresponds to 0.4 mrad precision at the near detector pit. Figure 2.14 shows an example of the neutrino beam profiles measured in the x and y directions.

Furthermore, the INGRID detector allows to monitor the neutrino beam intensity. Figure 2.15 shows an example of such intensity monitoring. It is normalized to 10^{14} protons on target.

A complete description of the INGRID detector and its capabilities can be found in Ref. [73].

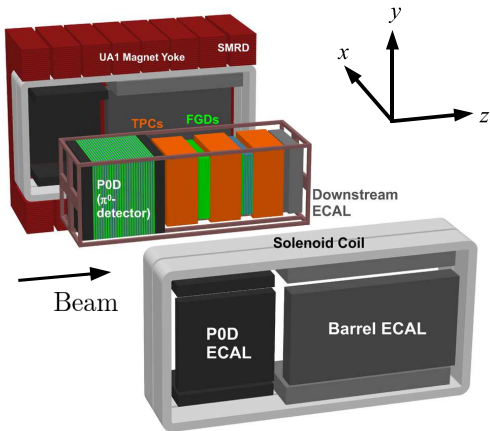


Figure 2.12: Layout of the off-axis detectors of ND280 embedded in the UA1 magnet [52]

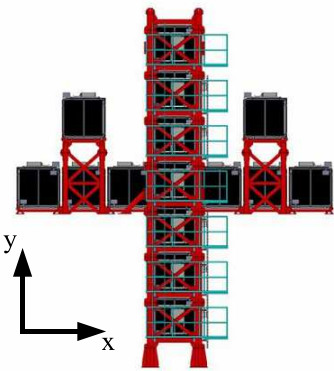


Figure 2.13: INGRID on-axis detector

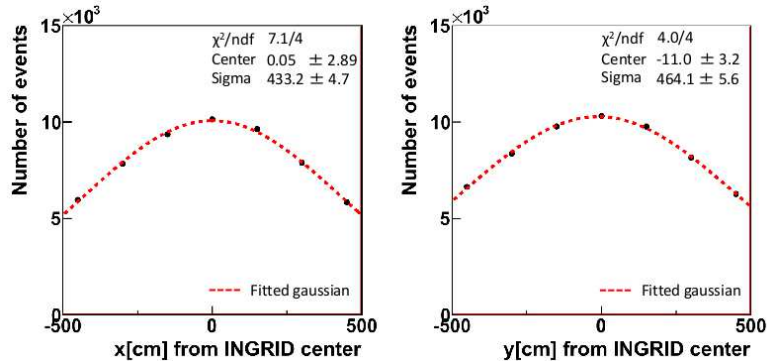


Figure 2.14: Example of Neutrino beam profiles for x (left) and y (right) directions as measured by INGRID [60].

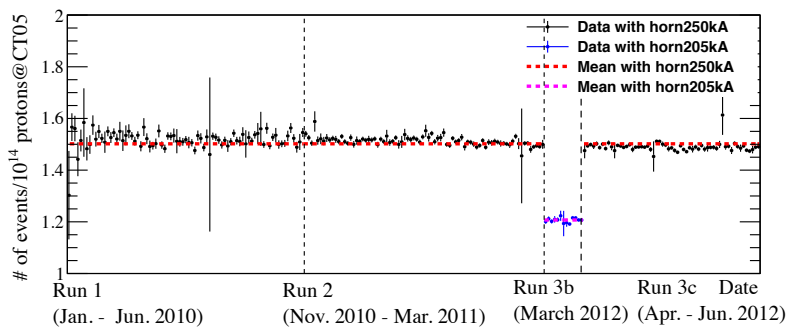


Figure 2.15: Neutrino events per 10^{14} POT measured by INGRID (points) overlaid with mean value (dashed lines). The error bar represents the statistical error on INGRID measurement [60].

The P0 detector

As mentioned earlier, π^0 particles cause a problem in the SK detector as they can easily be misidentified as an electron signal. A good knowledge of the interactions able to produce π^0 at SK is mandatory to reduce this background. The primary objective of the P0D is to measure the neutral current process $\nu_\mu + N \rightarrow \nu_\mu + N + \pi^0 + X$ on a water (H_2O) target with the same neutrino beam flux as reaches Super-Kamiokande. In addition the P0D will constrain the intrinsic ν_e content of the beam flux which is an irreducible background to the ν_e appearance measurement. The P0D detector is located off-axis, at the most upstream part of the UA1 magnet. It consists of two dimensional planes in the vertical and horizontal directions made out of scintillator bars. Each bar is read out with a single wavelength shifting fiber. The planes are interleaved with water bags that can be filled and emptied to allow a subtraction method to extract the cross-section on water. At the upstream and downstream part of the P0D detector, scintillator bar planes are interleaved with lead plates as can be seen in fig. 2.17. This layout improves the containment of electromagnetic showers and provides a veto region before and after the water target region to provide effective rejection of particles entering from interactions outside the P0D. The total target mass of water when the bags are full is measured as 1902 ± 16 kg.

A detailed description of the P0D and the current measurements of the total flux averaged neutrino induced neutral current elastic scattering cross-section can be found in Ref. [74].

The time projection chambers

Three time projection chambers (TPCs) are embedded inside the magnet. Two fine grained detectors are placed in between the second and the third TPC. The main role of the TPC is to track particles through ND280 in order to have good particle identification and precise momentum determination of these particles through the measured curvature of the tracks in the magnetic field. The UA1 magnet provides a magnetic field of approximately 0.2 T. Figure 2.16 shows a simplified drawing of the TPCs. When a charged particle flies through the gas mixture ($Ar : CF_4 : iC_4H_{10}$ (95:3:2)) of the TPCs, ionization of the atoms liberate electrons that drift in the electric field away from the central cathode to one of the readout planes. At the readout planes, electrons are accelerated by a higher electric field and they multiply. Twelve Micromegas modules at each sides of the TPCs are used to read out the collected charge signal on pads. The spacial information on the pads, combined with the arrival time information allowed to reconstruct the tracks in three dimensions.

A careful monitoring of the gas admixture as well as the pressure and temperature is mandatory for a precise knowledge of the electron drift velocity in the TPCs. In addition a calibration system produces a well defined pattern of photoelectrons by flashing a thin aluminum foil glued on the central cathode with a pulsed light. Measuring the signals of these photoelectrons allow to precisely monitor the electron drift velocity but also to monitor any distortion of the drifting direction due to inhomogeneities of the electric field or misalignment between the electric and magnetic fields.

The three TPCs have shown good spatial resolution performances, allowing to achieve a 10% resolution on the transverse momentum as can be seen on fig. 2.18.

The measurement of the energy loss, in conjunction with the momentum measurement, allow for particle identification in the TPCs. An example of energy loss as a function of momentum for negatively charged particles can be seen in fig. 2.19. The separation between electrons and muons is clear and the resolution of deposited energy obtained is about 7.8% for minimum ionizing particles, better than the design requirement of 10%.

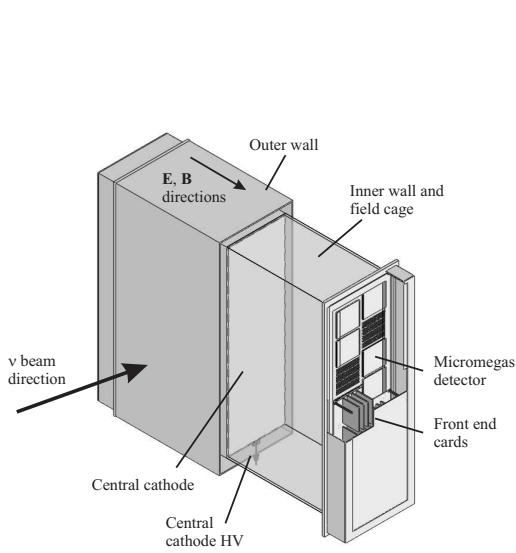


Figure 2.16: Technical drawing of the TPC design. The outer dimensions are approximately $2.3m \times 2.4m \times 1.0m$ [75].

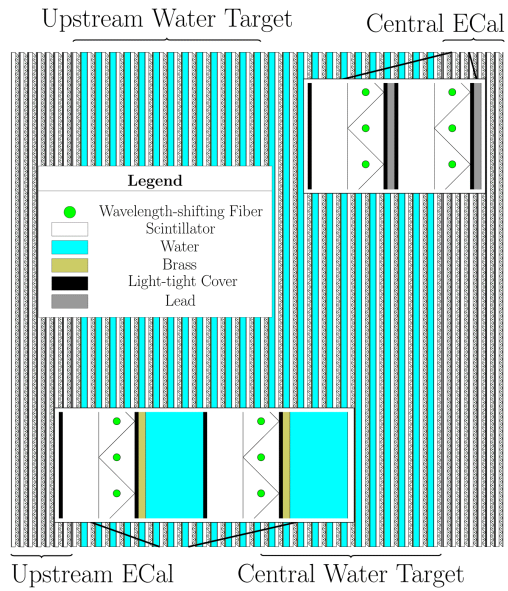


Figure 2.17: A schematic of the pi-zero detector. The beam is coming from the left and going right. Insets show details of the Water Target super-P0Dule layers and Central ECal layers [76].

The fine grained detectors

The ND280, as any neutrino detector, needs mass to increase the neutrino interaction rate. The Fine Grained Detectors (FGDs), placed in between the TPCs, help to bring this mass to the near detector complex. In addition, they are designed to track the charged particles so that their entire path across ND280 can be reconstructed with minimal dead spaces. The first FGD is composed only of scintillator planes mounted in the x and y planes, perpendicular to the neutrino beam direction. Its mass is about 1.1 tons. In the second FGD, layers of water have been inserted in between the scintillator planes. This allows complementary measurements with the P0D for neutrino water interaction cross-section. Comparing the interaction rates in the two FGDs permits separate determination of cross-sections on carbon and on water.

As for the P0D, the FGDs bars are read out with wavelength shifting fibers connected to photosensors. More about the design and performance of the FGDs can be found in Ref. [77].

The first FGD has already been used as a target for the measurement of neutrino carbon cross-section. Published results can be found in Ref. [56, 59].

The electromagnetic calorimeter

The Electromagnetic calorimeter (ECal) surrounds the P0D, the TPCs and the FGDs inside the UA1 magnet. Its main goal is to detect the outgoing photons as well as tracking the charged particles. The coverage of the electromagnetic calorimeter detector is almost hermetic to any particle exiting the inner detectors. Six Barrel-ECal modules surround the tracker volume on its four sides parallel to the z (beam) axis; one downstream module (Ds-ECal) covers the downstream exit of the tracker volume and six PoD-ECal modules surround the P0D detector volume.

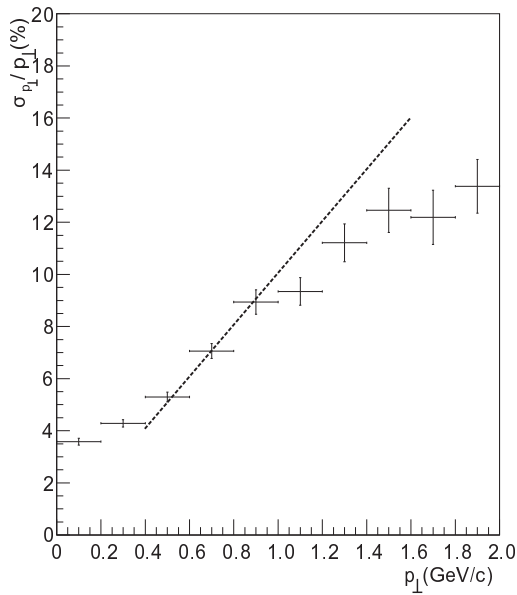


Figure 2.18: Momentum resolution for a single TPC is shown as a function of momentum perpendicular to the magnetic field as predicted by the Monte Carlo simulation of muons generated with the standard neutrino event generator of T2K. The dashed lines represents the momentum resolution goal.

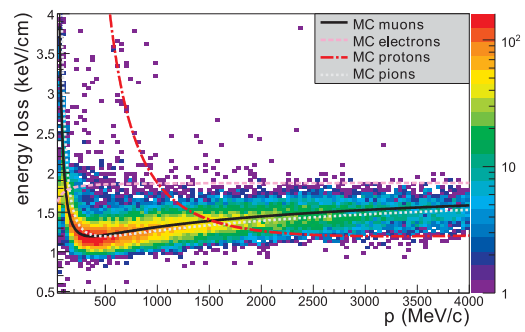


Figure 2.19: Distribution of the energy loss as a function of the momentum for negatively charged particles produced in neutrino interactions, compared to the expected curves for muons, electrons, protons, and pions.

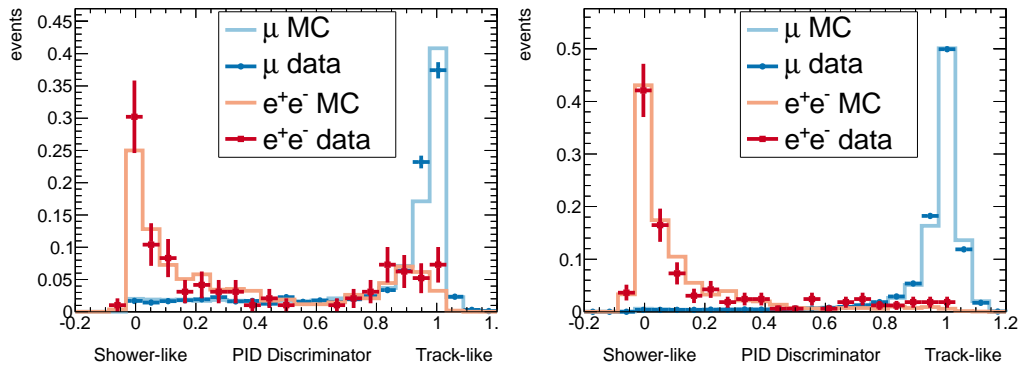


Figure 2.20: The discrimination between track-like (muon-like) and shower-like (electron-like) samples in the barrel-ECal (left) and in the Ds-ECal (right). Solid lines show Monte Carlo information and points show data [78].

The ECal uses plastic scintillator bars as active material with lead absorber planes interleaved in between the plastic bars. As for the other detector using scintillator bars, the light signal from the bar is transmitted to a wavelength shifting fibers running though the bar. The fibers are read out by MPPCs.

The ECal forms an important part of the ND280 and is essential to obtain good measurements of neutral particles and electron/positron showers that lead to correct particle identification and improved energy reconstruction. An example of the ECal capabilities for the particle identification is showed in fig. 2.20.

More details about the ECal can be found in Ref. [78].

The side muon range detector

The side muon range detector (SMRD) has three key functions. It records the muons escaping the inner detectors with large angles with respect to the beam direction and measures their momenta. It is also used to trigger on cosmic ray muons that enter ND280 as there is no overburden to protect the detector. Those cosmic ray events can later be used for detector calibration. Finally, it helps to identify interactions of the beam in the surrounding material of the inner detector, mainly the cavity walls and the iron of the magnet.

The UA1 magnet consists of sixteen flux return yokes which are grouped in pairs. Each yoke is made out of sixteen iron plates which are spaced at a distance of 17mm. The SMRD consists of a total of 440 scintillator modules which are inserted in these 17 mm air gaps between the iron plates. Due to the differently sized spaces for horizontal and vertical gaps, horizontal modules are composed of four scintillation counters with dimensions $875\text{mm} \times 167\text{mm} \times 7\text{mm}$ (lengthwidthheight) and vertical modules consist of five scintillation counters with dimensions $875\text{mm} \times 175\text{mm} \times 7\text{mm}$. The counter sizes have been optimized to maximize the active area in each magnet gap. In order to extract the light from the scintillator, a wavelength shifting fibers follow a serpentine route through the module as it is displayed in fig. 2.21. This configuration maximizes the light collection in the fiber. MPPCs identical to other inner detectors are used to read out the wavelength shifting fibers. In order to be able to measure high angle tracks with good precision, the SMRD needs to have an excellent time resolution. The timing resolution of counters, defined as the uncertainty on the time difference recorded at both end of the module ($(T_{left} - T_{right})/2$) was measured as function of light yield (fig. 2.22). The position resolution of a counter along its major axis based on both time difference between signals at both counter

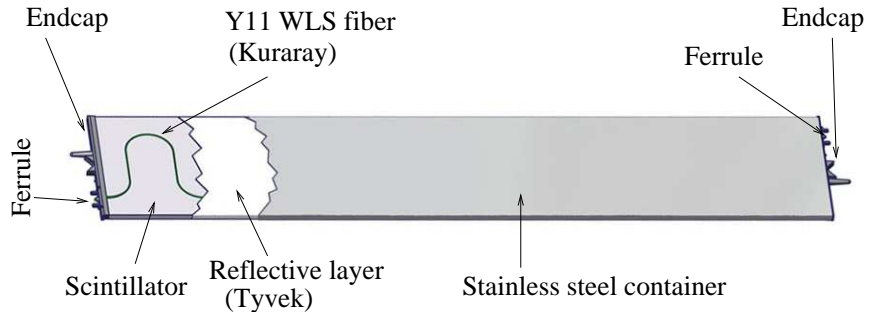


Figure 2.21: SMRD counter sliced view with the start of the serpentine route for the wavelength shifting fiber [79].

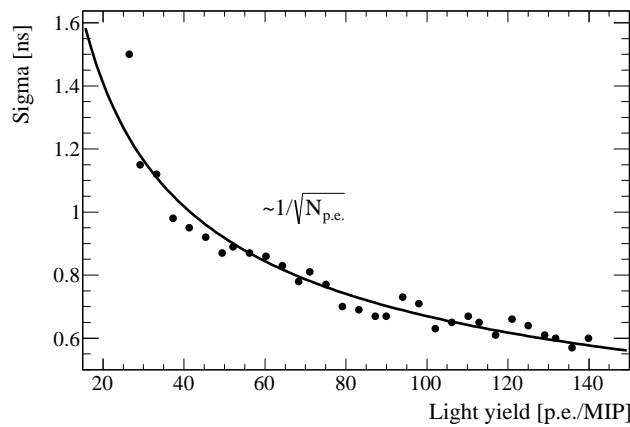


Figure 2.22: Time resolution of a SMRD counter versus light yield. The data are recorded in response to cosmic muons penetrating the center of the scintillator slab [79].

ends and the charge asymmetry between the signals was estimated and found to be of the order of 8.5 cm.

Detailed explanations about the SMRD calibration and performances can be found in Ref. [79].

2.2 The importance of an accurate neutrino flux predictions

T2K, as a long base line neutrino oscillation experiment, makes use of a near detector to constrain the predicted flux at the far detector. The oscillation parameters can be extracted from the signal observed in the far detector. In an ideal scenario, if the near and far detector would be identical in their construction and if the neutrino flux seen by both detector would be similar, most of the systematic uncertainties in a ratio of the far detector flux over the near detector flux (so-called far-to-near flux ratio) would cancel. And the oscillation parameters could be extracted with high precision though this far-to-near flux ratio. In reality, as we have seen in previous section, the near and far detector are quite different. Furthermore, the near detector is relatively close to the target and hence sees a line source of neutrinos, while the far detector sees a point-like source of neutrinos. This translates in a far-to-near flux ratio that is energy dependent as illustrated in fig. 2.23. It shows the predicted far-to-near flux ratio for the ν_μ flux as predicted with a T2K Monte-Carlo simulation of the neutrino beam.

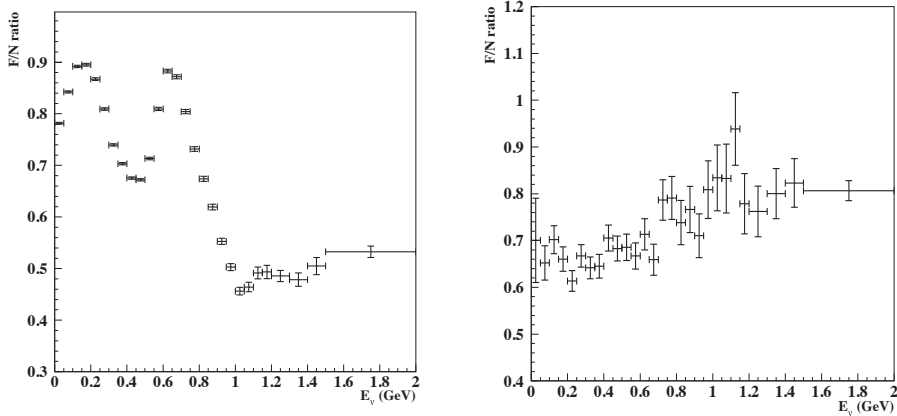


Figure 2.23: Far-to-near flux ratio for the ν_μ flux as a function of the neutrino energy

The systematic uncertainties related to the flux cancel to a limited extent but cannot be neglected as in the case of identical fluxes in the near and far detectors. Hence, it is mandatory to have a precise knowledge of the neutrino flux predictions in order to reach the T2K physics goals.

Monte-Carlo techniques can be used to predict the neutrino fluxes at the near and far detector. Hadron production models are needed to describe the production of hadrons (π and K) from the interactions of the primary proton beam on the graphite target. And a full simulation of the beam line is mandatory to model possible re-interactions of these hadrons before their decay to produce neutrinos. Previous studies [80] have shown that by using different hadronic models, the variation of the neutrino flux predictions at SK could be as large as a factor two. This is represented in fig. 2.24, where the three different models GFLUKA, GHEISHA and GCALOR were used. These differences are due to the limited knowledge on hadron interactions inside the

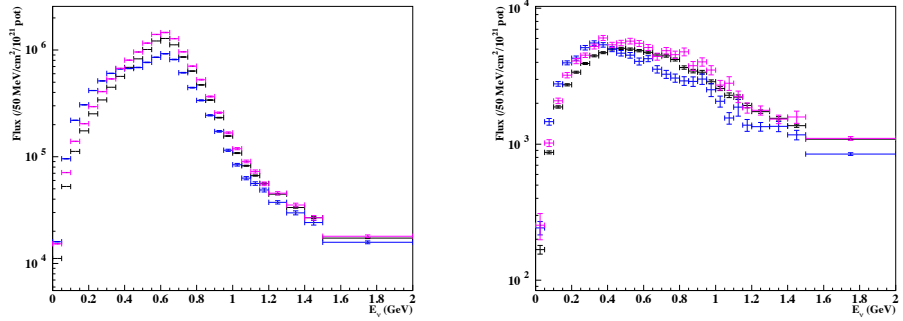


Figure 2.24: ν_μ (left) and ν_e (right) flux predictions at SK for GCALOR (black), GFLUKA (purple), GHEISHA (blue) [80].

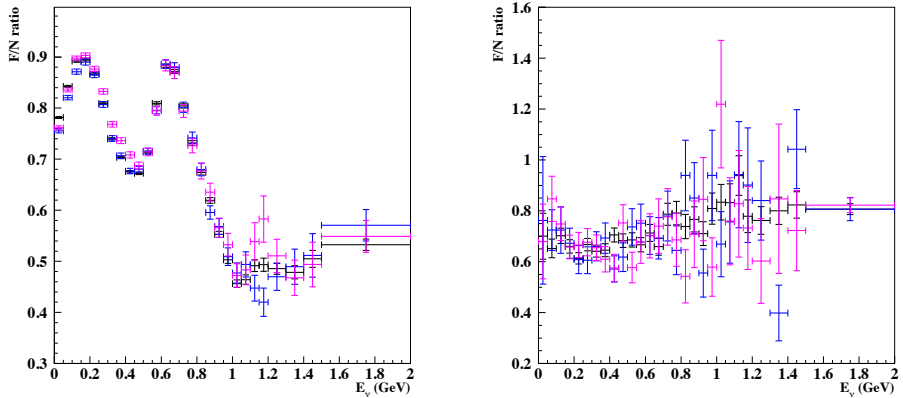


Figure 2.25: Far to near flux ratio for ν_μ (left) and ν_e (right) for GCALOR (black), GFLUKA (purple), GHEISHA (blue) [80].

graphite target. A factor two difference on the flux prediction would be directly translated as a factor two on the cross-section studies. This is of course unsatisfactory for the T2K physics goals on the neutrino cross-section measurements.

The differences on the far-to-near flux ratios using those three models can be seen in fig. 2.25. The variation is larger than the requested 3% to reach the T2K physics goals on the measurements of the oscillation parameters.

In order to reduce the uncertainties on the hadron production, it is thus mandatory to have experimental data that can be used to constrain the models.

2.3 The neutrino flux simulation

The prediction of the neutrino flux in T2K can be divided into three steps.

First, the simulation of the primary proton beam with the baffle and the graphite target is handled by the FLUKA 2011 hadronic model [81, 82]. This specific model was chosen as it was found to be the most accurate model for the simulation of hadron interaction in the energy range of T2K primary proton beam. All interactions are recorded and particles are traced until they exit the baffle or the target surface. The kinematic variables of the particles are saved at the exit point.

The second step of the simulation is handled by JNUBEAM. It is a GEANT3 simulation of the baffle, target, horn magnets, helium vessel, decay volume, beam dump, and muon monitor. The geometry of these components is based on the final mechanical drawings of the constructed beam line. JNUBEAM also includes planes at the positions of the INGRID, ND280, and SK detectors. Those planes are positioned in the simulation according to the latest survey results and the simulated neutrinos crossing those planes are saved. Hadronic interactions are modeled by GCALOR model in JNUBEAM. The generated particles of the first step are used as input for this second step. In JNUBEAM, the particles are propagated through the horns and the decay volume. Neutrinos produced from decaying particles are then forced to point to SK or a randomly chosen point in the near detector planes. The kinematic variables of the neutrino as well as the probability that the neutrino would fly through SK (or ND280) given the decay phase-space density are computed and saved. The neutrino flux and energy spectrum are obtained from these simulated events by weighting according to the saved probabilities. For each neutrino event, the full history of interactions, as well as the parameters of the primary beam proton are saved.

In the third step, a re-weighting procedure is applied to each neutrino event. Different hadron production data, including NA61/SHINE measurements are used to further constrain the hadronic models. As the full history of interactions are saved during the first and second step, it is easy to re-weight each interactions one-by-one using data sets. The final weight for each neutrino event will be computed as the product of each weight at each interaction.

2.3.1 Primary proton beam

The simulation starts with the primary proton beam at the most upstream face of the baffle. As discussed in section 2.1.2, the primary proton beam is well monitored with a number of different detectors along the beam line. The positions and angles of the protons are measured in both, the horizontal x and vertical y directions, perpendicular to the beam axis for each beam spill. The beam characteristics can then be described in terms of the distributions of the positions x and angle x' (respectively $y - y'$) of the protons. The shape of the proton beam in the $x - x'$ phase-space can be given in terms of the twiss parameters α , β , and γ which describe a general ellipse with area $\epsilon\pi$ according to

$$\gamma x^2 + 2\alpha x x' + \beta x'^2 = \epsilon \quad (2.3)$$

where the twiss parameters and the beam width are related by

$$2\sigma_x = \sqrt{\beta\epsilon} \quad (2.4)$$

Proton beam properties for each run period are obtained by reconstructing the beam profile at the baffle for each spill and summing the spill-by-spill profiles weighted by the number of protons in each spill. Table 2.1 summarizes those measurements for the different runs. Table 2.2 gives the uncertainties associated to these measurements.

The beam angle x' is given as θ_x in these tables.

For the FLUKA simulation, the position and angle of each primary proton at the baffle is generated by throwing two independent random variables r_1 and r_2 with mean 0 and variance 1 and computing the position and angle as:

$$\begin{pmatrix} x \\ x' \end{pmatrix} = \begin{pmatrix} \cos \theta & -\sin \theta \\ \sin \theta & \cos \theta \end{pmatrix} \begin{pmatrix} ar_1 \\ br_2 \end{pmatrix} + \begin{pmatrix} \bar{x} \\ \bar{x}' \end{pmatrix} \quad (2.5)$$

where θ is the angle of the semi-major axis of the ellipse with respect to the x axis and can be

Run	position [cm]	θ [mrad]	σ [cm]	ε [$\pi \cdot \text{mm} \cdot \text{mrad}$]	Twiss α
Run 1	X 0.037	-0.0044	0.4237	2.13	0.60
	Y 0.084	0.004	0.4167	2.29	-0.09
Run 2	X 0.015	-0.080	0.4037	5.27	0.16
	Y -0.005	-0.01	0.4083	5.17	0.14
Run 3b	X 0.0087	0.020	0.4134	6.50	0.16
	Y -0.0024	0.043	0.3973	5.30	0.25
Run 3c	X -0.0001	0.032	0.4033	4.94	0.33
	Y -0.0366	0.068	0.4220	6.02	0.34
Run 4	X 0.0032	0.042	0.3755	5.00	0.15
	Y -0.0865	0.182	0.4153	6.14	0.19
Run 5a	X -0.0003	-0.004	0.3960	3.09	0.01
	Y -0.1091	1.743	0.4214	4.08	0.05
Run 5b	X 0.0273	0.070	0.3844	3.50	-0.04
	Y -0.0242	0.159	0.4201	4.178	0.07
Run 5c	X 0.0451	-0.076	0.3891	3.98	-0.05
	Y -0.0435	0.130	0.4180	4.48	0.07
Run 6b	X 0.035	-0.030	0.4061	2.95	-0.02
	Y -0.0988	0.451	0.4367	4.22	0.29

Table 2.1: Summary of the beam conditions for runs 1 to 6b, calculated at baffle.

written in terms of the twiss parameters as

$$\theta = \frac{1}{2} \arctan \frac{2\alpha}{\gamma - \beta} \quad (2.6)$$

a and b are the half-lengths of the semi-major and semi-minor axes of the ellipse, respectively and are related to the twiss parameters by

$$a = \frac{1}{2} \sqrt{\frac{\epsilon}{\gamma + \alpha \tan \theta}} \quad (2.7)$$

$$b = \frac{1}{2} \sqrt{\frac{\epsilon}{\beta - \alpha \tan \theta}} \quad (2.8)$$

\bar{x} and \bar{x}' are the measured beam center and beam angle and correspond to x and θ_x in table 2.1.

The FLUKA transport code performs the simulation of all interactions in the baffle and the graphite target. The initial kinetic energy of the proton is set to 30 GeV in order to match the measured energy. The baffle is taken as a graphite block with dimensions $29 \times 40 \times 171.145 \text{ cm}^3$ and the target is modeled as a simple graphite rod 90cm long and 2.6cm in diameter. The geometry is presented in fig. 2.26. The volume along the beam axis is filled with helium.

The uncertainties on the measurements of the beam parameters have to be properly propagated into the final uncertainty of the neutrino flux at SK. Two groups of uncertainties are considered. Uncertainties related to the measurements of the average position and angle of the beam and uncertainties related to the width and divergence of the proton beam. The propagation of these uncertainties to the neutrino flux prediction will be further discussed later on in this chapter.

Run	ΔX [mm]	ΔY [mm]	$\Delta\theta_X$ [mrad]	$\Delta\theta_Y$ [mrad]	$\rho(Y, Y')$
Run 1	0.38	0.58	0.06	0.29	0.392
Run 2	0.27	0.62	0.06	0.32	0.398
Run 3b	0.28	0.58	0.06	0.29	0.427
Run 3c	0.36	0.58	0.07	0.28	0.417
Run 4	0.34	0.58	0.07	0.28	0.401
Run 5a to 5c	0.34	0.57	0.07	0.28	0.409
Run 6a to 6b	0.34	0.58	0.07	0.28	0.433

Table 2.2: Measured uncertainties of the position and angle of the beam, as well as the correlations between position and angle in Y for all run periods.

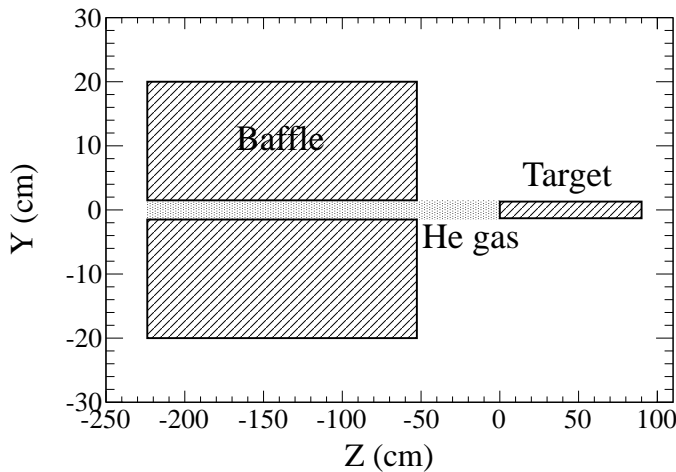


Figure 2.26: Two dimensional view of the geometrical set-up in the FLUKA simulation of the baffle and the target [60].

2.3.2 Sources of neutrino production

As already mentioned, particles are generated in JNUBEAM according to the recorded information from the FLUKA simulation. They are then traced through the horns, the decay volume and the beam dump until they decay to produce neutrinos or until their kinetic energy drops below 10MeV. In JNUBEAM, the GCALOR model is used for the hadronic interactions. The horn magnetic field collects and focuses the charged particles exiting the target surface. As explained in section 2.1.2, a toroidal magnetic field is generated in the horns. It is assumed that the current flows uniformly in the conductor. The magnetic field at radius r from the inner conductor is then calculated with the Ampere's law as

$$B(r) = \frac{\mu_0 I}{2\pi} \frac{r^2 - a^2}{b^2 - a^2} \quad (2.9)$$

where μ_0 is the magnetic permeability, I is the current and a and b are respectively the inner and outer radii of the inner conductor. The direction of the flow of the current determines whether T2K runs in neutrino or antineutrino mode.

In JNUBEAM seven particle species are considered as sources of neutrinos. These are π^\pm , K^\pm , K_L^0 and μ^\pm . Their decay products and branching fractions are listed in table 2.3

Particle	Decay Products	Branching Fraction (%)
π^+	$\rightarrow \mu^+ \nu_\mu$	99.9877
	$\rightarrow e^+ \nu_e$	1.23×10^{-4}
K^+	$\rightarrow \mu^+ \nu_\mu$	63.55
	$\rightarrow \pi^0 \mu^+ \nu_\mu$	3.353
	$\rightarrow \pi^0 e^+ \nu_e$	5.07
K_L^0	$\rightarrow \pi^- \mu^+ \nu_\mu$	27.04
	$\rightarrow \pi^- e^+ \nu_e$	40.55
μ^+	$\rightarrow e^+ \bar{\nu}_\mu \nu_e$	100

Table 2.3: Neutrino-producing decay modes considered in JNUBEAM and their branching ratio in percentage. Decay modes for $\bar{\nu}_\mu$ and $\bar{\nu}_e$ are omitted in this table. The π^- , K^- and μ^- modes are charge conjugates of the π^+ , K^+ and μ^+ modes, respectively.

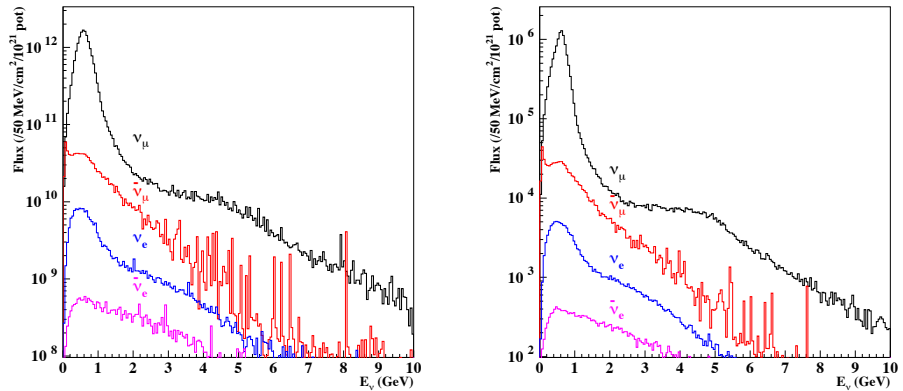


Figure 2.27: Energy spectra for ν_μ (black), $\bar{\nu}_\mu$ (red), ν_e (blue) and $\bar{\nu}_e$ (purple) at the ND280 near detector (left) and at the far detector (right) [80].

In the study of the $\nu_\mu \rightarrow \nu_e$ transition, direct ν_e contamination in the beam will be an irreducible background. It accounts for less than 1% in the energy range between 0 and 1.5 GeV but amounts up to 4.5% in the range between 1.5 and 3 GeV. Figure 2.27 shows the energy spectra for the different neutrino flavor normalized to 10^{21} simulated protons on target at ND280 and SK. To understand the reason of the relatively large amount of ν_e at higher energies, it is useful to study the contribution of each neutrino parent particle in the different energy ranges. As the full interaction history is recorded during the simulation, it is possible to identify the parents of any neutrino. Figure 2.28 shows the contribution of each parent particle type to the ν_μ flux at SK as an example. At the beam peak energy, pions clearly dominate the spectra. At higher energies, the kaons play the most important role and as they have a non negligible branching fraction to decay into ν_e , they are responsible for the major part of the 4.5% ν_e contamination to the ν_μ flux. A very detailed study of all the neutrino parent particles contribution was performed in Ref. [80]. A few conclusions can be drawn from fig. 2.28:

- a very good knowledge of pion production is mandatory to constrain the accuracy of the muon neutrino flux prediction
- a good knowledge of the kaon production is mandatory to constrain the irreducible ν_e

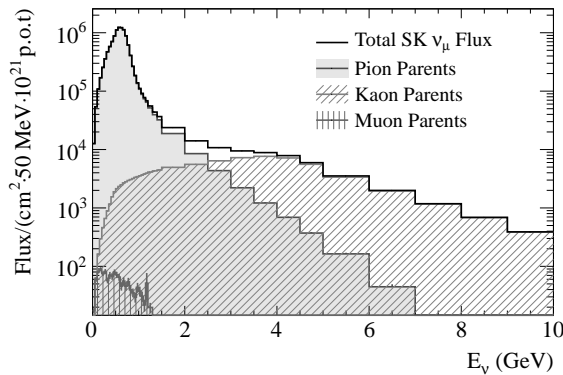


Figure 2.28: Contributions of neutrino parent particles

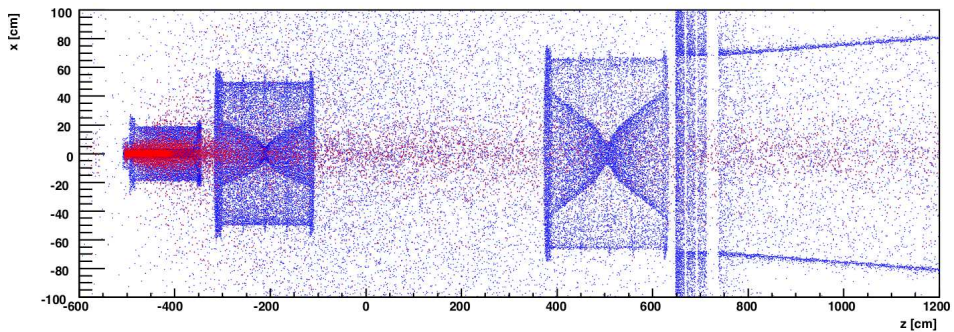


Figure 2.29: Position in the XZ plane of the production of the neutrino parent particles. Points in red correspond to parent particles produced inside the target or during the decay chain of a particle produced in the target. Blue points correspond to parent particles produced by re-interactions in the material of the beam line [80].

contamination in the ν_μ flux

The neutrino parent particles can be either produced in the graphite target or during re-interactions in the material of the beam line. For each neutrino event at SK (or ND280), thanks to the full record of the neutrino history, it is possible to determine production point of the neutrino parent particle. This can be seen in fig. 2.29. It shows the position in the XZ plane of the production of the neutrino parent particles. Points in red correspond to parent particles produced inside the target or during the decay chain of a particle produced in the target. Blue points correspond to parent particles produced by re-interactions in the material of the beam line. Red points along the beam axis and relatively far from the target are typically muons produced in pion decay.

To quantitatively understand the contribution of neutrino parent particles coming from re-interactions along the beam line, it is more useful to consider ratios of neutrino spectra. Considering neutrino fluxes at SK, we can compute ratios for each neutrino flavor by dividing two distributions: the distribution of the neutrino flux related only to those neutrinos that have parent particles produced in re-interactions outside the target and the distribution of the total neutrino flux. Figure 2.30 present these ratios for each neutrino flavors at SK. For the muon neutrino flux at SK, at the beam peak energy, around 10% of the neutrino flux comes from parent

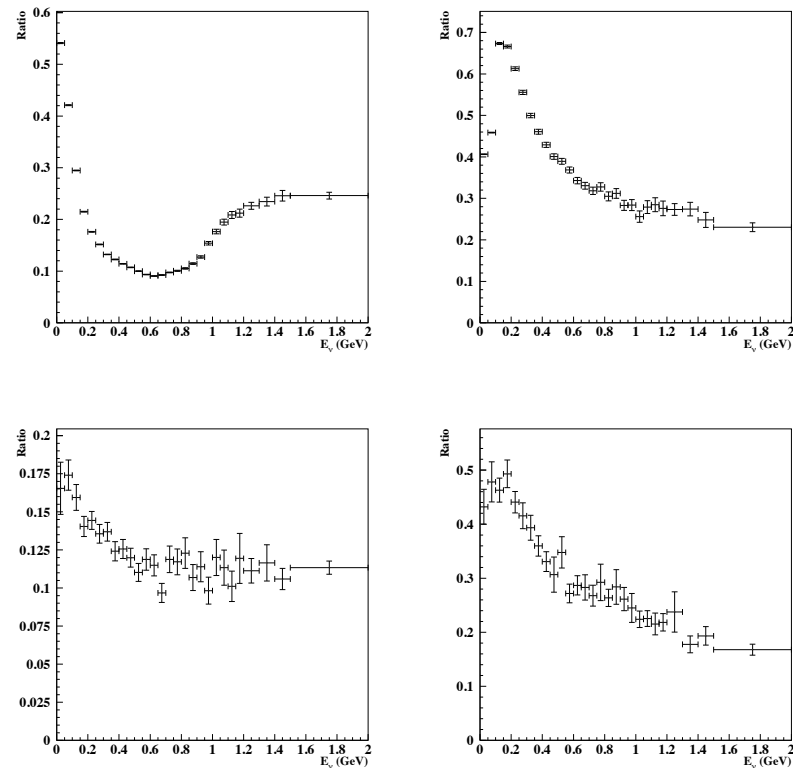


Figure 2.30: Ratios of neutrino flux related only to neutrinos having parent particles produced in re-interactions outside the target over total neutrino flux for ν_μ (top left), $\bar{\nu}_\mu$ (top right), ν_e (bottom left), $\bar{\nu}_e$ (bottom right) at SK [80].

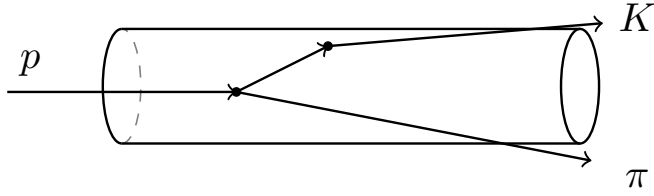


Figure 2.31: Schematic of the interactions in the target. The pion is labeled as secondary hadrons as it is a product of the interaction of the primary beam proton, the kaon is labeled as tertiary hadron as it has been produced in re-interaction.

particles produced in re-interactions in the beam line. 90% of the neutrino parent particles are due to interactions of primary protons within the graphite target. An important conclusion from fig. 2.30 has to be underlined: by having measurements of hadrons (pions and kaons) exiting the graphite target, one would be able to constrain 90% of the neutrino flux. This is a very strong motivation to conduct a hadron production measurement campaign using a replica of the T2K target.

The 90% contribution of the neutrino flux generated by parent hadrons being produced in the target can be further broken into sub-categories. The hadrons exiting the graphite target (and hence being modeled by FLUKA) can be divided into different categories. They are labeled as secondary hadrons if they are produced in interactions of the primary beam protons and tertiary hadrons if they are produced by interactions of hadrons other than the primary protons. Figure 2.31 shows a schematic of these labels.

In order to understand the contribution of secondary and tertiary hadrons responsible for the final neutrino flux, we plot again ratios of distributions. This time, the ratios correspond to dividing the distribution of the neutrino flux coming from tertiary interactions to the total neutrino flux. These ratios are computed for the SK detector and each neutrino flavor in fig. 2.32. For the ν_μ flux, at the beam peak energy, the component of the neutrinos produced by the tertiary hadrons account for 40% of the total neutrino flux. Around 60% of the ν_μ flux can then be constrained by using differential cross-section measurements for proton carbon at 30 GeV.

We can conclude that hadron production measurements from 30 GeV protons on a thin carbon target will help to constrain $\sim 60\%$ of the ν_μ at SK. By measuring particles exiting the surface of the T2K target, we could constrain up to 90% of the muon neutrino flux at SK.

For the thin target measurements, two relevant physics values can be used to constrain a model:

1. the mean number of hadrons produced at each proton-carbon interaction which corresponds to measuring the double differential hadron multiplicities in bins of momentum and polar angles (p, θ) of the produced hadrons.
2. the interaction rate of the 31 GeV/c protons with carbon which corresponds to measuring the production cross-section σ_{prod} of the reaction.

For measurements related to the number of particles exiting the T2K target, results should take the form of multiplicities as for the thin target but with an additional variable. The focusing properties of the horns is going to be different between the upstream part and the downstream part of the target. Thus the longitudinal distribution of the particles exiting the target surface will play a role in the distribution of the final neutrino spectra. It is then important to not only measure the integrated flux of hadron exiting the target over the full length, but also to

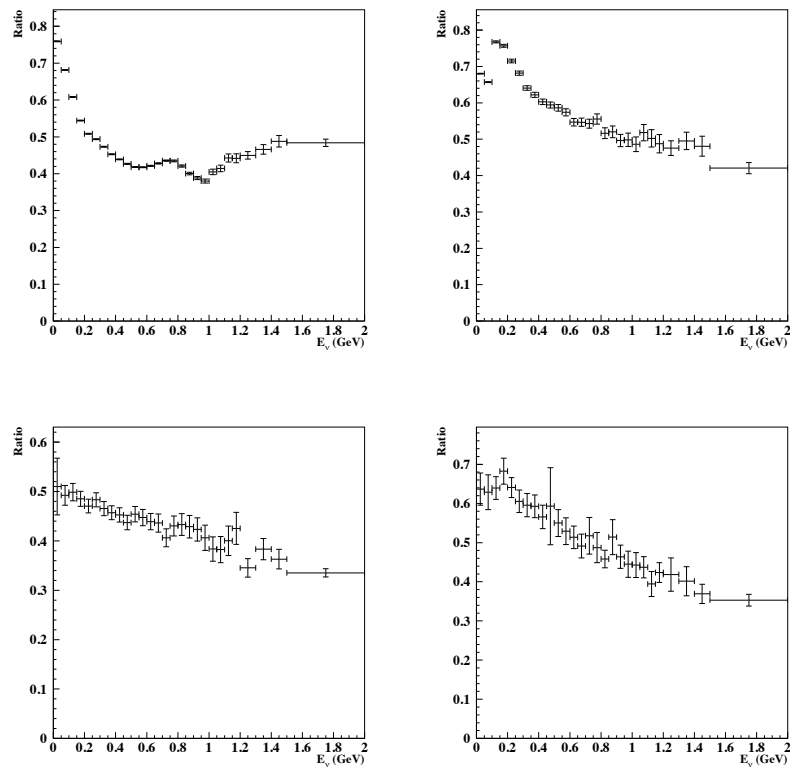


Figure 2.32: Ratio of tertiary to total contribution for ν_μ top left, $\bar{\nu}_\mu$ top right, ν_e bottom left, $\bar{\nu}_e$ bottom right neutrino fluxes at SK [80].

know the number of particles generated as a function of the position along the target surface. In other words, the 90cm long target has to be binned in its longitudinal direction. And the measurements of the number of hadrons exiting the target should be given in bins of momenta and polar angle (as for the thin target measurements) but also in longitudinal bins along the target surface. This leads to producing measurements in a (p, θ, z) binning. In order to determine the number of longitudinal bins that should be taken into account, a detailed study has been conducted by the T2K beam group. It is based on dividing the target into different number of bins and looking at the effect on the final neutrino spectra. When considering only one longitudinal bin, the FLUKA simulation was passed on to JNUBEAM, but instead of considering the exact longitudinal position of the exit point of the particle, only one point in the center of the target was set as the starting point of all the tracks in JNUBEAM. When considering two longitudinal bins, all particles simulated by FLUKA would be placed in two points along the target surface. This is illustrated in fig. 2.33. The neutrino flux was then evaluated with these specific configurations

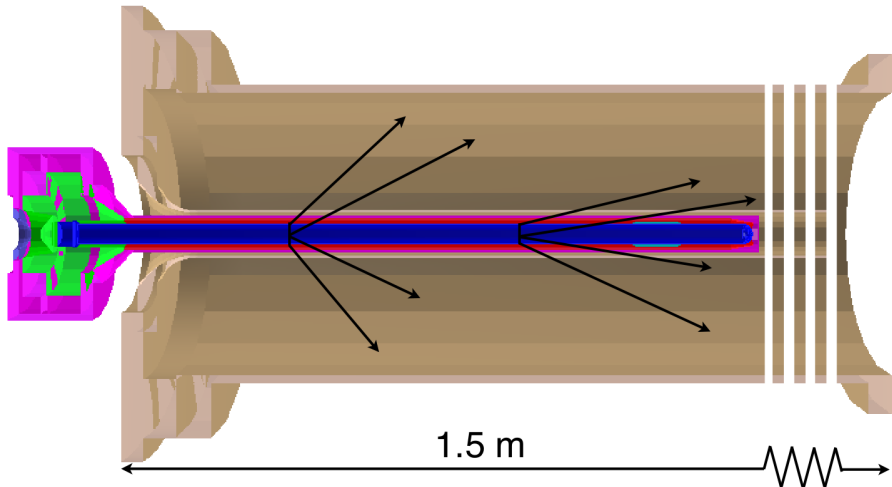


Figure 2.33: Schematic of the placement of the particles along the target surface for the study of the effect of the longitudinal binning on the neutrino flux predictions

and compared with the initial flux when the full information about FLUKA values are given to JNUBEAM. Figure 2.34 shows the muon neutrino flux at SK for different number of longitudinal bins. It can be noted that the position of the beam peak is not influenced by the number of longitudinal bins considered, but the overall shape of the spectra does. In order to fulfill the T2K physics requirements on the precision of the ν_μ flux at SK, at least 5 bins were requested. As the (p, θ) distributions of the produced hadrons are relatively different between the target surface and the downstream face of the target, it was decided to split the target into 6 bins: 5 bins of 18cm along the surface of the target and a 6th bin for the downstream face of the target. By considering 6 bins, it is then also possible to show the contribution of each z bin to the final neutrino flux as illustrated on fig. 2.35

The NA61/SHINE experiment, with its large spectrometer and excellent PID capabilities was found to be the best set-up to take hadron production data with a thin carbon target as well as with a replica of the T2K target. Hence a hadron production campaign was set up and data with a thin graphite target and a proton beam of 31 GeV/c were taken in 2007 and 2009. Data using a 31 GeV/c proton beam impinging on a replica of the T2K target were recorded in 2007, 2009 and 2010.

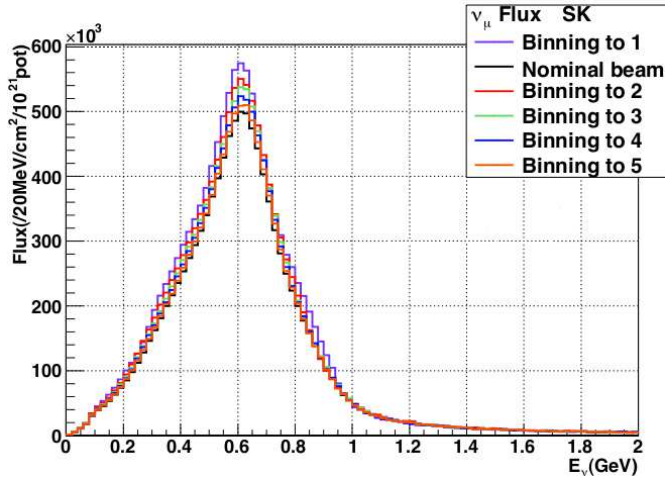


Figure 2.34: Effect of different number of bins along the target surface. The black curve shows the nominal neutrino flux prediction by placing precisely the particles at the exact exit position. Other curves show binning with 1 to 5 bins.

2.3.3 Re-weighting of the hadron production

Hadronic interactions in the target are modeled with FLUKA, outside of the target GCALOR is used. At the simulation level, the chain of hadronic interactions for each simulated event producing neutrinos is saved. Thus it is possible to re-weight each simulated hadronic event with measurements from different experiments. Currently, in the official T2K releases, only thin target measurements are used. As seen in the previous section, thin target measurements can provide two relevant physics values that can be used to re-weight the predicted hadron production:

- differential multiplicities of π^\pm , K^\pm and K_L^0 in the interactions of incident particle with the target, i.e. the number of particles being produced at each interaction point
- interaction cross-section, i.e. the probability for an incident particle of a given energy to interact with the target and produce secondary particles

In the first case, we will speak about multiplicity re-weighting while in the second case the production cross-section will be re-weighted. Some experiments measure inelastic cross-section σ_{inel} which is defined as the total cross-section minus the elastic component of the cross-section. NA61/SHINE gives its results in term of production cross-section which is related to the inelastic cross-section via

$$\sigma_{prod} = \sigma_{inel} - \sigma_{qe} \quad (2.10)$$

where σ_{qe} is the cross-section related to quasi-elastic process. The quasi-elastic scattering (also called elastic incoherent scattering) occurs when the incident proton scatters off an individual nucleon of the carbon atom. The scattered nucleon can have enough energy to escape the carbon atom, but no other particle is produced in the quasi-elastic reaction. Detailed study of elastic and quasi-elastic reactions have been conducted by Bellettini *et al.* for different materials and at different incident proton energies [83]. They showed the behavior of the differential cross-sections as function of momentum transfer. Figure 2.36 present their results where it can be seen that the elastic and quasi-elastic processes can be identified by different slopes in the exponential behavior of the differential cross-sections. By subtracting the quasi-elastic component to the inelastic cross-

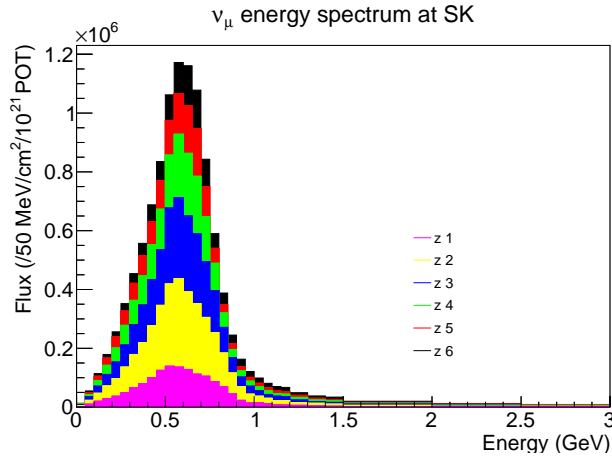


Figure 2.35: Stacked histograms showing the contribution of each different longitudinal bin to the muon neutrino flux at SK.

Experiment	Beam Mom.(GeV/c)	Target	Particles
NA61/SHINE	31	C	π^\pm, K^\pm, K_s^0
Eichten et al.	24	Be, Al	p, π^\pm, K^\pm
Allaby et al.	19.2	Be, Al	p, π^\pm, K^\pm
BNL-E910	6.4 - 17.5	Be	π^\pm

Table 2.4: Differential hadron production data used by T2K for the flux prediction

section, the production cross-section hence represents the rate of interactions where hadrons are produced in the final state. Table 2.4 summarizes the experiments used for their measurements of differential production of hadrons. Table 2.5 gives the list of data used for re-weighting of the interaction rates.

As already mentioned, NA61/SHINE conducted hadron production measurements dedicated to T2K. The thin target measurements comprises 6.7×10^5 registered events in 2007 and 5 million events in 2009. The 2007 data set was limited in statistics and only results for π^\pm and K^+ could be extracted. In 2009, thanks to the larger recorded statistics, seven particle species could be extracted with high precision, namely π^\pm, K^\pm , protons, and K_s^0 and Λ . The analysis phase space of NA61/SHINE allows to cover most of the phase space of interest for T2K. This is illustrated in fig. 2.37 as an example for π^\pm, K^\pm and K_s^0 . The color plots show the distributions for the different particle species that produce neutrinos passing through SK. The contours show the NA61/SHINE analysis phase space for each related particle species.

Meson multiplicity re-weighting

The multiplicity for a specific momentum p and polar angle θ is related to the differential cross-section by the production cross-section

$$\frac{d^2n}{dpd\theta}(p_{in}, A) = \frac{1}{\sigma_{prod}(p_{in}, A)} \frac{d^2\sigma}{dpd\theta}(p_{in}, A) \quad (2.11)$$

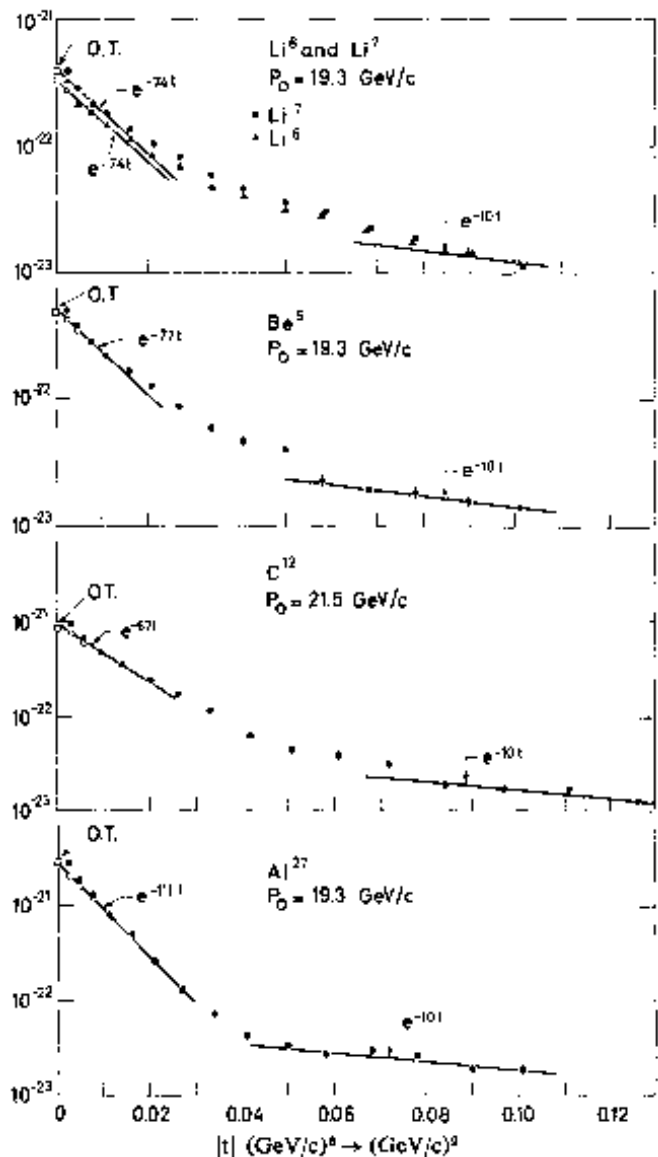


Figure 2.36: Differential cross-section as a function of momentum transfer $|t|$ from Bellettini [83]. The low $|t|$ region corresponds to the elastic interactions while the higher $|t|$ region is interpreted as the quasi-elastic interactions.

Data	Beam	Target	Beam Momentum (GeV/c)	Measurement
Abrams <i>et al.</i> [84]	K^\pm	C, Cu	1 – 3.3	σ_{inel}
Allaby <i>et al.</i> [85]	π^-, K^-	C, Al, ...	20 – 65	σ_{inel}
Allardyce <i>et al.</i> [86]	π^\pm	C, Al, ...	0.71 – 2	σ_{inel}
Bellettini <i>et al.</i> [83]	p	C, Al, ...	19.3, 21.5	σ_{inel}
Bobchenko <i>et al.</i> [87]	π^-, p	C, Al, ...	1.75 – 9	σ_{inel}
Carroll <i>et al.</i> [88]	π^\pm, K^\pm, p	C, Al, ...	60 – 280	σ_{prod}
Cronin <i>et al.</i> [89]	π^-	C, Al	0.73 – 1.33	σ_{inel}
Chen <i>et al.</i> [90]	p	C, Al, ...	1.53	σ_{inel}
Denisov <i>et al.</i> [91]	π^\pm, K^\pm, p	C, Al, ...	6 – 60	σ_{inel}
Longo <i>et al.</i> [92]	π^+, p	C, Al	3	σ_{inel}
NA61 [93]	p	C	31	σ_{prod}
Vlasov <i>et al.</i> [94]	π^-	C, Al	2 – 6.7	σ_{inel}

Table 2.5: Inelastic and production cross-section data used to re-weight hadron absorption probabilities.

where p_{in} is the incident nucleon momentum and A the target nucleus. The differential production weights can be simply given by the ratio of the measured multiplicity over the predicted value

$$W(p_{in}, A) = \frac{\left[\frac{d^2 n}{dp d\theta}(p_{in}, A) \right]_{data}}{\left[\frac{d^2 n}{dp d\theta}(p_{in}, A) \right]_{MC}} \quad (2.12)$$

As already mentioned, interactions of primary protons and subsequent interactions in the target are modeled by FLUKA and MC relates to this model, while for re-interactions outside of the target, MC is related to the GCALOR model.

The tuning of particle production from primary proton interactions is done directly with the NA61/SHINE pion, kaon and proton multiplicity data. The NA61/FLUKA tuning weights for the meson multiplicity data are shown in fig. 2.38.

For each interaction, the corresponding bin in these histograms is found and the weight is applied. The K_S^0 weights are calculated relative to the K_S^0 rate in the FLUKA thin target simulation, but the weights are applied for K_L^0 rate tuning as well. The weights extend beyond the phase space covered by NA61/SHINE. This is done by using a modified BMPT parametrization [38] to extrapolate the NA61/SHINE data.

The initial BMPT parametrization takes the form of eq. (2.13).

$$\left[E \frac{d^3 \sigma}{dp^3} \right]_{BMPT} = A(1 - x_R)^\alpha (1 + Bx_R) x_R^{-\beta} (1 + \frac{a}{x_R^\gamma} p_T + \frac{a^2}{2x_R^\delta} p_T^2) e^{-ap_T/x_R^\gamma}. \quad (2.13)$$

The parameterizations for π^- and K^- have additional factors of $r_0(1 + x_R)^{r_1}$ and $r_0(1 - x_R)^{r_1}$ respectively that are applied based on the observed ratios between positive and negative particle production. The K_S^0 data are fit with the same parameterized form as the K^+ since the data are still sparse and it is found that this form is sufficient. The values for the parameters $A, \alpha, B, \beta, a, \gamma, \delta, r_0$ and r_1 are derived from the fit to the data. The functional form is capable of describing known features of the particle production cross-section such as the exponential dependence with p_T and the flatness in the central rapidity region.

Since the BMPT formula depends on x_R or the outgoing particle energy, it describes symmetric forward/backward particle production in the center of mass frame. It is typically used to

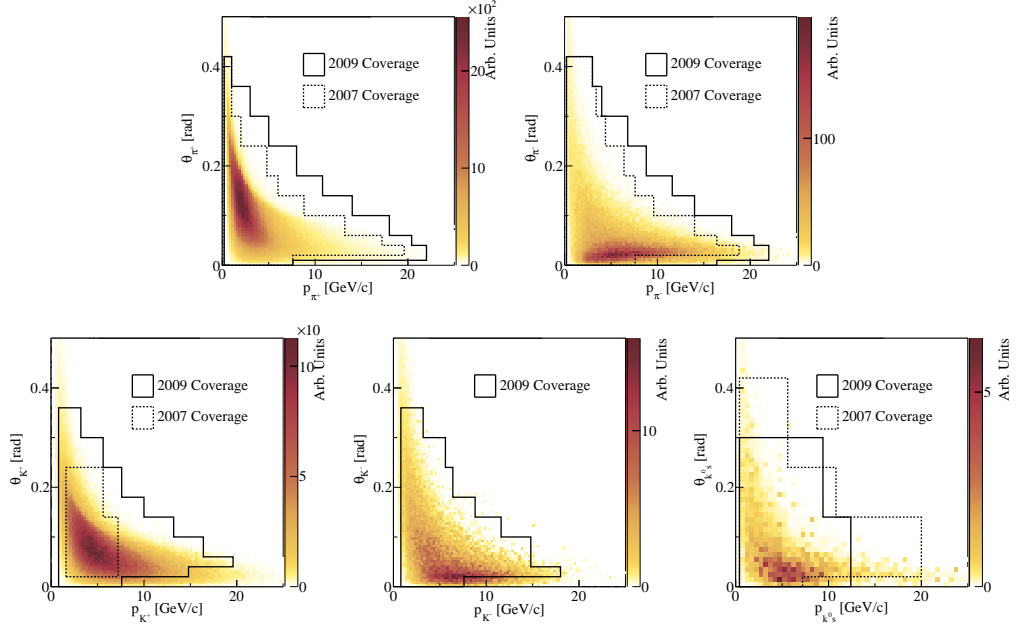


Figure 2.37: Phase space of π^\pm , K^\pm and K_s^0 that contribute to the neutrino flux at SK with the NA61/SHINE analysis phase space for each particle species overlaid on top.

describe forward production only, so this limitation is usually not a problem. However, some of the particle production relevant for the T2K flux prediction is in the backward hemisphere. We have modified the BMPT parametrization to introduce forward/backward asymmetry that can arise from particle re-interaction in the nucleus. The new form uses the original BMPT form to describe the scattering on a deuteron and then applies scaling to the desired nuclear target:

$$E \frac{d^3\sigma}{dp^3} = \left[\frac{A}{2} \right]^{(0.75 - 0.52x_F + 0.23x_F^2)(1 + 0.21p_T^2)} \left[E \frac{d^3\sigma}{dp^3} \right]_{BMPT} \quad (2.14)$$

Here x_F is the Feynman x variable, the longitudinal momentum of the outgoing particle in the center of mass frame divided by its maximum allowed momentum. The x_F dependence introduces a forward/backward asymmetry that is consistent with the target nucleus scaling derived from data. A is the atomic mass and the coefficients in the exponent are fixed to the values derived in the A scaling fits explained later.

The NA61/SHINE data are also used to tune the production of mesons in secondary (tertiary) interactions where a secondary (tertiary) proton or neutron interacts with the nucleus. This tuning requires some additional steps that are described in details below:

1. For incident neutrons we assume an isoscalar nuclear target (true for carbon) and apply an isospin rotation to the NA61/SHINE data. Under the assumption of isospin symmetry the multiplicities for $p + A \rightarrow \pi^+ + X$ are equal to $n + A \rightarrow \pi^- + X$ and $p + A \rightarrow \pi^- + X$ are equal to $n + A \rightarrow \pi^+ + X$.
2. Since the incident secondary (tertiary) proton or neutron has an energy less than the 30 GeV of the proton beam in NA61/SHINE, a scaling has to be applied to extrapolate the

NA61/SHINE measurements from 30 GeV down to the energy of the incident secondary (tertiary) proton or neutron.

3. For out-of-target interactions on Al, Ti or Fe, the NA61/SHINE measurements taken with a carbon target have to be scaled to these different target materials by using parametrized fits.

The scaling to different incident nucleon momenta is done assuming Feynman scaling. The Feynman variable x_F is defined as

$$x_F = \frac{p_L}{p_{L(max)}} \quad (2.15)$$

where p_L is the longitudinal momentum of the produced particle in the center of mass frame and $p_{L(max)}$ is the maximum allowed longitudinal momentum of the produced particle. The weights computed in eq. (2.12) are converted to x_F, p_T variables and applied to tertiary events based on the x_F and p_T of those events.

The extrapolation of the NA61/SHINE measurements to different target material (from carbon to aluminum for the horns for example) is carried out using the parametrization proposed by Bonesini based on works conducted by Barton and Skubic. This parametrization gives the dependence of the cross-section with respect to the target material A

$$E \frac{d^3\sigma(A_1)}{dp^3} = \left[\frac{A_1}{A_0} \right]^{\alpha(x_F, p_T)} E \frac{d^3\sigma(A_0)}{dp^3} \quad (2.16)$$

where:

$$\alpha(x_F, p_T) = (a + bx_F + cx_F^2)(d + ep_T^2). \quad (2.17)$$

The parameters a through e are determined by fitting the A -dependence in the data from Eichten *et al.* [39] and Allaby *et al.* [95]. The fit results and parameter values are discussed in Ref. [60].

Secondary baryon production re-weighting

In this tuning, the preliminary 2009 NA61/SHINE proton multiplicity data and the Allaby data are used to calculate the nominal secondary baryon weights. Protons, neutrons, Λ s and Σ s are included in this re-weighting. The Eichten and Allaby data sets are used to evaluate the material and momentum scaling parameters and uncertainties. Figure 2.39 shows the phase space covered by these three data sets on top of the proton spectra from a thin target FLUKA simulation. The Allaby data give access to the high x_F region. The most significant difference in the procedure for tuning baryons than that for mesons is the baryon number conservation constraint, which is used to constrain the integrated baryon multiplicity.

A parametrization is used to interpolate and extrapolate between the data points. Under the assumption of Feynman scaling, the parametrization should be independent of the beam energy, so the variables x_F and p_T are used. x_F is used instead of x_R , because there is an asymmetry in the NA61/SHINE data points around 0 momentum in the center of mass frame.

Unlike the meson tuning, baryon number conservation allows the integrated baryon multiplicity to be constrained. However, the simulation does not keep track of where every baryon came from in each event. The secondary baryon in a simulated event that produces a neutrino can be from the scattered incident proton, the break-up of the nucleus or from baryon/anti-baryon production. As a consequence of this, any given event can have one or more baryons. Therefore, only the leading baryon number is conserved in the weights calculation. The leading baryon is defined as the baryon in each event that has the largest p_L .

The region of the phase space that is well described by the BMPT parametrization (inside region) is weighted according to Equation 2.18 (same procedure as the meson tuning). This includes the region described by $0 < x_F < .84$ and any region covered by NA61/SHINE data bins. It was found that in the low p , high θ region and the high p region, the data are not well fit by the BMPT formula. Outside of this region (outside region), only leading baryons are reweighted. The factor applied is calculated such that the number of leading baryons (1 per event) remains a constant before and after the weighting procedure, which is shown in Equations 2.19 and 2.20. The weight applied in the outside region is a function of p and θ , because the ratio $\frac{M_{lead}}{M_{all}}$ varies with p and θ . Protons can be mutated into other baryons or neutrons can be ejected from the target, so in this calculation we include the phase-spaces of neutrons, Λ s and Σ s as outside regions. Fig. 2.40 shows the weights for the four baryon species.

$$W_{in}(p, \theta) = \frac{M_{BMPT}(p, \theta)}{M_{FLUKA}(p, \theta)} \quad (2.18)$$

Here the M s are the multiplicities from the BMPT fit data and from FLUKA MC in each kinematic bin.

$$W_{out}(p, \theta) = \frac{M_{nonLead}(p, \theta) + W_{lead}M_{lead}(p, \theta)}{M_{nonLead}(p, \theta) + M_{lead}(p, \theta)} = \frac{M_{all}(p, \theta) + (W_{lead} - 1)M_{lead}(p, \theta)}{M_{all}(p, \theta)} \quad (2.19)$$

Here $M_{all}(p, \theta)$ is the multiplicity from FLUKA MC, $M_{lead}(p, \theta)$ is the multiplicity only including leading baryons and $M_{nonLead}(p, \theta) = M_{all}(p, \theta) - M_{lead}(p, \theta)$. W_{lead} , which is a constant with p and θ is:

$$W_{lead} = \frac{N_{out} + N_{in} - N_{inScaled}}{N_{out}}. \quad (2.20)$$

N_{out} is the number of leading baryons in FLUKA MC in the outside region before the reweighting. N_{in} and $N_{inScaled}$ are the number of leading baryons in FLUKA MC in the inside region before and after the reweighting.

Hadron interaction rate re-weighting

In addition to re-weighting the multiplicities of hadrons produced at each interactions, it is also important to constrain the rate at which interactions occur. This is done by re-weighting the production cross-section. As mentioned earlier, many experiments publish their results as inelastic cross-sections. These results can be translated into production cross-section using eq. (2.10). The quasi-elastic cross-section can be extrapolated from hadron nucleon scattering data using the empirical equation

$$\sigma_{qe} = 0.8 (\sigma_{hp}^{el} + \sigma_{hn}^{el}) A^{1/3} \quad (2.21)$$

where σ_{hp}^{el} and σ_{hn}^{el} are the elastic cross-sections of the hadron h on the proton and neutron respectively. Equation (2.21) is based on the empirical equation from Bellettini [83] but has been slightly modified to include the elastic cross-section on neutron.

The re-weighting of the interaction rate models the change in the survival probability of particles as the cross-section changes, as well as the change in rate at a given interaction point. The probability that a particle with hadron production cross-section of σ_{prod} travels a distance

x and interacts in the infinitesimal length Δx to produce hadrons is:

$$P(x; \sigma_{prod}) = \int_x^{x+\Delta x} \sigma_{prod} \rho e^{-x' \sigma_{prod} \rho} dx' \quad (2.22)$$

$$= \Delta x \sigma_{prod} \rho e^{-x \sigma_{prod} \rho}. \quad (2.23)$$

Here, ρ is the density of nuclear targets in the material. When the production cross-section changes, $\sigma_{prod} \rightarrow \sigma'_{prod}$, the weight applied to model the change is the ratio of the probabilities:

$$W = \frac{P(x; \sigma'_{prod})}{P(x; \sigma_{prod})} \quad (2.24)$$

$$= \frac{\sigma'_{prod}}{\sigma_{prod}} e^{-x(\sigma'_{prod} - \sigma_{prod})\rho}. \quad (2.25)$$

The first factor in section 2.3.3 is the change in interaction probability at that point, while the second factor is the attenuation of the particle flux over the distance traveled. For a particle that decays or exit the target before interacting, the weight applied is:

$$W = e^{-x(\sigma'_{prod} - \sigma_{prod})\rho}. \quad (2.26)$$

Figure 2.41 shows the comparisons of the measured cross-sections for the different reactions listed in table 2.5 with FLUKA and GCALOR. FLUKA seems to be in reasonable agreement with the measurements while GCALOR shows significant deviations. It was thus decided not to apply any weights for the FLUKA cross-sections but to re-weight the GCALOR cross-sections with the FLUKA values.

The effect of the different re-weightings is illustrated in fig. 2.42. It shows the ratio of the hadron interaction re-weighted flux over the nominal flux for the different neutrino flavors at the SK far detector.

2.3.4 Uncertainties on the neutrino flux predictions

Uncertainties on the flux predictions are considered as coming from the following sources: the hadron production uncertainties, the proton beam profile, the off-axis angle, the target and horn alignment and the horn current and related magnetic field. The study of the variation of these different inputs on the predictions gives the uncertainties on the neutrino flux. Two different approaches are used, depending on the source considered.

If the considered error source has correlated parameters, the re-weighting method is used. The underlying parameters are varied according to their covariance and the flux prediction is re-weighted with each of N sets of the parameter values. The effect on the flux is evaluated by constructing a covariance matrix from the N re-weighted versions of the flux predictions:

$$V_{ij} = \frac{1}{N} \sum_{k=1}^{k=N} (\phi_{nom}^i - \phi_k^i)(\phi_{nom}^j - \phi_k^j). \quad (2.27)$$

ϕ_{nom}^i are the nominal flux and i specifies the neutrino energy bin, flavor and detector at which the flux is evaluated. Flux uncertainties evaluated with this method are the hadron interaction uncertainties and the proton beam profile uncertainties.

The second method is applied when the error source has no correlated parameters. In this case, the flux is simulated with all parameters varied by $\pm 1\sigma$. As for the first method a covariance

matrix is then calculated as:

$$V_{ij} = \frac{1}{2}[(\phi_{nom}^i - \phi_+^i)(\phi_{nom}^j - \phi_+^j) + (\phi_{nom}^i - \phi_-^i)(\phi_{nom}^j - \phi_-^j)]. \quad (2.28)$$

The ϕ_+^i and ϕ_-^i are the re-simulated flux for $+1\sigma$ and -1σ variations of the underlying parameter. The flux uncertainties evaluated with this method are related to the uncertainties on the beam line alignments and magnetic field strength.

The total covariance on the flux is finally simply computed as the sum of the covariances from each independent source of uncertainties.

Uncertainties on the meson multiplicity tuning

Systematic uncertainties on the neutrino flux are propagated from uncertainties on the meson multiplicity tuning data and methods. The sources of uncertainty, which will briefly be described below, include:

- The uncertainty on the NA61/SHINE multiplicity measurements.
- The phase space not covered by NA61/SHINE data.
- The center-of-mass energy scaling method.
- The target material scaling method.

NA61/SHINE provides both systematic and statistical errors for their multiplicity measurements. For most of the systematic uncertainties, it is assumed that all bins should be varied in a correlated manner when applying systematic variations. The exception is the reconstruction uncertainty, where it is assumed that only particle candidates originating in the same TPC are varied in a correlated manner. When applying these uncertainties to the T2K flux, we create a large covariance matrix for the π^\pm and K^\pm bins and perform systematic draws using the Cholesky decomposition method. The p^+ data are excluded from this procedure since the uncertainties on secondary (tertiary) proton tuning are dominated by the assumptions of how baryon conservation is applied. The K_S^0 systematic draws are done separately since NA61/SHINE currently does not supply correlations with the charged hadron data.

For the part of the phase space not covered by NA61/SHINE, we take the difference between the FLUKA model and the BMPT extrapolation and set that as the uncertainty. The effect is very small for the part of the flux from pion production, since the NA61/SHINE data covers almost all of the phase space relevant for the flux. The uncertainty is significant for the high energy flux coming from the high momentum forward kaon production.

For incident particle momenta different from 31 GeV/c, the implicit assumption in the tuning is that the tuning weights are constant under changes of beam energy when the weights are expressed as a function of x_F and p_T in the center of mass frame.

We can use alternative hadron production data measurements to tune the production from secondary (tertiary) proton and neutron interactions. None of the alternative data cover the full range of particle phase space relevant for T2K, so we group them together into sets that do. The grouped data are listed in Table 2.6. The approach is to tune the secondary (tertiary) production in the flux using these data and then take the difference from the flux when only NA61/SHINE data is used in the tuning as the uncertainty.

The target material scaling parameters are derived from fits to the BNL-802, Allaby and HARP data. The uncertainties on the parameters derived from these fits are propagated into the flux prediction as part of the target scaling uncertainty. In addition, we consider systematic

Data Set	p_{in} (GeV/c)	p_{out} (GeV/c)	θ_{out} (rad.)
$\sim 20 \text{ GeV/c } p + A \rightarrow \pi^\pm$			
Eichten <i>et al.</i> [39]	24.0	4.0-18.0	0.017-0.127
Dekkers <i>et al.</i> [96]	18.8,23.1	1.0-12.0	0.0-0.1
Allaby <i>et al.</i> [95]	19.2	6.0-16.0	0.013-0.07
BNL-E910 [97,98]	17.5	0.4-6.0	0.0-0.4
$\sim 13 \text{ GeV/c } p + A \rightarrow \pi^\pm$			
BNL-E802 [99]	14.6	0.5-4.5	0.1-0.9
BNL-E910 [97,98]	12.3	0.4-6.0	0.0-0.4
HARP [100]	12.0	0.5-8.0	0.025-0.25
$\sim 17 \text{ GeV/c } p + A \rightarrow K^\pm$			
BNL-E802 [99]	14.6	0.5-4.5	0.1-0.9
Allaby <i>et al.</i> [95]	19.2	6.0-16.0	0.013-0.07

Table 2.6: Data used to derive the target scaling dependence for double differential production. For the HARP data, only the 12 GeV/c incident proton data is used in the target scaling fit.

effects related to extrapolating this target scaling parameterization to an independent data set, namely the Eichten data.

At this time we are investigating the tuning of these interactions with HARP measurements of charged pion production in interactions with pions incident on nuclei [101]. While this tuning will not be applied to the current tuned flux prediction, the difference between the tuned flux and the flux without this tuning will be used as a systematic uncertainty. Four types of interactions are measured by HARP and will be tuned:

- $\pi^+ + A \rightarrow \pi^+ + X$
- $\pi^+ + A \rightarrow \pi^- + X$
- $\pi^- + A \rightarrow \pi^+ + X$
- $\pi^- + A \rightarrow \pi^- + X$

The HARP based tuning will be applied to C and Al interactions only.

The HARP experiment collected data with four incident pion momenta: 3, 5, 8, and 12 GeV/c [101].

After normalizing to the production cross-sections, the weights for the pion multiplicities in the FLUKA and GCALOR interactions are produced. These weights are applied as the tuning factors for $\pi^\pm + A \rightarrow \pi^\pm + X$ interactions in the flux simulation.

After the $\pi^\pm + A \rightarrow \pi^\pm + X$ interactions are tuned using the HARP data, the tuned flux is compared to the flux where the $\pi^\pm + A \rightarrow \pi^\pm + X$ interaction tuning is not applied. This tuning is not currently applied to the nominal flux prediction, but the magnitude of the tuning is applied as an uncertainty on the flux prediction.

Uncertainties on the baryon production tuning

Systematic uncertainties related to the secondary proton re-weighting can be computed by propagating the NA61/SHINE thin target results to the final neutrino flux prediction. This is done by generating a large set of throws. A Cholesky decomposition is performed on the covariance matrix describing the multiplicity uncertainties. For each throws, the decomposition

is used to compute new weights. As for the meson uncertainties, eq. (2.27) is used to estimate the uncertainty on the final neutrino flux.

In order to estimate an uncertainty related to the leading baryon constraint, different re-weighting methods have been tested. One of them is to only use the proton phase space for the leading baryon constraint. Neutron, Lambda's and Sigma's are not re-weighted. Instead of re-weighing all leading baryons to conserve the leading baryon constraint, only leading protons are re-weighted. Other methods are explained in Ref. [102].

Non-primary proton interactions in the target and proton interaction outside of the target material are not tuned in the current T2K flux prediction. Nevertheless, uncertainties related to these processes are estimated. As for the meson tuning, interactions are scaled to different incident proton momenta using the Feynman scaling. They are also scaled using the A scaling for different target material. The difference on the final neutrino flux prediction with and without these two additional scaling with respect to the nominal flux tuning is taken as the uncertainties on non-primary proton interactions inside the target and proton interactions outside the target material. Figure 2.44 shows the effect of the baryon production tuning with the related uncertainties as a function of the neutrino energy.

Uncertainties on the hadron production rate

As presented in fig. 2.41, FLUKA production cross-sections seems to be in reasonable agreement with the measured data sets while GCALOR shows important discrepancies. Available measurements of cross-sections cover different momentum ranges for different reactions (fig. 2.45) and are usually given as inelastic cross-section. Equation (2.10) allows to compute the production cross-section from the inelastic cross-sections given in table 2.5. Nevertheless, the evaluation of the quasi-elastic component is based on an empirical parametrization and not directly on data sets. In a conservative approach, the systematic uncertainty on the production cross-section was taken to be represented by the magnitude of the quasi-elastic correction.

The different components of uncertainty due to hadron interactions evaluated on the ND280 and SK flux predictions are summarized in fig. 2.46 and fig. 2.47.

Uncertainties on the proton beam and off-axis angle

To study the effects of the errors on the proton beam measurements, the different parameters given in table 2.1 were varied with respect to their uncertainties. It was observed that only the variation in the y direction (i.e. the beam center y and beam angle θ_y) was producing non negligible effects. This is because these parameters effectively change the off-axis angle at the far detector. Therefore, only these errors are considered in the evaluation of the flux uncertainty. The covariance matrix related to the proton beam uncertainty is constructed following eq. (2.27).

The neutrino flux uncertainty due to the error in the off-axis angle is evaluated by looking at a variation of the neutrino flux when SK and ND280 detectors are moved by 0.44 mrad in the JNUBEAM simulation. The effect can be seen in fig. 2.48.

Uncertainties on the target and horn alignment

Alignment of the beam line was surveyed after the installation of the target and horns. A difference of 1.2 mm (0.3 mm) in horizontal (vertical) direction between the target and the horn axis was measured at the downstream end, while the alignment of the upstream end was found to be centered on the horn axis to within 0.1 mm.

The observed displacement at the downstream end of the target translates into 1.3 mrad (0.1 mrad) rotation in the horizontal (vertical) plane of the downstream end relative to the target head.

The effect of the target alignment were studied by rotating the target in JNUBEAM by 1.3 (0.1) mrad in the horizontal (vertical) plane.

For the horn angular alignment, it was observed that only the rotation of the first horn could show significant effect. For neutrinos with energies below 7 GeV the fractional uncertainties due to these sources are under 3%.

Uncertainties on horn current and magnetic field

The uncertainty on the measured horn current is 1.3% and the magnetic field strength is consistent with the computed one within 2%. JNUBEAM simulations were performed with the different field uncertainties and it was observed that the effect on neutrino flux is less than 1% for energies up to 1 GeV and less than 4% for energies greater than 1 GeV.

Summary of uncertainties

All sources of uncertainties are summarized in fig. 2.49 for the different neutrino fluxes at the near and far detector. Uncertainties on the hadron production are dominant for all fluxes and across all energies.

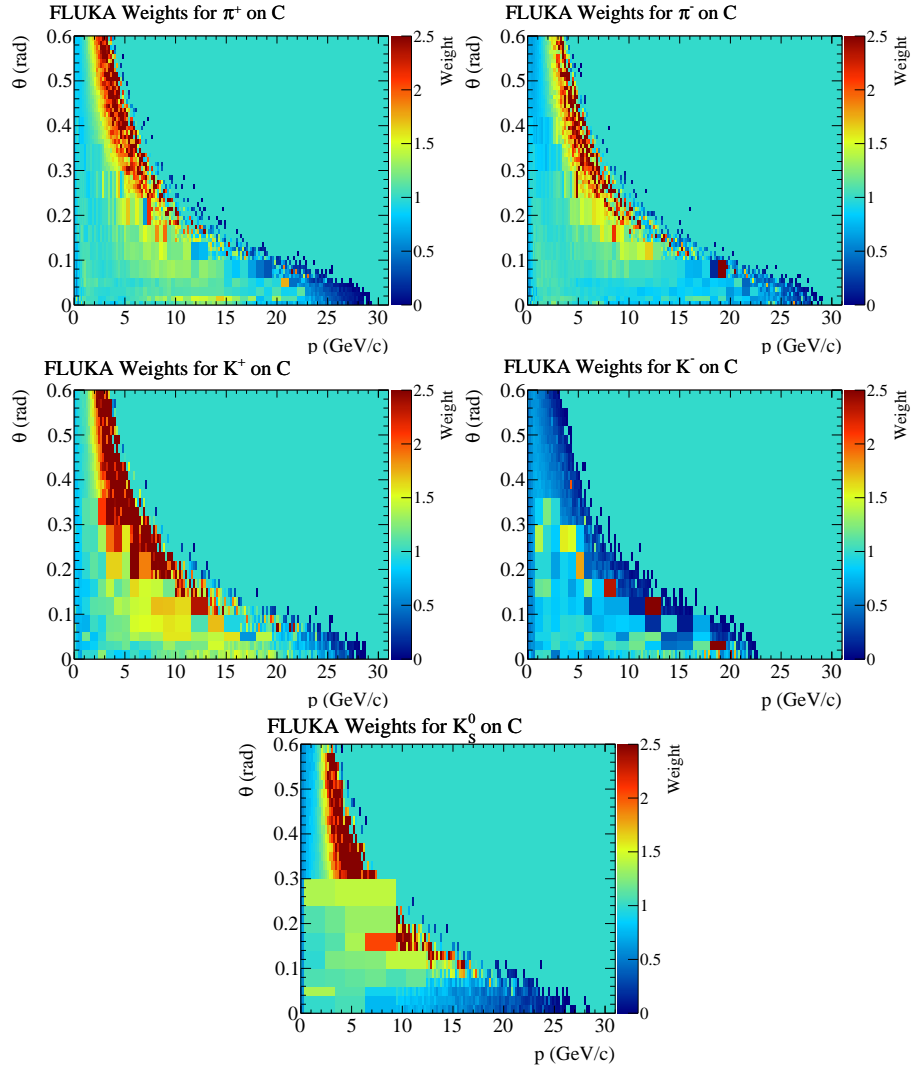


Figure 2.38: The meson multiplicity weights from NA61/SHINE data over FLUKA 2011. Outside the NA61/SHINE analysis phase-space, the weights are computed with respect to the BMPT fits to the NA61/SHINE data.

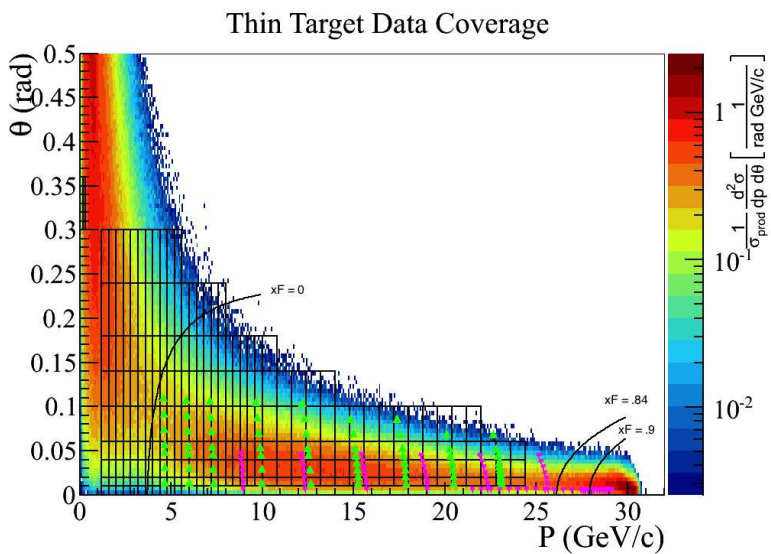


Figure 2.39: This figure shows the phase space covered by the different data sets and the FLUKA secondary proton distribution. The colored background is the FLUKA MC, rectangles are the NA61/SHINE bins, green triangles are the Eichten data and pink stars are the Allaby data. The Allaby and Eichten data were scaled according to the x_F scaling procedure in order to plot the data with the T2K beam energy. Lines of constant x_F are drawn, which are used as various cuts in the analysis.

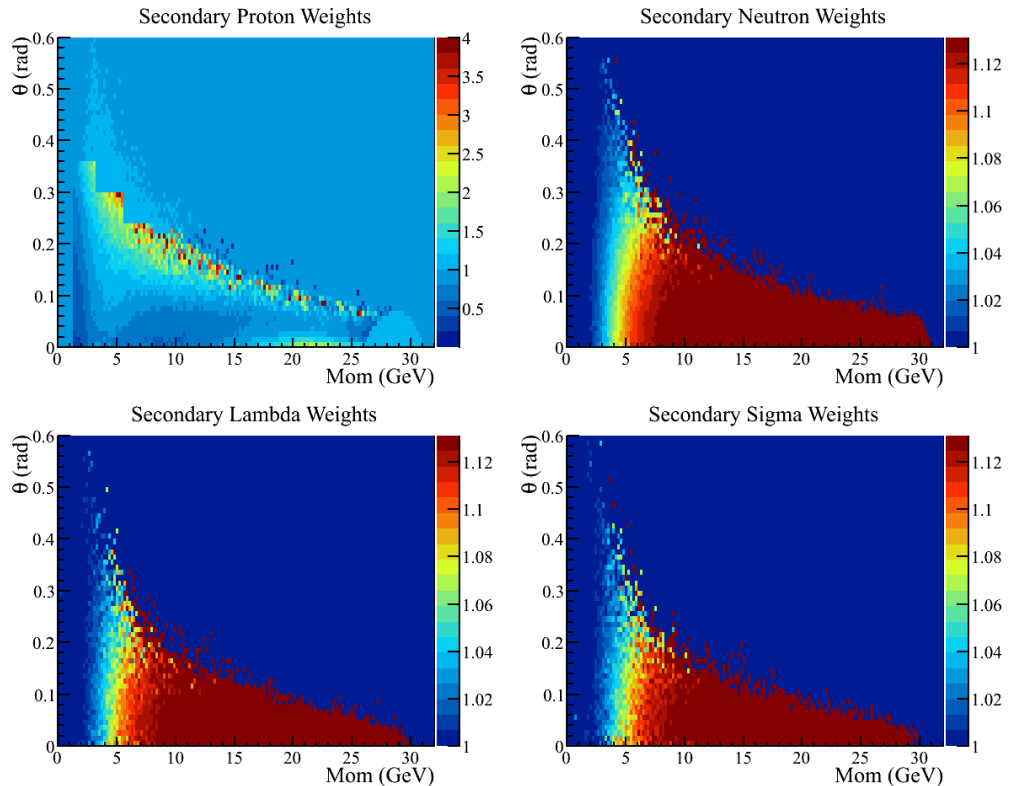


Figure 2.40: Secondary baryon weights for FLUKA MC are shown. These are the weights used to calculate the nominal neutrino flux in this flux release. The fading effect seen in the neutrons, Λ s and Σ s is a result of only tuning the leading baryons in these regions.

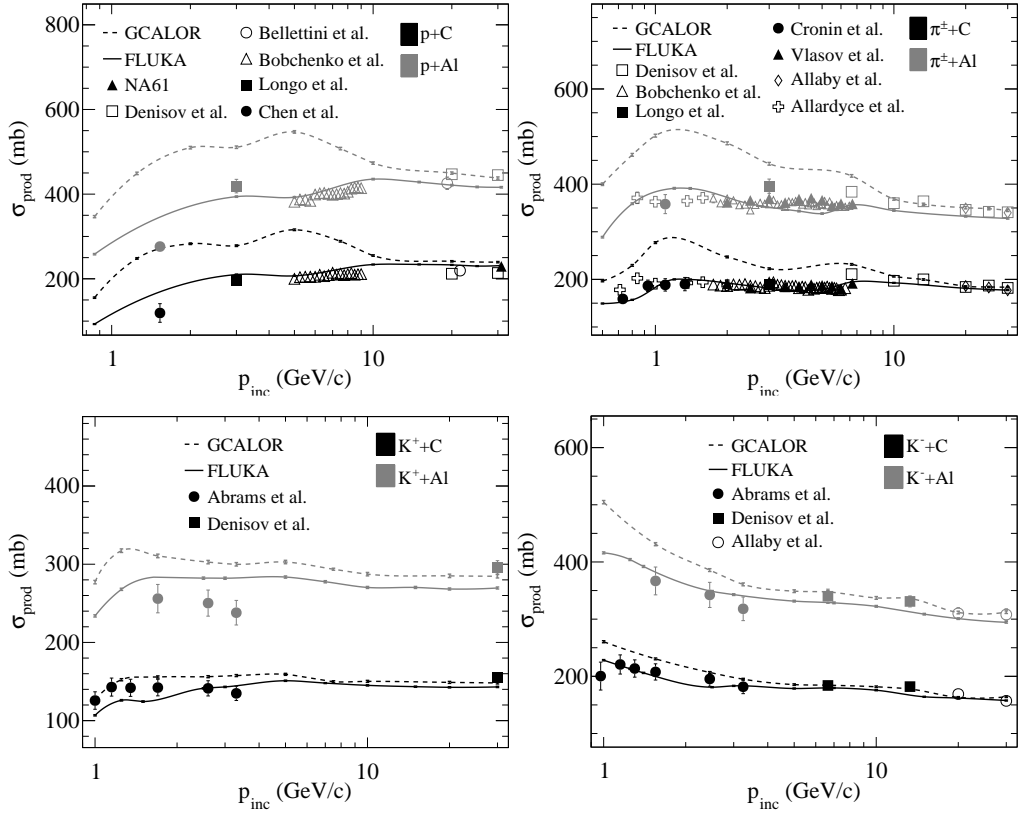


Figure 2.41: Comparisons of σ_{prod} measurements and the values used in the simulation (solid line for FLUKA and dashed line for GCALOR), for incident protons (top left) and charged pions (top right), K^+ (bottom left) and K^- (bottom right).

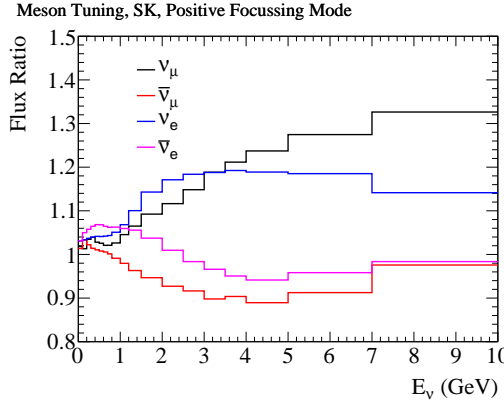


Figure 2.42: Ratio of the hadron interaction re-weighted flux over the nominal flux for ν_μ (black), $\bar{\nu}_\mu$ (red), ν_e (blue), $\bar{\nu}_e$ (magenta) at SK

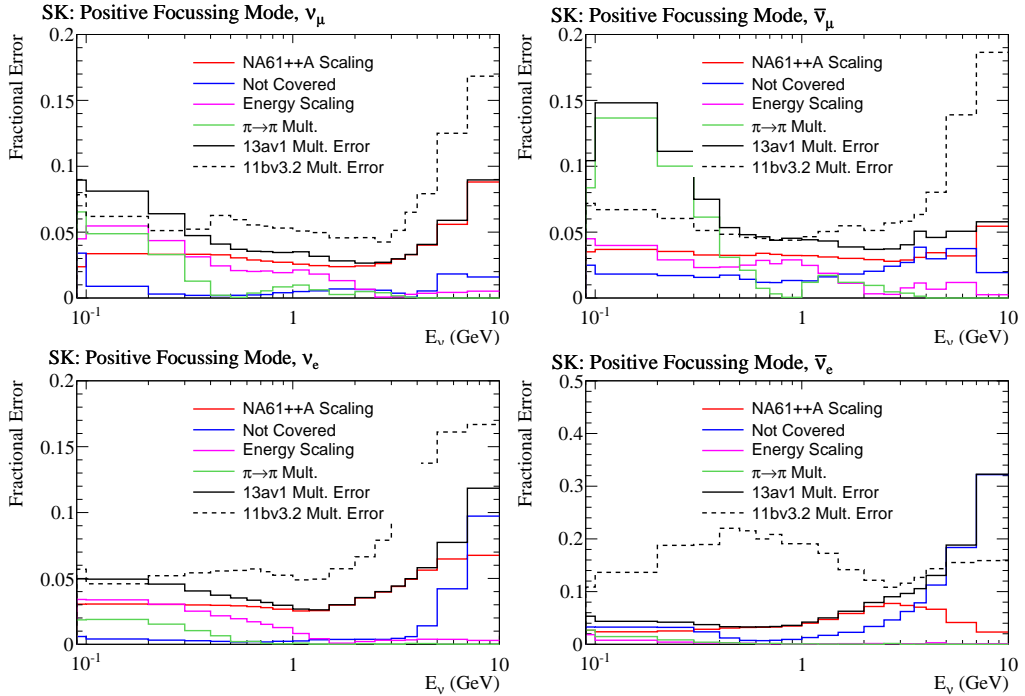


Figure 2.43: Meson multiplicity tuning uncertainties for SK fluxes in positive focussing horn mode operation; top left ν_μ , top right $\bar{\nu}_\mu$, bottom left ν_e and bottom right $\bar{\nu}_e$. The 13av1 labeled uncertainty is the current version of the estimated flux uncertainties in T2K as of summer 2015. It uses the latest preliminary results of NA61/SHINE thin target dataset recorded in 2009. The 11bv3.2 labeled uncertainty is the previous version of the estimated flux uncertainties that used the NA61/SHINE 2007 thin target data in the tuning.

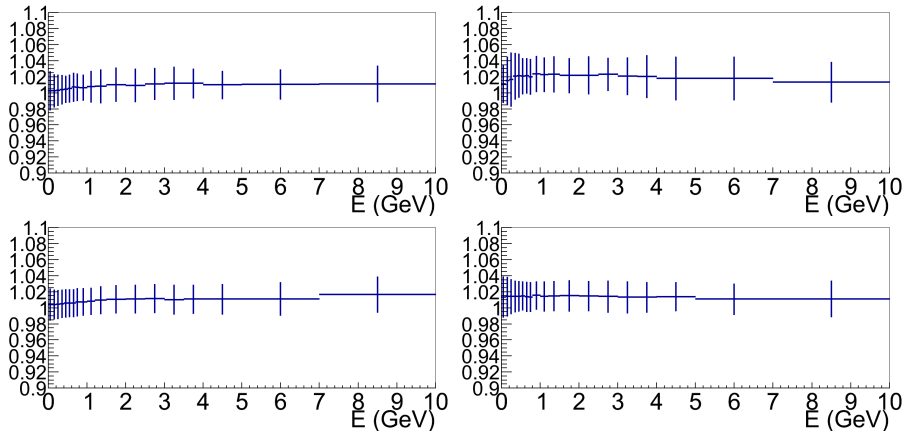


Figure 2.44: Relative effect of the baryon production tuning at SK for the ν_μ (top left), $\bar{\nu}_\mu$ (top right), ν_e (bottom left), $\bar{\nu}_e$ (bottom right) fluxes in positive focusing horn mode operation. The relative uncertainties are shown along with effect.

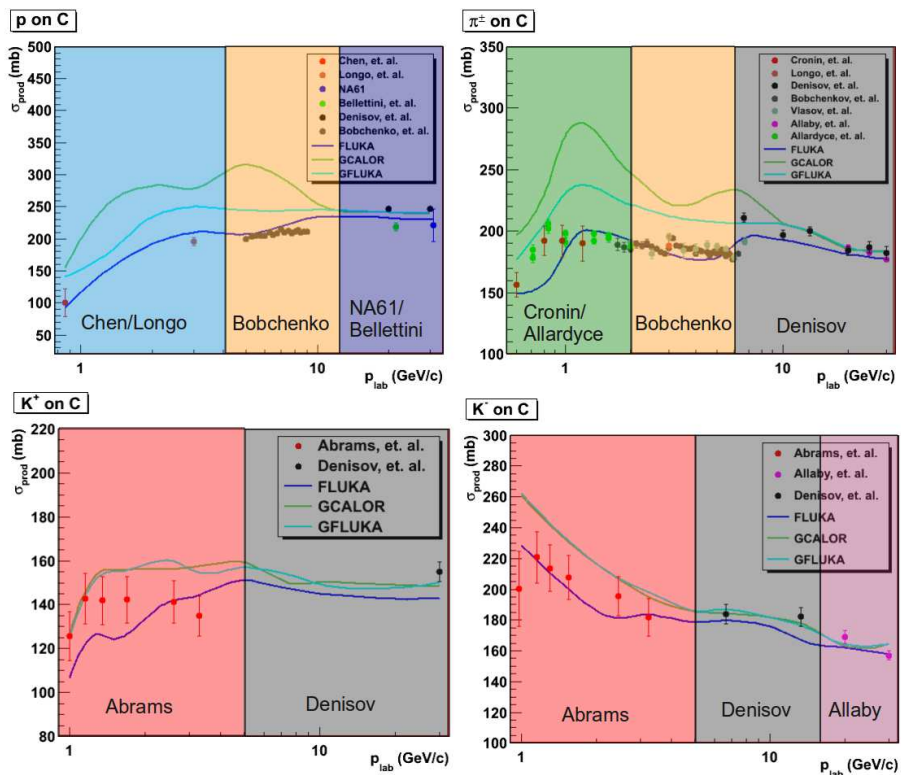


Figure 2.45: Different ranges considered for the production cross-section following the available data set from table 2.5.

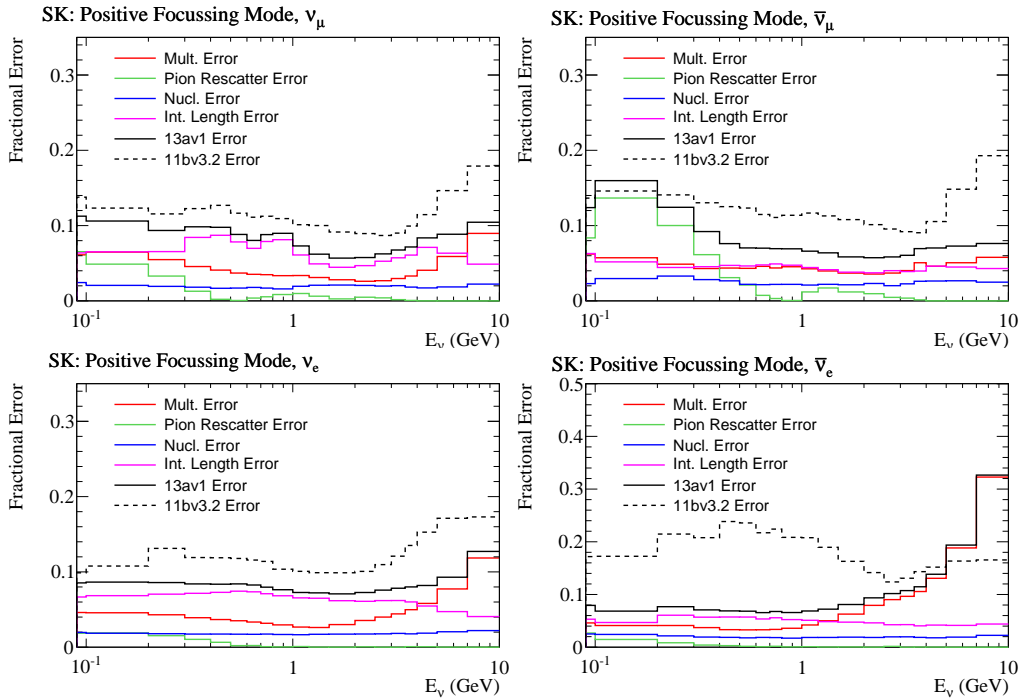


Figure 2.46: The hadron interaction model uncertainties evaluated for the different ND280 fluxes; top left ν_μ , top right $\bar{\nu}_\mu$, bottom left ν_e and bottom right $\bar{\nu}_e$. The 13av1 labeled uncertainty is the current version of the estimated flux uncertainties in T2K as of summer 2015. It uses the latest preliminary results of NA61/SHINE thin target dataset recorded in 2009. The 11bv3.2 labeled uncertainty is the previous version of the estimated flux uncertainties that used the NA61/SHINE 2007 thin target data in the tuning.

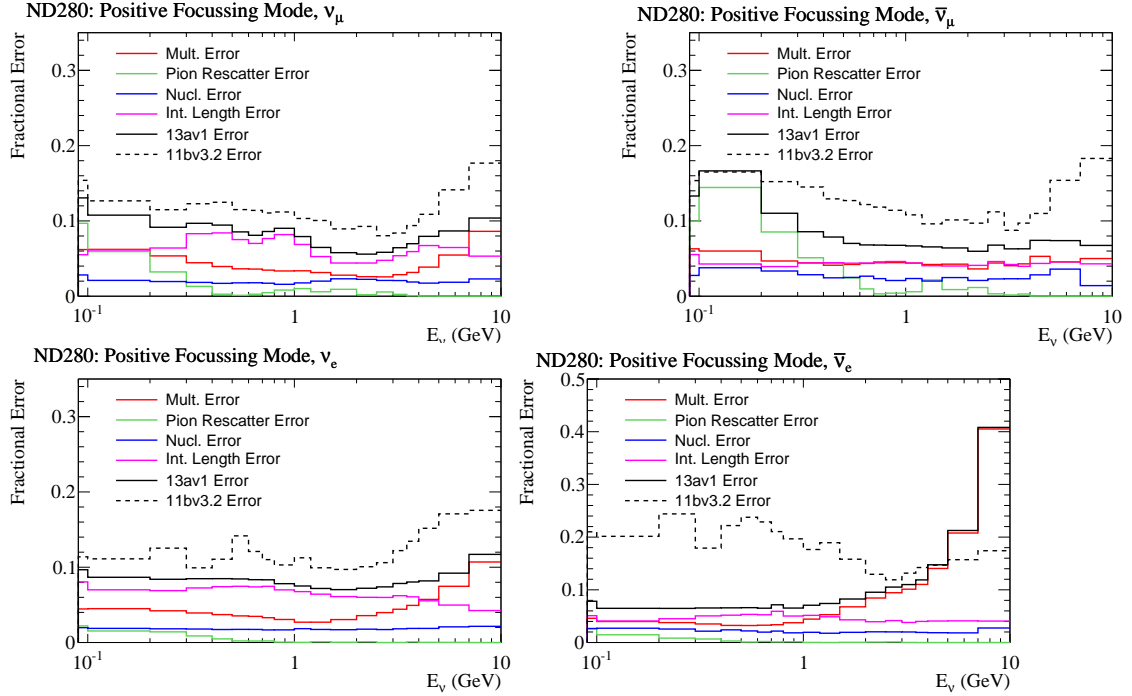


Figure 2.47: The hadron interaction model uncertainties evaluated for the different SK fluxes; top left ν_μ , top right $\bar{\nu}_\mu$, bottom left ν_e and bottom right $\bar{\nu}_e$. The 13av1 labeled uncertainty is the current version of the estimated flux uncertainties in T2K as of summer 2015. It uses the latest preliminary results of NA61/SHINE thin target dataset recorded in 2009. The 11bv3.2 labeled uncertainty is the previous version of the estimated flux uncertainties that used the NA61/SHINE 2007 thin target data in the tuning.

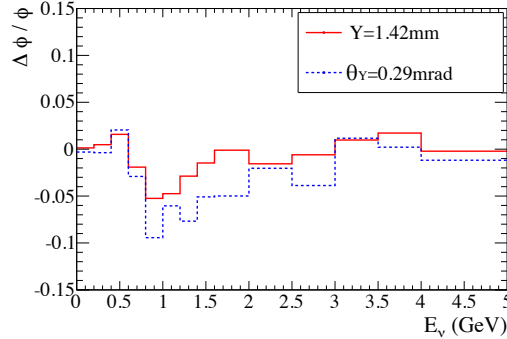


Figure 2.48: An example of the fractional change of SK ν_μ flux when the beam center position (Y) and center angle (θ_Y) measured in Run 1 are changed by 1σ , i.e. set to 1.42 mm and 0.29 mrad, respectively [60].

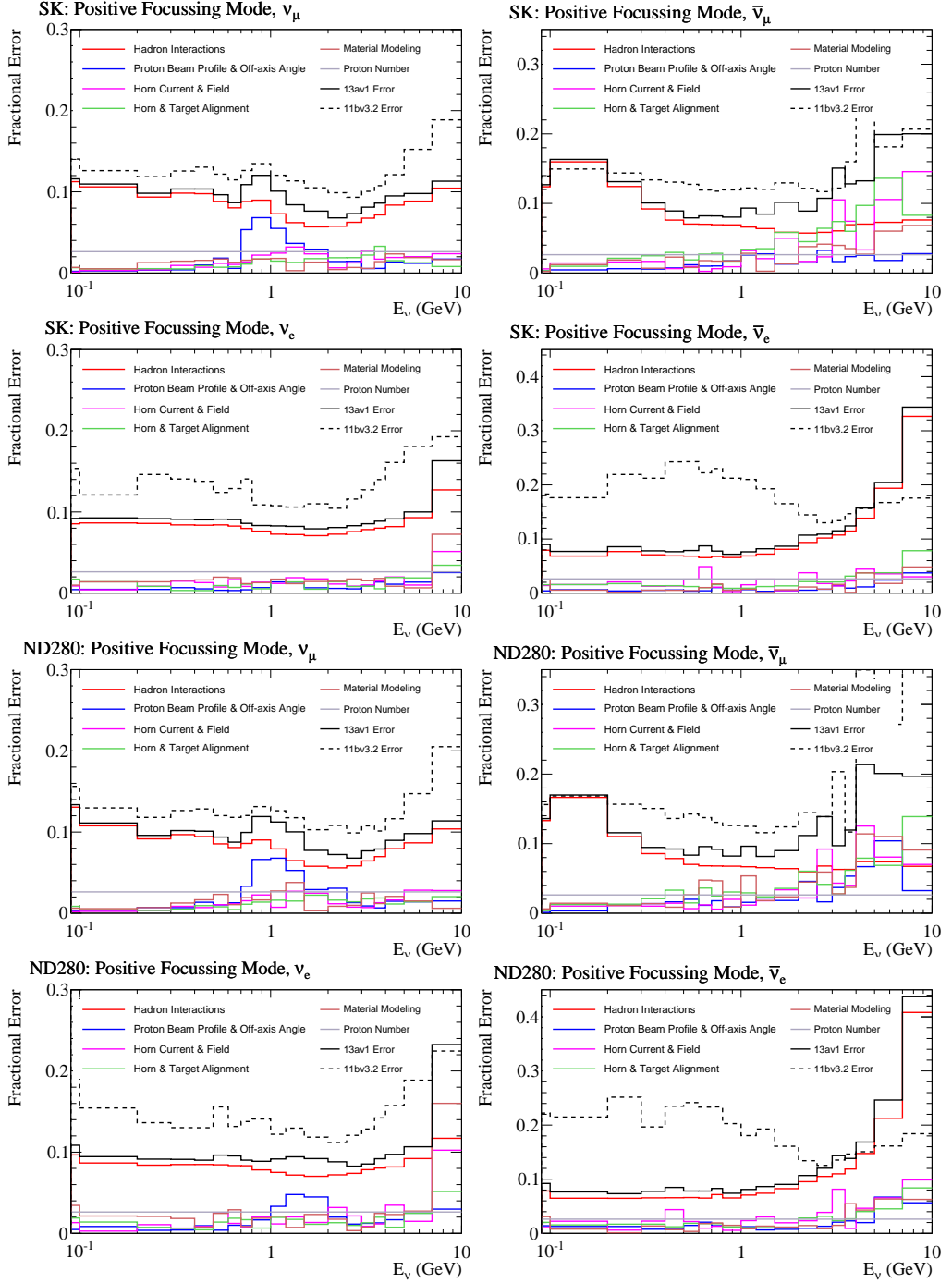


Figure 2.49: The total uncertainties evaluated for the SK flux predictions and the ND280 flux predictions. The 13av1 uncertainty is the current version. The 11bv3.2 is the previous version.

Chapter 3

The NA61/SHINE Experiment

NA61/SHINE (SPS Heavy ion and Neutrino physics Experiment) [103] is a fixed target experiment at the CERN SPS (Super Proton Synchrotron). It is a multi-purpose facility to study hadron production in hadron-proton, hadron-nucleus and nucleus-nucleus collisions. It has a rich physics program covering different topics:

- To study the properties of the onset of deconfinement [104] and search for the critical point of strongly interacting matter which is pursued by investigating p+p, p+Pb and nucleus-nucleus collisions
- Measurements of precise hadron production in order to improve predictions of neutrino beam flux in long baseline neutrino experiments
- Measurements of precise hadron production in order to improve simulations of cosmic-ray air showers

NA61/SHINE was proposed at CERN in November 2006. It inherited many of its components from the former NA49 experiment.

In this chapter we will only cover the information relevant to the neutrino program and more specifically, the hadron production campaign conducted for the T2K experiment.

3.1 Data sets for the T2K neutrino physics program

3.1.1 Data taking periods

Data taking periods conducted for the T2K experiment are summarised in table 3.1. These periods are divided into three different years and two target configurations.

Beam	(GeV/c)	graphite target	year	Nx10 ⁶
p	31	2cm “thin target”	2007	0.7
p	31	2cm “thin target”	2009	5.4
p	31	90cm “T2K replica”	2007	0.2
p	31	90cm “T2K replica”	2009	4
p	31	90cm “T2K replica”	2010	10

Table 3.1: Data taking periods for the T2K experiment

The so-called “thin target” is a graphite block of dimensions $2\text{cm}(L) \times 2.5\text{cm}(W) \times 2.5\text{cm}(H)$. The graphite grade was chosen to match as close as possible the T2K target graphite grade. The two centimetres of graphite in the beam direction are equivalent to 4% interaction length. The density of the thin target is $\rho = 1.84 \text{ g/cm}^3$ while for the T2K replica target $\rho = 1.831 \text{ g/cm}^3$.

The “T2K replica target” is made out of a 90cm long graphite rode with a diameter of 2.6 cm. Around the upstream end of the target, aluminium flanges are mounted so that the target could be fixed on a metallic frame of the NA61/SHINE experimental set-up. The target was delivered

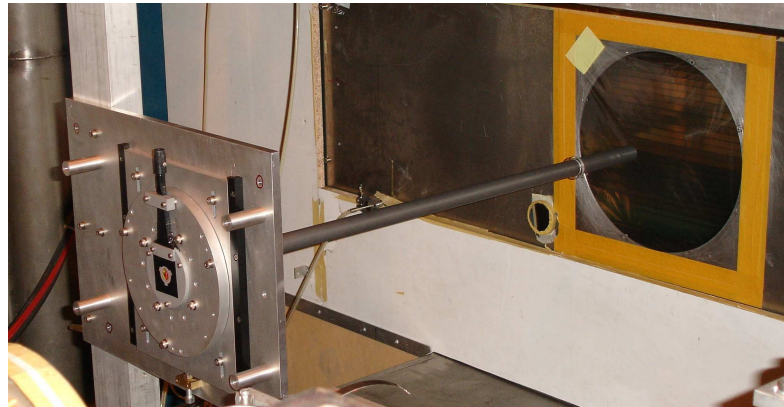


Figure 3.1: Photo of the T2K replica target mounted at NA61/SHINE. The aluminium flanges can be seen at the upstream part of the target (left).

to NA61/SHINE by the T2K collaboration. The density of the replica target is $\rho = 1.83 \text{ g/cm}^3$.

In 2007, a first run was recorded with a thin graphite target (2cm, equivalent to 4% interaction length). Even if the statistics was limited, seven particle species could be extracted: π^\pm , K^+ , K_s^0 protons and Λ . The thin target measurements allowed for the extraction of two different quantities: a production cross-section and double differential hadron productions in proton-carbon interactions at 31 GeV/c. The production cross-section relates to the rate at which 31 GeV/c protons interact with carbon to produce new particles. In the NA61/SHINE conventions, the quasi-elastic component of the total cross-section is subtracted from the inelastic cross-section to give the production cross-section:

$$\sigma_{prod} = \sigma_{inelastic} - \sigma_{quasi-elastic} \quad (3.1)$$

Double differential hadron productions $d^2n_\alpha/dpd\theta$ can also be called “multiplicities”. For the thin target data, they are defined with respect to the cross-sections σ_α as:

$$\frac{d^2n_\alpha}{dpd\theta} = \frac{1}{\sigma_{prod}} \frac{d^2\sigma_\alpha}{dpd\theta} \quad (3.2)$$

Multiplicities indicate the number of produced hadrons α as a function of angle and momentum with respect to incident beam protons. Three publications show these results [93, 105, 106].

Also in 2007, a pilot run was taken with the T2K replica target. The very limited dataset did not allow to provide precision measurements to the T2K collaboration. Nevertheless, it was effectively used to show a strong proof of principle regarding the feasibility of these measurements as well as their potential to constrain the T2K neutrino flux predictions. Spectra of positively charged pions were extracted and presented in the form of multiplicities. It is important to note that the definition of multiplicities is here slightly different with respect to the thin target

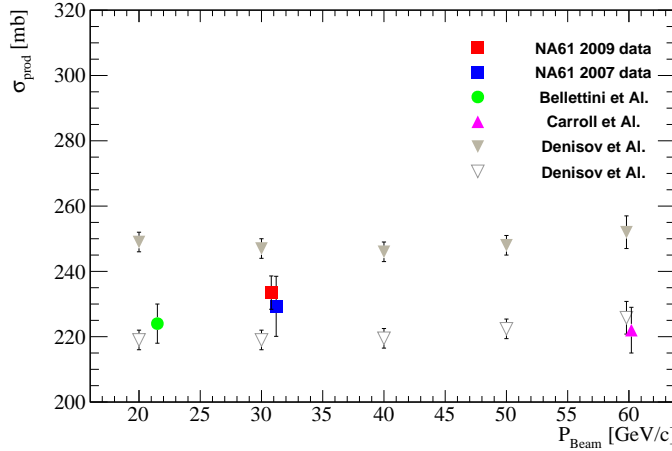


Figure 3.2: Production cross-section for the 2007 and 2009 data sets. Results from other experiments taken from Ref. [83, 88, 91] are shown for comparisons.

measurements. The number of produced hadrons is normalized to the number of protons on target. Hence, for the thin target measurements, multiplicities relate to the number of interacting protons while, for the T2K replica target measurements, they relates to number of incident protons on target. The results of these studies were published in Ref. [107].

During the 2009 period of data taking, large datasets were recorded for the thin target as well as for the T2K replica target. The thin target measurements have been analysed and are in the process of publication.

3.1.2 Thin target results

The production cross-section was found to be in agreement with the first 2007 results [108]. An improved method of analysis allowed for systematic uncertainties to be significantly reduced. The numerical values are:

$$\sigma_{prod} = 229.3 \pm 10.9 \text{ mb} \quad 2007 \quad (3.3)$$

$$\sigma_{prod} = 230.8^{+5.6}_{-4.7} \text{ mb} \quad \text{preliminary} \quad 2009 \quad (3.4)$$

Results for the 2007 and 2009 data are shown in fig. 3.2. Results of other measurements are displayed on the same plot for comparisons. Unfortunately it was not clear from the Denisov *et al.* [91] publication whether the quasi-elastic cross-section had been subtracted from the inelastic cross-section for the values quoted in the paper. Hence, two values are presented on fig. 3.2. For the lower values, the components of the quasi-elastic cross-section have been subtracted from the quoted published values.

Differential multiplicities are given in different polar angle intervals as a function of momentum. For the 2009 data set, the same six particle species as for 2007 could be extracted, and, in addition, K^- . Pion, kaon and proton spectra are given in fig. 3.3, fig. 3.4 and fig. 3.5. They are computed as a weighted average of the 2007 and 2009 results (except for K^-).

In the next chapters, the 2009 data set taken with the T2K replica target, will be discussed in great detail. Analysis technique, results and integration into the T2K neutrino flux predictions will be covered. The 2010 T2K replica target data set is in the final process of calibration. It comprises the largest statistical data set and covers the requirements made by T2K on hadron

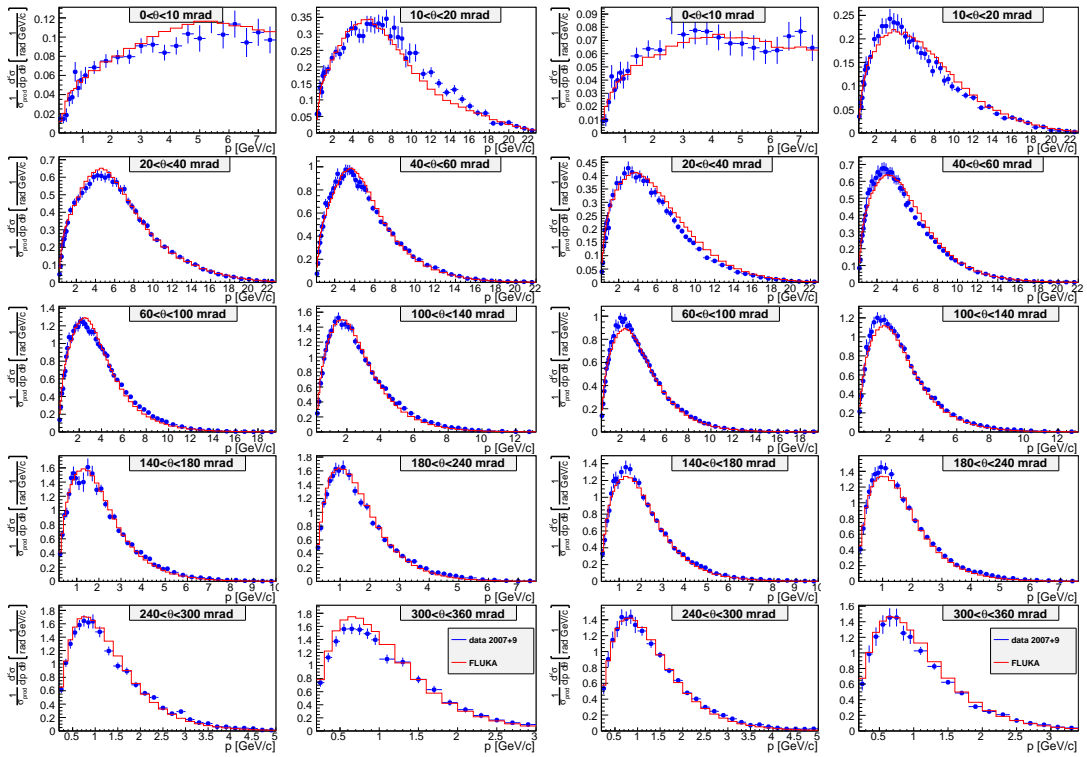


Figure 3.3: Multiplicities for positively charged pions (left) and negatively charged pions (right). Results are the weighted average of the 2007 and 2009 data sets.

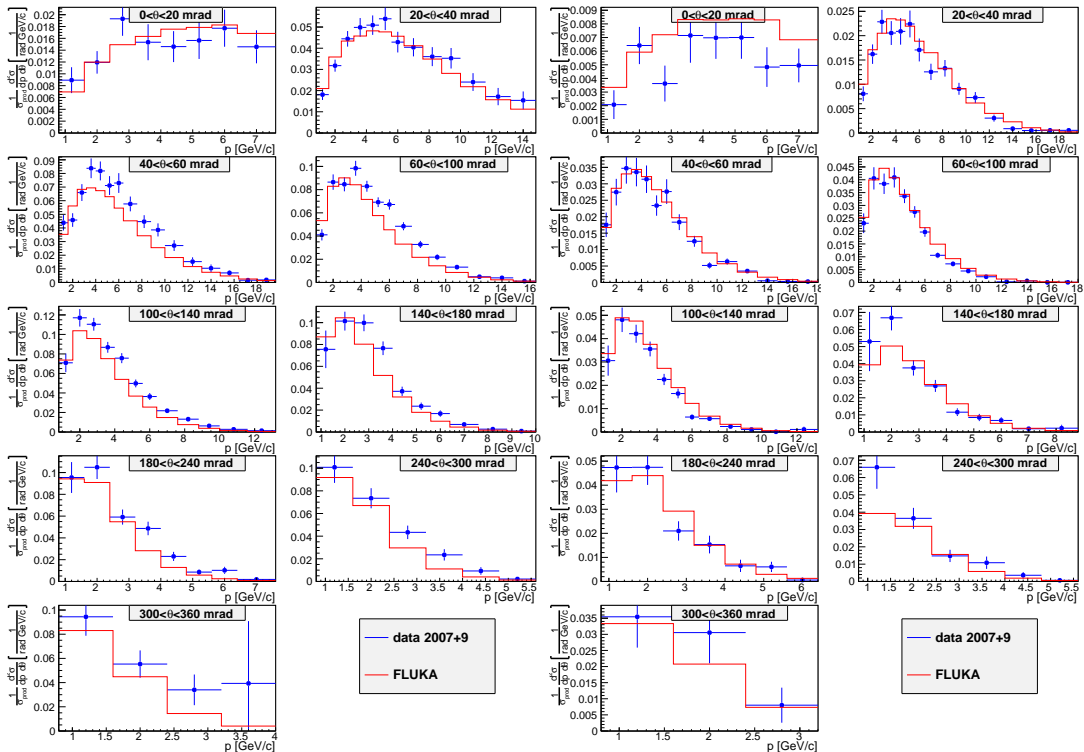


Figure 3.4: Multiplicities for positively charged kaons (left) and negatively charged kaons (right). Results for positively charged kaons are the weighted average of the 2007 and 2009 data sets. Results for negatively charged kaons have only been extracted for the 2009 data set.

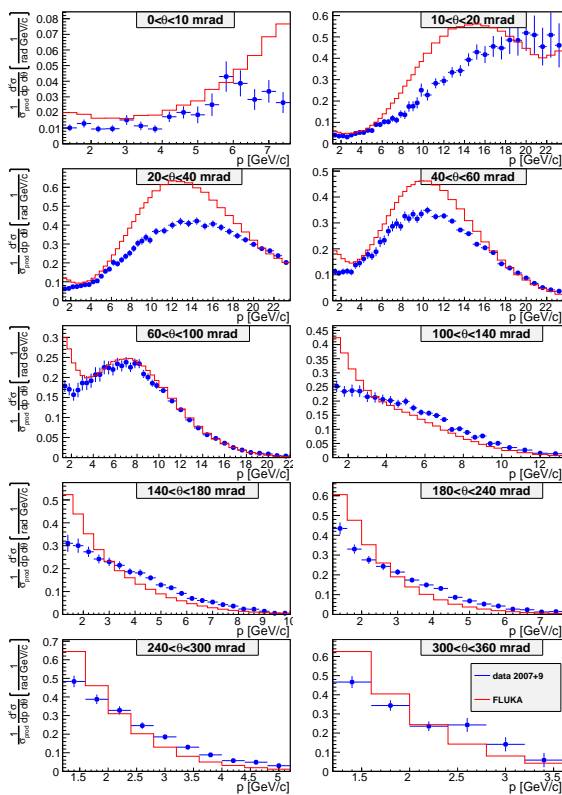


Figure 3.5: Multiplicities for protons. Results are the weighted average of the 2007 and 2009 data sets.

production measurements with a replica target.

3.2 The experimental setup

NA61/SHINE is served by the H2 beam line of the CERN North Area. The primary beam is extracted from the SPS and transported over 1km by bending and focusing magnets before impinging on the T2 target. The T2 target station hosts several beryllium plates of different lengths. The target plate inserted in the extracted beam is chosen to optimize the yield of the requested secondary particle momentum and type in the H2 beam line. Beams for NA61/SHINE are usually produced using a target length of 100 or 180mm. The H2 beam line can transport charged particles with a wide range of momenta from ~ 9 GeV/c up to the SPS energy of 400 GeV/c

The momentum selection in the beam is made in the vertical plane, as shown in Fig. 3.6 where the beamline basically consists of two large spectrometers able to select particles according to their rigidity. Thus the momentum-to-charge ratio $B\rho \approx 3.33p_b/Z$, where $B\rho$ in Tesla-meters, is set by the beam optics, p_b is the momentum of the beam particles in GeV/c, and Z the charge of the particle (in proton charge units). The beam spectrometer has an intrinsic resolution of

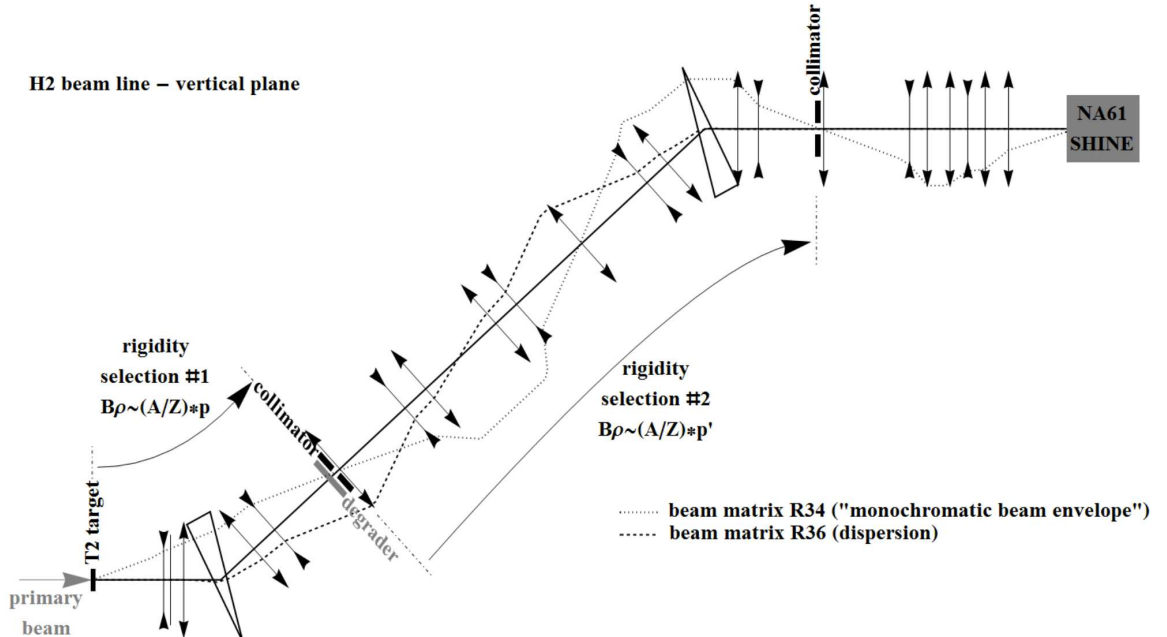


Figure 3.6: Schematic view of the vertical plane of the H2 beamline in the configuration used for the ion fragment separation. The dimensions are not to scale, e.g. the beamline is more than 600 m long, the height difference between T2 and the EHN1 is about 12 m, the aperture of the quadrupoles is ± 45 mm [103].

about 0.13% and a maximum rigidity acceptance of $\pm 1.7\%$.

Since the start of NA61/SHINE, the experimental set-up has been changed and upgraded with different new detectors. We will describe here the set-up as it was used in 2009 in detail and specifically for the T2K replica target measurements. A schematic drawing of the experiment is presented in fig. 3.7. It is composed of a target station, five Time Projection Chambers (TPC) and three Time of Flight (ToF) walls. Two TPCs are embedded in super-conducting magnets. They are called Vertex TPCs (VTPC1 and VTPC2). Two larger TPCs, called Main TPCs

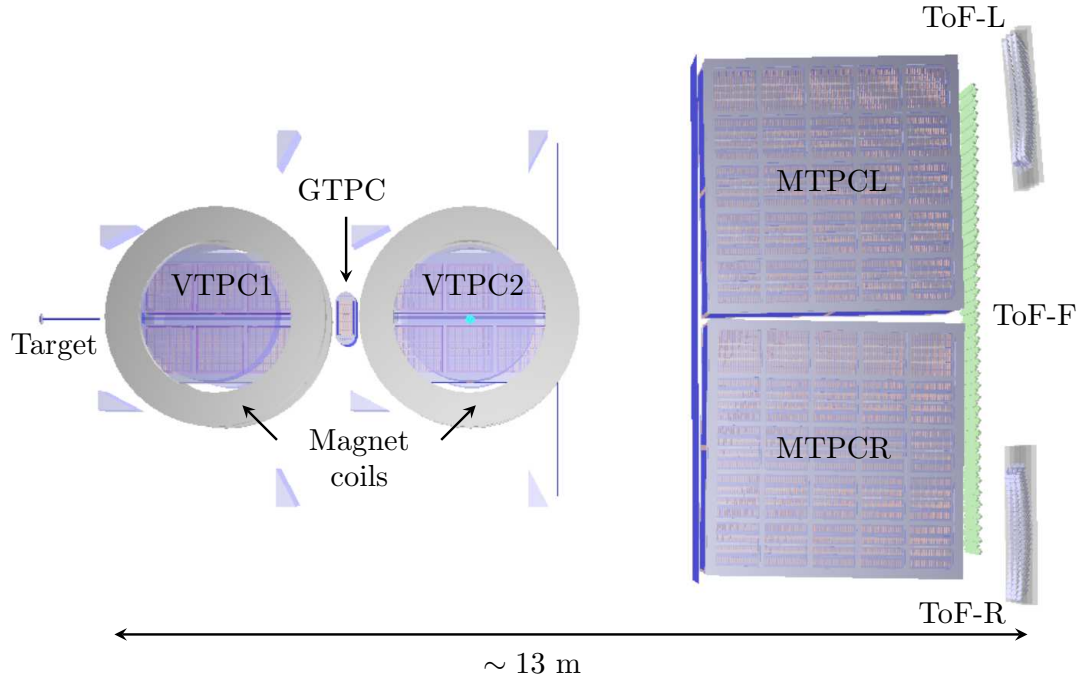


Figure 3.7: NA61/SHINE experimental set-up seen from above. The beam is coming from the left, impinging on the T2K replica target shown in this figure.

(MTPC), are located downstream of the magnets on both sides of the beam axis. The VTPCs are not instrumented along the beam axis and hence cannot record signal in the very forward region. The Gap TPC (GTPC) has been constructed to cover this area so that particles passing in between areas of the VTPCs, which are not instrumented, and also through the MTPCs can be reconstructed with the help of measured points in the GTPC.

The two identical super-conducting dipole magnets with a maximum total bending power of 9 Tm at currents of 5000 A have a width of 5700 mm and a length of 3600 mm. Their centres are approximately 2000 mm and 5800 mm downstream of the target respectively. The shape of the magnet yokes is such that the opening in the bending plane is maximized at the downstream end. Inside the magnets, a gap of 1000 mm between the upper and lower coils leaves room for the VTPCs. The magnetic field inside the sensitive volumes of the Vertex TPCs was precisely measured by Hall probes.

The standard configuration for data taking at beam momentum per nucleon of 150 GeV/c and higher is nominally 1.5 T, in the first magnet and 1.1 T in the second magnet. At lower beam momenta the fields are normally reduced proportionally to the beam momentum keeping the ratio of the two fields constant. Nevertheless, for the 2009 T2K replica target data sets, even if the beam energy was set at 30 GeV, the magnetic fields were set as for a 20 GeV/c proton beam. This was done in order to maximize the acceptance of the spectrometer with respect to the phase-space of interest for T2K.

detector	dimensions [mm]	hole [mm]	position [m]	material budget	
				[% λ_I]	[% X_0]
S1	$60 \times 60 \times 5$		-36.42	0.635	1.175
S2	$\phi = 28 \times 2$		-14.42	0.254	0.470
S3	$\phi = 26 \times 5$		-6.58	0.635	1.175
S4	$\phi = 20 \times 5$		-2.11	0.635	1.175
V0	$\phi = 80 \times 10$	$\phi = 10$	-14.16		
$V0^p$	$300 \times 300 \times 10$	$\phi = 20$	≈ -14		
V1	$100 \times 100 \times 10$	$\phi = 8$	-6.72		
$V1^p$	$300 \times 300 \times 10$	$\phi = 20$	-6.74		
BPD-1	$48 \times 48 \times 32.6$		-36.20	0.025	0.070
BPD-2	$48 \times 48 \times 32.6$		-14.90	0.025	0.070
BPD-3	$48 \times 48 \times 32.6$		-6.70	0.025	0.070
2009 thin target position			-5.810		
2009 T2K replica target position			-6.576		

Table 3.2: Summary of typical beam detector parameters: dimensions, positions along the beam-line (z coordinates) and their material budget (in terms of the nuclear interaction length λ_I and radiation length X_0). Positions of most of these detectors varied in time by a few cm due to dismounting and remounting in subsequent runs. Exceptions are BPD-3, V1 and $V1^p$, for which positions varied up to 50 cm depending on the employed target [103].

3.2.1 Beam line and triggers

The beam line between the T2 target and the NA61/SHINE target station is instrumented by a set of scintillation and Cherenkov counters as well as beam position detectors located upstream of the NA61/SHINE target station. It provides precise timing reference along with charge and position measurements of incoming beam particles. For the thin target data taking periods, an interaction counter located downstream of the target allowed to trigger on interactions in the target. For the 1.9 interaction length T2K replica target, this counter was not used in the trigger combination. Typical parameters of the scintillators and Beam Position Detectors (BPDs) are summarized in table 3.2.

The locations of the beam detectors are indicated in fig. 3.8. The first sketch (a) represents a typical example of locations for thin target measurements where the S4 counter is included in the trigger and plays the role of interaction counter. The second sketch (b) corresponds to the counters used for the T2K replica target measurements. The S3 counter was positioned at 5mm of the upstream face of the target and had an identical diameter to the target of precisely 2.6 cm. This allowed to define a trigger based on incident protons impinging on the upstream face of the T2K replica target.

The H2 beam line can transport and deliver positively and negatively charged hadrons (proton, pions, kaons) to NA61/SHINE. For given beam settings, i.e. rigidity selection, the momentum selected hadrons are mixed. In order to detect the desired hadrons, the beam line is equipped with a special differential Cherenkov counter, the Cherenkov Differential Counter with Achromatic Ring Focus (CEDAR) counter [109]. The counter has a sophisticated optical system that collects and focuses the Cherenkov photons onto the plane of a diaphragm, the opening of which can be tuned, in relation to a given gas pressure, so as to allow only the photons from the wanted species to pass through thus be detected by the 8 PMTs of the counter. The pressure range at which counts of a wanted hadron (p (\bar{p}) or π^+ (π^-), or K^+ (K^-)) per incident particle are maximal is found by performing a pressure scan in the domain where the wanted hadron peak is expected.

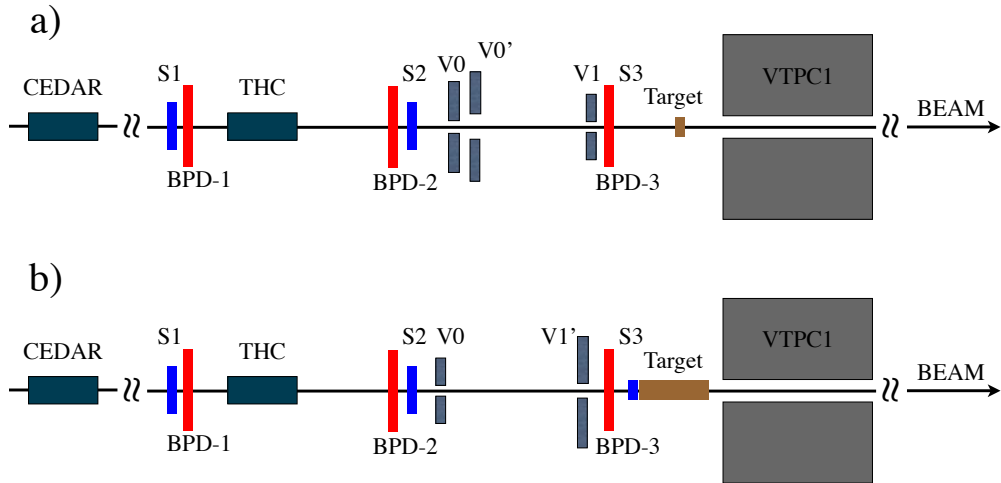


Figure 3.8: Schematic layout (horizontal cut in the beam plane, not to scale) of the beam detectors in two configurations of the beam line. a) for the thin target measurements where the S4 counter plays the role of interaction counter; b) for the T2K replica target measurements where the S3 counter insures that the proton beam hit the target upstream face.

The results of the gas pressure scan performed in the full relevant pressure range for beams at 13, 31 and 158 GeVc are presented in fig. 3.9. The final setting is the pressure corresponding to the center of the wanted hadron peak.

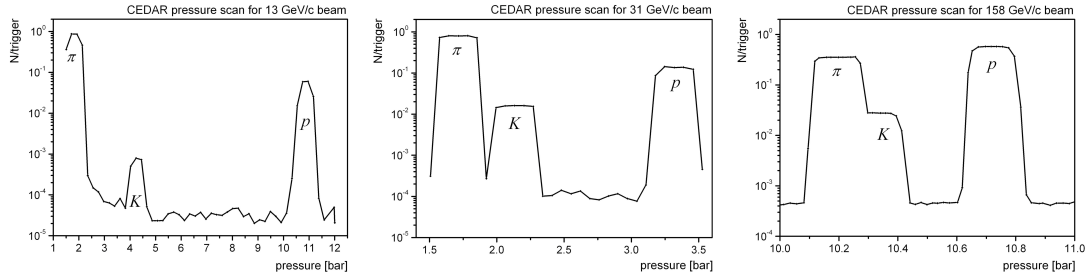


Figure 3.9: Counts of hadrons per incident beam particle from the CEDAR counter as a function of the gas pressure within the pressure range which covers maxima of pions, kaons and protons at 13 (left), 31 (middle) and 158 GeV/c (right) [103].

Under standard operational conditions, the detection efficiency of the detectors is better than 95%. The number of misidentified particles is lower than 0.8%. For the proton-carbon at 31 GeV/c, the trigger definition also required the signal from a carbon dioxide filled Threshold Cherenkov detector in anti-coincidence.

The first scintillator counter along the beam line is the S1 counter. It has to be reliable as a precise reference timing as it is used to give the start signal for the measurement of the time of flight. Hence it is equipped with four photomultipliers directly coupled to the scintillator. Scintillators labeled with the letter “V” in table 3.2 and fig. 3.8 are used as veto-counters in the trigger logic. The trigger is formed by combining several of the beam counters listed in table 3.2

and the Cherenkov detectors for beam particle identification.

The positions of the incoming beam particles in the transverse plane are measured by a telescope of three Beam Position Detectors (BPDs) placed along the beamline upstream of the target. These detectors are proportional chambers operated with Ar/CO_2 (85/15) gas mixture. Each BPD measures the position of the trigger-selected beam particle in two orthogonal directions independently using two planes of orthogonal strips. On each strip plane a charge distribution is induced with a width of about 5 strips on average. The reconstruction algorithm first searches for a cluster in each plane. The cluster is defined as a set of adjacent strips with signal amplitudes above a threshold value (to remove signals from pedestal fluctuations). Then, an average of the strip positions weighted with the signal amplitudes on the strips is calculated for the cluster to estimate the position of the beam particle (the so-called centroid method). A 3-dimensional point measured by a given BPD is built from two transverse coordinates measured by the two strip planes and the position of the BPD along the beamline. The trajectory of each beam particle is reconstructed as a straight line using a least square fit applied to the positions measured by the three BPDs in $x - z$ and $y - z$ planes independently.

3.2.2 Data calibration, reconstruction and simulation

The calibration procedure is largely based on the approach developed for the NA49 experiment [110] and consists of several consecutive steps resulting in optimized parameters for

1. detector geometry, drift velocity, and residual corrections,
2. magnetic field,
3. time-of-flight measurements, and
4. specific energy loss measurements.

Each step involved reconstruction of the data required to optimize a given set of calibration constants followed by verification procedures. Details of the procedure and quality assessment are presented in Ref. [111].

Reconstruction algorithms used for the analysis described in this thesis are based on those developed by the NA49 Collaboration [110]. The main steps of the reconstruction procedure are

1. cluster finding in the TPC raw data, and calculation of a cluster center of gravity and total charge,
2. reconstruction of local track segments in each TPC separately,
3. matching of track segments from different TPCs into global tracks,
4. track fitting through the magnetic field and determination of track parameters at the first measured TPC cluster,
5. determination of the interaction vertex as the intersection point of the incoming beam particle with the middle target plane,
6. refitting the particle trajectory using the interaction vertex as an additional point and determining the particle momentum at the interaction vertex, and
7. matching of ToF-F hits with the TPC tracks.

Simulation of the NA61 detector response consists of the following steps (see Ref. [80] for more details):

	VTPC-1	VTPC-2	MTPC-L/R	GAP-TPC
size (L×W×H) [cm]	250 × 200 × 98	250 × 200 × 98	390 × 390 × 180	30 × 81.5 × 70
No. of pads/TPC	26 886	27 648	63 360	672
Pad size [mm]	3.5 × 28(16)	3.5 × 28	3.6 × 40, 5.5 × 40	4 × 28
Drift length [cm]	66.60	66.60	111.74	58.97
Drift velocity [cm/μs]	1.4	1.4	2.3	1.3
Drift field [V/cm]	195	195	170	173
Drift voltage [kV]	13	13	19	10.2
gas mixture	Ar/CO ₂ (90/10)	Ar/CO ₂ (90/10)	Ar/CO ₂ (95/5)	Ar/CO ₂ (90/10)
# of sectors	2 × 3	2 × 3	5 × 5	1
# of padrows	72	72	90	7
# of pads/padrow	192	192	192, 128	96

Table 3.3: Parameters of the VTPCs and MTPCs. The pad length in the VTPC-1 equals 16 mm only in the two upstream sectors. In the MTPCs the 5 sectors closest to the beam have narrower pads and correspondingly more pads per pad row.

1. generation of p+C interactions at 31 GeV/c using the FLUKA [81, 82] model,
2. propagation of outgoing particles through the detector material using the GEANT 3.21 package [112], which takes into account the magnetic field as well as relevant physics processes, such as particle interactions and decays,
3. simulation of the detector response using dedicated NA61 packages which introduce distortions corresponding to all corrections applied to the real data,
4. storage of the simulated events in a file which has the same format as the raw data,
5. reconstruction of the simulated events with the same reconstruction chain as used for the real data, and
6. matching of the simulated and reconstructed tracks.

More detailed description of specific Monte-Carlo simulations for the T2K replica target data set will be discussed in section 3.3.

3.2.3 The Time Projection Chambers

The main tracking devices of NA61/SHINE are the four large time projection chambers, and the smaller gap TPC. As presented in fig. 3.7, the VTPCs are located in a magnetic field while the MTPCs are positioned downstream of the magnets, symmetrically about the beam line. The GTPC is mounted between the two VTPCs and is centered on the beam line for measuring particles produced with the smallest production angles.

The TPC are filled with a gaz mixture of argon and carbon dioxide. Details concerning the dimensions and main characteristics of the TPCs are given in table 3.3.

Charged particles, when traversing the TPCs, ionize the gas and leave a trace of electrons. These electrons drift with constant velocity under the influence of a vertical uniform electric field towards the top plate, where their position, arrival time and total number are measured with proportional wire chambers. In order to achieve high spatial resolution, the chamber top plates are subdivided into pads of about one square centimeter area each, making a total of about 180 000 for all TPC's. From the recorded arrival times of the track signals and the known pixel positions, a sequence of 3-dimensional measured points along the particle trajectories can be obtained.

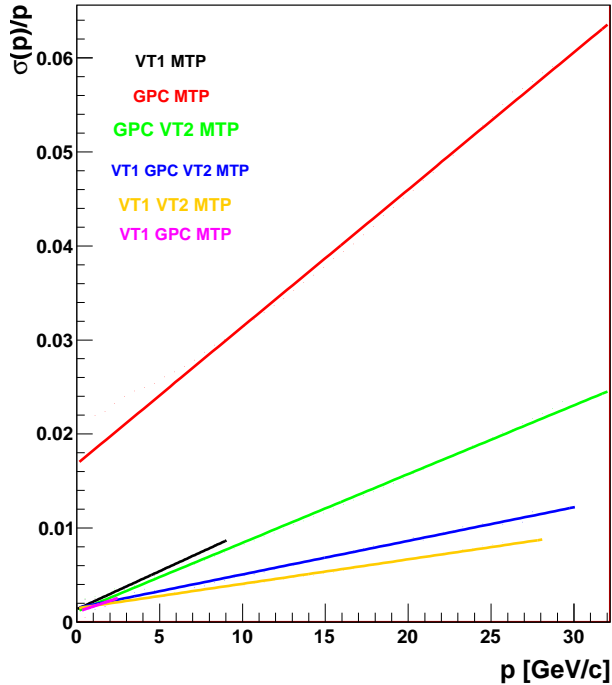


Figure 3.10: Momentum resolution as a function of the measured momentum for the 2009 T2K replica target data set. The forward going tracks going through GTPC MTPC show a lower resolution than those having a stronger bending.

The reconstruction of tracks through the entire NA61/SHINE set-up is based on these sequences of points and is done in three stages. First an algorithm reconstructs the tracks in each TPCs independently. Then the segments between the different TPCs are matched. Finally, parameters are computed for the globally reconstructed tracks matched between the TPCs.

The bending of the tracks through the magnetic field allows for the definition the momentum of the particles. The deposited charge along the track paths allows for the measurement of the energy loss.

The resolution of the momentum varies significantly with the different possible topologies of the tracks. For example, the longer tracks with stronger bending have a more precise momentum reconstruction than those going through the very forward region. This is illustrated on fig. 3.10, where the momentum resolution is plotted as a function of the measured momentum for different track topologies.

The specific energy loss in the TPCs for positively and negatively charged particles as a function of momentum is shown in fig. 3.11.

The energy loss resolution is $\sim 4\%$. It depends on the number of measured points. Tracks with higher measured points will have a better resolution. Figure 3.12 shows this behavior.

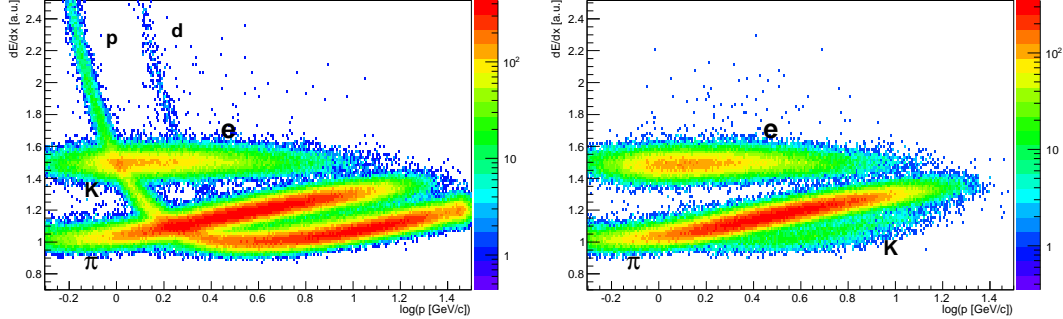


Figure 3.11: Specific energy losses in the TPCs for positively (left) and negatively (right) charged particles as a function of momentum. Data taken from the 2009 T2K replica target data set.

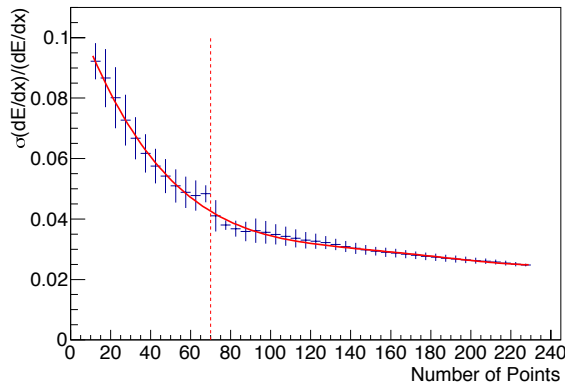


Figure 3.12: Resolution of the energy loss as a function of the number of measured points along the track.

3.2.4 The Forward Time Of Flight

The particle identification based only on energy loss cannot be performed in the momentum range of a few GeV/c. As can be seen in fig. 3.11, the Bether-Bloch curves overlap in this region. To resolve this problem, NA61/SHINE uses an additional and independent particle identification by Time of Flight (ToF) detectors. The particle's mass squared is obtained by combining the information from the particle's time of flight, t , with the track length, l , and momentum, p , measured in the TPCs:

$$m^2 = p^2 \left(\frac{c^2 t^2}{l^2} - 1 \right) \quad (3.5)$$

Two ToF walls, the ToF-L and ToF-R detectors, were inherited from NA49. Unfortunately their geometrical coverages are limited and do not span over the entire phase-space of interest for T2K. When operating at the T2K proton beam at 31 GeV/c, a large fraction of the tracks are produced by low-momentum particles which exit the spectrometer between ToF-L and ToF-R. The additional forward time of flight (ToF-F) wall was therefore constructed to provide full time of flight coverage of the downstream end of the MTPCs.

The ToF-F consists of modules, each containing eight scintillator bars. For the 2007 data taking periods, eight modules were installed, for a total of 64 scintillators. The ToF-F wall was

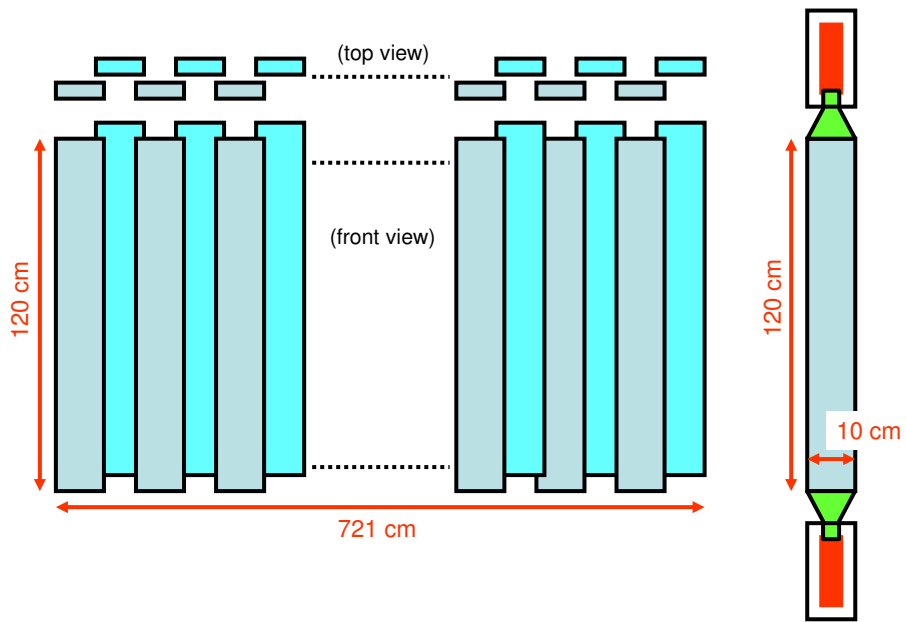


Figure 3.13: Schematic layout of scintillators in the ToF-F detector.

extended for the 2009-2010 periods by two more modules for a total of ten modules and 80 scintillator bars. The ToF-F is symmetric with respect to the beam axis. Half of the modules were placed on the left side, the other half placed on the right side. The size of each scintillator is $120 \times 10 \times 2.5\text{cm}^3$. They are staggered with 1cm overlap to ensure full coverage in the ToF-F geometrical acceptance. This configuration provides a total active area of $721 \times 120\text{cm}^2$ as illustrated in fig. 3.13. Each scintillator bar is read out on both sides with 2" Fast-Hamamatsu R1828 photomultipliers, for a total of 160 readout channels. The scintillators are plastic, Bicron BC-408 scintillators, with a scintillation rise time of 0.9 ns, a decay time of 2.1 ns and attenuation length of 210 cm. Their maximal emission wavelength is about 400 nm perfectly matching the PMT spectral response. In order to ensure proper optical contact between the PMTs and the light-guides, a 3 mm thick silicone cylinder matching the diameter of the PMT and light-guide is inserted at the interface.

The start signal is provided by the fast beam counter S1 of the central trigger system. The time measurement is carried out by LeCroy FASTBUS Time-to-Digital Converter (TDC) units digitizing the time in 12 bits dynamic range with a sampling time of 25 ps. The analog signals of the PMTs are converted by LeCroy Analog-to-Digital Converter (ADC) units into 12 bits. The time measurement, t , has an offset, t_0 , which is specific to each channel as it depends on cable length, PMT gain or constant fraction discriminator responses. t_0 was therefore carefully adjusted on a channel by channel basis by first assuming that all produced particles are pions and shifting the mean value of the $tof = t - t_\pi$ distribution accordingly. In a first iteration, this method allows to discriminate pions from protons and was then repeated by selecting only pions.

The mass-squared distribution and the resolution of its measurement as a function of momentum are presented in fig. 3.14. The intrinsic resolution of the ToF-F was also determined (see fig. 3.15). This was achieved by selecting particles that hit the region where the scintillat-

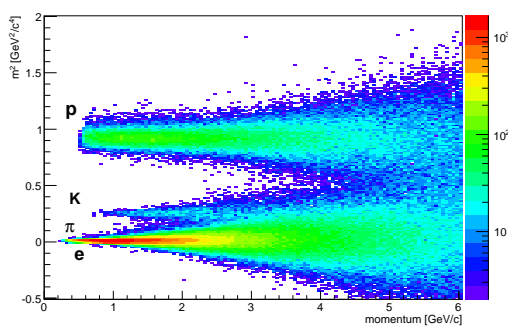


Figure 3.14: Mass squared versus momentum as measured by the ToF-F

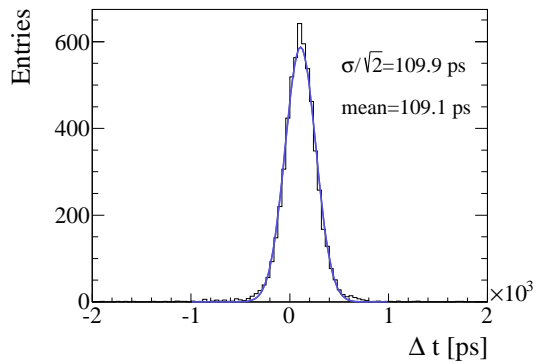


Figure 3.15: Distribution of the difference between a particle's time of flight measured independently by the overlapping scintillator bars of the ToF-F detector. The width of the distribution is about 155 ps, indicating a *tof* resolution of about 110 ps for a single measurement.

ors overlap and plotting the time difference between the two signals. The Gaussian fit to the distribution gives a resolution $\sigma_{tof} = \frac{155}{\sqrt{2}} \approx 110$ ps.

3.3 Monte-Carlo simulations

3.3.1 Specific Monte-Carlo productions for the T2K replica target

Dedicated Monte-Carlo productions have been generated for the simulation of 31 GeV/c protons with the thin carbon target and the T2K replica target. In order to be consistent with the T2K neutrino beam predictions, FLUKA2011 is also used in NA61/SHINE to generate all interactions inside the graphite target. The GEANT3 transport code is used to track the particles through the detector and GCALOR handles the interactions within the spectrometer material.

The full simulation chain is split into three parts:

1. First a standalone FLUKA simulation is run. The target geometry is precisely described as the one used for the data taking. For the T2K replica target, it consists of a 90cm long graphite rode with aluminum flanges. The target is positioned at the location given for the 2009 data taking period. The incident proton beam profile is simulated following the shape of the distributions for the positions and divergences of the specific data set to be analyzed. The momentum of the beam is set precisely at 30.92 GeV/c to match the beam momentum of the data. All interactions happening inside the target are stored at the simulation level and the position, momentum as well as polar and azimuthal angles of the particles exiting the target are recorded at the surface of the target and saved as output of the FLUKA simulation.
2. GEANT3 uses the variables at the surface of the target outputted by FLUKA to track the particles through the NA61/SHINE experimental setup. GCALOR handles all hadronic interactions in the spectrometer. Different effects are simulated, like the $\vec{E} \times \vec{B}$ effect that

take into account deviations of the drifted electrons due to the fact that the magnetic and electric fields are not perfectly aligned with each others.

3. The simulated tracks are finally reconstructed following the same reconstruction chain as the one applied to the data. All information from the FLUKA simulation through the simulated tracks until their reconstructions are stored in the final output files. This allows to get the full history of the simulation and to match the reconstructed tracks with the simulated tracks.

A total of 10 million protons on target have been simulated with the specific beam profile and target position for the 2009 T2K replica target analysis.

3.3.2 Flat phase-space simulations

The acceptance of the NA61/SHINE spectrometer is studied with dedicated Monte-Carlo productions. These are produced in so-called flat phase-space simulations. The idea is to generate the particles in GEANT3 not by following the FLUKA distributions at the surface of the target, but by considering flat distributions for the p , θ , ϕ variables and all the possible (x, y, z) coordinates corresponding to the surface of the target. For each of the 6 longitudinal bins in z , the (p, θ) phase-space is divided into bins of 0.2 GeV/c in momentum and 10 mrad in polar angle. In each of these bins, 400 particles are generated, following uniform distribution in ϕ and covering the entire possible ranges for the x and y coordinates on the surface of the target. Particles are then propagated through the detector and magnetic field with no simulation of physics processes such as decays, secondary interactions. The positions of the simulated clusters in the VTPCs are corrected for $\vec{E} \times \vec{B}$ effects. The geometrical acceptance of the spectrometer can then be studied by looking at the fraction of tracks crossing the detectors and fulfilling some analysis requirements. Acceptance maps will be presented and further discussed in section 4.4.3.

Chapter 4

The T2K Replica Target Analysis

The analysis of the T2K replica target presented in this chapter is based on the 2009 data set. The events recorded in 2007 have been analyzed and results have been published in Ref. [107] and in thesis [80]. The 2009 data set is more than one order of magnitude larger in statistics than the 2007 data set.

4.1 Incident proton beam

As explained in section 3.2.1, a set of counters placed in the proton beam line form the components of the trigger. Four different triggers are defined for the 2009 data set, marked as T1, T2, T3 and T4. Table 4.1 lists the different combinations of counters for each trigger for the four run periods. The NA61/SHINE beam line with the relevant counters for the 2009 T2K replica target data set is presented in fig. 4.1. The dimensions of the counters are given in section 3.2.1.

T1, T2 and T3 include the Cherenkov detector counters, allowing to select only protons as beam particles. T2 and T3 further require a hit in the S3 counter, which has the exact same diameter as the target and which is positioned at 5mm of the upstream face of the target. Hence, T2 and T3 can be seen as interaction triggers as they ensure that the incident beam proton is impinging on the target. T3 has an additional veto counter V0 with a smaller hole (1cm) than the V1' counter (4cm).

The measurements of interest for T2K are those when the incident beam particle can be identified as a proton and does hit the target. This corresponds to T2 and T3 triggers. T3 is a subset of T2. Hence considering the T2 trigger for the analysis of the data set allows to consider the larger available statistics.

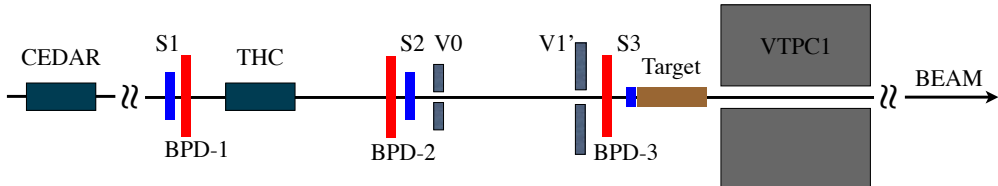


Figure 4.1: Schematic layout (horizontal cut in the beam plane, not to scale) of the beam detectors for the T2K replica target configuration.

T1	T2	T3	T4
$S1S2\bar{V}1' CED \bar{C}$	$S1S2S3\bar{V}1' CED \bar{C}$	$S1S2S3\bar{V}0\bar{V}1' CED \bar{C}$	$S1S2S3V1'$

Table 4.1: Combinations of counters for the different trigger settings.

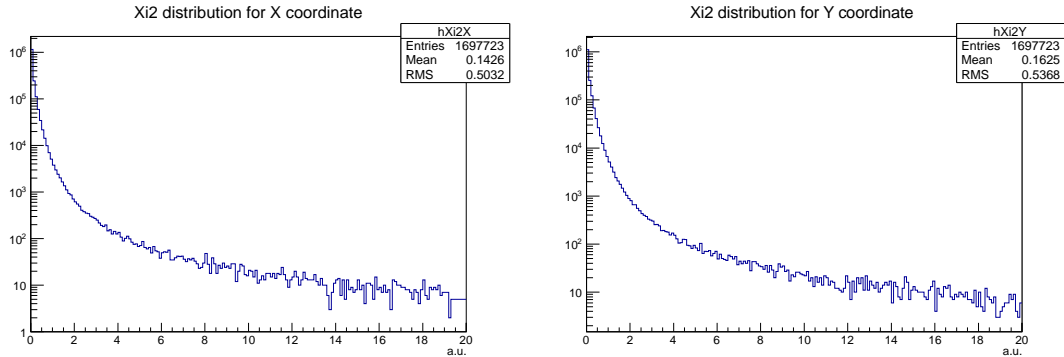


Figure 4.2: Distributions for the x (left) and y (right) coordinates of the chi-square for the fitted proton beam track in the BPDs.

The entire run period for the 2009 T2K replica target data taking represents 2.8 million events recorded and reconstructed. Selecting T2 gives a total of 2'312'504 events.

With the measurements of the three beam position detectors, the tracks of the beam particles are reconstructed by fitting two independent strait lines in the $x - z$ and $y - z$ planes. Least square fits use the measured clusters in each BPDs.

It is intuitively easy to understand that the hadron production along the T2K replica target will depend on the proton beam profile impinging on the target upstream face (we will discuss it in more details in the next chapter). Hence, it is important to be able to relate the final hadron spectra on the surface of the target with the characteristics of the primary beam. Thus it was decided to apply strict cuts on the measurements of the BPDs in order to have good precision on the reconstructed beam tracks. The requirements are to have properly reconstructed clusters in all three BPDs and to have a value for the chi-square of the fit smaller than 3,84. The distribution of the chi-square can be seen on fig. 4.2.

The initial statistics based on T2 trigger is reduced by 23% when applying these cuts on the BPDs, passing from 2'312'504 events to 1'687'454 events. If the T3 trigger is requested, and the same cuts on the reconstructed beam tracks are applied, the statistics falls down to 806'605 events.

The resolution on the proton beam tracks at the third BPD with the above cuts can be defined as the RMS of the distributions built as the difference between the position of the measured clusters and the predicted position from the fitted track. Figure 4.3 shows these distributions for the x and y coordinates.

The proton beam profile on the upstream face of the target can simply be computed as the extrapolation of the fitted beam tracks to the z position of the target. The two dimensional distributions of the T2 and T3 triggers in the $x - y$ plane are shown on fig. 4.4. The 2.6cm diameter black circle represents the edge of the target.

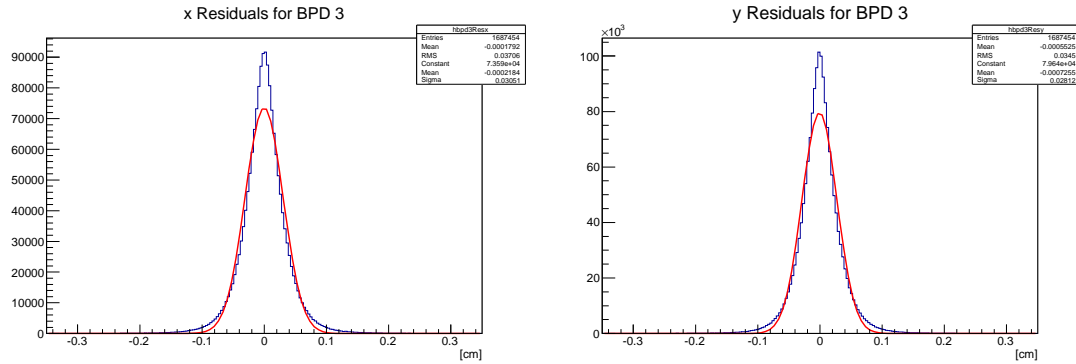


Figure 4.3: Distributions of the residuals at BPD3 for the x (left) and y (right) coordinates.

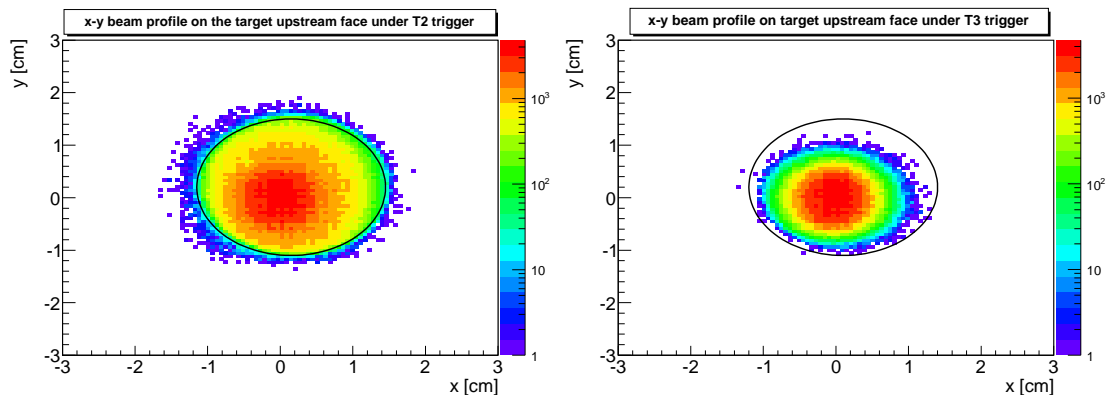


Figure 4.4: Distributions under T2 (left) and T3 (right) triggers of the proton beam profile at the z position of the target upstream face.

4.2 Determination of intersection point of track on target surface

Finding a vertex between the incident proton beam and the produced hadrons for a thin target experiment is a rather simple and unbiased task. The thin target used in NA61/SHINE is only a 4% interaction length graphite block. So, all re-interactions inside the target can be neglected and the longitudinal position of the interaction vertex can be fixed by the position of the thin target itself. This allows to apply a strong constraint on the determination of the x and y coordinates of the vertex and hence to determine whether a reconstructed track does originate from the target itself or from any decay or re-interaction within the detector.

For a thick target, such as the 1.9 interaction length graphite rode of the T2K replica target, the problem is different. Due to the fact that re-interactions and multiple scattering inside the target occur and cannot be neglected, trying to reconstruct an interaction vertex between the proton beam track and the measured hadron track would certainly produce biased results. Nevertheless, as seen in section 2.3.2, the final neutrino flux does depend on the longitudinal distribution of the hadrons exiting the target surface. Hence, it is important to be able to determine the exit position of the produced particles along the target surface.

The procedure is based on a backward extrapolation of the measured tracks in the TPCs. A Runge-Kutta method is used, taking into account the magnetic field map. The input variables of the method are the variables related to the first fitted point of the reconstructed tracks in the TPCs. The errors on the fitted points are propagated along with the method. The target is considered as a long cylinder. The position and the length of the cylinder are manually set. The backward extrapolation runs step-by-step. At each step, the distance in the transversal $x - y$ plan between the extrapolated point and the center of the cylinder is computed. If this distance gets smaller than the radius of the cylinder, it means that an intersection point can be computed. The Runge-Kutta method is then applied with smaller steps to precisely determine the (x, y, z) coordinates of the exit point of the track from the cylinder. If no intersection point can be found, the point of closest approach between the backward extrapolated track and the surface of the cylinder is recorded and assigned as the exit position.

Three reasons can be listed to explain that no intersection point of the track with the target surface is found. They are illustrated in fig. 4.5.

1. The track exits the target downstream face close to the edge. During the backward extrapolation the track misses the target and hence never crosses its surface. In this case, the point of closest approach will be assigned to the downstream face of the target.
2. The track is generated with a small angle at the upstream part of the target. Due to limited resolution on the reconstructed angle, the track becomes almost parallel to the target and hence never crosses its surface. The point of closest approach is then assigned to the upstream face of the target.
3. The track does not have precisely reconstructed ϕ and θ angles. Thus, the backward extrapolation approaches the target surface but never crosses it. In this case, a point of closest approach along the target surface is determined.

A combination of the first and the second or the first and the third reasons can also occur.

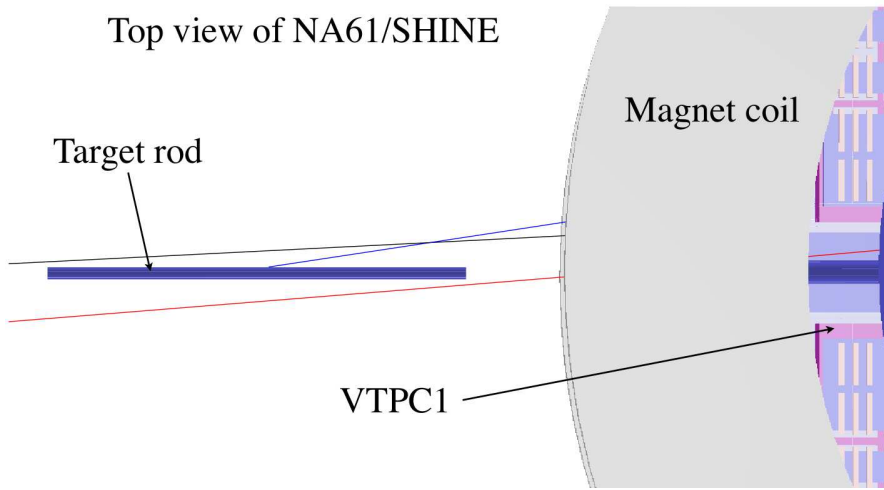


Figure 4.5: Example of tracks to determine the point of closest approach.

4.3 Target alignment and target position

A precise knowledge of the position of the target and its alignment along the beam line is mandatory in order to reconstruct the exit position of the produced hadrons at the surface of the target. The alignment of the target and its position with respect to the experimental setup are determined in two consecutive steps based on the data. The first step is based on the tracks extrapolated backward from the TPCs and allows to determine the alignment of the target within the beam line. The second step uses the tracks from the TPCs in conjunction with the beam tracks to compute the longitudinal and transversal positions of the target. A precise knowledge of the alignment of the TPCs with the BPDs is hence mandatory.

4.3.1 Target alignment

The first step uses a method that was developed for the 2007 data set. It allows to determine the alignment of the target along the beam line. In this method, reconstructed tracks in the TPCs are used. The 90cm long target is split into 17 slices. Each track reconstructed in the TPC is extrapolated backward and at the z position of each 17 slices, the distance of the track with respect to the nominal beam line is computed. For the slice at which this distance is minimal, the $x - y$ position is saved and assigned to that specific slice. For each slice, a 1.3cm radius circle is then moved step-by-step in the $x - y$ plan and for each step the number of tracks falling within the circle is computed. The central position for which the circle contains the maximum number of tracks is considered as the center of the target. Figure 4.6 shows the results for the x and y positions of the 17 slices as determined with this method. As can be seen, the positions for the x and y coordinates are constant over z . Hence it can be concluded that the target is correctly aligned along the beam line and no additional tilt will have to be considered in the analysis.

4.3.2 Target position

In the second step, the transversal and longitudinal positions of the target are determined. In order to reach a good precision, one can use the beam tracks in coordination with the T2 trigger. For each event being recorded with the T2 trigger, it is known that the proton beam hit the

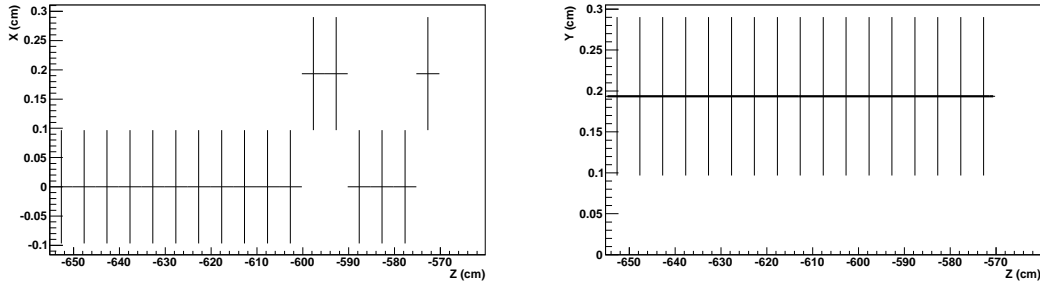


Figure 4.6: x (left) and y (right) positions for each 17 slices of the center of the 1.3cm radius circle at which the number of tracks within the circle is maximized.

upstream face of the target as it goes through the S3 counter. The left figure of 4.4 shows the two-dimensional $x - y$ distributions of the beam tracks. Fitting a circle of 1.3cm radius on this distribution by maximizing the number of entires in the circle gives the center of the target upstream face. It is found to be at $(x, y) = (0.16, 0.21)\text{cm}$ with respect to the NA61 coordinate system.

As this position is determined by using the beam tracks reconstructed from the BPDs information, and as the position of the particles exiting the target surface is determined by using the tracks from the TPCs, it is important to know the precision of the alignment between the BPDs and the TPCs. The determination of the precision on this alignment is based on the reconstruction of the vertexes between the beam tracks and the tracks from the TPCs for two independent sets of tracks flying through the spectrometer. The idea is to translate a potential misalignment in the transverse $x - y$ plan by looking for a shift in reconstructed distribution in the longitudinal z coordinate. In order to do so, two independent sets of tracks are considered. The first set comprises:

- tracks for positively charged particles scattering in the same direction as their bending in the magnetic field (i.e. $q \cdot p_x > 0$); they are called Right Side Tracks (RST)
- tracks for negatively charged particles scattering in the opposite direction as their bending in the magnetic field (i.e. $q \cdot p_x > 0$); they are called Wrong Side Tracks (WST)

They cover the side of positive x coordinate of VTPC1 and exit the target in the positive x direction. Right side tracks and wrong side tracks are presented in fig. 4.14 and will be further discussed in section 4.4.3. The second set comprises:

- positively charged particles for which $p_x < 0$; they are WST
- negatively charged particles for which $p_x < 0$; they are RST

This second set is associated with tracks exiting the target in the negative x direction. For both sets, tracks are extrapolated backward from the TPCs to the surface of a long cylinder of 1.5cm radius position at $(x, y) = (0.1, 0.2)\text{cm}$ as estimated in the first step determining the alignment of the target along the beam axis. From the point of closest approach of each track to the cylinder, a strait line is considered and the point where the distance between this line and the beam track is minimal is considered as the reconstructed vertex. The vertex distributions of the two sets of tracks should be identical if the BPDs and TPCs are correctly aligned. A transverse misalignment would be translated into a shift in the longitudinal direction of the vertex

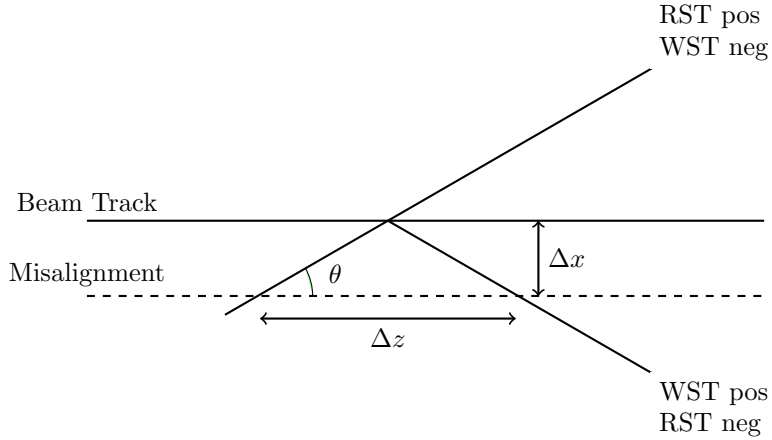


Figure 4.7: A transverse misalignment between the beam particles and the tracks extrapolated backward from the TPCs is translated into a longitudinal shift of the vertex distributions when comparing the two sets of tracks composed of positive RST and negative WST with positive WST and negative RST

distributions. Figure 4.7 represents schematically this procedure. The transverse misalignment can be related to the longitudinal shift in the vertex distributions by eq. (4.1)

$$\Delta x = \tan \theta \cdot (\Delta z / 2) \quad (4.1)$$

Considering tracks within a specific polar angle range θ allows to relate directly Δx with Δz .

In the case of a thin target, these vertexes can be unambiguously determined by using the whole set of data. When trying to reconstruct such vertexes for a thick target, specific cuts have to be applied in order to remove most of tracks originating from re-interactions inside the target. In our case, the following cuts were applied:

- consider only the beam tracks hitting the target outer part of the target upstream face; i.e. the beam tracks with a radial distance between 0.8 and 1.3cm from the coordinates $(x, y) = (0.16, 0.21)$ cm.
- consider only the beam tracks in the positive x coordinate when considering positive RST and negative WST, or beam tracks in the negative x coordinate when extrapolating positive WST or positive RST

Furthermore, to ensure the use of high quality tracks and to be able to translate a longitudinal shift into a transversal misalignment, the following two selections were applied:

- request a minimum number of reconstructed points along the tracks through the TPCs
- consider tracks exiting the cylinder with a polar angle $100 < \theta < 180$ mrad

In order to validate this procedure, a Monte-Carlo simulation was used where the exact longitudinal position of the target was known at $z = -658.51$ and the alignment between the simulated beam tracks and the TPCs was exact.

The distribution of the z vertexes can be seen in fig. 4.8.

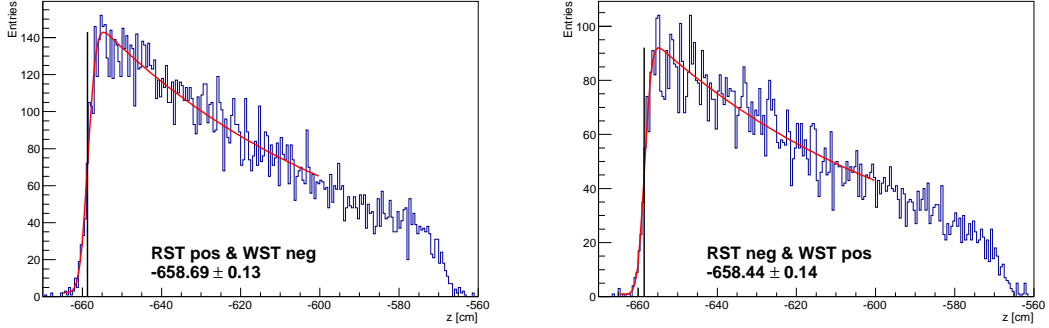


Figure 4.8: Distribution of the vertexes between the beam tracks and the reconstructed tracks in the TPCs along the z axis for the Monte-Carlo simulation.

In order to determine the target upstream face, the histograms are fitted with an exponentially modified gaussian function of the form of eq. (4.2).

$$f(x; \mu, \sigma, \lambda) = \frac{\lambda}{2} \exp\left[\frac{\lambda}{2}(2\mu + \lambda\sigma^2 - 2x)\right] \operatorname{erfc}\left(\frac{\mu + \lambda\sigma^2 - x}{\sqrt{2}\sigma}\right) \quad (4.2)$$

where $\operatorname{erfc}(x)$ is the complementary error function defined as

$$\operatorname{erfc}(x) = 1 - \operatorname{erf}(x) = \frac{2}{\sqrt{\pi}} \int_x^{\infty} e^{-t^2} dt$$

The reconstructed longitudinal position of the target can be simply computed as a weighted mean between the two sets of tracks. It is found to be $z = -658.57$.

The two results of both fits are in agreement within the statistical uncertainties. Hence, it shows that the above procedure works well and allows to determine the longitudinal z position of the target as well as to study a potential misalignment between the beam tracks and the tracks reconstructed from the TPC's

The results of the application of the same procedure to the data is presented through the distributions shown in fig. 4.9. As for the Monte-Carlo simulation, the histograms are fitted with a function of the form of eq. (4.2). We can conclude that the results are consistent within the statistical uncertainties.

The weighted average gives a position at $z = -657.62$ cm for the target upstream face and the difference of 0.36 cm can be considered as the resolution on the z position of the target upstream face. It can be further translated into an uncertainty of the BPDs-TPCs alignment of the order of 0.04 cm by using eq. (4.1).

Hence, the position of the target is set at $(x, y, z) = (0.16, 0.21, -657.62)$ cm in the NA61/SHINE coordinate system with uncertainties $(\delta x, \delta y, \delta z) = (0.04, 0.04, 0.36)$ cm.

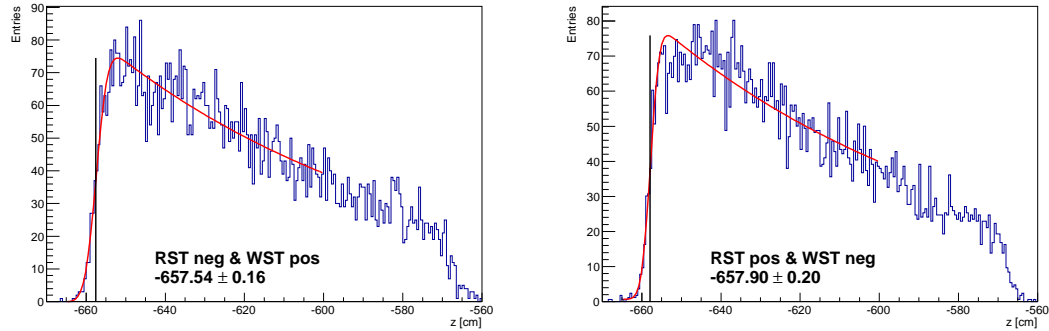


Figure 4.9: Distribution of the vertexes between the beam tracks and the reconstructed tracks in the TPCs along the z axis for the data.

4.4 Combined ToF-dE/dx analysis

The analysis of the reconstructed tracks in the NA61/SHINE detector is conducted in a set of steps.

First, a selection on the quality of the tracks is applied to ensure that they are well reconstructed and do originate from the target. The geometrical acceptance of the spectrometer is taken into account in order to remove the region where the acceptance varies rapidly. The selected tracks are filled in a second step into the different (p, θ, z) bins of the analysis phase-space. The third step consists of applying the combined ToF-dE/dx particle identification technique to each analysis bins to extract the number of pions in each bins. In a fourth step, Monte-Carlo based corrections are computed to correct the data for different effects like the limited geometrical acceptance of the spectrometer or the decay of particles in flight. Finally, the corrections are applied to the raw number of pions and spectra for the multiplicities of pions exiting the surface of the target are drawn.

4.4.1 Track selection

The track selection has to ensure that only well reconstructed tracks with high quality measurements and all requested variables by the analysis are considered. The list of requirements is as follows:

1. the track has a properly measured energy loss and an associated hit in the forward time of flight wall
2. the track has at least 30 points measured in the MTPCs and if the track crosses only VTPC1 and one MTPC, at least 20 points should be measured in VTPC1
3. forward going tracks flying through GTPC and MTPC without points in VTPCs should have at least 70 points measured in MTPCs
4. the azimuthal angle of the track should lie within a specified range, depending on the polar angle as follows:
5. the backward extrapolated point of closest approach to the target surface should touch the target surface within its uncertainty

$0 < \theta < 20$	$-60 < \phi < 60$ and $-120 < \phi < 120$
$20 < \theta < 40$	$-60 < \phi < 60$ and $-150 < \phi < 150$
$40 < \theta < 60$	$-40 < \phi < 40$ and $-145 < \phi < 145$
$60 < \theta < 100$	$-25 < \phi < 25$ and $-155 < \phi < 155$
$100 < \theta < 140$	$-15 < \phi < 15$ and $-165 < \phi < 165$
$\theta > 140$	$-10 < \phi < 10$ and $-170 < \phi < 170$

The first point of this list is of course mandatory for particle identification. The resolution of the energy loss depends on the number of measured clusters along the track as seen in fig. 3.12 of section 3.2.3. The scintillator bars of the forward time of flight wall are equipped with two PMTs, one at each side. During the 2009 data taking period of the T2K replica target, two bars had one deficient PMT. For these two bars, the time of flight is read from the single properly working channel while for the other bars, an averaged time between both PMTs is computed. In the case of multiple hits in a single bar, an averaged timing would give a biased result and would broaden the resolution of the computed mass squared. In order to remove this background, a cut is applied on the difference between the time recorded by the upper PMT and the lower one. If this difference is larger than 2 ns (≈ 30 cm), the track is discarded from the analysis and the forward time of flight is seen as being inefficient for this track. It is important to note that this efficiency is not due to a hardware problem or a failure in the construction of the ToF-F wall. It is only due to the fact that a precise value of the mass squared cannot be computed in a reliable manner.

The second point of the list is a cut on the quality of the reconstructed tracks. The momentum of the tracks is reconstructed with the help of the curvature in VTPC1 and VTPC2. For tracks emitted with large θ angle and flying directly from VTPC1 to MTPCs, at least 20 points are needed in order to have a less than 1% resolution on $\sigma(p)/p$. Very forward going particle pass close to the gap between the two MTPCs. In this region, re-interactions within the frame of the MTPCs are non negligible and the density of secondary tracks is higher. This causes potential mismatch in the reconstruction of global tracks between segments measured in the VTPCs and MTPCs. Requesting at least 30 points in the MTPCs gives a longer lever arm and higher precision on the matching between VTPCs and MTPCs track segments.

The third point of the list can be related to the geometrical acceptance of the spectrometer. Tracks with large azimuthal angle ϕ will mostly escape the TPCs and not reach the time of flight. A layout of the NA61/SHINE experiment as seen from the beam eye is illustrated in fig. 4.10. The distribution of the ϕ angle for the data after having requested a hit in the ToF-F wall is shown in fig. 4.11 for two different θ intervals to illustrate the $\phi - \theta$ dependence. As can be seen, the distribution is flat in certain regions of ϕ . The sharp edges correspond to the limited acceptance of the spectrometer. Keeping only those regions that are flat in ϕ allow to consider only those regions of the phase space with high acceptance. This limits the effect of the Monte-Carlo corrections for the acceptance and hence limit the probability to have biased corrections in the case the Monte-Carlo would not properly reproduce the detector acceptance in these regions.

The last point of the list is quite critical as it has to determine whether the measured track does originate from the target or should be assigned to a background track (track being produced by re-interaction in the detector material or a daughter particle from a decay in flight). During the procedure of backward extrapolation of the tracks from the first fitted point in the TPCs to the target surface, the uncertainties on the variables of the track are propagated as well. If the track, at its point of closest approach, reaches the target surface within its uncertainty, then it is considered as originating from the target.

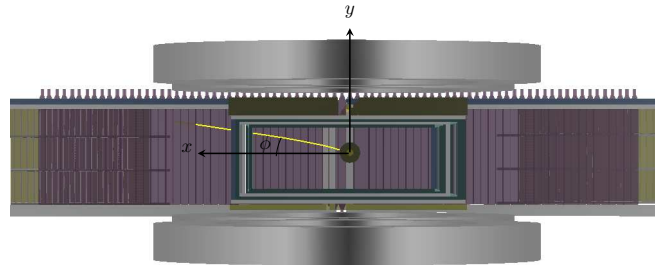


Figure 4.10: Layout of the NA61/SHINE detector showing the azimuthal coverage. The track shows the example of a positive pion of 3 GeV/c with a polar angle of 60 mrad and an azimuthal angle of 30 degrees.

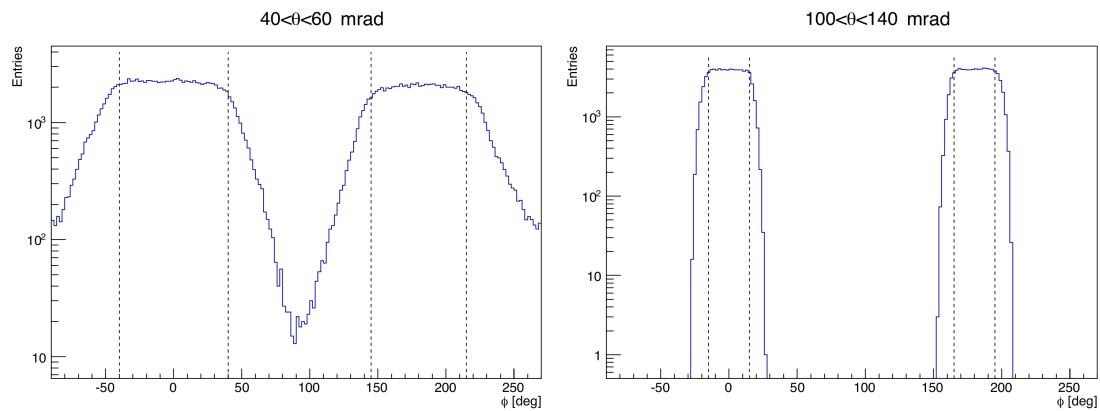


Figure 4.11: Distribution of the azimuthal angle ϕ of the tracks at the surface of the target. On the left for $40 < \theta < 60$ mrad and on the right for $100 < \theta < 140$ mrad.

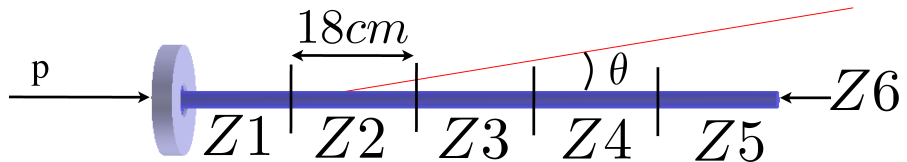


Figure 4.12: Sketch of the longitudinal binning of the target.

4.4.2 Analysis binning

In section 3.2, the energy loss in the TPCs and the time of flight measured by the ToF-F have been discussed. The T2K replica target analysis is based on the combination of the ToF and dE/dx values of the reconstructed tracks. This combined ToF- dE/dx analysis has been first developed and used for the thin target analysis of the 2007 data set [93]. As mentioned in section 2.3.2, the measured multiplicities for the T2K replica target analysis should be given in (p, θ, z) bins. The binning in z has been defined by the T2K requirements discussed in section 2.3.2. Five bins of 18cm along the target surface are considered and the downstream face of the target is the sixth longitudinal bin. A sketch of the binning is shown in fig. 4.12.

The determination of the binning in the (p, θ) phase-space is based on two considerations. It has to cover maximally the phase-space of interest for T2K but it also has to account for the available statistics from the 2009 data set. Requesting that each bin has more or less the same number of entries should allow to have equivalent statistical errors between the bins.

First, the binning for the polar angle was set. It is expected that the multiplicities varies rapidly with the polar angle. Hence the size of the bins was chosen to be relatively small. In order to determine the binning for the momentum with respect to each polar angle bins, a simple statistical method is used which consists of searching to have equiprobable bins. The cumulative distribution is built by summing the entries for one specific longitudinal bin and polar angle bin along the momentum axis. The vertical axis of the cumulative distribution is then marked by equidistant points. The ranges of the momentum bins are finally read on the horizontal axis.

The analysis binning defined with the above method can be seen on fig. 4.13. The color plot represents the pions exiting the target surface and contributing to the ν_μ flux at SK. Most part of the phase space of interest for T2K is well covered by the analysis binning.

4.4.3 Geometrical acceptance

The track topologies in the NA61/SHINE spectrometer are divided into two categories as already mentioned in section 4.3.2. The so-called Right Side Tracks (RST) are those which fulfill the requirement $p_x \cdot q > 0$ (see section 4.3.2). Their trajectory are bent away of the beam axis. The Wrong Side Tracks (WST) are defined by $p_x \cdot q < 0$. In other words, these tracks are steered back to the beam axis by the magnetic field. Figure 4.14 shows these two track topologies for different polar angles and momenta. Different parts of the (p, θ) phase-space are covered either by both topologies or by only one of the two track topologies. Particles with low momentum will have higher curvature. In this case, RST will often leave the spectrometer before reaching the ToF-F. WST, on the contrary, will be brought back into the detector and hence will better cover large angles. For high momentum tracks, at small polar angles, WST pass along the beam axis in between the two MTPCs and do not have enough reconstructed points to be considered in the analysis. RST, on the contrary, cross at least GTPC and one MTPC. They better cover high momentum particle exiting the target with small polar angle. Figure 4.15 and fig. 4.16 show the acceptance maps for RST and WST.

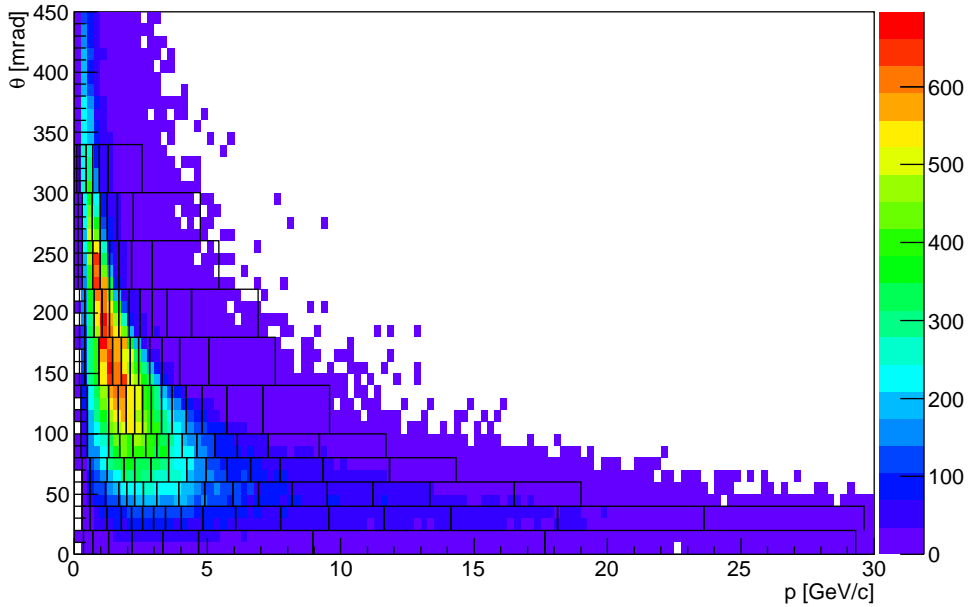


Figure 4.13: Analysis binning overlaid on the (p, θ) distributions of the pion parent particles exiting the target surface and producing ν_μ at SK.

These maps are built with the flat phase-space simulations described in section 3.3.2. The acceptance is computed as a ratio of the number of tracks passing the analysis cuts normalized to the total number of tracks in each bin. It is interesting to note that the acceptance of the spectrometer does not strongly depend on the longitudinal binning. Nevertheless some small differences can be seen and hence it was decided to consider each z bin independently. In order to reduce the dependency of the Monte-Carlo corrections to the model used for the simulation, it is important to consider only the topologies with high acceptance. Hence, a selection is done for each analysis bin and each topology. If the acceptance exceeds 90% for both topologies, then all the tracks are kept for particle identification. Otherwise, only the topology with the higher acceptance is considered.

A strong cross-check of the RST and WST acceptance estimates described above can be done by comparing the extracted particle yields for both topologies in the regions of high acceptance (i.e. where the acceptance is higher than 90%). Such validations have been done and allow to validate this procedure and confirm the accurate matching of the description of the detector setup by the Monte-Carlo simulation.

4.4.4 Particle identification

The combination of the information on the measured energy loss and mass squared for each track is used for the identification of the particle species. The dE/dx distributions allow to clearly distinguish electrons and pions from protons and kaons at momentum higher than 4 GeV/c. In the region from 1 to 4 GeV/c, the different distributions for the different particle species overlap. This is precisely where the mass squared distributions are well separated. Proton and kaon peaks

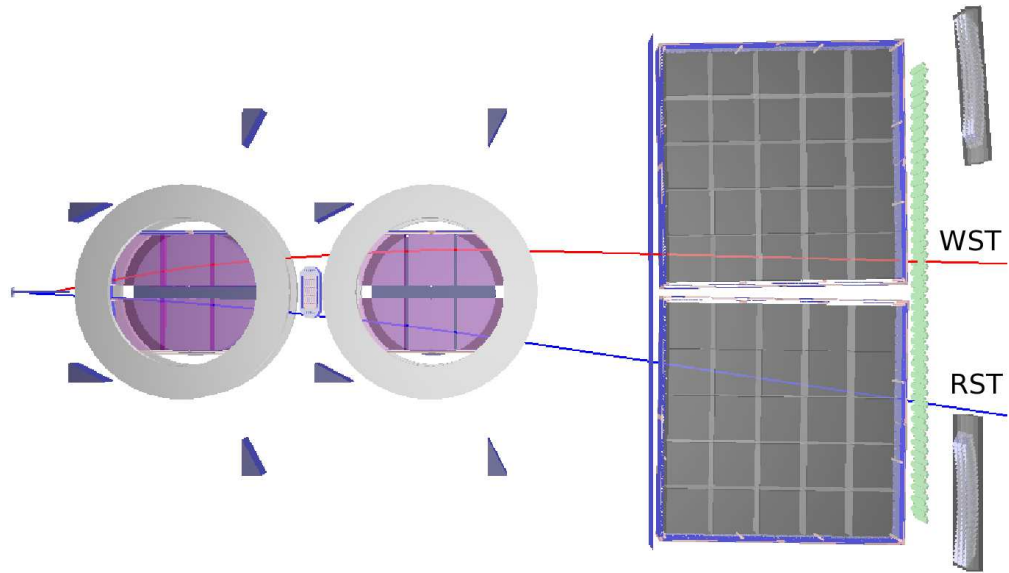


Figure 4.14: Representation of Wrong Side Track (WST) in red and Right Side Track (RST) in blue.

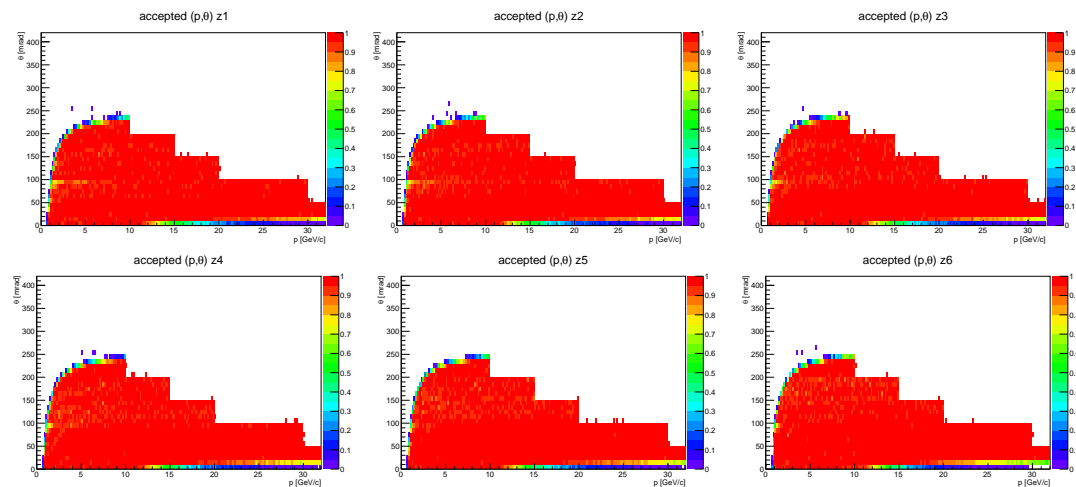


Figure 4.15: Right side tracks acceptance maps for the different longitudinal bins z in the (p, θ) phase-space. The acceptance is defined as the fraction of tracks that passes the analysis cuts.

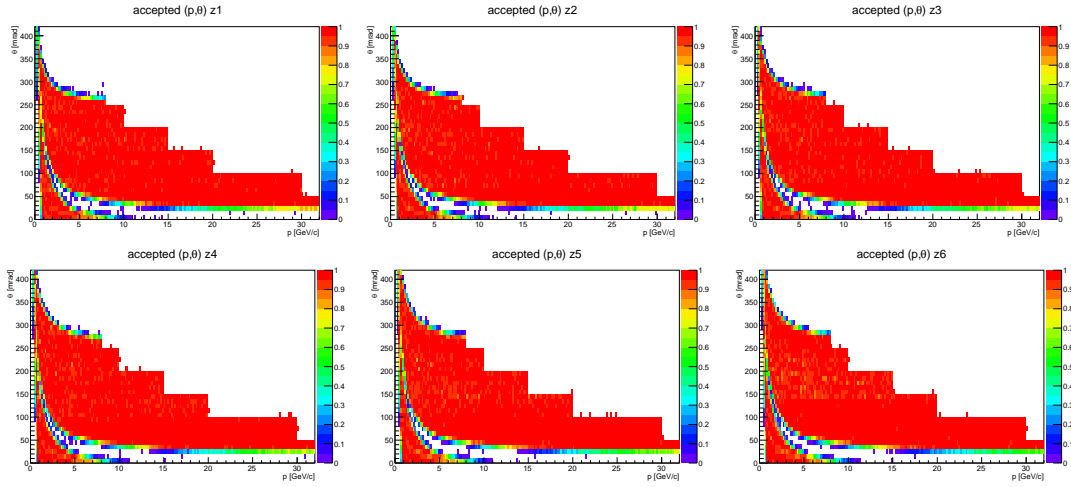


Figure 4.16: Wrong side tracks acceptance maps for the different longitudinal bins z in the (p, θ) phase-space. The acceptance is defined as the fraction of tracks that passes the analysis cuts.

can be distinguished from pion and electron peaks. Hence, by combining the mass square and energy loss information, it is possible to identify particles over the entire range of momenta.

For each (p, θ, z) analysis bin, two-dimensional histograms in m^2 versus dE/dx are filled for both, positively and negatively charged particles. Example of these histograms are presented in fig. 4.17.

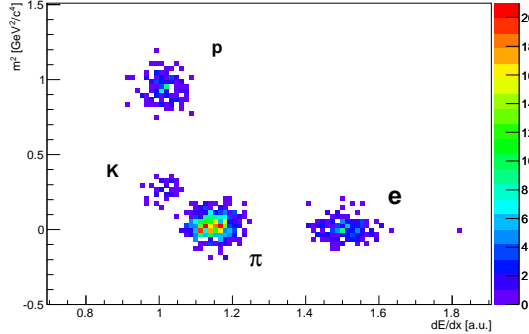


Figure 4.17: Example of a two-dimensional $m^2 - dE/dx$ distribution for positively charged particles in the second longitudinal bin $z2$ in the polar angle interval $60 < \theta < 80$ mrad and momentum $2.27 < p < 2.88$ GeV/c.

It is assumed that four two-dimensional gaussian functions describe the two-dimensional distributions of each particle species. The global probability distribution function can thus be written as

$$f(x_{dE/dx}, x_{m^2}; \alpha) = \sum_{j=\pi, K, p, e} \frac{A^j}{2\pi\sigma_{dE/dx}^j \sigma_{m^2}^j} \exp \left[\frac{(x_{dE/dx} - \mu_{dE/dx}^j)^2}{2\sigma_{dE/dx}^{j2}} + \frac{(x_{m^2} - \mu_{m^2}^j)^2}{2\sigma_{m^2}^{j2}} \right] \quad (4.3)$$

α is a vector with 20 components. They are given as:

- $\sigma_{dE/dx}^j$: width for the dE/dx projection of the two-dimensional gaussian distribution for the particle species j
- $\sigma_{m^2}^j$: width for the m^2 projection of the two-dimensional gaussian distribution for the particle species j
- $\mu_{dE/dx}^j$: mean value for dE/dx projection of the two-dimensional gaussian distribution for the particle species j
- $\mu_{m^2}^j$: mean value for m^2 projection of the two-dimensional gaussian distribution for the particle species j
- A^j : normalization factor of the two-dimensional distribution for the particle species j

The determination of the components is done by fitting the two-dimensional $m^2 - dE/dx$ distribution for each (p, θ, z) bins with the global probability distribution function in eq. (4.3) with the binned maximum likelihood method. The probability distribution function being normalized, the parameter A^j is thus related to the number of particles for each species j as returned by the fits.

A precise initialization of the fit parameters has to be done in order to have a properly converging minimization of the fitting algorithm. The initialization is handled as follows:

Initialization of $\mu_{dE/dx}^j$ and $\sigma_{dE/dx}^j$

The initialization of $\mu_{dE/dx}^j$ and $\sigma_{dE/dx}^j$ is based on the parametrization of the dE/dx distributions by Bethe-Bloch curves. In order to fit the energy loss distribution of each particle species separately, some simple selection can be applied. In the case of protons, for example, using the m^2 information at low momentum allows to clearly identify them. At higher momenta, a cut on the measured dE/dx allows to significantly remove pions. A quite clean sub-sample of protons remain and the energy loss of this sub-sample can be plotted as a function of momentum. The determination of $\sigma_{dE/dx}^j$ is done by taking slices of the two-dimensional distributions along the momentum axis. Each slice is fitted with a simple gaussian. The result of the fit returns directly the width of the distribution for each momentum slice as well as the mean value. As mentioned in section 3.2.3, the resolution of the energy loss depends on the number of measured points along the tracks. By applying the analysis cuts on the number of measured cluster in the TPCs, we saw that this resolution is fairly constant around 4%. This is confirmed by fig. 4.18, where the width of the fitted gaussian for each momentum slice is presented.

Fitting the mean value of each slices allows to get the parametrization of the Bethe-Bloch function that describes the energy loss. It is expected that the Bethe-Bloch curves for the different particle species should fall on top of each others when they are expressed as a function of $\beta\gamma$. Due to limited detector resolution, one can see some differences between the curves as presented on fig. 4.19. Proton and kaon curves overlay well on top of each others while a small shift for the pion curve can be observed. Nevertheless, this discrepancy is small enough to be neglected. Furthermore, these curves are only used as the initialization of the two-dimensional fit parameters and hence will be later on allowed to vary during the fitting procedure of the $m^2 - dE/dx$ distributions.

Figure 4.20 shows the different curves as a function of momentum for each particle species. They are superimposed on the dE/dx distributions.

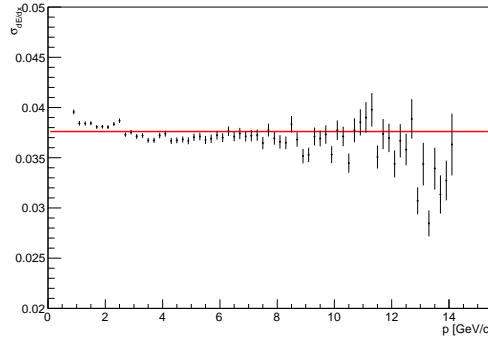


Figure 4.18: Parameterization of the dE/dx resolution for pion-like particles used for the initialization of the two-dimensional fits

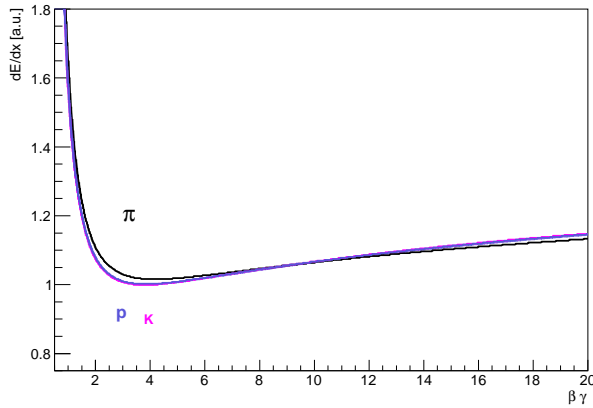


Figure 4.19: Bethe-Bloch curves for the different particle species. Theoretically, they should all fall on the same curve. Some small differences can be seen at low $\beta\gamma$.

Initialization of $\mu_{m^2}^j$ and $\sigma_{m^2}^j$

As in the case of the energy loss, slices in momentum are considered in the mass squared versus momentum distributions. Each slice is fitted with a simple gaussian function. The width of the gaussian gives the estimation of $\sigma_{m^2}^j$, while the mean returns $\mu_{m^2}^j$. The mass squared distribution is expected to be independent of the momentum. Hence, the means for the different slices in momentum for each particle species is fitted with a straight line. The width of the gaussians for each different slices should vary as a function of the square of the momentum. The uncertainty on the computed mass squared is dominated by the error on the time of flight. Hence, from eq. (3.5) we get

$$\delta m^2 = \frac{p^2 c^2 t}{l^2} \delta t \quad (4.4)$$

Protons and kaons are well separated at low momentum. Hence, they can be directly parameterized. Pions and electrons cannot be distinguished directly. Nevertheless, the information on the energy loss can be used to separate them and remain with one of the two particle species in the

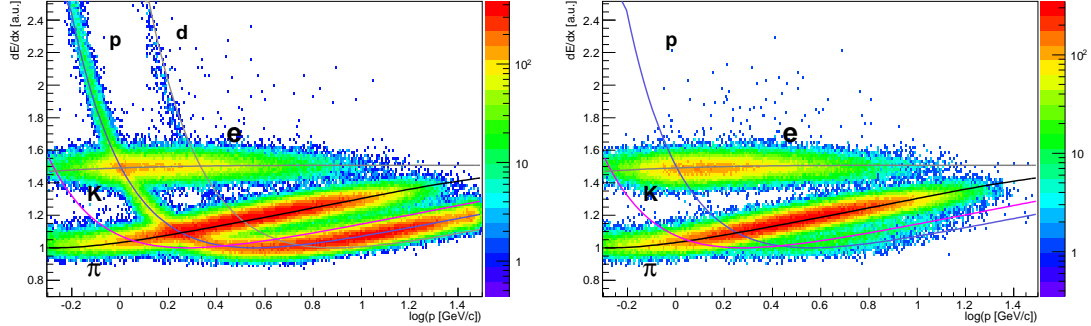


Figure 4.20: The dE/dx distributions as a function of momentum for positive particles (left) and negative particles (right) with the Bethe-Bloch curves superimposed.

mass squared distribution.

Figure 4.21 shows the result of the fits overlaid on the two-dimensional distributions. The

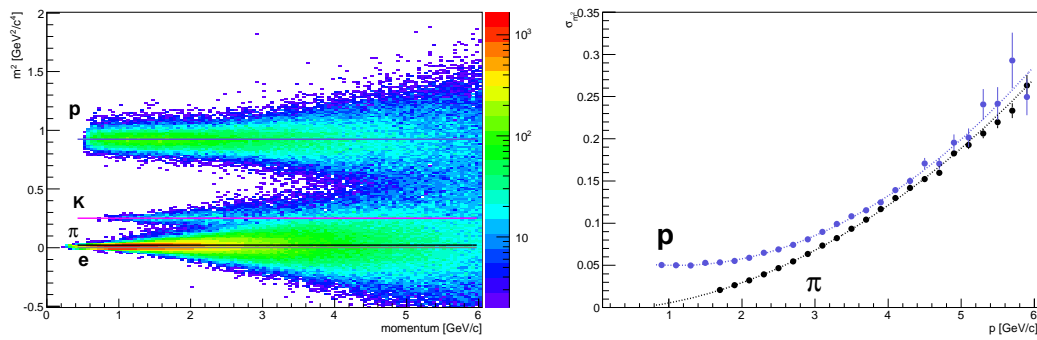


Figure 4.21: Mass squared distribution and resolution as functions of momentum.

mean of the mass squared have been fitted with a strait line, while the error has been fitted with a second order polynomial function.

Initialization of the amplitude factors A^j

The integral of each of the four bi-dimensional gaussian functions has to be initialized in order to have a rapidly converging fitting algorithm. From the initial parameters for the means of the mass squared and energy loss, an ellipse for each particle species with axis equal to three times the value of the width of m^2 and dE/dx is considered. The total number of entries lying in the ellipses gives the initial value for the amplitude of the gaussians.

Two-dimensional fit results

For the fitting procedure, all parameters are initialized as explained above. None of the parameters are fixed but different constrains are set to each parameter limit. For pions, $\mu_{dE/dx}^j$ and $\sigma_{dE/dx}^j$ are allowed to vary by 20% around their initial values while $\mu_{m^2}^j$ and $\sigma_{m^2}^j$ can vary by

25%. For electrons, $\sigma_{dE/dx}^j$ can vary by 25% but $\mu_{dE/dx}^j$ is limited within 7% of its initial value set at 1.5. This ensures that at high momenta (typically above ~ 8 GeV/c) the electron peak will not interfere with the pion peak. Kaons and protons are not well separated through the dE/dx distributions, hence the constraints on the limits of $\mu_{dE/dx}^j$ for those two particle species is tighter and the parameter is only allowed to vary within 5% around its initial value. These tight constraints for protons and kaons are actually specially important for the extraction of kaon and proton yields. Nevertheless, also in our case, where we extract pion yields, it is important to have a correct definition of other particle species as we still fit the full two-dimensional distributions with a sum of four gaussians describing the four different particle species.

Typical results of the fit procedure can be seen in fig. 4.22. It shows an example of the two-dimensional distribution m^2 versus dE/dx . The result for the fitted function given in eq. (4.3) is overlaid as a contour plot. The projections of the fit results on the m^2 and dE/dx axis show that the particle species can be well separated and the function of a sum of four two-dimensional gaussians fits correctly the data.

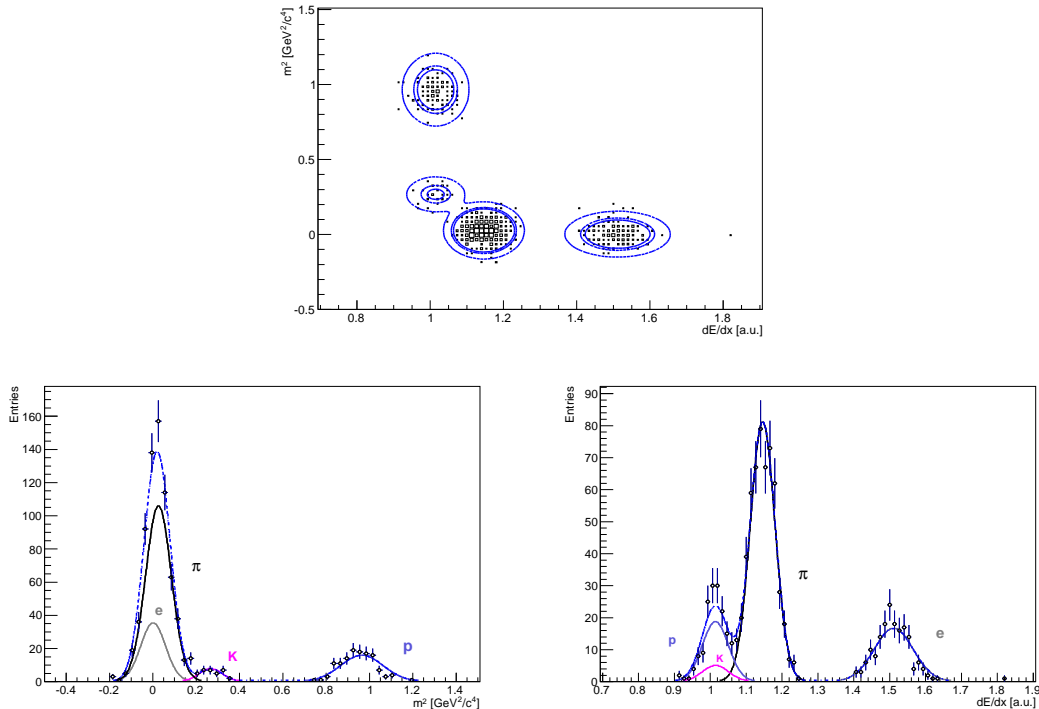


Figure 4.22: Two dimensional histogram with contour plot showing the fit result for the second longitudinal bin $z2$ in the polar angle bin $60 < \theta < 80$ mrad and momentum $2.27 < p < 2.88$ GeV/c (top). The different particle species are well separated in different ‘islands’. Bottom plots show the projection on the m^2 (left) and dE/dx (right) axes.

The integral of the four two-dimensional gaussians returns the fitted particle yields. The uncertainties on the fitted amplitude for pions are thus propagated as the statistical uncertainties of the pion multiplicities.

4.4.5 Monte-Carlo corrections

The raw particle yields as returned by the fitting procedure have to be corrected for different effects like the limited acceptance of the NA61/SHINE spectrometer or the decay of particles in flight. The corrections are based on a Monte-Carlo simulation. As mentioned in section 3.3.1, 10 million events have been produced with the specific beam characteristics of the 2009 data set as well as the same target alignment and position. The corrections to be applied to the raw particle yields are computed bin-by-bin as the ratio between the number of reconstructed tracks passing the analysis cuts over the number of simulated tracks. The global corrections can be split into different factors. They are presented for the angular interval between 60 and 80 mrad in fig. 4.23 (see appendix A for the correction factors of the entire phase space). The different factors can be listed as follows:

- ϕ_{cut} : as mentioned in section 4.4.1, the acceptance of the NA61/SHINE spectrometer is limited for the ϕ angle ranges. In order to avoid having a rapidly varying acceptance, specific cut on the ϕ angle depending on the polar ranges are applied. Hence the ϕ_{cut} corrections depend on the θ bins.
- π loss : the combined ToF-dE/dx analysis requests to have a hit in the forward time of flight wall. Nevertheless, pions exiting the target can be lost before reaching the scintillator wall. Two main reasons can be mentioned. The pions can interact within the detector materials, or they can decay before reaching the ToF-F. The second case is the dominant effect. The exponential behavior of this effect related to particle decaying in flight can be observed in fig. 4.23.
- reconstruction efficiency : not all the tracks crossing the detector can be reconstructed. Either due to a failure of the reconstruction procedure or due to some hardware inefficiency in some specific part of the TPCs, it is expected that a very small amount of tracks will be missing at the analysis level. The amplitude of such a correction had been carefully estimated for the 2007 analysis [113] and the same value is used here.
- ToF-F efficiency : the efficiency of the forward time of flight is measured as the ratio between the number of tracks crossing the scintillator wall over the number of tracks having a properly computed m^2 value. As can be seen in the figures of the correction factors, this efficiency is around 98%. The very small inefficiency of the forward ToF-F is mainly due to double hits in a same scintillator bar. In order to have a properly computed mass squared value, a cut on the time difference recorded by the upper and lower PMTs of the scintillator is applied. The 2% inefficiency of the ToF-F is mainly due to this cut.
- Feed-down : particle exiting the target surface can only be identified when they start crossing the spectrometer. Nevertheless, it can happen that a short lived particle exit the target surface and decays before entering the TPCs. This could be for example the case for a kaon exiting the target and decaying into a pion before VTPC1. The reconstruction and identification of such a track would be misidentified and wrongly attributed to a pion being emitted from the target. The same can be true for particles being produced in interactions in the detector material.

In principle, statistical errors on the final corrected pion spectra receive contributions from the finite statistics of both the data as well as the simulated events used to obtain the correction factors. The dominating contribution is the uncertainty of the data which is returned by the maximum likelihood method. The Monte Carlo statistics were higher than the data statistics by a factor 10, hence the related uncertainties are by more than a factor 3 smaller. Added in quadrature to the statistical uncertainties of the data, these errors become negligible.

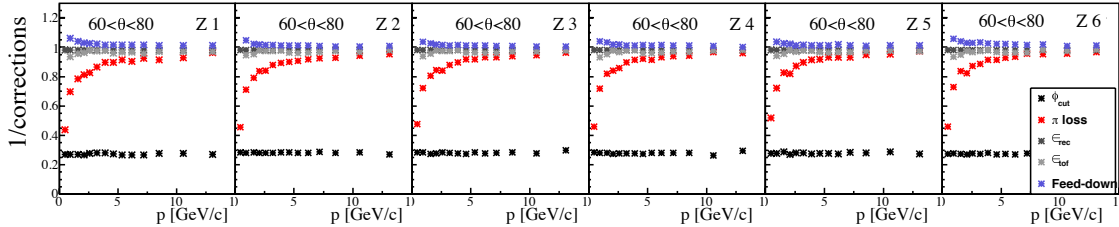


Figure 4.23: Correction factors for positively charged pions, in the polar angle range from 60 to 80 mrad, and for the six longitudinal bins as a function of momentum.

4.5 Systematic uncertainties

Six different components are considered for the systematic uncertainties in the case of the T2K replica target analysis. Each of the six components is described in detail below. Five of them are similar to the thin target analysis, only the last one is specific to the backward extrapolation procedure.

- PID : as stated by eq. (4.3), it is assumed that the dE/dx distribution for the different particle species in each of the (p, θ, z) bin can be described by a single gaussian. This is not exactly correct. The width of the energy loss distribution is correlated to the number of measured clusters along the track. And it is obvious that different tracks entering in the same (p, θ, z) analysis bin will have different measured number of points. In order to estimate the size of this effect on the final pion spectra, eq. (4.3) was modified such that two gaussians with the same mean value but different width would be considered to fit the dE/dx distribution. At low momenta, the particle identification is strongly constrained but the ToF-F information and hence the amplitude of the error due to describing the energy loss by a single gaussian is expected to be negligible. At higher momenta, when the resolution of the time of flight does not allow to distinguish the different particle species, using two gaussians instead of a single gaussian in the fitting procedure does show some small but non negligible effect as it is illustrated on fig. 4.24 to fig. 4.26.
- Feed-down : the correction factor for feed-down is computed based on Monte-Carlo simulations produced with FLUKA as hadron model. Thus, this correction is strongly model dependent and an uncertainty on this model had to be assigned. As for the thin target analysis [93], it was decided to consider a 30% uncertainty on the amplitude of the correction as the systematic uncertainty on this correction factor.
- reconstruction efficiency : following the thin target analysis, a constant 2% uncertainty on the efficiency of the reconstruction procedure is assigned.
- ToF-F efficiency : the correction for the ToF-F efficiency is computed based on the data. It depends on the different slabs, but also on the momentum of the different analysis bins. This dependence is small but not negligible. A constant 2% over the entire phase space is hence assigned as the systematic uncertainty. An uncertainty computed for each slab would be more accurate. Unfortunately, the limited statistics of the 2009 data set did not allow to have enough hits in the slabs at the two extremities of the ToF-F in order to have a statistically accurate estimation of the uncertainty.
- π loss : as mentioned above, the loss of pions can be regarded as tracks being measured in the TPCs and aiming for the ToF-F acceptance but not having a recorded hit in the

ToF-F. The corrections related to this effect are computed via the precisely known pion decay which should be model independent. Hence, by varying the number of requested measured points in the MTPCs, it is not expected to see differences on the final spectra. Any variations would represent the error on the amplitude of the pion loss correction.

- backward extrapolation : the estimation of the uncertainty due to the backward extrapolation procedure is based on the accuracy with which the target position is known. As stated in section 4.3, the position of the target and the uncertainties on this position are

$$(x, y, z) = (0.16, 0.21, -657.62) \text{ cm} \quad (4.5)$$

$$(\delta x, \delta y, \delta z) = (0.04, 0.04, 0.36) \text{ cm} \quad (4.6)$$

The main goal of the backward extrapolation is to attach to each track a specific longitudinal z bin as well as parameters of the momentum and polar angle at the surface of the target. By shifting the target from the relative uncertainties on the different coordinates, the number of tracks exiting from each different (p, θ, z) bin will vary. This variation is taken as the systematic uncertainties on the final spectra due to the backward extrapolation.

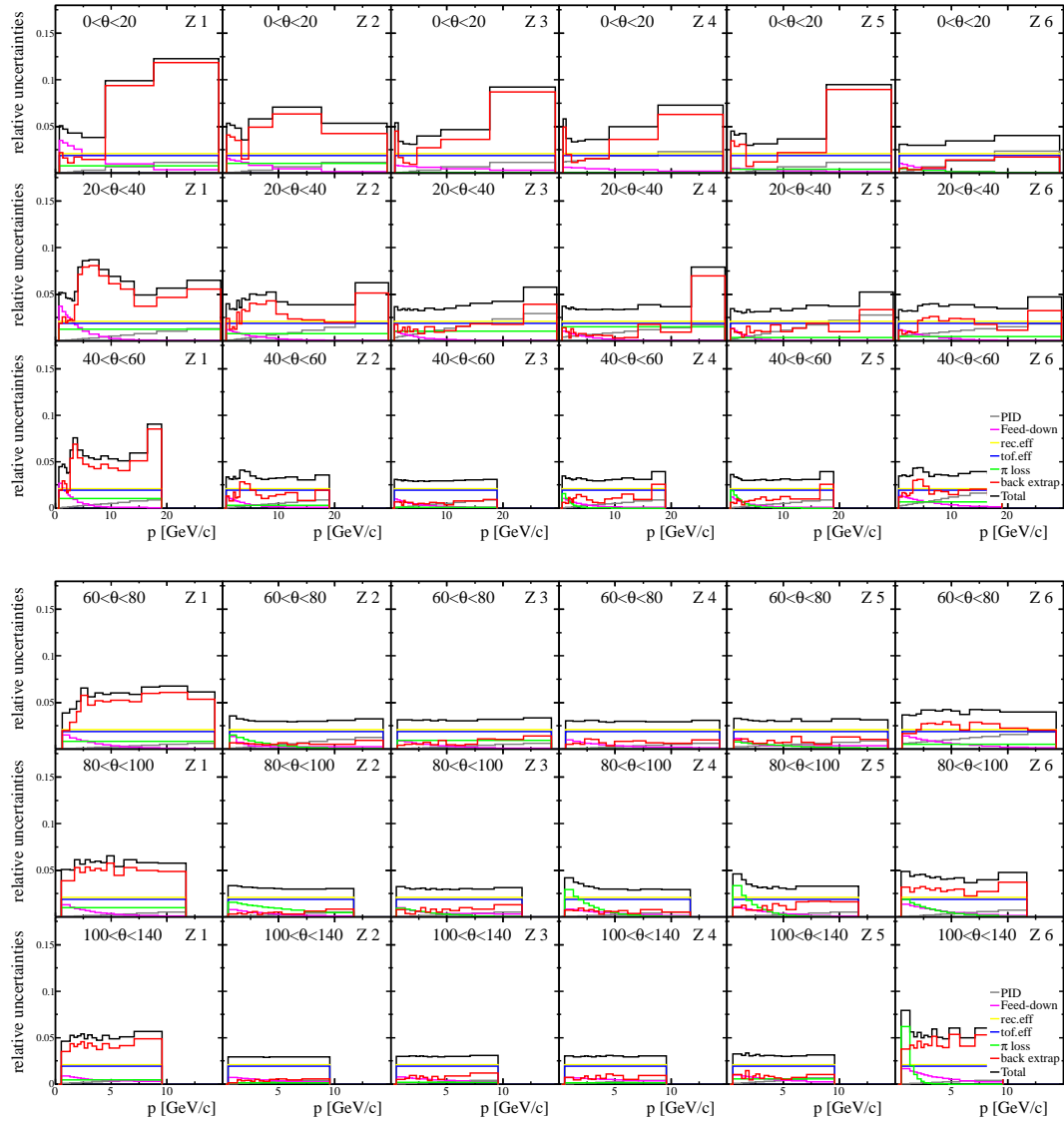


Figure 4.24: Components of the systematic uncertainties for positively charged pions, in the polar angle range from 0 to 140 mrad, and for the six longitudinal bins as a function of momentum.

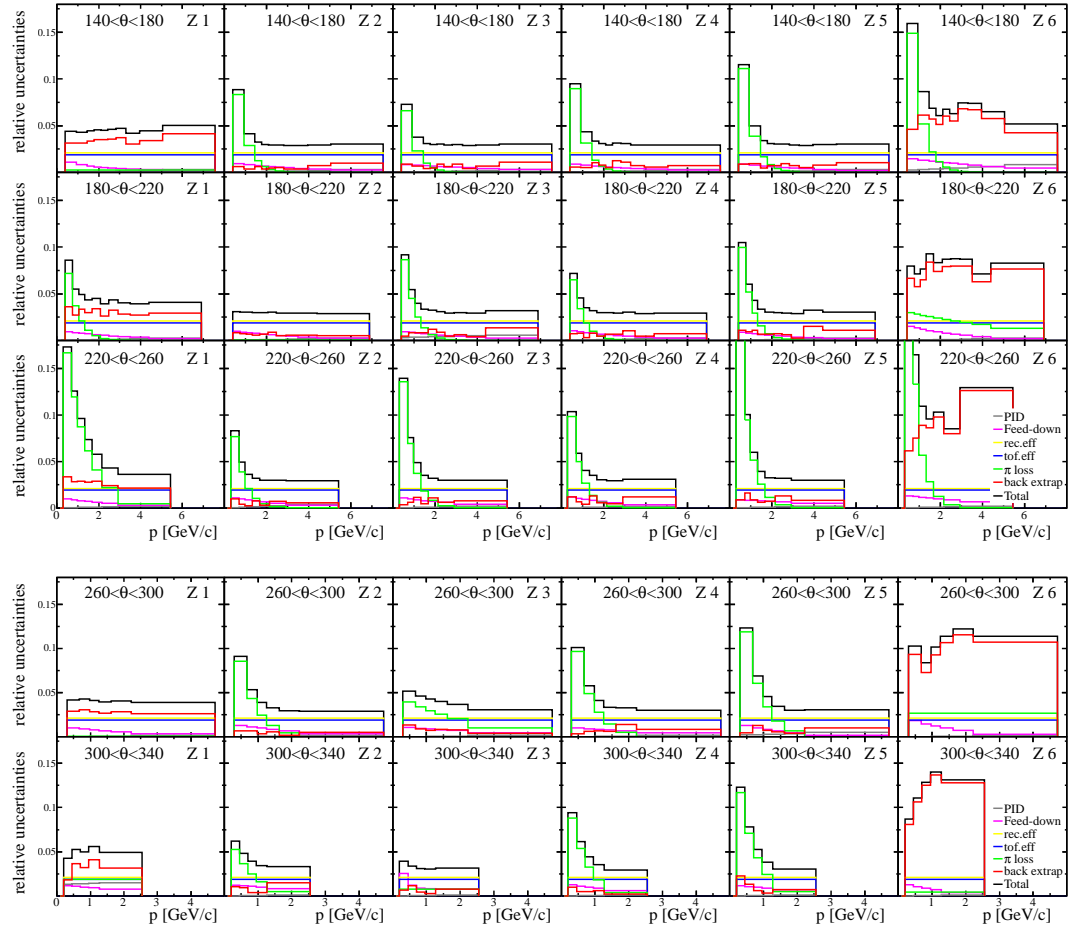


Figure 4.25: Components of the systematic uncertainties for positively charged pions, in the polar angle range from 140 to 340 mrad, and for the six longitudinal bins as a function of momentum.

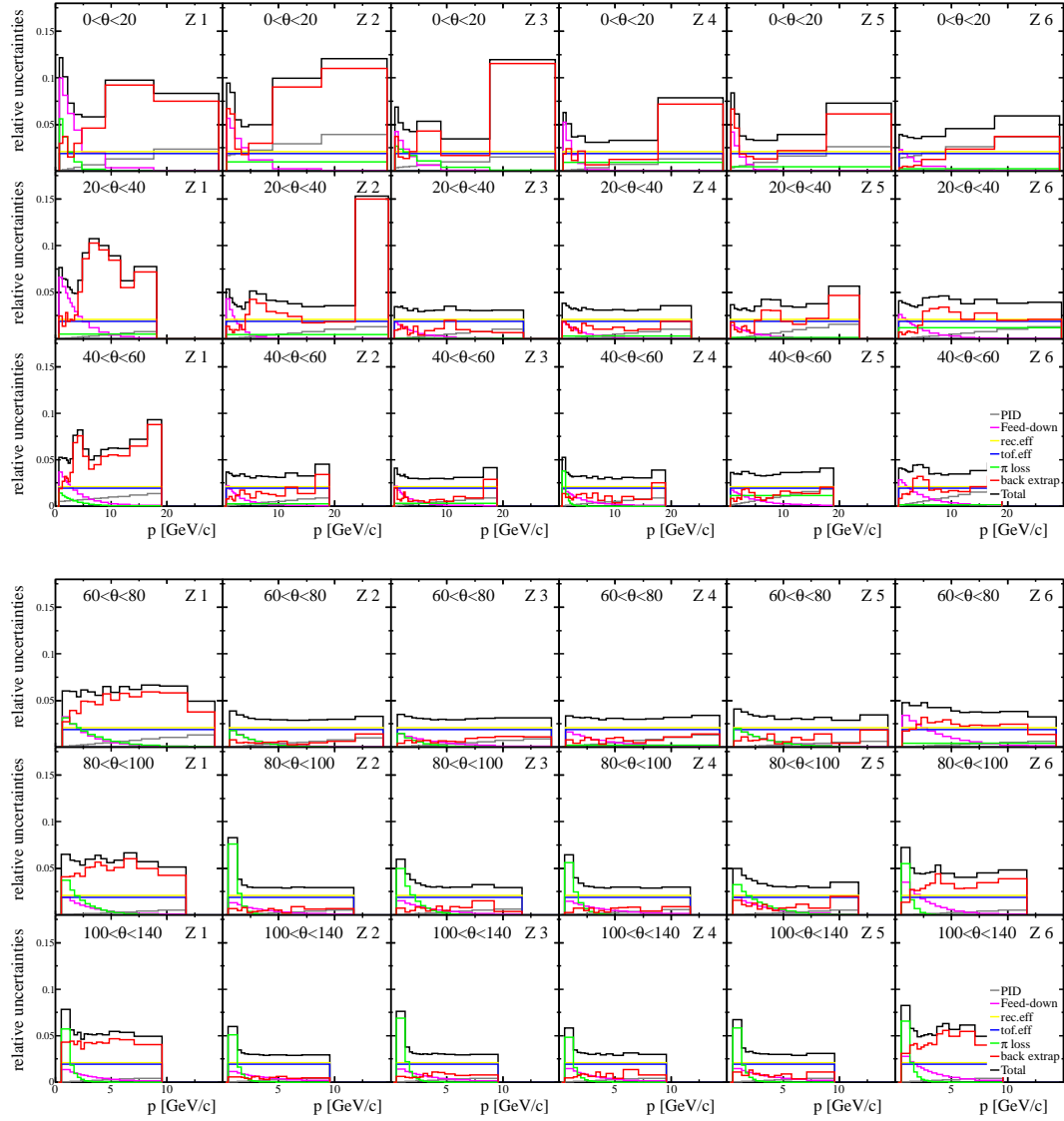


Figure 4.26: Components of the systematic uncertainties for negatively charged pions, in the polar angle range from 0 to 140 mrad, and for the six longitudinal bins as a function of momentum.

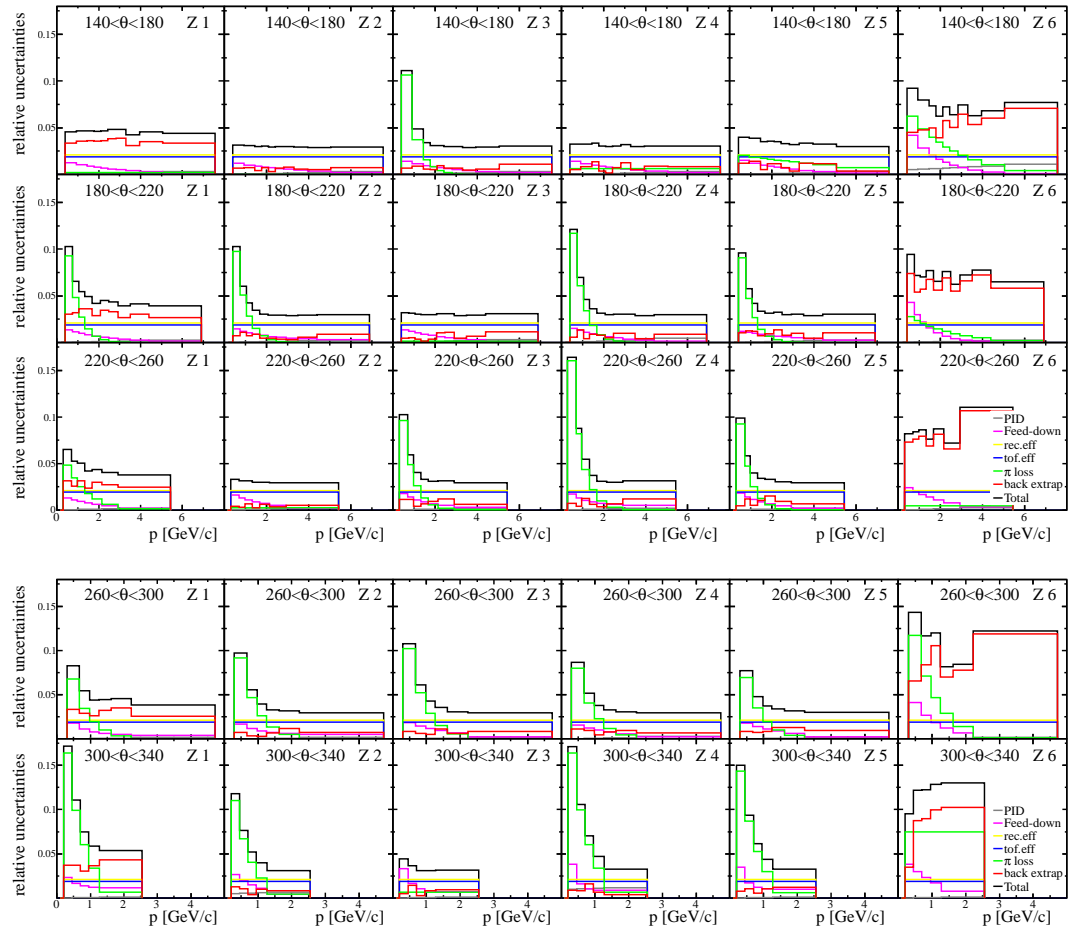


Figure 4.27: Components of the systematic uncertainties for negatively charged pions, in the polar angle range from 140 to 340 mrad, and for the six longitudinal bins as a function of momentum.

4.6 Results

Differential multiplicities of positively and negatively charged pions emitted from the T2K replica target exposed to a 31 GeV/c proton beam are presented in fig. 4.28 to fig. 4.31. The results are corrected for the different components presented in section 4.4.5.

The black points are the NA61/SHINE measurements with the errors bars representing the statistical and systematic uncertainties added in quadrature. For comparison, the FLUKA2011 predictions are presented as splines in blue. The NA61/SHINE data and the FLUKA predictions are normalized to the number of protons on target. The numerical values of the NA61/SHINE measurements for each (p, θ, z) bins can be found in the tables of appendix D.

Relative statistical and systematic uncertainties are presented in fig. 4.32 to fig. 4.35.

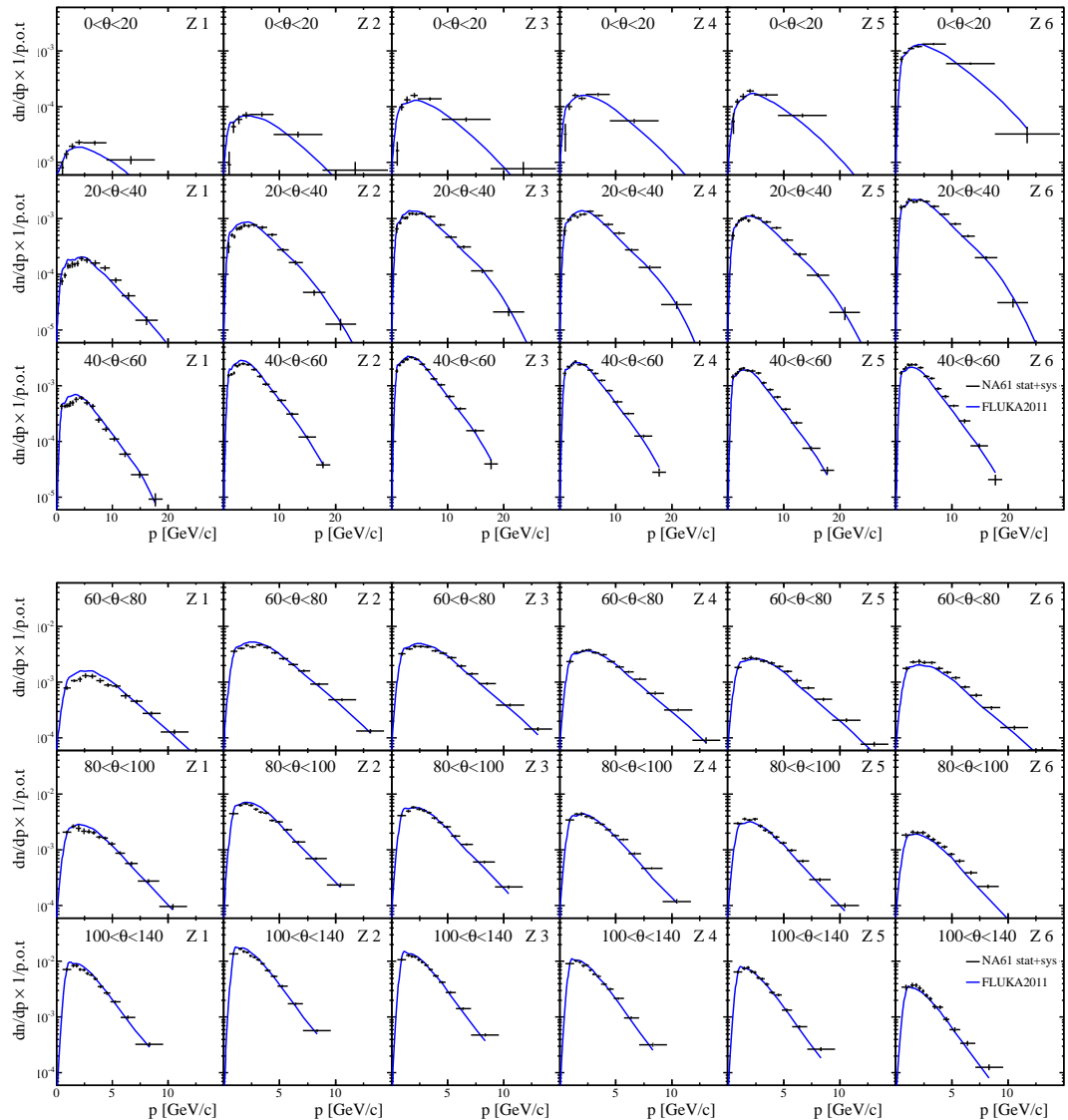


Figure 4.28: Fully corrected spectra for positively charged pions, in the polar angle range from 0 to 140 mrad, and for the six longitudinal bins as a function of momentum. The normalization is done on the number of protons on target.

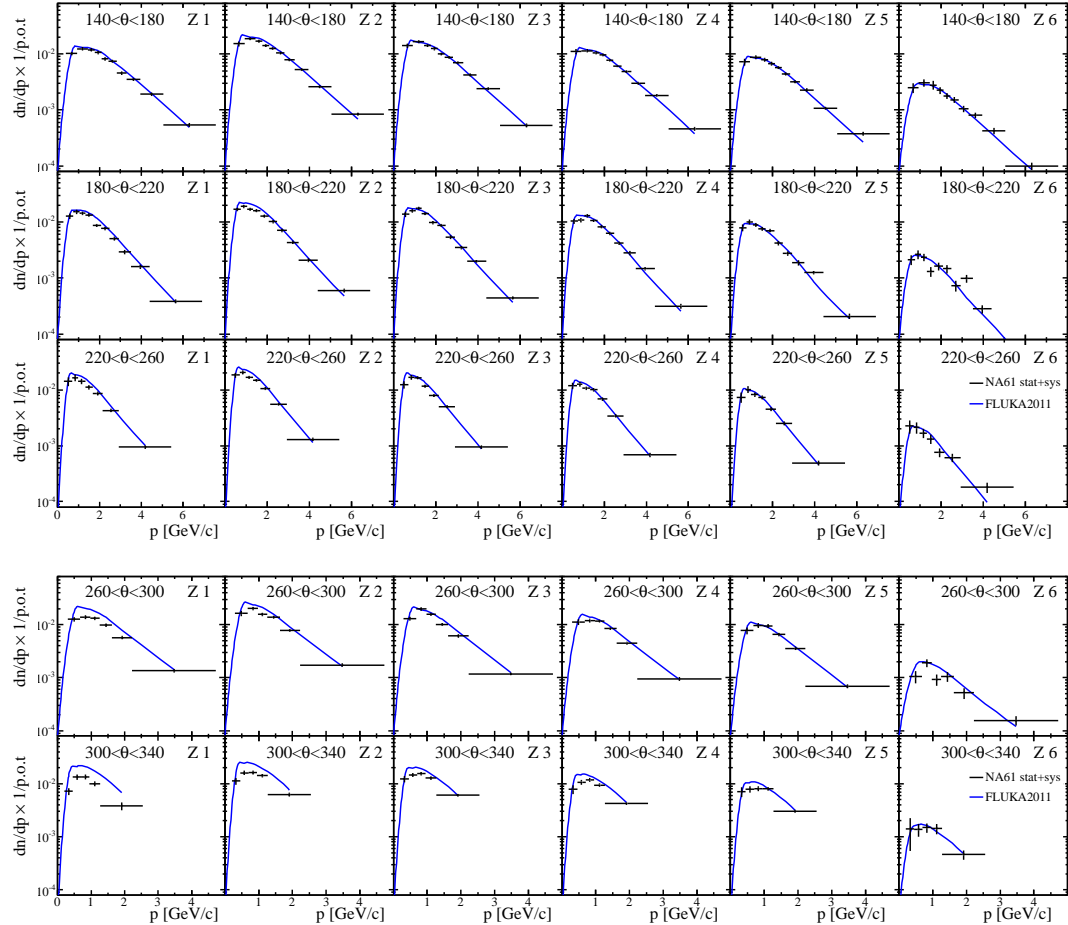


Figure 4.29: Fully corrected spectra for positively charged pions, in the polar angle range from 140 to 340 mrad, and for the six longitudinal bins as a function of momentum. The normalization is done on the number of protons on target.

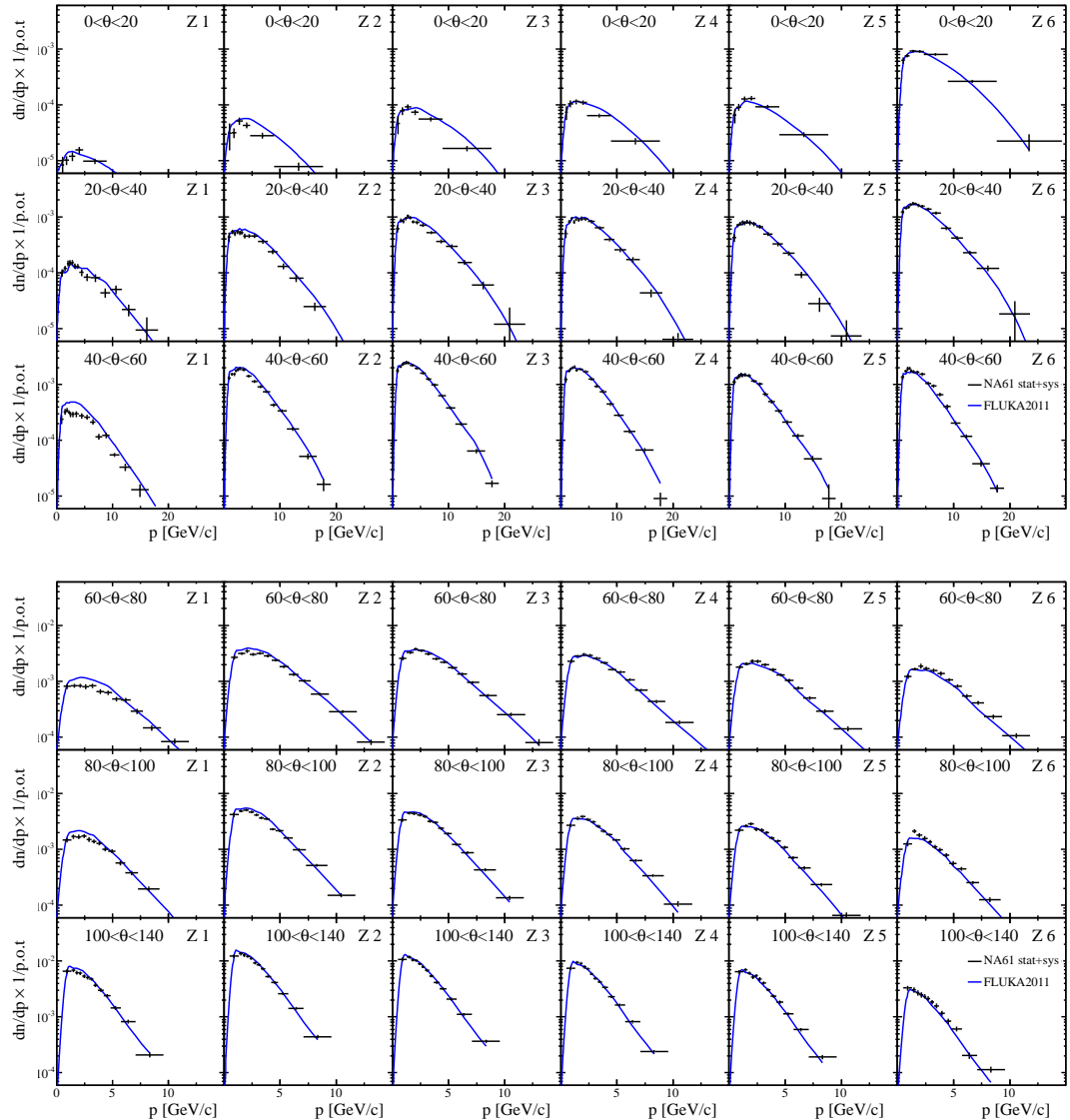


Figure 4.30: Fully corrected spectra for negatively charged pions, in the polar angle range from 0 to 140 mrad, and for the six longitudinal bins as a function of momentum. The normalization is done on the number of protons on target.

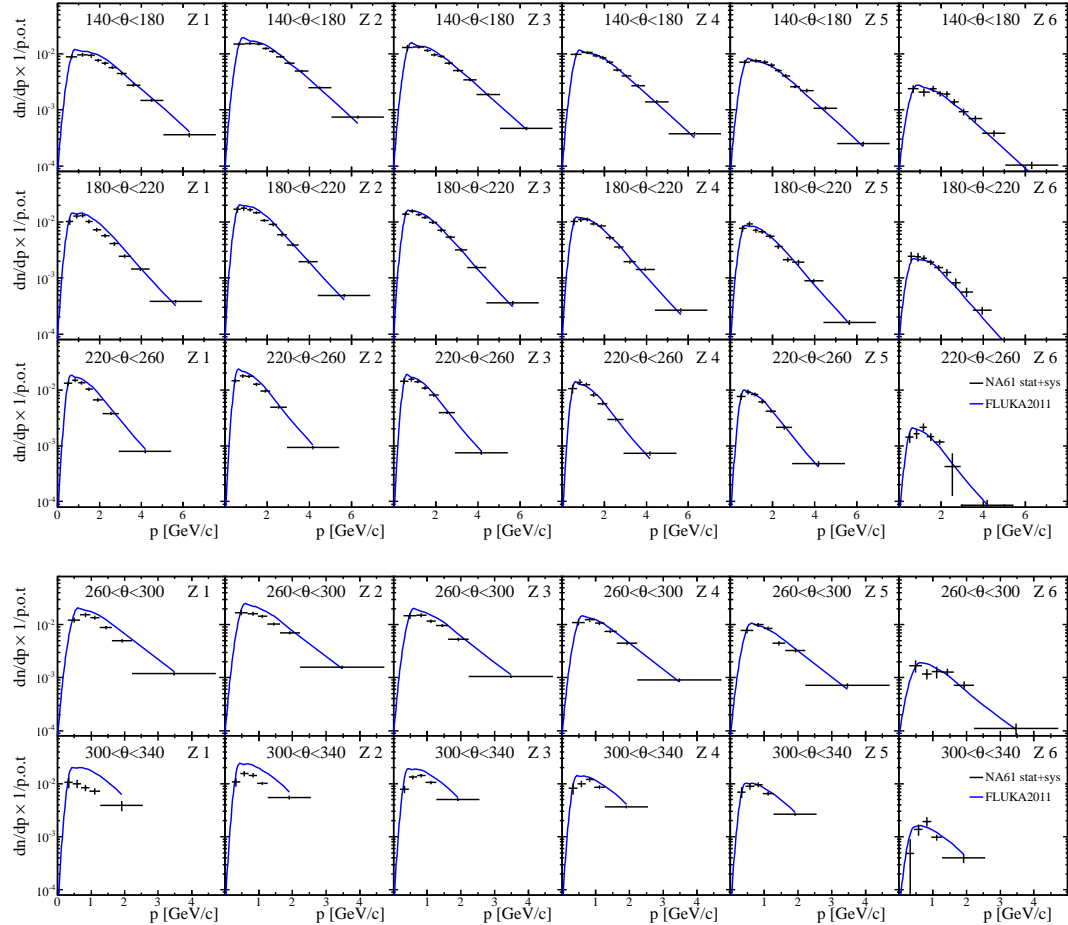


Figure 4.31: Fully corrected spectra for negatively charged pions, in the polar angle range from 140 to 340 mrad, and for the six longitudinal bins as a function of momentum. The normalization is done on the number of protons on target.

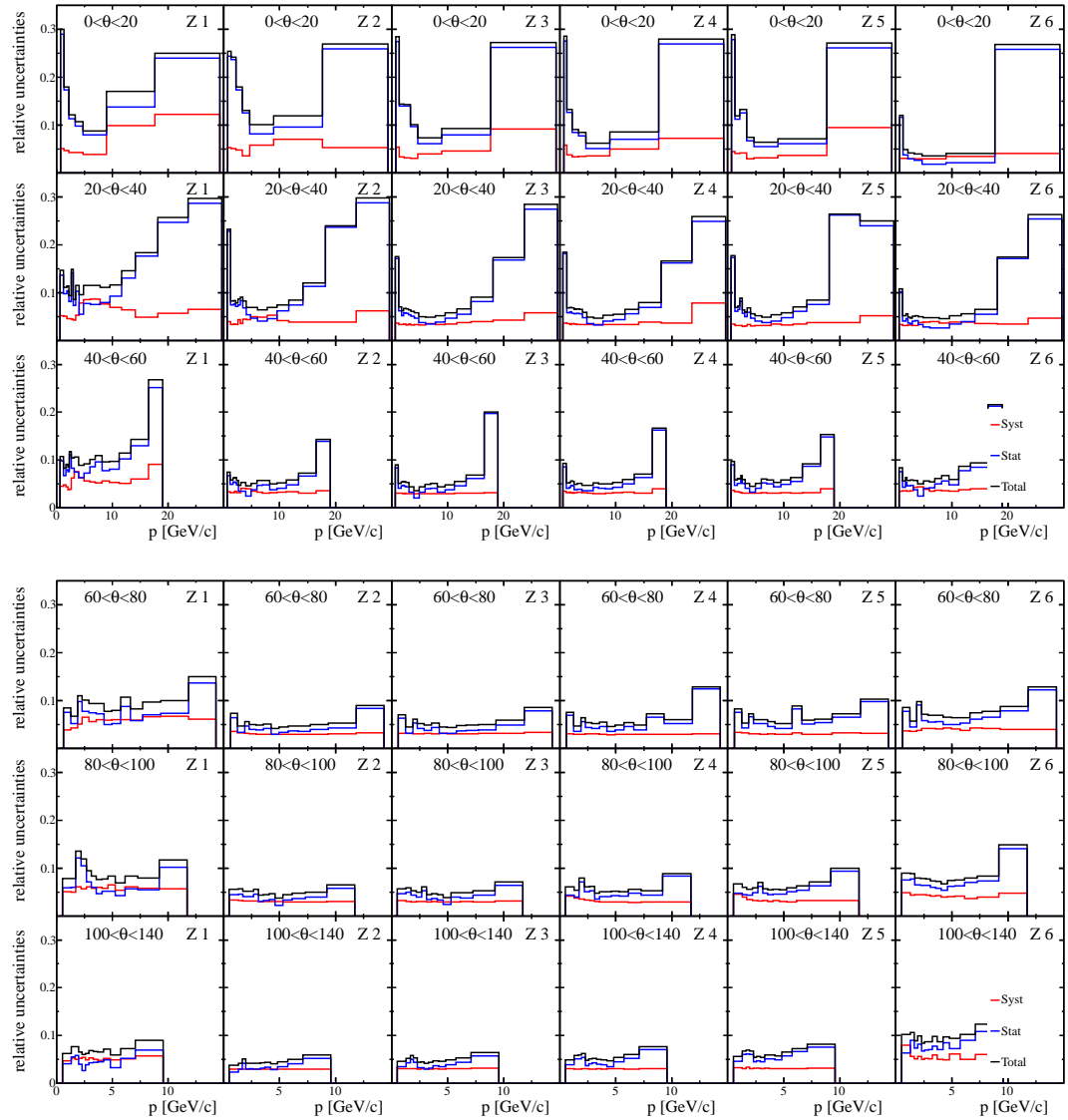


Figure 4.32: Statistical and systematic uncertainties for positively charged pions, in the polar angle range from 0 to 140 mrad, and for the six longitudinal bins as a function of momentum.

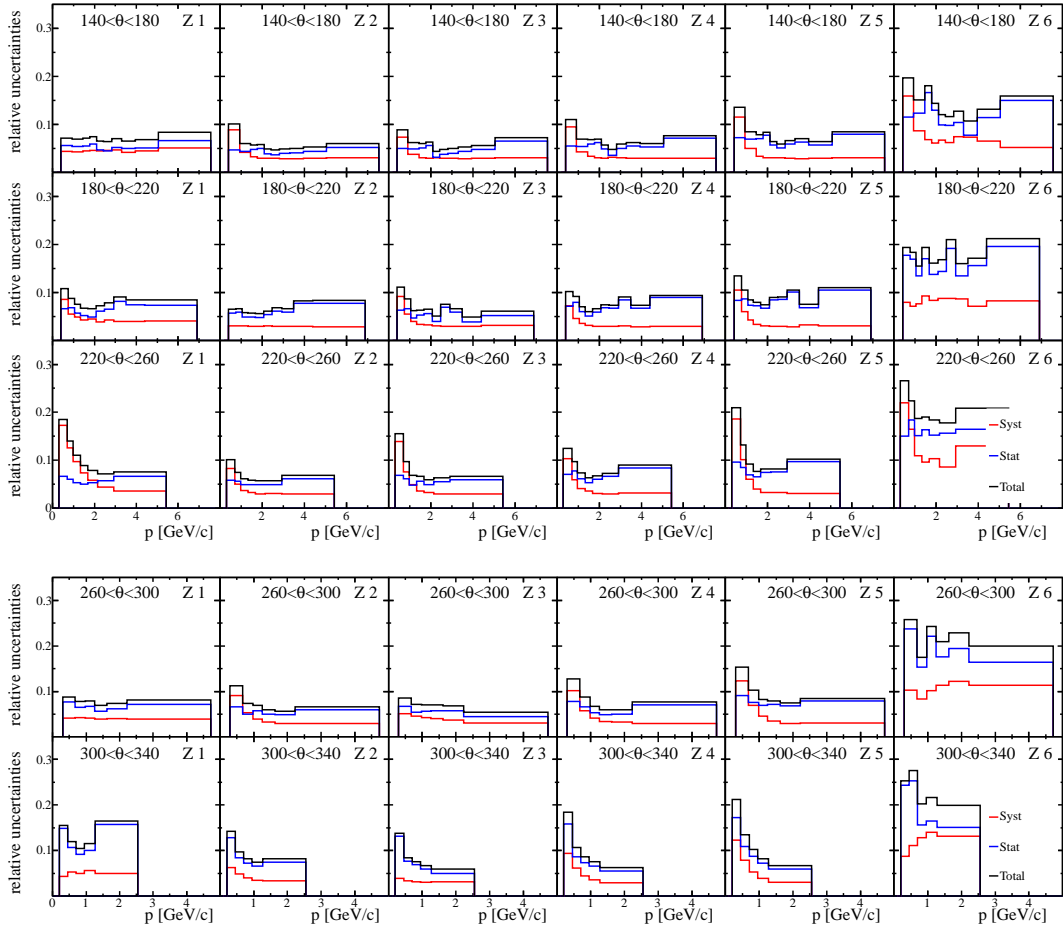


Figure 4.33: Statistical and systematic uncertainties for positively charged pions, in the polar angle range from 140 to 340 mrad, and for the six longitudinal bins as a function of momentum.

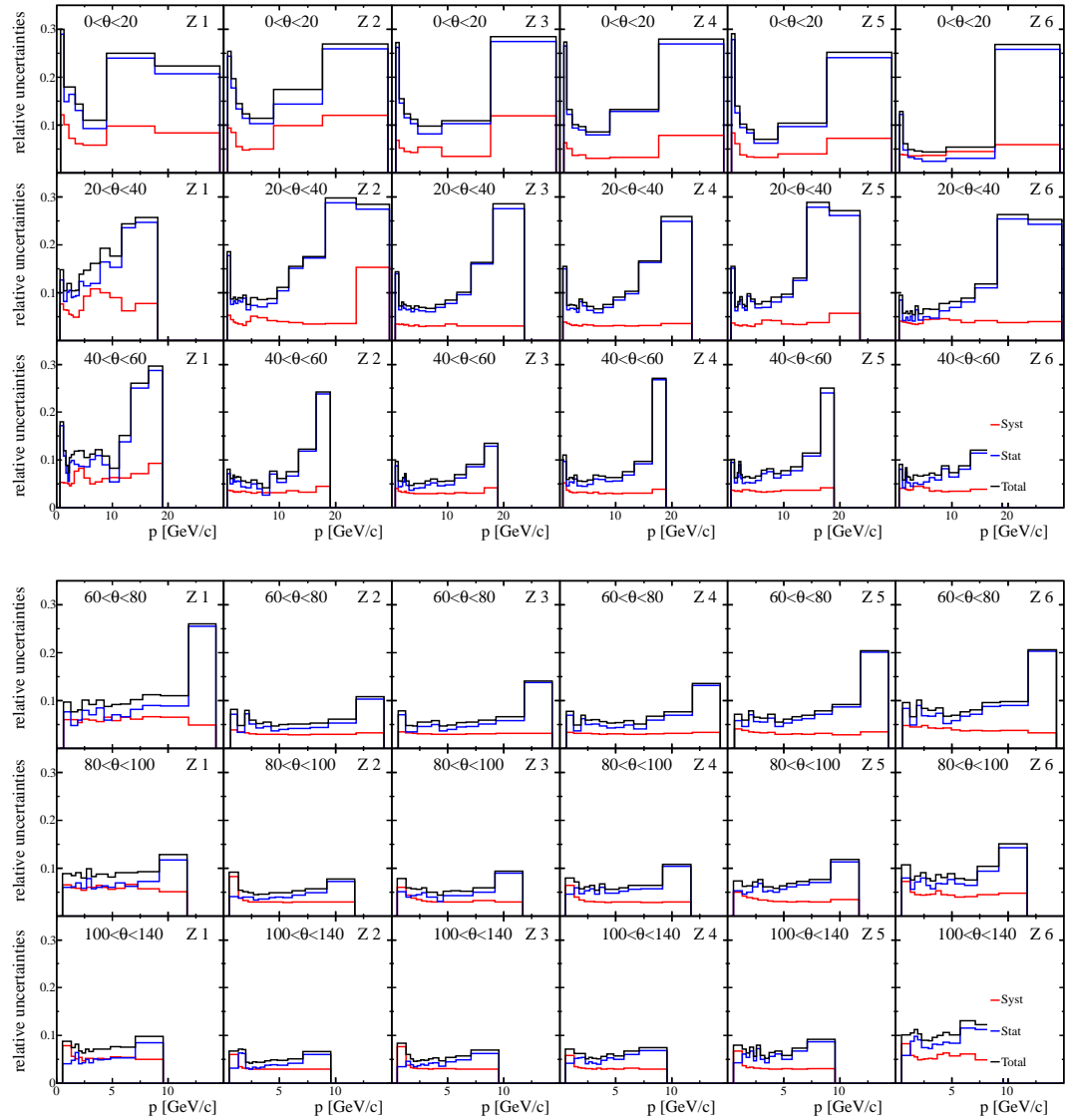


Figure 4.34: Statistical and systematic uncertainties for negatively charged pions, in the polar angle range from 0 to 140 mrad, and for the six longitudinal bins as a function of momentum.

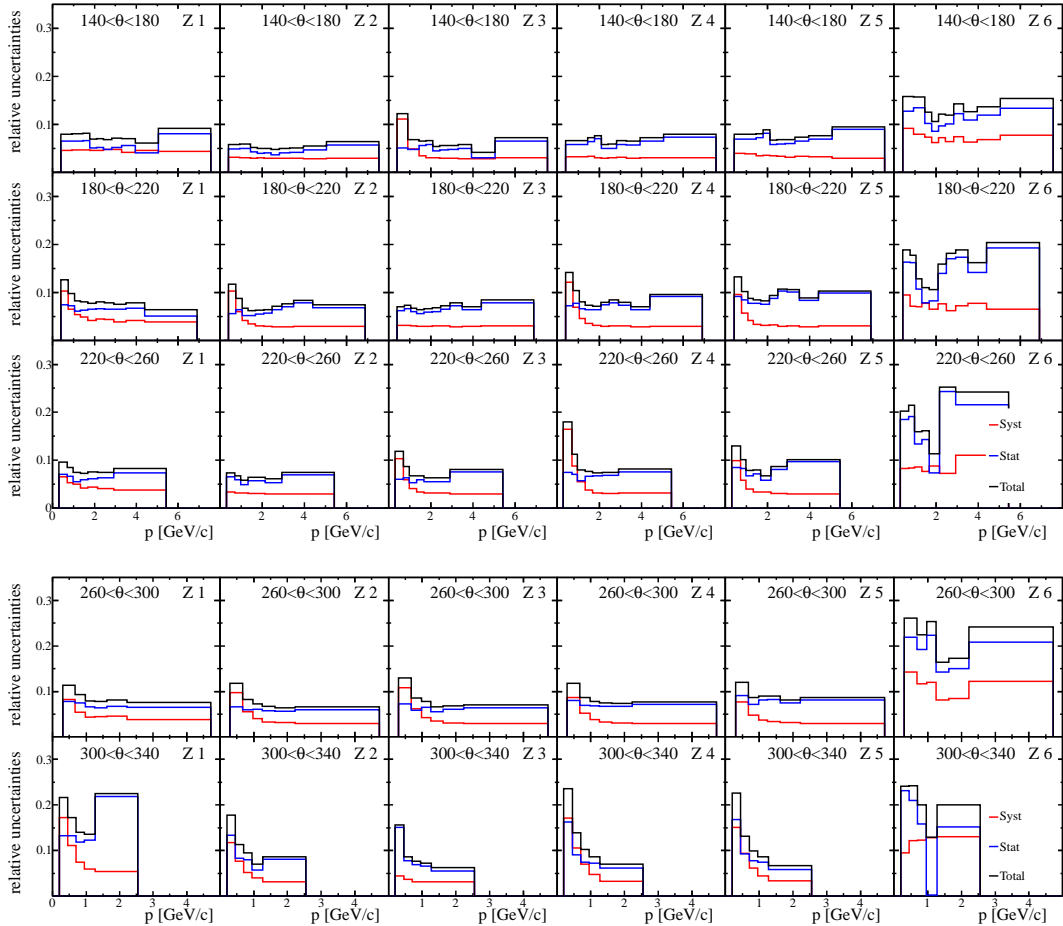


Figure 4.35: Statistical and systematic uncertainties for negatively charged pions, in the polar angle range from 140 to 340 mrad, and for the six longitudinal bins as a function of momentum.

4.7 Comparisons of thin target and T2K replica target results using the T2K hadron production re-weighting procedure

By slightly modifying the T2K hadron production re-weighting procedure presented in section 2.3.3, it is possible to re-weight the hadron production of all pions exiting the surface of the T2K replica target after the FLUKA simulation. This gives a way to compare the thin target results from NA61/SHINE with the T2K replica target results for the pion multiplicities.

The re-weighting procedure can be split into two parts as explained in section 2.3.3: a first part related to multiplicities re-weighting and a second part related to interaction rate re-weighting. It is thus interesting to apply the two different parts of the procedure individually and look at the effects on the pion spectra.

For the multiplicity re-weighting, the NA61/SHINE thin target data for π^\pm , K^\pm , K^0 and protons are used. The results can be seen in fig. 4.38 to fig. 4.49 for the different (p, θ, z) bins. The effect is mainly an increase of the number of pions exiting the target surface and it is larger for the upstream part of the target than for the downstream longitudinal bins.

The re-weighting of the interaction rate is done by varying the value of the production cross-sections for different incident particle momenta with respect to the quasi-elastic cross-section.

The quasi-elastic component is computed following eq. (2.21). Figure 4.36 shows the components of σ_{hp}^{el} and σ_{hn}^{el} as well as σ_{qe} as a function of momentum p . Technically, σ'_{prod} is estimated from the nominal σ_{prod}^{FLUKA} by adding a fraction “ S ” of the quasi-elastic production cross-section following eq. (4.7).

$$\sigma'_{prod} = \sigma_{prod}^{FLUKA} + S \cdot \sigma_{qe} \quad (4.7)$$

The quasi-elastic cross-section σ_{qe} is computed following the extended Bellettini’s formula based on the elastic cross-section of proton-proton and proton-neutron interactions.

$$\sigma_{qe} = 0.8(\sigma_{pp}^{el} + \sigma_{pn}^{el})A^{1/3} \quad (4.8)$$

In the FLUKA model, the interactions are either flagged as elastic or inelastic. For interactions at momentum higher than 5 GeV/c, the interactions flagged as elastic contains also the quasi-elastic part of the cross-section. Hence, for momentum equal or lower than 5 GeV/c, the quasi-elastic component of the interaction should be subtracted from the FLUKA values in order to be compared with data. Following this prescription and using eq. (4.8) to subtract the quasi-elastic component of the cross-section in FLUKA, fig. 4.37 shows the values of the production cross-sections for FLUKA in black. Different data sets are presented for comparisons. Two sets of points are displayed for the results quoted by Denisov. From the published values, it is not clear whether the inelastic or production cross-section has been measured. The higher values are the quoted results while for the lower values the quasi-elastic part has been subtracted (again using Bellettini’s formula eq. (4.8)).

It can be seen that FLUKA predictions are a bit higher than the available measurements. Using eq. (4.7) and assuming a scaling factor of $S = -0.6$, the FLUKA predictions can be re-computed. The black curve in fig. 4.37 represents these new values for the production cross-sections.

In order to clearly see the effect of both, the multiplicity re-weighting and the interaction rate re-weighting, we first apply only the multiplicity re-weighting and then add to it the interaction rate re-weighting. Figure 4.38 to fig. 4.43 present the results for the positively charged pions. Figure 4.44 to fig. 4.49 present the results for the negatively charged pions. In both cases, the tuning of the interaction rate has been done with a scaling factor $S = -0.6$, corresponding to

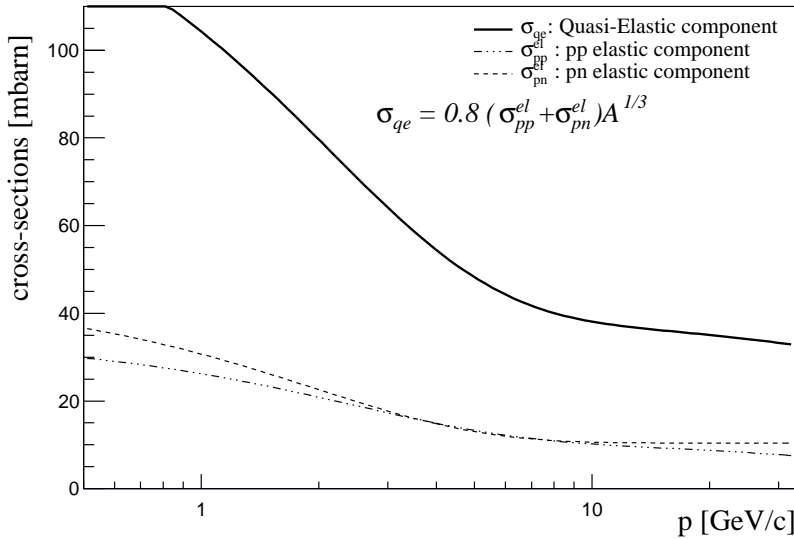


Figure 4.36: pp and pn elastic cross-sections and σ_{qe} as computed in eq. (2.21) as function of momentum p .

the values shown in fig. 4.37.

Modifying the multiplicities seems to increase the spectra. This is consistent with the observed comparisons of thin target results and FLUKA predictions, where the thin target spectra are on average higher than the FLUKA spectra. So, tuning the multiplicities does not allow to find an explanation for the discrepancies between the T2K replica target results and FLUKA simulation.

Changing the interaction rate shows a drop in the predictions, specially for the upstream part of the target in lower momentum ranges. While it has a tendency to increase the spectra at higher momentum and for the downstream part of the target. This tends to bring a better agreement between the NA61/SHINE measurements and the FLUKA model. A larger value of the scaling factor S would give an even better agreement on the level of the T2K replica target multiplicities but would start to bring tensions in the comparisons of the production cross-sections. It is important to note that only the production cross-section for proton-carbon interactions has been modified. Tuning pion-carbon production cross-section might also help to reduce the remaining tensions.

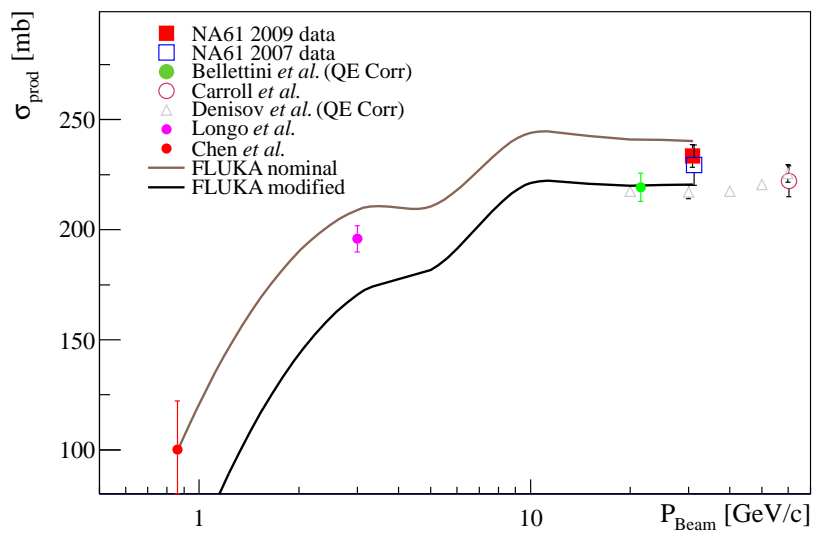


Figure 4.37: Nominal and modified Fluka production cross-sections compared with available data. The modified FLUKA production cross-section has been computed from the nominal values of the FLUKA production cross-section σ_{prod}^{FLUKA} and using eq. (4.7) with a scaling factor $S = -0.6$ and a quasi-elastic cross-section σ_{qe} given by eq. (4.8).

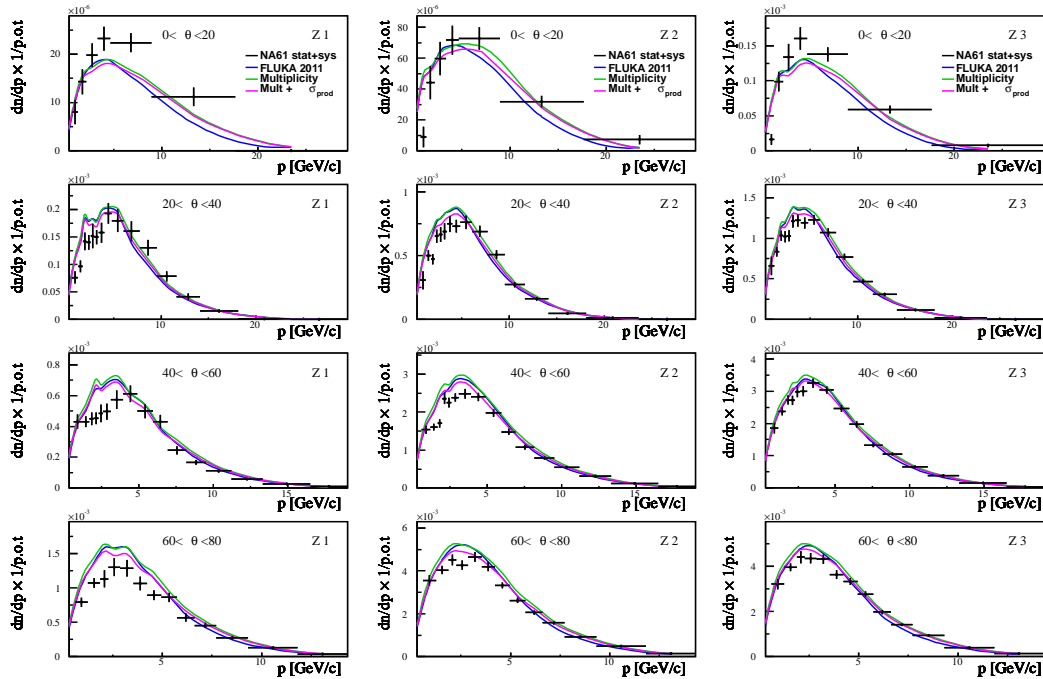


Figure 4.38: T2K replica target results for positively charged pions with nominal FLUKA predictions (blue), FLUKA re-weighted for the multiplicities (green) and FLUKA re-weighted for multiplicities and production cross-section σ_{prod} for the three upstream longitudinal bins and in the polar angles between 0 and 80 mrad plotted as a function of momentum

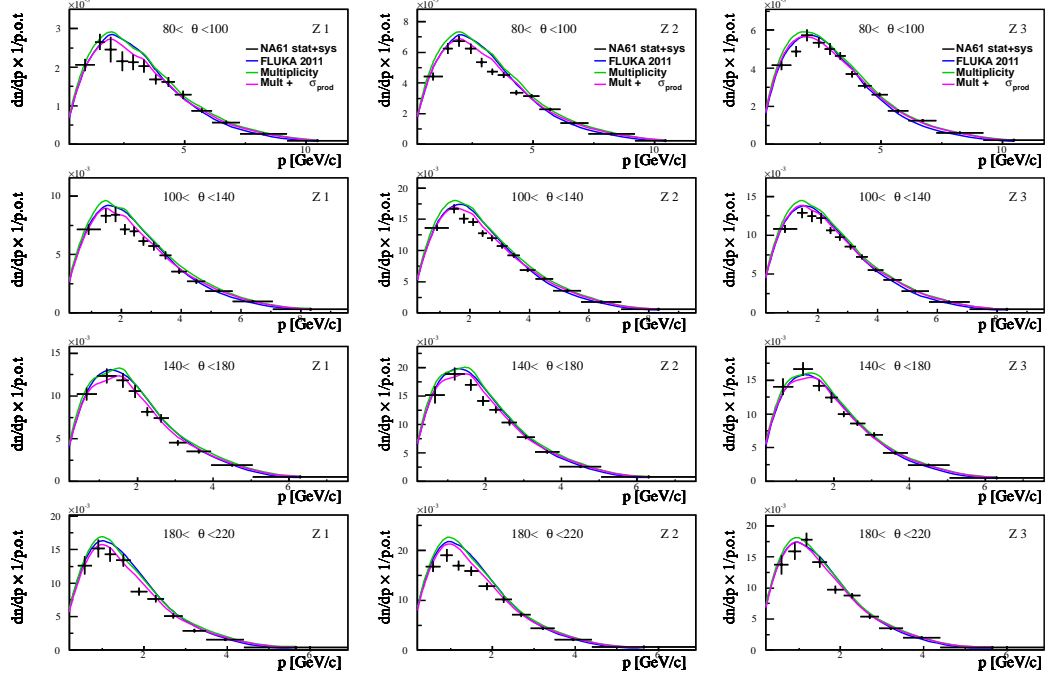


Figure 4.39: T2K replica target results for positively charged pions with nominal FLUKA predictions (blue), FLUKA re-weighted for the multiplicities (green) and FLUKA re-weighted for multiplicities and production cross-section σ_{prod} for the three upstream longitudinal bins and in the polar angles between 80 and 220 mrad plotted as a function of momentum

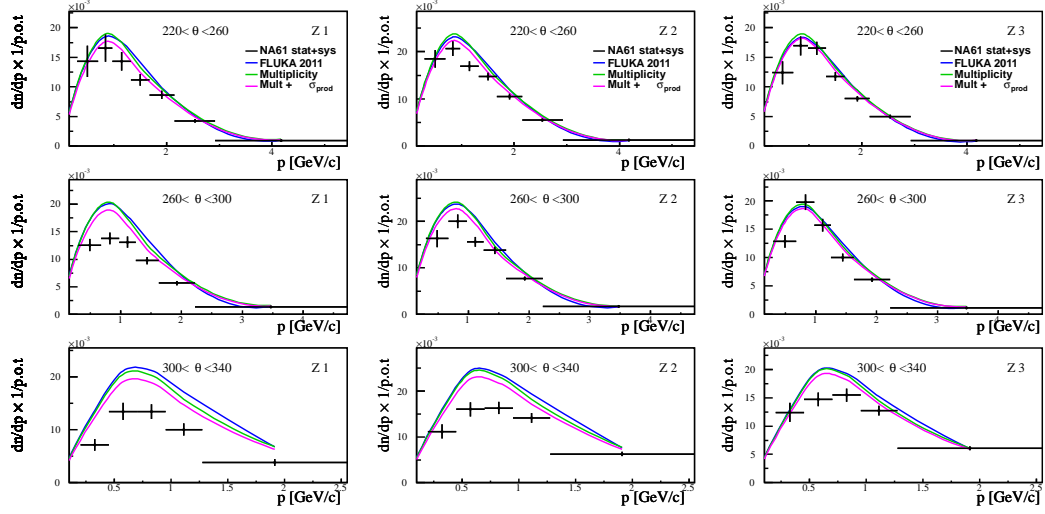


Figure 4.40: T2K replica target results for positively charged pions with nominal FLUKA predictions (blue), FLUKA re-weighted for the multiplicities (green) and FLUKA re-weighted for multiplicities and production cross-section σ_{prod} for the three upstream longitudinal bins and in the polar angles between 220 and 340 mrad plotted as a function of momentum

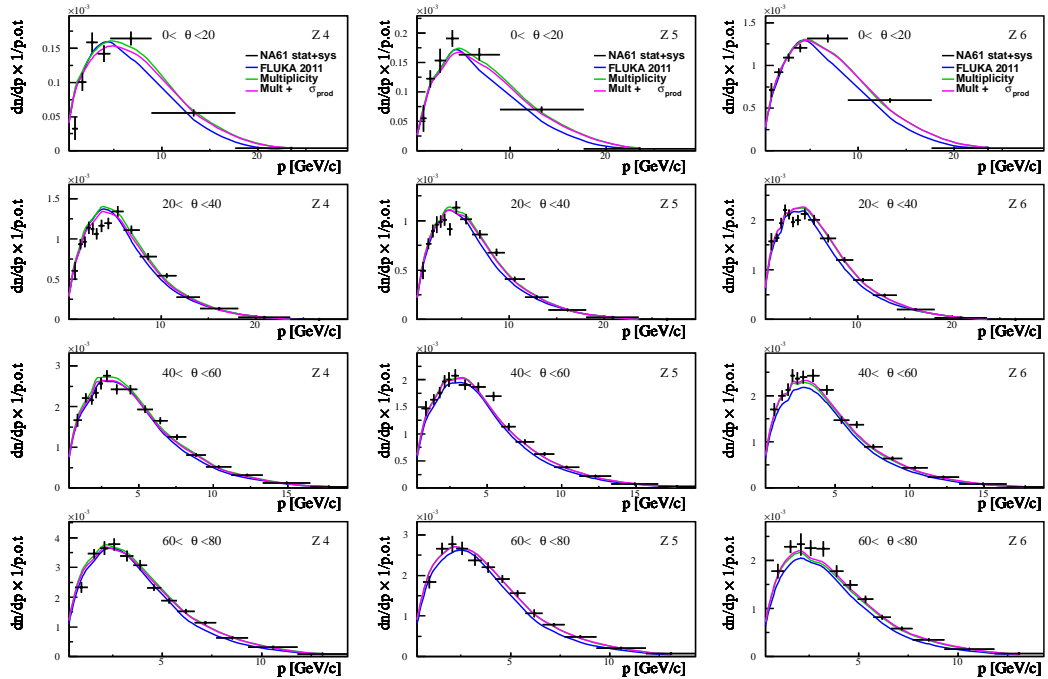


Figure 4.41: T2K replica target results for positively charged pions with nominal FLUKA predictions (blue), FLUKA re-weighted for the multiplicities (green) and FLUKA re-weighted for multiplicities and production cross-section σ_{prod} for the three downstream longitudinal bins and in the polar angles between 0 and 80 mrad plotted as a function of momentum

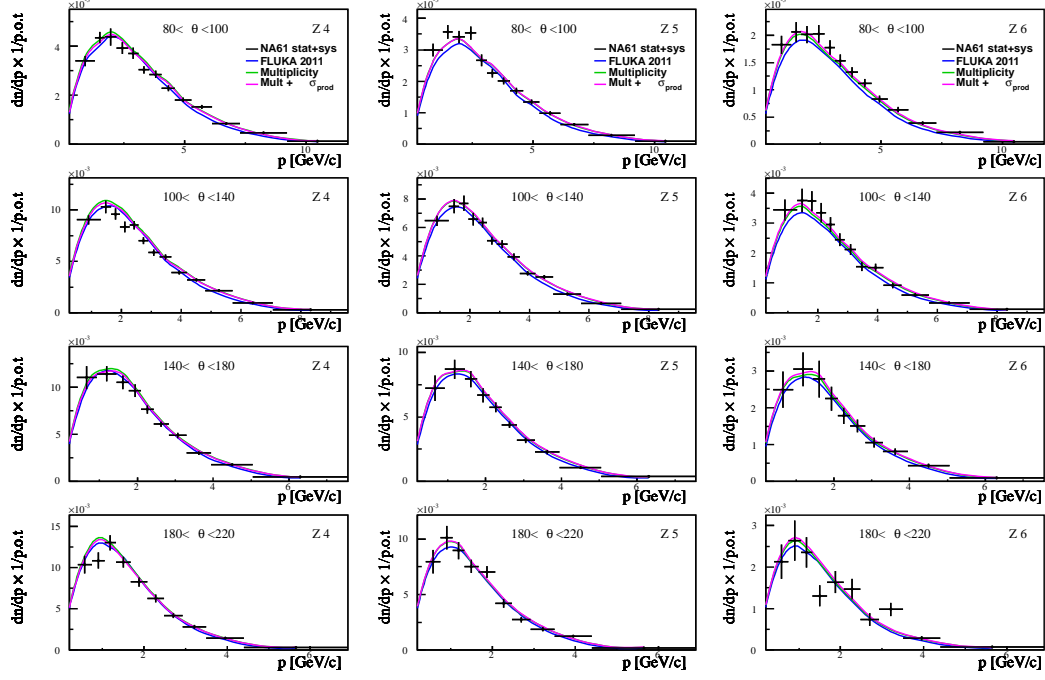


Figure 4.42: T2K replica target results for positively charged pions with nominal FLUKA predictions (blue), FLUKA re-weighted for the multiplicities (green) and FLUKA re-weighted for multiplicities and production cross-section σ_{prod} for the three downstream longitudinal bins and in the polar angles between 80 and 220 mrad plotted as a function of momentum

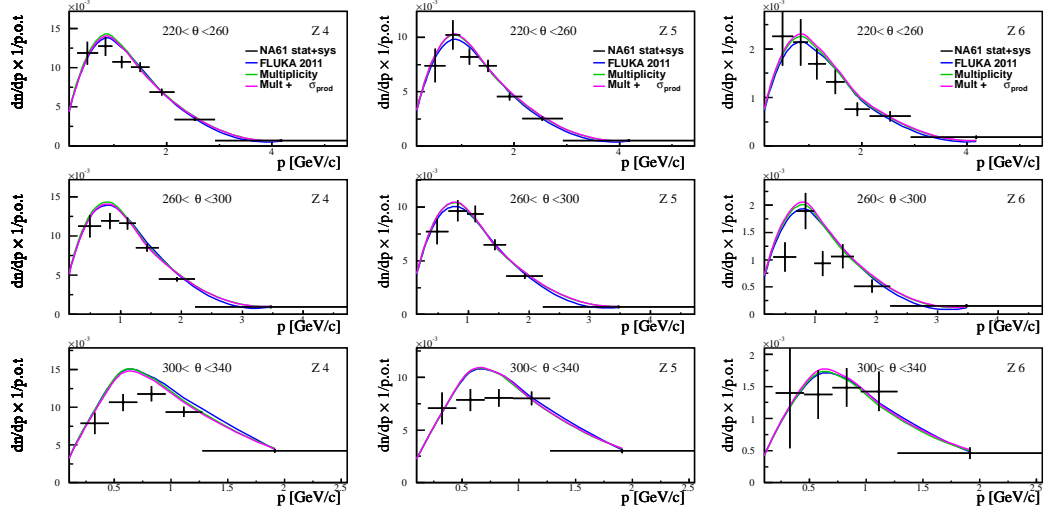


Figure 4.43: T2K replica target results for positively charged pions with nominal FLUKA predictions (blue), FLUKA re-weighted for the multiplicities (green) and FLUKA re-weighted for multiplicities and production cross-section σ_{prod} for the three downstream longitudinal bins and in the polar angles between 220 and 340 mrad plotted as a function of momentum

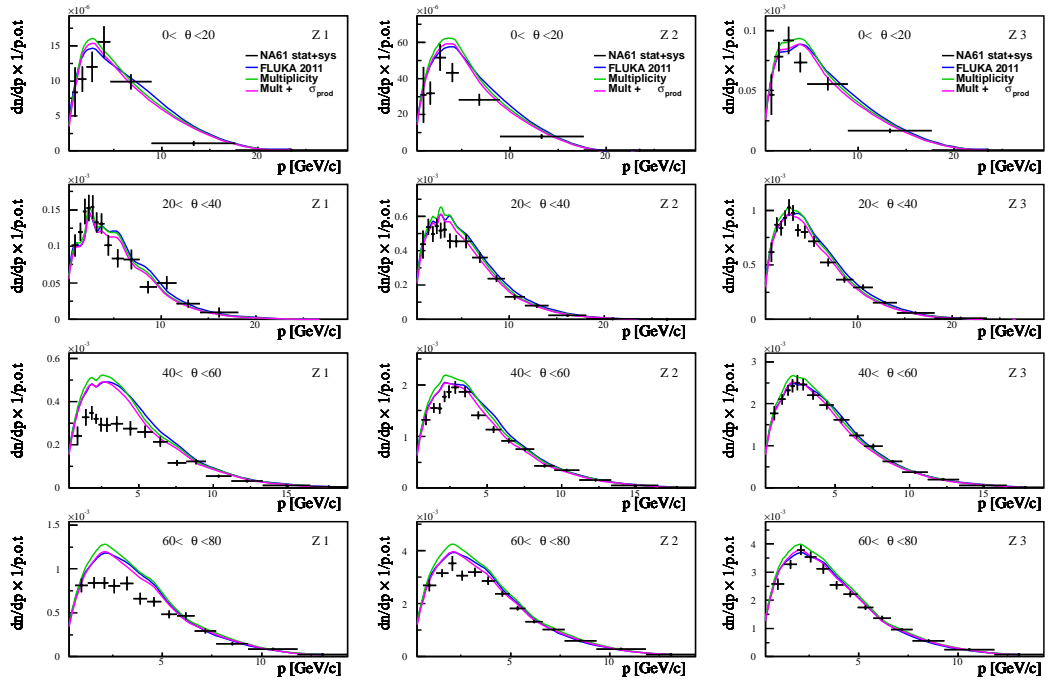


Figure 4.44: T2K replica target results for negatively charged pions with nominal FLUKA predictions (blue), FLUKA re-weighted for the multiplicities (green) and FLUKA re-weighted for multiplicities and production cross-section σ_{prod} for the three upstream longitudinal bins and in the polar angles between 0 and 80 mrad plotted as a function of momentum

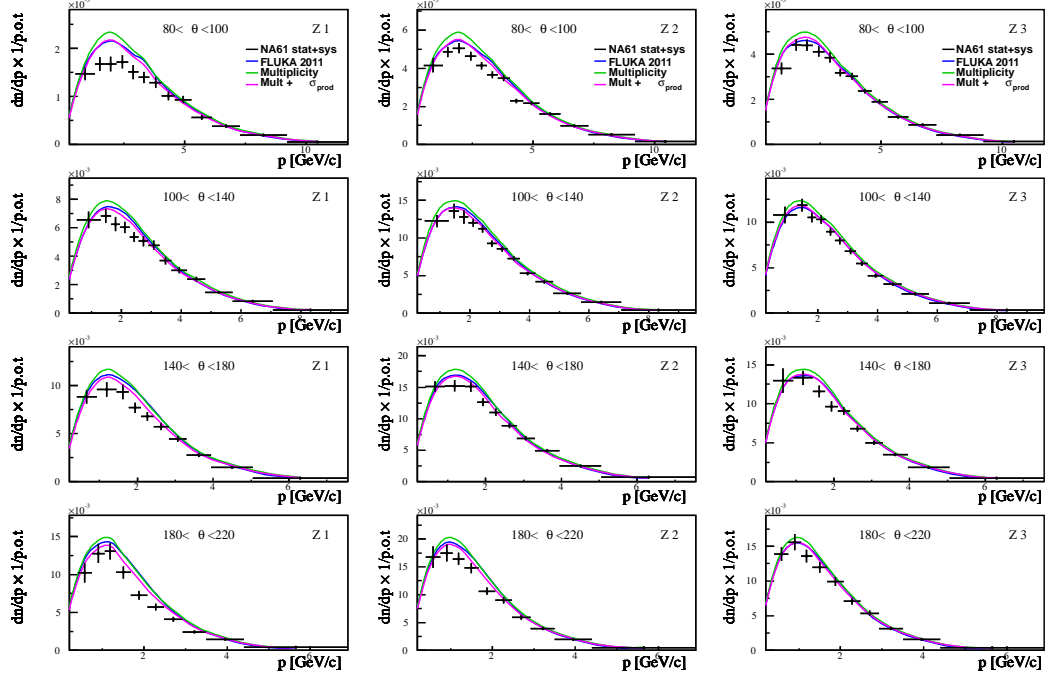


Figure 4.45: T2K replica target results for negatively charged pions with nominal FLUKA predictions (blue), FLUKA re-weighted for the multiplicities (green) and FLUKA re-weighted for multiplicities and production cross-section σ_{prod} for the three upstream longitudinal bins and in the polar angles between 80 and 220 mrad plotted as a function of momentum

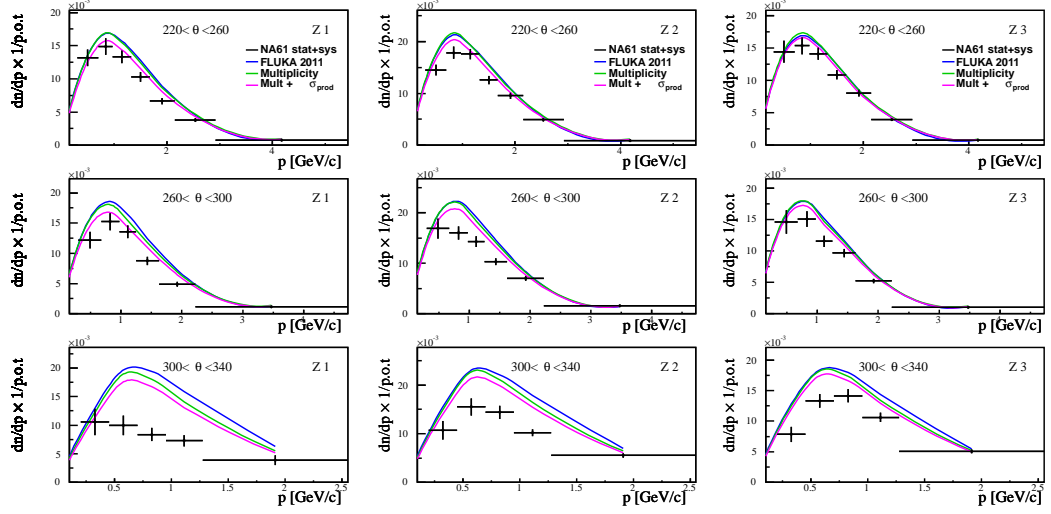


Figure 4.46: T2K replica target results for negatively charged pions with nominal FLUKA predictions (blue), FLUKA re-weighted for the multiplicities (green) and FLUKA re-weighted for multiplicities and production cross-section σ_{prod} for the three upstream longitudinal bins and in the polar angles between 220 and 340 mrad plotted as a function of momentum

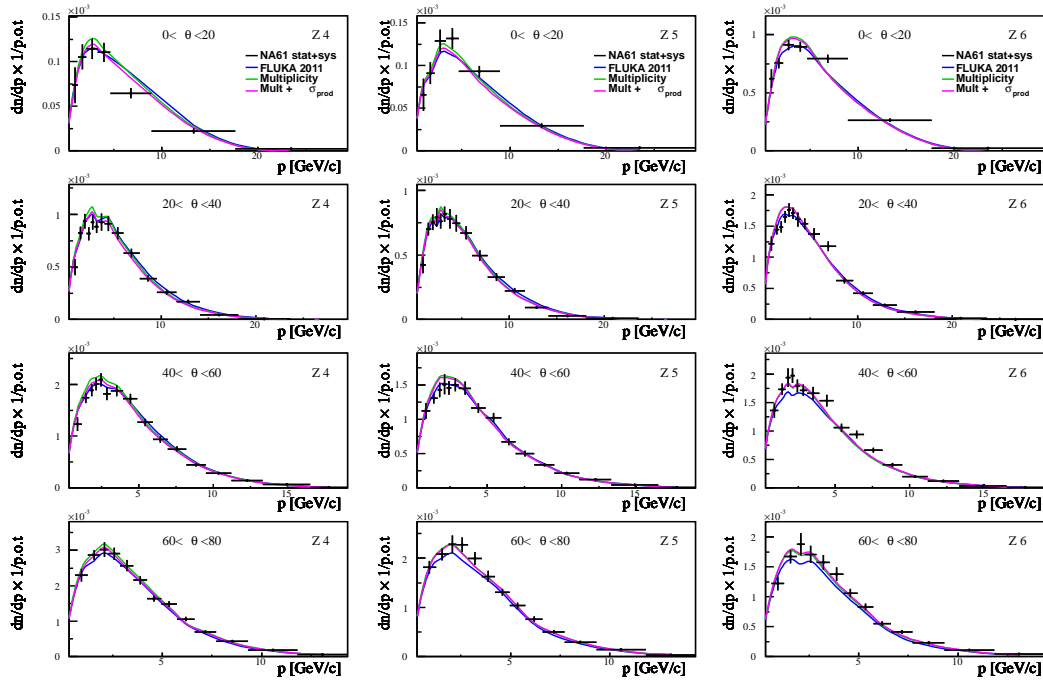


Figure 4.47: T2K replica target results for negatively charged pions with nominal FLUKA predictions (blue), FLUKA re-weighted for the multiplicities (green) and FLUKA re-weighted for multiplicities and production cross-section σ_{prod} for the three downstream longitudinal bins and in the polar angles between 0 and 80 mrad plotted as a function of momentum

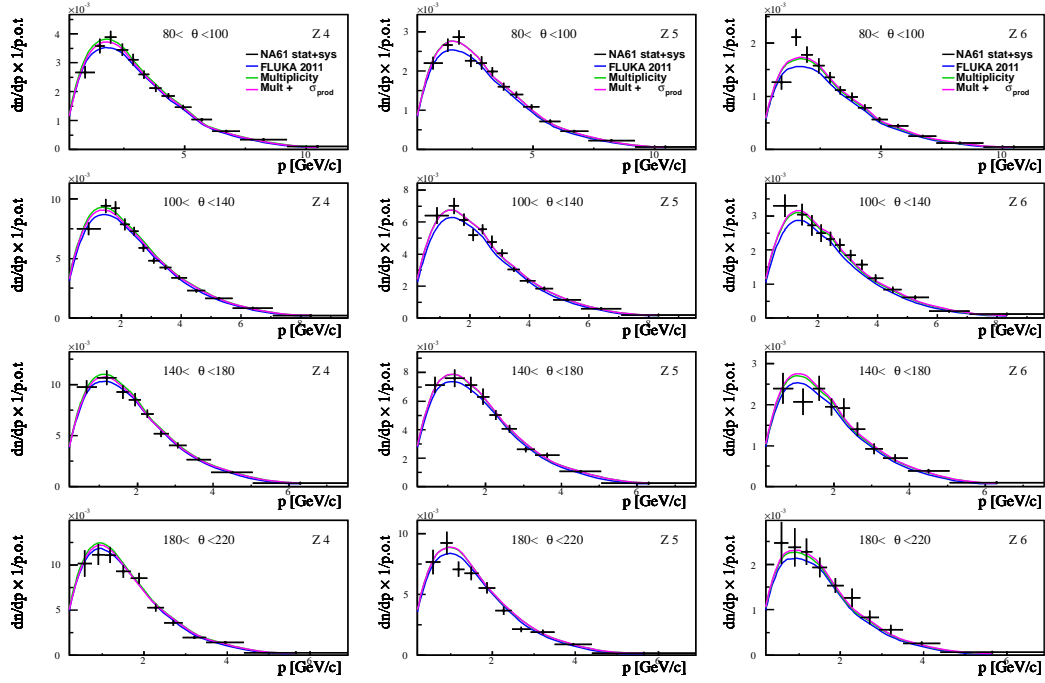


Figure 4.48: T2K replica target results for negatively charged pions with nominal FLUKA predictions (blue), FLUKA re-weighted for the multiplicities (green) and FLUKA re-weighted for multiplicities and production cross-section σ_{prod} for the three downstream longitudinal bins and in the polar angles between 80 and 220 mrad plotted as a function of momentum

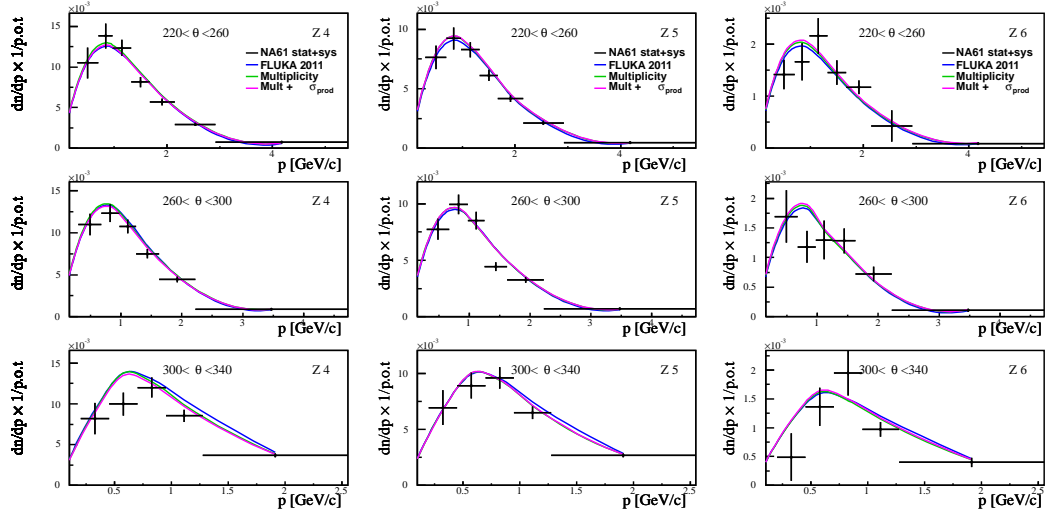


Figure 4.49: T2K replica target results for negatively charged pions with nominal FLUKA predictions (blue), FLUKA re-weighted for the multiplicities (green) and FLUKA re-weighted for multiplicities and production cross-section σ_{prod} for the three downstream longitudinal bins and in the polar angles between 220 and 340 mrad plotted as a function of momentum

Chapter 5

Implementation of the T2K Replica Target Results in the T2K Neutrino Flux Prediction

A first trial of implementing the T2K replica target results of the 2007 dataset was developed and presented in a published article [107]. The method proposes to re-weight the predictions of the model used in the T2K beam MC for the simulation of hadronic interactions in the target by computing re-weighting factors in bins of (p, θ, z) within the NA61 simulation. The weights are defined as:

$$w(p, \theta, z) = N_{NA61}^{data}(p, \theta, z) / N_{NA61}^{MC}(p, \theta, z) \quad (5.1)$$

where N_{NA61}^{data} are the NA61/SHINE measured yields at the surface of the target without any corrections (i.e. raw yields) and N_{NA61}^{MC} are the reconstructed yields obtained from the NA61/SHINE simulation based on the same model as used in T2K. This method has the advantage of being rather straightforward as no corrections for the pion spectra need to be computed. Furthermore, the systematic uncertainties on the computed weights are estimated to be small as most of the components of the systematics would cancel in the ratio. Unfortunately it has the disadvantage of being quite rigid in the sense that the hadronic models used in T2K and in NA61/SHINE to compute the weights have to be exactly the same in order for the weights to be consistently applied. Hence, it was decided, for the 2009 data set, to compute correction factors and deliver corrected pion spectra. Re-weighting factors can then be computed in bins of (p, θ, z) as

$$w(p, \theta, z) = N_{NA61}^{corr}(p, \theta, z) / N_{T2K}^{sim}(p, \theta, z) \quad (5.2)$$

where N_{NA61}^{corr} are the NA61 measured yields at the surface of the target, corrected for various efficiencies, detector geometrical acceptance and particle losses (i.e. absolute yields), and N_{T2K}^{sim} are the yields of emitted particles simulated within the hadronic model used in T2K (i.e. FLUKA 2011).

5.1 Calculation of neutrino flux using T2K Replica Target Results

The implementation of the T2K replica target results within the T2K neutrino flux prediction can follow the same main stream as the one for the thin target re-weighting procedure. The major modification to be introduced is to save the relevant parameters of the particles exiting the surface of the graphite target at the level of the FLUKA simulation. This specific entry is added to the already existing history chain for each produced neutrino. Recording these parameters allows, once the full neutrino beam simulation is completed, to come back to each pion exiting the surface of the target and being parent of neutrinos. The neutrinos are then assigned a weight which is dependant on the (p, θ, z) parameters of the pions at the surface of the target and being computed as in eq. (5.2).

It is important to note that only neutrinos that have a pion parent particle exiting the surface of the target can be re-weighted following this procedure in the present analysis (as Kaon spectra at the surface of the target have not been extracted yet). Figure 5.1 shows the parent particles for the different neutrino species at SK.

Figure 5.2 and fig. 5.3 present the fraction of parent particles that can be re-weighted with the T2K replica target results from NA61/SHINE. The solid blue line represent the fraction of neutrinos for which parent particles are generated by re-interactions along the beam line or by a particle being any other hadrons than a pion exiting the target surface. Hence, it represent the fraction of the neutrino flux that cannot be constrained by the present T2K replica target results from the 2009 data set. The dashed black line represent the fraction of the neutrino flux for which parent particles are generated by re-interactions along the beam line. By extracting not only pions but also kaons from the T2K replica target measurements, this dashed line would represent the remaining fraction of the neutrino flux that cannot be re-weighted directly with the T2K replica target measurements.

Other particle species exiting the target surface are re-weighted following the already existing thin target procedure. Re-interactions outside of the target (in the focusing horns and along the beam line) are also tuned with the nominal T2K neutrino flux calculation (based on thin target data).

In order to compare, in a consistent way, the neutrino flux prediction re-weighted with the thin target procedure and with the T2K replica target results, it is important to consider the exact same settings for the entire flux computation. As the weights related to the T2K replica target dataset have been computed with the NA61/SHINE beam profile, this same beam profile is used to run a full neutrino flux simulation within JNUBEAM. A direct comparison between thin target and T2K replica target re-weighting procedures can then be done.

In order to study the different effects of the thin target tuning, the neutrino flux at SK is first re-weighted for the multiplicity only (fig. 5.4 left) and then for the multiplicity and production cross-section for proton-Carbon interactions (fig. 5.4 right).

As in the case of the pion spectra, the production cross-section is modified by a factor of -0.6 of the quasi-elastic component. It corresponds roughly to lowering the value of the FLUKA production cross-section for p+C@31 GeV/c from 241 mbarn to 221 mbarn. Figure 4.37 shows the modified values over the full momentum range.

The results presented in fig. 5.4 are consistent with those obtained in section 4.7. At high neutrino energy, the ratio tends to one. This is simply due to the fact that the dominant part of the spectra comes from kaon parent particles and hence cannot be re-weighted with the T2K replica target measurements obtained in the present analysis. At lower energy spectra, where the pion parent particles dominate, the thin target tuning predicts a higher neutrino flux at SK. This is in agreement with the pion spectra, where the thin target tuning inflates the predictions

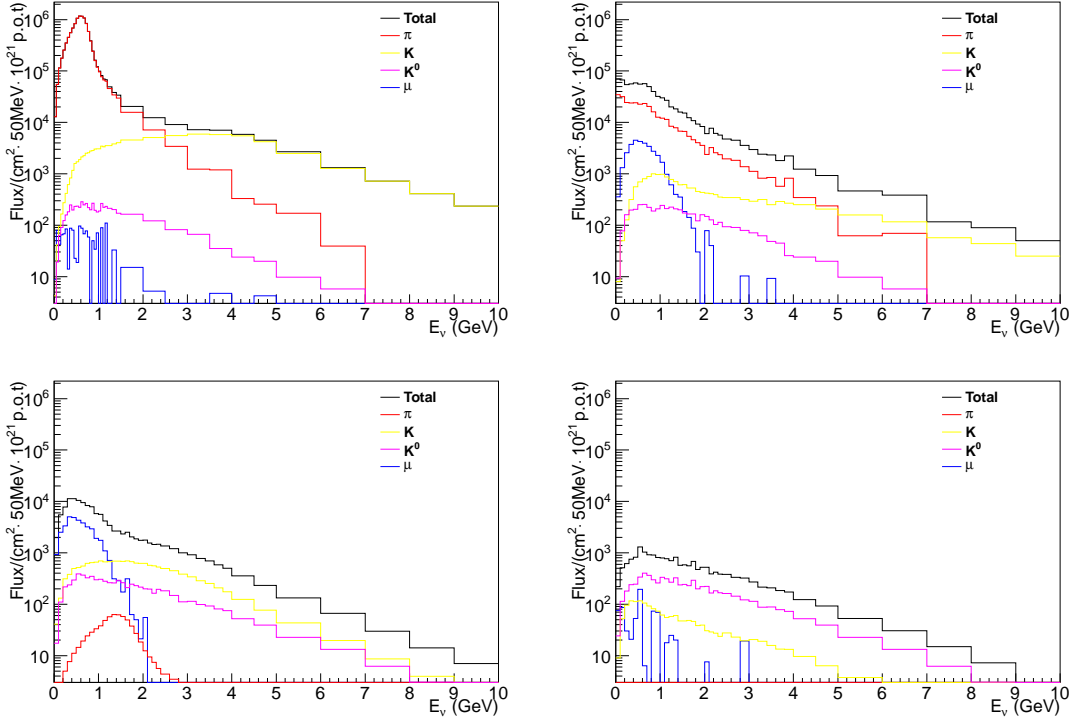


Figure 5.1: Spectra of neutrino parent particles for ν_μ (top left), $\bar{\nu}_\mu$ (top right), ν_e (bottom left) and $\bar{\nu}_e$ (bottom right) at SK calculated using JNUBEAM.

of the number of pions exiting the target surface. By lowering the proton-carbon production cross-section, reduced spectra are obtained for the predictions of the number of pions exiting the surface of the graphite target. This gets translated into a smaller ν_μ flux prediction for neutrinos at SK.

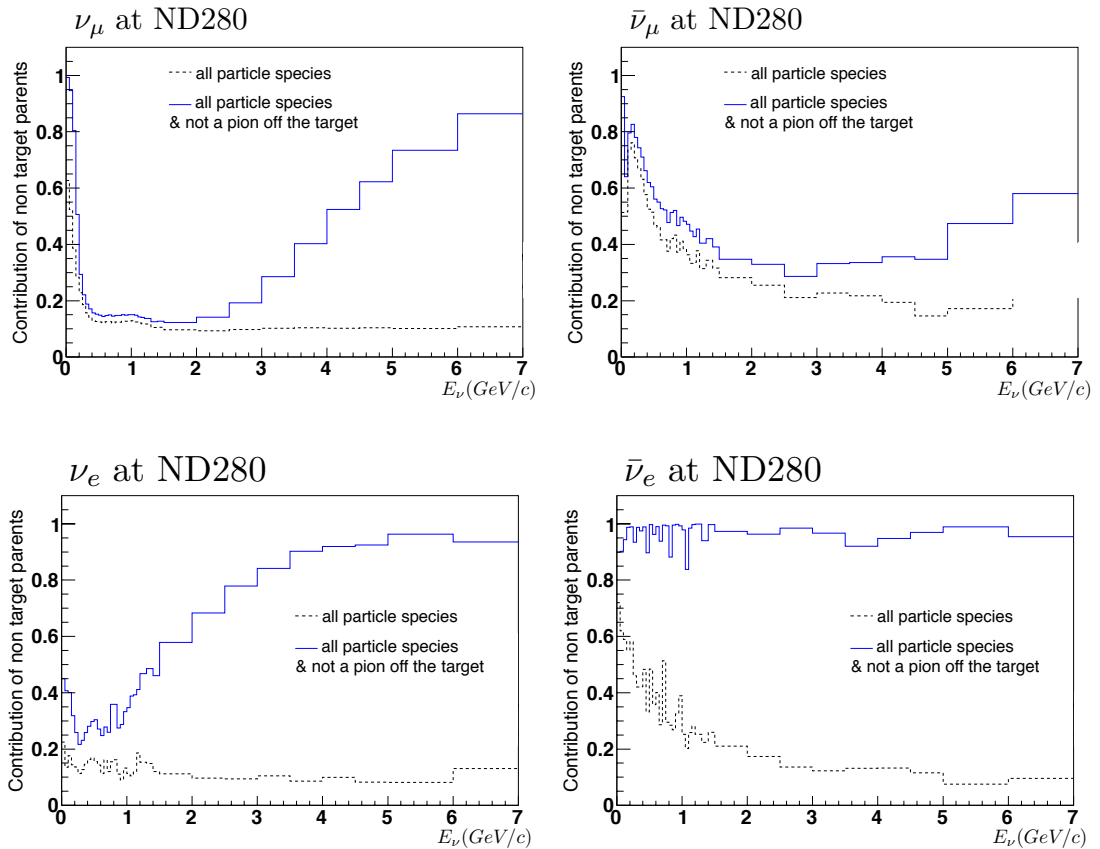


Figure 5.2: Fraction of neutrino fluxes at ND280 generated by re-interactions along the beam line (solid blue line) and by particles not being a pion when exiting the target surface (dashed black line) as calculated using JNUBEAM.

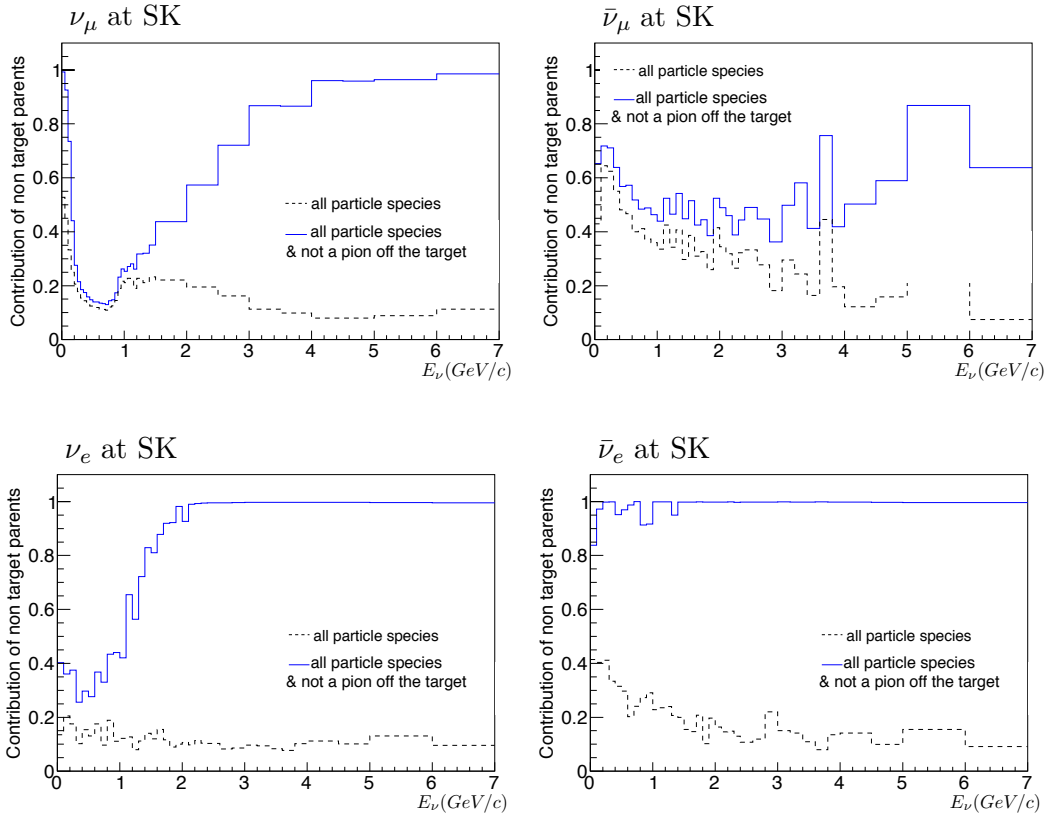


Figure 5.3: Fraction of neutrino fluxes at SK generated by re-interactions along the beam line (solid blue line) and by particles not being a pion when exiting the target surface (dashed black line) as calculated using JNUBEAM.

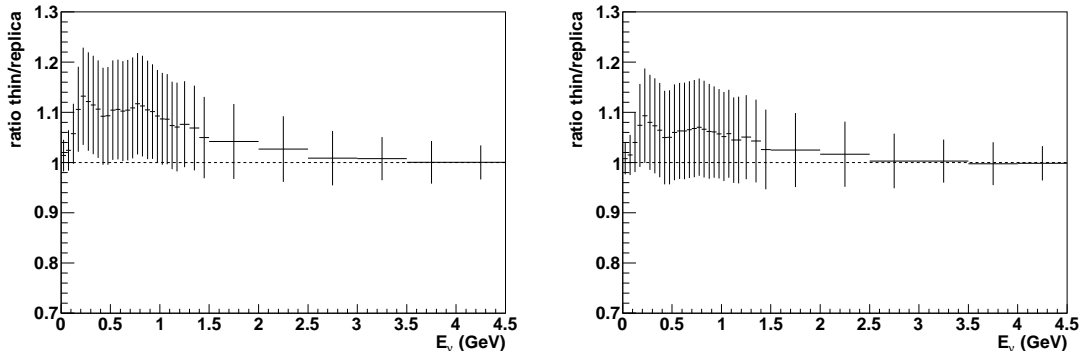


Figure 5.4: Ratio of ν_μ flux re-weighted with thin target procedure over T2K replica target. Left plot shows result when the production cross-section is not re-weighted, on the right the production is rescaled by -0.6 of the quasi-elastic contribution

5.2 Flux systematics using T2K replica target data

The propagation of the T2K replica target results to the final neutrino flux predictions is done via the weights computed as

$$w(p, \theta, z) = N_{NA61}^{corr}(p, \theta, z) / N_{T2K}^{sim}(p, \theta, z) \quad (5.3)$$

For each neutrino energy bin i , one can write the contribution of the re-weighting factors, for each (p, θ, z) bin j as a linear combination

$$E_{\nu_i} = \sum_{j=1}^N a_{ij} \cdot \omega_j \quad \text{where} \quad \omega_j = \frac{n_j^{NA61}}{n_j^{FLUKA}} \quad (5.4)$$

and the coefficients a_{ij} are related to the contribution of each (p, θ, z) bins to each neutrino energy bins. Graphical representation of the a_{ij} coefficients are presented in fig. 5.5 for the ν_μ flux prediction at SK and in fig. 5.6 for the $\bar{\nu}_\mu$ flux prediction at SK. They show the contributions of each pion (p, θ, z) bin to the different neutrino energy bins. The abscissa are subdivided into

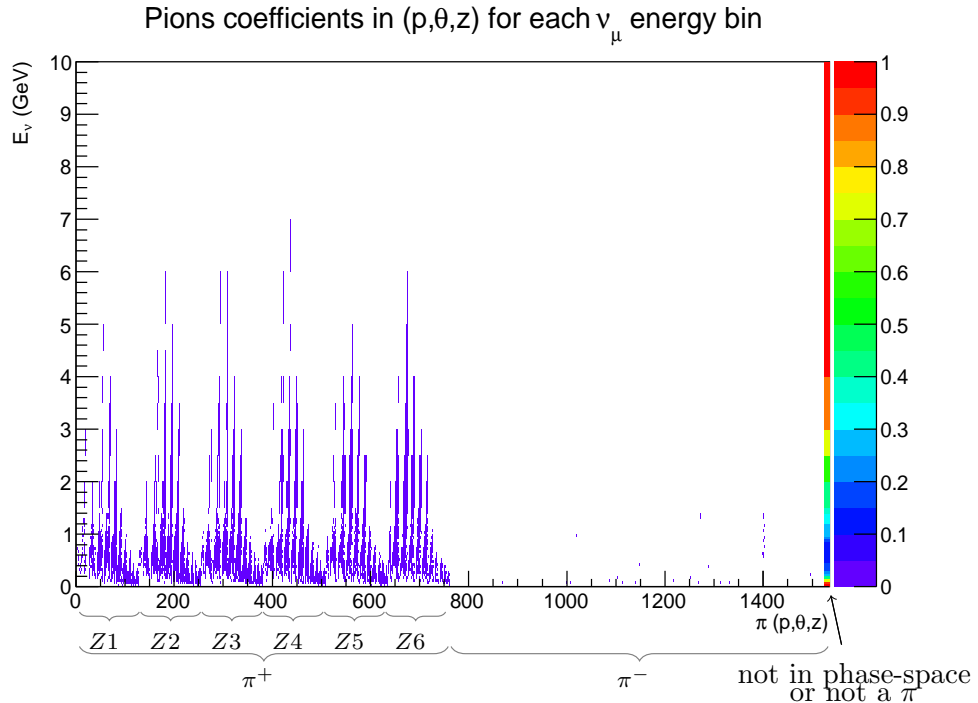


Figure 5.5: Coefficient matrix for pions exiting the target surface contributing to each bin of the ν_μ spectra at SK

different bins. Positively charged pions span over the first part of the axis. This part is further divided into the six different longitudinal bins z . Each z bin is divided into the eleven polar angle θ bins. Finally, each θ bin is subdivided into momentum p bins. This gives a total of 762 bins for both pion species. The very last bin along the abscissa represents the fraction of each neutrino energy bin that is not generated by pions exiting the target surface, and hence cannot be directly re-weighted by the T2K replica target results.

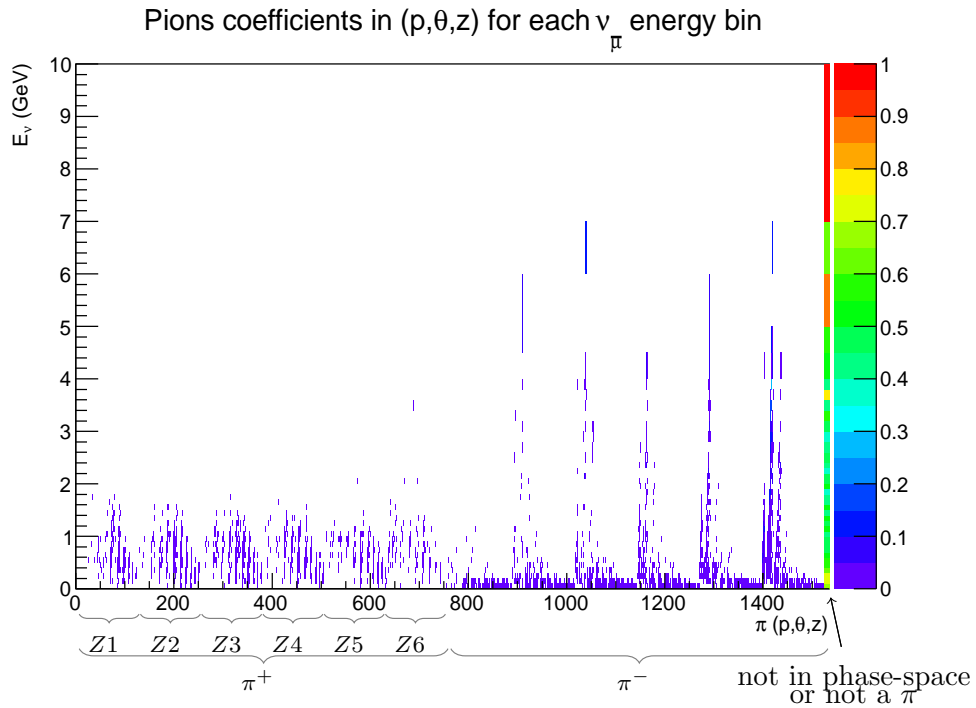


Figure 5.6: Coefficient matrix for pions exiting the target surface contributing to each bin of the $\bar{\nu}_\mu$ spectra at SK

Propagating the T2K replica target uncertainties means propagating the uncertainties on the weights ω_j .

Two methods can be considered:

1. propagation via an “overall 1σ shift” of the T2K replica target results, for each error source treated as independent

$$\sigma_{Y_i} = f_i(X_j + \sigma_{X_j}) - f_i(X_j) \quad \text{where} \quad Y_i = f_i(X_j) \equiv E_{\nu_i}; X_j \equiv \omega_j \quad (5.5)$$

In this notation, σ_{X_j} represents the uncertainties on the weights ω_j and $f_i(X_j)$ is the linear combination related to the neutrino bin energy i . Propagating σ_X to $f_i(X)$ due to an overall 1σ shift on X_j can be written as:

$$\sigma_{f_i} = f_i(X_j + \sigma_{X_j}) - f_i(X_j) = \sum_j a_{ij}(x_j + \sigma_{x_j}) - \sum_j a_{ij}x_j = \sum_j a_{ij}\sigma_{x_j} \quad (5.6)$$

In this case, it should be noted that the statistical error is also shifted by 1σ for all bins at the same time, hence treated as fully correlated between all bins.

2. propagation via “covariance matrices” for each error source

$$C_Y = F_X \cdot C_X \cdot F_X^T \quad (5.7)$$

with

$$F_X = \begin{pmatrix} a_{11} & \dots & a_{1n} \\ \vdots & \ddots & \vdots \\ a_{p1} & \dots & a_{pn} \end{pmatrix} \quad \text{and} \quad C_X = \begin{pmatrix} \sigma_{x_1}^2 & \dots & \sigma_{x_1, x_n} \\ \sigma_{x_2, x_1} & \dots & \sigma_{x_2, x_n} \\ \vdots & \ddots & \vdots \\ \sigma_{x_n, x_1} & \dots & \sigma_{x_n}^2 \end{pmatrix} \quad (5.8)$$

$c_{1,1}$ gives the uncertainty on $Y_1 = f_1(X)$. It can be written as:

$$\sigma_{y_1}^2 = \sum_j (a_{1j})^2 \sigma_{x_j}^2 + \sum_{i \neq j} \sum \frac{\partial f_1}{\partial x_i} \frac{\partial f_1}{\partial x_j} \sigma_{x_i, x_j} \quad (5.9)$$

Assuming all variables X_j are fully correlated: $\sigma_{x_i, x_j} = \sigma_{x_i} \cdot \sigma_{x_j}$

$$\sigma_{y_1}^2 = \sum_j (a_{1j})^2 \sigma_{x_j}^2 + \sum_{i \neq j} \sum 2 \cdot a_{ij} \sigma_{x_i} \sigma_{x_j} \quad (5.10)$$

which is the square of eq. (5.6).

The two procedures have been processed. Assuming fully correlated variables in the second method showed the same results as those computed with the first method. This insures that the coded algorithm is correct.

Figure 5.7 shows the results of propagating the T2K replica target uncertainties to the final neutrino flux. The different components of the systematic uncertainties from the T2K replica target results are considered as not correlated between each others, while, for each component, the (p, θ, z) bins are taken as fully correlated. For the statistical uncertainties, the (p, θ, z) bins are treated as not correlated between each others. It is very important so stress again, that these plots are build by considering only those neutrinos being directly produced by pions exiting the target surface and not interacting along the beam line. It corresponds to around 90% of the ν_μ flux at the beam peak energy but rapidly fall to less than 40% above 2 GeV (as seen in fig. 5.3).

In other words, the 4% uncertainty on the neutrino flux quoted in fig. 5.7 for the ν_μ spectra around the beam peak energy represents 90% of the total systematic uncertainty due to hadronic interactions for the neutrino flux. While at 3 GeV the 4% uncertainty represent only 30% of the total uncertainty.

The propagation of uncertainties for the ν_e and $\bar{\nu}_e$ fluxes are not presented. The contribution of these fluxes that can be re-weighted with the T2K replica target results is too small to be of interest (see fig. 5.3).

A detailed study of the systematic uncertainties due to other particle species and to re-interactions along the beam line would be mandatory in order to have a consistent comparison between the thin target re-weighting procedure and the T2K replica target re-weighting. Nevertheless, it can be foreseen that the final outcome based on the T2K replica re-weighting procedure will be very competitive. While the thin target procedure will always have to take into account many additional uncertainties (as for example the error related to the interaction length used by the models, see fig. 2.46 and fig. 2.47), a procedure base on the T2K replica target measurements will not have further sources of systematic uncertainties than those already included in the present analysis.

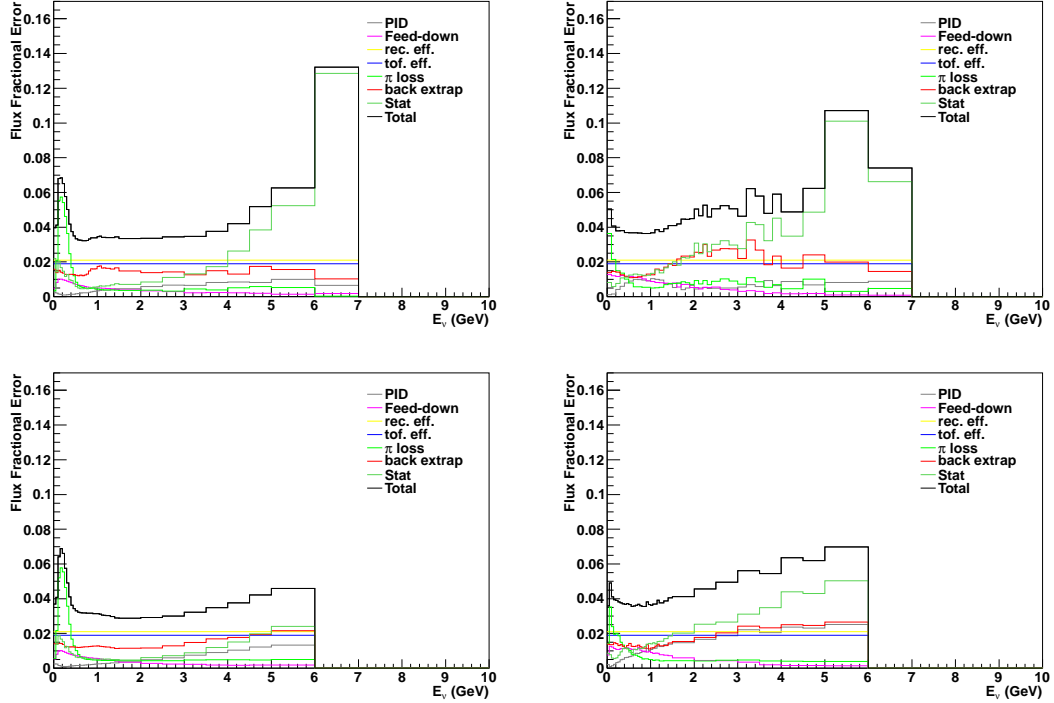


Figure 5.7: Propagated statistical and systematic uncertainties for the T2K replica target results to the ν_μ (left) and $\bar{\nu}_\mu$ (right) fluxes at SK (top) and ND280 (bottom). The statistical uncertainties are considered as not being correlated between the different NA61/SHINE analysis bins, while for each component of the systematic uncertainties the correlation is considered to be maximal. The different components of the systematic uncertainties are considered as not being correlated between each others.

5.3 Proton Beam Profiles

In the above sections, all calculations have been done based on the NA61/SHINE beam profile. Nevertheless, the pion spectra at the surface of the target depend on the initial proton beam profile hitting the target upstream face. This is presented in the figures of appendix C, where two different FLUKA simulations of four million protons on target have been produced. For the first simulation, the measured NA61/SHINE parameters of the proton beam are used as input. The second simulation is based on the measured T2K parameters for the run 4 (table 2.1). Figure 5.8 shows the distribution of the divergence versus position of the proton beam at the surface of the target for the x and y coordinates and for NA61/SHINE and T2K.

Figure 5.9 presents the radial distributions for NA61/SHINE and T2K. One can see that the T2K proton beam is narrower than the one of NA61/SHINE.

In order to show that the T2K replica target measurements can be properly used for the T2K neutrino flux prediction, it is important to illustrate the possibility to extrapolate those measurements to the beam profile as set in T2K. To conduct this study, the two different FLUKA simulations presented in appendix C are used.

The goal is to prove that, starting with the NA61/SHINE pion spectra and re-weighting

them for the differences in beam profiles, it is possible to reconstruct the T2K pion spectra at the surface of the target.

The proton beam distributions at the upstream face of the target can be subdivided into radial and azimuthal angle bins (r, ϕ) . Figure 5.10 shows the distributions in the (x, y) coordinates for the NA61/SHINE and the T2K beams as well as the ratio of the T2K over the NA61/SHINE distribution. The binning is overlaid on top of the distributions. Figure 5.11 represents the number of entries in each beam bin, with the ratio of the T2K over NA61/SHINE beam.

The radial binning is chosen relatively fine in order not to average out the differences over large areas.

For each (p, θ, z) bin it is possible to write a linear combination of the contribution of each beam bin, such that the number π_i of pions in the (p, θ, z) bin i related to the number of proton beam b_j in each beam bin j is:

$$\pi_i^{N,T} = \sum_j c_{ij}^{N,T} b_j^{N,T} \quad (5.11)$$

where the components c_{ij} are the contribution coefficients of each beam bin to the (p, θ, z) bins. The indices N and T stands for the specific NA61/SHINE and T2K beam profiles respectively.

If the beam bins are fine enough with respect to the variations of the different beam profiles, it could be expected that the $c_{ij}^{N,T}$ are independent of the beam distribution. Indeed, each proton hitting a specific position of the target upstream face will follow the same physics processes inside the target, independently of the fact that it has been produced under the T2K or the NA61/SHINE beam profile. If this is true, the re-weighted NA61/SHINE pion spectra at the surface of the target could be written as:

$$\pi_i^{N_r} = \sum_j c_{ij} d_j b_j^N \quad (5.12)$$

where d_j are the components of the ratio of the T2K beam bins over the NA61/SHINE beam bins (as presented in fig. 5.11). N_r stands here for re-weighted NA61/SHINE spectra.

Showing that:

$$\frac{\pi_i^{N_r}}{\pi_i^T} = 1 \quad (5.13)$$

for each (p, θ, z) bins i are consistent with one would prove that the coefficients c_{ij} are indeed independent of the beam profiles. Furthermore, it proves that a procedure can be followed to re-weight any pion spectra at the surface of the target with different beam profiles (which is what is needed to implement directly the NA61/SHINE measurements in the T2K neutrino flux prediction).

To qualitatively prove the above mentioned assertions, we start with the NA61/SHINE pion spectra and the related beam profile. The c_{ij} coefficients can be computed and presented under the form of a matrix. For each pion exiting the target surface, the contribution of each beam bin is recorded. A two dimensional histogram is then filled with, on the horizontal axis, the different (r, ϕ) bins and on the vertical axis the different (p, θ, z) bins. 20 bins are considered in the radial direction, 8 bins divide the 360 degrees of the azimuthal angle. This gives a total of 160 bins for the horizontal axis, while the usual analysis binning introduced in chapter 4 is used for the vertical axis.

Figure 5.12 shows this histogram as computed with the NA61/SHINE simulation for positively charged pions.

The histogram is normalized such that the sum of each row is one. Hence, the content of each bin (i, j) represent the fractional contribution of each beam bin j to each (p, θ, z) bin i of

the pion spectra. It should be noted that there is no normalization for the beam bin area.

Using the 4 million protons on target simulation for NA61/SHINE and T2K and using the matrix element of fig. 5.12 as the coefficients c_{ij} , the d_j elements as presented in fig. 5.11, it is strait forward to compute the ratios of eq. (5.13).

The estimation of the uncertainties on these ratios has to be computed as the propagation of the uncertainties on the number of entries in the different (r, ϕ) and (p, θ, z) bins. It is expected that the distributions of the number of events in the (r, ϕ) bins follow a Poisson distribution as these bins are filled by randomly drawing event on given histograms produced from the data. The drawings are completely independent with each others and hence the uncertainties on the number of entries on each (r, ϕ) bins can be estimated as the square root of this number of entries. The statistical uncertainties on the number of entries in each of the (p, θ, z) bins are also expected to follow a Poisson distribution. But it might actually depend on the underlying computations included in the FLUKA model. In order to proof that the number of events in each (p, θ, z) bin does follow a Poisson distribution, we build 100 samples of 4 millions protons on target. In order not to have to run 100 times a FLUKA simulation of 4 millions protons on target (which would be quite expensive in computer resources), a bootstrap method is used [114].

For one sample of 4 million protons on target (the NA61/SHINE sample is chosen here), we produce 100 bootstrap samples by randomly drawing events on the initial sample. This leads to 100 samples of 4 million protons on target for the NA61/SHINE beam configuration. For each (p, θ, z) bin we then have 100 entries given by the bootstrap samples with which we can build a distribution histogram. These histograms can then be fitted with a Poisson distribution.. As can be seen on fig. 5.13, where three examples for three different (p, θ, z) bins are displayed, the distribution does follow a Poisson distribution. Hence, the uncertainties on the number of entries on each (p, θ, z) bin can be estimated as the square root of the number of entry in each bin.

The final results of the ratios of eq. (5.13) and their statistical uncertainties can be plotted in the same format as used to present the pion multiplicities (i.e. in the different longitudinal bins Z , for each polar angle bins θ as a function of momentum p).

Figure 5.14 to fig. 5.19 present these results. By fitting the ratios in each (p, θ, z) bin with a strait line, it turns out that no significant deviations (within statistical uncertainties) are present. In the region of lower Monte-Carlo statistics (typically for the upstream part of the target and at small polar angle intervals) the fluctuations as well as the uncertainties are larger as expected.

The consistency of these results allow to prove that, starting with given pion multiplicities at the surface of the target for a specific beam profile, and given a second beam distribution, it is possible to infer the multiplicities of pions at the surface of the target for this second beam configuration. Hence, by applying the re-weighted method to the measured NA61/SHINE measurements of the T2K replica target, it is possible to directly implement these measurements in the T2K flux prediction for the specific T2K beam profile.

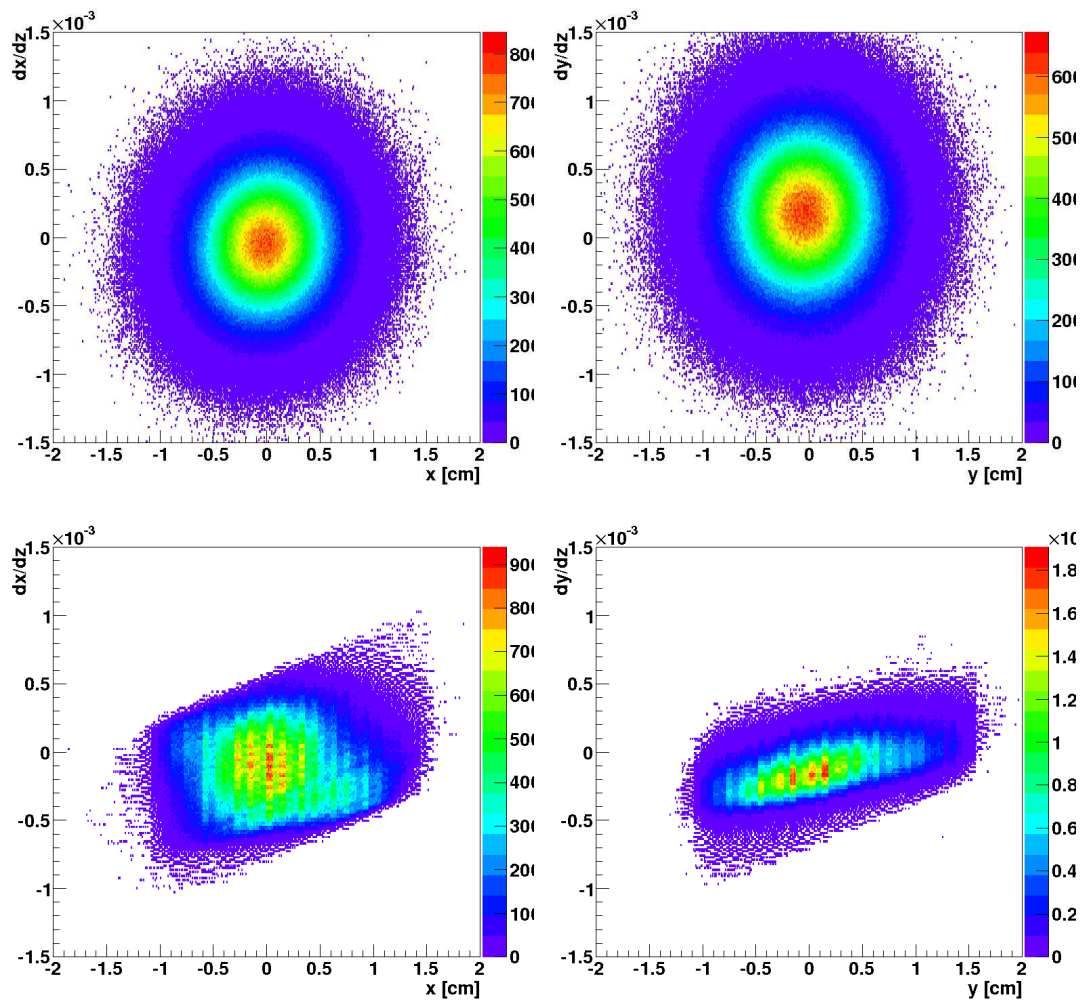


Figure 5.8: Proton beam divergence versus momentum for T2K (top) and NA61/SHINE (bottom) for the x coordinate (left) and y coordinate (right) at the upstream face of the target

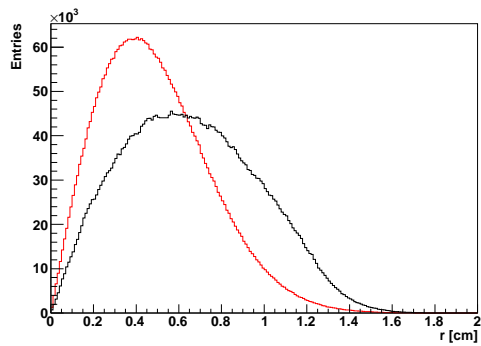


Figure 5.9: Radial distributions for the NA61/SHINE (black) and T2K (red) beam profiles at the upstream face of the target

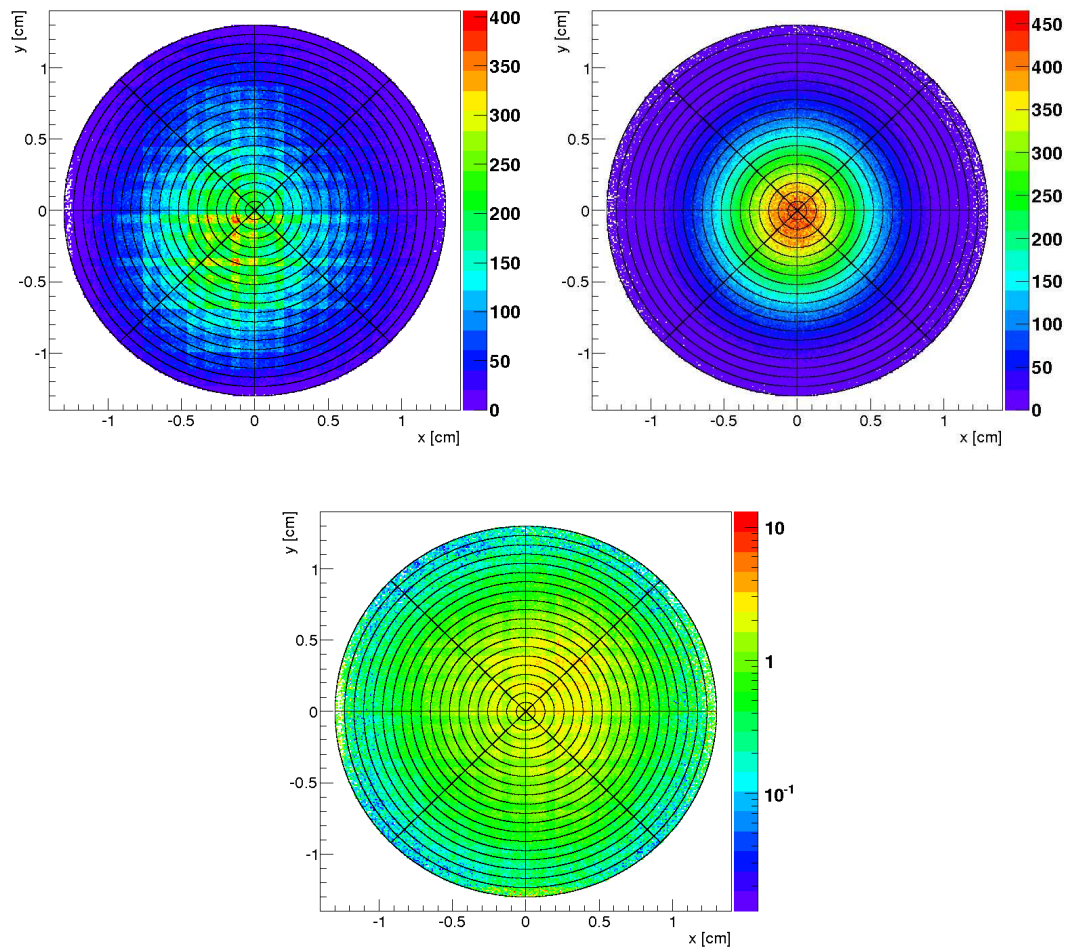


Figure 5.10: (x, y) distributions of the proton beams at the surface of the target for NA61/SHINE (top left) and for T2K (top right). The ratio of these two distributions is shown in the bottom plot. The (r, ϕ) binning is overlaid on top of the color histograms

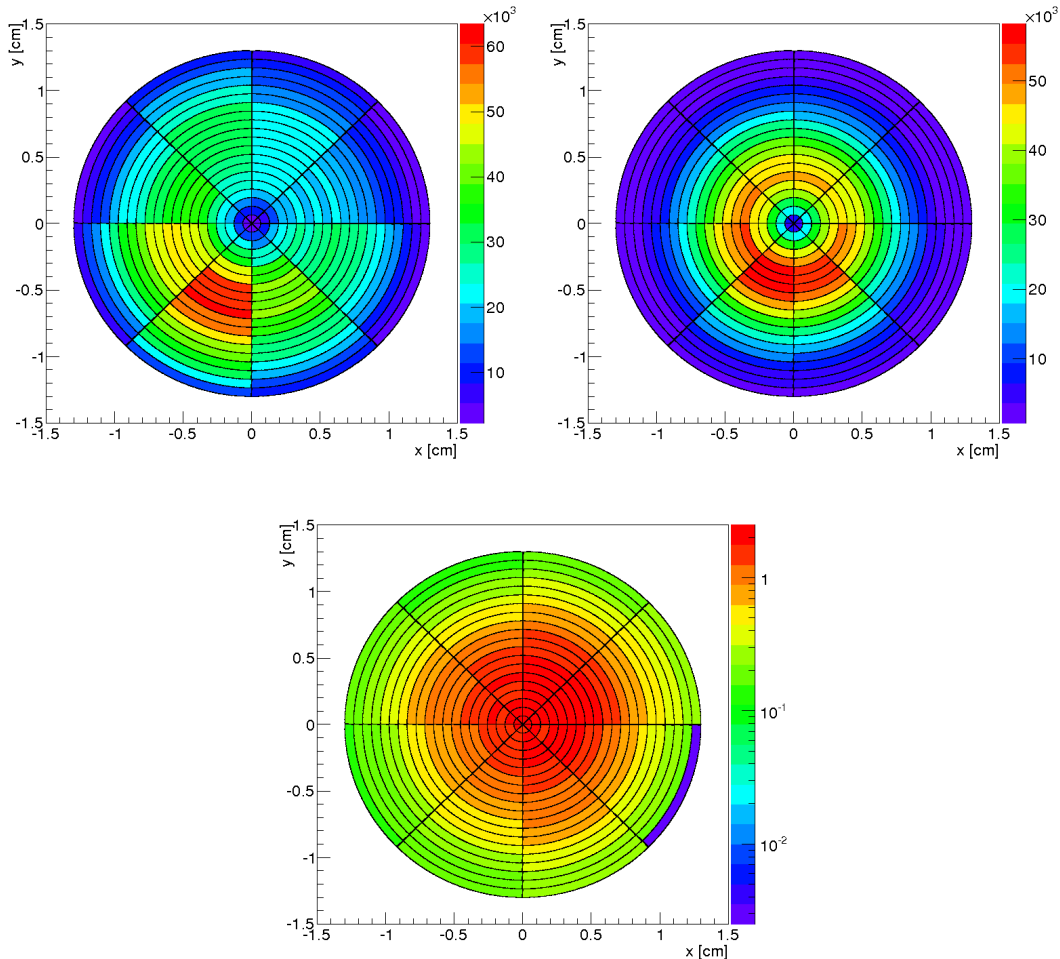


Figure 5.11: (r, ϕ) distributions of the proton beams at the surface of the target for NA61/SHINE (top left) and for T2K (top right). The ratio of these two distributions is shown in the bottom plot. The (r, ϕ) binning is overlaid on top of the color histograms

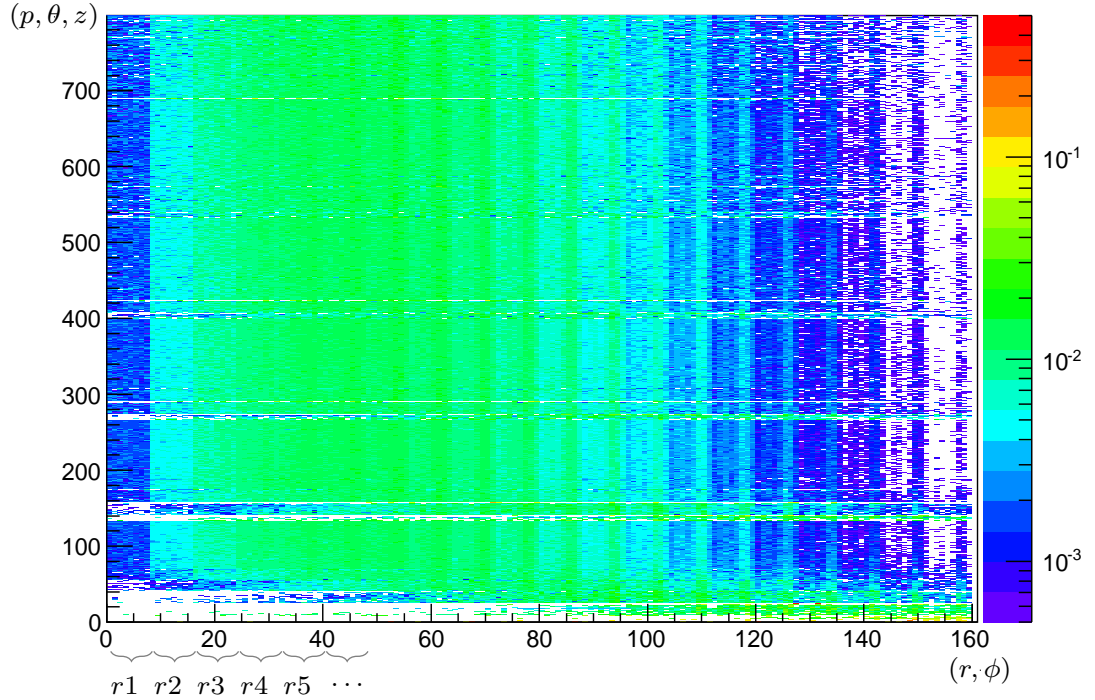


Figure 5.12: Two dimensional distribution showing the contribution of each beam bin to the different (p, θ, z) bins for positively charged pions using the NA61/SHINE simulation. The normalization is such that the sum over each row is one.

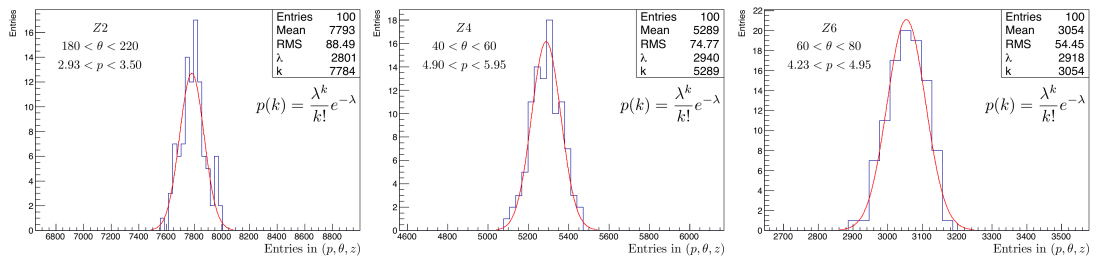


Figure 5.13: Distributions of the number of entries in three different (p, θ, z) bins generated by using the 100 bootstrap samples. The left plot is for the second longitudinal bin Z2, polar interval between 180 and 220 mrad and momentum between 2.93 and 3.50 GeV/c. The middle plot is for the fourth longitudinal bin Z4, polar interval between 40 and 60 mrad and momentum between 4.90 and 5.95 GeV/c. The right plot is for the downstream face of the target (i.e. Z6 bin), polar interval between 60 and 80 mrad and momentum between 4.23 and 4.95 GeV/c.

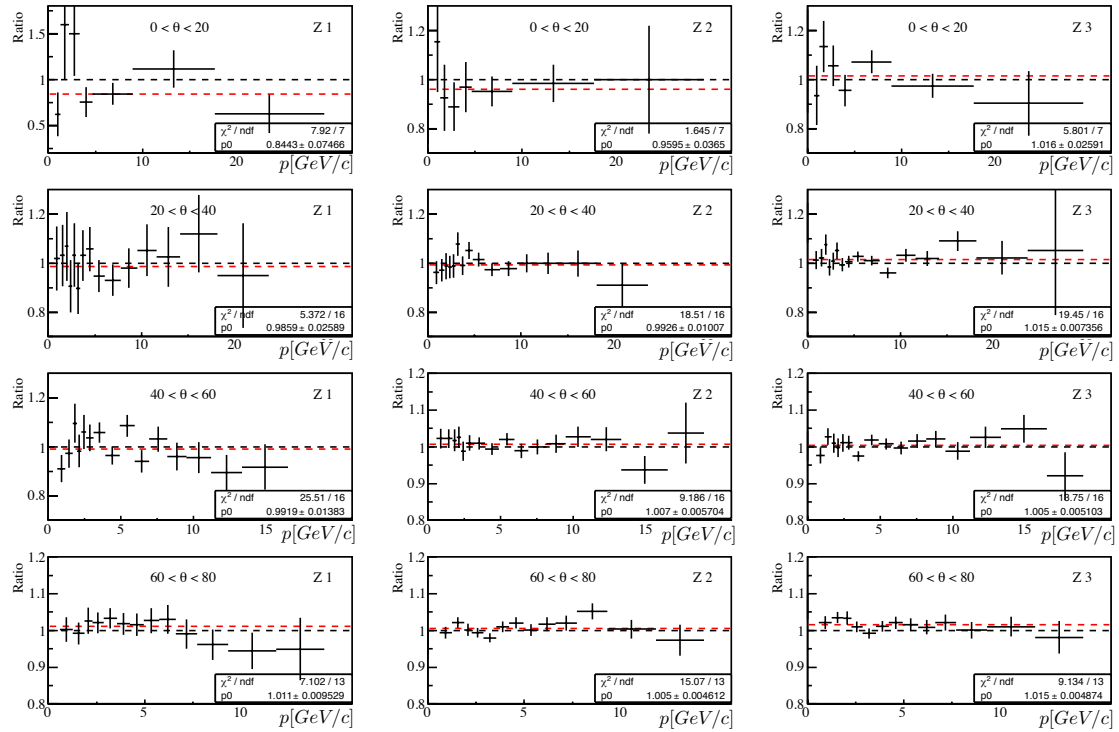


Figure 5.14: Ratio of re-weighted NA61/SHINE π^+ spectra with respect to the T2K beam profile over the T2K simulated π^+ spectra for the three upstream longitudinal bins and in the polar angles between 0 and 80 mrad plotted as a function of momentum

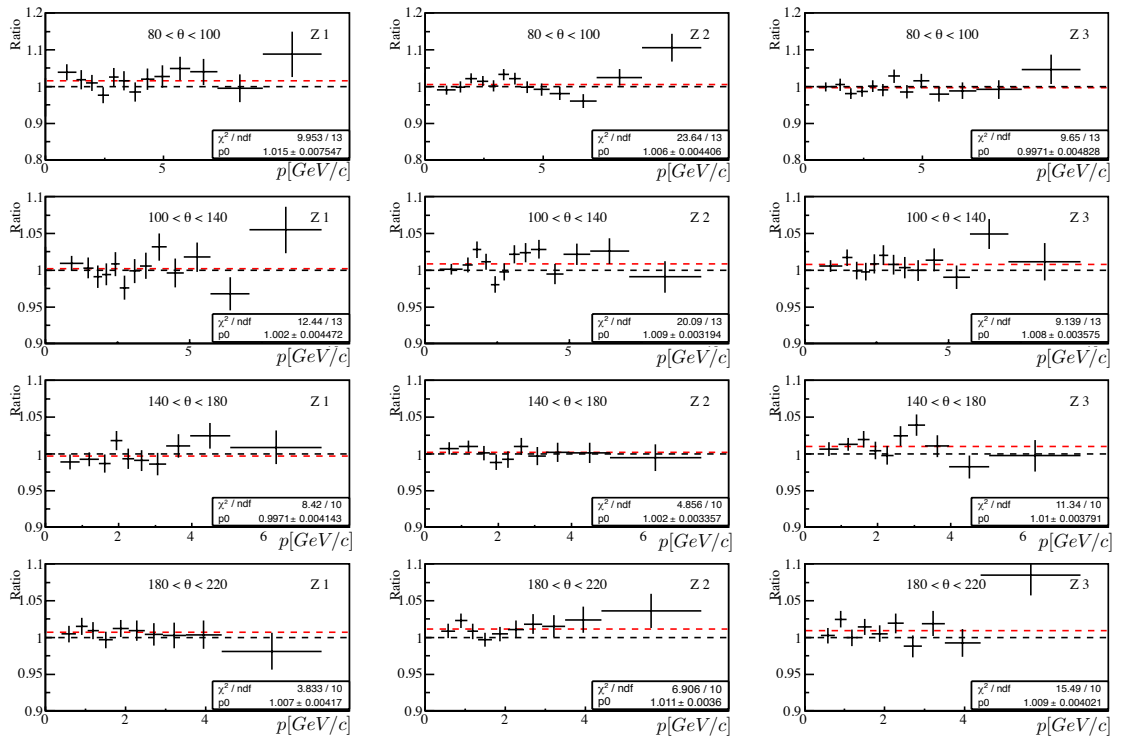


Figure 5.15: Ratio of re-weighted NA61/SHINE π^+ spectra with respect to the T2K beam profile over the T2K simulated π^+ spectra for the three upstream longitudinal bins and in the polar angles between 80 and 220 mrad plotted as a function of momentum

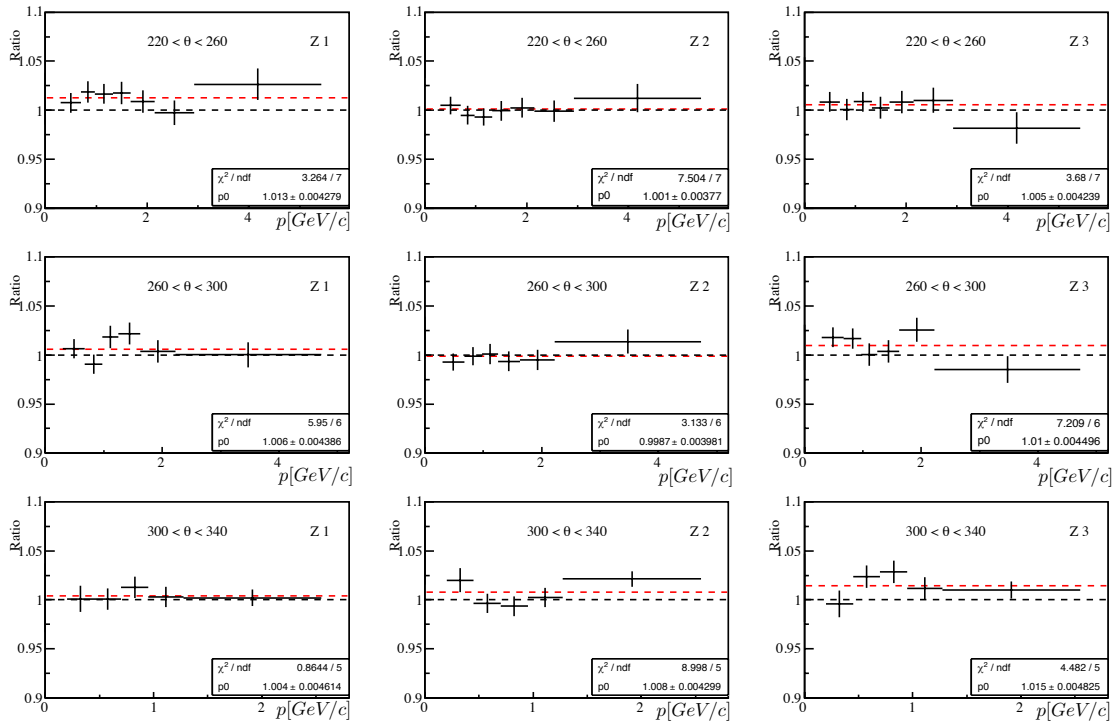


Figure 5.16: Ratio of re-weighted NA61/SHINE π^+ spectra with respect to the T2K beam profile over the T2K simulated π^+ spectra for the three upstream longitudinal bins and in the polar angles between 220 and 340 mrad plotted as a function of momentum

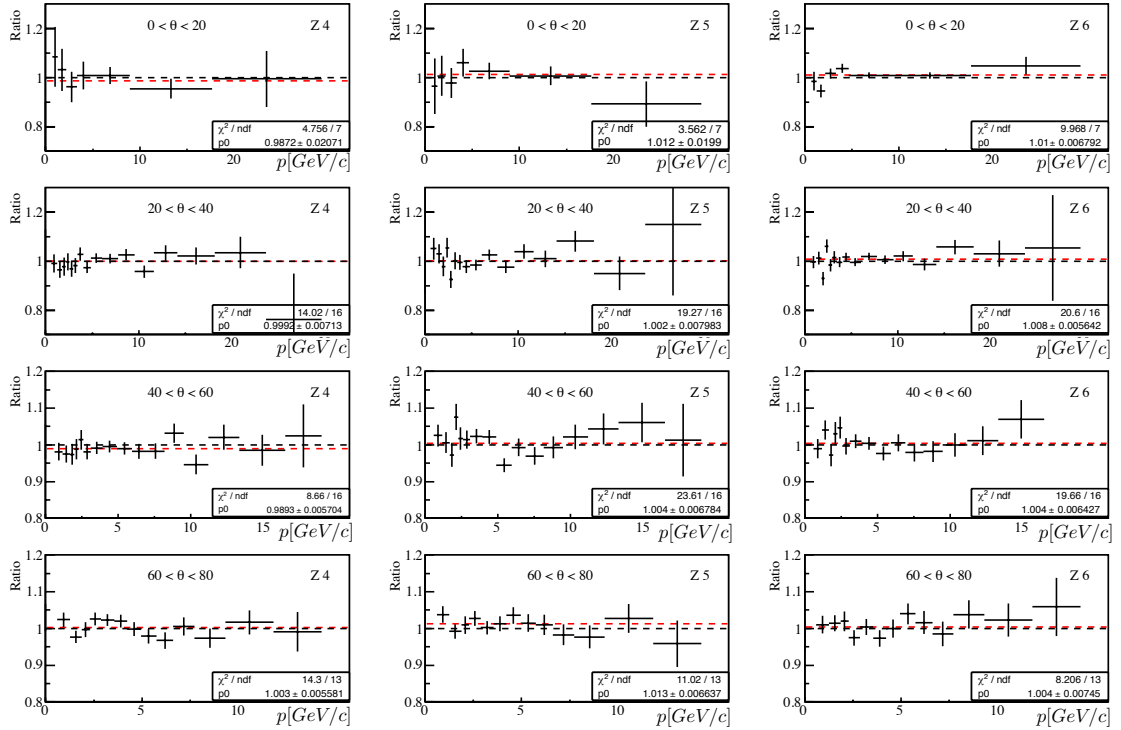


Figure 5.17: Ratio of re-weighted NA61/SHINE π^+ spectra with respect to the T2K beam profile over the T2K simulated π^+ spectra for the three downstream longitudinal bins and in the polar angles between 0 and 80 mrad plotted as a function of momentum

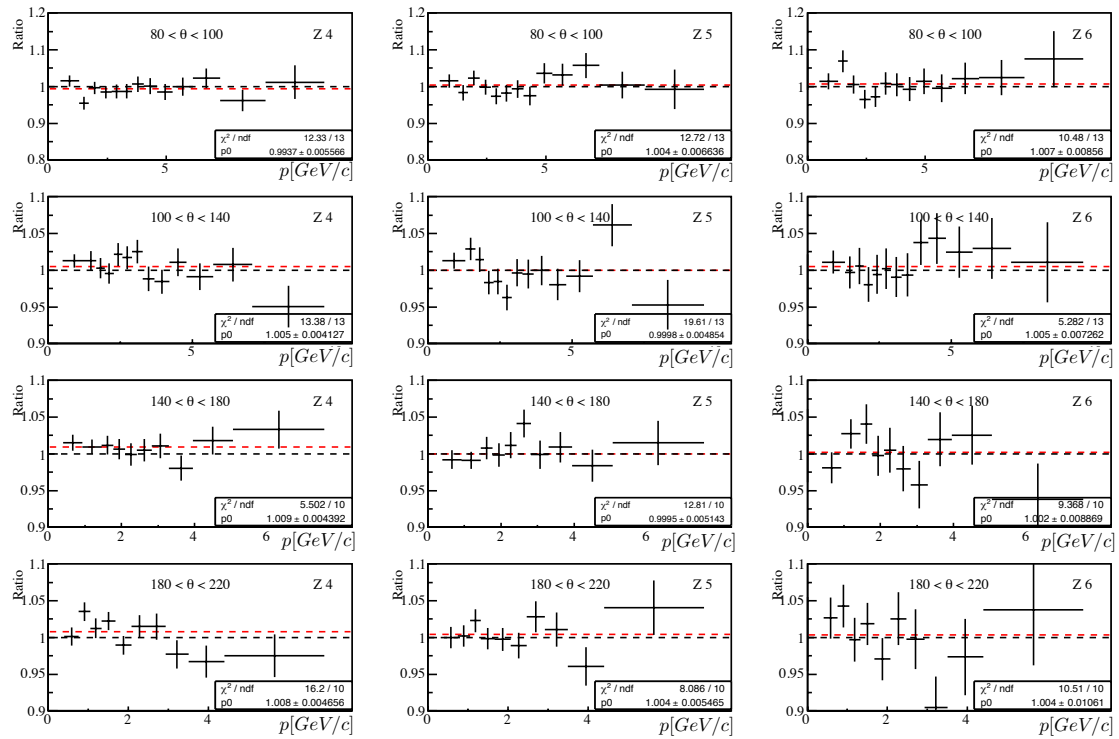


Figure 5.18: Ratio of re-weighted NA61/SHINE π^+ spectra with respect to the T2K beam profile over the T2K simulated π^+ spectra for the three downstream longitudinal bins and in the polar angles between 80 and 220 mrad plotted as a function of momentum

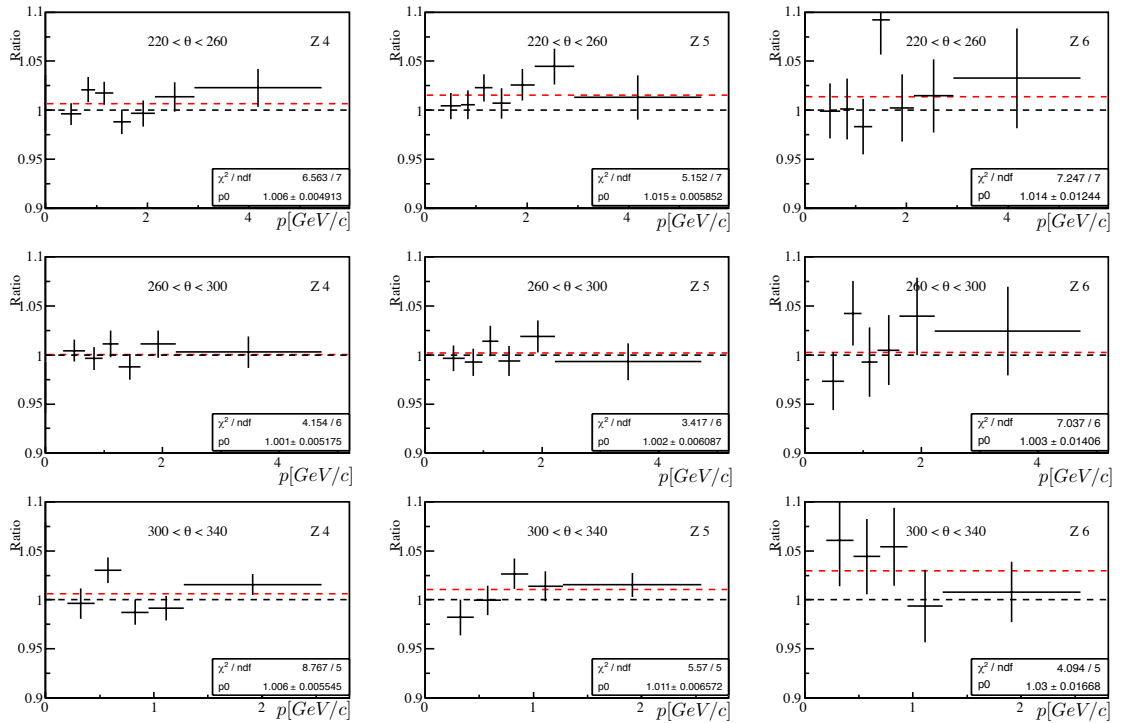


Figure 5.19: Ratio of re-weighted NA61/SHINE π^+ spectra with respect to the T2K beam profile over the T2K simulated π^+ spectra for the three downstream longitudinal bins and in the polar angles between 220 and 340 mrad plotted as a function of momentum

Chapter 6

Conclusion

Three goals have been reached through the work of this thesis. They can be listed as:

1. the extraction of π^+ and π^- spectra at the surface of the T2K replica target for the 2009 dataset recorded in NA61/SHINE
2. the comparisons of these spectra with the FLUKA model and the description of the discrepancies between the data and the FLUKA model by using the NA61/SHINE thin target results and a re-weighting algorithm developed by the T2K beam group
3. the implementation of the T2K replica target results and the propagation of their uncertainties within the T2K neutrino beam simulation to constrain the T2K neutrino flux predictions

To extract π^+ and π^- spectra at the surface of the target, different steps have been done. The proper understanding of the NA61/SHINE beam has allowed to select the beam protons of interest and determine the parameters of the NA61/SHINE beam (section 4.1). The careful study of the reconstructed events in the spectrometer has been mandatory to compute the geometrical acceptance of the experimental setup (section 4.4.3), to determine the relevant cuts for the analysis (section 4.4.1) and to define the analysis binning (section 4.4.2). The precise determination of the target position (section 4.3.2) as well as an accurate knowledge of the alignment of the beam with respect to the spectrometer (section 4.3.1) has showed to be very important to reduce systematic uncertainties on the final spectra. The particle identification has been performed following the combined ToF-dE/dx method (section 4.4.4). Dedicated Monte-Carlo simulations, using FLUKA as hadron generator for the interactions of the incident beam protons with the T2K replica target, have been produced in order to match the NA61/SHINE beam profile and the target position of the 2009 dataset. Correction factors based on these Monte-Carlo simulations have been computed and applied to the raw pion spectra (section 4.4.5). Finally, systematic uncertainties on the pion spectra have been estimated. They are at the level of 4% for the central part of the target and go up to 14% for the first and last longitudinal bins (section 4.5).

In order to better constrain the neutrino flux predictions based on the FLUKA hadron production model in T2K, detailed comparisons of the T2K replica target results with the FLUKA predictions are mandatory. The modification of the re-weighting code developed by the T2K beam group has allowed to find a strategy to compare the NA61/SHINE thin target results with the T2K replica target results (section 4.7). It also allowed to have a deeper understanding of the discrepancies between the predicted pion spectra as given by FLUKA and the T2K replica target

results from NA61/SHINE. In particular, it has showed the important effect of re-weighting the FLUKA production cross-section at each interactions inside the target on the predicted pion spectra at the surface of the target. And hence, it has stressed the importance of a better understanding of the different components of the cross-sections and the need for consistent definitions of these components through carefully determining which reactions are included into, either the elastic, the quasi-elastic or the inelastic components of the cross-sections.

The implementation of the T2K replica target measurements into the T2K neutrino beam prediction and the propagation of the related uncertainties has been the ultimate goal of this thesis. The already existing framework of the T2K neutrino beam predictions has been the basis of this implementation. A first study to determine which part of the predicted neutrino flux could be re-weighted using the T2K replica target results was mandatory to estimate the potential effect of constraining the T2K neutrino flux prediction with the T2K replica target measurements from NA61/SHINE. Specific modifications have been carried out to the already existing framework in order to be able to apply to weighting factors to the relevant pions at the surface of the target (section 5.1). A new framework for the propagation of the uncertainties on the T2K replica target measurements to the final neutrino flux predictions has been developed (section 5.2). It allowed to show the strong potential of reducing the uncertainties on the final neutrino flux and confirmed the importance of the dedicated T2K replica target measurements for the future improvements on the accuracy of the predicted neutrino flux predictions in T2K. The uncertainties on the 90% of the muon neutrino flux at SK begin generated by the pions exiting the target surface could be lower down to 4% by using the T2K replica target measurements. Finally, a short study has showed the importance of taking into account the characteristics of the proton beam profiles for the determination of the produced pions at the surface of the target (section 5.3). In particular, it was showed that a re-weighing method could be used to translate the pion spectra at the surface of the target from one specific proton beam profile to another known profile. And in this sense, proving that the T2K replica target measurements with the NA61/SHINE proton beam profile can be used to constrain the pion production off the target in case of different proton beam profiles.

Future accelerator based long base line neutrino experiments will open the way to high precision measurements of the neutrino mixing parameters. In order to reach their goals, these experiments plan to have high proton beam power. They also count on reducing the systematic uncertainties estimated in the present long base line experiments. As showed in chapter 2, the error on the neutrino flux predictions is one of the components that can be further reduced by using dedicated hadron production measurements. The NA61/SHINE experiment has proved its success in taking such measurements.

As presented in this thesis, the analysis of the 2009 data set is dominated by statistical uncertainties. The 2010 data set, with its 10 million events recorded, will allow to drastically reduce this uncertainty and kaon spectra will surely be available, allowing to also constrain the neutrino predictions at higher energies. The phase-space of interest for T2K will be better covered as the NA61/SHINE analysis binning could eventually be increased, specially for large polar angles. For small angles, the data taken with higher magnetic field settings, will allow to better cover the very forward going tracks exiting the downstream face of the target.

The systematic uncertainties for the T2K replica target analysis are well controlled and understood (most of them are identical to the thin target analysis and hence have been extensively studied for different data sets). The larger component coming from the backward extrapolation could still be reduced with the 2010 data set as the high recorded statistics should allow to get better precision on the BPD-TPC alignment.

If new measurements with a replica target in NA61/SHINE were to be taken, it would be interesting to study the optimal location to place the target. Bringing it closer to the VTPC1

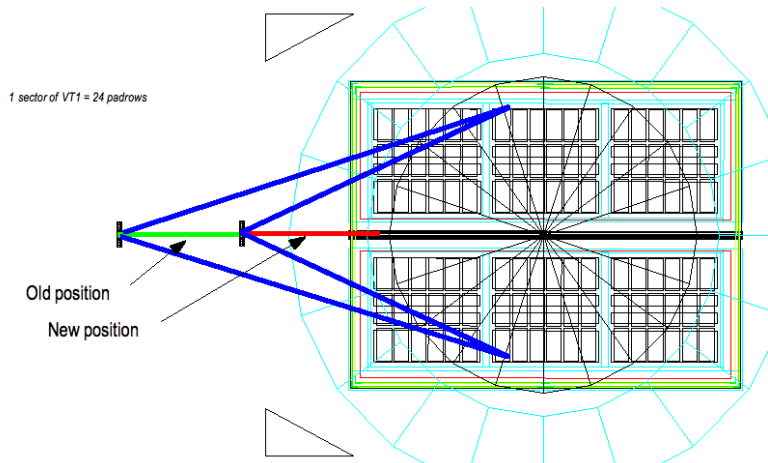


Figure 6.1: Example of a new proposed position for a replica target closer to the central part of VTPC1.

would reduce the long backward extrapolation and increase the precision of the measured variables at the surface of the target. Ideally, the replica target could be position closer to the central part of VTPC1. Figure 6.1 shows an example for a new proposed target position [115]. In this case, a much shorter backward extrapolation would be needed. The contribution of the feed-down corrections would be smaller and the particle identification would be better. Nevertheless, a careful study of the acceptance would be mandatory to be sure that the phase-space of interest would still be well covered.

The successful data taking of hadron production by NA61/SHINE for T2K has encouraged other long baseline neutrino projects to consider using the NA61/SHINE set-up for their own studies. We can cite the LBNE (lately re-named DUNE) experiment which has already some members being part of NA61/SHINE to set up a new specific hadron production campaign. First data for $p - C$ interactions at 60 GeV/c should be taken in fall 2015. The full proposed campaign plans to scan different reactions at different energies. By using graphite, aluminum and beryllium targets, different re-interactions along the beam line will be better constrained. The scaling between different target materials can also be better studied. Using different incident beam momenta (between 30 and 120 GeV/c) allows to more precisely re-weight primary and secondary interactions as well as to cross-check the energy scaling described in chapter 2. When using higher momentum beam particles, the very forward region of the NA61/SHINE spectrometer becomes more important. Hence a proposition to build new so-called forward TPCs has been submitted. One or two TPCs could be mounted along the beam line. In conjunction with the GTPC, they would allow to reconstruct very forward going tracks and hence better cover the phase-space of interest for the LBNE (DUNE) experiment.

The LBNO proposal as well as the Hyper-Kamiokande experiment mentioned also in their letter of intent the importance of dedicated hadron production experiments to reach their physics goal and the specific role that NA61/SHINE will have to play.

Appendix A

Pion correction factors

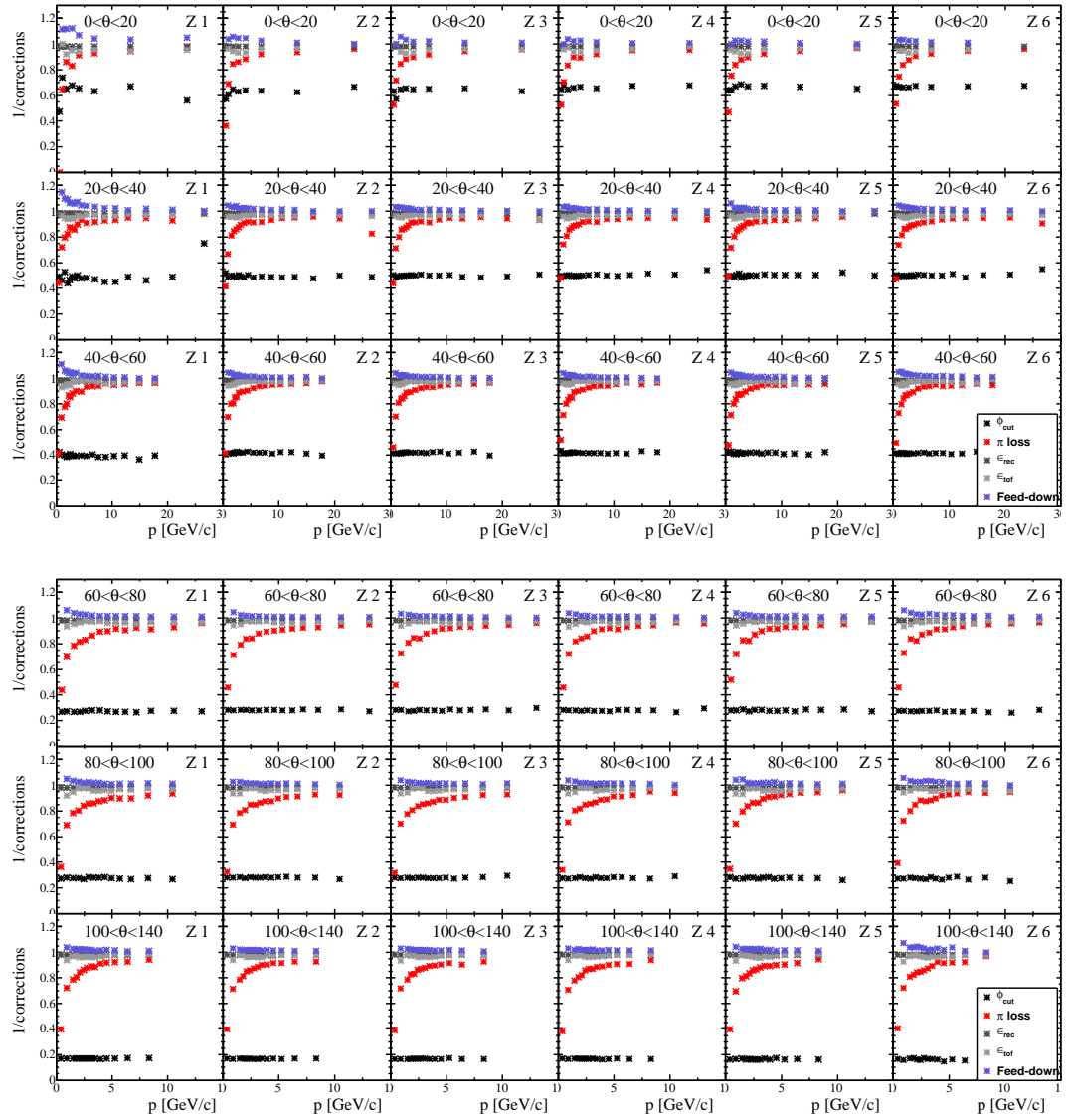


Figure A.1: Corrections factors for positively charged pions, in the polar angle range from 0 to 140 mrad, and for the six longitudinal bins as a function of momentum.

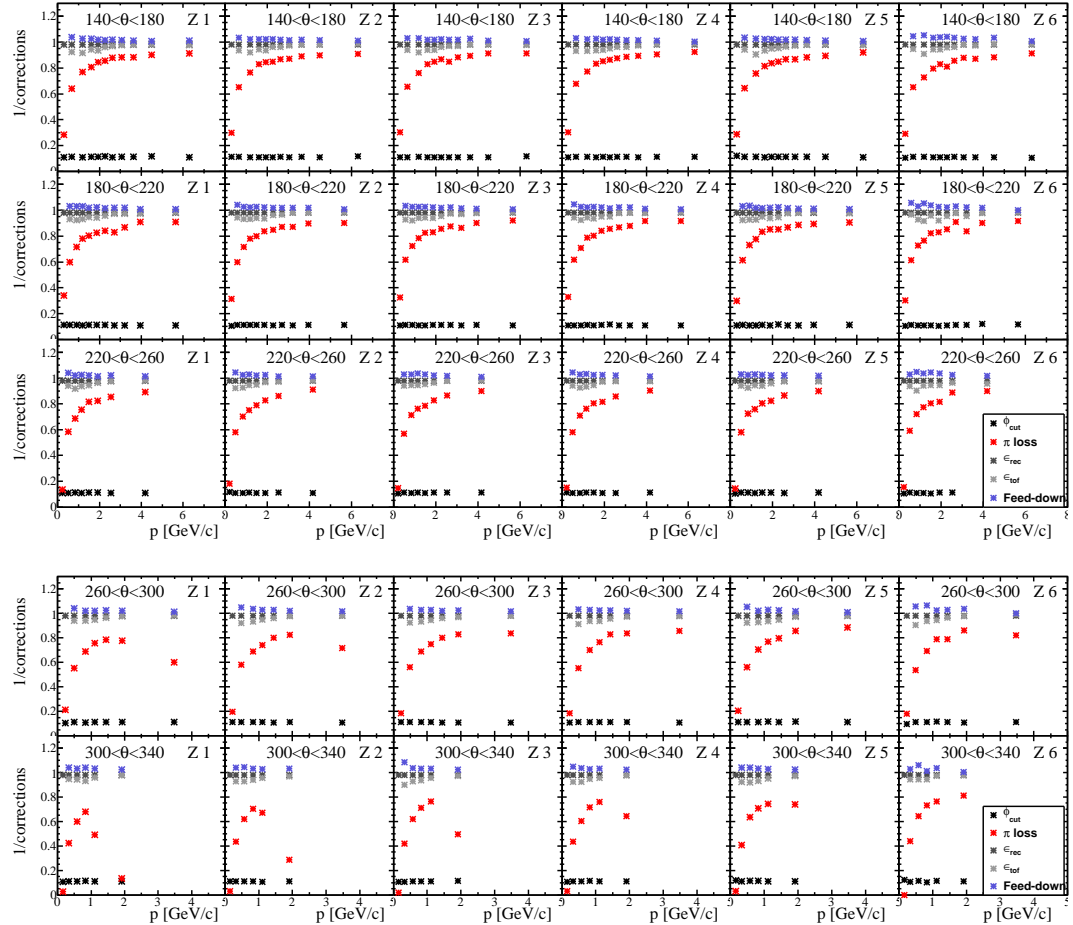


Figure A.2: Corrections factors for positively charged pions, in the polar angle range from 140 to 340 mrad, and for the six longitudinal bins as a function of momentum.

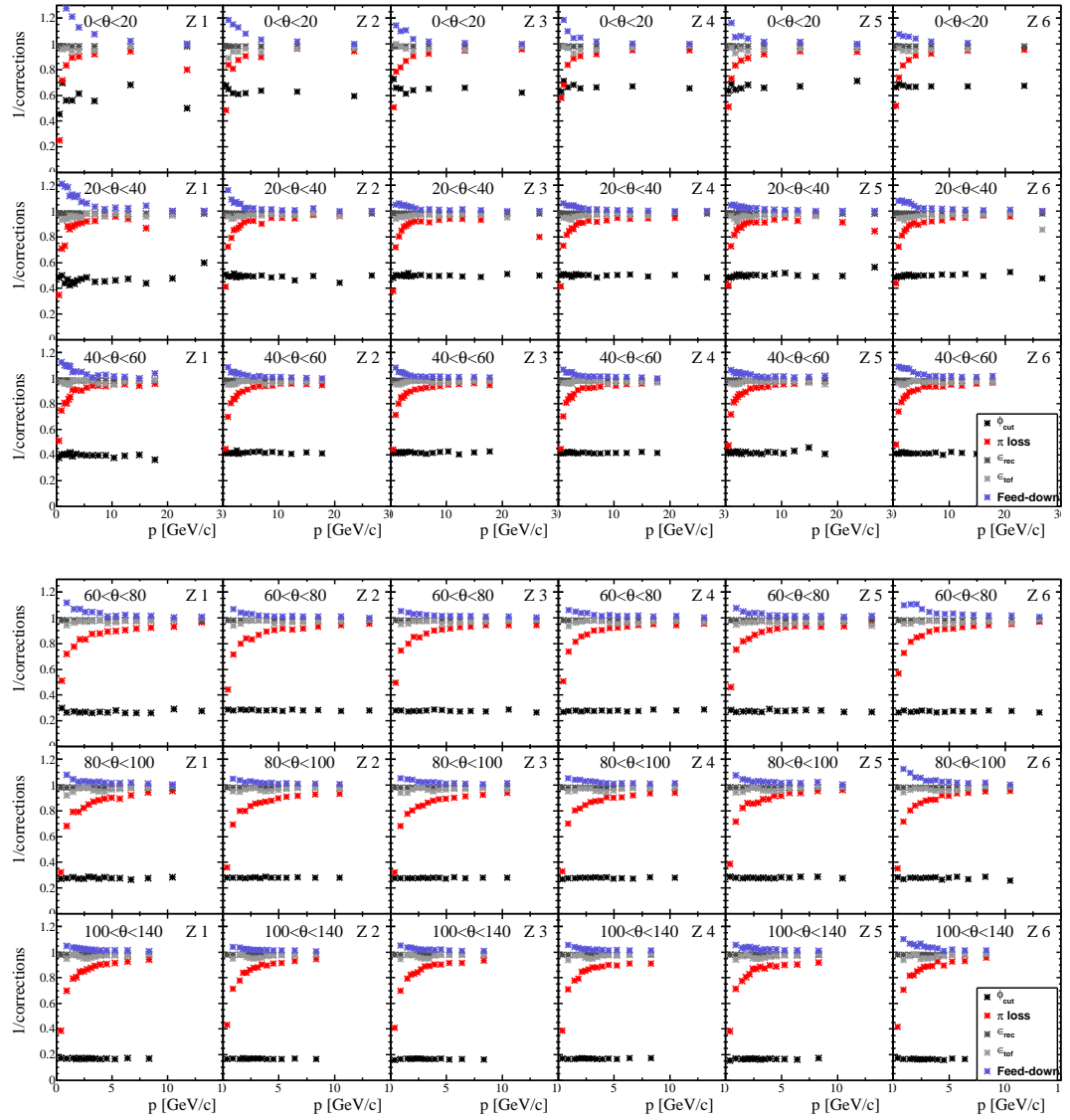


Figure A.3: Corrections factors for negatively charged pions, in the polar angle range from 0 to 140 mrad, and for the six longitudinal bins as a function of momentum.

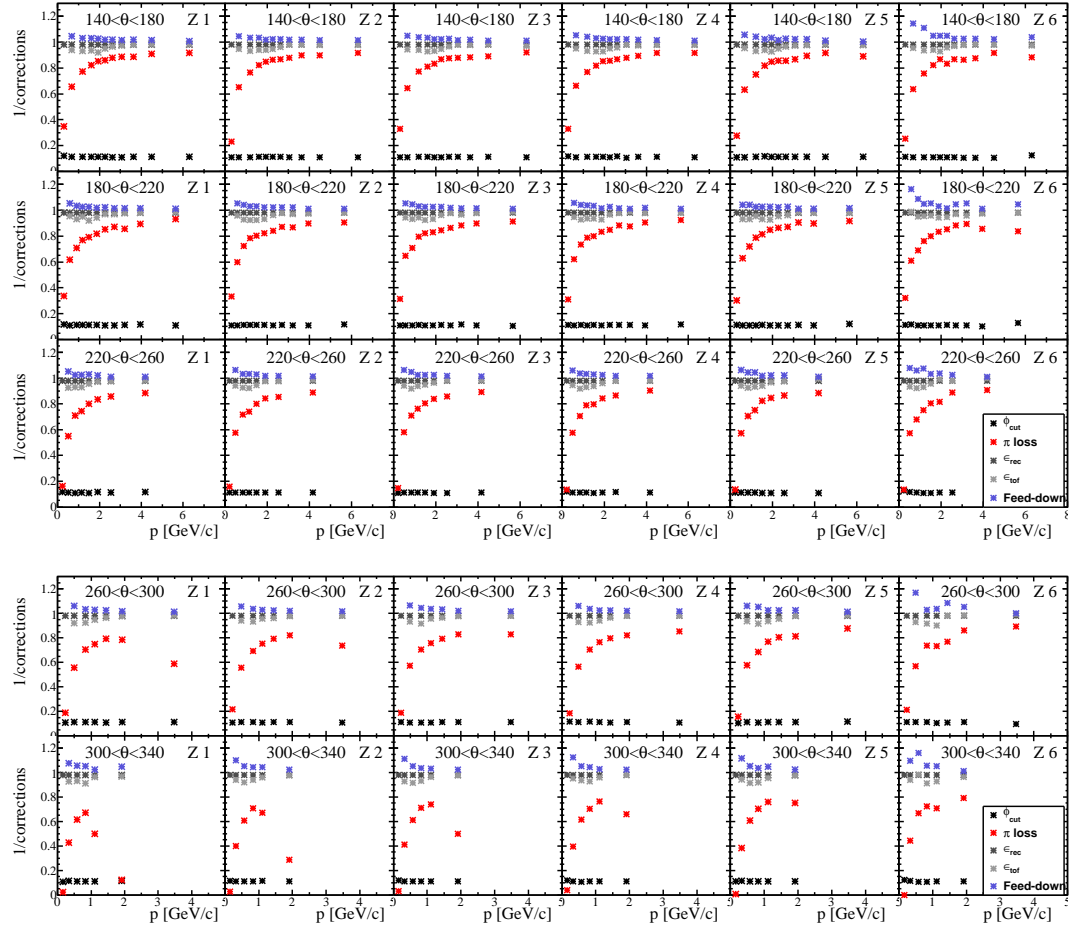


Figure A.4: Corrections factors for negatively charged pions, in the polar angle range from 140 to 340 mrad, and for the six longitudinal bins as a function of momentum.

Appendix B

T2K replica target weights

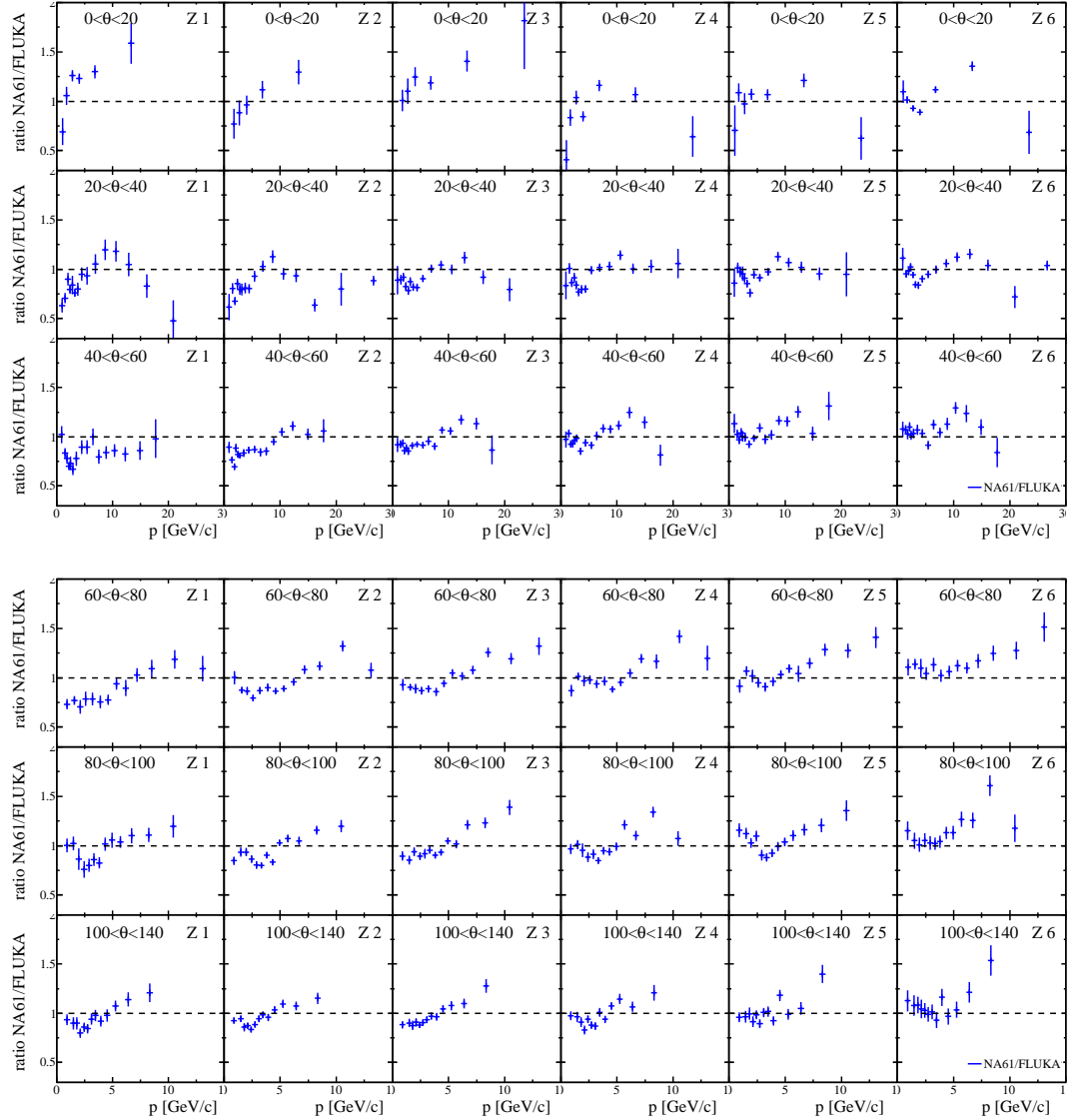


Figure B.1: T2K replica target weights for positively charged pions computed as the ratio of the NA61/SHINE measurements over the FLUKA 2011 predictions, in the polar angle range from 0 to 140 mrad, and for the six longitudinal bins as a function of momentum. The normalization is done on the number of protons on target.

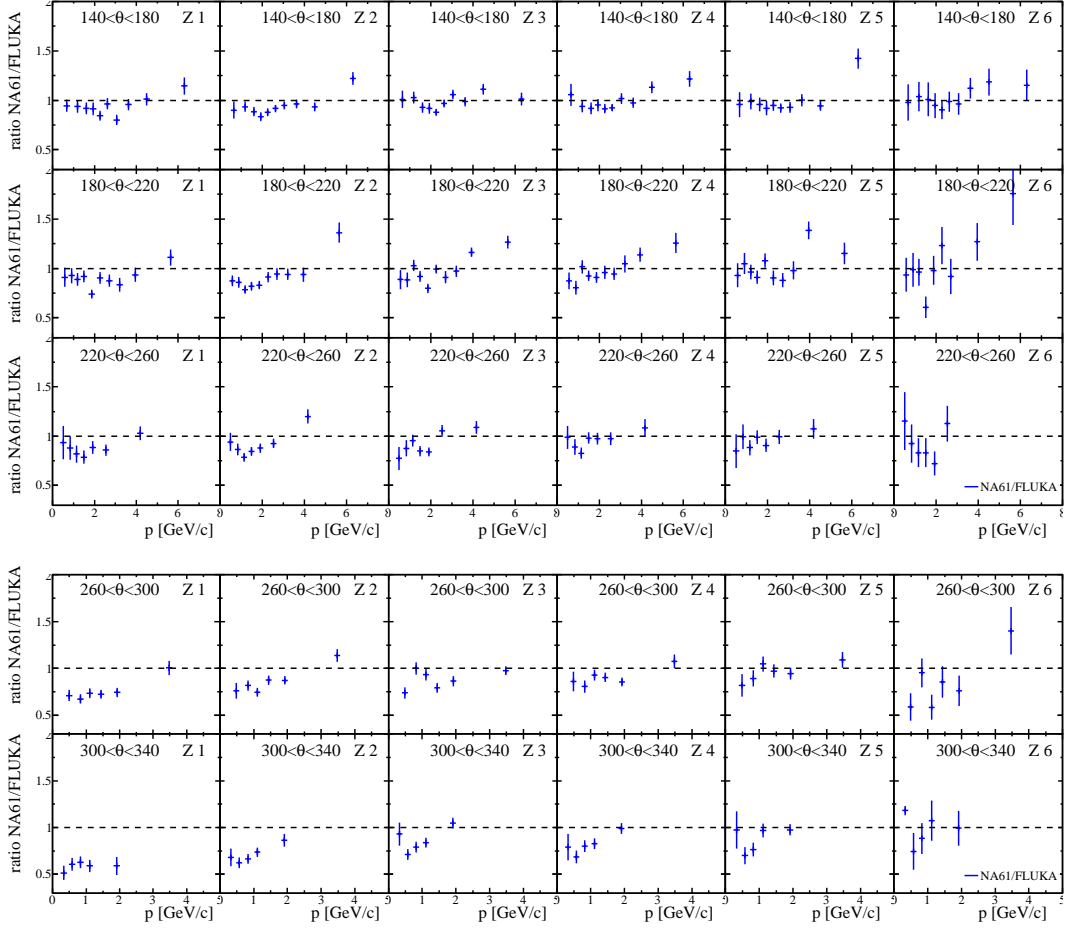


Figure B.2: T2K replica target weights for positively charged pions computed as the ratio of the NA61/SHINE measurements over the FLUKA 2011 predictions, in the polar angle range from 140 to 340 mrad, and for the six longitudinal bins as a function of momentum. The normalization is done on the number of protons on target.

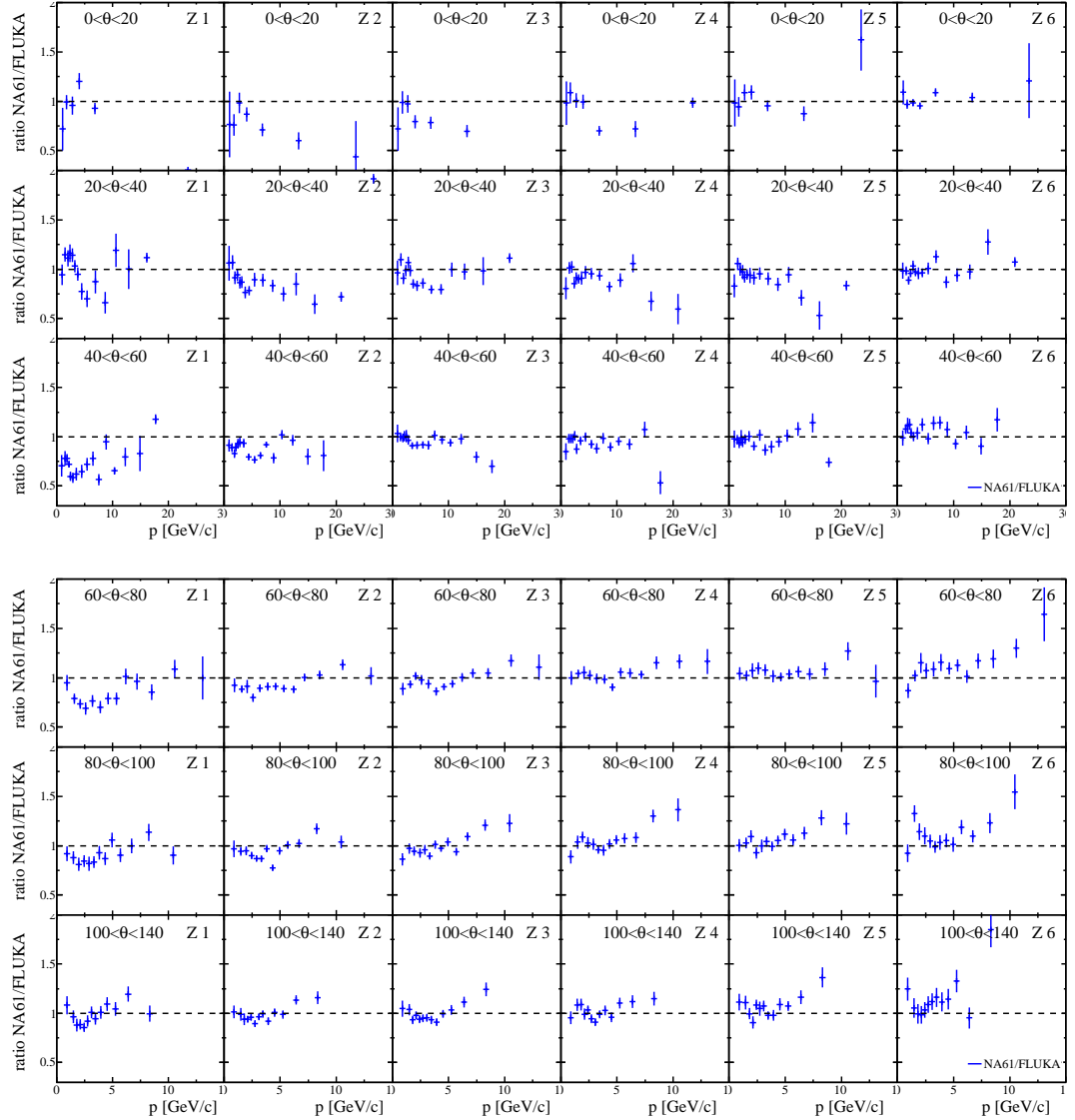


Figure B.3: T2K replica target weights for negatively charged pions computed as the ratio of the NA61/SHINE measurements over the FLUKA 2011 predictions, in the polar angle range from 0 to 140 mrad, and for the six longitudinal bins as a function of momentum. The normalization is done on the number of protons on target.

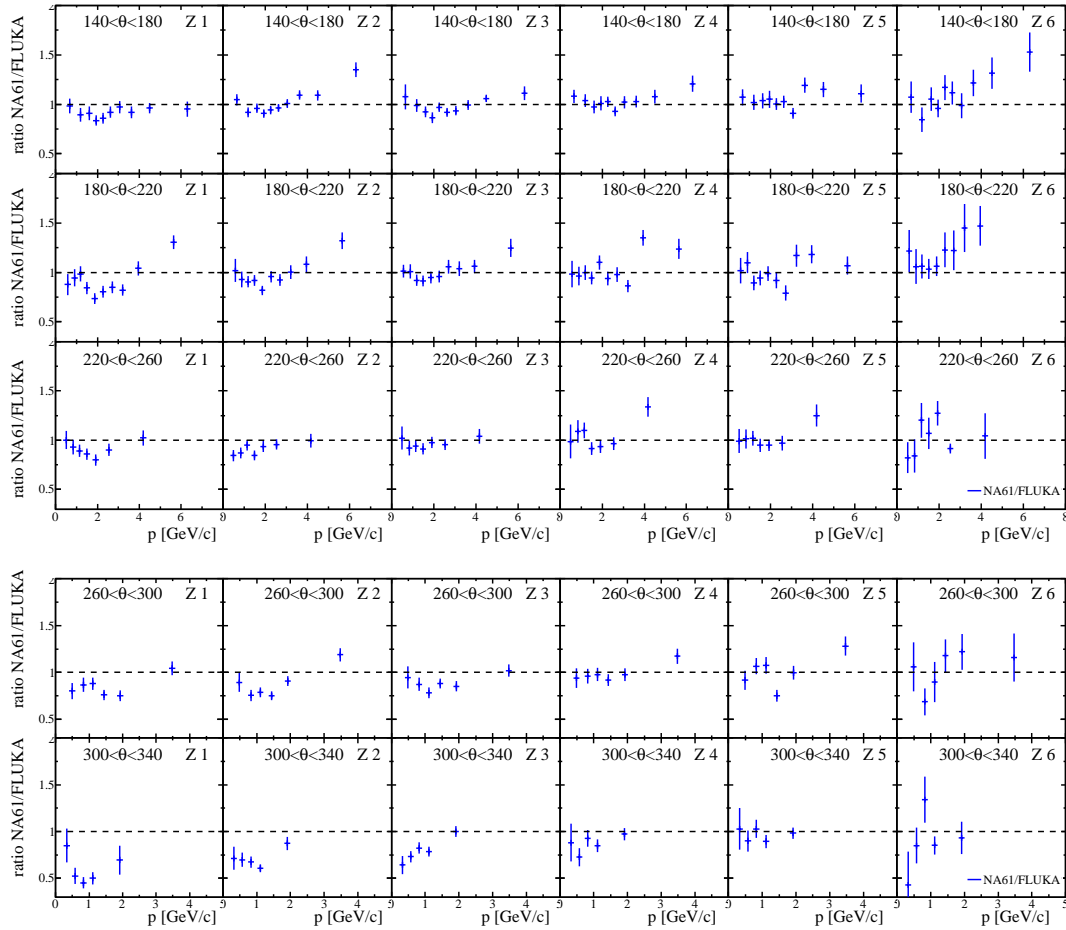


Figure B.4: T2K replica target weights for negatively charged pions computed as the ratio of the NA61/SHINE measurements over the FLUKA 2011 predictions, in the polar angle range from 140 to 340 mrad, and for the six longitudinal bins as a function of momentum. The normalization is done on the number of protons on target.

Appendix C

Comparisons of pions spectra at the surface of the target for different beam profiles

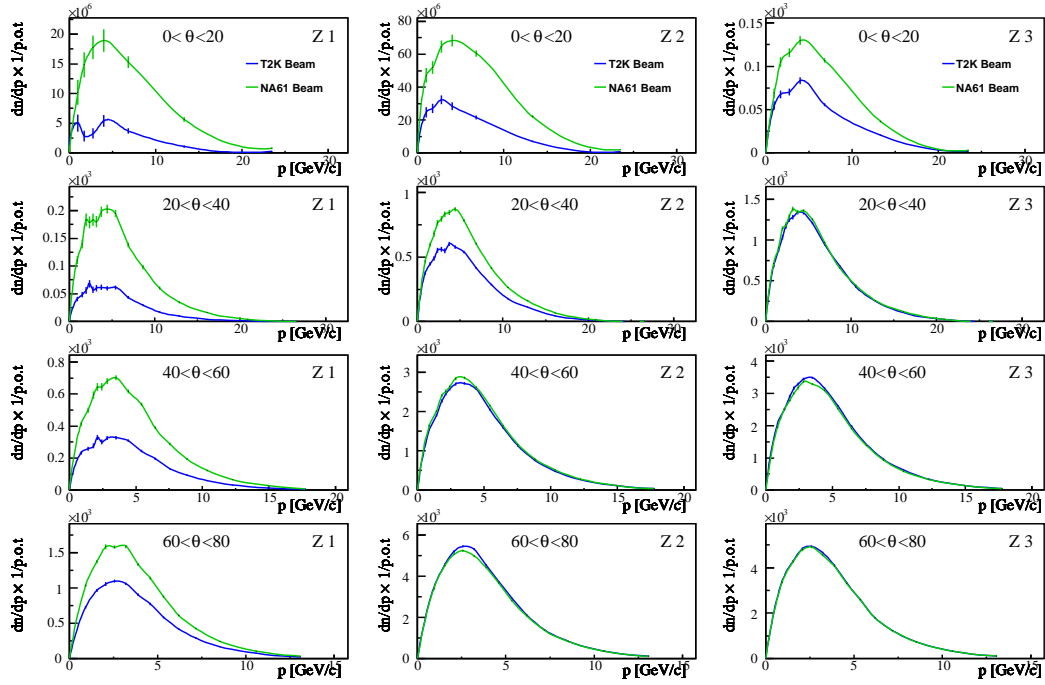


Figure C.1: Positively charged pion spectra at the surface of the target produced with FLUKA for the NA61/SHINE beam profile (green) and the T2K beam profile (blue) for the three upstream longitudinal bins and in the polar angles between 0 and 80 mrad plotted as a function of momentum. The spectra are normalized to momentum bin size and number of protons on target

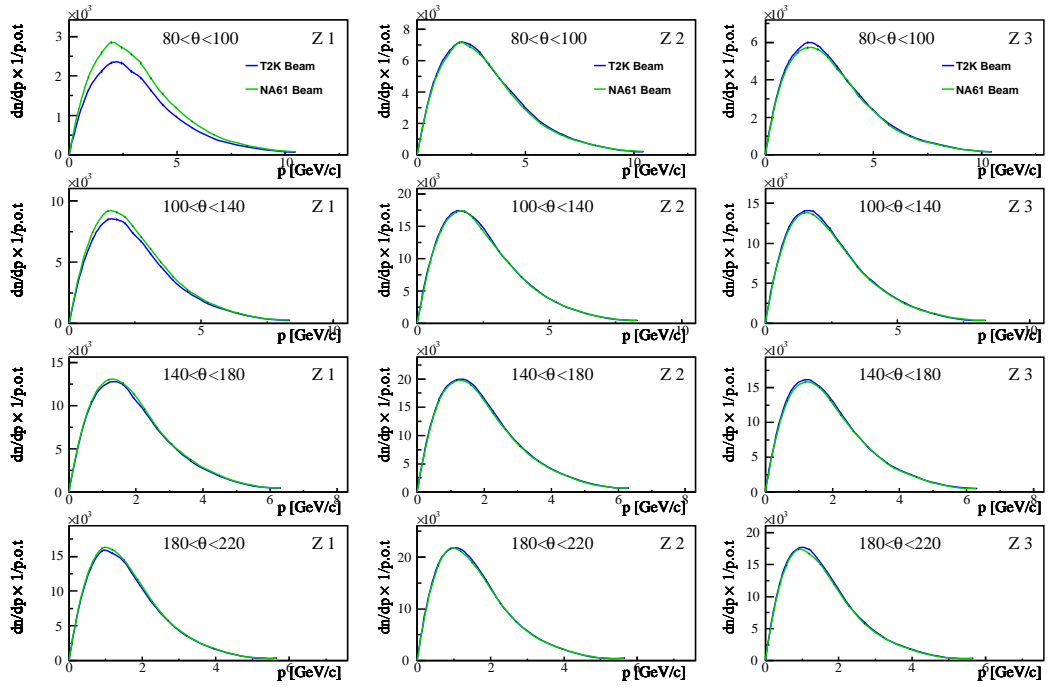


Figure C.2: Positively charged pion spectra at the surface of the target produced with FLUKA for the NA61/SHINE beam profile (green) and the T2K beam profile (blue) for the three upstream longitudinal bins and in the polar angles between 80 and 220 mrad plotted as a function of momentum. The spectra are normalized to momentum bin size and number of protons on target

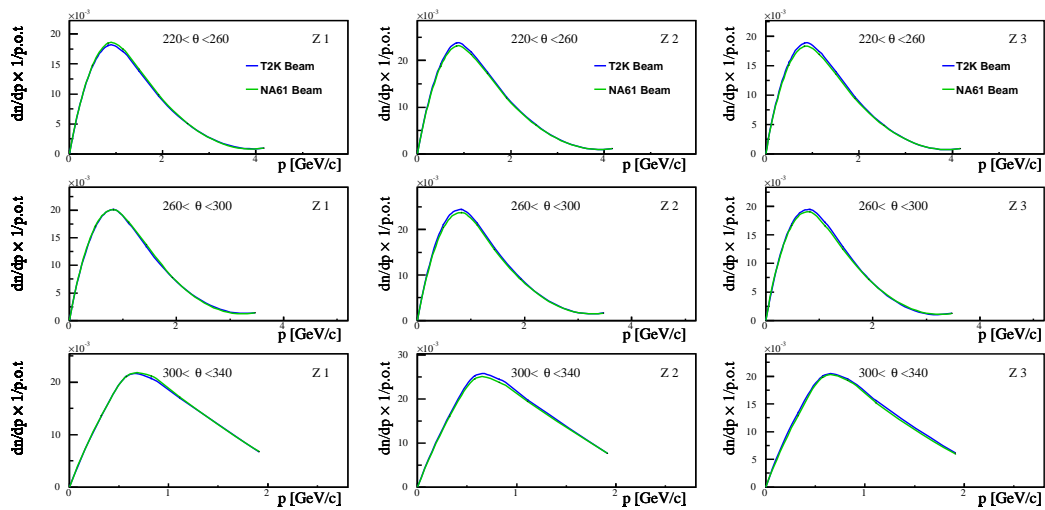


Figure C.3: Positively charged pion spectra at the surface of the target produced with FLUKA for the NA61/SHINE beam profile (green) and the T2K beam profile (blue) for the three upstream longitudinal bins and in the polar angles between 220 and 340 mrad plotted as a function of momentum. The spectra are normalized to momentum bin size and number of protons on target

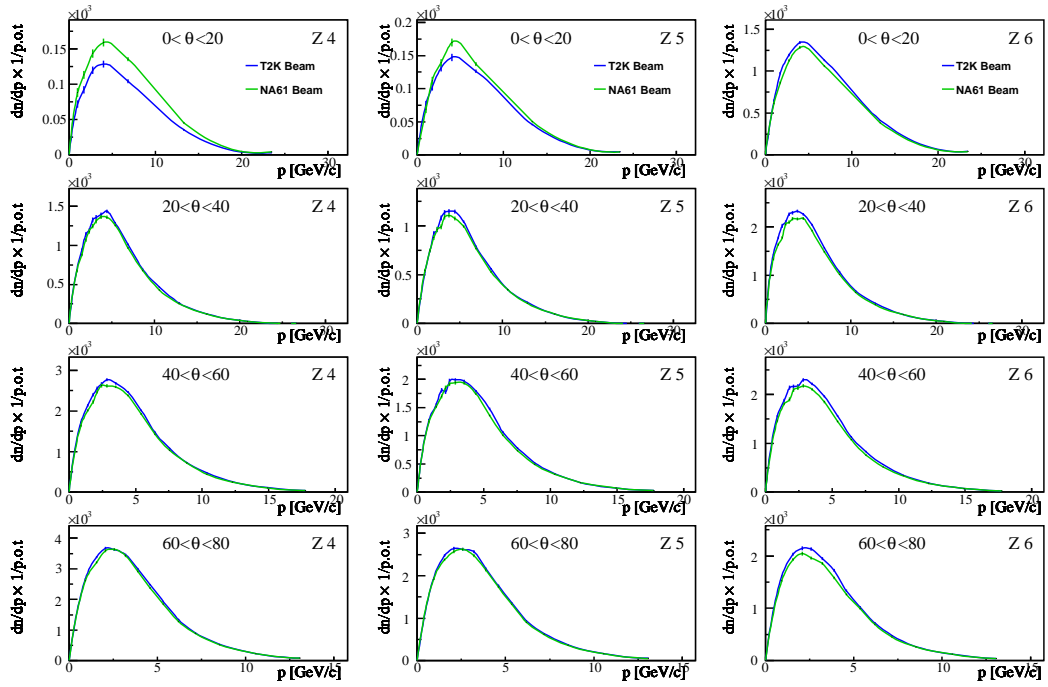


Figure C.4: Positively charged pion spectra at the surface of the target produced with FLUKA for the NA61/SHINE beam profile (green) and the T2K beam profile (blue) for the three downstream longitudinal bins and in the polar angles between 0 and 80 mrad plotted as a function of momentum. The spectra are normalized to momentum bin size and number of protons on target

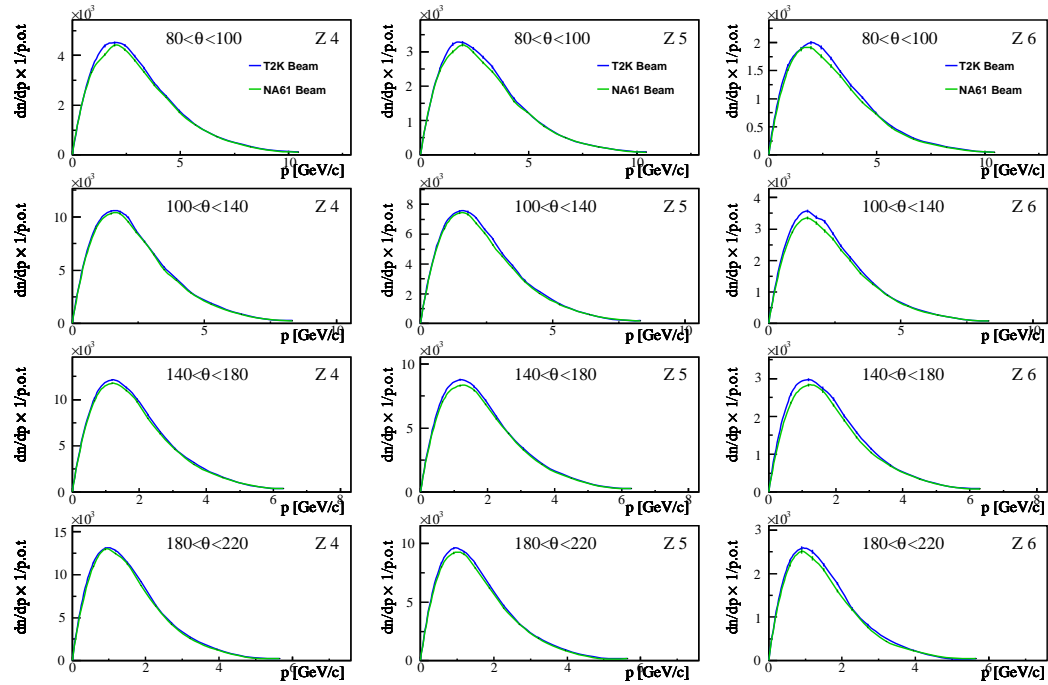


Figure C.5: Positively charged pion spectra at the surface of the target produced with FLUKA for the NA61/SHINE beam profile (green) and the T2K beam profile (blue) for the three downstream longitudinal bins and in the polar angles between 80 and 220 mrad plotted as a function of momentum. The spectra are normalized to momentum bin size and number of protons on target

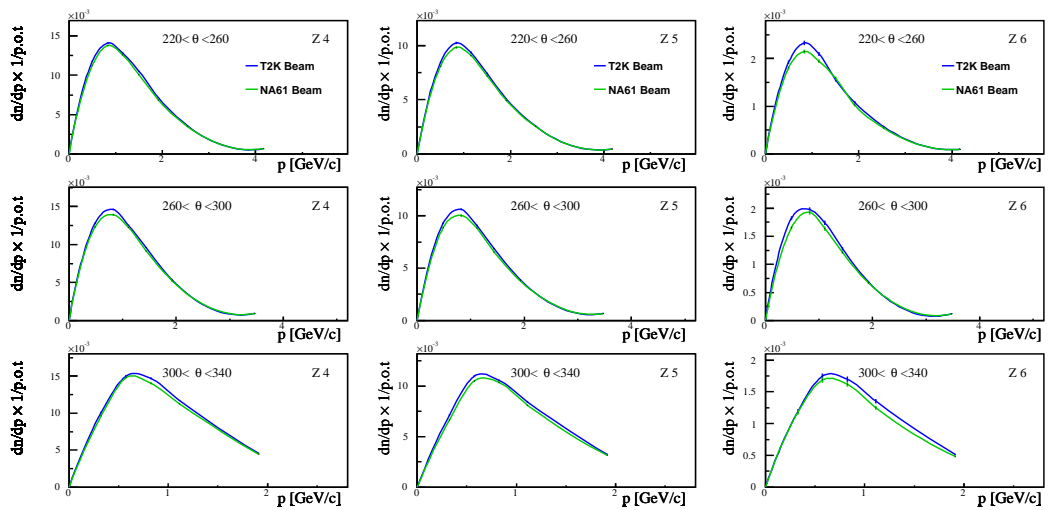


Figure C.6: Positively charged pion spectra at the surface of the target produced with FLUKA for the NA61/SHINE beam profile (green) and the T2K beam profile (blue) for the three downstream longitudinal bins and in the polar angles between 220 and 340 mrad plotted as a function of momentum. The spectra are normalized to momentum bin size and number of protons on target

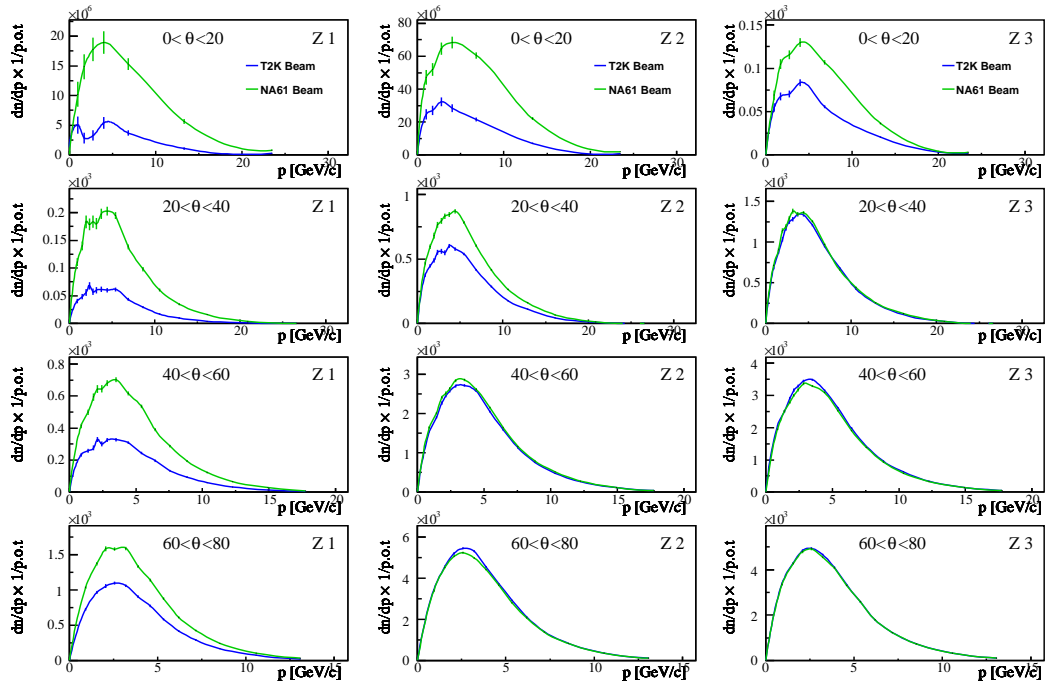


Figure C.7: Negatively charged pion spectra at the surface of the target produced with FLUKA for the NA61/SHINE beam profile (green) and the T2K beam profile (blue) for the three upstream longitudinal bins and in the polar angles between 0 and 80 mrad plotted as a function of momentum. The spectra are normalized to momentum bin size and number of protons on target

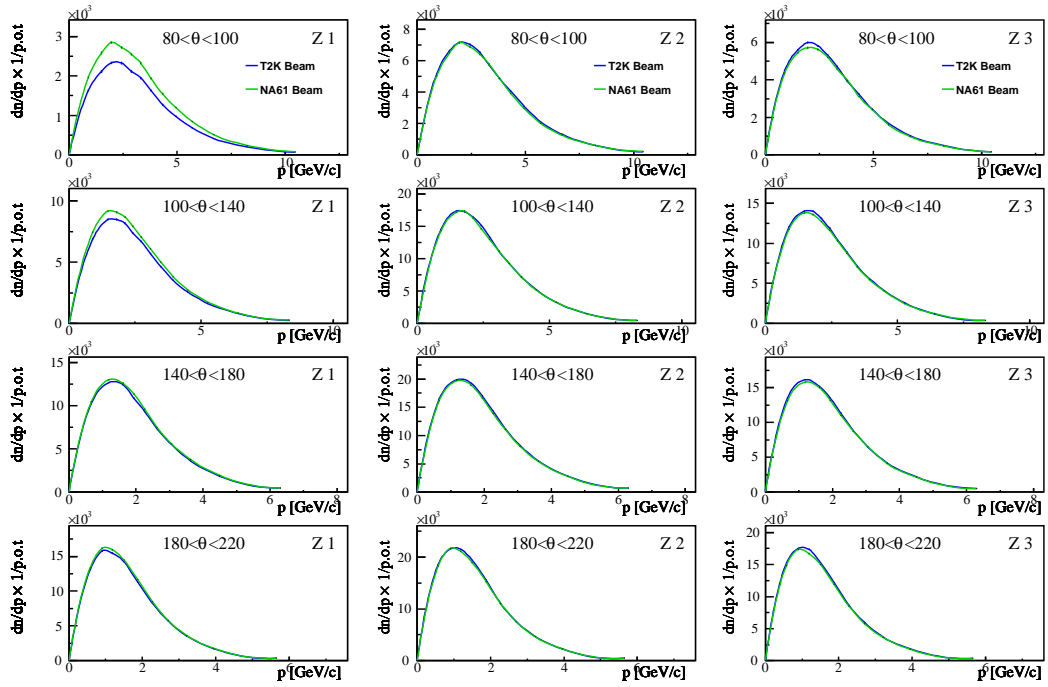


Figure C.8: Negatively charged pion spectra at the surface of the target produced with FLUKA for the NA61/SHINE beam profile (green) and the T2K beam profile (blue) for the three upstream longitudinal bins and in the polar angles between 80 and 220 mrad plotted as a function of momentum. The spectra are normalized to momentum bin size and number of protons on target

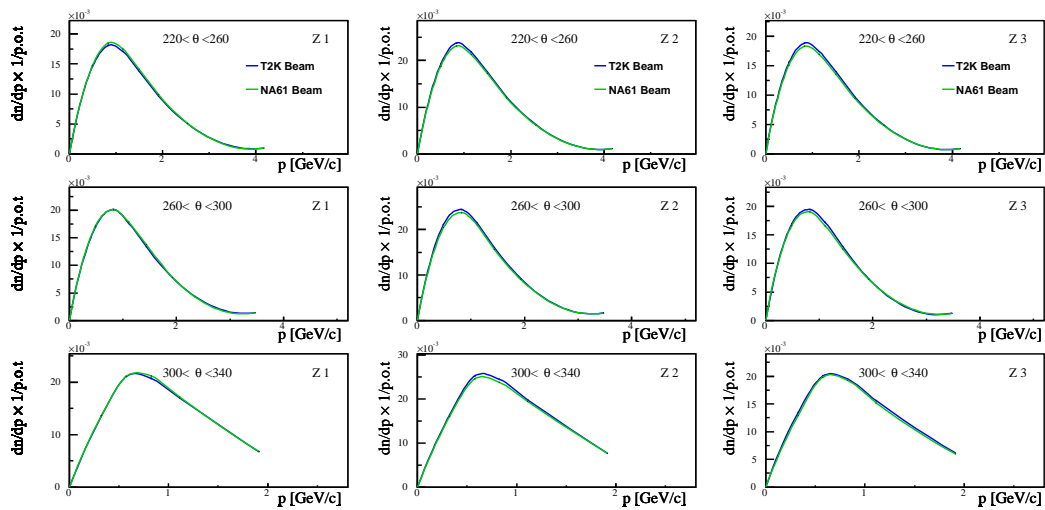


Figure C.9: Negatively charged pion spectra at the surface of the target produced with FLUKA for the NA61/SHINE beam profile (green) and the T2K beam profile (blue) for the three upstream longitudinal bins and in the polar angles between 220 and 340 mrad plotted as a function of momentum. The spectra are normalized to momentum bin size and number of protons on target

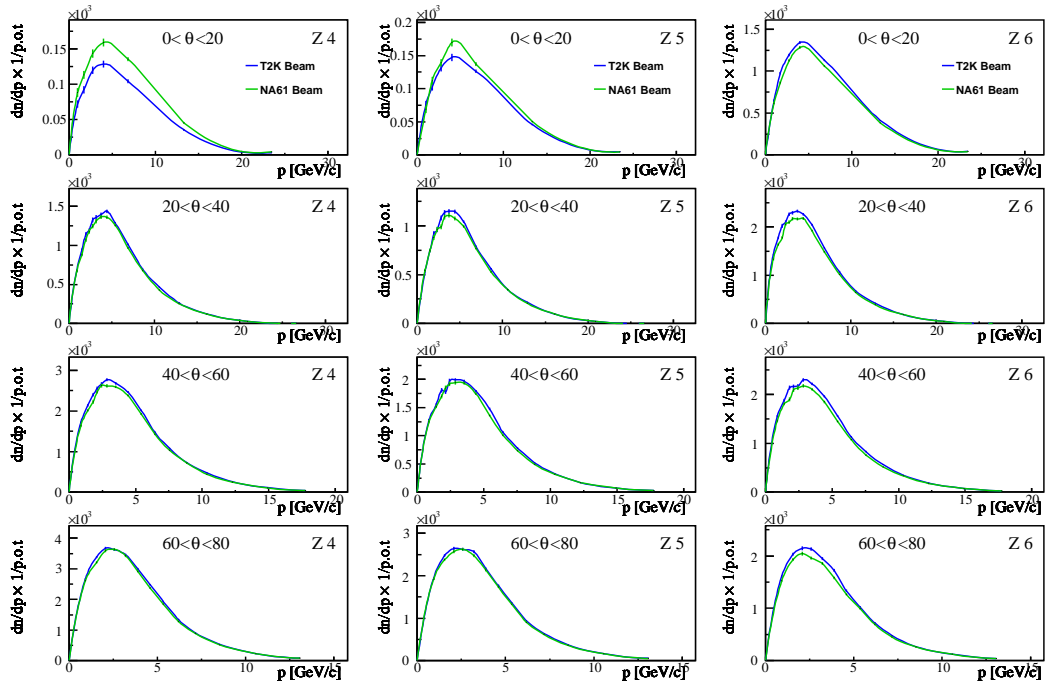


Figure C.10: Negatively charged pion spectra at the surface of the target produced with FLUKA for the NA61/SHINE beam profile (green) and the T2K beam profile (blue) for the three downstream longitudinal bins and in the polar angles between 0 and 80 mrad plotted as a function of momentum. The spectra are normalized to momentum bin size and number of protons on target

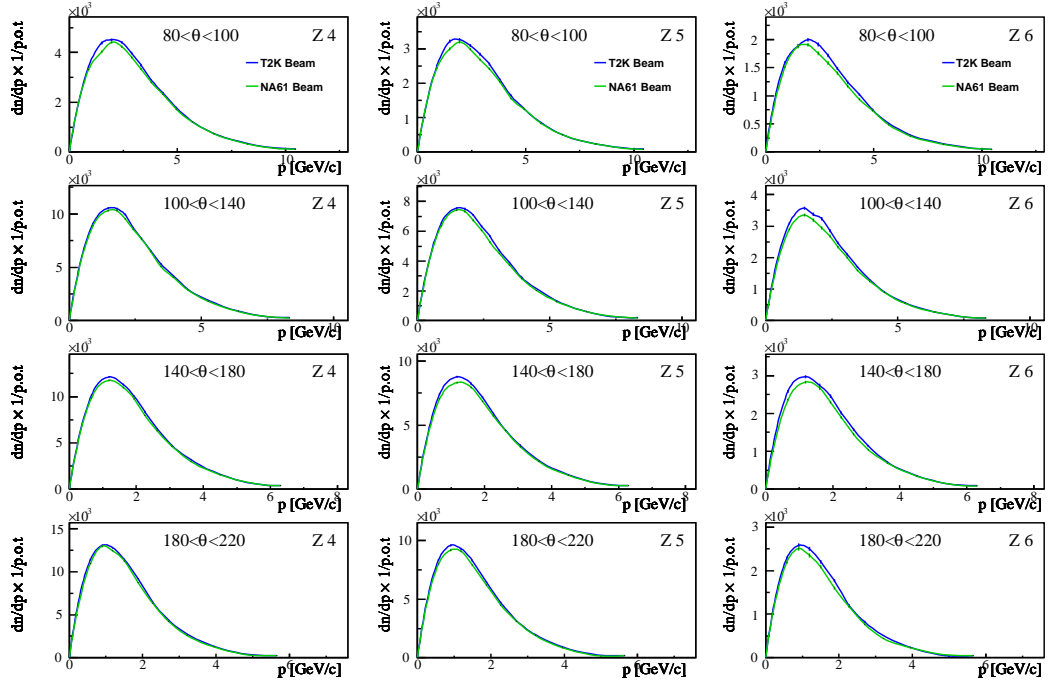


Figure C.11: Negatively charged pion spectra at the surface of the target produced with FLUKA for the NA61/SHINE beam profile (green) and the T2K beam profile (blue) for the three downstream longitudinal bins and in the polar angles between 80 and 220 mrad plotted as a function of momentum. The spectra are normalized to momentum bin size and number of protons on target

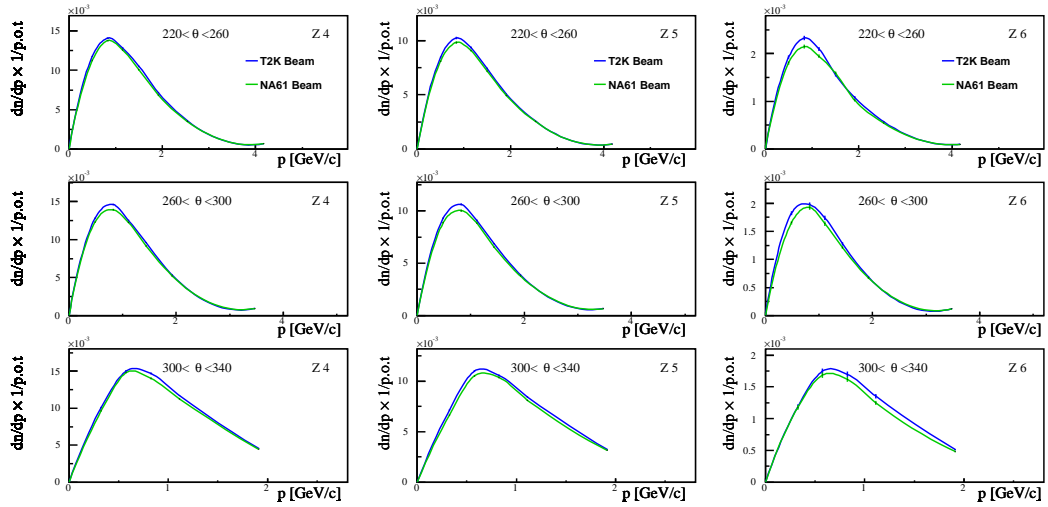


Figure C.12: Negatively charged pion spectra at the surface of the target produced with FLUKA for the NA61/SHINE beam profile (green) and the T2K beam profile (blue) for the three downstream longitudinal bins and in the polar angles between 220 and 340 mrad plotted as a function of momentum. The spectra are normalized to momentum bin size and number of protons on target

Appendix D

Numerical Tables

Table D.1 shows the numerical values of the positively charged pion multiplicities for each (p, θ, z) bins with the related statistical and systematic uncertainties.

Table D.2 shows the numerical values of the negatively charged pion multiplicities for each (p, θ, z) bins with the related statistical and systematic uncertainties.

Table D.1: Multiplicities of π^+ for the different (p, θ, z) bins with related statistical and systematic uncertainties

z	θ [mrad]	p [GeV/c]	$d\pi^+ / dp$ [/(GeV/c)/p.o.t]	Δ_{stat}	$\Delta_{stat}\%$	Δ_{sys}	$\Delta_{sys}\%$
z 1	0 - 20	0.7 - 1.3	$8.077 \cdot 10^{-6}$	$2.518 \cdot 10^{-6}$	0.312	$4.125 \cdot 10^{-7}$	0.051
		1.3 - 2.175	$1.429 \cdot 10^{-5}$	$2.482 \cdot 10^{-6}$	0.174	$6.719 \cdot 10^{-7}$	0.047
		2.175 - 3.325	$1.981 \cdot 10^{-5}$	$2.246 \cdot 10^{-6}$	0.113	$8.558 \cdot 10^{-7}$	0.043
		3.325 - 4.675	$2.323 \cdot 10^{-5}$	$2.287 \cdot 10^{-6}$	0.098	$9.996 \cdot 10^{-7}$	0.043
		4.675 - 8.95	$2.239 \cdot 10^{-5}$	$1.779 \cdot 10^{-6}$	0.079	$8.601 \cdot 10^{-7}$	0.038
		8.95 - 17.65	$1.121 \cdot 10^{-5}$	$1.549 \cdot 10^{-6}$	0.138	$1.112 \cdot 10^{-6}$	0.099
	20 - 40	0.6 - 1.23	$7.614 \cdot 10^{-5}$	$1.045 \cdot 10^{-5}$	0.137	$3.971 \cdot 10^{-6}$	0.052
		1.23 - 1.775	$9.646 \cdot 10^{-5}$	$9.499 \cdot 10^{-6}$	0.098	$4.945 \cdot 10^{-6}$	0.051
		1.775 - 2.15	$1.421 \cdot 10^{-4}$	$1.480 \cdot 10^{-5}$	0.104	$6.556 \cdot 10^{-6}$	0.046
		2.15 - 2.575	$1.401 \cdot 10^{-4}$	$1.151 \cdot 10^{-5}$	0.082	$6.389 \cdot 10^{-6}$	0.046
		2.575 - 2.975	$1.516 \cdot 10^{-4}$	$2.154 \cdot 10^{-5}$	0.142	$6.837 \cdot 10^{-6}$	0.045
		2.975 - 3.425	$1.497 \cdot 10^{-4}$	$1.109 \cdot 10^{-5}$	0.074	$6.437 \cdot 10^{-6}$	0.043
		3.425 - 4.025	$1.576 \cdot 10^{-4}$	$1.620 \cdot 10^{-5}$	0.103	$8.334 \cdot 10^{-6}$	0.053
		4.025 - 4.825	$1.929 \cdot 10^{-4}$	$1.065 \cdot 10^{-5}$	0.055	$1.525 \cdot 10^{-5}$	0.079
		4.825 - 6.05	$1.795 \cdot 10^{-4}$	$1.394 \cdot 10^{-5}$	0.078	$1.540 \cdot 10^{-5}$	0.086
		6.05 - 7.75	$1.602 \cdot 10^{-4}$	$1.206 \cdot 10^{-5}$	0.075	$1.394 \cdot 10^{-5}$	0.087
		7.75 - 9.55	$1.304 \cdot 10^{-4}$	$1.042 \cdot 10^{-5}$	0.080	$1.001 \cdot 10^{-5}$	0.077
		9.55 - 11.625	$7.825 \cdot 10^{-5}$	$7.300 \cdot 10^{-6}$	0.093	$5.426 \cdot 10^{-6}$	0.069
		11.625 - 14.125	$4.120 \cdot 10^{-5}$	$5.402 \cdot 10^{-6}$	0.131	$2.635 \cdot 10^{-6}$	0.064
		14.125 - 18.125	$1.513 \cdot 10^{-5}$	$2.672 \cdot 10^{-6}$	0.177	$7.465 \cdot 10^{-7}$	0.049
		18.125 - 23.625	$1.626 \cdot 10^{-6}$	$8.198 \cdot 10^{-7}$	0.504	$9.253 \cdot 10^{-8}$	0.057
		23.625 - 29.625	$4.607 \cdot 10^{-7}$	$4.703 \cdot 10^{-7}$	1.021	$1.734 \cdot 10^{-7}$	0.377
	40 - 60	0.6 - 1.175	$4.304 \cdot 10^{-4}$	$4.215 \cdot 10^{-5}$	0.098	$1.912 \cdot 10^{-5}$	0.044
		1.175 - 1.675	$4.310 \cdot 10^{-4}$	$2.891 \cdot 10^{-5}$	0.067	$2.033 \cdot 10^{-5}$	0.047
		1.675 - 1.975	$4.503 \cdot 10^{-4}$	$3.598 \cdot 10^{-5}$	0.080	$1.964 \cdot 10^{-5}$	0.044
		1.975 - 2.275	$4.531 \cdot 10^{-4}$	$3.423 \cdot 10^{-5}$	0.076	$1.712 \cdot 10^{-5}$	0.038
		2.275 - 2.6	$4.844 \cdot 10^{-4}$	$5.390 \cdot 10^{-5}$	0.111	$1.845 \cdot 10^{-5}$	0.038
		2.6 - 3.1	$4.956 \cdot 10^{-4}$	$4.103 \cdot 10^{-5}$	0.083	$3.093 \cdot 10^{-5}$	0.062
		3.1 - 3.925	$5.728 \cdot 10^{-4}$	$4.266 \cdot 10^{-5}$	0.074	$4.330 \cdot 10^{-5}$	0.076
		3.925 - 4.9	$6.121 \cdot 10^{-4}$	$3.881 \cdot 10^{-5}$	0.063	$3.815 \cdot 10^{-5}$	0.062
		4.9 - 5.95	$4.996 \cdot 10^{-4}$	$3.633 \cdot 10^{-5}$	0.073	$2.798 \cdot 10^{-5}$	0.056
		5.95 - 6.92	$4.315 \cdot 10^{-4}$	$3.700 \cdot 10^{-5}$	0.086	$2.330 \cdot 10^{-5}$	0.054
		6.92 - 8.175	$2.444 \cdot 10^{-4}$	$2.346 \cdot 10^{-5}$	0.096	$1.277 \cdot 10^{-5}$	0.052
		8.175 - 9.5	$1.678 \cdot 10^{-4}$	$1.293 \cdot 10^{-5}$	0.077	$9.430 \cdot 10^{-6}$	0.056
		9.5 - 11.2	$1.119 \cdot 10^{-4}$	$9.035 \cdot 10^{-6}$	0.081	$5.906 \cdot 10^{-6}$	0.053
		11.2 - 13.325	$5.938 \cdot 10^{-5}$	$6.082 \cdot 10^{-6}$	0.102	$3.004 \cdot 10^{-6}$	0.051
		13.325 - 16.5	$2.569 \cdot 10^{-5}$	$3.339 \cdot 10^{-6}$	0.130	$1.528 \cdot 10^{-6}$	0.059
		16.5 - 19	$9.333 \cdot 10^{-6}$	$2.349 \cdot 10^{-6}$	0.252	$8.447 \cdot 10^{-7}$	0.091
	60 - 80	0.6 - 1.25	$7.913 \cdot 10^{-4}$	$5.973 \cdot 10^{-5}$	0.075	$3.065 \cdot 10^{-5}$	0.039
		1.25 - 1.875	$1.068 \cdot 10^{-3}$	$5.530 \cdot 10^{-5}$	0.052	$4.612 \cdot 10^{-5}$	0.043
		1.875 - 2.275	$1.131 \cdot 10^{-3}$	$1.107 \cdot 10^{-4}$	0.098	$5.800 \cdot 10^{-5}$	0.051
		2.275 - 2.875	$1.301 \cdot 10^{-3}$	$1.006 \cdot 10^{-4}$	0.077	$8.544 \cdot 10^{-5}$	0.066
		2.875 - 3.55	$1.283 \cdot 10^{-3}$	$9.605 \cdot 10^{-5}$	0.075	$7.234 \cdot 10^{-5}$	0.056

Table D.1: Multiplicities of π^+ for the different (p, θ, z) bins with related statistical and systematic uncertainties

z	θ	p	$d\mathbf{n}^{\pi^+}/dp$	Δ_{stat}	$\Delta_{stat}\%$	Δ_{sys}	$\Delta_{sys}\%$
	[mrad]	[GeV/c]	[/ (GeV/c)/p.o.t]				
		3.55 - 4.225	$1.066 \cdot 10^{-3}$	$7.736 \cdot 10^{-5}$	0.073	$6.417 \cdot 10^{-5}$	0.060
		4.225 - 4.95	$8.913 \cdot 10^{-4}$	$4.473 \cdot 10^{-5}$	0.050	$5.265 \cdot 10^{-5}$	0.059
		4.95 - 5.75	$8.620 \cdot 10^{-4}$	$4.536 \cdot 10^{-5}$	0.053	$5.195 \cdot 10^{-5}$	0.060
		5.75 - 6.625	$5.684 \cdot 10^{-4}$	$5.006 \cdot 10^{-5}$	0.088	$3.433 \cdot 10^{-5}$	0.060
		6.625 - 7.725	$4.530 \cdot 10^{-4}$	$2.648 \cdot 10^{-5}$	0.058	$2.665 \cdot 10^{-5}$	0.059
		7.725 - 9.325	$2.758 \cdot 10^{-4}$	$1.940 \cdot 10^{-5}$	0.070	$1.839 \cdot 10^{-5}$	0.067
		9.325 - 11.825	$1.290 \cdot 10^{-4}$	$9.542 \cdot 10^{-6}$	0.074	$8.753 \cdot 10^{-6}$	0.068
		11.825 - 14.325	$4.090 \cdot 10^{-5}$	$5.609 \cdot 10^{-6}$	0.137	$2.522 \cdot 10^{-6}$	0.062
80 - 100	0.5 - 1.3		$2.059 \cdot 10^{-3}$	$1.219 \cdot 10^{-4}$	0.059	$1.052 \cdot 10^{-4}$	0.051
	1.3 - 1.7		$2.652 \cdot 10^{-3}$	$1.613 \cdot 10^{-4}$	0.061	$1.338 \cdot 10^{-4}$	0.050
	1.7 - 2.2		$2.456 \cdot 10^{-3}$	$2.979 \cdot 10^{-4}$	0.121	$1.510 \cdot 10^{-4}$	0.061
	2.2 - 2.675		$2.155 \cdot 10^{-3}$	$2.260 \cdot 10^{-4}$	0.105	$1.226 \cdot 10^{-4}$	0.057
	2.675 - 3.1		$2.132 \cdot 10^{-3}$	$1.533 \cdot 10^{-4}$	0.072	$1.314 \cdot 10^{-4}$	0.062
	3.1 - 3.55		$2.033 \cdot 10^{-3}$	$1.224 \cdot 10^{-4}$	0.060	$1.194 \cdot 10^{-4}$	0.059
	3.55 - 4.05		$1.679 \cdot 10^{-3}$	$7.987 \cdot 10^{-5}$	0.048	$1.009 \cdot 10^{-4}$	0.060
	4.05 - 4.6		$1.616 \cdot 10^{-3}$	$8.374 \cdot 10^{-5}$	0.052	$9.421 \cdot 10^{-5}$	0.058
	4.6 - 5.275		$1.283 \cdot 10^{-3}$	$6.747 \cdot 10^{-5}$	0.053	$8.397 \cdot 10^{-5}$	0.065
	5.275 - 6.125		$8.748 \cdot 10^{-4}$	$3.782 \cdot 10^{-5}$	0.043	$4.724 \cdot 10^{-5}$	0.054
	6.125 - 7.275		$5.669 \cdot 10^{-4}$	$3.273 \cdot 10^{-5}$	0.058	$3.471 \cdot 10^{-5}$	0.061
	7.275 - 9.2		$2.772 \cdot 10^{-4}$	$1.520 \cdot 10^{-5}$	0.055	$1.621 \cdot 10^{-5}$	0.058
	9.2 - 11.7		$9.667 \cdot 10^{-5}$	$9.847 \cdot 10^{-6}$	0.102	$5.561 \cdot 10^{-6}$	0.058
100 - 140	0.5 - 1.3		$7.149 \cdot 10^{-3}$	$2.910 \cdot 10^{-4}$	0.041	$3.312 \cdot 10^{-4}$	0.046
	1.3 - 1.65		$8.342 \cdot 10^{-3}$	$4.556 \cdot 10^{-4}$	0.055	$4.395 \cdot 10^{-4}$	0.053
	1.65 - 1.95		$8.433 \cdot 10^{-3}$	$4.853 \cdot 10^{-4}$	0.058	$4.228 \cdot 10^{-4}$	0.050
	1.95 - 2.275		$7.148 \cdot 10^{-3}$	$2.838 \cdot 10^{-4}$	0.040	$3.707 \cdot 10^{-4}$	0.052
	2.275 - 2.575		$6.990 \cdot 10^{-3}$	$1.857 \cdot 10^{-4}$	0.027	$3.782 \cdot 10^{-4}$	0.054
	2.575 - 2.9		$6.145 \cdot 10^{-3}$	$2.342 \cdot 10^{-4}$	0.038	$2.989 \cdot 10^{-4}$	0.049
	2.9 - 3.275		$5.732 \cdot 10^{-3}$	$2.435 \cdot 10^{-4}$	0.042	$3.023 \cdot 10^{-4}$	0.053
	3.275 - 3.675		$4.916 \cdot 10^{-3}$	$2.144 \cdot 10^{-4}$	0.044	$2.458 \cdot 10^{-4}$	0.050
	3.675 - 4.2		$3.553 \cdot 10^{-3}$	$1.590 \cdot 10^{-4}$	0.045	$1.676 \cdot 10^{-4}$	0.047
	4.2 - 4.8		$2.705 \cdot 10^{-3}$	$1.324 \cdot 10^{-4}$	0.049	$1.414 \cdot 10^{-4}$	0.052
	4.8 - 5.725		$1.867 \cdot 10^{-3}$	$6.108 \cdot 10^{-5}$	0.033	$9.065 \cdot 10^{-5}$	0.049
	5.725 - 7.075		$9.963 \cdot 10^{-4}$	$5.119 \cdot 10^{-5}$	0.051	$5.055 \cdot 10^{-5}$	0.051
	7.075 - 9.575		$3.263 \cdot 10^{-4}$	$2.247 \cdot 10^{-5}$	0.069	$1.851 \cdot 10^{-5}$	0.057
140 - 180	0.4 - 0.925		$1.023 \cdot 10^{-2}$	$5.744 \cdot 10^{-4}$	0.056	$4.496 \cdot 10^{-4}$	0.044
	0.925 - 1.45		$1.237 \cdot 10^{-2}$	$6.688 \cdot 10^{-4}$	0.054	$5.344 \cdot 10^{-4}$	0.043
	1.45 - 1.775		$1.182 \cdot 10^{-2}$	$6.582 \cdot 10^{-4}$	0.056	$5.269 \cdot 10^{-4}$	0.045
	1.775 - 2.1		$1.055 \cdot 10^{-2}$	$6.226 \cdot 10^{-4}$	0.059	$4.807 \cdot 10^{-4}$	0.046
	2.1 - 2.425		$8.167 \cdot 10^{-3}$	$3.842 \cdot 10^{-4}$	0.047	$3.708 \cdot 10^{-4}$	0.045
	2.425 - 2.825		$7.388 \cdot 10^{-3}$	$3.323 \cdot 10^{-4}$	0.045	$3.403 \cdot 10^{-4}$	0.046
	2.825 - 3.3		$4.526 \cdot 10^{-3}$	$2.348 \cdot 10^{-4}$	0.052	$2.139 \cdot 10^{-4}$	0.047
	3.3 - 3.95		$3.534 \cdot 10^{-3}$	$1.787 \cdot 10^{-4}$	0.051	$1.479 \cdot 10^{-4}$	0.042
	3.95 - 5.05		$1.909 \cdot 10^{-3}$	$9.770 \cdot 10^{-5}$	0.051	$8.551 \cdot 10^{-5}$	0.045

Table D.1: Multiplicities of π^+ for the different (p, θ, z) bins with related statistical and systematic uncertainties

z	θ	p	$d\pi^+ / dp$	Δ_{stat}	$\Delta_{stat}\%$	Δ_{sys}	$\Delta_{sys}\%$
		[mrad]	[(GeV/c)/p.o.t]				
180 - 220	5.05 - 7.55		$5.422 \cdot 10^{-4}$	$3.604 \cdot 10^{-5}$	0.066	$2.747 \cdot 10^{-5}$	0.051
	0.4 - 0.75		$1.264 \cdot 10^{-2}$	$8.432 \cdot 10^{-4}$	0.067	$1.085 \cdot 10^{-3}$	0.086
	0.75 - 1.05		$1.519 \cdot 10^{-2}$	$1.038 \cdot 10^{-3}$	0.068	$8.376 \cdot 10^{-4}$	0.055
	1.05 - 1.325		$1.431 \cdot 10^{-2}$	$8.131 \cdot 10^{-4}$	0.057	$7.053 \cdot 10^{-4}$	0.049
	1.325 - 1.675		$1.340 \cdot 10^{-2}$	$6.971 \cdot 10^{-4}$	0.052	$5.809 \cdot 10^{-4}$	0.043
	1.675 - 2.075		$8.703 \cdot 10^{-3}$	$4.230 \cdot 10^{-4}$	0.049	$3.930 \cdot 10^{-4}$	0.045
	2.075 - 2.475		$7.670 \cdot 10^{-3}$	$4.715 \cdot 10^{-4}$	0.061	$3.017 \cdot 10^{-4}$	0.039
	2.475 - 2.925		$5.079 \cdot 10^{-3}$	$3.331 \cdot 10^{-4}$	0.066	$2.207 \cdot 10^{-4}$	0.043
	2.925 - 3.5		$2.906 \cdot 10^{-3}$	$2.367 \cdot 10^{-4}$	0.081	$1.171 \cdot 10^{-4}$	0.040
	3.5 - 4.4		$1.590 \cdot 10^{-3}$	$1.194 \cdot 10^{-4}$	0.075	$6.273 \cdot 10^{-5}$	0.039
	4.4 - 6.9		$3.846 \cdot 10^{-4}$	$2.838 \cdot 10^{-5}$	0.074	$1.584 \cdot 10^{-5}$	0.041
220 - 260	0.3 - 0.7		$1.432 \cdot 10^{-2}$	$9.454 \cdot 10^{-4}$	0.066	$2.475 \cdot 10^{-3}$	0.173
	0.7 - 0.975		$1.660 \cdot 10^{-2}$	$9.960 \cdot 10^{-4}$	0.060	$2.088 \cdot 10^{-3}$	0.126
	0.975 - 1.325		$1.432 \cdot 10^{-2}$	$7.488 \cdot 10^{-4}$	0.052	$1.380 \cdot 10^{-3}$	0.096
	1.325 - 1.675		$1.117 \cdot 10^{-2}$	$5.556 \cdot 10^{-4}$	0.050	$8.200 \cdot 10^{-4}$	0.073
	1.675 - 2.15		$8.654 \cdot 10^{-3}$	$4.548 \cdot 10^{-4}$	0.053	$4.989 \cdot 10^{-4}$	0.058
	2.15 - 2.925		$4.280 \cdot 10^{-3}$	$2.424 \cdot 10^{-4}$	0.057	$1.848 \cdot 10^{-4}$	0.043
	2.925 - 5.425		$9.485 \cdot 10^{-4}$	$6.312 \cdot 10^{-5}$	0.067	$3.400 \cdot 10^{-5}$	0.036
	260 - 300		$1.258 \cdot 10^{-2}$	$9.651 \cdot 10^{-4}$	0.077	$5.268 \cdot 10^{-4}$	0.042
	0.675 - 0.975		$1.381 \cdot 10^{-2}$	$8.955 \cdot 10^{-4}$	0.065	$5.896 \cdot 10^{-4}$	0.043
	0.975 - 1.25		$1.311 \cdot 10^{-2}$	$8.786 \cdot 10^{-4}$	0.067	$5.377 \cdot 10^{-4}$	0.041
300 - 340	1.25 - 1.625		$9.763 \cdot 10^{-3}$	$5.554 \cdot 10^{-4}$	0.057	$3.880 \cdot 10^{-4}$	0.040
	1.625 - 2.225		$5.681 \cdot 10^{-3}$	$3.486 \cdot 10^{-4}$	0.061	$2.306 \cdot 10^{-4}$	0.041
	2.225 - 4.725		$1.347 \cdot 10^{-3}$	$9.618 \cdot 10^{-5}$	0.071	$5.241 \cdot 10^{-5}$	0.039
	0.2 - 0.45		$7.184 \cdot 10^{-3}$	$1.069 \cdot 10^{-3}$	0.149	$3.058 \cdot 10^{-4}$	0.043
	0.45 - 0.7		$1.346 \cdot 10^{-2}$	$1.440 \cdot 10^{-3}$	0.107	$7.105 \cdot 10^{-4}$	0.053
	0.7 - 0.95		$1.342 \cdot 10^{-2}$	$1.225 \cdot 10^{-3}$	0.091	$6.672 \cdot 10^{-4}$	0.050
	0.95 - 1.275		$1.001 \cdot 10^{-2}$	$1.008 \cdot 10^{-3}$	0.101	$5.615 \cdot 10^{-4}$	0.056
	1.275 - 2.55		$3.812 \cdot 10^{-3}$	$6.000 \cdot 10^{-4}$	0.157	$1.883 \cdot 10^{-4}$	0.049
	z 2 0 - 20		$9.065 \cdot 10^{-6}$	$6.625 \cdot 10^{-6}$	0.731	$4.842 \cdot 10^{-7}$	0.053
	1.3 - 2.175		$4.431 \cdot 10^{-5}$	$1.048 \cdot 10^{-5}$	0.236	$2.276 \cdot 10^{-6}$	0.051
20 - 40	2.175 - 3.325		$5.968 \cdot 10^{-5}$	$1.036 \cdot 10^{-5}$	0.174	$2.881 \cdot 10^{-6}$	0.048
	3.325 - 4.675		$7.179 \cdot 10^{-5}$	$9.008 \cdot 10^{-6}$	0.125	$2.574 \cdot 10^{-6}$	0.036
	4.675 - 8.95		$7.273 \cdot 10^{-5}$	$5.961 \cdot 10^{-6}$	0.082	$4.252 \cdot 10^{-6}$	0.058
	8.95 - 17.65		$3.196 \cdot 10^{-5}$	$3.056 \cdot 10^{-6}$	0.096	$2.261 \cdot 10^{-6}$	0.071
	17.65 - 29.3		$7.273 \cdot 10^{-6}$	$3.051 \cdot 10^{-6}$	0.419	$3.888 \cdot 10^{-7}$	0.053
	0.6 - 1.23		$3.079 \cdot 10^{-4}$	$7.050 \cdot 10^{-5}$	0.229	$1.231 \cdot 10^{-5}$	0.040
	1.23 - 1.775		$5.017 \cdot 10^{-4}$	$3.763 \cdot 10^{-5}$	0.075	$1.704 \cdot 10^{-5}$	0.034
	1.775 - 2.15		$4.732 \cdot 10^{-4}$	$3.618 \cdot 10^{-5}$	0.076	$1.643 \cdot 10^{-5}$	0.035
	2.15 - 2.575		$6.529 \cdot 10^{-4}$	$4.655 \cdot 10^{-5}$	0.071	$2.186 \cdot 10^{-5}$	0.033
	2.575 - 2.975		$6.664 \cdot 10^{-4}$	$4.973 \cdot 10^{-5}$	0.075	$2.916 \cdot 10^{-5}$	0.044
	2.975 - 3.425		$6.900 \cdot 10^{-4}$	$5.782 \cdot 10^{-5}$	0.084	$2.470 \cdot 10^{-5}$	0.036
	3.425 - 4.025		$7.487 \cdot 10^{-4}$	$5.157 \cdot 10^{-5}$	0.069	$3.403 \cdot 10^{-5}$	0.045

Table D.1: Multiplicities of π^+ for the different (p, θ, z) bins with related statistical and systematic uncertainties

z	θ	p	$d\eta^{\pi^+}/dp$	Δ_{stat}	$\Delta_{stat}\%$	Δ_{sys}	$\Delta_{sys}\%$
	[mrad]	[GeV/c]	[/ (GeV/c)/p.o.t]				
	4.025 - 4.825		$7.310 \cdot 10^{-4}$	$3.954 \cdot 10^{-5}$	0.054	$3.231 \cdot 10^{-5}$	0.044
	4.825 - 6.05		$7.615 \cdot 10^{-4}$	$3.604 \cdot 10^{-5}$	0.047	$3.834 \cdot 10^{-5}$	0.050
	6.05 - 7.75		$6.900 \cdot 10^{-4}$	$2.860 \cdot 10^{-5}$	0.041	$3.414 \cdot 10^{-5}$	0.049
	7.75 - 9.55		$5.093 \cdot 10^{-4}$	$2.341 \cdot 10^{-5}$	0.046	$2.683 \cdot 10^{-5}$	0.053
	9.55 - 11.625		$2.722 \cdot 10^{-4}$	$1.693 \cdot 10^{-5}$	0.062	$1.139 \cdot 10^{-5}$	0.042
	11.625 - 14.125		$1.611 \cdot 10^{-4}$	$1.206 \cdot 10^{-5}$	0.075	$6.251 \cdot 10^{-6}$	0.039
	14.125 - 18.125		$4.714 \cdot 10^{-5}$	$5.351 \cdot 10^{-6}$	0.114	$1.833 \cdot 10^{-6}$	0.039
	18.125 - 23.625		$1.289 \cdot 10^{-5}$	$3.045 \cdot 10^{-6}$	0.236	$4.983 \cdot 10^{-7}$	0.039
	23.625 - 29.625		$8.348 \cdot 10^{-7}$	$1.084 \cdot 10^{-5}$	12.988	$5.213 \cdot 10^{-8}$	0.062
40 - 60	0.6 - 1.175		$1.535 \cdot 10^{-3}$	$1.023 \cdot 10^{-4}$	0.067	$5.147 \cdot 10^{-5}$	0.034
	1.175 - 1.675		$1.603 \cdot 10^{-3}$	$7.736 \cdot 10^{-5}$	0.048	$5.009 \cdot 10^{-5}$	0.031
	1.675 - 1.975		$1.702 \cdot 10^{-3}$	$9.178 \cdot 10^{-5}$	0.054	$5.263 \cdot 10^{-5}$	0.031
	1.975 - 2.275		$2.357 \cdot 10^{-3}$	$1.251 \cdot 10^{-4}$	0.053	$8.066 \cdot 10^{-5}$	0.034
	2.275 - 2.6		$2.247 \cdot 10^{-3}$	$1.066 \cdot 10^{-4}$	0.047	$7.061 \cdot 10^{-5}$	0.031
	2.6 - 3.1		$2.383 \cdot 10^{-3}$	$8.199 \cdot 10^{-5}$	0.034	$7.542 \cdot 10^{-5}$	0.032
	3.1 - 3.925		$2.482 \cdot 10^{-3}$	$8.512 \cdot 10^{-5}$	0.034	$1.008 \cdot 10^{-4}$	0.041
	3.925 - 4.9		$2.404 \cdot 10^{-3}$	$5.736 \cdot 10^{-5}$	0.024	$9.405 \cdot 10^{-5}$	0.039
	4.9 - 5.95		$1.982 \cdot 10^{-3}$	$7.371 \cdot 10^{-5}$	0.037	$6.876 \cdot 10^{-5}$	0.035
	5.95 - 6.92		$1.481 \cdot 10^{-3}$	$6.933 \cdot 10^{-5}$	0.047	$4.739 \cdot 10^{-5}$	0.032
	6.92 - 8.175		$1.076 \cdot 10^{-3}$	$5.126 \cdot 10^{-5}$	0.048	$3.297 \cdot 10^{-5}$	0.031
	8.175 - 9.5		$7.924 \cdot 10^{-4}$	$2.991 \cdot 10^{-5}$	0.038	$2.506 \cdot 10^{-5}$	0.032
	9.5 - 11.2		$5.492 \cdot 10^{-4}$	$2.240 \cdot 10^{-5}$	0.041	$1.777 \cdot 10^{-5}$	0.032
	11.2 - 13.325		$3.111 \cdot 10^{-4}$	$1.483 \cdot 10^{-5}$	0.048	$1.042 \cdot 10^{-5}$	0.033
	13.325 - 16.5		$1.199 \cdot 10^{-4}$	$7.910 \cdot 10^{-6}$	0.066	$3.662 \cdot 10^{-6}$	0.031
	16.5 - 19		$3.836 \cdot 10^{-5}$	$5.310 \cdot 10^{-6}$	0.138	$1.358 \cdot 10^{-6}$	0.035
60 - 80	0.6 - 1.25		$3.552 \cdot 10^{-3}$	$2.273 \cdot 10^{-4}$	0.064	$1.268 \cdot 10^{-4}$	0.036
	1.25 - 1.875		$4.040 \cdot 10^{-3}$	$1.379 \cdot 10^{-4}$	0.034	$1.314 \cdot 10^{-4}$	0.033
	1.875 - 2.275		$4.504 \cdot 10^{-3}$	$2.119 \cdot 10^{-4}$	0.047	$1.418 \cdot 10^{-4}$	0.031
	2.275 - 2.875		$4.270 \cdot 10^{-3}$	$1.702 \cdot 10^{-4}$	0.040	$1.312 \cdot 10^{-4}$	0.031
	2.875 - 3.55		$4.643 \cdot 10^{-3}$	$1.823 \cdot 10^{-4}$	0.039	$1.399 \cdot 10^{-4}$	0.030
	3.55 - 4.225		$4.199 \cdot 10^{-3}$	$1.753 \cdot 10^{-4}$	0.042	$1.251 \cdot 10^{-4}$	0.030
	4.225 - 4.95		$3.326 \cdot 10^{-3}$	$9.887 \cdot 10^{-5}$	0.030	$9.895 \cdot 10^{-5}$	0.030
	4.95 - 5.75		$2.624 \cdot 10^{-3}$	$8.792 \cdot 10^{-5}$	0.034	$7.864 \cdot 10^{-5}$	0.030
	5.75 - 6.625		$2.058 \cdot 10^{-3}$	$7.511 \cdot 10^{-5}$	0.036	$6.109 \cdot 10^{-5}$	0.030
	6.625 - 7.725		$1.579 \cdot 10^{-3}$	$5.729 \cdot 10^{-5}$	0.036	$4.761 \cdot 10^{-5}$	0.030
	7.725 - 9.325		$9.180 \cdot 10^{-4}$	$3.639 \cdot 10^{-5}$	0.040	$2.773 \cdot 10^{-5}$	0.030
	9.325 - 11.825		$4.816 \cdot 10^{-4}$	$2.080 \cdot 10^{-5}$	0.043	$1.482 \cdot 10^{-5}$	0.031
	11.825 - 14.325		$1.340 \cdot 10^{-4}$	$1.120 \cdot 10^{-5}$	0.084	$4.383 \cdot 10^{-6}$	0.033
80 - 100	0.5 - 1.3		$4.420 \cdot 10^{-3}$	$2.000 \cdot 10^{-4}$	0.045	$1.479 \cdot 10^{-4}$	0.033
	1.3 - 1.7		$6.238 \cdot 10^{-3}$	$2.895 \cdot 10^{-4}$	0.046	$2.050 \cdot 10^{-4}$	0.033
	1.7 - 2.2		$6.722 \cdot 10^{-3}$	$2.736 \cdot 10^{-4}$	0.041	$2.167 \cdot 10^{-4}$	0.032
	2.2 - 2.675		$6.233 \cdot 10^{-3}$	$2.566 \cdot 10^{-4}$	0.041	$1.993 \cdot 10^{-4}$	0.032
	2.675 - 3.1		$5.345 \cdot 10^{-3}$	$2.459 \cdot 10^{-4}$	0.046	$1.700 \cdot 10^{-4}$	0.032

Table D.1: Multiplicities of π^+ for the different (p, θ, z) bins with related statistical and systematic uncertainties

z	θ	p	$d\pi^+ / dp$	Δ_{stat}	$\Delta_{stat}\%$	Δ_{sys}	$\Delta_{sys}\%$
	[mrad]	[GeV/c]	[/ (GeV/c)/p.o.t]				
100 - 140	3.1 - 3.55		$4.736 \cdot 10^{-3}$	$1.449 \cdot 10^{-4}$	0.031	$1.471 \cdot 10^{-4}$	0.031
	3.55 - 4.05		$4.525 \cdot 10^{-3}$	$1.464 \cdot 10^{-4}$	0.032	$1.400 \cdot 10^{-4}$	0.031
	4.05 - 4.6		$3.364 \cdot 10^{-3}$	$1.182 \cdot 10^{-4}$	0.035	$1.035 \cdot 10^{-4}$	0.031
	4.6 - 5.275		$3.141 \cdot 10^{-3}$	$7.193 \cdot 10^{-5}$	0.023	$9.588 \cdot 10^{-5}$	0.031
	5.275 - 6.125		$2.282 \cdot 10^{-3}$	$7.796 \cdot 10^{-5}$	0.034	$6.843 \cdot 10^{-5}$	0.030
	6.125 - 7.275		$1.389 \cdot 10^{-3}$	$5.162 \cdot 10^{-5}$	0.037	$4.127 \cdot 10^{-5}$	0.030
	7.275 - 9.2		$6.968 \cdot 10^{-4}$	$2.774 \cdot 10^{-5}$	0.040	$2.087 \cdot 10^{-5}$	0.030
	9.2 - 11.7		$2.372 \cdot 10^{-4}$	$1.381 \cdot 10^{-5}$	0.058	$7.228 \cdot 10^{-6}$	0.030
	0.5 - 1.3		$1.365 \cdot 10^{-2}$	$3.086 \cdot 10^{-4}$	0.023	$4.001 \cdot 10^{-4}$	0.029
	1.3 - 1.65		$1.669 \cdot 10^{-2}$	$4.876 \cdot 10^{-4}$	0.029	$4.915 \cdot 10^{-4}$	0.029
	1.65 - 1.95		$1.511 \cdot 10^{-2}$	$6.339 \cdot 10^{-4}$	0.042	$4.420 \cdot 10^{-4}$	0.029
	1.95 - 2.275		$1.457 \cdot 10^{-2}$	$4.262 \cdot 10^{-4}$	0.029	$4.264 \cdot 10^{-4}$	0.029
	2.275 - 2.575		$1.272 \cdot 10^{-2}$	$3.833 \cdot 10^{-4}$	0.030	$3.713 \cdot 10^{-4}$	0.029
	2.575 - 2.9		$1.197 \cdot 10^{-2}$	$3.504 \cdot 10^{-4}$	0.029	$3.476 \cdot 10^{-4}$	0.029
	2.9 - 3.275		$1.075 \cdot 10^{-2}$	$3.190 \cdot 10^{-4}$	0.030	$3.142 \cdot 10^{-4}$	0.029
	3.275 - 3.675		$9.196 \cdot 10^{-3}$	$2.876 \cdot 10^{-4}$	0.031	$2.667 \cdot 10^{-4}$	0.029
	3.675 - 4.2		$6.886 \cdot 10^{-3}$	$2.265 \cdot 10^{-4}$	0.033	$1.988 \cdot 10^{-4}$	0.029
	4.2 - 4.8		$5.437 \cdot 10^{-3}$	$1.526 \cdot 10^{-4}$	0.028	$1.586 \cdot 10^{-4}$	0.029
	4.8 - 5.725		$3.592 \cdot 10^{-3}$	$1.227 \cdot 10^{-4}$	0.034	$1.049 \cdot 10^{-4}$	0.029
	5.725 - 7.075		$1.742 \cdot 10^{-3}$	$6.987 \cdot 10^{-5}$	0.040	$5.056 \cdot 10^{-5}$	0.029
	7.075 - 9.575		$5.679 \cdot 10^{-4}$	$2.915 \cdot 10^{-5}$	0.051	$1.663 \cdot 10^{-5}$	0.029
140 - 180	0.4 - 0.925		$1.520 \cdot 10^{-2}$	$7.223 \cdot 10^{-4}$	0.048	$1.348 \cdot 10^{-3}$	0.089
	0.925 - 1.45		$1.885 \cdot 10^{-2}$	$8.335 \cdot 10^{-4}$	0.044	$7.853 \cdot 10^{-4}$	0.042
	1.45 - 1.775		$1.693 \cdot 10^{-2}$	$8.092 \cdot 10^{-4}$	0.048	$5.489 \cdot 10^{-4}$	0.032
	1.775 - 2.1		$1.413 \cdot 10^{-2}$	$7.129 \cdot 10^{-4}$	0.050	$4.255 \cdot 10^{-4}$	0.030
	2.1 - 2.425		$1.256 \cdot 10^{-2}$	$4.888 \cdot 10^{-4}$	0.039	$3.715 \cdot 10^{-4}$	0.030
	2.425 - 2.825		$1.034 \cdot 10^{-2}$	$3.794 \cdot 10^{-4}$	0.037	$3.049 \cdot 10^{-4}$	0.029
	2.825 - 3.3		$7.793 \cdot 10^{-3}$	$3.073 \cdot 10^{-4}$	0.039	$2.266 \cdot 10^{-4}$	0.029
	3.3 - 3.95		$5.226 \cdot 10^{-3}$	$2.161 \cdot 10^{-4}$	0.041	$1.516 \cdot 10^{-4}$	0.029
	3.95 - 5.05		$2.610 \cdot 10^{-3}$	$1.154 \cdot 10^{-4}$	0.044	$7.730 \cdot 10^{-5}$	0.030
	5.05 - 7.55		$8.407 \cdot 10^{-4}$	$4.374 \cdot 10^{-5}$	0.052	$2.547 \cdot 10^{-5}$	0.030
	180 - 220	0.4 - 0.75	$1.677 \cdot 10^{-2}$	$9.586 \cdot 10^{-4}$	0.057	$5.234 \cdot 10^{-4}$	0.031
	0.75 - 1.05		$1.906 \cdot 10^{-2}$	$1.133 \cdot 10^{-3}$	0.059	$5.849 \cdot 10^{-4}$	0.031
220 - 260	1.05 - 1.325		$1.695 \cdot 10^{-2}$	$8.367 \cdot 10^{-4}$	0.049	$5.143 \cdot 10^{-4}$	0.030
	1.325 - 1.675		$1.584 \cdot 10^{-2}$	$7.803 \cdot 10^{-4}$	0.049	$4.747 \cdot 10^{-4}$	0.030
	1.675 - 2.075		$1.280 \cdot 10^{-2}$	$6.111 \cdot 10^{-4}$	0.048	$3.835 \cdot 10^{-4}$	0.030
	2.075 - 2.475		$1.015 \cdot 10^{-2}$	$5.454 \cdot 10^{-4}$	0.054	$3.084 \cdot 10^{-4}$	0.030
	2.475 - 2.925		$7.076 \cdot 10^{-3}$	$4.337 \cdot 10^{-4}$	0.061	$2.082 \cdot 10^{-4}$	0.029
	2.925 - 3.5		$4.337 \cdot 10^{-3}$	$2.570 \cdot 10^{-4}$	0.059	$1.272 \cdot 10^{-4}$	0.029
	3.5 - 4.4		$2.075 \cdot 10^{-3}$	$1.611 \cdot 10^{-4}$	0.078	$6.075 \cdot 10^{-5}$	0.029
	4.4 - 6.9		$5.983 \cdot 10^{-4}$	$4.670 \cdot 10^{-5}$	0.078	$1.740 \cdot 10^{-5}$	0.029
	0.3 - 0.7		$1.845 \cdot 10^{-2}$	$1.077 \cdot 10^{-3}$	0.058	$1.529 \cdot 10^{-3}$	0.083
	0.7 - 0.975		$2.066 \cdot 10^{-2}$	$1.154 \cdot 10^{-3}$	0.056	$1.018 \cdot 10^{-3}$	0.049

Table D.1: Multiplicities of π^+ for the different (p, θ, z) bins with related statistical and systematic uncertainties

z	θ	p	$d\pi^+ / dp$	Δ_{stat}	$\Delta_{stat}\%$	Δ_{sys}	$\Delta_{sys}\%$
	[mrad]	[GeV/c]	[/ (GeV/c)/p.o.t]				
260 - 300	0.975 - 1.325	1.697·10 ⁻²	8.231·10 ⁻⁴	0.049	6.156·10 ⁻⁴	0.036	
	1.325 - 1.675	1.479·10 ⁻²	7.122·10 ⁻⁴	0.048	4.729·10 ⁻⁴	0.032	
	1.675 - 2.15	1.053·10 ⁻²	5.128·10 ⁻⁴	0.049	3.113·10 ⁻⁴	0.030	
	2.15 - 2.925	5.573·10 ⁻³	2.687·10 ⁻⁴	0.048	1.659·10 ⁻⁴	0.030	
	2.925 - 5.425	1.301·10 ⁻³	7.952·10 ⁻⁵	0.061	3.809·10 ⁻⁵	0.029	
	0.3 - 0.675	1.631·10 ⁻²	1.085·10 ⁻³	0.067	1.486·10 ⁻³	0.091	
	0.675 - 0.975	2.004·10 ⁻²	1.006·10 ⁻³	0.050	1.072·10 ⁻³	0.053	
	0.975 - 1.25	1.563·10 ⁻²	8.975·10 ⁻⁴	0.057	6.078·10 ⁻⁴	0.039	
	1.25 - 1.625	1.378·10 ⁻²	6.930·10 ⁻⁴	0.050	4.514·10 ⁻⁴	0.033	
	1.625 - 2.225	7.720·10 ⁻³	3.744·10 ⁻⁴	0.048	2.289·10 ⁻⁴	0.030	
300 - 340	2.225 - 4.725	1.734·10 ⁻³	1.036·10 ⁻⁴	0.060	5.043·10 ⁻⁵	0.029	
	0.2 - 0.45	1.120·10 ⁻²	1.435·10 ⁻³	0.128	6.937·10 ⁻⁴	0.062	
	0.45 - 0.7	1.603·10 ⁻²	1.349·10 ⁻³	0.084	7.761·10 ⁻⁴	0.048	
	0.7 - 0.95	1.630·10 ⁻²	1.169·10 ⁻³	0.072	6.441·10 ⁻⁴	0.040	
	0.95 - 1.275	1.416·10 ⁻²	9.287·10 ⁻⁴	0.066	4.872·10 ⁻⁴	0.034	
z 3	1.275 - 2.55	6.282·10 ⁻³	4.674·10 ⁻⁴	0.074	2.100·10 ⁻⁴	0.033	
	0 - 20	0.7 - 1.3	1.626·10 ⁻⁵	7.442·10 ⁻⁶	0.458	8.759·10 ⁻⁷	0.054
	1.3 - 2.175	9.886·10 ⁻⁵	1.379·10 ⁻⁵	0.139	3.362·10 ⁻⁶	0.034	
	2.175 - 3.325	1.336·10 ⁻⁴	1.868·10 ⁻⁵	0.140	4.196·10 ⁻⁶	0.031	
	3.325 - 4.675	1.603·10 ⁻⁴	1.549·10 ⁻⁵	0.097	4.946·10 ⁻⁶	0.031	
	4.675 - 8.95	1.379·10 ⁻⁴	8.465·10 ⁻⁶	0.061	5.510·10 ⁻⁶	0.040	
	8.95 - 17.65	5.895·10 ⁻⁵	4.710·10 ⁻⁶	0.080	2.744·10 ⁻⁶	0.047	
	17.65 - 29.3	7.833·10 ⁻⁶	2.360·10 ⁻⁶	0.301	7.227·10 ⁻⁷	0.092	
	20 - 40	0.6 - 1.23	6.585·10 ⁻⁴	1.128·10 ⁻⁴	0.171	2.427·10 ⁻⁵	0.037
	1.23 - 1.775	8.357·10 ⁻⁴	5.187·10 ⁻⁵	0.062	2.786·10 ⁻⁵	0.033	
40 - 60	1.775 - 2.15	1.032·10 ⁻³	5.416·10 ⁻⁵	0.052	3.466·10 ⁻⁵	0.034	
	2.15 - 2.575	1.019·10 ⁻³	5.941·10 ⁻⁵	0.058	3.561·10 ⁻⁵	0.035	
	2.575 - 2.975	1.030·10 ⁻³	5.910·10 ⁻⁵	0.057	3.389·10 ⁻⁵	0.033	
	2.975 - 3.425	1.212·10 ⁻³	6.550·10 ⁻⁵	0.054	4.234·10 ⁻⁵	0.035	
	3.425 - 4.025	1.219·10 ⁻³	6.286·10 ⁻⁵	0.052	4.022·10 ⁻⁵	0.033	
	4.025 - 4.825	1.191·10 ⁻³	5.662·10 ⁻⁵	0.048	4.049·10 ⁻⁵	0.034	
	4.825 - 6.05	1.229·10 ⁻³	4.656·10 ⁻⁵	0.038	4.016·10 ⁻⁵	0.033	
	6.05 - 7.75	1.069·10 ⁻³	3.703·10 ⁻⁵	0.035	3.793·10 ⁻⁵	0.035	
	7.75 - 9.55	7.711·10 ⁻⁴	3.028·10 ⁻⁵	0.039	2.611·10 ⁻⁵	0.034	
	9.55 - 11.625	4.679·10 ⁻⁴	2.192·10 ⁻⁵	0.047	1.636·10 ⁻⁵	0.035	
	11.625 - 14.125	3.081·10 ⁻⁴	1.697·10 ⁻⁵	0.055	1.160·10 ⁻⁵	0.038	
	14.125 - 18.125	1.143·10 ⁻⁴	9.332·10 ⁻⁶	0.082	4.598·10 ⁻⁶	0.040	
	18.125 - 23.625	2.131·10 ⁻⁵	3.578·10 ⁻⁶	0.168	9.080·10 ⁻⁷	0.043	
	23.625 - 29.625	3.545·10 ⁻⁷	3.602·10 ⁻⁷	1.016	2.053·10 ⁻⁸	0.058	
40 - 60	0.6 - 1.175	1.860·10 ⁻³	1.560·10 ⁻⁴	0.084	5.688·10 ⁻⁵	0.031	
	1.175 - 1.675	2.371·10 ⁻³	9.675·10 ⁻⁵	0.041	7.183·10 ⁻⁵	0.030	
	1.675 - 1.975	2.728·10 ⁻³	1.230·10 ⁻⁴	0.045	8.195·10 ⁻⁵	0.030	
	1.975 - 2.275	2.714·10 ⁻³	1.258·10 ⁻⁴	0.046	7.979·10 ⁻⁵	0.029	

Table D.1: Multiplicities of π^+ for the different (p, θ, z) bins with related statistical and systematic uncertainties

z	θ	p	$d\pi^+ / dp$	Δ_{stat}	$\Delta_{stat}\%$	Δ_{sys}	$\Delta_{sys}\%$
	[mrad]	[GeV/c]	[/ (GeV/c)/p.o.t]				
60 - 80	2.275 - 2.6	2.979·10 ⁻³	1.333·10 ⁻⁴	0.045	9.005·10 ⁻⁵	0.030	
	2.6 - 3.1	2.997·10 ⁻³	1.320·10 ⁻⁴	0.044	8.892·10 ⁻⁵	0.030	
	3.1 - 3.925	3.248·10 ⁻³	1.060·10 ⁻⁴	0.033	9.586·10 ⁻⁵	0.030	
	3.925 - 4.9	3.032·10 ⁻³	6.146·10 ⁻⁵	0.020	8.788·10 ⁻⁵	0.029	
	4.9 - 5.95	2.462·10 ⁻³	8.040·10 ⁻⁵	0.033	7.159·10 ⁻⁵	0.029	
	5.95 - 6.92	1.970·10 ⁻³	7.705·10 ⁻⁵	0.039	5.708·10 ⁻⁵	0.029	
	6.92 - 8.175	1.331·10 ⁻³	5.443·10 ⁻⁵	0.041	3.897·10 ⁻⁵	0.029	
	8.175 - 9.5	1.051·10 ⁻³	3.399·10 ⁻⁵	0.032	3.075·10 ⁻⁵	0.029	
	9.5 - 11.2	6.516·10 ⁻⁴	2.435·10 ⁻⁵	0.037	1.893·10 ⁻⁵	0.029	
	11.2 - 13.325	3.915·10 ⁻⁴	1.776·10 ⁻⁵	0.045	1.172·10 ⁻⁵	0.030	
	13.325 - 16.5	1.569·10 ⁻⁴	9.569·10 ⁻⁶	0.061	4.745·10 ⁻⁶	0.030	
	16.5 - 19	3.980·10 ⁻⁵	7.867·10 ⁻⁶	0.198	1.237·10 ⁻⁶	0.031	
	0.6 - 1.25	3.205·10 ⁻³	2.021·10 ⁻⁴	0.063	1.011·10 ⁻⁴	0.032	
	1.25 - 1.875	3.956·10 ⁻³	1.266·10 ⁻⁴	0.032	1.241·10 ⁻⁴	0.031	
	1.875 - 2.275	4.395·10 ⁻³	2.325·10 ⁻⁴	0.053	1.372·10 ⁻⁴	0.031	
	2.275 - 2.875	4.343·10 ⁻³	1.818·10 ⁻⁴	0.042	1.349·10 ⁻⁴	0.031	
	2.875 - 3.55	4.310·10 ⁻³	1.627·10 ⁻⁴	0.038	1.351·10 ⁻⁴	0.031	
	3.55 - 4.225	3.632·10 ⁻³	1.580·10 ⁻⁴	0.044	1.114·10 ⁻⁴	0.031	
	4.225 - 4.95	3.323·10 ⁻³	1.043·10 ⁻⁴	0.031	1.055·10 ⁻⁴	0.032	
	4.95 - 5.75	2.766·10 ⁻³	8.913·10 ⁻⁵	0.032	8.470·10 ⁻⁵	0.031	
	5.75 - 6.625	1.969·10 ⁻³	7.281·10 ⁻⁵	0.037	6.004·10 ⁻⁵	0.030	
80 - 100	6.625 - 7.725	1.408·10 ⁻³	5.409·10 ⁻⁵	0.038	4.320·10 ⁻⁵	0.031	
	7.725 - 9.325	9.348·10 ⁻⁴	3.633·10 ⁻⁵	0.039	3.009·10 ⁻⁵	0.032	
	9.325 - 11.825	3.881·10 ⁻⁴	1.923·10 ⁻⁵	0.050	1.251·10 ⁻⁵	0.032	
	11.825 - 14.325	1.452·10 ⁻⁴	1.149·10 ⁻⁵	0.079	4.890·10 ⁻⁶	0.034	
	0.5 - 1.3	4.147·10 ⁻³	1.961·10 ⁻⁴	0.047	1.354·10 ⁻⁴	0.033	
	1.3 - 1.7	4.878·10 ⁻³	2.445·10 ⁻⁴	0.050	1.503·10 ⁻⁴	0.031	
	1.7 - 2.2	5.734·10 ⁻³	2.497·10 ⁻⁴	0.044	1.733·10 ⁻⁴	0.030	
	2.2 - 2.675	5.345·10 ⁻³	2.125·10 ⁻⁴	0.040	1.622·10 ⁻⁴	0.030	
	2.675 - 3.1	5.009·10 ⁻³	2.677·10 ⁻⁴	0.053	1.554·10 ⁻⁴	0.031	
	3.1 - 3.55	4.651·10 ⁻³	1.604·10 ⁻⁴	0.034	1.382·10 ⁻⁴	0.030	
	3.55 - 4.05	3.683·10 ⁻³	1.343·10 ⁻⁴	0.036	1.116·10 ⁻⁴	0.030	
100 - 140	4.05 - 4.6	3.080·10 ⁻³	1.048·10 ⁻⁴	0.034	9.063·10 ⁻⁵	0.029	
	4.6 - 5.275	2.607·10 ⁻³	6.391·10 ⁻⁵	0.025	7.865·10 ⁻⁵	0.030	
	5.275 - 6.125	1.753·10 ⁻³	6.958·10 ⁻⁵	0.040	5.194·10 ⁻⁵	0.030	
	6.125 - 7.275	1.252·10 ⁻³	4.767·10 ⁻⁵	0.038	3.818·10 ⁻⁵	0.031	
	7.275 - 9.2	6.016·10 ⁻⁴	2.666·10 ⁻⁵	0.044	1.810·10 ⁻⁵	0.030	
	9.2 - 11.7	2.148·10 ⁻⁴	1.373·10 ⁻⁵	0.064	6.826·10 ⁻⁶	0.032	
	0.5 - 1.3	1.082·10 ⁻²	3.723·10 ⁻⁴	0.034	3.230·10 ⁻⁴	0.030	
	1.3 - 1.65	1.289·10 ⁻²	5.483·10 ⁻⁴	0.043	3.842·10 ⁻⁴	0.030	
	1.65 - 1.95	1.245·10 ⁻²	6.198·10 ⁻⁴	0.050	3.801·10 ⁻⁴	0.031	
	1.95 - 2.275	1.219·10 ⁻²	5.274·10 ⁻⁴	0.043	3.720·10 ⁻⁴	0.031	
	2.275 - 2.575	1.064·10 ⁻²	3.415·10 ⁻⁴	0.032	3.144·10 ⁻⁴	0.030	

Table D.1: Multiplicities of π^+ for the different (p, θ, z) bins with related statistical and systematic uncertainties

z	θ [mrad]	p [GeV/c]	$d\pi^+ / dp$ [/(GeV/c)/p.o.t]	Δ_{stat}	$\Delta_{stat}\%$	Δ_{sys}	$\Delta_{sys}\%$
140 - 180	2.575 - 2.9	$9.734 \cdot 10^{-3}$	$3.176 \cdot 10^{-4}$	0.033	$2.946 \cdot 10^{-4}$	0.030	
	2.9 - 3.275	$8.524 \cdot 10^{-3}$	$2.514 \cdot 10^{-4}$	0.029	$2.545 \cdot 10^{-4}$	0.030	
	3.275 - 3.675	$7.214 \cdot 10^{-3}$	$2.292 \cdot 10^{-4}$	0.032	$2.103 \cdot 10^{-4}$	0.029	
	3.675 - 4.2	$5.524 \cdot 10^{-3}$	$1.998 \cdot 10^{-4}$	0.036	$1.653 \cdot 10^{-4}$	0.030	
	4.2 - 4.8	$4.255 \cdot 10^{-3}$	$1.466 \cdot 10^{-4}$	0.034	$1.246 \cdot 10^{-4}$	0.029	
	4.8 - 5.725	$2.782 \cdot 10^{-3}$	$1.072 \cdot 10^{-4}$	0.039	$8.349 \cdot 10^{-5}$	0.030	
	5.725 - 7.075	$1.414 \cdot 10^{-3}$	$6.176 \cdot 10^{-5}$	0.044	$4.246 \cdot 10^{-5}$	0.030	
	7.075 - 9.575	$4.755 \cdot 10^{-4}$	$2.685 \cdot 10^{-5}$	0.056	$1.478 \cdot 10^{-5}$	0.031	
	0.4 - 0.925	$1.406 \cdot 10^{-2}$	$7.003 \cdot 10^{-4}$	0.050	$1.029 \cdot 10^{-3}$	0.073	
	0.925 - 1.45	$1.664 \cdot 10^{-2}$	$8.174 \cdot 10^{-4}$	0.049	$6.334 \cdot 10^{-4}$	0.038	
	1.45 - 1.775	$1.420 \cdot 10^{-2}$	$7.308 \cdot 10^{-4}$	0.051	$4.429 \cdot 10^{-4}$	0.031	
	1.775 - 2.1	$1.243 \cdot 10^{-2}$	$6.999 \cdot 10^{-4}$	0.056	$3.731 \cdot 10^{-4}$	0.030	
	2.1 - 2.425	$9.952 \cdot 10^{-3}$	$3.200 \cdot 10^{-4}$	0.032	$3.036 \cdot 10^{-4}$	0.031	
	2.425 - 2.825	$8.615 \cdot 10^{-3}$	$3.269 \cdot 10^{-4}$	0.038	$2.557 \cdot 10^{-4}$	0.030	
	2.825 - 3.3	$6.913 \cdot 10^{-3}$	$2.726 \cdot 10^{-4}$	0.039	$2.090 \cdot 10^{-4}$	0.030	
	3.3 - 3.95	$4.215 \cdot 10^{-3}$	$1.876 \cdot 10^{-4}$	0.044	$1.230 \cdot 10^{-4}$	0.029	
	3.95 - 5.05	$2.406 \cdot 10^{-3}$	$1.147 \cdot 10^{-4}$	0.048	$7.113 \cdot 10^{-5}$	0.030	
	5.05 - 7.55	$5.298 \cdot 10^{-4}$	$3.482 \cdot 10^{-5}$	0.066	$1.628 \cdot 10^{-5}$	0.031	
180 - 220	0.4 - 0.75	$1.373 \cdot 10^{-2}$	$8.661 \cdot 10^{-4}$	0.063	$1.259 \cdot 10^{-3}$	0.092	
	0.75 - 1.05	$1.592 \cdot 10^{-2}$	$1.063 \cdot 10^{-3}$	0.067	$8.722 \cdot 10^{-4}$	0.055	
	1.05 - 1.325	$1.778 \cdot 10^{-2}$	$8.425 \cdot 10^{-4}$	0.047	$7.101 \cdot 10^{-4}$	0.040	
	1.325 - 1.675	$1.416 \cdot 10^{-2}$	$7.596 \cdot 10^{-4}$	0.054	$4.758 \cdot 10^{-4}$	0.034	
	1.675 - 2.075	$9.753 \cdot 10^{-3}$	$5.511 \cdot 10^{-4}$	0.057	$3.159 \cdot 10^{-4}$	0.032	
	2.075 - 2.475	$8.778 \cdot 10^{-3}$	$3.547 \cdot 10^{-4}$	0.040	$2.704 \cdot 10^{-4}$	0.031	
	2.475 - 2.925	$5.395 \cdot 10^{-3}$	$3.738 \cdot 10^{-4}$	0.069	$1.599 \cdot 10^{-4}$	0.030	
	2.925 - 3.5	$3.489 \cdot 10^{-3}$	$2.054 \cdot 10^{-4}$	0.059	$1.040 \cdot 10^{-4}$	0.030	
	3.5 - 4.4	$1.991 \cdot 10^{-3}$	$7.771 \cdot 10^{-5}$	0.039	$5.843 \cdot 10^{-5}$	0.029	
	4.4 - 6.9	$4.388 \cdot 10^{-4}$	$2.291 \cdot 10^{-5}$	0.052	$1.408 \cdot 10^{-5}$	0.032	
220 - 260	0.3 - 0.7	$1.238 \cdot 10^{-2}$	$8.439 \cdot 10^{-4}$	0.068	$1.724 \cdot 10^{-3}$	0.139	
	0.7 - 0.975	$1.692 \cdot 10^{-2}$	$1.027 \cdot 10^{-3}$	0.061	$1.279 \cdot 10^{-3}$	0.076	
	0.975 - 1.325	$1.653 \cdot 10^{-2}$	$7.865 \cdot 10^{-4}$	0.048	$8.059 \cdot 10^{-4}$	0.049	
	1.325 - 1.675	$1.175 \cdot 10^{-2}$	$6.602 \cdot 10^{-4}$	0.056	$4.114 \cdot 10^{-4}$	0.035	
	1.675 - 2.15	$8.016 \cdot 10^{-3}$	$3.912 \cdot 10^{-4}$	0.049	$2.575 \cdot 10^{-4}$	0.032	
	2.15 - 2.925	$4.993 \cdot 10^{-3}$	$2.751 \cdot 10^{-4}$	0.055	$1.483 \cdot 10^{-4}$	0.030	
	2.925 - 5.425	$9.495 \cdot 10^{-4}$	$5.603 \cdot 10^{-5}$	0.059	$2.811 \cdot 10^{-5}$	0.030	
	260 - 300	$0.3 - 0.675$	$1.289 \cdot 10^{-2}$	$8.724 \cdot 10^{-4}$	0.068	$6.641 \cdot 10^{-4}$	0.052
300 - 340	0.675 - 0.975	$1.977 \cdot 10^{-2}$	$1.068 \cdot 10^{-3}$	0.054	$9.119 \cdot 10^{-4}$	0.046	
	0.975 - 1.25	$1.576 \cdot 10^{-2}$	$8.823 \cdot 10^{-4}$	0.056	$6.732 \cdot 10^{-4}$	0.043	
	1.25 - 1.625	$1.002 \cdot 10^{-2}$	$5.774 \cdot 10^{-4}$	0.058	$4.019 \cdot 10^{-4}$	0.040	
	1.625 - 2.225	$6.115 \cdot 10^{-3}$	$3.525 \cdot 10^{-4}$	0.058	$2.241 \cdot 10^{-4}$	0.037	
	2.225 - 4.725	$1.175 \cdot 10^{-3}$	$5.252 \cdot 10^{-5}$	0.045	$3.621 \cdot 10^{-5}$	0.031	
	0.2 - 0.45	$1.243 \cdot 10^{-2}$	$1.636 \cdot 10^{-3}$	0.132	$4.875 \cdot 10^{-4}$	0.039	
	0.45 - 0.7	$1.471 \cdot 10^{-2}$	$1.131 \cdot 10^{-3}$	0.077	$4.954 \cdot 10^{-4}$	0.034	

Table D.1: Multiplicities of π^+ for the different (p, θ, z) bins with related statistical and systematic uncertainties

z	θ	p	$d\pi^+ / dp$	Δ_{stat}	$\Delta_{stat}\%$	Δ_{sys}	$\Delta_{sys}\%$
		[mrad]	[(GeV/c)/p.o.t]				
z 4	0 - 20	0.7 - 0.95	1.550·10 ⁻²	1.062·10 ⁻³	0.069	4.808·10 ⁻⁴	0.031
		0.95 - 1.275	1.276·10 ⁻²	7.607·10 ⁻⁴	0.060	3.901·10 ⁻⁴	0.031
		1.275 - 2.55	6.060·10 ⁻³	3.015·10 ⁻⁴	0.050	1.901·10 ⁻⁴	0.031
		0.7 - 1.3	3.260·10 ⁻⁵	1.678·10 ⁻⁵	0.515	1.904·10 ⁻⁶	0.058
		1.3 - 2.175	1.010·10 ⁻⁴	1.282·10 ⁻⁵	0.127	3.783·10 ⁻⁶	0.037
		2.175 - 3.325	1.589·10 ⁻⁴	1.349·10 ⁻⁵	0.085	5.386·10 ⁻⁶	0.034
		3.325 - 4.675	1.424·10 ⁻⁴	1.102·10 ⁻⁵	0.077	4.954·10 ⁻⁶	0.035
		4.675 - 8.95	1.644·10 ⁻⁴	8.345·10 ⁻⁶	0.051	5.935·10 ⁻⁶	0.036
		8.95 - 17.65	5.542·10 ⁻⁵	3.889·10 ⁻⁶	0.070	2.760·10 ⁻⁶	0.050
		17.65 - 29.3	3.683·10 ⁻⁶	1.299·10 ⁻⁶	0.353	2.685·10 ⁻⁷	0.073
20 - 40	0.6 - 1.23	0.6 - 1.23	6.035·10 ⁻⁴	1.094·10 ⁻⁴	0.181	2.236·10 ⁻⁵	0.037
		1.23 - 1.775	9.352·10 ⁻⁴	5.458·10 ⁻⁵	0.058	3.318·10 ⁻⁵	0.035
		1.775 - 2.15	9.643·10 ⁻⁴	5.827·10 ⁻⁵	0.060	3.273·10 ⁻⁵	0.034
		2.15 - 2.575	1.140·10 ⁻³	6.568·10 ⁻⁵	0.058	4.112·10 ⁻⁵	0.036
		2.575 - 2.975	1.126·10 ⁻³	6.286·10 ⁻⁵	0.056	3.908·10 ⁻⁵	0.035
		2.975 - 3.425	1.065·10 ⁻³	6.081·10 ⁻⁵	0.057	3.601·10 ⁻⁵	0.034
		3.425 - 4.025	1.164·10 ⁻³	6.532·10 ⁻⁵	0.056	3.989·10 ⁻⁵	0.034
		4.025 - 4.825	1.195·10 ⁻³	5.719·10 ⁻⁵	0.048	4.090·10 ⁻⁵	0.034
		4.825 - 6.05	1.344·10 ⁻³	4.807·10 ⁻⁵	0.036	4.532·10 ⁻⁵	0.034
		6.05 - 7.75	1.113·10 ⁻³	3.695·10 ⁻⁵	0.033	3.769·10 ⁻⁵	0.034
40 - 60	0.6 - 1.175	7.75 - 9.55	7.831·10 ⁻⁴	3.182·10 ⁻⁵	0.041	2.661·10 ⁻⁵	0.034
		9.55 - 11.625	5.433·10 ⁻⁴	2.391·10 ⁻⁵	0.044	1.837·10 ⁻⁵	0.034
		11.625 - 14.125	2.763·10 ⁻⁴	1.546·10 ⁻⁵	0.056	9.438·10 ⁻⁶	0.034
		14.125 - 18.125	1.333·10 ⁻⁴	9.217·10 ⁻⁶	0.069	5.170·10 ⁻⁶	0.039
		18.125 - 23.625	2.854·10 ⁻⁵	4.632·10 ⁻⁶	0.162	1.047·10 ⁻⁶	0.037
		23.625 - 29.625	4.960·10 ⁻⁶	2.555·10 ⁻⁶	0.515	3.918·10 ⁻⁷	0.079
		0.6 - 1.175	1.669·10 ⁻³	1.431·10 ⁻⁴	0.086	5.760·10 ⁻⁵	0.035
		1.175 - 1.675	2.211·10 ⁻³	8.910·10 ⁻⁵	0.040	7.025·10 ⁻⁵	0.032
		1.675 - 1.975	2.166·10 ⁻³	9.161·10 ⁻⁵	0.042	7.016·10 ⁻⁵	0.032
		1.975 - 2.275	2.341·10 ⁻³	1.089·10 ⁻⁴	0.047	7.363·10 ⁻⁵	0.031
60 - 80	0.6 - 1.25	2.275 - 2.6	2.572·10 ⁻³	1.180·10 ⁻⁴	0.046	7.731·10 ⁻⁵	0.030
		2.6 - 3.1	2.760·10 ⁻³	1.031·10 ⁻⁴	0.037	8.573·10 ⁻⁵	0.031
		3.1 - 3.925	2.428·10 ⁻³	9.339·10 ⁻⁵	0.038	7.868·10 ⁻⁵	0.032
		3.925 - 4.9	2.420·10 ⁻³	8.490·10 ⁻⁵	0.035	7.586·10 ⁻⁵	0.031
		4.9 - 5.95	1.933·10 ⁻³	6.915·10 ⁻⁵	0.036	5.772·10 ⁻⁵	0.030
		5.95 - 6.92	1.656·10 ⁻³	6.998·10 ⁻⁵	0.042	4.848·10 ⁻⁵	0.029
		6.92 - 8.175	1.252·10 ⁻³	5.046·10 ⁻⁵	0.040	3.648·10 ⁻⁵	0.029
		8.175 - 9.5	8.165·10 ⁻⁴	3.185·10 ⁻⁵	0.039	2.469·10 ⁻⁵	0.030
		9.5 - 11.2	5.186·10 ⁻⁴	2.220·10 ⁻⁵	0.043	1.598·10 ⁻⁵	0.031
		11.2 - 13.325	3.163·10 ⁻⁴	1.571·10 ⁻⁵	0.050	1.030·10 ⁻⁵	0.033
	13.325 - 16.5	13.325 - 16.5	1.253·10 ⁻⁴	7.951·10 ⁻⁶	0.063	3.854·10 ⁻⁶	0.031
		16.5 - 19	2.844·10 ⁻⁵	4.613·10 ⁻⁶	0.162	1.113·10 ⁻⁶	0.039
		0.6 - 1.25	2.332·10 ⁻³	1.624·10 ⁻⁴	0.070	7.127·10 ⁻⁵	0.031

Table D.1: Multiplicities of π^+ for the different (p, θ, z) bins with related statistical and systematic uncertainties

z	θ	p	$d\pi^+ / dp$	Δ_{stat}	$\Delta_{stat}\%$	Δ_{sys}	$\Delta_{sys}\%$
	[mrad]	[GeV/c]	[/ (GeV/c)/p.o.t]				
	1.25 - 1.875		$3.458 \cdot 10^{-3}$	$1.237 \cdot 10^{-4}$	0.036	$1.045 \cdot 10^{-4}$	0.030
	1.875 - 2.275		$3.651 \cdot 10^{-3}$	$2.065 \cdot 10^{-4}$	0.057	$1.088 \cdot 10^{-4}$	0.030
	2.275 - 2.875		$3.777 \cdot 10^{-3}$	$1.674 \cdot 10^{-4}$	0.044	$1.174 \cdot 10^{-4}$	0.031
	2.875 - 3.55		$3.385 \cdot 10^{-3}$	$1.430 \cdot 10^{-4}$	0.042	$1.044 \cdot 10^{-4}$	0.031
	3.55 - 4.225		$3.077 \cdot 10^{-3}$	$1.424 \cdot 10^{-4}$	0.046	$9.130 \cdot 10^{-5}$	0.030
	4.225 - 4.95		$2.317 \cdot 10^{-3}$	$8.272 \cdot 10^{-5}$	0.036	$6.708 \cdot 10^{-5}$	0.029
	4.95 - 5.75		$1.882 \cdot 10^{-3}$	$7.356 \cdot 10^{-5}$	0.039	$5.614 \cdot 10^{-5}$	0.030
	5.75 - 6.625		$1.515 \cdot 10^{-3}$	$6.923 \cdot 10^{-5}$	0.046	$4.533 \cdot 10^{-5}$	0.030
	6.625 - 7.725		$1.138 \cdot 10^{-3}$	$4.411 \cdot 10^{-5}$	0.039	$3.417 \cdot 10^{-5}$	0.030
	7.725 - 9.325		$6.341 \cdot 10^{-4}$	$4.174 \cdot 10^{-5}$	0.066	$1.870 \cdot 10^{-5}$	0.029
	9.325 - 11.825		$3.209 \cdot 10^{-4}$	$1.679 \cdot 10^{-5}$	0.052	$9.497 \cdot 10^{-6}$	0.030
	11.825 - 14.325		$9.091 \cdot 10^{-5}$	$1.134 \cdot 10^{-5}$	0.125	$2.806 \cdot 10^{-6}$	0.031
80 - 100	0.5 - 1.3		$3.399 \cdot 10^{-3}$	$1.490 \cdot 10^{-4}$	0.044	$1.437 \cdot 10^{-4}$	0.042
	1.3 - 1.7		$4.355 \cdot 10^{-3}$	$1.717 \cdot 10^{-4}$	0.039	$1.635 \cdot 10^{-4}$	0.038
	1.7 - 2.2		$4.380 \cdot 10^{-3}$	$3.141 \cdot 10^{-4}$	0.072	$1.569 \cdot 10^{-4}$	0.036
	2.2 - 2.675		$3.928 \cdot 10^{-3}$	$2.019 \cdot 10^{-4}$	0.051	$1.311 \cdot 10^{-4}$	0.033
	2.675 - 3.1		$3.713 \cdot 10^{-3}$	$1.978 \cdot 10^{-4}$	0.053	$1.201 \cdot 10^{-4}$	0.032
	3.1 - 3.55		$3.038 \cdot 10^{-3}$	$1.096 \cdot 10^{-4}$	0.036	$9.496 \cdot 10^{-5}$	0.031
	3.55 - 4.05		$2.855 \cdot 10^{-3}$	$1.168 \cdot 10^{-4}$	0.041	$8.606 \cdot 10^{-5}$	0.030
	4.05 - 4.6		$2.285 \cdot 10^{-3}$	$9.350 \cdot 10^{-5}$	0.041	$6.896 \cdot 10^{-5}$	0.030
	4.6 - 5.275		$1.813 \cdot 10^{-3}$	$7.819 \cdot 10^{-5}$	0.043	$5.394 \cdot 10^{-5}$	0.030
	5.275 - 6.125		$1.521 \cdot 10^{-3}$	$6.409 \cdot 10^{-5}$	0.042	$4.526 \cdot 10^{-5}$	0.030
	6.125 - 7.275		$8.559 \cdot 10^{-4}$	$4.076 \cdot 10^{-5}$	0.048	$2.485 \cdot 10^{-5}$	0.029
	7.275 - 9.2		$4.706 \cdot 10^{-4}$	$2.063 \cdot 10^{-5}$	0.044	$1.406 \cdot 10^{-5}$	0.030
	9.2 - 11.7		$1.197 \cdot 10^{-4}$	$1.007 \cdot 10^{-5}$	0.084	$3.517 \cdot 10^{-6}$	0.029
100 - 140	0.5 - 1.3		$9.039 \cdot 10^{-3}$	$3.486 \cdot 10^{-4}$	0.039	$2.722 \cdot 10^{-4}$	0.030
	1.3 - 1.65		$1.030 \cdot 10^{-2}$	$5.182 \cdot 10^{-4}$	0.050	$3.037 \cdot 10^{-4}$	0.029
	1.65 - 1.95		$9.606 \cdot 10^{-3}$	$4.881 \cdot 10^{-4}$	0.051	$2.831 \cdot 10^{-4}$	0.029
	1.95 - 2.275		$8.344 \cdot 10^{-3}$	$4.491 \cdot 10^{-4}$	0.054	$2.482 \cdot 10^{-4}$	0.030
	2.275 - 2.575		$8.523 \cdot 10^{-3}$	$3.119 \cdot 10^{-4}$	0.037	$2.585 \cdot 10^{-4}$	0.030
	2.575 - 2.9		$7.017 \cdot 10^{-3}$	$2.864 \cdot 10^{-4}$	0.041	$2.071 \cdot 10^{-4}$	0.030
	2.9 - 3.275		$5.864 \cdot 10^{-3}$	$2.482 \cdot 10^{-4}$	0.042	$1.725 \cdot 10^{-4}$	0.029
	3.275 - 3.675		$5.427 \cdot 10^{-3}$	$2.159 \cdot 10^{-4}$	0.040	$1.648 \cdot 10^{-4}$	0.030
	3.675 - 4.2		$3.928 \cdot 10^{-3}$	$1.504 \cdot 10^{-4}$	0.038	$1.160 \cdot 10^{-4}$	0.030
	4.2 - 4.8		$3.214 \cdot 10^{-3}$	$1.106 \cdot 10^{-4}$	0.034	$9.879 \cdot 10^{-5}$	0.031
	4.8 - 5.725		$2.164 \cdot 10^{-3}$	$9.615 \cdot 10^{-5}$	0.044	$6.555 \cdot 10^{-5}$	0.030
	5.725 - 7.075		$9.664 \cdot 10^{-4}$	$5.047 \cdot 10^{-5}$	0.052	$2.829 \cdot 10^{-5}$	0.029
	7.075 - 9.575		$3.183 \cdot 10^{-4}$	$2.241 \cdot 10^{-5}$	0.070	$9.641 \cdot 10^{-6}$	0.030
140 - 180	0.4 - 0.925		$1.102 \cdot 10^{-2}$	$6.138 \cdot 10^{-4}$	0.056	$1.045 \cdot 10^{-3}$	0.095
	0.925 - 1.45		$1.141 \cdot 10^{-2}$	$6.218 \cdot 10^{-4}$	0.054	$4.946 \cdot 10^{-4}$	0.043
	1.45 - 1.775		$1.052 \cdot 10^{-2}$	$6.268 \cdot 10^{-4}$	0.060	$3.559 \cdot 10^{-4}$	0.034
	1.775 - 2.1		$9.650 \cdot 10^{-3}$	$6.031 \cdot 10^{-4}$	0.062	$2.991 \cdot 10^{-4}$	0.031
	2.1 - 2.425		$7.647 \cdot 10^{-3}$	$3.725 \cdot 10^{-4}$	0.049	$2.268 \cdot 10^{-4}$	0.030

Table D.1: Multiplicities of π^+ for the different (p, θ, z) bins with related statistical and systematic uncertainties

z	θ	p	$d\pi^+ / dp$	Δ_{stat}	$\Delta_{stat}\%$	Δ_{sys}	$\Delta_{sys}\%$
	[mrad]	[GeV/c]	[/ (GeV/c)/p.o.t]				
180 - 220	2.425 - 2.825	6.076·10 ⁻³	2.173·10 ⁻⁴	0.036	1.914·10 ⁻⁴	0.031	
	2.825 - 3.3	4.889·10 ⁻³	2.468·10 ⁻⁴	0.050	1.514·10 ⁻⁴	0.031	
	3.3 - 3.95	3.016·10 ⁻³	1.654·10 ⁻⁴	0.055	8.948·10 ⁻⁵	0.030	
	3.95 - 5.05	1.794·10 ⁻³	9.477·10 ⁻⁵	0.053	5.250·10 ⁻⁵	0.029	
	5.05 - 7.55	4.625·10 ⁻⁴	3.289·10 ⁻⁵	0.071	1.367·10 ⁻⁵	0.030	
	0.4 - 0.75	1.035·10 ⁻²	7.444·10 ⁻⁴	0.072	7.456·10 ⁻⁴	0.072	
	0.75 - 1.05	1.086·10 ⁻²	8.672·10 ⁻⁴	0.080	4.980·10 ⁻⁴	0.046	
	1.05 - 1.325	1.301·10 ⁻²	7.865·10 ⁻⁴	0.060	4.606·10 ⁻⁴	0.035	
	1.325 - 1.675	1.065·10 ⁻²	5.463·10 ⁻⁴	0.051	3.428·10 ⁻⁴	0.032	
	1.675 - 2.075	8.263·10 ⁻³	4.924·10 ⁻⁴	0.060	2.477·10 ⁻⁴	0.030	
	2.075 - 2.475	6.247·10 ⁻³	4.246·10 ⁻⁴	0.068	1.866·10 ⁻⁴	0.030	
	2.475 - 2.925	4.176·10 ⁻³	2.796·10 ⁻⁴	0.067	1.239·10 ⁻⁴	0.030	
	2.925 - 3.5	2.800·10 ⁻³	2.383·10 ⁻⁴	0.085	8.568·10 ⁻⁵	0.031	
	3.5 - 4.4	1.466·10 ⁻³	9.883·10 ⁻⁵	0.067	4.259·10 ⁻⁵	0.029	
	4.4 - 6.9	3.162·10 ⁻⁴	2.828·10 ⁻⁵	0.089	9.329·10 ⁻⁶	0.030	
220 - 260	0.3 - 0.7	1.185·10 ⁻²	8.281·10 ⁻⁴	0.070	1.225·10 ⁻³	0.103	
	0.7 - 0.975	1.273·10 ⁻²	9.856·10 ⁻⁴	0.077	7.466·10 ⁻⁴	0.059	
	0.975 - 1.325	1.073·10 ⁻²	6.525·10 ⁻⁴	0.061	4.317·10 ⁻⁴	0.040	
	1.325 - 1.675	1.008·10 ⁻²	5.345·10 ⁻⁴	0.053	3.516·10 ⁻⁴	0.035	
	1.675 - 2.15	6.892·10 ⁻³	4.106·10 ⁻⁴	0.060	2.086·10 ⁻⁴	0.030	
	2.15 - 2.925	3.421·10 ⁻³	2.266·10 ⁻⁴	0.066	1.002·10 ⁻⁴	0.029	
	2.925 - 5.425	6.843·10 ⁻⁴	5.724·10 ⁻⁵	0.084	2.125·10 ⁻⁵	0.031	
260 - 300	0.3 - 0.675	1.126·10 ⁻²	8.766·10 ⁻⁴	0.078	1.139·10 ⁻³	0.101	
	0.675 - 0.975	1.193·10 ⁻²	7.879·10 ⁻⁴	0.066	6.899·10 ⁻⁴	0.058	
	0.975 - 1.25	1.162·10 ⁻²	6.124·10 ⁻⁴	0.053	4.776·10 ⁻⁴	0.041	
	1.25 - 1.625	8.528·10 ⁻³	4.179·10 ⁻⁴	0.049	2.846·10 ⁻⁴	0.033	
	1.625 - 2.225	4.494·10 ⁻³	2.242·10 ⁻⁴	0.050	1.470·10 ⁻⁴	0.033	
	2.225 - 4.725	9.484·10 ⁻⁴	6.712·10 ⁻⁵	0.071	2.838·10 ⁻⁵	0.030	
	300 - 340	0.2 - 0.45	7.869·10 ⁻³	1.245·10 ⁻³	0.158	7.402·10 ⁻⁴	0.094
z 5	0 - 20	0.45 - 0.7	1.063·10 ⁻²	9.206·10 ⁻⁴	0.087	6.566·10 ⁻⁴	0.062
	0.7 - 0.95	1.177·10 ⁻²	8.658·10 ⁻⁴	0.074	5.234·10 ⁻⁴	0.044	
	0.95 - 1.275	9.391·10 ⁻³	6.200·10 ⁻⁴	0.066	3.321·10 ⁻⁴	0.035	
	1.275 - 2.55	4.263·10 ⁻³	2.335·10 ⁻⁴	0.055	1.249·10 ⁻⁴	0.029	
	0.7 - 1.3	5.529·10 ⁻⁵	2.250·10 ⁻⁵	0.407	2.505·10 ⁻⁶	0.045	
	1.3 - 2.175	1.226·10 ⁻⁴	1.379·10 ⁻⁵	0.113	5.053·10 ⁻⁶	0.041	
	2.175 - 3.325	1.535·10 ⁻⁴	1.931·10 ⁻⁵	0.126	6.517·10 ⁻⁶	0.042	
	3.325 - 4.675	1.910·10 ⁻⁴	1.294·10 ⁻⁵	0.068	5.742·10 ⁻⁶	0.030	
	4.675 - 8.95	1.638·10 ⁻⁴	9.118·10 ⁻⁶	0.056	5.173·10 ⁻⁶	0.032	
	8.95 - 17.65	7.000·10 ⁻⁵	4.304·10 ⁻⁶	0.061	2.582·10 ⁻⁶	0.037	
20 - 40	17.65 - 29.3	3.486·10 ⁻⁶	1.307·10 ⁻⁶	0.375	3.318·10 ⁻⁷	0.095	
	0.6 - 1.23	4.950·10 ⁻⁴	8.612·10 ⁻⁵	0.174	1.704·10 ⁻⁵	0.034	
	1.23 - 1.775	7.656·10 ⁻⁴	4.702·10 ⁻⁵	0.061	2.466·10 ⁻⁵	0.032	
	1.775 - 2.15	8.954·10 ⁻⁴	5.864·10 ⁻⁵	0.065	2.829·10 ⁻⁵	0.032	

Table D.1: Multiplicities of π^+ for the different (p, θ, z) bins with related statistical and systematic uncertainties

z	θ	p	$d\mathbf{n}^{\pi^+}/dp$	Δ_{stat}	$\Delta_{stat}\%$	Δ_{sys}	$\Delta_{sys}\%$
	[mrad]	[GeV/c]	[/ (GeV/c)/p.o.t]				
40 - 60	2.15 - 2.575	9.609·10 ⁻⁴	7.949·10 ⁻⁵	0.083	3.014·10 ⁻⁵	0.031	
	2.575 - 2.975	9.917·10 ⁻⁴	5.668·10 ⁻⁵	0.057	2.976·10 ⁻⁵	0.030	
	2.975 - 3.425	1.011·10 ⁻³	5.110·10 ⁻⁵	0.051	3.064·10 ⁻⁵	0.030	
	3.425 - 4.025	9.147·10 ⁻⁴	5.425·10 ⁻⁵	0.059	3.061·10 ⁻⁵	0.033	
	4.025 - 4.825	1.135·10 ⁻³	5.328·10 ⁻⁵	0.047	3.496·10 ⁻⁵	0.031	
	4.825 - 6.05	1.016·10 ⁻³	4.205·10 ⁻⁵	0.041	3.195·10 ⁻⁵	0.031	
	6.05 - 7.75	8.610·10 ⁻⁴	3.225·10 ⁻⁵	0.037	2.701·10 ⁻⁵	0.031	
	7.75 - 9.55	6.778·10 ⁻⁴	2.786·10 ⁻⁵	0.041	2.359·10 ⁻⁵	0.035	
	9.55 - 11.625	4.095·10 ⁻⁴	1.956·10 ⁻⁵	0.048	1.331·10 ⁻⁵	0.032	
	11.625 - 14.125	2.267·10 ⁻⁴	1.398·10 ⁻⁵	0.062	7.874·10 ⁻⁶	0.035	
	14.125 - 18.125	9.710·10 ⁻⁵	7.332·10 ⁻⁶	0.076	3.718·10 ⁻⁶	0.038	
	18.125 - 23.625	2.072·10 ⁻⁵	5.425·10 ⁻⁶	0.262	7.766·10 ⁻⁷	0.037	
	0.6 - 1.175	1.467·10 ⁻³	1.315·10 ⁻⁴	0.090	5.326·10 ⁻⁵	0.036	
	1.175 - 1.675	1.635·10 ⁻³	7.651·10 ⁻⁵	0.047	5.475·10 ⁻⁵	0.033	
	1.675 - 1.975	1.761·10 ⁻³	8.935·10 ⁻⁵	0.051	5.840·10 ⁻⁵	0.033	
	1.975 - 2.275	1.967·10 ⁻³	9.925·10 ⁻⁵	0.050	6.312·10 ⁻⁵	0.032	
	2.275 - 2.6	2.006·10 ⁻³	1.197·10 ⁻⁴	0.060	6.322·10 ⁻⁵	0.032	
	2.6 - 3.1	2.073·10 ⁻³	1.044·10 ⁻⁴	0.050	6.220·10 ⁻⁵	0.030	
	3.1 - 3.925	1.906·10 ⁻³	7.748·10 ⁻⁵	0.041	5.721·10 ⁻⁵	0.030	
	3.925 - 4.9	1.866·10 ⁻³	6.044·10 ⁻⁵	0.032	5.600·10 ⁻⁵	0.030	
	4.9 - 5.95	1.692·10 ⁻³	6.813·10 ⁻⁵	0.040	5.124·10 ⁻⁵	0.030	
	5.95 - 6.92	1.130·10 ⁻³	5.805·10 ⁻⁵	0.051	3.505·10 ⁻⁵	0.031	
60 - 80	6.92 - 8.175	8.532·10 ⁻⁴	4.219·10 ⁻⁵	0.049	2.544·10 ⁻⁵	0.030	
	8.175 - 9.5	6.310·10 ⁻⁴	2.748·10 ⁻⁵	0.044	1.897·10 ⁻⁵	0.030	
	9.5 - 11.2	3.842·10 ⁻⁴	1.876·10 ⁻⁵	0.049	1.203·10 ⁻⁵	0.031	
	11.2 - 13.325	2.185·10 ⁻⁴	1.203·10 ⁻⁵	0.055	6.664·10 ⁻⁶	0.031	
	13.325 - 16.5	7.533·10 ⁻⁵	6.508·10 ⁻⁶	0.086	2.331·10 ⁻⁶	0.031	
	16.5 - 19	3.060·10 ⁻⁵	4.517·10 ⁻⁶	0.148	1.198·10 ⁻⁶	0.039	
	0.6 - 1.25	1.833·10 ⁻³	1.387·10 ⁻⁴	0.076	6.108·10 ⁻⁵	0.033	
	1.25 - 1.875	2.662·10 ⁻³	1.136·10 ⁻⁴	0.043	8.597·10 ⁻⁵	0.032	
	1.875 - 2.275	2.765·10 ⁻³	1.825·10 ⁻⁴	0.066	8.572·10 ⁻⁵	0.031	
	2.275 - 2.875	2.660·10 ⁻³	1.401·10 ⁻⁴	0.053	8.059·10 ⁻⁵	0.030	
	2.875 - 3.55	2.372·10 ⁻³	1.231·10 ⁻⁴	0.052	7.121·10 ⁻⁵	0.030	
	3.55 - 4.225	2.195·10 ⁻³	1.021·10 ⁻⁴	0.047	6.764·10 ⁻⁵	0.031	
	4.225 - 4.95	1.908·10 ⁻³	8.092·10 ⁻⁵	0.042	5.736·10 ⁻⁵	0.030	
	4.95 - 5.75	1.557·10 ⁻³	6.593·10 ⁻⁵	0.042	4.683·10 ⁻⁵	0.030	
	5.75 - 6.625	1.067·10 ⁻³	8.879·10 ⁻⁵	0.083	3.450·10 ⁻⁵	0.032	
	6.625 - 7.725	7.836·10 ⁻⁴	3.974·10 ⁻⁵	0.051	2.365·10 ⁻⁵	0.030	
	7.725 - 9.325	4.910·10 ⁻⁴	2.656·10 ⁻⁵	0.054	1.465·10 ⁻⁵	0.030	
	9.325 - 11.825	2.094·10 ⁻⁴	1.359·10 ⁻⁵	0.065	6.791·10 ⁻⁶	0.032	
80 - 100	11.825 - 14.325	7.761·10 ⁻⁵	7.611·10 ⁻⁶	0.098	2.456·10 ⁻⁶	0.032	
	0.5 - 1.3	2.991·10 ⁻³	1.453·10 ⁻⁴	0.049	1.387·10 ⁻⁴	0.046	
	1.3 - 1.7	3.565·10 ⁻³	1.606·10 ⁻⁴	0.045	1.428·10 ⁻⁴	0.040	

Table D.1: Multiplicities of π^+ for the different (p, θ, z) bins with related statistical and systematic uncertainties

z	θ	p	$d\pi^+ / dp$	Δ_{stat}	$\Delta_{stat}\%$	Δ_{sys}	$\Delta_{sys}\%$
	[mrad]	[GeV/c]	[/ (GeV/c)/p.o.t]				
100 - 140	1.7 - 2.2		$3.405 \cdot 10^{-3}$	$1.512 \cdot 10^{-4}$	0.044	$1.201 \cdot 10^{-4}$	0.035
	2.2 - 2.675		$3.533 \cdot 10^{-3}$	$1.749 \cdot 10^{-4}$	0.050	$1.166 \cdot 10^{-4}$	0.033
	2.675 - 3.1		$2.673 \cdot 10^{-3}$	$1.668 \cdot 10^{-4}$	0.062	$8.491 \cdot 10^{-5}$	0.032
	3.1 - 3.55		$2.254 \cdot 10^{-3}$	$1.077 \cdot 10^{-4}$	0.048	$7.278 \cdot 10^{-5}$	0.032
	3.55 - 4.05		$2.018 \cdot 10^{-3}$	$9.186 \cdot 10^{-5}$	0.046	$6.137 \cdot 10^{-5}$	0.030
	4.05 - 4.6		$1.693 \cdot 10^{-3}$	$7.752 \cdot 10^{-5}$	0.046	$5.492 \cdot 10^{-5}$	0.032
	4.6 - 5.275		$1.342 \cdot 10^{-3}$	$6.150 \cdot 10^{-5}$	0.046	$4.196 \cdot 10^{-5}$	0.031
	5.275 - 6.125		$9.870 \cdot 10^{-4}$	$5.080 \cdot 10^{-5}$	0.051	$2.939 \cdot 10^{-5}$	0.030
	6.125 - 7.275		$6.342 \cdot 10^{-4}$	$3.441 \cdot 10^{-5}$	0.054	$2.089 \cdot 10^{-5}$	0.033
	7.275 - 9.2		$2.925 \cdot 10^{-4}$	$1.867 \cdot 10^{-5}$	0.064	$9.699 \cdot 10^{-6}$	0.033
	9.2 - 11.7		$1.016 \cdot 10^{-4}$	$9.584 \cdot 10^{-6}$	0.094	$3.353 \cdot 10^{-6}$	0.033
	0.5 - 1.3		$6.490 \cdot 10^{-3}$	$2.934 \cdot 10^{-4}$	0.045	$2.091 \cdot 10^{-4}$	0.032
	1.3 - 1.65		$7.499 \cdot 10^{-3}$	$4.463 \cdot 10^{-4}$	0.060	$2.306 \cdot 10^{-4}$	0.031
	1.65 - 1.95		$7.701 \cdot 10^{-3}$	$4.664 \cdot 10^{-4}$	0.061	$2.566 \cdot 10^{-4}$	0.033
	1.95 - 2.275		$6.584 \cdot 10^{-3}$	$3.962 \cdot 10^{-4}$	0.060	$1.990 \cdot 10^{-4}$	0.030
	2.275 - 2.575		$6.357 \cdot 10^{-3}$	$2.813 \cdot 10^{-4}$	0.044	$1.976 \cdot 10^{-4}$	0.031
	2.575 - 2.9		$5.072 \cdot 10^{-3}$	$2.360 \cdot 10^{-4}$	0.047	$1.606 \cdot 10^{-4}$	0.032
	2.9 - 3.275		$4.838 \cdot 10^{-3}$	$2.161 \cdot 10^{-4}$	0.045	$1.464 \cdot 10^{-4}$	0.030
	3.275 - 3.675		$3.941 \cdot 10^{-3}$	$1.980 \cdot 10^{-4}$	0.050	$1.219 \cdot 10^{-4}$	0.031
	3.675 - 4.2		$2.785 \cdot 10^{-3}$	$1.412 \cdot 10^{-4}$	0.051	$8.515 \cdot 10^{-5}$	0.031
	4.2 - 4.8		$2.518 \cdot 10^{-3}$	$1.214 \cdot 10^{-4}$	0.048	$7.618 \cdot 10^{-5}$	0.030
	4.8 - 5.725		$1.324 \cdot 10^{-3}$	$7.573 \cdot 10^{-5}$	0.057	$3.960 \cdot 10^{-5}$	0.030
140 - 180	5.725 - 7.075		$6.692 \cdot 10^{-4}$	$4.390 \cdot 10^{-5}$	0.066	$2.034 \cdot 10^{-5}$	0.030
	7.075 - 9.575		$2.675 \cdot 10^{-4}$	$2.008 \cdot 10^{-5}$	0.075	$8.397 \cdot 10^{-6}$	0.031
	0.4 - 0.925		$7.217 \cdot 10^{-3}$	$5.204 \cdot 10^{-4}$	0.072	$8.326 \cdot 10^{-4}$	0.115
	0.925 - 1.45		$8.701 \cdot 10^{-3}$	$6.027 \cdot 10^{-4}$	0.069	$4.325 \cdot 10^{-4}$	0.050
	1.45 - 1.775		$7.937 \cdot 10^{-3}$	$5.611 \cdot 10^{-4}$	0.071	$2.693 \cdot 10^{-4}$	0.034
	1.775 - 2.1		$6.679 \cdot 10^{-3}$	$5.191 \cdot 10^{-4}$	0.078	$2.086 \cdot 10^{-4}$	0.031
	2.1 - 2.425		$5.737 \cdot 10^{-3}$	$3.260 \cdot 10^{-4}$	0.057	$1.739 \cdot 10^{-4}$	0.030
	2.425 - 2.825		$4.395 \cdot 10^{-3}$	$2.234 \cdot 10^{-4}$	0.051	$1.342 \cdot 10^{-4}$	0.031
	2.825 - 3.3		$3.191 \cdot 10^{-3}$	$1.896 \cdot 10^{-4}$	0.059	$9.476 \cdot 10^{-5}$	0.030
	3.3 - 3.95		$2.274 \cdot 10^{-3}$	$1.447 \cdot 10^{-4}$	0.064	$6.633 \cdot 10^{-5}$	0.029
	3.95 - 5.05		$1.071 \cdot 10^{-3}$	$6.087 \cdot 10^{-5}$	0.057	$3.185 \cdot 10^{-5}$	0.030
180 - 220	5.05 - 7.55		$3.756 \cdot 10^{-4}$	$2.984 \cdot 10^{-5}$	0.079	$1.146 \cdot 10^{-5}$	0.031
	0.4 - 0.75		$7.944 \cdot 10^{-3}$	$6.676 \cdot 10^{-4}$	0.084	$8.326 \cdot 10^{-4}$	0.105
	0.75 - 1.05		$1.011 \cdot 10^{-2}$	$8.741 \cdot 10^{-4}$	0.086	$6.129 \cdot 10^{-4}$	0.061
	1.05 - 1.325		$8.953 \cdot 10^{-3}$	$6.575 \cdot 10^{-4}$	0.073	$3.840 \cdot 10^{-4}$	0.043
	1.325 - 1.675		$7.531 \cdot 10^{-3}$	$5.449 \cdot 10^{-4}$	0.072	$2.544 \cdot 10^{-4}$	0.034
	1.675 - 2.075		$7.022 \cdot 10^{-3}$	$4.750 \cdot 10^{-4}$	0.068	$2.153 \cdot 10^{-4}$	0.031
	2.075 - 2.475		$4.206 \cdot 10^{-3}$	$3.584 \cdot 10^{-4}$	0.085	$1.259 \cdot 10^{-4}$	0.030
	2.475 - 2.925		$2.736 \cdot 10^{-3}$	$2.359 \cdot 10^{-4}$	0.086	$8.069 \cdot 10^{-5}$	0.029
	2.925 - 3.5		$1.873 \cdot 10^{-3}$	$1.891 \cdot 10^{-4}$	0.101	$5.384 \cdot 10^{-5}$	0.029
	3.5 - 4.4		$1.249 \cdot 10^{-3}$	$8.519 \cdot 10^{-5}$	0.068	$4.038 \cdot 10^{-5}$	0.032

Table D.1: Multiplicities of π^+ for the different (p, θ, z) bins with related statistical and systematic uncertainties

z	θ	p	$d\eta\pi^+ / dp$	Δ_{stat}	$\Delta_{stat}\%$	Δ_{sys}	$\Delta_{sys}\%$
	[mrad]	[GeV/c]	[/ (GeV/c)/p.o.t]				
220 - 260	4.4 - 6.9	2.068·10 ⁻⁴	2.184·10 ⁻⁵	0.106	6.328·10 ⁻⁶	0.031	
	0.3 - 0.7	7.403·10 ⁻³	7.066·10 ⁻⁴	0.095	1.377·10 ⁻³	0.186	
	0.7 - 0.975	1.023·10 ⁻²	8.655·10 ⁻⁴	0.085	1.027·10 ⁻³	0.100	
	0.975 - 1.325	8.220·10 ⁻³	5.679·10 ⁻⁴	0.069	4.910·10 ⁻⁴	0.060	
	1.325 - 1.675	7.379·10 ⁻³	4.803·10 ⁻⁴	0.065	2.915·10 ⁻⁴	0.040	
	1.675 - 2.15	4.556·10 ⁻³	3.406·10 ⁻⁴	0.075	1.466·10 ⁻⁴	0.032	
	2.15 - 2.925	2.531·10 ⁻³	1.907·10 ⁻⁴	0.075	8.108·10 ⁻⁵	0.032	
	2.925 - 5.425	4.912·10 ⁻⁴	4.776·10 ⁻⁵	0.097	1.475·10 ⁻⁵	0.030	
	0.3 - 0.675	7.725·10 ⁻³	7.047·10 ⁻⁴	0.091	9.500·10 ⁻⁴	0.123	
	0.675 - 0.975	9.653·10 ⁻³	7.299·10 ⁻⁴	0.076	6.648·10 ⁻⁴	0.069	
260 - 300	0.975 - 1.25	9.377·10 ⁻³	6.467·10 ⁻⁴	0.069	4.293·10 ⁻⁴	0.046	
	1.25 - 1.625	6.495·10 ⁻³	4.617·10 ⁻⁴	0.071	2.257·10 ⁻⁴	0.035	
	1.625 - 2.225	3.562·10 ⁻³	2.431·10 ⁻⁴	0.068	1.069·10 ⁻⁴	0.030	
	2.225 - 4.725	6.880·10 ⁻⁴	5.420·10 ⁻⁵	0.079	2.104·10 ⁻⁵	0.031	
	0.2 - 0.45	7.058·10 ⁻³	1.216·10 ⁻³	0.172	8.679·10 ⁻⁴	0.123	
	0.45 - 0.7	7.844·10 ⁻³	8.567·10 ⁻⁴	0.109	6.140·10 ⁻⁴	0.078	
	0.7 - 0.95	8.054·10 ⁻³	7.030·10 ⁻⁴	0.087	4.254·10 ⁻⁴	0.053	
	0.95 - 1.275	7.994·10 ⁻³	5.733·10 ⁻⁴	0.072	3.077·10 ⁻⁴	0.038	
	1.275 - 2.55	3.023·10 ⁻³	1.780·10 ⁻⁴	0.059	9.204·10 ⁻⁵	0.030	
	0.7 - 1.3	7.106·10 ⁻⁴	8.258·10 ⁻⁵	0.116	2.212·10 ⁻⁵	0.031	
z 6 0 - 20	1.3 - 2.175	9.193·10 ⁻⁴	3.528·10 ⁻⁵	0.038	2.832·10 ⁻⁵	0.031	
	2.175 - 3.325	1.094·10 ⁻³	3.207·10 ⁻⁵	0.029	3.292·10 ⁻⁵	0.030	
	3.325 - 4.675	1.204·10 ⁻³	3.207·10 ⁻⁵	0.027	3.588·10 ⁻⁵	0.030	
	4.675 - 8.95	1.314·10 ⁻³	2.500·10 ⁻⁵	0.019	3.965·10 ⁻⁵	0.030	
	8.95 - 17.65	5.904·10 ⁻⁴	1.259·10 ⁻⁵	0.021	2.038·10 ⁻⁵	0.035	
	17.65 - 29.3	3.274·10 ⁻⁵	1.073·10 ⁻⁵	0.328	1.332·10 ⁻⁶	0.041	
	0.6 - 1.23	1.567·10 ⁻³	1.608·10 ⁻⁴	0.103	5.293·10 ⁻⁵	0.034	
	1.23 - 1.775	1.644·10 ⁻³	6.728·10 ⁻⁵	0.041	5.287·10 ⁻⁵	0.032	
	1.775 - 2.15	1.932·10 ⁻³	8.804·10 ⁻⁵	0.046	6.209·10 ⁻⁵	0.032	
	2.15 - 2.575	2.202·10 ⁻³	8.026·10 ⁻⁵	0.036	7.181·10 ⁻⁵	0.033	
20 - 40	2.575 - 2.975	2.113·10 ⁻³	7.260·10 ⁻⁵	0.034	6.840·10 ⁻⁵	0.032	
	2.975 - 3.425	1.959·10 ⁻³	7.936·10 ⁻⁵	0.041	6.259·10 ⁻⁵	0.032	
	3.425 - 4.025	1.999·10 ⁻³	8.319·10 ⁻⁵	0.042	6.382·10 ⁻⁵	0.032	
	4.025 - 4.825	2.122·10 ⁻³	7.078·10 ⁻⁵	0.033	7.974·10 ⁻⁵	0.038	
	4.825 - 6.05	2.005·10 ⁻³	5.671·10 ⁻⁵	0.028	7.877·10 ⁻⁵	0.039	
	6.05 - 7.75	1.633·10 ⁻³	4.439·10 ⁻⁵	0.027	6.531·10 ⁻⁵	0.040	
	7.75 - 9.55	1.198·10 ⁻³	3.200·10 ⁻⁵	0.027	4.452·10 ⁻⁵	0.037	
	9.55 - 11.625	7.901·10 ⁻⁴	2.774·10 ⁻⁵	0.035	3.083·10 ⁻⁵	0.039	
	11.625 - 14.125	4.866·10 ⁻⁴	1.965·10 ⁻⁵	0.040	1.891·10 ⁻⁵	0.039	
	14.125 - 18.125	1.969·10 ⁻⁴	1.078·10 ⁻⁵	0.055	7.158·10 ⁻⁶	0.036	
40 - 60	18.125 - 23.625	3.093·10 ⁻⁵	5.289·10 ⁻⁶	0.171	1.073·10 ⁻⁶	0.035	
	23.625 - 29.625	2.405·10 ⁻⁶	2.409·10 ⁻⁶	1.002	1.138·10 ⁻⁷	0.047	
0.6 - 1.175	1.701·10 ⁻³	1.286·10 ⁻⁴	0.076	5.832·10 ⁻⁵	0.034		

Table D.1: Multiplicities of π^+ for the different (p, θ, z) bins with related statistical and systematic uncertainties

z	θ	p	$d\pi^+ / dp$	Δ_{stat}	$\Delta_{stat}\%$	Δ_{sys}	$\Delta_{sys}\%$	
	[mrad]	[GeV/c]	[/ (GeV/c)/p.o.t]					
60 - 80	1.175 - 1.675	1.998·10 ⁻³	8.591·10 ⁻⁵	0.043	7.142·10 ⁻⁵	0.036		
	1.675 - 1.975	2.127·10 ⁻³	1.120·10 ⁻⁴	0.053	7.490·10 ⁻⁵	0.035		
	1.975 - 2.275	2.428·10 ⁻³	1.109·10 ⁻⁴	0.046	8.245·10 ⁻⁵	0.034		
	2.275 - 2.6	2.370·10 ⁻³	1.091·10 ⁻⁴	0.046	8.055·10 ⁻⁵	0.034		
	2.6 - 3.1	2.398·10 ⁻³	1.106·10 ⁻⁴	0.046	8.373·10 ⁻⁵	0.035		
	3.1 - 3.925	2.428·10 ⁻³	8.999·10 ⁻⁵	0.037	1.044·10 ⁻⁴	0.043		
	3.925 - 4.9	2.126·10 ⁻³	5.075·10 ⁻⁵	0.024	9.245·10 ⁻⁵	0.043		
	4.9 - 5.95	1.471·10 ⁻³	5.984·10 ⁻⁵	0.041	5.670·10 ⁻⁵	0.039		
	5.95 - 6.92	1.366·10 ⁻³	5.640·10 ⁻⁵	0.041	4.664·10 ⁻⁵	0.034		
	6.92 - 8.175	8.965·10 ⁻⁴	4.432·10 ⁻⁵	0.049	3.216·10 ⁻⁵	0.036		
	8.175 - 9.5	6.426·10 ⁻⁴	3.619·10 ⁻⁵	0.056	2.290·10 ⁻⁵	0.036		
	9.5 - 11.2	4.369·10 ⁻⁴	2.077·10 ⁻⁵	0.048	1.512·10 ⁻⁵	0.035		
	11.2 - 13.325	2.334·10 ⁻⁴	1.811·10 ⁻⁵	0.078	8.729·10 ⁻⁶	0.037		
	13.325 - 16.5	8.465·10 ⁻⁵	7.189·10 ⁻⁶	0.085	3.309·10 ⁻⁶	0.039		
	16.5 - 19	2.081·10 ⁻⁵	4.423·10 ⁻⁶	0.213	7.780·10 ⁻⁷	0.037		
	0.6 - 1.25	1.777·10 ⁻³	1.379·10 ⁻⁴	0.078	6.544·10 ⁻⁵	0.037		
	1.25 - 1.875	2.286·10 ⁻³	1.025·10 ⁻⁴	0.045	8.308·10 ⁻⁵	0.036		
	1.875 - 2.275	2.336·10 ⁻³	2.118·10 ⁻⁴	0.091	8.886·10 ⁻⁵	0.038		
	2.275 - 2.875	2.253·10 ⁻³	1.311·10 ⁻⁴	0.058	9.450·10 ⁻⁵	0.042		
	2.875 - 3.55	2.242·10 ⁻³	1.232·10 ⁻⁴	0.055	9.429·10 ⁻⁵	0.042		
	3.55 - 4.225	1.778·10 ⁻³	9.957·10 ⁻⁵	0.056	7.306·10 ⁻⁵	0.041		
	4.225 - 4.95	1.492·10 ⁻³	7.406·10 ⁻⁵	0.050	6.383·10 ⁻⁵	0.043		
	4.95 - 5.75	1.191·10 ⁻³	5.934·10 ⁻⁵	0.050	4.870·10 ⁻⁵	0.041		
	5.75 - 6.625	8.197·10 ⁻⁴	4.320·10 ⁻⁵	0.053	3.068·10 ⁻⁵	0.037		
	6.625 - 7.725	5.823·10 ⁻⁴	3.565·10 ⁻⁵	0.061	2.490·10 ⁻⁵	0.043		
	7.725 - 9.325	3.485·10 ⁻⁴	2.289·10 ⁻⁵	0.066	1.472·10 ⁻⁵	0.042		
	9.325 - 11.825	1.526·10 ⁻⁴	1.203·10 ⁻⁵	0.079	6.092·10 ⁻⁶	0.040		
	11.825 - 14.325	6.154·10 ⁻⁵	7.556·10 ⁻⁶	0.123	2.449·10 ⁻⁶	0.040		
80 - 100	0.5 - 1.3	1.827·10 ⁻³	1.380·10 ⁻⁴	0.076	8.904·10 ⁻⁵	0.049		
	1.3 - 1.7	2.063·10 ⁻³	1.599·10 ⁻⁴	0.078	9.012·10 ⁻⁵	0.044		
	1.7 - 2.2	2.016·10 ⁻³	1.327·10 ⁻⁴	0.066	9.121·10 ⁻⁵	0.045		
	2.2 - 2.675	2.031·10 ⁻³	1.313·10 ⁻⁴	0.065	9.246·10 ⁻⁵	0.046		
	2.675 - 3.1	1.775·10 ⁻³	1.142·10 ⁻⁴	0.064	7.726·10 ⁻⁵	0.044		
	3.1 - 3.55	1.537·10 ⁻³	9.226·10 ⁻⁵	0.060	6.456·10 ⁻⁵	0.042		
	3.55 - 4.05	1.323·10 ⁻³	7.658·10 ⁻⁵	0.058	5.698·10 ⁻⁵	0.043		
	4.05 - 4.6	1.121·10 ⁻³	6.088·10 ⁻⁵	0.054	4.523·10 ⁻⁵	0.040		
	4.6 - 5.275	8.343·10 ⁻⁴	5.206·10 ⁻⁵	0.062	3.434·10 ⁻⁵	0.041		
	5.275 - 6.125	6.350·10 ⁻⁴	4.006·10 ⁻⁵	0.063	2.661·10 ⁻⁵	0.042		
	6.125 - 7.275	3.881·10 ⁻⁴	2.729·10 ⁻⁵	0.070	1.436·10 ⁻⁵	0.037		
	7.275 - 9.2	2.230·10 ⁻⁴	1.645·10 ⁻⁵	0.074	8.902·10 ⁻⁶	0.040		
	9.2 - 11.7	5.033·10 ⁻⁵	7.114·10 ⁻⁶	0.141	2.398·10 ⁻⁶	0.048		
	100 - 140	0.5 - 1.3	3.443·10 ⁻³	2.181·10 ⁻⁴	0.063	2.739·10 ⁻⁴	0.080	
	1.3 - 1.65	3.755·10 ⁻³	3.364·10 ⁻⁴	0.090	2.103·10 ⁻⁴	0.056		

Table D.1: Multiplicities of π^+ for the different (p, θ, z) bins with related statistical and systematic uncertainties

z	θ	p	$d\pi^+ / dp$	Δ_{stat}	$\Delta_{stat}\%$	Δ_{sys}	$\Delta_{sys}\%$
	[mrad]	[GeV/c]	[/ (GeV/c)/p.o.t]				
140 - 180	1.65 - 1.95	3.736·10 ⁻³	2.727·10 ⁻⁴	0.073	1.897·10 ⁻⁴	0.051	
	1.95 - 2.275	3.352·10 ⁻³	2.739·10 ⁻⁴	0.082	1.866·10 ⁻⁴	0.056	
	2.275 - 2.575	2.962·10 ⁻³	1.978·10 ⁻⁴	0.067	1.469·10 ⁻⁴	0.050	
	2.575 - 2.9	2.455·10 ⁻³	1.704·10 ⁻⁴	0.069	1.283·10 ⁻⁴	0.052	
	2.9 - 3.275	2.115·10 ⁻³	1.484·10 ⁻⁴	0.070	1.077·10 ⁻⁴	0.051	
	3.275 - 3.675	1.551·10 ⁻³	1.208·10 ⁻⁴	0.078	9.164·10 ⁻⁵	0.059	
	3.675 - 4.2	1.513·10 ⁻³	1.060·10 ⁻⁴	0.070	7.586·10 ⁻⁵	0.050	
	4.2 - 4.8	9.161·10 ⁻⁴	7.700·10 ⁻⁵	0.084	4.462·10 ⁻⁵	0.049	
	4.8 - 5.725	5.993·10 ⁻⁴	4.302·10 ⁻⁵	0.072	3.628·10 ⁻⁵	0.061	
	5.725 - 7.075	3.377·10 ⁻⁴	3.019·10 ⁻⁵	0.089	1.687·10 ⁻⁵	0.050	
	7.075 - 9.575	1.257·10 ⁻⁴	1.354·10 ⁻⁵	0.108	7.557·10 ⁻⁶	0.060	
	0.4 - 0.925	2.496·10 ⁻³	2.883·10 ⁻⁴	0.116	3.977·10 ⁻⁴	0.159	
	0.925 - 1.45	3.050·10 ⁻³	3.768·10 ⁻⁴	0.124	2.642·10 ⁻⁴	0.087	
	1.45 - 1.775	2.782·10 ⁻³	4.638·10 ⁻⁴	0.167	1.915·10 ⁻⁴	0.069	
	1.775 - 2.1	2.250·10 ⁻³	2.920·10 ⁻⁴	0.130	1.375·10 ⁻⁴	0.061	
	2.1 - 2.425	1.782·10 ⁻³	1.765·10 ⁻⁴	0.099	1.209·10 ⁻⁴	0.068	
	2.425 - 2.825	1.510·10 ⁻³	1.484·10 ⁻⁴	0.098	9.483·10 ⁻⁵	0.063	
	2.825 - 3.3	1.052·10 ⁻³	1.094·10 ⁻⁴	0.104	7.861·10 ⁻⁵	0.075	
	3.3 - 3.95	8.095·10 ⁻⁴	6.311·10 ⁻⁵	0.078	5.972·10 ⁻⁵	0.074	
	3.95 - 5.05	4.272·10 ⁻⁴	4.883·10 ⁻⁵	0.114	2.776·10 ⁻⁵	0.065	
	5.05 - 7.55	9.979·10 ⁻⁵	1.497·10 ⁻⁵	0.150	5.192·10 ⁻⁶	0.052	
180 - 220	0.4 - 0.75	2.124·10 ⁻³	3.763·10 ⁻⁴	0.177	1.698·10 ⁻⁴	0.080	
	0.75 - 1.05	2.631·10 ⁻³	4.458·10 ⁻⁴	0.169	1.880·10 ⁻⁴	0.071	
	1.05 - 1.325	2.354·10 ⁻³	3.170·10 ⁻⁴	0.135	1.810·10 ⁻⁴	0.077	
	1.325 - 1.675	1.304·10 ⁻³	2.221·10 ⁻⁴	0.170	1.213·10 ⁻⁴	0.093	
	1.675 - 2.075	1.637·10 ⁻³	2.259·10 ⁻⁴	0.138	1.368·10 ⁻⁴	0.084	
	2.075 - 2.475	1.464·10 ⁻³	2.107·10 ⁻⁴	0.144	1.279·10 ⁻⁴	0.087	
	2.475 - 2.925	7.317·10 ⁻⁴	1.401·10 ⁻⁴	0.191	6.403·10 ⁻⁵	0.088	
	2.925 - 3.5	9.802·10 ⁻⁴	1.318·10 ⁻⁴	0.134	8.542·10 ⁻⁵	0.087	
	3.5 - 4.4	2.811·10 ⁻⁴	4.390·10 ⁻⁵	0.156	2.002·10 ⁻⁵	0.071	
	4.4 - 6.9	7.425·10 ⁻⁵	1.453·10 ⁻⁵	0.196	6.140·10 ⁻⁶	0.083	
220 - 260	0.3 - 0.7	2.257·10 ⁻³	3.383·10 ⁻⁴	0.150	4.963·10 ⁻⁴	0.220	
	0.7 - 0.975	2.134·10 ⁻³	3.917·10 ⁻⁴	0.183	2.750·10 ⁻⁴	0.129	
	0.975 - 1.325	1.690·10 ⁻³	2.562·10 ⁻⁴	0.152	1.852·10 ⁻⁴	0.110	
	1.325 - 1.675	1.325·10 ⁻³	2.170·10 ⁻⁴	0.164	1.267·10 ⁻⁴	0.096	
	1.675 - 2.15	7.620·10 ⁻⁴	1.159·10 ⁻⁴	0.152	7.839·10 ⁻⁵	0.103	
	2.15 - 2.925	6.128·10 ⁻⁴	9.544·10 ⁻⁵	0.156	5.228·10 ⁻⁵	0.085	
	2.925 - 5.425	1.808·10 ⁻⁴	2.963·10 ⁻⁵	0.164	2.341·10 ⁻⁵	0.130	
	0.3 - 0.675	1.049·10 ⁻³	2.487·10 ⁻⁴	0.237	1.076·10 ⁻⁴	0.103	
260 - 300	0.675 - 0.975	1.893·10 ⁻³	2.911·10 ⁻⁴	0.154	1.587·10 ⁻⁴	0.084	
	0.975 - 1.25	9.299·10 ⁻⁴	2.055·10 ⁻⁴	0.221	9.429·10 ⁻⁵	0.101	
	1.25 - 1.625	1.063·10 ⁻³	1.865·10 ⁻⁴	0.176	1.208·10 ⁻⁴	0.114	
	1.625 - 2.225	5.162·10 ⁻⁴	1.000·10 ⁻⁴	0.194	6.305·10 ⁻⁵	0.122	

Table D.1: Multiplicities of π^+ for the different (p, θ, z) bins with related statistical and systematic uncertainties

z	θ [mrad]	p [GeV/c]	dn^{π^+}/dp [/(GeV/c)/p.o.t]	Δ_{stat}	$\Delta_{stat}\%$	Δ_{sys}	$\Delta_{sys}\%$
300 - 340	2.225 - 4.725	1.563·10 ⁻⁴	2.558·10 ⁻⁵	0.164	1.783·10 ⁻⁵	0.114	
	0.2 - 0.45	1.401·10 ⁻³	8.544·10 ⁻⁴	0.610	1.218·10 ⁻⁴	0.087	
	0.45 - 0.7	1.374·10 ⁻³	3.476·10 ⁻⁴	0.253	1.523·10 ⁻⁴	0.111	
	0.7 - 0.95	1.482·10 ⁻³	2.323·10 ⁻⁴	0.157	1.905·10 ⁻⁴	0.129	
	0.95 - 1.275	1.422·10 ⁻³	2.344·10 ⁻⁴	0.165	1.991·10 ⁻⁴	0.140	
	1.275 - 2.55	4.627·10 ⁻⁴	6.969·10 ⁻⁵	0.151	6.070·10 ⁻⁵	0.131	

Table D.2: Multiplicities of π^- for the different (p, θ, z) bins with related statistical and systematic uncertainties

z	θ [mrad]	p [GeV/c]	$d\mathbf{n}^{\pi^-}/dp$ [/(GeV/c)/p.o.t]	Δ_{stat}	$\Delta_{stat}\%$	Δ_{sys}	$\Delta_{sys}\%$
z 1	0 - 20	0.7 - 1.3	$8.380 \cdot 10^{-6}$	$3.384 \cdot 10^{-6}$	0.404	$1.020 \cdot 10^{-6}$	0.122
		1.3 - 2.175	$1.025 \cdot 10^{-5}$	$1.524 \cdot 10^{-6}$	0.149	$1.036 \cdot 10^{-6}$	0.101
		2.175 - 3.325	$1.199 \cdot 10^{-5}$	$1.970 \cdot 10^{-6}$	0.164	$8.722 \cdot 10^{-7}$	0.073
		3.325 - 4.675	$1.558 \cdot 10^{-5}$	$2.034 \cdot 10^{-6}$	0.131	$9.516 \cdot 10^{-7}$	0.061
		4.675 - 8.95	$9.882 \cdot 10^{-6}$	$9.210 \cdot 10^{-7}$	0.093	$5.781 \cdot 10^{-7}$	0.058
		8.95 - 17.65	$1.057 \cdot 10^{-6}$	$3.439 \cdot 10^{-7}$	0.325	$1.033 \cdot 10^{-7}$	0.098
		17.65 - 29.3	$8.818 \cdot 10^{-8}$	$1.826 \cdot 10^{-8}$	0.207	$7.369 \cdot 10^{-9}$	0.084
		0.6 - 1.23	$1.012 \cdot 10^{-4}$	$1.285 \cdot 10^{-5}$	0.127	$7.734 \cdot 10^{-6}$	0.076
		1.23 - 1.775	$1.199 \cdot 10^{-4}$	$9.838 \cdot 10^{-6}$	0.082	$7.726 \cdot 10^{-6}$	0.064
20 - 40	20 - 40	1.775 - 2.15	$1.476 \cdot 10^{-4}$	$1.490 \cdot 10^{-5}$	0.101	$9.378 \cdot 10^{-6}$	0.064
		2.15 - 2.575	$1.525 \cdot 10^{-4}$	$1.605 \cdot 10^{-5}$	0.105	$8.498 \cdot 10^{-6}$	0.056
		2.575 - 2.975	$1.536 \cdot 10^{-4}$	$1.386 \cdot 10^{-5}$	0.090	$8.110 \cdot 10^{-6}$	0.053
		2.975 - 3.425	$1.329 \cdot 10^{-4}$	$1.217 \cdot 10^{-5}$	0.092	$6.535 \cdot 10^{-6}$	0.049
		3.425 - 4.025	$1.312 \cdot 10^{-4}$	$1.231 \cdot 10^{-5}$	0.094	$6.381 \cdot 10^{-6}$	0.049
		4.025 - 4.825	$1.014 \cdot 10^{-4}$	$1.255 \cdot 10^{-5}$	0.124	$6.388 \cdot 10^{-6}$	0.063
		4.825 - 6.05	$8.361 \cdot 10^{-5}$	$9.529 \cdot 10^{-6}$	0.114	$7.744 \cdot 10^{-6}$	0.093
		6.05 - 7.75	$8.207 \cdot 10^{-5}$	$9.830 \cdot 10^{-6}$	0.120	$8.841 \cdot 10^{-6}$	0.108
		7.75 - 9.55	$4.426 \cdot 10^{-5}$	$7.293 \cdot 10^{-6}$	0.165	$4.427 \cdot 10^{-6}$	0.100
		9.55 - 11.625	$5.012 \cdot 10^{-5}$	$7.651 \cdot 10^{-6}$	0.153	$4.484 \cdot 10^{-6}$	0.089
		11.625 - 14.125	$2.197 \cdot 10^{-5}$	$5.175 \cdot 10^{-6}$	0.236	$1.370 \cdot 10^{-6}$	0.062
		14.125 - 18.125	$9.583 \cdot 10^{-6}$	$6.457 \cdot 10^{-6}$	0.674	$7.450 \cdot 10^{-7}$	0.078
		18.125 - 23.625	$0.000 \cdot 10^0$	$0.000 \cdot 10^0$	0.000	$0.000 \cdot 10^0$	0.000
		23.625 - 29.625	$0.000 \cdot 10^0$	$0.000 \cdot 10^0$	0.000	$0.000 \cdot 10^0$	0.000
40 - 60	40 - 60	0.6 - 1.175	$2.408 \cdot 10^{-4}$	$4.134 \cdot 10^{-5}$	0.172	$1.258 \cdot 10^{-5}$	0.052
		1.175 - 1.675	$3.273 \cdot 10^{-4}$	$3.521 \cdot 10^{-5}$	0.108	$1.689 \cdot 10^{-5}$	0.052
		1.675 - 1.975	$3.486 \cdot 10^{-4}$	$2.514 \cdot 10^{-5}$	0.072	$1.816 \cdot 10^{-5}$	0.052
		1.975 - 2.275	$3.210 \cdot 10^{-4}$	$1.752 \cdot 10^{-5}$	0.055	$1.584 \cdot 10^{-5}$	0.049
		2.275 - 2.6	$2.938 \cdot 10^{-4}$	$2.787 \cdot 10^{-5}$	0.095	$1.347 \cdot 10^{-5}$	0.046
		2.6 - 3.1	$2.923 \cdot 10^{-4}$	$2.890 \cdot 10^{-5}$	0.099	$1.491 \cdot 10^{-5}$	0.051
		3.1 - 3.925	$2.979 \cdot 10^{-4}$	$2.697 \cdot 10^{-5}$	0.091	$2.269 \cdot 10^{-5}$	0.076
		3.925 - 4.9	$2.758 \cdot 10^{-4}$	$2.398 \cdot 10^{-5}$	0.087	$2.263 \cdot 10^{-5}$	0.082
		4.9 - 5.95	$2.607 \cdot 10^{-4}$	$2.229 \cdot 10^{-5}$	0.086	$1.606 \cdot 10^{-5}$	0.062
		5.95 - 6.92	$2.149 \cdot 10^{-4}$	$2.170 \cdot 10^{-5}$	0.101	$1.074 \cdot 10^{-5}$	0.050
		6.92 - 8.175	$1.164 \cdot 10^{-4}$	$1.272 \cdot 10^{-5}$	0.109	$6.263 \cdot 10^{-6}$	0.054
		8.175 - 9.5	$1.224 \cdot 10^{-4}$	$1.094 \cdot 10^{-5}$	0.089	$7.474 \cdot 10^{-6}$	0.061
		9.5 - 11.2	$5.471 \cdot 10^{-5}$	$2.956 \cdot 10^{-6}$	0.054	$3.424 \cdot 10^{-6}$	0.063
		11.2 - 13.325	$3.329 \cdot 10^{-5}$	$4.595 \cdot 10^{-6}$	0.138	$2.065 \cdot 10^{-6}$	0.062
		13.325 - 16.5	$1.306 \cdot 10^{-5}$	$3.276 \cdot 10^{-6}$	0.251	$9.364 \cdot 10^{-7}$	0.072
		16.5 - 19	$4.708 \cdot 10^{-6}$	$3.568 \cdot 10^{-6}$	0.758	$4.374 \cdot 10^{-7}$	0.093
60 - 80	60 - 80	0.6 - 1.25	$8.124 \cdot 10^{-4}$	$6.212 \cdot 10^{-5}$	0.076	$4.897 \cdot 10^{-5}$	0.060
		1.25 - 1.875	$8.427 \cdot 10^{-4}$	$4.054 \cdot 10^{-5}$	0.048	$5.047 \cdot 10^{-5}$	0.060
		1.875 - 2.275	$8.386 \cdot 10^{-4}$	$4.966 \cdot 10^{-5}$	0.059	$4.549 \cdot 10^{-5}$	0.054
		2.275 - 2.875	$8.052 \cdot 10^{-4}$	$6.437 \cdot 10^{-5}$	0.080	$4.964 \cdot 10^{-5}$	0.062

Table D.2: Multiplicities of π^- for the different (p, θ, z) bins with related statistical and systematic uncertainties

z	θ	p	$d\pi^-/dp$	Δ_{stat}	$\Delta_{stat}\%$	Δ_{sys}	$\Delta_{sys}\%$
		[mrad]	[(GeV/c)/p.o.t]				
		2.875 - 3.55	$8.348 \cdot 10^{-4}$	$5.846 \cdot 10^{-5}$	0.070	$4.958 \cdot 10^{-5}$	0.059
		3.55 - 4.225	$6.635 \cdot 10^{-4}$	$5.596 \cdot 10^{-5}$	0.084	$3.705 \cdot 10^{-5}$	0.056
		4.225 - 4.95	$6.254 \cdot 10^{-4}$	$3.735 \cdot 10^{-5}$	0.060	$4.067 \cdot 10^{-5}$	0.065
		4.95 - 5.75	$4.827 \cdot 10^{-4}$	$3.425 \cdot 10^{-5}$	0.071	$2.833 \cdot 10^{-5}$	0.059
		5.75 - 6.625	$4.640 \cdot 10^{-4}$	$3.102 \cdot 10^{-5}$	0.067	$3.022 \cdot 10^{-5}$	0.065
		6.625 - 7.725	$2.921 \cdot 10^{-4}$	$2.376 \cdot 10^{-5}$	0.081	$1.804 \cdot 10^{-5}$	0.062
		7.725 - 9.325	$1.486 \cdot 10^{-4}$	$1.339 \cdot 10^{-5}$	0.090	$9.891 \cdot 10^{-6}$	0.067
		9.325 - 11.825	$8.482 \cdot 10^{-5}$	$7.520 \cdot 10^{-6}$	0.089	$5.585 \cdot 10^{-6}$	0.066
		11.825 - 14.325	$2.350 \cdot 10^{-5}$	$5.991 \cdot 10^{-6}$	0.255	$1.157 \cdot 10^{-6}$	0.049
80 - 100	0.5 - 1.3		$1.469 \cdot 10^{-3}$	$8.923 \cdot 10^{-5}$	0.061	$9.549 \cdot 10^{-5}$	0.065
	1.3 - 1.7		$1.677 \cdot 10^{-3}$	$1.029 \cdot 10^{-4}$	0.061	$9.869 \cdot 10^{-5}$	0.059
	1.7 - 2.2		$1.674 \cdot 10^{-3}$	$1.171 \cdot 10^{-4}$	0.070	$9.709 \cdot 10^{-5}$	0.058
	2.2 - 2.675		$1.719 \cdot 10^{-3}$	$1.005 \cdot 10^{-4}$	0.058	$9.246 \cdot 10^{-5}$	0.054
	2.675 - 3.1		$1.509 \cdot 10^{-3}$	$1.183 \cdot 10^{-4}$	0.078	$9.057 \cdot 10^{-5}$	0.060
	3.1 - 3.55		$1.395 \cdot 10^{-3}$	$7.981 \cdot 10^{-5}$	0.057	$8.380 \cdot 10^{-5}$	0.060
	3.55 - 4.05		$1.289 \cdot 10^{-3}$	$7.795 \cdot 10^{-5}$	0.060	$8.249 \cdot 10^{-5}$	0.064
	4.05 - 4.6		$1.012 \cdot 10^{-3}$	$6.395 \cdot 10^{-5}$	0.063	$6.133 \cdot 10^{-5}$	0.061
	4.6 - 5.275		$9.340 \cdot 10^{-4}$	$5.622 \cdot 10^{-5}$	0.060	$5.232 \cdot 10^{-5}$	0.056
	5.275 - 6.125		$5.679 \cdot 10^{-4}$	$3.944 \cdot 10^{-5}$	0.069	$3.330 \cdot 10^{-5}$	0.059
	6.125 - 7.275		$3.822 \cdot 10^{-4}$	$2.369 \cdot 10^{-5}$	0.062	$2.547 \cdot 10^{-5}$	0.067
	7.275 - 9.2		$1.978 \cdot 10^{-4}$	$1.445 \cdot 10^{-5}$	0.073	$1.134 \cdot 10^{-5}$	0.057
	9.2 - 11.7		$5.235 \cdot 10^{-5}$	$6.153 \cdot 10^{-6}$	0.118	$2.692 \cdot 10^{-6}$	0.051
100 - 140	0.5 - 1.3		$6.566 \cdot 10^{-3}$	$2.625 \cdot 10^{-4}$	0.040	$5.138 \cdot 10^{-4}$	0.078
	1.3 - 1.65		$6.853 \cdot 10^{-3}$	$3.295 \cdot 10^{-4}$	0.048	$3.861 \cdot 10^{-4}$	0.056
	1.65 - 1.95		$6.270 \cdot 10^{-3}$	$3.994 \cdot 10^{-4}$	0.064	$3.195 \cdot 10^{-4}$	0.051
	1.95 - 2.275		$6.033 \cdot 10^{-3}$	$2.424 \cdot 10^{-4}$	0.040	$3.218 \cdot 10^{-4}$	0.053
	2.275 - 2.575		$5.348 \cdot 10^{-3}$	$2.294 \cdot 10^{-4}$	0.043	$2.471 \cdot 10^{-4}$	0.046
	2.575 - 2.9		$5.077 \cdot 10^{-3}$	$2.506 \cdot 10^{-4}$	0.049	$2.625 \cdot 10^{-4}$	0.052
	2.9 - 3.275		$4.780 \cdot 10^{-3}$	$2.012 \cdot 10^{-4}$	0.042	$2.465 \cdot 10^{-4}$	0.052
	3.275 - 3.675		$3.698 \cdot 10^{-3}$	$1.864 \cdot 10^{-4}$	0.050	$1.871 \cdot 10^{-4}$	0.051
	3.675 - 4.2		$3.025 \cdot 10^{-3}$	$1.479 \cdot 10^{-4}$	0.049	$1.568 \cdot 10^{-4}$	0.052
	4.2 - 4.8		$2.389 \cdot 10^{-3}$	$1.197 \cdot 10^{-4}$	0.050	$1.211 \cdot 10^{-4}$	0.051
	4.8 - 5.725		$1.452 \cdot 10^{-3}$	$7.693 \cdot 10^{-5}$	0.053	$7.936 \cdot 10^{-5}$	0.055
	5.725 - 7.075		$8.221 \cdot 10^{-4}$	$4.330 \cdot 10^{-5}$	0.053	$4.410 \cdot 10^{-5}$	0.054
	7.075 - 9.575		$2.081 \cdot 10^{-4}$	$1.751 \cdot 10^{-5}$	0.084	$1.028 \cdot 10^{-5}$	0.049
140 - 180	0.4 - 0.925		$8.848 \cdot 10^{-3}$	$5.811 \cdot 10^{-4}$	0.066	$4.040 \cdot 10^{-4}$	0.046
	0.925 - 1.45		$9.598 \cdot 10^{-3}$	$6.285 \cdot 10^{-4}$	0.065	$4.509 \cdot 10^{-4}$	0.047
	1.45 - 1.775		$9.339 \cdot 10^{-3}$	$6.240 \cdot 10^{-4}$	0.067	$4.369 \cdot 10^{-4}$	0.047
	1.775 - 2.1		$7.687 \cdot 10^{-3}$	$3.956 \cdot 10^{-4}$	0.051	$3.546 \cdot 10^{-4}$	0.046
	2.1 - 2.425		$6.789 \cdot 10^{-3}$	$3.568 \cdot 10^{-4}$	0.053	$3.160 \cdot 10^{-4}$	0.047
	2.425 - 2.825		$5.736 \cdot 10^{-3}$	$2.778 \cdot 10^{-4}$	0.048	$2.760 \cdot 10^{-4}$	0.048
	2.825 - 3.3		$4.455 \cdot 10^{-3}$	$2.327 \cdot 10^{-4}$	0.052	$2.150 \cdot 10^{-4}$	0.048
	3.3 - 3.95		$2.782 \cdot 10^{-3}$	$1.561 \cdot 10^{-4}$	0.056	$1.178 \cdot 10^{-4}$	0.042

Table D.2: Multiplicities of π^- for the different (p, θ, z) bins with related statistical and systematic uncertainties

z	θ	p	$d\mathbf{n}^{\pi^-}/dp$	Δ_{stat}	$\Delta_{stat}\%$	Δ_{sys}	$\Delta_{sys}\%$
	[mrad]	[GeV/c]	[/ (GeV/c)/p.o.t]				
180 - 220	3.95 - 5.05	1.471·10 ⁻³	5.967·10 ⁻⁵	0.041	6.708·10 ⁻⁵	0.046	
	5.05 - 7.55	3.604·10 ⁻⁴	2.912·10 ⁻⁵	0.081	1.589·10 ⁻⁵	0.044	
	0.4 - 0.75	1.021·10 ⁻²	7.574·10 ⁻⁴	0.074	1.050·10 ⁻³	0.103	
	0.75 - 1.05	1.278·10 ⁻²	9.291·10 ⁻⁴	0.073	8.409·10 ⁻⁴	0.066	
	1.05 - 1.325	1.305·10 ⁻²	8.057·10 ⁻⁴	0.062	7.119·10 ⁻⁴	0.055	
	1.325 - 1.675	1.027·10 ⁻²	6.524·10 ⁻⁴	0.064	5.043·10 ⁻⁴	0.049	
	1.675 - 2.075	7.252·10 ⁻³	4.709·10 ⁻⁴	0.065	3.034·10 ⁻⁴	0.042	
	2.075 - 2.475	5.683·10 ⁻³	3.761·10 ⁻⁴	0.066	2.580·10 ⁻⁴	0.045	
	2.475 - 2.925	4.092·10 ⁻³	2.693·10 ⁻⁴	0.066	1.789·10 ⁻⁴	0.044	
	2.925 - 3.5	2.444·10 ⁻³	1.589·10 ⁻⁴	0.065	9.629·10 ⁻⁵	0.039	
220 - 260	3.5 - 4.4	1.457·10 ⁻³	9.793·10 ⁻⁵	0.067	6.059·10 ⁻⁵	0.042	
	4.4 - 6.9	3.800·10 ⁻⁴	1.959·10 ⁻⁵	0.052	1.493·10 ⁻⁵	0.039	
	0.3 - 0.7	1.317·10 ⁻²	9.187·10 ⁻⁴	0.070	8.584·10 ⁻⁴	0.065	
	0.7 - 0.975	1.486·10 ⁻²	9.809·10 ⁻⁴	0.066	7.800·10 ⁻⁴	0.052	
	0.975 - 1.325	1.332·10 ⁻²	7.339·10 ⁻⁴	0.055	6.676·10 ⁻⁴	0.050	
	1.325 - 1.675	1.029·10 ⁻²	6.088·10 ⁻⁴	0.059	4.285·10 ⁻⁴	0.042	
	1.675 - 2.15	6.639·10 ⁻³	4.058·10 ⁻⁴	0.061	2.872·10 ⁻⁴	0.043	
	2.15 - 2.925	3.796·10 ⁻³	2.382·10 ⁻⁴	0.063	1.521·10 ⁻⁴	0.040	
	2.925 - 5.425	7.966·10 ⁻⁴	5.829·10 ⁻⁵	0.073	3.002·10 ⁻⁵	0.038	
	0.3 - 0.675	1.222·10 ⁻²	9.516·10 ⁻⁴	0.078	1.011·10 ⁻³	0.083	
260 - 300	0.675 - 0.975	1.524·10 ⁻²	1.147·10 ⁻³	0.075	8.270·10 ⁻⁴	0.054	
	0.975 - 1.25	1.354·10 ⁻²	8.887·10 ⁻⁴	0.066	5.947·10 ⁻⁴	0.044	
	1.25 - 1.625	8.744·10 ⁻³	5.598·10 ⁻⁴	0.064	3.890·10 ⁻⁴	0.044	
	1.625 - 2.225	4.926·10 ⁻³	3.313·10 ⁻⁴	0.067	2.252·10 ⁻⁴	0.046	
	2.225 - 4.725	1.200·10 ⁻³	7.839·10 ⁻⁵	0.065	4.635·10 ⁻⁵	0.039	
	0.2 - 0.45	1.056·10 ⁻²	1.395·10 ⁻³	0.132	1.815·10 ⁻³	0.172	
	0.45 - 0.7	9.958·10 ⁻³	1.318·10 ⁻³	0.132	1.106·10 ⁻³	0.111	
	0.7 - 0.95	8.351·10 ⁻³	9.854·10 ⁻⁴	0.118	6.228·10 ⁻⁴	0.075	
	0.95 - 1.275	7.275·10 ⁻³	8.923·10 ⁻⁴	0.123	4.275·10 ⁻⁴	0.059	
	1.275 - 2.55	3.871·10 ⁻³	8.468·10 ⁻⁴	0.219	2.075·10 ⁻⁴	0.054	
z 2 0 - 20	0.7 - 1.3	3.089·10 ⁻⁵	1.512·10 ⁻⁵	0.490	2.918·10 ⁻⁶	0.094	
	1.3 - 2.175	3.190·10 ⁻⁵	5.666·10 ⁻⁶	0.178	2.702·10 ⁻⁶	0.085	
	2.175 - 3.325	5.163·10 ⁻⁵	6.927·10 ⁻⁶	0.134	2.859·10 ⁻⁶	0.055	
	3.325 - 4.675	4.325·10 ⁻⁵	4.926·10 ⁻⁶	0.114	2.059·10 ⁻⁶	0.048	
	4.675 - 8.95	2.836·10 ⁻⁵	2.917·10 ⁻⁶	0.103	1.413·10 ⁻⁶	0.050	
	8.95 - 17.65	7.983·10 ⁻⁶	1.145·10 ⁻⁶	0.143	7.947·10 ⁻⁷	0.100	
	17.65 - 29.3	4.000·10 ⁻⁷	3.632·10 ⁻⁷	0.908	4.826·10 ⁻⁸	0.121	
	0.6 - 1.23	4.372·10 ⁻⁴	7.762·10 ⁻⁵	0.178	2.335·10 ⁻⁵	0.053	
	1.23 - 1.775	5.390·10 ⁻⁴	4.055·10 ⁻⁵	0.075	2.365·10 ⁻⁵	0.044	
	1.775 - 2.15	4.991·10 ⁻⁴	4.122·10 ⁻⁵	0.083	1.931·10 ⁻⁵	0.039	
20 - 40	2.15 - 2.575	5.437·10 ⁻⁴	4.246·10 ⁻⁵	0.078	1.990·10 ⁻⁵	0.037	
	2.575 - 2.975	5.179·10 ⁻⁴	4.313·10 ⁻⁵	0.083	1.784·10 ⁻⁵	0.034	
	2.975 - 3.425	5.242·10 ⁻⁴	4.254·10 ⁻⁵	0.081	1.849·10 ⁻⁵	0.035	

Table D.2: Multiplicities of π^- for the different (p, θ, z) bins with related statistical and systematic uncertainties

z	θ	p	$d\pi^-/dp$	Δ_{stat}	$\Delta_{stat}\%$	Δ_{sys}	$\Delta_{sys}\%$
	[mrad]	[GeV/c]	[/ (GeV/c)/p.o.t]				
		3.425 - 4.025	$4.576 \cdot 10^{-4}$	$4.064 \cdot 10^{-5}$	0.089	$1.474 \cdot 10^{-5}$	0.032
		4.025 - 4.825	$4.566 \cdot 10^{-4}$	$2.939 \cdot 10^{-5}$	0.064	$1.806 \cdot 10^{-5}$	0.040
		4.825 - 6.05	$4.560 \cdot 10^{-4}$	$3.352 \cdot 10^{-5}$	0.074	$2.351 \cdot 10^{-5}$	0.052
		6.05 - 7.75	$3.604 \cdot 10^{-4}$	$2.558 \cdot 10^{-5}$	0.071	$1.739 \cdot 10^{-5}$	0.048
		7.75 - 9.55	$2.375 \cdot 10^{-4}$	$1.832 \cdot 10^{-5}$	0.077	$9.872 \cdot 10^{-6}$	0.042
		9.55 - 11.625	$1.311 \cdot 10^{-4}$	$1.359 \cdot 10^{-5}$	0.104	$5.280 \cdot 10^{-6}$	0.040
		11.625 - 14.125	$8.038 \cdot 10^{-5}$	$1.212 \cdot 10^{-5}$	0.151	$3.054 \cdot 10^{-6}$	0.038
		14.125 - 18.125	$2.505 \cdot 10^{-5}$	$4.321 \cdot 10^{-6}$	0.172	$8.625 \cdot 10^{-7}$	0.034
		18.125 - 23.625	$4.705 \cdot 10^{-6}$	$4.592 \cdot 10^{-6}$	0.976	$1.674 \cdot 10^{-7}$	0.036
		23.625 - 29.625	$4.929 \cdot 10^{-7}$	$4.576 \cdot 10^{-7}$	0.928	$7.557 \cdot 10^{-8}$	0.153
40 - 60		0.6 - 1.175	$1.325 \cdot 10^{-3}$	$9.470 \cdot 10^{-5}$	0.071	$4.870 \cdot 10^{-5}$	0.037
		1.175 - 1.675	$1.552 \cdot 10^{-3}$	$7.742 \cdot 10^{-5}$	0.050	$5.457 \cdot 10^{-5}$	0.035
		1.675 - 1.975	$1.538 \cdot 10^{-3}$	$9.194 \cdot 10^{-5}$	0.060	$5.103 \cdot 10^{-5}$	0.033
		1.975 - 2.275	$1.774 \cdot 10^{-3}$	$9.594 \cdot 10^{-5}$	0.054	$5.699 \cdot 10^{-5}$	0.032
		2.275 - 2.6	$1.862 \cdot 10^{-3}$	$1.047 \cdot 10^{-4}$	0.056	$6.138 \cdot 10^{-5}$	0.033
		2.6 - 3.1	$1.947 \cdot 10^{-3}$	$1.069 \cdot 10^{-4}$	0.055	$6.340 \cdot 10^{-5}$	0.033
		3.1 - 3.925	$1.861 \cdot 10^{-3}$	$8.147 \cdot 10^{-5}$	0.044	$6.389 \cdot 10^{-5}$	0.034
		3.925 - 4.9	$1.411 \cdot 10^{-3}$	$5.838 \cdot 10^{-5}$	0.041	$4.509 \cdot 10^{-5}$	0.032
		4.9 - 5.95	$1.133 \cdot 10^{-3}$	$5.612 \cdot 10^{-5}$	0.050	$3.414 \cdot 10^{-5}$	0.030
		5.95 - 6.92	$9.163 \cdot 10^{-4}$	$3.621 \cdot 10^{-5}$	0.040	$2.985 \cdot 10^{-5}$	0.033
		6.92 - 8.175	$7.487 \cdot 10^{-4}$	$1.983 \cdot 10^{-5}$	0.026	$2.371 \cdot 10^{-5}$	0.032
		8.175 - 9.5	$4.302 \cdot 10^{-4}$	$3.007 \cdot 10^{-5}$	0.070	$1.350 \cdot 10^{-5}$	0.031
		9.5 - 11.2	$3.404 \cdot 10^{-4}$	$1.799 \cdot 10^{-5}$	0.053	$1.048 \cdot 10^{-5}$	0.031
		11.2 - 13.325	$1.591 \cdot 10^{-4}$	$1.060 \cdot 10^{-5}$	0.067	$5.663 \cdot 10^{-6}$	0.036
		13.325 - 16.5	$5.175 \cdot 10^{-5}$	$6.100 \cdot 10^{-6}$	0.118	$1.670 \cdot 10^{-6}$	0.032
		16.5 - 19	$1.632 \cdot 10^{-5}$	$3.884 \cdot 10^{-6}$	0.238	$7.353 \cdot 10^{-7}$	0.045
60 - 80		0.6 - 1.25	$2.698 \cdot 10^{-3}$	$1.930 \cdot 10^{-4}$	0.072	$1.051 \cdot 10^{-4}$	0.039
		1.25 - 1.875	$3.151 \cdot 10^{-3}$	$1.059 \cdot 10^{-4}$	0.034	$1.088 \cdot 10^{-4}$	0.035
		1.875 - 2.275	$3.526 \cdot 10^{-3}$	$2.554 \cdot 10^{-4}$	0.072	$1.148 \cdot 10^{-4}$	0.033
		2.275 - 2.875	$3.058 \cdot 10^{-3}$	$1.550 \cdot 10^{-4}$	0.051	$9.555 \cdot 10^{-5}$	0.031
		2.875 - 3.55	$3.189 \cdot 10^{-3}$	$1.357 \cdot 10^{-4}$	0.043	$9.609 \cdot 10^{-5}$	0.030
		3.55 - 4.225	$2.864 \cdot 10^{-3}$	$1.328 \cdot 10^{-4}$	0.046	$8.520 \cdot 10^{-5}$	0.030
		4.225 - 4.95	$2.380 \cdot 10^{-3}$	$8.659 \cdot 10^{-5}$	0.036	$7.021 \cdot 10^{-5}$	0.029
		4.95 - 5.75	$1.830 \cdot 10^{-3}$	$7.349 \cdot 10^{-5}$	0.040	$5.394 \cdot 10^{-5}$	0.029
		5.75 - 6.625	$1.325 \cdot 10^{-3}$	$5.606 \cdot 10^{-5}$	0.042	$3.839 \cdot 10^{-5}$	0.029
		6.625 - 7.725	$1.018 \cdot 10^{-3}$	$4.273 \cdot 10^{-5}$	0.042	$2.964 \cdot 10^{-5}$	0.029
		7.725 - 9.325	$5.958 \cdot 10^{-4}$	$2.651 \cdot 10^{-5}$	0.045	$1.756 \cdot 10^{-5}$	0.029
		9.325 - 11.825	$2.871 \cdot 10^{-4}$	$1.526 \cdot 10^{-5}$	0.053	$8.657 \cdot 10^{-6}$	0.030
		11.825 - 14.325	$8.194 \cdot 10^{-5}$	$8.461 \cdot 10^{-6}$	0.103	$2.718 \cdot 10^{-6}$	0.033
80 - 100		0.5 - 1.3	$4.162 \cdot 10^{-3}$	$1.685 \cdot 10^{-4}$	0.040	$3.444 \cdot 10^{-4}$	0.083
		1.3 - 1.7	$4.861 \cdot 10^{-3}$	$1.838 \cdot 10^{-4}$	0.038	$1.865 \cdot 10^{-4}$	0.038
		1.7 - 2.2	$5.062 \cdot 10^{-3}$	$2.036 \cdot 10^{-4}$	0.040	$1.635 \cdot 10^{-4}$	0.032
		2.2 - 2.675	$4.647 \cdot 10^{-3}$	$1.838 \cdot 10^{-4}$	0.040	$1.385 \cdot 10^{-4}$	0.030

Table D.2: Multiplicities of π^- for the different (p, θ, z) bins with related statistical and systematic uncertainties

z	θ [mrad]	p [GeV/c]	$d\mathbf{n}^{\pi^-}/dp$ [/(GeV/c)/p.o.t]	Δ_{stat}	$\Delta_{stat}\%$	Δ_{sys}	$\Delta_{sys}\%$
100 - 140	2.675 - 3.1	$4.137 \cdot 10^{-3}$	$1.410 \cdot 10^{-4}$	0.034	$1.220 \cdot 10^{-4}$	0.029	
	3.1 - 3.55	$3.658 \cdot 10^{-3}$	$1.313 \cdot 10^{-4}$	0.036	$1.076 \cdot 10^{-4}$	0.029	
	3.55 - 4.05	$3.489 \cdot 10^{-3}$	$1.261 \cdot 10^{-4}$	0.036	$1.022 \cdot 10^{-4}$	0.029	
	4.05 - 4.6	$2.295 \cdot 10^{-3}$	$9.043 \cdot 10^{-5}$	0.039	$6.801 \cdot 10^{-5}$	0.030	
	4.6 - 5.275	$2.162 \cdot 10^{-3}$	$8.603 \cdot 10^{-5}$	0.040	$6.320 \cdot 10^{-5}$	0.029	
	5.275 - 6.125	$1.595 \cdot 10^{-3}$	$6.270 \cdot 10^{-5}$	0.039	$4.580 \cdot 10^{-5}$	0.029	
	6.125 - 7.275	$9.875 \cdot 10^{-4}$	$4.312 \cdot 10^{-5}$	0.044	$2.959 \cdot 10^{-5}$	0.030	
	7.275 - 9.2	$5.208 \cdot 10^{-4}$	$2.550 \cdot 10^{-5}$	0.049	$1.530 \cdot 10^{-5}$	0.029	
	9.2 - 11.7	$1.524 \cdot 10^{-4}$	$1.100 \cdot 10^{-5}$	0.072	$4.523 \cdot 10^{-6}$	0.030	
	0.5 - 1.3	$1.226 \cdot 10^{-2}$	$3.776 \cdot 10^{-4}$	0.031	$7.315 \cdot 10^{-4}$	0.060	
	1.3 - 1.65	$1.360 \cdot 10^{-2}$	$8.506 \cdot 10^{-4}$	0.063	$4.686 \cdot 10^{-4}$	0.034	
	1.65 - 1.95	$1.281 \cdot 10^{-2}$	$8.000 \cdot 10^{-4}$	0.062	$3.998 \cdot 10^{-4}$	0.031	
	1.95 - 2.275	$1.204 \cdot 10^{-2}$	$3.785 \cdot 10^{-4}$	0.031	$3.619 \cdot 10^{-4}$	0.030	
	2.275 - 2.575	$1.122 \cdot 10^{-2}$	$3.334 \cdot 10^{-4}$	0.030	$3.322 \cdot 10^{-4}$	0.030	
	2.575 - 2.9	$9.263 \cdot 10^{-3}$	$3.101 \cdot 10^{-4}$	0.033	$2.753 \cdot 10^{-4}$	0.030	
	2.9 - 3.275	$8.548 \cdot 10^{-3}$	$2.701 \cdot 10^{-4}$	0.032	$2.537 \cdot 10^{-4}$	0.030	
	3.275 - 3.675	$7.244 \cdot 10^{-3}$	$2.387 \cdot 10^{-4}$	0.033	$2.110 \cdot 10^{-4}$	0.029	
	3.675 - 4.2	$5.275 \cdot 10^{-3}$	$1.961 \cdot 10^{-4}$	0.037	$1.527 \cdot 10^{-4}$	0.029	
140 - 180	4.2 - 4.8	$4.168 \cdot 10^{-3}$	$1.617 \cdot 10^{-4}$	0.039	$1.213 \cdot 10^{-4}$	0.029	
	4.8 - 5.725	$2.602 \cdot 10^{-3}$	$9.805 \cdot 10^{-5}$	0.038	$7.623 \cdot 10^{-5}$	0.029	
	5.725 - 7.075	$1.434 \cdot 10^{-3}$	$5.989 \cdot 10^{-5}$	0.042	$4.138 \cdot 10^{-5}$	0.029	
	7.075 - 9.575	$4.441 \cdot 10^{-4}$	$2.639 \cdot 10^{-5}$	0.059	$1.288 \cdot 10^{-5}$	0.029	
	0.4 - 0.925	$1.513 \cdot 10^{-2}$	$7.413 \cdot 10^{-4}$	0.049	$4.778 \cdot 10^{-4}$	0.032	
	0.925 - 1.45	$1.523 \cdot 10^{-2}$	$7.709 \cdot 10^{-4}$	0.051	$4.716 \cdot 10^{-4}$	0.031	
	1.45 - 1.775	$1.509 \cdot 10^{-2}$	$6.440 \cdot 10^{-4}$	0.043	$4.526 \cdot 10^{-4}$	0.030	
	1.775 - 2.1	$1.262 \cdot 10^{-2}$	$5.057 \cdot 10^{-4}$	0.040	$3.837 \cdot 10^{-4}$	0.030	
	2.1 - 2.425	$1.102 \cdot 10^{-2}$	$4.540 \cdot 10^{-4}$	0.041	$3.247 \cdot 10^{-4}$	0.029	
	2.425 - 2.825	$8.916 \cdot 10^{-3}$	$3.308 \cdot 10^{-4}$	0.037	$2.668 \cdot 10^{-4}$	0.030	
	2.825 - 3.3	$6.888 \cdot 10^{-3}$	$2.797 \cdot 10^{-4}$	0.041	$2.063 \cdot 10^{-4}$	0.030	
	3.3 - 3.95	$4.939 \cdot 10^{-3}$	$2.064 \cdot 10^{-4}$	0.042	$1.450 \cdot 10^{-4}$	0.029	
	3.95 - 5.05	$2.478 \cdot 10^{-3}$	$1.169 \cdot 10^{-4}$	0.047	$7.220 \cdot 10^{-5}$	0.029	
	5.05 - 7.55	$7.496 \cdot 10^{-4}$	$4.296 \cdot 10^{-5}$	0.057	$2.212 \cdot 10^{-5}$	0.030	
180 - 220	0.4 - 0.75	$1.677 \cdot 10^{-2}$	$9.355 \cdot 10^{-4}$	0.056	$1.725 \cdot 10^{-3}$	0.103	
	0.75 - 1.05	$1.748 \cdot 10^{-2}$	$1.123 \cdot 10^{-3}$	0.064	$1.060 \cdot 10^{-3}$	0.061	
	1.05 - 1.325	$1.645 \cdot 10^{-2}$	$8.612 \cdot 10^{-4}$	0.052	$6.962 \cdot 10^{-4}$	0.042	
	1.325 - 1.675	$1.480 \cdot 10^{-2}$	$7.696 \cdot 10^{-4}$	0.052	$5.129 \cdot 10^{-4}$	0.035	
	1.675 - 2.075	$1.061 \cdot 10^{-2}$	$5.858 \cdot 10^{-4}$	0.055	$3.253 \cdot 10^{-4}$	0.031	
	2.075 - 2.475	$8.987 \cdot 10^{-3}$	$5.139 \cdot 10^{-4}$	0.057	$2.665 \cdot 10^{-4}$	0.030	
	2.475 - 2.925	$5.919 \cdot 10^{-3}$	$3.836 \cdot 10^{-4}$	0.065	$1.728 \cdot 10^{-4}$	0.029	
	2.925 - 3.5	$3.924 \cdot 10^{-3}$	$2.763 \cdot 10^{-4}$	0.070	$1.138 \cdot 10^{-4}$	0.029	
	3.5 - 4.4	$1.970 \cdot 10^{-3}$	$1.547 \cdot 10^{-4}$	0.079	$5.772 \cdot 10^{-5}$	0.029	
	4.4 - 6.9	$4.859 \cdot 10^{-4}$	$3.306 \cdot 10^{-5}$	0.068	$1.460 \cdot 10^{-5}$	0.030	
220 - 260	0.3 - 0.7	$1.450 \cdot 10^{-2}$	$9.448 \cdot 10^{-4}$	0.065	$4.771 \cdot 10^{-4}$	0.033	

Table D.2: Multiplicities of π^- for the different (p, θ, z) bins with related statistical and systematic uncertainties

z	θ	p	$d\pi^-/dp$	Δ_{stat}	$\Delta_{stat}\%$	Δ_{sys}	$\Delta_{sys}\%$
		[mrad]	[(GeV/c)/p.o.t]				
		0.7 - 0.975	$1.781 \cdot 10^{-2}$	$1.052 \cdot 10^{-3}$	0.059	$5.595 \cdot 10^{-4}$	0.031
		0.975 - 1.325	$1.759 \cdot 10^{-2}$	$8.537 \cdot 10^{-4}$	0.049	$5.475 \cdot 10^{-4}$	0.031
		1.325 - 1.675	$1.258 \cdot 10^{-2}$	$7.185 \cdot 10^{-4}$	0.057	$3.760 \cdot 10^{-4}$	0.030
		1.675 - 2.15	$9.575 \cdot 10^{-3}$	$5.420 \cdot 10^{-4}$	0.057	$2.862 \cdot 10^{-4}$	0.030
		2.15 - 2.925	$4.912 \cdot 10^{-3}$	$2.615 \cdot 10^{-4}$	0.053	$1.427 \cdot 10^{-4}$	0.029
		2.925 - 5.425	$9.266 \cdot 10^{-4}$	$6.364 \cdot 10^{-5}$	0.069	$2.687 \cdot 10^{-5}$	0.029
260 - 300	0.3 - 0.675	1.688 $\cdot 10^{-2}$	$1.123 \cdot 10^{-3}$	0.067	$1.643 \cdot 10^{-3}$	0.097	
	0.675 - 0.975	$1.600 \cdot 10^{-2}$	$9.566 \cdot 10^{-4}$	0.060	$8.929 \cdot 10^{-4}$	0.056	
	0.975 - 1.25	$1.430 \cdot 10^{-2}$	$8.678 \cdot 10^{-4}$	0.061	$5.690 \cdot 10^{-4}$	0.040	
	1.25 - 1.625	$1.033 \cdot 10^{-2}$	$5.986 \cdot 10^{-4}$	0.058	$3.418 \cdot 10^{-4}$	0.033	
	1.625 - 2.225	$7.031 \cdot 10^{-3}$	$3.939 \cdot 10^{-4}$	0.056	$2.239 \cdot 10^{-4}$	0.032	
	2.225 - 4.725	$1.568 \cdot 10^{-3}$	$9.298 \cdot 10^{-5}$	0.059	$4.674 \cdot 10^{-5}$	0.030	
	300 - 340	0.2 - 0.45	$1.075 \cdot 10^{-2}$	$1.434 \cdot 10^{-3}$	0.133	$1.265 \cdot 10^{-3}$	0.118
		0.45 - 0.7	$1.550 \cdot 10^{-2}$	$1.292 \cdot 10^{-3}$	0.083	$1.183 \cdot 10^{-3}$	0.076
		0.7 - 0.95	$1.441 \cdot 10^{-2}$	$1.143 \cdot 10^{-3}$	0.079	$7.516 \cdot 10^{-4}$	0.052
		0.95 - 1.275	$1.024 \cdot 10^{-2}$	$5.870 \cdot 10^{-4}$	0.057	$4.062 \cdot 10^{-4}$	0.040
		1.275 - 2.55	$5.523 \cdot 10^{-3}$	$4.461 \cdot 10^{-4}$	0.081	$1.706 \cdot 10^{-4}$	0.031
z 3	0 - 20	0.7 - 1.3	$4.671 \cdot 10^{-5}$	$1.653 \cdot 10^{-5}$	0.354	$3.208 \cdot 10^{-6}$	0.069
		1.3 - 2.175	$7.837 \cdot 10^{-5}$	$1.145 \cdot 10^{-5}$	0.146	$4.086 \cdot 10^{-6}$	0.052
		2.175 - 3.325	$9.183 \cdot 10^{-5}$	$1.056 \cdot 10^{-5}$	0.115	$4.109 \cdot 10^{-6}$	0.045
		3.325 - 4.675	$7.346 \cdot 10^{-5}$	$7.608 \cdot 10^{-6}$	0.104	$3.133 \cdot 10^{-6}$	0.043
		4.675 - 8.95	$5.558 \cdot 10^{-5}$	$4.560 \cdot 10^{-6}$	0.082	$2.985 \cdot 10^{-6}$	0.054
		8.95 - 17.65	$1.667 \cdot 10^{-5}$	$1.723 \cdot 10^{-6}$	0.103	$5.790 \cdot 10^{-7}$	0.035
		17.65 - 29.3	$4.499 \cdot 10^{-7}$	$4.481 \cdot 10^{-7}$	0.996	$5.388 \cdot 10^{-8}$	0.120
	20 - 40	0.6 - 1.23	$6.157 \cdot 10^{-4}$	$8.619 \cdot 10^{-5}$	0.140	$2.150 \cdot 10^{-5}$	0.035
		1.23 - 1.775	$8.697 \cdot 10^{-4}$	$5.623 \cdot 10^{-5}$	0.065	$2.951 \cdot 10^{-5}$	0.034
		1.775 - 2.15	$8.352 \cdot 10^{-4}$	$6.033 \cdot 10^{-5}$	0.072	$2.922 \cdot 10^{-5}$	0.035
		2.15 - 2.575	$9.295 \cdot 10^{-4}$	$6.278 \cdot 10^{-5}$	0.068	$3.071 \cdot 10^{-5}$	0.033
		2.575 - 2.975	$1.027 \cdot 10^{-3}$	$6.599 \cdot 10^{-5}$	0.064	$3.423 \cdot 10^{-5}$	0.033
		2.975 - 3.425	$9.766 \cdot 10^{-4}$	$6.375 \cdot 10^{-5}$	0.065	$2.979 \cdot 10^{-5}$	0.031
		3.425 - 4.025	$8.166 \cdot 10^{-4}$	$4.926 \cdot 10^{-5}$	0.060	$2.489 \cdot 10^{-5}$	0.030
		4.025 - 4.825	$8.020 \cdot 10^{-4}$	$5.218 \cdot 10^{-5}$	0.065	$2.609 \cdot 10^{-5}$	0.033
		4.825 - 6.05	$7.142 \cdot 10^{-4}$	$4.480 \cdot 10^{-5}$	0.063	$2.101 \cdot 10^{-5}$	0.029
		6.05 - 7.75	$5.227 \cdot 10^{-4}$	$3.137 \cdot 10^{-5}$	0.060	$1.582 \cdot 10^{-5}$	0.030
		7.75 - 9.55	$3.659 \cdot 10^{-4}$	$2.543 \cdot 10^{-5}$	0.069	$1.130 \cdot 10^{-5}$	0.031
		9.55 - 11.625	$2.946 \cdot 10^{-4}$	$2.287 \cdot 10^{-5}$	0.078	$1.031 \cdot 10^{-5}$	0.035
		11.625 - 14.125	$1.541 \cdot 10^{-4}$	$1.481 \cdot 10^{-5}$	0.096	$4.750 \cdot 10^{-6}$	0.031
		14.125 - 18.125	$6.049 \cdot 10^{-5}$	$9.716 \cdot 10^{-6}$	0.161	$1.847 \cdot 10^{-6}$	0.031
		18.125 - 23.625	$1.199 \cdot 10^{-5}$	$1.198 \cdot 10^{-5}$	1.000	$3.714 \cdot 10^{-7}$	0.031
		23.625 - 29.625	$0.000 \cdot 10^0$	$0.000 \cdot 10^0$	0.000	$0.000 \cdot 10^0$	0.000
40 - 60	0.6 - 1.175	$1.777 \cdot 10^{-3}$	$1.560 \cdot 10^{-4}$	0.088	$7.221 \cdot 10^{-5}$	0.041	
	1.175 - 1.675	$2.105 \cdot 10^{-3}$	$9.274 \cdot 10^{-5}$	0.044	$7.146 \cdot 10^{-5}$	0.034	
	1.675 - 1.975	$2.315 \cdot 10^{-3}$	$1.033 \cdot 10^{-4}$	0.045	$7.528 \cdot 10^{-5}$	0.033	

Table D.2: Multiplicities of π^- for the different (p, θ, z) bins with related statistical and systematic uncertainties

z	θ	p	$d\mathbf{n}^{\pi^-}/dp$	Δ_{stat}	$\Delta_{stat}\%$	Δ_{sys}	$\Delta_{sys}\%$
	[mrad]	[GeV/c]	[/ (GeV/c)/p.o.t]				
	1.975 - 2.275		$2.430 \cdot 10^{-3}$	$1.304 \cdot 10^{-4}$	0.054	$7.871 \cdot 10^{-5}$	0.032
	2.275 - 2.6		$2.497 \cdot 10^{-3}$	$1.569 \cdot 10^{-4}$	0.063	$8.537 \cdot 10^{-5}$	0.034
	2.6 - 3.1		$2.462 \cdot 10^{-3}$	$1.136 \cdot 10^{-4}$	0.046	$7.753 \cdot 10^{-5}$	0.031
	3.1 - 3.925		$2.203 \cdot 10^{-3}$	$7.966 \cdot 10^{-5}$	0.036	$6.593 \cdot 10^{-5}$	0.030
	3.925 - 4.9		$1.966 \cdot 10^{-3}$	$8.006 \cdot 10^{-5}$	0.041	$5.839 \cdot 10^{-5}$	0.030
	4.9 - 5.95		$1.620 \cdot 10^{-3}$	$6.666 \cdot 10^{-5}$	0.041	$4.759 \cdot 10^{-5}$	0.029
	5.95 - 6.92		$1.254 \cdot 10^{-3}$	$6.027 \cdot 10^{-5}$	0.048	$3.643 \cdot 10^{-5}$	0.029
	6.92 - 8.175		$9.952 \cdot 10^{-4}$	$5.133 \cdot 10^{-5}$	0.052	$2.942 \cdot 10^{-5}$	0.030
	8.175 - 9.5		$6.285 \cdot 10^{-4}$	$2.859 \cdot 10^{-5}$	0.045	$1.870 \cdot 10^{-5}$	0.030
	9.5 - 11.2		$3.814 \cdot 10^{-4}$	$1.805 \cdot 10^{-5}$	0.047	$1.122 \cdot 10^{-5}$	0.029
	11.2 - 13.325		$1.979 \cdot 10^{-4}$	$1.228 \cdot 10^{-5}$	0.062	$6.130 \cdot 10^{-6}$	0.031
	13.325 - 16.5		$6.414 \cdot 10^{-5}$	$5.502 \cdot 10^{-6}$	0.086	$1.970 \cdot 10^{-6}$	0.031
	16.5 - 19		$1.689 \cdot 10^{-5}$	$2.172 \cdot 10^{-6}$	0.129	$7.020 \cdot 10^{-7}$	0.042
60 - 80	0.6 - 1.25		$2.574 \cdot 10^{-3}$	$1.820 \cdot 10^{-4}$	0.071	$9.046 \cdot 10^{-5}$	0.035
	1.25 - 1.875		$3.280 \cdot 10^{-3}$	$1.159 \cdot 10^{-4}$	0.035	$1.086 \cdot 10^{-4}$	0.033
	1.875 - 2.275		$3.785 \cdot 10^{-3}$	$1.308 \cdot 10^{-4}$	0.035	$1.189 \cdot 10^{-4}$	0.031
	2.275 - 2.875		$3.538 \cdot 10^{-3}$	$1.630 \cdot 10^{-4}$	0.046	$1.099 \cdot 10^{-4}$	0.031
	2.875 - 3.55		$3.117 \cdot 10^{-3}$	$1.436 \cdot 10^{-4}$	0.046	$9.527 \cdot 10^{-5}$	0.031
	3.55 - 4.225		$2.541 \cdot 10^{-3}$	$1.267 \cdot 10^{-4}$	0.050	$7.533 \cdot 10^{-5}$	0.030
	4.225 - 4.95		$2.207 \cdot 10^{-3}$	$8.123 \cdot 10^{-5}$	0.037	$6.574 \cdot 10^{-5}$	0.030
	4.95 - 5.75		$1.747 \cdot 10^{-3}$	$6.917 \cdot 10^{-5}$	0.040	$5.160 \cdot 10^{-5}$	0.030
	5.75 - 6.625		$1.370 \cdot 10^{-3}$	$6.158 \cdot 10^{-5}$	0.045	$4.039 \cdot 10^{-5}$	0.029
	6.625 - 7.725		$9.563 \cdot 10^{-4}$	$4.404 \cdot 10^{-5}$	0.046	$2.904 \cdot 10^{-5}$	0.030
	7.725 - 9.325		$5.575 \cdot 10^{-4}$	$2.831 \cdot 10^{-5}$	0.051	$1.716 \cdot 10^{-5}$	0.031
	9.325 - 11.825		$2.568 \cdot 10^{-4}$	$1.497 \cdot 10^{-5}$	0.058	$8.095 \cdot 10^{-6}$	0.032
	11.825 - 14.325		$8.121 \cdot 10^{-5}$	$1.116 \cdot 10^{-5}$	0.137	$2.577 \cdot 10^{-6}$	0.032
80 - 100	0.5 - 1.3		$3.369 \cdot 10^{-3}$	$1.714 \cdot 10^{-4}$	0.051	$2.020 \cdot 10^{-4}$	0.060
	1.3 - 1.7		$4.418 \cdot 10^{-3}$	$1.743 \cdot 10^{-4}$	0.039	$1.943 \cdot 10^{-4}$	0.044
	1.7 - 2.2		$4.398 \cdot 10^{-3}$	$1.895 \cdot 10^{-4}$	0.043	$1.655 \cdot 10^{-4}$	0.038
	2.2 - 2.675		$4.117 \cdot 10^{-3}$	$1.849 \cdot 10^{-4}$	0.045	$1.417 \cdot 10^{-4}$	0.034
	2.675 - 3.1		$3.852 \cdot 10^{-3}$	$1.898 \cdot 10^{-4}$	0.049	$1.240 \cdot 10^{-4}$	0.032
	3.1 - 3.55		$3.182 \cdot 10^{-3}$	$1.276 \cdot 10^{-4}$	0.040	$9.708 \cdot 10^{-5}$	0.031
	3.55 - 4.05		$3.035 \cdot 10^{-3}$	$1.209 \cdot 10^{-4}$	0.040	$9.123 \cdot 10^{-5}$	0.030
	4.05 - 4.6		$2.364 \cdot 10^{-3}$	$7.301 \cdot 10^{-5}$	0.031	$7.263 \cdot 10^{-5}$	0.031
	4.6 - 5.275		$1.903 \cdot 10^{-3}$	$8.178 \cdot 10^{-5}$	0.043	$5.583 \cdot 10^{-5}$	0.029
	5.275 - 6.125		$1.219 \cdot 10^{-3}$	$5.277 \cdot 10^{-5}$	0.043	$3.670 \cdot 10^{-5}$	0.030
	6.125 - 7.275		$8.671 \cdot 10^{-4}$	$3.717 \cdot 10^{-5}$	0.043	$2.584 \cdot 10^{-5}$	0.030
	7.275 - 9.2		$4.275 \cdot 10^{-4}$	$2.138 \cdot 10^{-5}$	0.050	$1.400 \cdot 10^{-5}$	0.033
	9.2 - 11.7		$1.359 \cdot 10^{-4}$	$1.215 \cdot 10^{-5}$	0.089	$3.984 \cdot 10^{-6}$	0.029
100 - 140	0.5 - 1.3		$1.080 \cdot 10^{-2}$	$3.736 \cdot 10^{-4}$	0.035	$8.222 \cdot 10^{-4}$	0.076
	1.3 - 1.65		$1.187 \cdot 10^{-2}$	$5.467 \cdot 10^{-4}$	0.046	$4.495 \cdot 10^{-4}$	0.038
	1.65 - 1.95		$1.052 \cdot 10^{-2}$	$4.092 \cdot 10^{-4}$	0.039	$3.420 \cdot 10^{-4}$	0.033
	1.95 - 2.275		$1.031 \cdot 10^{-2}$	$3.514 \cdot 10^{-4}$	0.034	$3.176 \cdot 10^{-4}$	0.031

Table D.2: Multiplicities of π^- for the different (p, θ, z) bins with related statistical and systematic uncertainties

z	θ	p	$d\pi^-/dp$	Δ_{stat}	$\Delta_{stat}\%$	Δ_{sys}	$\Delta_{sys}\%$
	[mrad]	[GeV/c]	[/ (GeV/c)/p.o.t]				
	2.275 - 2.575		$8.958 \cdot 10^{-3}$	$3.222 \cdot 10^{-4}$	0.036	$2.698 \cdot 10^{-4}$	0.030
	2.575 - 2.9		$7.973 \cdot 10^{-3}$	$3.115 \cdot 10^{-4}$	0.039	$2.383 \cdot 10^{-4}$	0.030
	2.9 - 3.275		$6.825 \cdot 10^{-3}$	$2.541 \cdot 10^{-4}$	0.037	$2.084 \cdot 10^{-4}$	0.031
	3.275 - 3.675		$5.445 \cdot 10^{-3}$	$2.240 \cdot 10^{-4}$	0.041	$1.618 \cdot 10^{-4}$	0.030
	3.675 - 4.2		$4.130 \cdot 10^{-3}$	$1.748 \cdot 10^{-4}$	0.042	$1.268 \cdot 10^{-4}$	0.031
	4.2 - 4.8		$3.210 \cdot 10^{-3}$	$1.147 \cdot 10^{-4}$	0.036	$9.796 \cdot 10^{-5}$	0.031
	4.8 - 5.725		$2.093 \cdot 10^{-3}$	$9.361 \cdot 10^{-5}$	0.045	$6.269 \cdot 10^{-5}$	0.030
	5.725 - 7.075		$1.108 \cdot 10^{-3}$	$5.388 \cdot 10^{-5}$	0.049	$3.268 \cdot 10^{-5}$	0.029
	7.075 - 9.575		$3.639 \cdot 10^{-4}$	$2.269 \cdot 10^{-5}$	0.062	$1.082 \cdot 10^{-5}$	0.030
140 - 180	0.4 - 0.925		$1.294 \cdot 10^{-2}$	$6.559 \cdot 10^{-4}$	0.051	$1.442 \cdot 10^{-3}$	0.111
	0.925 - 1.45		$1.332 \cdot 10^{-2}$	$6.394 \cdot 10^{-4}$	0.048	$6.535 \cdot 10^{-4}$	0.049
	1.45 - 1.775		$1.160 \cdot 10^{-2}$	$6.488 \cdot 10^{-4}$	0.056	$3.990 \cdot 10^{-4}$	0.034
	1.775 - 2.1		$9.654 \cdot 10^{-3}$	$5.664 \cdot 10^{-4}$	0.059	$3.008 \cdot 10^{-4}$	0.031
	2.1 - 2.425		$9.056 \cdot 10^{-3}$	$4.056 \cdot 10^{-4}$	0.045	$2.825 \cdot 10^{-4}$	0.031
	2.425 - 2.825		$6.784 \cdot 10^{-3}$	$3.214 \cdot 10^{-4}$	0.047	$2.032 \cdot 10^{-4}$	0.030
	2.825 - 3.3		$5.004 \cdot 10^{-3}$	$2.390 \cdot 10^{-4}$	0.048	$1.487 \cdot 10^{-4}$	0.030
	3.3 - 3.95		$3.469 \cdot 10^{-3}$	$1.744 \cdot 10^{-4}$	0.050	$1.011 \cdot 10^{-4}$	0.029
	3.95 - 5.05		$1.871 \cdot 10^{-3}$	$5.740 \cdot 10^{-5}$	0.031	$5.467 \cdot 10^{-5}$	0.029
	5.05 - 7.55		$4.677 \cdot 10^{-4}$	$3.057 \cdot 10^{-5}$	0.065	$1.433 \cdot 10^{-5}$	0.031
180 - 220	0.4 - 0.75		$1.387 \cdot 10^{-2}$	$8.663 \cdot 10^{-4}$	0.062	$4.430 \cdot 10^{-4}$	0.032
	0.75 - 1.05		$1.560 \cdot 10^{-2}$	$1.039 \cdot 10^{-3}$	0.067	$4.883 \cdot 10^{-4}$	0.031
	1.05 - 1.325		$1.357 \cdot 10^{-2}$	$8.157 \cdot 10^{-4}$	0.060	$4.142 \cdot 10^{-4}$	0.031
	1.325 - 1.675		$1.198 \cdot 10^{-2}$	$6.790 \cdot 10^{-4}$	0.057	$3.581 \cdot 10^{-4}$	0.030
	1.675 - 2.075		$9.909 \cdot 10^{-3}$	$5.865 \cdot 10^{-4}$	0.059	$2.944 \cdot 10^{-4}$	0.030
	2.075 - 2.475		$7.079 \cdot 10^{-3}$	$4.304 \cdot 10^{-4}$	0.061	$2.197 \cdot 10^{-4}$	0.031
	2.475 - 2.925		$5.350 \cdot 10^{-3}$	$3.519 \cdot 10^{-4}$	0.066	$1.659 \cdot 10^{-4}$	0.031
	2.925 - 3.5		$3.157 \cdot 10^{-3}$	$2.298 \cdot 10^{-4}$	0.073	$9.205 \cdot 10^{-5}$	0.029
	3.5 - 4.4		$1.550 \cdot 10^{-3}$	$9.909 \cdot 10^{-5}$	0.064	$4.562 \cdot 10^{-5}$	0.029
	4.4 - 6.9		$3.586 \cdot 10^{-4}$	$2.819 \cdot 10^{-5}$	0.079	$1.107 \cdot 10^{-5}$	0.031
220 - 260	0.3 - 0.7		$1.443 \cdot 10^{-2}$	$8.599 \cdot 10^{-4}$	0.060	$1.479 \cdot 10^{-3}$	0.102
	0.7 - 0.975		$1.536 \cdot 10^{-2}$	$9.700 \cdot 10^{-4}$	0.063	$9.125 \cdot 10^{-4}$	0.059
	0.975 - 1.325		$1.412 \cdot 10^{-2}$	$7.521 \cdot 10^{-4}$	0.053	$5.698 \cdot 10^{-4}$	0.040
	1.325 - 1.675		$1.088 \cdot 10^{-2}$	$6.393 \cdot 10^{-4}$	0.059	$3.594 \cdot 10^{-4}$	0.033
	1.675 - 2.15		$8.054 \cdot 10^{-3}$	$4.440 \cdot 10^{-4}$	0.055	$2.500 \cdot 10^{-4}$	0.031
	2.15 - 2.925		$3.953 \cdot 10^{-3}$	$2.185 \cdot 10^{-4}$	0.055	$1.232 \cdot 10^{-4}$	0.031
	2.925 - 5.425		$7.538 \cdot 10^{-4}$	$5.690 \cdot 10^{-5}$	0.075	$2.200 \cdot 10^{-5}$	0.029
260 - 300	0.3 - 0.675		$1.462 \cdot 10^{-2}$	$1.061 \cdot 10^{-3}$	0.073	$1.578 \cdot 10^{-3}$	0.108
	0.675 - 0.975		$1.508 \cdot 10^{-2}$	$8.915 \cdot 10^{-4}$	0.059	$9.251 \cdot 10^{-4}$	0.061
	0.975 - 1.25		$1.154 \cdot 10^{-2}$	$7.482 \cdot 10^{-4}$	0.065	$4.940 \cdot 10^{-4}$	0.043
	1.25 - 1.625		$9.671 \cdot 10^{-3}$	$5.394 \cdot 10^{-4}$	0.056	$3.424 \cdot 10^{-4}$	0.035
	1.625 - 2.225		$5.244 \cdot 10^{-3}$	$3.198 \cdot 10^{-4}$	0.061	$1.596 \cdot 10^{-4}$	0.030
	2.225 - 4.725		$1.053 \cdot 10^{-3}$	$6.761 \cdot 10^{-5}$	0.064	$3.140 \cdot 10^{-5}$	0.030
300 - 340	0.2 - 0.45		$7.848 \cdot 10^{-3}$	$1.180 \cdot 10^{-3}$	0.150	$3.471 \cdot 10^{-4}$	0.044

Table D.2: Multiplicities of π^- for the different (p, θ, z) bins with related statistical and systematic uncertainties

z	θ	p	$d\mathbf{n}^{\pi^-}/dp$	Δ_{stat}	$\Delta_{stat}\%$	Δ_{sys}	$\Delta_{sys}\%$
	[mrad]	[GeV/c]	[/ (GeV/c)/p.o.t]				
z 4	0 - 20	0.45 - 0.7	$1.330 \cdot 10^{-2}$	$1.032 \cdot 10^{-3}$	0.078	$4.858 \cdot 10^{-4}$	0.037
		0.7 - 0.95	$1.415 \cdot 10^{-2}$	$9.822 \cdot 10^{-4}$	0.069	$4.390 \cdot 10^{-4}$	0.031
		0.95 - 1.275	$1.062 \cdot 10^{-2}$	$6.970 \cdot 10^{-4}$	0.066	$3.316 \cdot 10^{-4}$	0.031
		1.275 - 2.55	$5.086 \cdot 10^{-3}$	$2.768 \cdot 10^{-4}$	0.054	$1.598 \cdot 10^{-4}$	0.031
		0.7 - 1.3	$7.372 \cdot 10^{-5}$	$1.958 \cdot 10^{-5}$	0.266	$4.657 \cdot 10^{-6}$	0.063
		1.3 - 2.175	$1.053 \cdot 10^{-4}$	$1.287 \cdot 10^{-5}$	0.122	$5.343 \cdot 10^{-6}$	0.051
		2.175 - 3.325	$1.146 \cdot 10^{-4}$	$1.082 \cdot 10^{-5}$	0.094	$4.218 \cdot 10^{-6}$	0.037
		3.325 - 4.675	$1.106 \cdot 10^{-4}$	$9.915 \cdot 10^{-6}$	0.090	$4.175 \cdot 10^{-6}$	0.038
		4.675 - 8.95	$6.474 \cdot 10^{-5}$	$5.160 \cdot 10^{-6}$	0.080	$2.002 \cdot 10^{-6}$	0.031
		8.95 - 17.65	$2.244 \cdot 10^{-5}$	$2.889 \cdot 10^{-6}$	0.129	$7.465 \cdot 10^{-7}$	0.033
		17.65 - 29.3	$2.193 \cdot 10^{-6}$	$1.453 \cdot 10^{-6}$	0.662	$1.733 \cdot 10^{-7}$	0.079
		0.6 - 1.23	$4.979 \cdot 10^{-4}$	$7.465 \cdot 10^{-5}$	0.150	$1.922 \cdot 10^{-5}$	0.039
		1.23 - 1.775	$8.216 \cdot 10^{-4}$	$5.280 \cdot 10^{-5}$	0.064	$2.953 \cdot 10^{-5}$	0.036
		1.775 - 2.15	$9.349 \cdot 10^{-4}$	$6.334 \cdot 10^{-5}$	0.068	$3.147 \cdot 10^{-5}$	0.034
		2.15 - 2.575	$8.162 \cdot 10^{-4}$	$5.517 \cdot 10^{-5}$	0.068	$2.628 \cdot 10^{-5}$	0.032
20 - 40		2.575 - 2.975	$9.242 \cdot 10^{-4}$	$6.086 \cdot 10^{-5}$	0.066	$3.049 \cdot 10^{-5}$	0.033
		2.975 - 3.425	$8.816 \cdot 10^{-4}$	$5.196 \cdot 10^{-5}$	0.059	$2.820 \cdot 10^{-5}$	0.032
		3.425 - 4.025	$9.273 \cdot 10^{-4}$	$7.592 \cdot 10^{-5}$	0.082	$2.817 \cdot 10^{-5}$	0.030
		4.025 - 4.825	$9.123 \cdot 10^{-4}$	$6.587 \cdot 10^{-5}$	0.072	$3.086 \cdot 10^{-5}$	0.034
		4.825 - 6.05	$8.227 \cdot 10^{-4}$	$5.214 \cdot 10^{-5}$	0.063	$2.658 \cdot 10^{-5}$	0.032
		6.05 - 7.75	$6.336 \cdot 10^{-4}$	$3.693 \cdot 10^{-5}$	0.058	$1.957 \cdot 10^{-5}$	0.031
		7.75 - 9.55	$3.907 \cdot 10^{-4}$	$2.706 \cdot 10^{-5}$	0.069	$1.202 \cdot 10^{-5}$	0.031
		9.55 - 11.625	$2.569 \cdot 10^{-4}$	$2.177 \cdot 10^{-5}$	0.085	$8.121 \cdot 10^{-6}$	0.032
		11.625 - 14.125	$1.715 \cdot 10^{-4}$	$1.688 \cdot 10^{-5}$	0.098	$5.251 \cdot 10^{-6}$	0.031
		14.125 - 18.125	$4.353 \cdot 10^{-5}$	$7.127 \cdot 10^{-6}$	0.164	$1.370 \cdot 10^{-6}$	0.031
		18.125 - 23.625	$6.493 \cdot 10^{-6}$	$1.914 \cdot 10^{-6}$	0.295	$2.322 \cdot 10^{-7}$	0.036
		23.625 - 29.625	$0.000 \cdot 10^0$	$0.000 \cdot 10^0$	0.000	$0.000 \cdot 10^0$	0.000
40 - 60		0.6 - 1.175	$1.231 \cdot 10^{-3}$	$1.196 \cdot 10^{-4}$	0.097	$6.426 \cdot 10^{-5}$	0.052
		1.175 - 1.675	$1.738 \cdot 10^{-3}$	$7.998 \cdot 10^{-5}$	0.046	$6.258 \cdot 10^{-5}$	0.036
		1.675 - 1.975	$1.887 \cdot 10^{-3}$	$1.008 \cdot 10^{-4}$	0.053	$6.372 \cdot 10^{-5}$	0.034
		1.975 - 2.275	$2.006 \cdot 10^{-3}$	$1.087 \cdot 10^{-4}$	0.054	$6.494 \cdot 10^{-5}$	0.032
		2.275 - 2.6	$2.087 \cdot 10^{-3}$	$1.076 \cdot 10^{-4}$	0.052	$6.559 \cdot 10^{-5}$	0.031
		2.6 - 3.1	$1.816 \cdot 10^{-3}$	$1.088 \cdot 10^{-4}$	0.060	$5.744 \cdot 10^{-5}$	0.032
		3.1 - 3.925	$1.878 \cdot 10^{-3}$	$8.527 \cdot 10^{-5}$	0.045	$6.031 \cdot 10^{-5}$	0.032
		3.925 - 4.9	$1.720 \cdot 10^{-3}$	$7.653 \cdot 10^{-5}$	0.044	$5.545 \cdot 10^{-5}$	0.032
		4.9 - 5.95	$1.267 \cdot 10^{-3}$	$6.186 \cdot 10^{-5}$	0.049	$3.827 \cdot 10^{-5}$	0.030
		5.95 - 6.92	$9.384 \cdot 10^{-4}$	$5.638 \cdot 10^{-5}$	0.060	$3.004 \cdot 10^{-5}$	0.032
		6.92 - 8.175	$7.516 \cdot 10^{-4}$	$4.454 \cdot 10^{-5}$	0.059	$2.203 \cdot 10^{-5}$	0.029
		8.175 - 9.5	$4.461 \cdot 10^{-4}$	$2.437 \cdot 10^{-5}$	0.055	$1.372 \cdot 10^{-5}$	0.031
		9.5 - 11.2	$2.847 \cdot 10^{-4}$	$1.591 \cdot 10^{-5}$	0.056	$8.258 \cdot 10^{-6}$	0.029
		11.2 - 13.325	$1.451 \cdot 10^{-4}$	$9.956 \cdot 10^{-6}$	0.069	$4.460 \cdot 10^{-6}$	0.031
		13.325 - 16.5	$6.666 \cdot 10^{-5}$	$6.135 \cdot 10^{-6}$	0.092	$2.007 \cdot 10^{-6}$	0.030
		16.5 - 19	$9.028 \cdot 10^{-6}$	$2.423 \cdot 10^{-6}$	0.268	$3.495 \cdot 10^{-7}$	0.039

Table D.2: Multiplicities of π^- for the different (p, θ, z) bins with related statistical and systematic uncertainties

z	θ [mrad]	p [GeV/c]	$d\pi^-/dp$ [/(GeV/c)/p.o.t]	Δ_{stat}	$\Delta_{stat}\%$	Δ_{sys}	$\Delta_{sys}\%$
60 - 80	0.6 - 1.25	$2.301 \cdot 10^{-3}$		$1.609 \cdot 10^{-4}$	0.070	$7.766 \cdot 10^{-5}$	0.034
	1.25 - 1.875	$2.863 \cdot 10^{-3}$		$1.056 \cdot 10^{-4}$	0.037	$9.121 \cdot 10^{-5}$	0.032
	1.875 - 2.275	$3.022 \cdot 10^{-3}$		$1.876 \cdot 10^{-4}$	0.062	$9.602 \cdot 10^{-5}$	0.032
	2.275 - 2.875	$2.903 \cdot 10^{-3}$		$1.441 \cdot 10^{-4}$	0.050	$9.330 \cdot 10^{-5}$	0.032
	2.875 - 3.55	$2.568 \cdot 10^{-3}$		$1.321 \cdot 10^{-4}$	0.051	$7.951 \cdot 10^{-5}$	0.031
	3.55 - 4.225	$2.157 \cdot 10^{-3}$		$1.021 \cdot 10^{-4}$	0.047	$6.409 \cdot 10^{-5}$	0.030
	4.225 - 4.95	$1.634 \cdot 10^{-3}$		$6.984 \cdot 10^{-5}$	0.043	$5.044 \cdot 10^{-5}$	0.031
	4.95 - 5.75	$1.482 \cdot 10^{-3}$		$6.518 \cdot 10^{-5}$	0.044	$4.612 \cdot 10^{-5}$	0.031
	5.75 - 6.625	$1.062 \cdot 10^{-3}$		$5.259 \cdot 10^{-5}$	0.050	$3.205 \cdot 10^{-5}$	0.030
	6.625 - 7.725	$7.024 \cdot 10^{-4}$		$2.876 \cdot 10^{-5}$	0.041	$2.094 \cdot 10^{-5}$	0.030
	7.725 - 9.325	$4.379 \cdot 10^{-4}$		$2.614 \cdot 10^{-5}$	0.060	$1.343 \cdot 10^{-5}$	0.031
	9.325 - 11.825	$1.843 \cdot 10^{-4}$		$1.276 \cdot 10^{-5}$	0.069	$5.941 \cdot 10^{-6}$	0.032
	11.825 - 14.325	$5.985 \cdot 10^{-5}$		$7.879 \cdot 10^{-6}$	0.132	$2.053 \cdot 10^{-6}$	0.034
	80 - 100	0.5 - 1.3	$2.673 \cdot 10^{-3}$	$1.242 \cdot 10^{-4}$	0.046	$1.731 \cdot 10^{-4}$	0.065
	1.3 - 1.7	$3.584 \cdot 10^{-3}$		$2.108 \cdot 10^{-4}$	0.059	$1.440 \cdot 10^{-4}$	0.040
	1.7 - 2.2	$3.881 \cdot 10^{-3}$		$1.813 \cdot 10^{-4}$	0.047	$1.317 \cdot 10^{-4}$	0.034
	2.2 - 2.675	$3.450 \cdot 10^{-3}$		$1.843 \cdot 10^{-4}$	0.053	$1.071 \cdot 10^{-4}$	0.031
	2.675 - 3.1	$3.100 \cdot 10^{-3}$		$1.771 \cdot 10^{-4}$	0.057	$9.526 \cdot 10^{-5}$	0.031
	3.1 - 3.55	$2.592 \cdot 10^{-3}$		$1.183 \cdot 10^{-4}$	0.046	$7.671 \cdot 10^{-5}$	0.030
	3.55 - 4.05	$2.122 \cdot 10^{-3}$		$1.278 \cdot 10^{-4}$	0.060	$6.286 \cdot 10^{-5}$	0.030
	4.05 - 4.6	$1.852 \cdot 10^{-3}$		$8.999 \cdot 10^{-5}$	0.049	$5.404 \cdot 10^{-5}$	0.029
	4.6 - 5.275	$1.463 \cdot 10^{-3}$		$7.038 \cdot 10^{-5}$	0.048	$4.355 \cdot 10^{-5}$	0.030
100 - 140	5.275 - 6.125	$1.031 \cdot 10^{-3}$		$5.330 \cdot 10^{-5}$	0.052	$3.085 \cdot 10^{-5}$	0.030
	6.125 - 7.275	$6.268 \cdot 10^{-4}$		$3.550 \cdot 10^{-5}$	0.057	$1.875 \cdot 10^{-5}$	0.030
	7.275 - 9.2	$3.372 \cdot 10^{-4}$		$1.937 \cdot 10^{-5}$	0.057	$9.799 \cdot 10^{-6}$	0.029
	9.2 - 11.7	$1.060 \cdot 10^{-4}$		$1.106 \cdot 10^{-5}$	0.104	$3.205 \cdot 10^{-6}$	0.030
	0.5 - 1.3	$7.493 \cdot 10^{-3}$		$3.125 \cdot 10^{-4}$	0.042	$4.355 \cdot 10^{-4}$	0.058
	1.3 - 1.65	$9.415 \cdot 10^{-3}$		$4.894 \cdot 10^{-4}$	0.052	$3.264 \cdot 10^{-4}$	0.035
	1.65 - 1.95	$9.209 \cdot 10^{-3}$		$4.837 \cdot 10^{-4}$	0.053	$2.950 \cdot 10^{-4}$	0.032
	1.95 - 2.275	$7.845 \cdot 10^{-3}$		$4.226 \cdot 10^{-4}$	0.054	$2.453 \cdot 10^{-4}$	0.031
	2.275 - 2.575	$7.299 \cdot 10^{-3}$		$2.959 \cdot 10^{-4}$	0.041	$2.244 \cdot 10^{-4}$	0.031
	2.575 - 2.9	$5.890 \cdot 10^{-3}$		$2.637 \cdot 10^{-4}$	0.045	$1.762 \cdot 10^{-4}$	0.030
	2.9 - 3.275	$4.835 \cdot 10^{-3}$		$2.026 \cdot 10^{-4}$	0.042	$1.436 \cdot 10^{-4}$	0.030
	3.275 - 3.675	$4.246 \cdot 10^{-3}$		$1.688 \cdot 10^{-4}$	0.040	$1.310 \cdot 10^{-4}$	0.031
	3.675 - 4.2	$3.401 \cdot 10^{-3}$		$1.608 \cdot 10^{-4}$	0.047	$9.966 \cdot 10^{-5}$	0.029
	4.2 - 4.8	$2.309 \cdot 10^{-3}$		$1.212 \cdot 10^{-4}$	0.053	$6.953 \cdot 10^{-5}$	0.030
	4.8 - 5.725	$1.647 \cdot 10^{-3}$		$8.125 \cdot 10^{-5}$	0.049	$4.760 \cdot 10^{-5}$	0.029
	5.725 - 7.075	$8.160 \cdot 10^{-4}$		$4.880 \cdot 10^{-5}$	0.060	$2.572 \cdot 10^{-5}$	0.032
	7.075 - 9.575	$2.388 \cdot 10^{-4}$		$1.626 \cdot 10^{-5}$	0.068	$7.080 \cdot 10^{-6}$	0.030
140 - 180	0.4 - 0.925	$9.791 \cdot 10^{-3}$		$5.668 \cdot 10^{-4}$	0.058	$3.205 \cdot 10^{-4}$	0.033
	0.925 - 1.45	$1.070 \cdot 10^{-2}$		$6.198 \cdot 10^{-4}$	0.058	$3.464 \cdot 10^{-4}$	0.032
	1.45 - 1.775	$9.291 \cdot 10^{-3}$		$5.980 \cdot 10^{-4}$	0.064	$3.124 \cdot 10^{-4}$	0.034
	1.775 - 2.1	$8.534 \cdot 10^{-3}$		$5.978 \cdot 10^{-4}$	0.070	$2.612 \cdot 10^{-4}$	0.031

Table D.2: Multiplicities of π^- for the different (p, θ, z) bins with related statistical and systematic uncertainties

z	θ	p	$d\mathbf{n}^{\pi^-}/dp$	Δ_{stat}	$\Delta_{stat}\%$	Δ_{sys}	$\Delta_{sys}\%$
	[mrad]	[GeV/c]	[/ (GeV/c)/p.o.t]				
	2.1 - 2.425		$7.138 \cdot 10^{-3}$	$3.552 \cdot 10^{-4}$	0.050	$2.152 \cdot 10^{-4}$	0.030
	2.425 - 2.825		$5.196 \cdot 10^{-3}$	$2.625 \cdot 10^{-4}$	0.051	$1.597 \cdot 10^{-4}$	0.031
	2.825 - 3.3		$4.056 \cdot 10^{-3}$	$2.378 \cdot 10^{-4}$	0.059	$1.304 \cdot 10^{-4}$	0.032
	3.3 - 3.95		$2.680 \cdot 10^{-3}$	$1.546 \cdot 10^{-4}$	0.058	$8.025 \cdot 10^{-5}$	0.030
	3.95 - 5.05		$1.393 \cdot 10^{-3}$	$9.172 \cdot 10^{-5}$	0.066	$4.265 \cdot 10^{-5}$	0.031
	5.05 - 7.55		$3.743 \cdot 10^{-4}$	$2.752 \cdot 10^{-5}$	0.074	$1.138 \cdot 10^{-5}$	0.030
180 - 220	0.4 - 0.75		$1.016 \cdot 10^{-2}$	$7.404 \cdot 10^{-4}$	0.073	$1.234 \cdot 10^{-3}$	0.121
	0.75 - 1.05		$1.114 \cdot 10^{-2}$	$8.627 \cdot 10^{-4}$	0.077	$7.788 \cdot 10^{-4}$	0.070
	1.05 - 1.325		$1.110 \cdot 10^{-2}$	$7.389 \cdot 10^{-4}$	0.067	$5.119 \cdot 10^{-4}$	0.046
	1.325 - 1.675		$9.301 \cdot 10^{-3}$	$5.969 \cdot 10^{-4}$	0.064	$3.367 \cdot 10^{-4}$	0.036
	1.675 - 2.075		$8.510 \cdot 10^{-3}$	$5.468 \cdot 10^{-4}$	0.064	$2.692 \cdot 10^{-4}$	0.032
	2.075 - 2.475		$5.269 \cdot 10^{-3}$	$3.917 \cdot 10^{-4}$	0.074	$1.574 \cdot 10^{-4}$	0.030
	2.475 - 2.925		$3.601 \cdot 10^{-3}$	$2.836 \cdot 10^{-4}$	0.079	$1.101 \cdot 10^{-4}$	0.031
	2.925 - 3.5		$1.971 \cdot 10^{-3}$	$1.451 \cdot 10^{-4}$	0.074	$5.996 \cdot 10^{-5}$	0.030
	3.5 - 4.4		$1.434 \cdot 10^{-3}$	$9.248 \cdot 10^{-5}$	0.064	$4.153 \cdot 10^{-5}$	0.029
	4.4 - 6.9		$2.654 \cdot 10^{-4}$	$2.430 \cdot 10^{-5}$	0.092	$7.990 \cdot 10^{-6}$	0.030
220 - 260	0.3 - 0.7		$1.049 \cdot 10^{-2}$	$7.755 \cdot 10^{-4}$	0.074	$1.720 \cdot 10^{-3}$	0.164
	0.7 - 0.975		$1.383 \cdot 10^{-2}$	$9.649 \cdot 10^{-4}$	0.070	$1.210 \cdot 10^{-3}$	0.088
	0.975 - 1.325		$1.235 \cdot 10^{-2}$	$7.082 \cdot 10^{-4}$	0.057	$6.730 \cdot 10^{-4}$	0.054
	1.325 - 1.675		$8.144 \cdot 10^{-3}$	$5.404 \cdot 10^{-4}$	0.066	$3.029 \cdot 10^{-4}$	0.037
	1.675 - 2.15		$5.685 \cdot 10^{-3}$	$3.799 \cdot 10^{-4}$	0.067	$1.758 \cdot 10^{-4}$	0.031
	2.15 - 2.925		$2.932 \cdot 10^{-3}$	$1.990 \cdot 10^{-4}$	0.068	$8.746 \cdot 10^{-5}$	0.030
	2.925 - 5.425		$7.276 \cdot 10^{-4}$	$5.490 \cdot 10^{-5}$	0.075	$2.268 \cdot 10^{-5}$	0.031
	0.3 - 0.675		$1.099 \cdot 10^{-2}$	$8.823 \cdot 10^{-4}$	0.080	$9.542 \cdot 10^{-4}$	0.087
	0.675 - 0.975		$1.234 \cdot 10^{-2}$	$8.621 \cdot 10^{-4}$	0.070	$6.409 \cdot 10^{-4}$	0.052
	0.975 - 1.25		$1.075 \cdot 10^{-2}$	$7.321 \cdot 10^{-4}$	0.068	$4.092 \cdot 10^{-4}$	0.038
260 - 300	1.25 - 1.625		$7.491 \cdot 10^{-3}$	$5.053 \cdot 10^{-4}$	0.067	$2.454 \cdot 10^{-4}$	0.033
	1.625 - 2.225		$4.456 \cdot 10^{-3}$	$2.987 \cdot 10^{-4}$	0.067	$1.371 \cdot 10^{-4}$	0.031
	2.225 - 4.725		$9.050 \cdot 10^{-4}$	$6.458 \cdot 10^{-5}$	0.071	$2.655 \cdot 10^{-5}$	0.029
	0.2 - 0.45		$8.183 \cdot 10^{-3}$	$1.328 \cdot 10^{-3}$	0.162	$1.402 \cdot 10^{-3}$	0.171
	0.45 - 0.7		$9.966 \cdot 10^{-3}$	$9.068 \cdot 10^{-4}$	0.091	$1.052 \cdot 10^{-3}$	0.106
	0.7 - 0.95		$1.201 \cdot 10^{-2}$	$8.877 \cdot 10^{-4}$	0.074	$8.422 \cdot 10^{-4}$	0.070
	0.95 - 1.275		$8.527 \cdot 10^{-3}$	$6.117 \cdot 10^{-4}$	0.072	$4.001 \cdot 10^{-4}$	0.047
	1.275 - 2.55		$3.674 \cdot 10^{-3}$	$2.273 \cdot 10^{-4}$	0.062	$1.205 \cdot 10^{-4}$	0.033
	0.7 - 1.3		$6.543 \cdot 10^{-5}$	$1.819 \cdot 10^{-5}$	0.278	$5.492 \cdot 10^{-6}$	0.084
	1.3 - 2.175		$9.114 \cdot 10^{-5}$	$1.144 \cdot 10^{-5}$	0.126	$5.580 \cdot 10^{-6}$	0.061
z 5	2.175 - 3.325		$1.288 \cdot 10^{-4}$	$1.228 \cdot 10^{-5}$	0.095	$4.883 \cdot 10^{-6}$	0.038
	3.325 - 4.675		$1.315 \cdot 10^{-4}$	$1.101 \cdot 10^{-5}$	0.084	$4.500 \cdot 10^{-6}$	0.034
	4.675 - 8.95		$9.296 \cdot 10^{-5}$	$5.836 \cdot 10^{-6}$	0.063	$3.082 \cdot 10^{-6}$	0.033
	8.95 - 17.65		$2.941 \cdot 10^{-5}$	$2.842 \cdot 10^{-6}$	0.097	$1.166 \cdot 10^{-6}$	0.040
	17.65 - 29.3		$3.881 \cdot 10^{-6}$	$9.343 \cdot 10^{-7}$	0.241	$2.822 \cdot 10^{-7}$	0.073
	0.6 - 1.23		$4.238 \cdot 10^{-4}$	$6.391 \cdot 10^{-5}$	0.151	$1.552 \cdot 10^{-5}$	0.037
	1.23 - 1.775		$7.014 \cdot 10^{-4}$	$4.392 \cdot 10^{-5}$	0.063	$2.289 \cdot 10^{-5}$	0.033

Table D.2: Multiplicities of π^- for the different (p, θ, z) bins with related statistical and systematic uncertainties

z	θ	p	$d\pi^-/dp$	Δ_{stat}	$\Delta_{stat}\%$	Δ_{sys}	$\Delta_{sys}\%$
	[mrad]	[GeV/c]	[/ (GeV/c)/p.o.t]				
		1.775 - 2.15	$7.542 \cdot 10^{-4}$	$5.711 \cdot 10^{-5}$	0.076	$2.384 \cdot 10^{-5}$	0.032
		2.15 - 2.575	$7.910 \cdot 10^{-4}$	$6.805 \cdot 10^{-5}$	0.086	$2.467 \cdot 10^{-5}$	0.031
		2.575 - 2.975	$7.632 \cdot 10^{-4}$	$5.205 \cdot 10^{-5}$	0.068	$2.498 \cdot 10^{-5}$	0.033
		2.975 - 3.425	$8.170 \cdot 10^{-4}$	$5.188 \cdot 10^{-5}$	0.064	$2.702 \cdot 10^{-5}$	0.033
		3.425 - 4.025	$7.808 \cdot 10^{-4}$	$7.224 \cdot 10^{-5}$	0.093	$2.426 \cdot 10^{-5}$	0.031
		4.025 - 4.825	$7.476 \cdot 10^{-4}$	$6.072 \cdot 10^{-5}$	0.081	$2.248 \cdot 10^{-5}$	0.030
		4.825 - 6.05	$6.708 \cdot 10^{-4}$	$4.591 \cdot 10^{-5}$	0.068	$2.368 \cdot 10^{-5}$	0.035
		6.05 - 7.75	$4.954 \cdot 10^{-4}$	$3.443 \cdot 10^{-5}$	0.070	$2.105 \cdot 10^{-5}$	0.042
		7.75 - 9.55	$3.289 \cdot 10^{-4}$	$2.645 \cdot 10^{-5}$	0.080	$1.384 \cdot 10^{-5}$	0.042
		9.55 - 11.625	$2.235 \cdot 10^{-4}$	$2.027 \cdot 10^{-5}$	0.091	$7.855 \cdot 10^{-6}$	0.035
		11.625 - 14.125	$9.275 \cdot 10^{-5}$	$1.167 \cdot 10^{-5}$	0.126	$3.154 \cdot 10^{-6}$	0.034
		14.125 - 18.125	$2.801 \cdot 10^{-5}$	$8.053 \cdot 10^{-6}$	0.288	$1.063 \cdot 10^{-6}$	0.038
		18.125 - 23.625	$7.425 \cdot 10^{-6}$	$6.901 \cdot 10^{-6}$	0.929	$4.229 \cdot 10^{-7}$	0.057
		23.625 - 29.625	$0.000 \cdot 10^0$	$0.000 \cdot 10^0$	0.000	$0.000 \cdot 10^0$	0.000
40 - 60	0.6 - 1.175	$1.124 \cdot 10^{-3}$	$1.065 \cdot 10^{-4}$	0.095	$4.050 \cdot 10^{-5}$	0.036	
	1.175 - 1.675	$1.305 \cdot 10^{-3}$	$6.731 \cdot 10^{-5}$	0.052	$4.516 \cdot 10^{-5}$	0.035	
	1.675 - 1.975	$1.426 \cdot 10^{-3}$	$9.126 \cdot 10^{-5}$	0.064	$4.992 \cdot 10^{-5}$	0.035	
	1.975 - 2.275	$1.507 \cdot 10^{-3}$	$1.356 \cdot 10^{-4}$	0.090	$5.203 \cdot 10^{-5}$	0.035	
	2.275 - 2.6	$1.456 \cdot 10^{-3}$	$8.850 \cdot 10^{-5}$	0.061	$4.917 \cdot 10^{-5}$	0.034	
	2.6 - 3.1	$1.501 \cdot 10^{-3}$	$7.663 \cdot 10^{-5}$	0.051	$5.576 \cdot 10^{-5}$	0.037	
	3.1 - 3.925	$1.451 \cdot 10^{-3}$	$7.706 \cdot 10^{-5}$	0.053	$5.401 \cdot 10^{-5}$	0.037	
	3.925 - 4.9	$1.164 \cdot 10^{-3}$	$6.011 \cdot 10^{-5}$	0.052	$4.097 \cdot 10^{-5}$	0.035	
	4.9 - 5.95	$1.022 \cdot 10^{-3}$	$5.814 \cdot 10^{-5}$	0.057	$3.389 \cdot 10^{-5}$	0.033	
	5.95 - 6.92	$6.723 \cdot 10^{-4}$	$4.769 \cdot 10^{-5}$	0.071	$2.175 \cdot 10^{-5}$	0.032	
	6.92 - 8.175	$5.005 \cdot 10^{-4}$	$3.754 \cdot 10^{-5}$	0.075	$1.651 \cdot 10^{-5}$	0.033	
	8.175 - 9.5	$3.379 \cdot 10^{-4}$	$2.102 \cdot 10^{-5}$	0.062	$1.155 \cdot 10^{-5}$	0.034	
	9.5 - 11.2	$2.140 \cdot 10^{-4}$	$1.455 \cdot 10^{-5}$	0.068	$7.757 \cdot 10^{-6}$	0.036	
	11.2 - 13.325	$1.201 \cdot 10^{-4}$	$9.299 \cdot 10^{-6}$	0.077	$4.336 \cdot 10^{-6}$	0.036	
	13.325 - 16.5	$4.719 \cdot 10^{-5}$	$5.093 \cdot 10^{-6}$	0.108	$1.737 \cdot 10^{-6}$	0.037	
	16.5 - 19	$9.003 \cdot 10^{-6}$	$7.379 \cdot 10^{-6}$	0.820	$3.697 \cdot 10^{-7}$	0.041	
60 - 80	0.6 - 1.25	$1.812 \cdot 10^{-3}$	$1.058 \cdot 10^{-4}$	0.058	$7.385 \cdot 10^{-5}$	0.041	
	1.25 - 1.875	$2.082 \cdot 10^{-3}$	$9.570 \cdot 10^{-5}$	0.046	$7.927 \cdot 10^{-5}$	0.038	
	1.875 - 2.275	$2.281 \cdot 10^{-3}$	$1.599 \cdot 10^{-4}$	0.070	$7.981 \cdot 10^{-5}$	0.035	
	2.275 - 2.875	$2.271 \cdot 10^{-3}$	$1.283 \cdot 10^{-4}$	0.057	$7.610 \cdot 10^{-5}$	0.034	
	2.875 - 3.55	$1.996 \cdot 10^{-3}$	$1.097 \cdot 10^{-4}$	0.055	$6.476 \cdot 10^{-5}$	0.032	
	3.55 - 4.225	$1.628 \cdot 10^{-3}$	$1.027 \cdot 10^{-4}$	0.063	$5.446 \cdot 10^{-5}$	0.033	
	4.225 - 4.95	$1.309 \cdot 10^{-3}$	$6.033 \cdot 10^{-5}$	0.046	$3.904 \cdot 10^{-5}$	0.030	
	4.95 - 5.75	$1.036 \cdot 10^{-3}$	$5.554 \cdot 10^{-5}$	0.054	$3.083 \cdot 10^{-5}$	0.030	
	5.75 - 6.625	$7.637 \cdot 10^{-4}$	$4.507 \cdot 10^{-5}$	0.059	$2.350 \cdot 10^{-5}$	0.031	
	6.625 - 7.725	$5.026 \cdot 10^{-4}$	$3.157 \cdot 10^{-5}$	0.063	$1.498 \cdot 10^{-5}$	0.030	
	7.725 - 9.325	$2.950 \cdot 10^{-4}$	$2.107 \cdot 10^{-5}$	0.071	$9.494 \cdot 10^{-6}$	0.032	
	9.325 - 11.825	$1.430 \cdot 10^{-4}$	$1.245 \cdot 10^{-5}$	0.087	$4.165 \cdot 10^{-6}$	0.029	
	11.825 - 14.325	$3.556 \cdot 10^{-5}$	$7.160 \cdot 10^{-6}$	0.201	$1.227 \cdot 10^{-6}$	0.035	

Table D.2: Multiplicities of π^- for the different (p, θ, z) bins with related statistical and systematic uncertainties

z	θ [mrad]	p [GeV/c]	$d\mathbf{n}^{\pi^-}/dp$ [/(GeV/c)/p.o.t]	Δ_{stat}	$\Delta_{stat}\%$	Δ_{sys}	$\Delta_{sys}\%$
80 - 100	0.5 - 1.3	$2.205 \cdot 10^{-3}$	$1.183 \cdot 10^{-4}$	0.054	$1.097 \cdot 10^{-4}$	0.050	
	1.3 - 1.7	$2.661 \cdot 10^{-3}$	$1.230 \cdot 10^{-4}$	0.046	$1.128 \cdot 10^{-4}$	0.042	
	1.7 - 2.2	$2.864 \cdot 10^{-3}$	$1.445 \cdot 10^{-4}$	0.050	$1.107 \cdot 10^{-4}$	0.039	
	2.2 - 2.675	$2.268 \cdot 10^{-3}$	$1.387 \cdot 10^{-4}$	0.061	$8.387 \cdot 10^{-5}$	0.037	
	2.675 - 3.1	$2.205 \cdot 10^{-3}$	$1.507 \cdot 10^{-4}$	0.068	$7.411 \cdot 10^{-5}$	0.034	
	3.1 - 3.55	$1.986 \cdot 10^{-3}$	$1.013 \cdot 10^{-4}$	0.051	$6.673 \cdot 10^{-5}$	0.034	
	3.55 - 4.05	$1.601 \cdot 10^{-3}$	$8.520 \cdot 10^{-5}$	0.053	$5.041 \cdot 10^{-5}$	0.031	
	4.05 - 4.6	$1.399 \cdot 10^{-3}$	$6.965 \cdot 10^{-5}$	0.050	$4.256 \cdot 10^{-5}$	0.030	
	4.6 - 5.275	$1.089 \cdot 10^{-3}$	$6.106 \cdot 10^{-5}$	0.056	$3.312 \cdot 10^{-5}$	0.030	
	5.275 - 6.125	$7.126 \cdot 10^{-4}$	$4.355 \cdot 10^{-5}$	0.061	$2.142 \cdot 10^{-5}$	0.030	
	6.125 - 7.275	$4.624 \cdot 10^{-4}$	$3.013 \cdot 10^{-5}$	0.065	$1.437 \cdot 10^{-5}$	0.031	
	7.275 - 9.2	$2.342 \cdot 10^{-4}$	$1.645 \cdot 10^{-5}$	0.070	$6.941 \cdot 10^{-6}$	0.030	
	9.2 - 11.7	$6.623 \cdot 10^{-5}$	$7.519 \cdot 10^{-6}$	0.114	$2.318 \cdot 10^{-6}$	0.035	
100 - 140	0.5 - 1.3	$6.412 \cdot 10^{-3}$	$2.717 \cdot 10^{-4}$	0.042	$4.301 \cdot 10^{-4}$	0.067	
	1.3 - 1.65	$7.015 \cdot 10^{-3}$	$4.313 \cdot 10^{-4}$	0.061	$2.566 \cdot 10^{-4}$	0.037	
	1.65 - 1.95	$6.145 \cdot 10^{-3}$	$3.324 \cdot 10^{-4}$	0.054	$2.008 \cdot 10^{-4}$	0.033	
	1.95 - 2.275	$5.198 \cdot 10^{-3}$	$3.500 \cdot 10^{-4}$	0.067	$1.717 \cdot 10^{-4}$	0.033	
	2.275 - 2.575	$5.550 \cdot 10^{-3}$	$2.569 \cdot 10^{-4}$	0.046	$1.727 \cdot 10^{-4}$	0.031	
	2.575 - 2.9	$4.763 \cdot 10^{-3}$	$3.459 \cdot 10^{-4}$	0.073	$1.472 \cdot 10^{-4}$	0.031	
	2.9 - 3.275	$4.065 \cdot 10^{-3}$	$2.002 \cdot 10^{-4}$	0.049	$1.227 \cdot 10^{-4}$	0.030	
	3.275 - 3.675	$3.042 \cdot 10^{-3}$	$1.287 \cdot 10^{-4}$	0.042	$9.155 \cdot 10^{-5}$	0.030	
	3.675 - 4.2	$2.344 \cdot 10^{-3}$	$1.321 \cdot 10^{-4}$	0.056	$6.927 \cdot 10^{-5}$	0.030	
	4.2 - 4.8	$1.839 \cdot 10^{-3}$	$1.113 \cdot 10^{-4}$	0.061	$5.455 \cdot 10^{-5}$	0.030	
	4.8 - 5.725	$1.144 \cdot 10^{-3}$	$5.630 \cdot 10^{-5}$	0.049	$3.435 \cdot 10^{-5}$	0.030	
	5.725 - 7.075	$5.950 \cdot 10^{-4}$	$4.013 \cdot 10^{-5}$	0.067	$1.717 \cdot 10^{-5}$	0.029	
	7.075 - 9.575	$1.920 \cdot 10^{-4}$	$1.668 \cdot 10^{-5}$	0.087	$5.874 \cdot 10^{-6}$	0.031	
140 - 180	0.4 - 0.925	$7.137 \cdot 10^{-3}$	$4.925 \cdot 10^{-4}$	0.069	$2.857 \cdot 10^{-4}$	0.040	
	0.925 - 1.45	$7.598 \cdot 10^{-3}$	$5.297 \cdot 10^{-4}$	0.070	$2.942 \cdot 10^{-4}$	0.039	
	1.45 - 1.775	$7.137 \cdot 10^{-3}$	$5.149 \cdot 10^{-4}$	0.072	$2.508 \cdot 10^{-4}$	0.035	
	1.775 - 2.1	$6.302 \cdot 10^{-3}$	$5.150 \cdot 10^{-4}$	0.082	$2.256 \cdot 10^{-4}$	0.036	
	2.1 - 2.425	$5.014 \cdot 10^{-3}$	$2.904 \cdot 10^{-4}$	0.058	$1.763 \cdot 10^{-4}$	0.035	
	2.425 - 2.825	$4.069 \cdot 10^{-3}$	$2.422 \cdot 10^{-4}$	0.060	$1.358 \cdot 10^{-4}$	0.033	
	2.825 - 3.3	$2.605 \cdot 10^{-3}$	$1.570 \cdot 10^{-4}$	0.060	$8.368 \cdot 10^{-5}$	0.032	
	3.3 - 3.95	$2.213 \cdot 10^{-3}$	$1.442 \cdot 10^{-4}$	0.065	$7.410 \cdot 10^{-5}$	0.033	
	3.95 - 5.05	$1.069 \cdot 10^{-3}$	$7.427 \cdot 10^{-5}$	0.070	$3.479 \cdot 10^{-5}$	0.033	
	5.05 - 7.55	$2.505 \cdot 10^{-4}$	$2.264 \cdot 10^{-5}$	0.090	$7.463 \cdot 10^{-6}$	0.030	
180 - 220	0.4 - 0.75	$7.675 \cdot 10^{-3}$	$7.024 \cdot 10^{-4}$	0.092	$7.390 \cdot 10^{-4}$	0.096	
	0.75 - 1.05	$9.236 \cdot 10^{-3}$	$7.809 \cdot 10^{-4}$	0.085	$5.320 \cdot 10^{-4}$	0.058	
	1.05 - 1.325	$7.079 \cdot 10^{-3}$	$5.472 \cdot 10^{-4}$	0.077	$2.970 \cdot 10^{-4}$	0.042	
	1.325 - 1.675	$6.748 \cdot 10^{-3}$	$5.244 \cdot 10^{-4}$	0.078	$2.284 \cdot 10^{-4}$	0.034	
	1.675 - 2.075	$5.550 \cdot 10^{-3}$	$4.213 \cdot 10^{-4}$	0.076	$1.761 \cdot 10^{-4}$	0.032	
	2.075 - 2.475	$3.667 \cdot 10^{-3}$	$3.230 \cdot 10^{-4}$	0.088	$1.190 \cdot 10^{-4}$	0.032	
	2.475 - 2.925	$2.132 \cdot 10^{-3}$	$2.195 \cdot 10^{-4}$	0.103	$6.418 \cdot 10^{-5}$	0.030	

Table D.2: Multiplicities of π^- for the different (p, θ, z) bins with related statistical and systematic uncertainties

z	θ	p	$d\pi^-/dp$	Δ_{stat}	$\Delta_{stat}\%$	Δ_{sys}	$\Delta_{sys}\%$
	[mrad]	[GeV/c]	[/ (GeV/c)/p.o.t]				
220 - 260	2.925 - 3.5	1.902·10 ⁻³	1.926·10 ⁻⁴	0.101	5.811·10 ⁻⁵	0.031	
	3.5 - 4.4	8.973·10 ⁻⁴	7.513·10 ⁻⁵	0.084	2.614·10 ⁻⁵	0.029	
	4.4 - 6.9	1.623·10 ⁻⁴	1.600·10 ⁻⁵	0.099	4.952·10 ⁻⁶	0.031	
	0.3 - 0.7	7.617·10 ⁻³	6.425·10 ⁻⁴	0.084	7.510·10 ⁻⁴	0.099	
	0.7 - 0.975	9.221·10 ⁻³	7.642·10 ⁻⁴	0.083	5.346·10 ⁻⁴	0.058	
	0.975 - 1.325	8.277·10 ⁻³	5.586·10 ⁻⁴	0.067	3.303·10 ⁻⁴	0.040	
	1.325 - 1.675	6.128·10 ⁻³	4.373·10 ⁻⁴	0.071	2.072·10 ⁻⁴	0.034	
	1.675 - 2.15	4.184·10 ⁻³	2.418·10 ⁻⁴	0.058	1.387·10 ⁻⁴	0.033	
	2.15 - 2.925	2.126·10 ⁻³	1.718·10 ⁻⁴	0.081	6.432·10 ⁻⁵	0.030	
	2.925 - 5.425	4.835·10 ⁻⁴	4.659·10 ⁻⁵	0.096	1.413·10 ⁻⁵	0.029	
260 - 300	0.3 - 0.675	7.747·10 ⁻³	7.070·10 ⁻⁴	0.091	5.988·10 ⁻⁴	0.077	
	0.675 - 0.975	9.935·10 ⁻³	7.143·10 ⁻⁴	0.072	4.750·10 ⁻⁴	0.048	
	0.975 - 1.25	8.514·10 ⁻³	6.946·10 ⁻⁴	0.082	3.178·10 ⁻⁴	0.037	
	1.25 - 1.625	4.426·10 ⁻³	3.663·10 ⁻⁴	0.083	1.503·10 ⁻⁴	0.034	
	1.625 - 2.225	3.264·10 ⁻³	2.449·10 ⁻⁴	0.075	1.041·10 ⁻⁴	0.032	
	2.225 - 4.725	7.122·10 ⁻⁴	5.800·10 ⁻⁵	0.081	2.139·10 ⁻⁵	0.030	
300 - 340	0.2 - 0.45	6.947·10 ⁻³	1.170·10 ⁻³	0.168	1.045·10 ⁻³	0.150	
	0.45 - 0.7	8.908·10 ⁻³	8.234·10 ⁻⁴	0.092	8.339·10 ⁻⁴	0.094	
	0.7 - 0.95	9.589·10 ⁻³	7.449·10 ⁻⁴	0.078	5.879·10 ⁻⁴	0.061	
	0.95 - 1.275	6.485·10 ⁻³	4.817·10 ⁻⁴	0.074	2.830·10 ⁻⁴	0.044	
	1.275 - 2.55	2.666·10 ⁻³	1.564·10 ⁻⁴	0.059	8.759·10 ⁻⁵	0.033	
z 6	0 - 20	0.7 - 1.3	6.216·10 ⁻⁴	7.625·10 ⁻⁵	0.123	2.444·10 ⁻⁵	0.039
		1.3 - 2.175	7.545·10 ⁻⁴	3.621·10 ⁻⁵	0.048	2.841·10 ⁻⁵	0.038
		2.175 - 3.325	9.115·10 ⁻⁴	3.009·10 ⁻⁵	0.033	3.289·10 ⁻⁵	0.036
		3.325 - 4.675	8.952·10 ⁻⁴	2.682·10 ⁻⁵	0.030	3.174·10 ⁻⁵	0.035
		4.675 - 8.95	7.936·10 ⁻⁴	1.918·10 ⁻⁵	0.024	2.961·10 ⁻⁵	0.037
		8.95 - 17.65	2.643·10 ⁻⁴	8.013·10 ⁻⁶	0.030	1.202·10 ⁻⁵	0.045
		17.65 - 29.3	2.249·10 ⁻⁵	7.444·10 ⁻⁶	0.331	1.338·10 ⁻⁶	0.060
		0.6 - 1.23	1.217·10 ⁻³	1.037·10 ⁻⁴	0.085	5.012·10 ⁻⁵	0.041
		1.23 - 1.775	1.445·10 ⁻³	6.018·10 ⁻⁵	0.042	5.589·10 ⁻⁵	0.039
		1.775 - 2.15	1.486·10 ⁻³	7.263·10 ⁻⁵	0.049	5.596·10 ⁻⁵	0.038
20 - 40	20 - 40	2.15 - 2.575	1.650·10 ⁻³	6.946·10 ⁻⁵	0.042	6.115·10 ⁻⁵	0.037
		2.575 - 2.975	1.763·10 ⁻³	9.064·10 ⁻⁵	0.051	6.346·10 ⁻⁵	0.036
		2.975 - 3.425	1.710·10 ⁻³	7.021·10 ⁻⁵	0.041	6.026·10 ⁻⁵	0.035
		3.425 - 4.025	1.606·10 ⁻³	1.036·10 ⁻⁴	0.064	5.510·10 ⁻⁵	0.034
		4.025 - 4.825	1.538·10 ⁻³	6.685·10 ⁻⁵	0.043	5.567·10 ⁻⁵	0.036
		4.825 - 6.05	1.374·10 ⁻³	6.816·10 ⁻⁵	0.050	6.040·10 ⁻⁵	0.044
		6.05 - 7.75	1.178·10 ⁻³	5.596·10 ⁻⁵	0.048	5.348·10 ⁻⁵	0.045
		7.75 - 9.55	6.257·10 ⁻⁴	3.875·10 ⁻⁵	0.062	2.905·10 ⁻⁵	0.046
		9.55 - 11.625	4.206·10 ⁻⁴	2.919·10 ⁻⁵	0.069	1.794·10 ⁻⁵	0.043
		11.625 - 14.125	2.299·10 ⁻⁴	1.850·10 ⁻⁵	0.080	8.747·10 ⁻⁶	0.038
		14.125 - 18.125	1.207·10 ⁻⁴	1.336·10 ⁻⁵	0.111	5.118·10 ⁻⁶	0.042
		18.125 - 23.625	1.839·10 ⁻⁵	1.261·10 ⁻⁵	0.686	7.041·10 ⁻⁷	0.038

Table D.2: Multiplicities of π^- for the different (p, θ, z) bins with related statistical and systematic uncertainties

z	θ [mrad]	p [GeV/c]	$d\mathbf{n}^{\pi^-}/dp$ [/(GeV/c)/p.o.t]	Δ_{stat}	$\Delta_{stat}\%$	Δ_{sys}	$\Delta_{sys}\%$
40 - 60	0.6 - 1.175	$1.357 \cdot 10^{-3}$		$1.096 \cdot 10^{-4}$	0.081	$5.555 \cdot 10^{-5}$	0.041
	1.175 - 1.675	$1.734 \cdot 10^{-3}$		$7.200 \cdot 10^{-5}$	0.042	$6.929 \cdot 10^{-5}$	0.040
	1.675 - 1.975	$1.936 \cdot 10^{-3}$		$1.441 \cdot 10^{-4}$	0.074	$7.472 \cdot 10^{-5}$	0.039
	1.975 - 2.275	$1.969 \cdot 10^{-3}$		$1.031 \cdot 10^{-4}$	0.052	$7.438 \cdot 10^{-5}$	0.038
	2.275 - 2.6	$1.792 \cdot 10^{-3}$		$9.356 \cdot 10^{-5}$	0.052	$6.561 \cdot 10^{-5}$	0.037
	2.6 - 3.1	$1.715 \cdot 10^{-3}$		$7.676 \cdot 10^{-5}$	0.045	$6.332 \cdot 10^{-5}$	0.037
	3.1 - 3.925	$1.663 \cdot 10^{-3}$		$8.618 \cdot 10^{-5}$	0.052	$7.332 \cdot 10^{-5}$	0.044
	3.925 - 4.9	$1.534 \cdot 10^{-3}$		$7.483 \cdot 10^{-5}$	0.049	$6.826 \cdot 10^{-5}$	0.044
	4.9 - 5.95	$1.058 \cdot 10^{-3}$		$5.724 \cdot 10^{-5}$	0.054	$4.385 \cdot 10^{-5}$	0.041
	5.95 - 6.92	$9.408 \cdot 10^{-4}$		$5.940 \cdot 10^{-5}$	0.063	$3.260 \cdot 10^{-5}$	0.035
	6.92 - 8.175	$6.655 \cdot 10^{-4}$		$3.881 \cdot 10^{-5}$	0.058	$2.333 \cdot 10^{-5}$	0.035
	8.175 - 9.5	$4.041 \cdot 10^{-4}$		$3.282 \cdot 10^{-5}$	0.081	$1.359 \cdot 10^{-5}$	0.034
	9.5 - 11.2	$2.045 \cdot 10^{-4}$		$1.315 \cdot 10^{-5}$	0.064	$7.049 \cdot 10^{-6}$	0.034
	11.2 - 13.325	$1.190 \cdot 10^{-4}$		$9.626 \cdot 10^{-6}$	0.081	$4.114 \cdot 10^{-6}$	0.035
	13.325 - 16.5	$3.838 \cdot 10^{-5}$		$4.368 \cdot 10^{-6}$	0.114	$1.470 \cdot 10^{-6}$	0.038
	16.5 - 19	$1.379 \cdot 10^{-5}$		$2.129 \cdot 10^{-6}$	0.154	$6.366 \cdot 10^{-7}$	0.046
60 - 80	0.6 - 1.25	$1.222 \cdot 10^{-3}$		$1.022 \cdot 10^{-4}$	0.084	$5.849 \cdot 10^{-5}$	0.048
	1.25 - 1.875	$1.669 \cdot 10^{-3}$		$8.211 \cdot 10^{-5}$	0.049	$7.446 \cdot 10^{-5}$	0.045
	1.875 - 2.275	$1.876 \cdot 10^{-3}$		$1.693 \cdot 10^{-4}$	0.090	$8.426 \cdot 10^{-5}$	0.045
	2.275 - 2.875	$1.707 \cdot 10^{-3}$		$1.164 \cdot 10^{-4}$	0.068	$8.156 \cdot 10^{-5}$	0.048
	2.875 - 3.55	$1.573 \cdot 10^{-3}$		$1.055 \cdot 10^{-4}$	0.067	$6.720 \cdot 10^{-5}$	0.043
	3.55 - 4.225	$1.377 \cdot 10^{-3}$		$1.010 \cdot 10^{-4}$	0.073	$5.828 \cdot 10^{-5}$	0.042
	4.225 - 4.95	$1.061 \cdot 10^{-3}$		$5.579 \cdot 10^{-5}$	0.053	$4.535 \cdot 10^{-5}$	0.043
	4.95 - 5.75	$8.259 \cdot 10^{-4}$		$4.788 \cdot 10^{-5}$	0.058	$3.230 \cdot 10^{-5}$	0.039
	5.75 - 6.625	$5.491 \cdot 10^{-4}$		$3.704 \cdot 10^{-5}$	0.067	$2.047 \cdot 10^{-5}$	0.037
	6.625 - 7.725	$4.110 \cdot 10^{-4}$		$2.922 \cdot 10^{-5}$	0.071	$1.547 \cdot 10^{-5}$	0.038
	7.725 - 9.325	$2.345 \cdot 10^{-4}$		$2.066 \cdot 10^{-5}$	0.088	$8.733 \cdot 10^{-6}$	0.037
	9.325 - 11.825	$1.074 \cdot 10^{-4}$		$9.674 \cdot 10^{-6}$	0.090	$4.113 \cdot 10^{-6}$	0.038
	11.825 - 14.325	$4.338 \cdot 10^{-5}$		$8.816 \cdot 10^{-6}$	0.203	$1.408 \cdot 10^{-6}$	0.032
80 - 100	0.5 - 1.3	$1.259 \cdot 10^{-3}$		$9.975 \cdot 10^{-5}$	0.079	$9.129 \cdot 10^{-5}$	0.073
	1.3 - 1.7	$2.107 \cdot 10^{-3}$		$1.195 \cdot 10^{-4}$	0.057	$1.063 \cdot 10^{-4}$	0.050
	1.7 - 2.2	$1.780 \cdot 10^{-3}$		$1.269 \cdot 10^{-4}$	0.071	$7.978 \cdot 10^{-5}$	0.045
	2.2 - 2.675	$1.572 \cdot 10^{-3}$		$1.248 \cdot 10^{-4}$	0.079	$6.909 \cdot 10^{-5}$	0.044
	2.675 - 3.1	$1.353 \cdot 10^{-3}$		$8.707 \cdot 10^{-5}$	0.064	$6.133 \cdot 10^{-5}$	0.045
	3.1 - 3.55	$1.112 \cdot 10^{-3}$		$6.380 \cdot 10^{-5}$	0.057	$5.119 \cdot 10^{-5}$	0.046
	3.55 - 4.05	$9.859 \cdot 10^{-4}$		$6.762 \cdot 10^{-5}$	0.069	$5.256 \cdot 10^{-5}$	0.053
	4.05 - 4.6	$7.893 \cdot 10^{-4}$		$5.339 \cdot 10^{-5}$	0.068	$3.525 \cdot 10^{-5}$	0.045
	4.6 - 5.275	$5.641 \cdot 10^{-4}$		$4.329 \cdot 10^{-5}$	0.077	$2.507 \cdot 10^{-5}$	0.044
	5.275 - 6.125	$4.464 \cdot 10^{-4}$		$3.026 \cdot 10^{-5}$	0.068	$1.800 \cdot 10^{-5}$	0.040
	6.125 - 7.275	$2.529 \cdot 10^{-4}$		$1.621 \cdot 10^{-5}$	0.064	$1.026 \cdot 10^{-5}$	0.041
	7.275 - 9.2	$1.263 \cdot 10^{-4}$		$1.190 \cdot 10^{-5}$	0.094	$5.704 \cdot 10^{-6}$	0.045
	9.2 - 11.7	$4.664 \cdot 10^{-5}$		$6.679 \cdot 10^{-6}$	0.143	$2.264 \cdot 10^{-6}$	0.049
100 - 140	0.5 - 1.3	$3.296 \cdot 10^{-3}$		$1.900 \cdot 10^{-4}$	0.058	$2.717 \cdot 10^{-4}$	0.082

Table D.2: Multiplicities of π^- for the different (p, θ, z) bins with related statistical and systematic uncertainties

z	θ	p	$d\pi^-/dp$	Δ_{stat}	$\Delta_{stat}\%$	Δ_{sys}	$\Delta_{sys}\%$
	[mrad]	[GeV/c]	[/ (GeV/c)/p.o.t]				
140 - 180	1.3 - 1.65		$3.036 \cdot 10^{-3}$	$2.672 \cdot 10^{-4}$	0.088	$1.746 \cdot 10^{-4}$	0.058
	1.65 - 1.95		$2.723 \cdot 10^{-3}$	$2.650 \cdot 10^{-4}$	0.097	$1.493 \cdot 10^{-4}$	0.055
	1.95 - 2.275		$2.494 \cdot 10^{-3}$	$2.261 \cdot 10^{-4}$	0.091	$1.218 \cdot 10^{-4}$	0.049
	2.275 - 2.575		$2.324 \cdot 10^{-3}$	$1.735 \cdot 10^{-4}$	0.075	$1.151 \cdot 10^{-4}$	0.050
	2.575 - 2.9		$2.145 \cdot 10^{-3}$	$1.586 \cdot 10^{-4}$	0.074	$1.087 \cdot 10^{-4}$	0.051
	2.9 - 3.275		$1.842 \cdot 10^{-3}$	$1.323 \cdot 10^{-4}$	0.072	$9.567 \cdot 10^{-5}$	0.052
	3.275 - 3.675		$1.572 \cdot 10^{-3}$	$1.287 \cdot 10^{-4}$	0.082	$7.913 \cdot 10^{-5}$	0.050
	3.675 - 4.2		$1.169 \cdot 10^{-3}$	$9.346 \cdot 10^{-5}$	0.080	$6.979 \cdot 10^{-5}$	0.060
	4.2 - 4.8		$8.324 \cdot 10^{-4}$	$7.143 \cdot 10^{-5}$	0.086	$5.234 \cdot 10^{-5}$	0.063
	4.8 - 5.725		$6.085 \cdot 10^{-4}$	$5.069 \cdot 10^{-5}$	0.083	$3.461 \cdot 10^{-5}$	0.057
	5.725 - 7.075		$2.019 \cdot 10^{-4}$	$2.317 \cdot 10^{-5}$	0.115	$1.240 \cdot 10^{-5}$	0.061
	7.075 - 9.575		$1.143 \cdot 10^{-4}$	$1.285 \cdot 10^{-5}$	0.112	$5.615 \cdot 10^{-6}$	0.049
	0.4 - 0.925		$2.397 \cdot 10^{-3}$	$3.067 \cdot 10^{-4}$	0.128	$2.216 \cdot 10^{-4}$	0.092
	0.925 - 1.45		$2.071 \cdot 10^{-3}$	$2.797 \cdot 10^{-4}$	0.135	$1.647 \cdot 10^{-4}$	0.080
	1.45 - 1.775		$2.398 \cdot 10^{-3}$	$2.450 \cdot 10^{-4}$	0.102	$1.759 \cdot 10^{-4}$	0.073
	1.775 - 2.1		$1.948 \cdot 10^{-3}$	$1.679 \cdot 10^{-4}$	0.086	$1.214 \cdot 10^{-4}$	0.062
	2.1 - 2.425		$1.918 \cdot 10^{-3}$	$1.869 \cdot 10^{-4}$	0.097	$1.384 \cdot 10^{-4}$	0.072
	2.425 - 2.825		$1.397 \cdot 10^{-3}$	$1.410 \cdot 10^{-4}$	0.101	$8.983 \cdot 10^{-5}$	0.064
180 - 220	2.825 - 3.3		$9.250 \cdot 10^{-4}$	$1.131 \cdot 10^{-4}$	0.122	$6.874 \cdot 10^{-5}$	0.074
	3.3 - 3.95		$7.008 \cdot 10^{-4}$	$7.649 \cdot 10^{-5}$	0.109	$4.431 \cdot 10^{-5}$	0.063
	3.95 - 5.05		$3.833 \cdot 10^{-4}$	$4.563 \cdot 10^{-5}$	0.119	$2.606 \cdot 10^{-5}$	0.068
	5.05 - 7.55		$1.040 \cdot 10^{-4}$	$1.386 \cdot 10^{-5}$	0.133	$8.044 \cdot 10^{-6}$	0.077
	0.4 - 0.75		$2.468 \cdot 10^{-3}$	$4.030 \cdot 10^{-4}$	0.163	$2.332 \cdot 10^{-4}$	0.094
	0.75 - 1.05		$2.373 \cdot 10^{-3}$	$3.842 \cdot 10^{-4}$	0.162	$1.707 \cdot 10^{-4}$	0.072
	1.05 - 1.325		$2.274 \cdot 10^{-3}$	$2.437 \cdot 10^{-4}$	0.107	$1.600 \cdot 10^{-4}$	0.070
	1.325 - 1.675		$1.929 \cdot 10^{-3}$	$1.517 \cdot 10^{-4}$	0.079	$1.490 \cdot 10^{-4}$	0.077
	1.675 - 2.075		$1.535 \cdot 10^{-3}$	$1.275 \cdot 10^{-4}$	0.083	$1.006 \cdot 10^{-4}$	0.066
	2.075 - 2.475		$1.262 \cdot 10^{-3}$	$1.763 \cdot 10^{-4}$	0.140	$9.632 \cdot 10^{-5}$	0.076
	2.475 - 2.925		$8.310 \cdot 10^{-4}$	$1.413 \cdot 10^{-4}$	0.170	$5.211 \cdot 10^{-5}$	0.063
	2.925 - 3.5		$5.672 \cdot 10^{-4}$	$9.861 \cdot 10^{-5}$	0.174	$4.111 \cdot 10^{-5}$	0.072
	3.5 - 4.4		$2.646 \cdot 10^{-4}$	$3.763 \cdot 10^{-5}$	0.142	$2.060 \cdot 10^{-5}$	0.078
	4.4 - 6.9		$6.975 \cdot 10^{-5}$	$1.348 \cdot 10^{-5}$	0.193	$4.537 \cdot 10^{-6}$	0.065
220 - 260	0.3 - 0.7		$1.413 \cdot 10^{-3}$	$2.607 \cdot 10^{-4}$	0.184	$1.160 \cdot 10^{-4}$	0.082
	0.7 - 0.975		$1.660 \cdot 10^{-3}$	$3.167 \cdot 10^{-4}$	0.191	$1.641 \cdot 10^{-4}$	0.099
	0.975 - 1.325		$2.156 \cdot 10^{-3}$	$2.890 \cdot 10^{-4}$	0.134	$1.852 \cdot 10^{-4}$	0.086
	1.325 - 1.675		$1.454 \cdot 10^{-3}$	$2.075 \cdot 10^{-4}$	0.143	$1.103 \cdot 10^{-4}$	0.076
	1.675 - 2.15		$1.167 \cdot 10^{-3}$	$8.523 \cdot 10^{-5}$	0.073	$1.017 \cdot 10^{-4}$	0.087
	2.15 - 2.925		$4.251 \cdot 10^{-4}$	$2.984 \cdot 10^{-4}$	0.702	$3.062 \cdot 10^{-5}$	0.072
	2.925 - 5.425		$8.645 \cdot 10^{-5}$	$1.868 \cdot 10^{-5}$	0.216	$9.540 \cdot 10^{-6}$	0.110
260 - 300	0.3 - 0.675		$1.692 \cdot 10^{-3}$	$3.704 \cdot 10^{-4}$	0.219	$2.420 \cdot 10^{-4}$	0.143
	0.675 - 0.975		$1.182 \cdot 10^{-3}$	$2.271 \cdot 10^{-4}$	0.192	$1.379 \cdot 10^{-4}$	0.117
	0.975 - 1.25		$1.295 \cdot 10^{-3}$	$2.890 \cdot 10^{-4}$	0.223	$1.556 \cdot 10^{-4}$	0.120
	1.25 - 1.625		$1.282 \cdot 10^{-3}$	$1.826 \cdot 10^{-4}$	0.142	$1.047 \cdot 10^{-4}$	0.082

Table D.2: Multiplicities of π^- for the different (p, θ, z) bins with related statistical and systematic uncertainties

z	θ [mrad]	p [GeV/c]	$d\mathbf{n}^{\pi^-}/dp$ [/(GeV/c)/p.o.t]	Δ_{stat}	$\Delta_{stat}\%$	Δ_{sys}	$\Delta_{sys}\%$
300 - 340	1.625 - 2.225		$7.216 \cdot 10^{-4}$	$1.087 \cdot 10^{-4}$	0.151	$6.081 \cdot 10^{-5}$	0.084
	2.225 - 4.725		$1.094 \cdot 10^{-4}$	$2.282 \cdot 10^{-5}$	0.209	$1.334 \cdot 10^{-5}$	0.122
	0.2 - 0.45		$4.895 \cdot 10^{-4}$	$4.077 \cdot 10^{-4}$	0.833	$4.660 \cdot 10^{-5}$	0.095
	0.45 - 0.7		$1.363 \cdot 10^{-3}$	$2.856 \cdot 10^{-4}$	0.210	$1.662 \cdot 10^{-4}$	0.122
	0.7 - 0.95		$1.947 \cdot 10^{-3}$	$3.089 \cdot 10^{-4}$	0.159	$2.382 \cdot 10^{-4}$	0.122
	0.95 - 1.275		$9.706 \cdot 10^{-4}$	$1.657 \cdot 10^{-6}$	0.002	$1.249 \cdot 10^{-4}$	0.129
	1.275 - 2.55		$3.984 \cdot 10^{-4}$	$6.062 \cdot 10^{-5}$	0.152	$5.185 \cdot 10^{-5}$	0.130

Bibliography

- [1] J. Chadwick, “The intensity distribution in the magnetic spectrum of beta particles from radium (B + C),” *Verh.Phys.Gesell.*, vol. 16, pp. 383–391, 1914.
- [2] J. Chadwick, “The Existence of a Neutron,” *Proc. R. Soc. Lond. A*, vol. 136, pp. 692–708, 1932.
- [3] J. Chadwick, “Possible Existence of a Neutron,” *Nature*, vol. 129, p. 312, 1932.
- [4] E. Fermi, “An attempt of a theory of beta radiation. 1.,” *Z.Phys.*, vol. 88, pp. 161–177, 1934.
- [5] C. Cowan, F. Reines, F. Harrison, H. Kruse, and A. McGuire, “Detection of the free neutrino: A Confirmation,” *Science*, vol. 124, pp. 103–104, 1956.
- [6] F. Reines, C. Cowan, F. Harrison, A. McGuire, and H. Kruse, “Detection of the free anti-neutrino,” *Phys.Rev.*, vol. 117, pp. 159–173, 1960.
- [7] T. Lee and C.-N. Yang, “Question of Parity Conservation in Weak Interactions,” *Phys.Rev.*, vol. 104, pp. 254–258, 1956.
- [8] C. Wu, E. Ambler, R. Hayward, D. Hoppes, and R. Hudson, “Experimental Test of Parity Conservation in Beta Decay,” *Phys.Rev.*, vol. 105, pp. 1413–1414, 1957.
- [9] M. Goldhaber, L. Grodzins, and A. Sunyar, “Helicity of Neutrinos,” *Phys.Rev.*, vol. 109, pp. 1015–1017, 1958.
- [10] J. Bahcall, W. A. Fowler, J. Iben, I., and R. Sears, “Solar neutrino flux,” *Astrophys.J.*, vol. 137, pp. 344–346, 1963.
- [11] B. Cleveland, T. Daily, J. Davis, Raymond, J. R. Distel, K. Lande, *et al.*, “Measurement of the solar electron neutrino flux with the Homestake chlorine detector,” *Astrophys.J.*, vol. 496, pp. 505–526, 1998.
- [12] B. Pontecorvo, “Mesonium and anti-mesonium,” *Sov.Phys.JETP*, vol. 6, p. 429, 1957.
- [13] G. Danby, J. Gaillard, K. A. Goulianos, L. Lederman, N. B. Mistry, *et al.*, “Observation of High-Energy Neutrino Reactions and the Existence of Two Kinds of Neutrinos,” *Phys.Rev.Lett.*, vol. 9, pp. 36–44, 1962.
- [14] Y. Fukuda *et al.*, “Evidence for oscillation of atmospheric neutrinos,” *Phys.Rev.Lett.*, vol. 81, pp. 1562–1567, 1998.

- [15] Q. Ahmad *et al.*, “Direct evidence for neutrino flavor transformation from neutral current interactions in the Sudbury Neutrino Observatory,” *Phys.Rev.Lett.*, vol. 89, p. 011301, 2002.
- [16] S. Chatrchyan *et al.*, “Observation of a new boson at a mass of 125 gev with the cms experiment at the lhc,” *Phys.Lett.*, vol. B716, pp. 30–61, 2012.
- [17] G. Aad *et al.*, “Observation of a new particle in the search for the standard model higgs boson with the atlas detector at the lhc,” *Phys.Lett.*, vol. B716, pp. 1–29, 2012.
- [18] S. Schael *et al.*, “Precision electroweak measurements on the Z resonance,” *Phys.Rept.*, vol. 427, pp. 257–454, 2006.
- [19] F. Englert and R. Brout, “Broken symmetry and the mass of gauge vector mesons,” *Phys. Rev. Lett.*, vol. 13, pp. 321–323, Aug. 1964.
- [20] P. W. Higgs, “Broken symmetries and the masses of gauge bosons,” *Phys. Rev. Lett.*, vol. 13, pp. 508–509, Oct. 1964.
- [21] J. Goldstone, A. Salam, and S. Weinberg, “Broken Symmetries,” *Phys.Rev.*, vol. 127, pp. 965–970, 1962.
- [22] A. Blondel, E. Gaverini, N. Serra, and M. Shaposhnikov, “Search for Heavy Right Handed Neutrinos at the FCC-ee,” 2014.
- [23] M. Schwartz, “Feasibility of using high-energy neutrinos to study the weak interactions,” *Phys.Rev.Lett.*, vol. 4, pp. 306–307, 1960.
- [24] B. Pontecorvo, “Electron and Muon Neutrinos,” *Sov.Phys.JETP*, vol. 10, pp. 1236–1240, 1960.
- [25] F. Hasert, H. Faissner, W. Krenz, J. Von Krogh, D. Lanske, *et al.*, “Search for Elastic ν_μ Electron Scattering,” *Phys.Lett.*, vol. B46, pp. 121–124, 1973.
- [26] F. Hasert *et al.*, “Observation of Neutrino Like Interactions Without Muon Or Electron in the Gargamelle Neutrino Experiment,” *Phys.Lett.*, vol. B46, pp. 138–140, 1973.
- [27] “Bubble chamber: D meson production and decay.” Dec 1978.
- [28] H. Abramowicz, J. de Groot, J. Knobloch, J. May, P. Palazzi, *et al.*, “Experimental Study of Opposite Sign Dimuons Produced in Neutrino and anti-neutrinos Interactions,” *Z.Phys.*, vol. C15, p. 19, 1982.
- [29] T. Araki *et al.*, “Measurement of neutrino oscillation with KamLAND: Evidence of spectral distortion,” *Phys.Rev.Lett.*, vol. 94, p. 081801, 2005.
- [30] S. van der Meer, “A directive device for charged particles and its use in an enhanced neutrino beam,” 1961.
- [31] F. Garcia and W. Pellico, “FNAL Proton Source High Intensity Operations and Beam Loss Control,” 2012.
- [32] S. Childress and J. Strait, “Long baseline neutrino beams at Fermilab,” *J.Phys.Conf.Ser.*, vol. 408, p. 012007, 2013.

- [33] D. Autiero, I. Efthymiopoulos, A. Ferrari, E. Gschwendtner, A. Guglielmi, *et al.*, “CNGS neutrino beam for long base-line experiments: Present status and perspectives,” *Nucl.Phys.Proc.Suppl.*, vol. 189, pp. 263–270, 2009.
- [34] T. Ishida, “T2HK: J-PARC upgrade plan for future and beyond T2K,” 2013.
- [35] C. Adams *et al.*, “The Long-Baseline Neutrino Experiment: Exploring Fundamental Symmetries of the Universe,” 2013.
- [36] R. e. a. Steerenberg, “Design Study for a Short Base Line Neutrino Facility at CERN,” *IPAC 2013 TUPEA052*.
- [37] A. Stahl, C. Wiebusch, A. Guler, M. Kamiscioglu, R. Sever, *et al.*, “Expression of Interest for a very long baseline neutrino oscillation experiment (LBNO),” 2012.
- [38] M. Bonesini, A. Marchionni, F. Pietropaolo, and T. Tabarelli de Fatis, “On Particle production for high-energy neutrino beams,” *Eur.Phys.J.*, vol. C20, pp. 13–27, 2001.
- [39] T. Eichten *et al.*, “Particle production in proton interactions in nuclei at 24 GeV/c,” *Nucl.Phys. B*, vol. 44, 1972.
- [40] D. Barton, G. Brandenburg, W. Busza, T. Dobrowolski, J. Friedman, *et al.*, “Experimental Study of the α -Dependence of Inclusive Hadron Fragmentation,” *Phys.Rev.*, vol. D27, p. 2580, 1983.
- [41] P. Skubic, O. Overseth, K. J. Heller, M. Sheaff, L. Pondrom, *et al.*, “Neutral Strange Particle Production by 300-GeV Protons,” *Phys.Rev.*, vol. D18, pp. 3115–3144, 1978.
- [42] J. Paley *et al.*, “Measurement of Charged Pion Production Yields off the NuMI Target,” *Phys.Rev.*, vol. D90, p. 032001, 2014.
- [43] J. Paley, “FNAL JETP seminar,” Apr 8, 2014.
- [44] F. An *et al.*, “Observation of electron-antineutrino disappearance at Daya Bay,” *Phys.Rev.Lett.*, vol. 108, p. 171803, 2012.
- [45] M. Gonzalez-Garcia, M. Maltoni, and T. Schwetz, “Updated fit to three neutrino mixing: status of leptonic CP violation,” 2014.
- [46] J. Blietschau *et al.*, “Total Cross-Sections for electron-neutrino and anti-electron-neutrino Interactions and Search for Neutrino Oscillations and Decay,” *Nucl.Phys.*, vol. B133, p. 205, 1978.
- [47] J. Formaggio and G. Zeller, “From eV to EeV: Neutrino Cross Sections Across Energy Scales,” *Rev.Mod.Phys.*, vol. 84, p. 1307, 2012.
- [48] D. Casper *Nucl. Phys. Proc. Suppl.*, vol. 112, p. 161, 2002.
- [49] T. Leitner and U. Mosel, “Neutrino-nucleus scattering reexamined: Quasielastic scattering and pion production entanglement and implications for neutrino energy reconstruction,” *Phys.Rev.*, vol. C81, p. 064614, 2010.
- [50] J. Dorenbosch *et al.*, “Experimental verification of the universality of electron-neutrino and muon-neutrino coupling to the neutral weak current,” *Phys. Lett.*, vol. B180, p. 303, 1986.

- [51] J. V. Allaby *et al.*, “Test of the universality of the electron-neutrino and muon-neutrino coupling to the charged weak current,” *Phys. Lett.*, vol. B179, p. 301, 1986.
- [52] K. Abe *et al.*, “The T2K Experiment,” *Nucl.Instrum.Meth.*, vol. A659, pp. 106–135, 2011.
- [53] K. Abe *et al.*, “Indication of Electron Neutrino Appearance from an Accelerator-produced Off-axis Muon Neutrino Beam,” *Phys.Rev.Lett.*, vol. 107, p. 041801, 2011.
- [54] K. Abe *et al.*, “Evidence of Electron Neutrino Appearance in a Muon Neutrino Beam,” *Phys.Rev.*, vol. D88, no. 3, p. 032002, 2013.
- [55] K. Abe *et al.*, “Observation of Electron Neutrino Appearance in a Muon Neutrino Beam,” *Phys.Rev.Lett.*, vol. 112, p. 061802, 2014.
- [56] K. Abe *et al.*, “Measurement of the Inclusive NuMu Charged Current Cross Section on Carbon in the Near Detector of the T2K Experiment,” *Phys.Rev.*, vol. D87, p. 092003, 2013.
- [57] K. Abe *et al.*, “Measurement of the inclusive ν_μ charged current cross section on iron and hydrocarbon in the T2K on-axis neutrino beam,” *Phys.Rev.*, vol. D90, p. 052010, 2014.
- [58] K. Abe *et al.*, “Measurement of the neutrino-oxygen neutral-current interaction cross section by observing nuclear de-excitation γ -rays,” 2014.
- [59] K. Abe *et al.*, “Measurement of the Inclusive Electron Neutrino Charged Current Cross Section on Carbon with the T2K Near Detector,” 2014.
- [60] K. Abe *et al.*, “The T2K Neutrino Flux Prediction,” *Phys.Rev.*, vol. D87, p. 012001, 2013.
- [61] A. Renshaw *et al.*, “First indication of terrestrial matter effects on solar neutrino oscillation,” *Phys.Rev.Lett.*, vol. 112, p. 091805, 2014.
- [62] K. Abe *et al.*, “Solar neutrino results in super-kamiokande-iii,” *Phys. Rev.*, vol. D83, p. 052010, 2011.
- [63] J. Cravens *et al.*, “Solar neutrino measurements in super-kamiokande-ii,” *Phys. Rev.*, vol. D78, p. 032002, 2008.
- [64] J. Hosaka *et al.*, “Solar neutrino measurements in super-kamiokande-i,” *Phys. Rev.*, vol. D73, p. 112001, 2006.
- [65] Y. Fukuda *et al.*, “Measurements of the solar neutrino flux from Super-Kamiokande’s first 300 days,” *Phys.Rev.Lett.*, vol. 81, pp. 1158–1162, 1998.
- [66] Y. Ashie *et al.*, “Evidence for an oscillatory signature in atmospheric neutrino oscillation,” *Phys.Rev.Lett.*, vol. 93, p. 101801, 2004.
- [67] C. Regis *et al.*, “Search for proton decay into muon plus neutral kaon in super-kamiokande i, ii, and iii,” *Phys. Rev.*, vol. D86, p. 012006, 2012.
- [68] K. Abe *et al.*, “A search for nucleon decay via $n \rightarrow \bar{\nu} p i^0$ and $p \rightarrow \bar{\nu} p i^+$ in super-kamiokande,” *Phys.Rev.Lett.*, vol. 113, p. 121802, 2014.
- [69] K. Abe *et al.*, “Calibration of the super-kamiokande detector,” *Nucl.Instrum.Meth.*, vol. A737, pp. 253–272, 2014.

[70] K. Abe, T. Abe, H. Aihara, Y. Fukuda, Y. Hayato, *et al.*, “Letter of Intent: The Hyper-Kamiokande Experiment — Detector Design and Physics Potential —,” 2011.

[71] S. Bhadra, M. Cadabeschi, P. de Perio, V. Galymov, M. Hartz, *et al.*, “Optical Transition Radiation Monitor for the T2K Experiment,” *Nucl.Instrum.Meth.*, vol. A703, pp. 45–58, 2013.

[72] A. Ichikawa, “Design concept of the magnetic horn system for the T2K neutrino beam,” *Nucl.Instrum.Meth.*, vol. A690, pp. 27–33, 2012.

[73] K. Abe, N. Abgrall, Y. Ajima, H. Aihara, J. Albert, *et al.*, “Measurements of the T2K neutrino beam properties using the INGRID on-axis near detector,” *Nucl.Instrum.Meth.*, vol. A694, pp. 211–223, 2012.

[74] D. G. Ruterbories, “Measurement of the total flux averaged neutrino induced neutral current elastic scattering cross section with the T2K Pi-Zero detector,” 2014.

[75] N. Abgrall *et al.*, “Time Projection Chambers for the T2K Near Detectors,” *Nucl.Instrum.Meth.*, vol. A637, pp. 25–46, 2011.

[76] S. Assylbekov, G. Barr, B. Berger, H. Berns, D. Beznosko, *et al.*, “The T2K ND280 Off-Axis Pi-Zero Detector,” *Nucl.Instrum.Meth.*, vol. A686, pp. 48–63, 2012.

[77] P. Amaudruz *et al.*, “The T2K Fine-Grained Detectors,” *Nucl.Instrum.Meth.*, vol. A696, pp. 1–31, 2012.

[78] D. Allan *et al.*, “The Electromagnetic Calorimeter for the T2K Near Detector ND280,” *JINST*, vol. 8, p. P10019, 2013.

[79] S. Aoki, G. Barr, M. Batkiewicz, J. Blocki, J. Brinson, *et al.*, “The T2K Side Muon Range Detector,” *Nucl.Instrum.Meth.*, vol. A698, pp. 135–146, 2013.

[80] N. Abgrall, “Constraining neutrino flux predictions with hadron production data: the NA61/SHINE measurements for the T2K experiment.,” *CERN-THESIS-2011-165*, 2011.

[81] A. Ferrari, P. R. Sala, A. Fasso, and J. Ranft, “FLUKA: A multi-particle transport code (Program version 2005),” 2005.

[82] T. Bohlen, F. Cerutti, M. Chin, A. Fasso, A. Ferrari, P. Ortega, A. Mairani, P. Sala, G. Smirnov, and V. Vlachoudis, “The FLUKA Code: Developments and Challenges for High Energy and Medical Applications,” *Nuclear Data Sheets*, vol. 120, pp. 211–214, 2014.

[83] G. Bellettini, “Proton-nuclei cross sections at 20 GeV,” *Nucl.Phys.*, vol. 79, pp. 609–624, 1966.

[84] R. Abrams, R. Cool, G. Giacomelli, T. Kycia, B. Leontic, *et al.*, “Total cross-sections of K+-mesons and anti-protons on nucleons up to 3.3-GeV/c,” *Phys.Rev.*, vol. D1, pp. 1917–1935, 1970.

[85] J. Allaby, Y. Bushnin, Y. Gorin, S. Denisov, G. Giacomelli, *et al.*, “Total and absorption cross-sections of pi-, k- and anti-p in the momentum range 20-65 gev/c,” *Yad.Fiz.*, vol. 12, pp. 538–557, 1970.

[86] B. Allardice, C. Batty, D. Baugh, E. Friedman, G. Heymann, *et al.*, “Pion reaction cross-sections and nuclear sizes,” *Nucl.Phys.*, vol. A209, pp. 1–51, 1973.

[87] B. Bobchenko, A. Boklei, A. Vlasov, L. Vorobev, N. Goryainov, *et al.*, “Measurements of total inelastic cross-sections from proton interactions with nuclei in the momentum range from 5-GeV/c to 9-GeV/c and pi- mesons with nuclei in the momentum range from 1.75-GeV/c to 6.5-GeV/c,” *Sov.J.Nucl.Phys.*, vol. 30, p. 805, 1979.

[88] A. Carroll, I.-H. Chiang, T. Kycia, K. Li, M. Marx, *et al.*, “Absorption Cross-Sections of pi+-, K+-, p and anti-p on Nuclei Between 60-GeV/c and 280-GeV/c,” *Phys.Lett.*, vol. B80, p. 319, 1979.

[89] J. Cronin, R. Cool, and A. Abashian, “Cross Sections of Nuclei for High-Energy Pions,” *Phys.Rev.*, vol. 107, pp. 1121–1130, 1957.

[90] F. F. Chen, C. P. Leavitt, and A. M. Shapiro, “Attenuation cross sections for 860-mev protons,” *Phys. Rev.*, vol. 99, pp. 857–871, Aug 1955.

[91] S. Denisov, S. Donskov, Y. Gorin, R. Krasnokutsky, A. Petrukhin, *et al.*, “Absorption cross-sections for pions, kaons, protons and anti-protons on complex nuclei in the 6-GeV/c to 60-GeV/c momentum range,” *Nucl.Phys.*, vol. B61, pp. 62–76, 1973.

[92] M. J. Longo and B. J. Moyer, “Nucleon and Nuclear Cross Sections for Positive Pions and Protons above 1.4 Bev/c,” *Phys.Rev.*, vol. 125, pp. 701–713, 1962.

[93] N. Abgrall *et al.*, “Measurements of Cross Sections and Charged Pion Spectra in Proton-Carbon Interactions at 31 GeV/c,” *Phys.Rev.*, vol. C84, p. 034604, 2011.

[94] V. Fedorov, Y. Grishuk, M. Kosov, G. Leksin, N. Pivnyuk, *et al.*, “Total Inelastic Cross-Sections for pi Mesons on Nuclei in the 2-GeV/c to 6-GeV/c Momentum Range,” *Sov.J.Nucl.Phys.*, vol. 27, p. 222, 1978.

[95] J. V. Allaby *et al.*, “High-energy particle spectra from proton interactions at 19.2 GeV/c,” Tech. Rep. 70-12, CERN, 1970.

[96] D. Dekkers, J. Geibel, R. Mermot, G. Weber, T. Willitts, *et al.*, “Experimental Study of Particle Production at Small Angles in Nucleon-Nucleon Collisions at 19 and 23 GeV/c,” *Phys.Rev.*, vol. 137, pp. B962–B978, 1965.

[97] I. Chemakin *et al.*, “Pion production by protons on a thin beryllium target at 6.4, 12.3, and 17.5 gev/c incident proton momenta,” *Phys. Rev. C*, vol. 77, p. 015209, Jan 2008.

[98] I. Chemakin *et al.*, “Erratum: Pion production by protons on a thin beryllium target at 6.4, 12.3, and 17.5 gev/c incident proton momenta,” *Phys. Rev. C*, vol. 77, p. 049903, Apr 2008.

[99] T. Abbott *et al.*, “Measurement of particle production in proton induced reactions at 14.6-GeV/c,” *Phys.Rev.*, vol. D45, pp. 3906–3920, 1992.

[100] M. Apollonio *et al.*, “Forward production of charged pions with incident protons on nuclear targets at the CERN PS,” *Phys.Rev.*, vol. C80, p. 035208, 2009.

[101] M. Apollonio *et al.*, “Forward production of charged pions with incident pi+- on nuclear targets measured at the CERN PS,” *Nucl.Phys.*, vol. A821, pp. 118–192, 2009.

[102] T. B. Group, “Flux Prediction and Uncertainty Updates with NA61 2009 Thin Target Data and Negative Focussing Mode Predictions,” *T2K*, vol. Technical Note, 2015.

- [103] N. Abgrall *et al.*, “NA61/SHINE facility at the CERN SPS: beams and detector system,” *JINST*, vol. 9, p. P06005, 2014.
- [104] M. Gazdzicki, M. Gorenstein, and P. Seyboth, “Onset of deconfinement in nucleus-nucleus collisions: Review for pedestrians and experts,” *Acta Phys.Polon.*, vol. B42, pp. 307–351, 2011.
- [105] N. Abgrall *et al.*, “Measurement of Production Properties of Positively Charged Kaons in Proton-Carbon Interactions at 31 GeV/c,” *Phys.Rev.*, vol. C85, p. 035210, 2012.
- [106] N. Abgrall *et al.*, “Measurements of production properties of K_S^0 mesons and *Lambda* hyperons in proton-carbon interactions at 31 GeV/c,” *Phys.Rev.*, vol. C89, no. 2, p. 025205, 2014.
- [107] N. Abgrall *et al.*, “Pion emission from the T2K replica target: method, results and application,” *Nucl.Instrum.Meth.*, vol. A701, pp. 99–114, 2013.
- [108] C. Strabel, “Evaluation of Particle Yields in 30 GeV Proton-Carbon Inelastic Interactions for Estimating the T2K Neutrino Flux,” *ETH-19538, CERN-THESIS-2011-295*, 2011.
- [109] C. Bovet, S. Milner, and A. Placci, “The Cedar Project. Cherenkov Differential Counters with Achromatic Ring Focus,” *IEEE Trans.Nucl.Sci.*, vol. 25, pp. 572–576, 1978.
- [110] S. Afanasiev *et al.*, “The na49 large acceptance hadron detector,” *Nuclear Instruments and Methods in Physics Research Section A: Accelerators, Spectrometers, Detectors and Associated Equipment*, vol. 430, no. 2-3, pp. 210 – 244, 1999.
- [111] N. Abgrall *et al.*, “Calibration and analysis of the 2007 data,” 2008.
- [112] F. C. R. Brun, “GEANT Detector Description and Simulation Tool,” *CERN Program Library Long Writeup W5013*, 1993.
- [113] S. Murphy, “Measurement of charged Pion and Kaon production cross sections with NA61/SHINE for T2K,” *CERN-THESIS-2012-093*, 2012.
- [114] B. Efron, “Bootstrap method: another look at the jackknife,” *Ann. Statist.*, vol. 7, pp. 1–26, 1979.
- [115] A. Korzenev, “Target (thin and replica) position for the Neutrino programme of NA61,” *NA61/SHINE internal meeting*, October 2014.